BINARY PHASE DIAGRAMS
FROM A CUBIC EQUATION OF STATE

by

GLENN THOMAS HONG

B.S., State University of New York at Albany
(1976)

SUBMITTED TO THE DEPARTMENT OF
CHEMICAL ENGINEERING IN PARTIAL
FULFILLMENT OF THE
REQUIREMENTS FOR THE
DEGREE OF

DOCTOR OF SCIENCE

at the

MASSACHUSETTS INSTITUTE OF TECHNOLOGY

August, 1981

Signature of Author ______________
Department of Chemical Engineering
August 27, 1981

Certified by ______________
Michael Modell
Thesis Supervisor

Accepted by ______________
Glenn C. Williams
Chairman, Department Committee

BINARY PHASE DIAGRAMS
FROM A CUBIC EQUATION OF STATE

by

GLENN THOMAS HONG

Submitted to the Department of Chemical Engineering
on August 27, 1981 in partial fulfillment of the
requirements for the Degree of Doctor of Science in
Chemical Engineering

ABSTRACT

A methodology is developed for generating binary P-T-x diagrams over extensive ranges of temperature and pressure. The Peng-Robinson equation of state is used with a constant interaction parameter to generate semiquantitative P-T-x diagrams over the entire fluid range for four binary systems. The systems considered are n-hexadecane - carbon dioxide, naphthalene - carbon dioxide, naphthalene - ethylene, and benzene - water. These systems exhibit various types of liquid-liquid immiscibilities and critical phenomena. In addition, the naphthalene systems involve formation of a solid phase. Predictions include two-phase and three-phase equilibrium, azeotropic points, critical lines, critical end points, and spinodal curves. Fugacity-composition plots are shown to be a valuable tool in phase equilibrium calculations, and for defining stable, metastable, and unstable equilibria. Failure to consider metastable and unstable equilibria can result in erroneous predictions. The method is useful in the evaluation and design of phase equilibrium processes, especially those involving supercritical fluids. It is also of value in experimental studies, since it points out regions of the P-T-x space which merit detailed attention.

Thesis Supervisor: Dr. Michael Modell
Title: Associate Professor of
Chemical Engineering

Acknowledgements

Professor Michael Modell is gratefully acknowledged for his superb guidance throughout the course of this work. It has indeed been a pleasure knowing him as a teacher, advisor, and friend. Helpful suggestions along the way were provided by Fred Putnam, R.C.Reid, and Costas Vayenas, the members of my thesis committee. Their assistance is very much appreciated. Jeff Tester provided some much needed editorial comment down the home stretch, and deserves a special note of thanks.

My stay at MIT has been made enjoyable through acquaintance with many faculty and fellow grad students, especially those involved with the Chem E intramural teams. I will miss them when my athletic card expires. My colleague from SUNY Albany, Frank Bates, has always been the best of friends, and lent some measure of excitement to an otherwise drab existence.

Finally, I would like to thank my family for their encouragement of my academic endeavors. This thesis is dedicated to them. My deepest love and thanks are for my wife Karen, without whom this thesis would be handwritten and minus about 300 diagrams. Patience is one of her virtues.

TABLE OF CONTENTS

List of Tables

List of Figures

Chapter 1 Summary

1.1. Introduction

This thesis is concerned with the generation of binary phase diagrams from a cubic equation of state over extensive ranges of temperature and pressure. Research on this topic was motivated by the unique solvent properties exhibited by a substance somewhat above its critical temperature and pressure, known as a supercritical fluid. Supercritical fluid technology is a relatively recent development. Effective evaluation and use of the technology is aided by knowledge of a system's overall phase behavior, and it is the object of this work to show how such a knowledge may be acquired for binary systems. The techniques developed illustrate the need for careful application of the mathematical criteria which define phase equilibrium. The systems covered are n-hexadecane - CO_2, naphthalene - CO_2, naphthalene - ethylene, and benzene - water. Each has been characterized by a complete set of P-T-x diagrams. For reference in the following discussion, Table 1.1 lists physical constants of the compounds considered.

1.2. Solubility in Supercritical Fluids

Table 1.1

Constants of Pure Components

Substance	T_c(K)	P_c(atm)	actual v_c(m^3/kgmol)	predicted v_c(m^3/kgmol)	actual ρ_c(kg/m^3)	predicted ρ_c(kg/m^3)	actual Z_c	ω
Ethylene (C_2H_4)	282.4	49.7	0.129	0.143	217	196	0.276	0.085
Carbon dioxide (CO_2)	304.2	72.8	0.094	0.105	468	419	0.274	0.225
Benzene (C_6H_6)	562.1	48.3	0.259	0.293	301	266	0.271	0.212
Water (H_2O)	647.3	217.6	0.056	0.075	321	240	0.229	0.344
n-Hexadecane ($C_{16}H_{34}$)	717.0	14.0	-	1.290	-	175	-	0.742
Naphthalene ($C_{10}H_8$)	748.4	40.0	0.410	0.471	312	272	0.267	0.302

Note - The P-R equation predicts a universal Z_c of 0.307.

Solubility effects in a supercritical fluid are best illustrated by example. Figure 1.1 gives a solubility "map" for the system naphthalene - carbon dioxide near the critical point of carbon dioxide. Tracing a particular isobar in this diagram shows how the concentration of naphthalene in the carbon dioxide fluid phase varies with temperature. The lines in the diagram represent saturated solutions, i.e., there is always a pure solid naphthalene phase present (naphthalene's normal melting point is 80°C). Above about 75 atm an isobar gives the composition of a saturated CO_2 fluid in equilibrium with solid naphthalene. For any lower pressure, there is a temperature at which three phases coexist - pure solid, saturated liquid, and saturated vapor. The composition of the saturated liquid and vapor at 65 atm are shown in the figure by a tieline; the locus of all these tieline compositions for various pressures is given by the dashed line. If the solid-liquid-vapor (SLV or SLG) locus is traced to higher temperatures (and pressures), it is found that the liquid-vapor tielines converge to the critical point labelled in the diagram. At this point the near-critical liquid and near-critical vapor phases become indistinguishable, or, in other words, the vapor-liquid critical phenomenon is observed in the presence of a solid phase. The occurrence of the critical phenomenon between two phases in the presence of a third characterizes a special class of critical points known as critical end points. The critical point in Figure 1.1 is known as a lower critical end

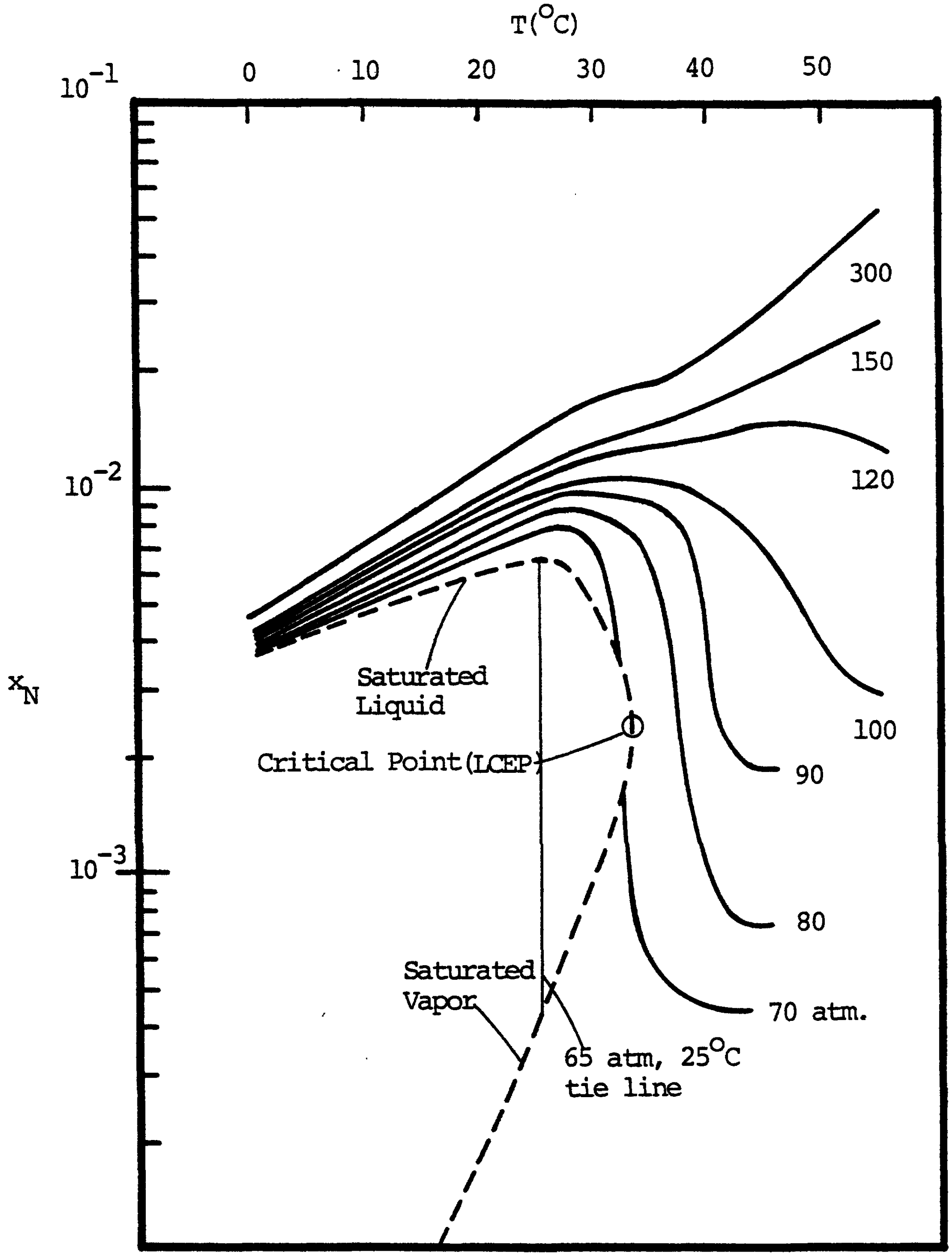

Figure 1.1. The experimental solubility map for the naphthalene (N) - carbon dioxide system. Isobars indicate the mole fraction of naphthalene in solution. The dashed line corresponds to a three-phase solid-liquid-vapor equilibrium. This equilibrium terminates at LCEP, the lower critical end point.

point (LCEP), a designation which will become clear in the following sections.

The effects of temperature and pressure on solubility may be observed in Figure 1.1. Along the 300 atm isobar, solubility increases continuously with temperature due to the increasing activity of the solid phase. At 55°C, the concentration of naphthalene in the supercritical fluid phase is about 5 mole percent, or 15 weight percent. While this compares unfavorably with traditional nonpolar solvents, it is nevertheless a significant quantity of naphthalene.

At 80 atm, solubility decreases sharply with temperature at about 35°C. This is the near critical region, where a slight increase in temperature leads to a large decrease in the density of the fluid. The fluid phase naphthalene concentration drops as the CO_2 loses much of its solvent power. Moving beyond the critical region toward higher temperatures, the density changes again become small and the isobar reverts to a positive slope.

1.3. Phase Diagrams

A full understanding of phase behavior in the supercritical fluid region requires an understanding of its context, the binary P-T-x space. These diagrams may exhibit a multitude of different shapes, some of them quite complex. A P-T projection for the simplest type of binary phase behavior is shown in Figure 1.2. A diagram of this type does not give compositional information on the mixture. The figure contains the P-T diagrams of the two pure components A and B which comprise the system, and these are of the usual shape. The sublimation, fusion, and vaporization curves for each component meet at the triple point. The vaporization curves terminate at pure component critical points. The other lines in the diagrams represent univariant states of mixtures of A and B. The dashed line connecting CP_A and CP_B represents the mixture critical line. Composition varies along this line from pure A to pure B. There are four three-phase lines shown, S_AS_BG, S_AS_BL (eutectic line), S_ALG, and S_BLG. These lines all intersect at the quadruple point Q, where the four phases S_A, G, L, and S_B all coexist at the same temperature and pressure.

For systems where the solubility of solid B in the liquid phase is very low, and the temperature of TP_B is higher than that of CP_A, the S_BLG liquid phase near the quadruple point is almost pure A. When this low solubility persists to temperatures above the critical point of A, the S_BLG line cuts the LG critical locus to give a lower critical end point (LCEP) as shown in Figure 1.3. The segment of the S_BLG line starting from TP_B similarly intersects the

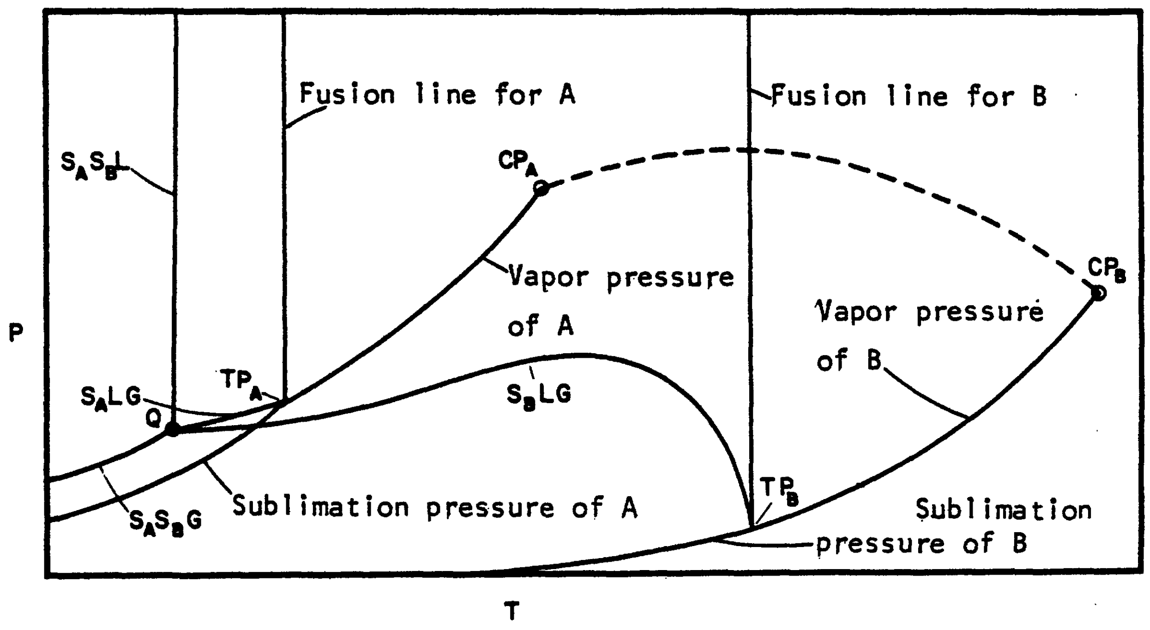

Figure 1.2. The P-T projection for a system in which the liquid phases are completely miscible, and the solid phases are completely immiscible. Triple points are denoted by TP and the quadruple point by Q. S_A and S_B are the pure solids.

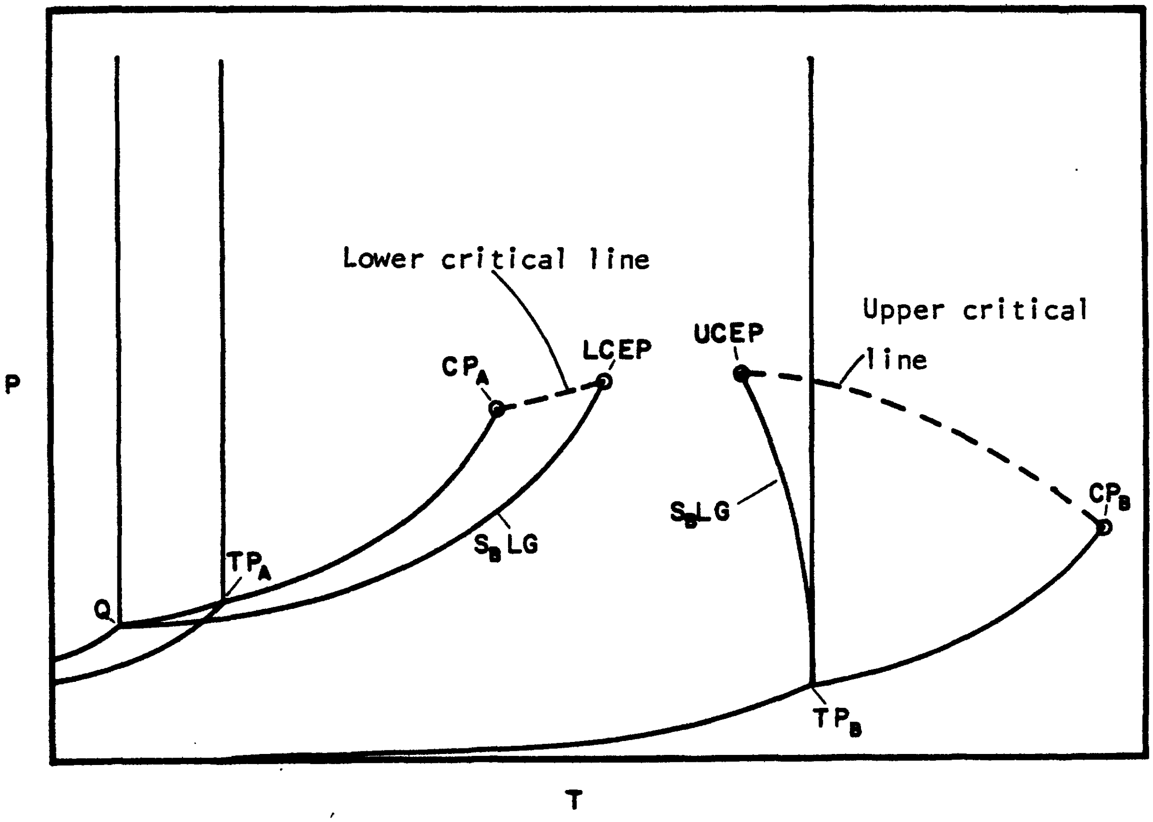

Figure 1.3. The P-T projection of a system in which the gas-liquid critical line is cut by the S_BLG line. The length of the lower critical line has been greatly exaggerated. The LCEP is typically within a few °C of CP_A.

critical line at an upper critical end point (UCEP). At temperatures between the critical end points, the fluid phase critical phenomenon is not observed at any pressure. Consequently, this region is designated as the supercritical fluid region. The critical point in Figure 1.3 was, as noted, a lower critical end point. An upper critical end point did not appear in that diagram.

1.4. The Equation of State

Generation of phase diagrams of the type shown in the previous section requires fugacity expressions for the solid phase and for a component in a fluid phase. The first of these is easily obtained from an equation for the sublimation pressure of the solid. To represent the gaseous, fluid, and liquid phases present, the Peng-Robinson (P-R) equation of state was used. This equation was felt to represent the best compromise between simplicity and accuracy in attaining the desired goal.

The P-R equation is

$$P = \frac{RT}{v-b} - \frac{a}{v(v+b) + b(v+b)} \tag{1.1}$$

It is a modified van der Waals type equation. The parameter b is associated with the volume occupied by the molecules, and the temperature dependent parameter a = a(T) with the attractive forces between molecules. The equation is cubic in volume, so that volume may be analytically determined if pressure and temperature are specified. Using equation (1.1), an expresssion for the fugacity of a component in a mixture may be derived and used in the calculation of phase equilibria. For a binary system, an empirical interaction parameter, δ_{12}, must often be employed to obtain reasonable agreement with experimental data.

1.5. Theoretical Aspects

Equilibrium of phases requires that the phases be of equal temperature and pressure, and that the fugacity (or chemical potential) of a given component be the same in every phase. It has been found that plots of fugacity versus composition, at constant temperature and pressure, provide an excellent means of visualizing the criterion of equal fugacities. Consider Figure 1.4, which is a plot of n-hexadecane (subscript H) fugacity versus n-hexadecane mole fraction for the n-hexadecane -carbon dioxide system, at a temperature of 300 K and a pressure of 0.1 atm. The systems represented by this diagram are a result of mixing liquid

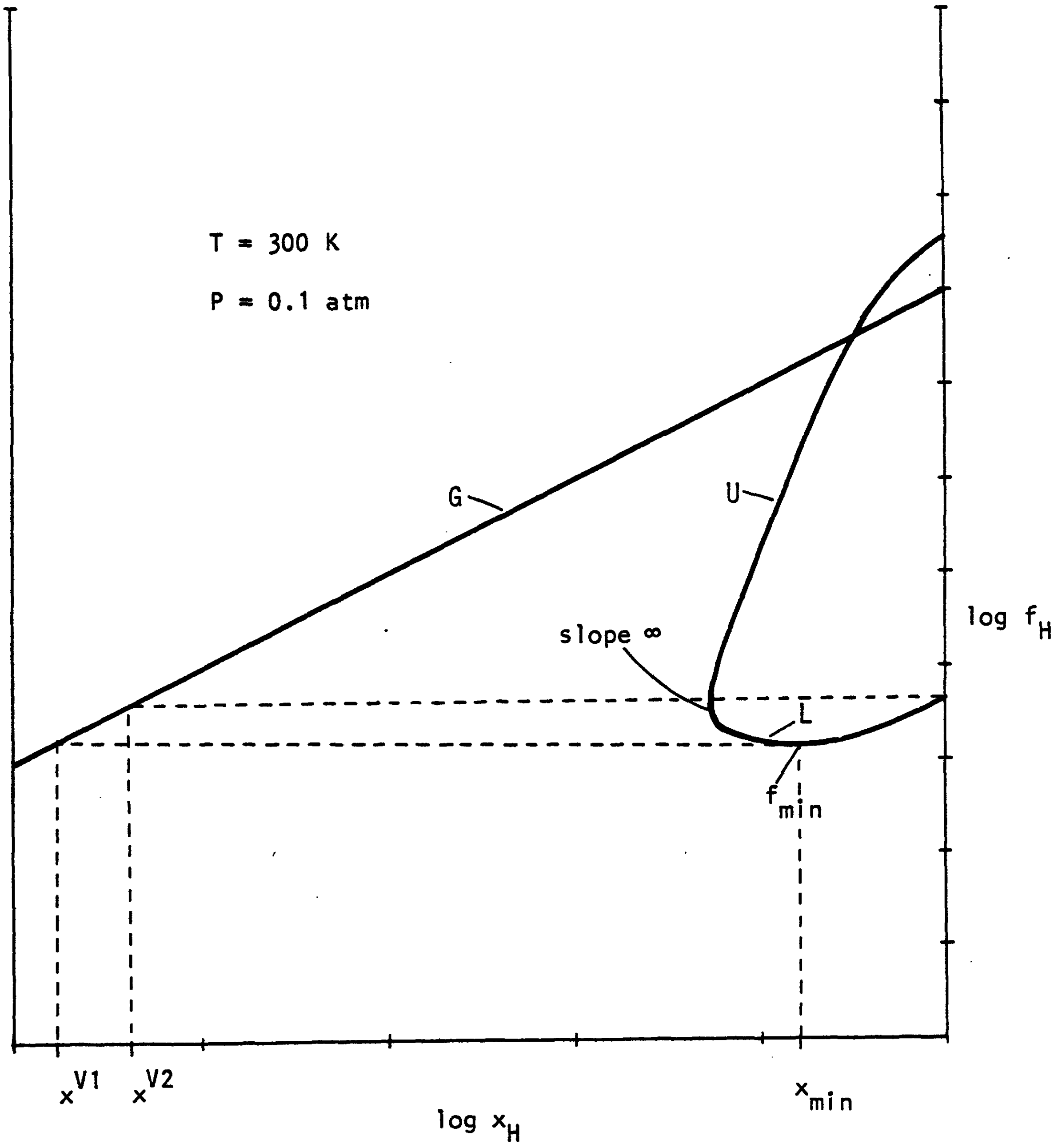

Figure 1.4. An f_H-x_H plot for n-hexadecane - carbon dioxide. Segment G is the gaseous root, segment U is the mechanically unstable root, and segment L is the liquid root. Segments U and L start at the slope infinity and continue to the pure hexadecane axis.

n-C_{16} with gaseous CO_2, and VLE is to be expected if the two components are present in a certain range of proportions. The most striking feature of the plot is that there are actually two separate curves. Segment G is essentially linear over the entire range of composition, with a slope of unity and an intercept at the pure C_{16} axis of 0.1 atm. This is the equivalent of ideal gas behavior, since

$$f_H = x_H P = P_H \tag{1.2}$$

where P_H is the partial pressure of C_{16}. The second curve appears when the cubic equation (1.4) gives three real roots. In the composition range from the infinity in $\frac{df_H}{dx_H}$ to $x_H = 1$, segment G corresponds to the high volume (gaseous) root, segment L to the low volume (liquid) root, and segment U to the middle volume root. Between the slope infinity and x_{min}, $\frac{df_H}{dx_H}$ for segment L is negative, indicating that the liquid phase is materially unstable in this composition range. For x_H greater than x_{min}, $\frac{df_H}{dx_H} > 0$, and segment L represents a stable or metastable liquid phase. Segment U appears to be materially stable in this plot. As with the middle volume root for pure component systems, however, it violates the criterion of mechanical stability (i.e.,

$\left(\frac{\partial P}{\partial V}\right)_{T,x} > 0$) and thus does not represent stable conditions. As indicated by the crossing of segments G and U in the graph, the middle volume root does not always give the middle fugacity root.

Suppose now that suitable quantities of C_{16} and CO_2 are present in the system so that two phases exist with compositions x^V and x^L, and fugacity f_H^E. The f-x plot shows that x^L must lie between x_{min} and $x_H = 1$, and furthermore, that f_H^E is between $f_H(x_{min})$ and $f_H(x_H = 1)$. For the coexisting vapor phase, which must lie on the straight line segment, equality of fugacities requires that

$$x^{V1} \leq x^V \leq x^{V2} \tag{1.3}$$

This limiting procedure illustrates the usefulness of the f-x plots in determining two phase equilibrium, and is one of the steps in the phase equilibrium algorithm developed in this thesis. To find the actual compositions for VLE, it is of course necessary to match partial fugacities of carbon dioxide as well.

Fugacity-composition plots may have many shapes other than that given in Figure 1.4. Figure 1.5 depicts an f-x curve with a closed loop, chosen to illustrate a special case of phase stability discovered in this work. Generally speaking, if one starts with a stable system and moves

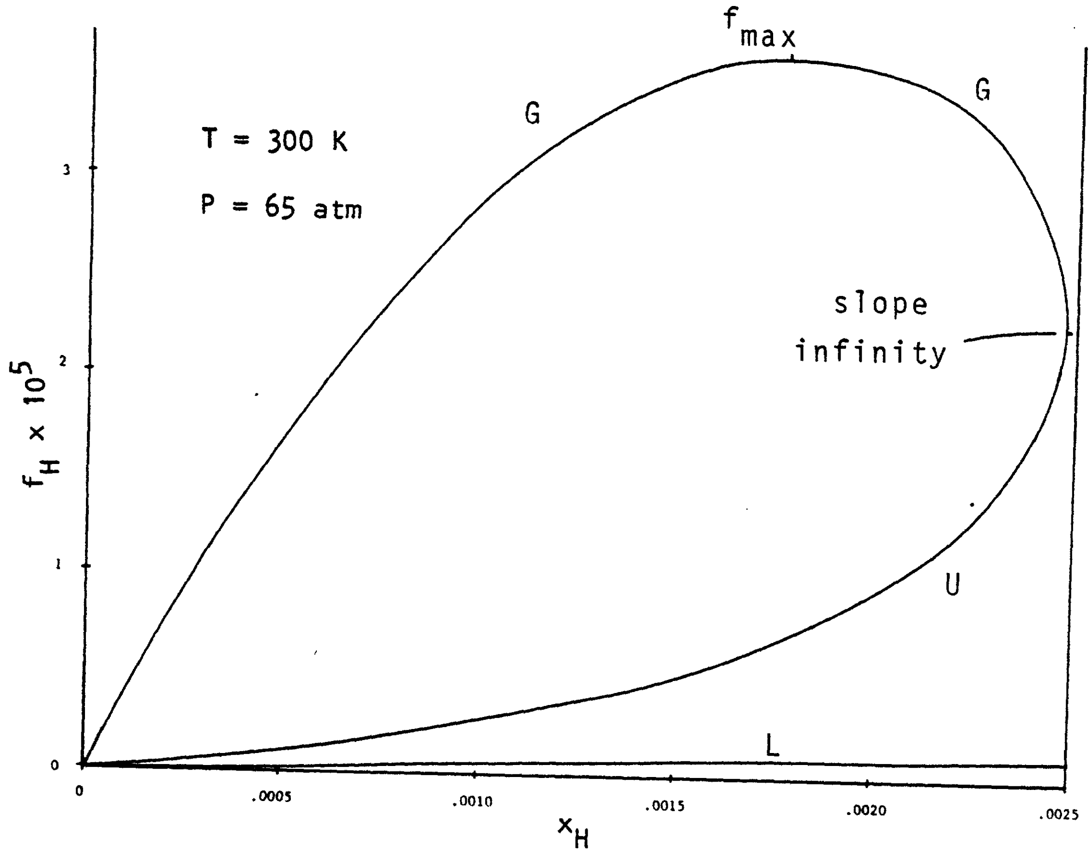

Figure 1.5. A Cartesian plot illustrating the closed loop behavior of the f_H- x_H curve at conditions near CO_2's vapor pressure.

continuously toward the limit of stability, the highest order stability criterion will be the first (or among the first) to be violated. For binary systems, this means that a stable system will violate the criterion of material stability before the criterion of mechanical stability, so that it is sufficient to check only the former to ascertain phase stability. This is shown in Figure 1.5 by tracing the stable gaseous root with increasing x_H. At f_{max}, the material stability criterion is violated as $\frac{df_H}{dx_H}$ becomes negative. The mechanical stability criterion is not violated until the composition of the slope infinity is reached. A special case arises, however, when the stable gaseous or liquid root is traced with decreasing x_H. Since all three roots join at the origin, it is possible to follow segment G or L to $x_H = 0$, and then proceed with increasing x_H along segment U. In this instance, the mechanical stability criterion has been violated without a violation of the material stability criterion. In light of this possibility, a discontinuity in $\frac{df_H}{dx_H}$ must be treated as a violation of the stability criterion. Upon tracing a stable system through such a discontinuity, it is necessary to evaluate all stability criteria, not just the one of highest order, to determine phase stability.

Fugacity-composition plots may be used in the determination of critical points, since an f-x plot exhibits a horizontal inflection at such a point. It is more convenient, however, to evaluate two alternate criteria for this purpose. The first criterion of criticality, which corresponds to the material stability criterion, is given by:

$$L1 = \begin{vmatrix} A_{xx} & A_{xv} \\ A_{xv} & A_{vv} \end{vmatrix} = A_{xx}A_{vv} - A_{xv}^2 \geq 0 \qquad (1.4)$$

For a stable system, L1>0. At the limit of stability, i.e., on the spinodal curve, L1=0. Spinodal points correspond to extrema in an f-x plot. The L1 criterion is not strictly equivalent to the $\frac{df_H}{dx_H}$ criterion since these two quantities differ in sign in a region of mechanical instability. For this reason, it is best to treat material stability as undefined in a region of mechanical instability. The second criterion of criticality is

$$M1 = \begin{vmatrix} A_{vv} & A_{xv} \\ \frac{\partial L1}{\partial v} & \frac{\partial L1}{\partial x} \end{vmatrix} = A_{xxx}A_{vv}^2 - A_{vvv}A_{xx}A_{xv} - 3A_{vv}A_{xv}A_{vxx} + 2A_{xv}^2 + A_{vv}A_{vvx}A_{xx} \geq 0 \qquad (1.5)$$

Points of M1=0 correspond to inflection points in an f-x plot. At a critical point, both L1 and M1 equal zero. This work has shown that the M1=0 criterion may be replaced by the criterion $\left(\frac{\partial L1}{\partial x}\right)_{T,P} = 0$ in critical point determinations. This must be so because a critical point is a terminus of a spinodal surface. As the critical temperature and pressure are approached, two points of L1=0 may be brought arbitrarily close to one another in composition. At the critical point, the two L1 zeroes coincide (see Figure 1.10).

1.6. The n-Hexadecane - Carbon Dioxide System

The considerations of the preceding sections make it possible to determine overall phase behavior in binary systems, provided sufficient data is available to allow the choice of an appropriate interaction parameter. For the C_{16} - CO_2 system, P-T measurements along the upper critical line provide the requisite information. Figure 1.6 shows the upper critical line generated for various values of δ_{12} (using the L1=0 and M1=0 criteria), and illustrates the marked effect of this parameter on the predictions. The experimental upper critical line starts from the critical point of C_{16}, rises to a pressure maximum, falls to a pressure minimum, and thereafter runs steeply to higher pressures and temperatures. On the basis of this curve, a δ_{12} of 0.081 was selected as giving the best overall fit.

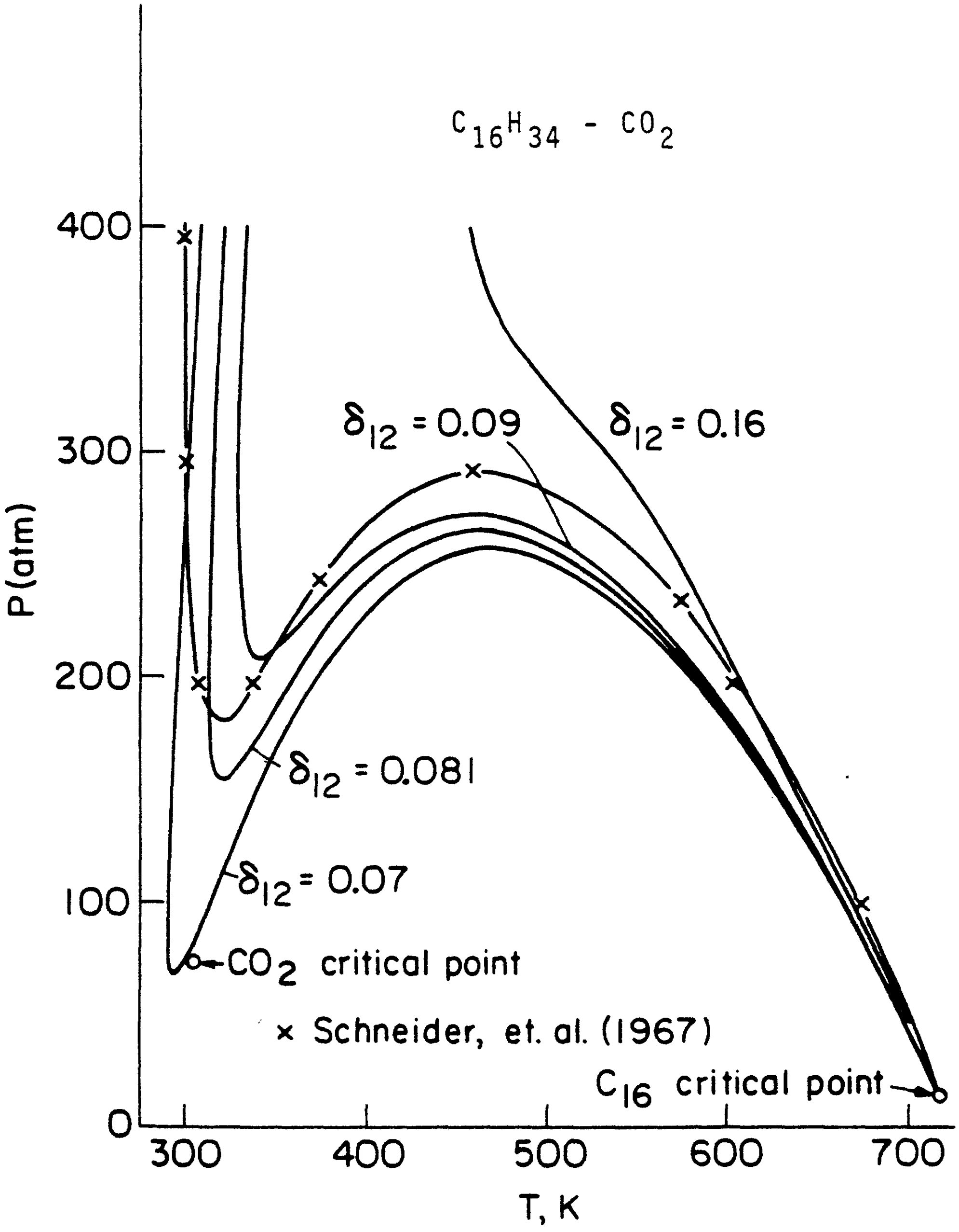

Figure 1.6. The P-T projection for the C_{16}-CO_2 system showing the effect of δ_{12} on the predicted upper critical line. The pure CO_2 critical point has also been included, although it is not a part of this line.

No solids form in this pressure and temperature regime.

Figure 1.6 includes the critical point of CO_2, which serves as a starting point for the lower critical line. Figure 1.7 is an enlargement of the P-T projection in this region. The lower critical line intersects the three-phase L_1L_2G line at an LCEP analogous to that shown in Figures 1.1 and 1.3. Now, however, the liquid-vapor critical phenomenon occurs in the presence of a second liquid phase. The critical line continues past the LCEP in a metastable fashion, until being terminated at a cusp by the unstable critical line. The unstable critical line is the terminus of an unstable binodal surface.

The three-phase line in Figure 1.7 is predicted by noting the intersection of binodal curves at a given temperature or pressure. Figure 1.8 illustrates qualitatively the shape of the T-x section expected on the basis of the measured critical loci. The three binodal regions intersect at a common temperature to give a three-phase L_1-L_2-G tieline. At the high temperature end, the G-L_2 region terminates at a point along the upper critical line. The G-L_1 region, on the other hand, terminates at the CO_2 vapor pressure point (i.e., the boiling point of CO_2 at 70 atm). The L_1-L_2 region extends off the plot to lower temperatures, where it will eventually terminate due to solid formation.

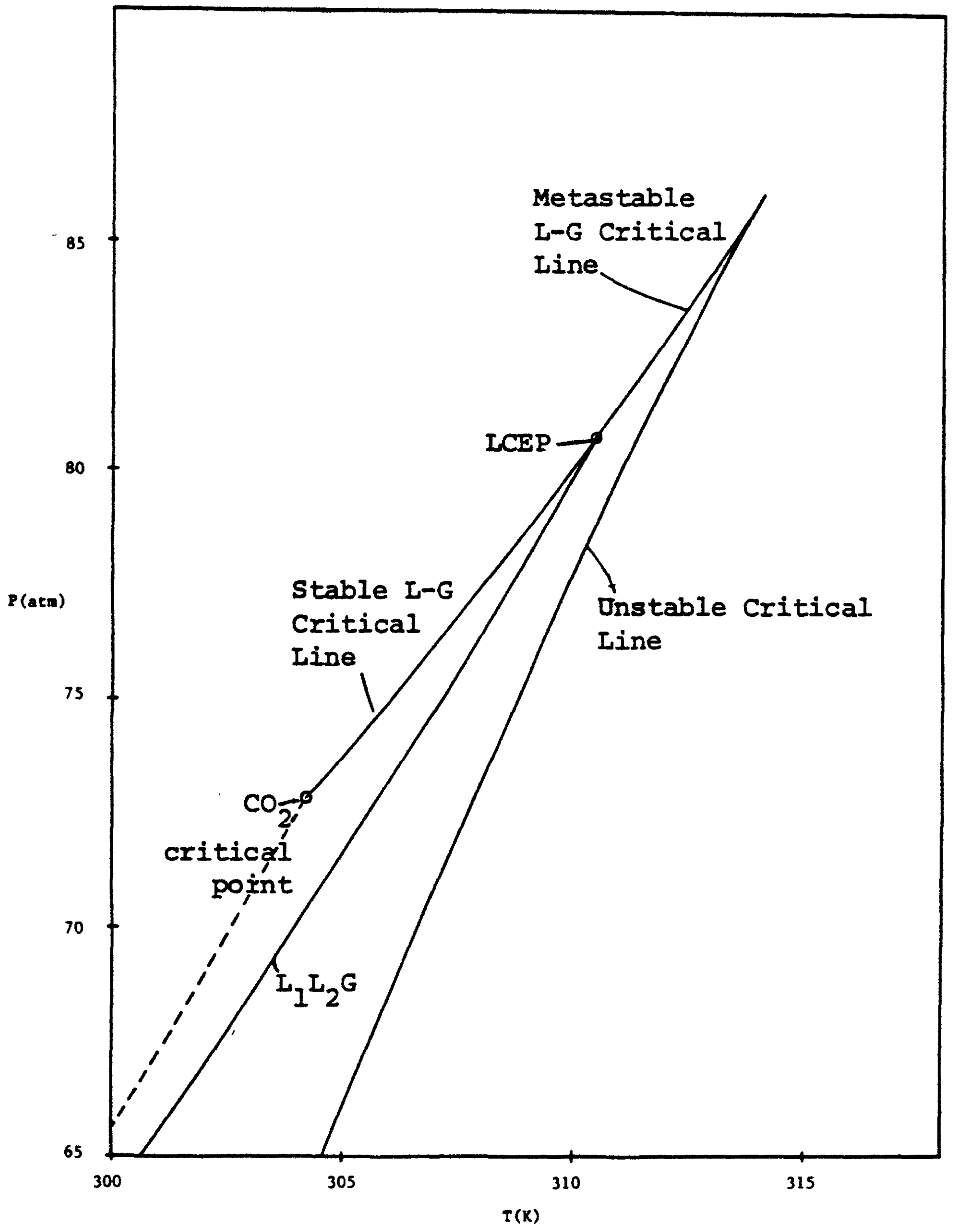

Figure 1.7. The P-T projection of the lower critical line for C_{16}-CO_2. The stable critical line is metastable between LCEP and the cusp.

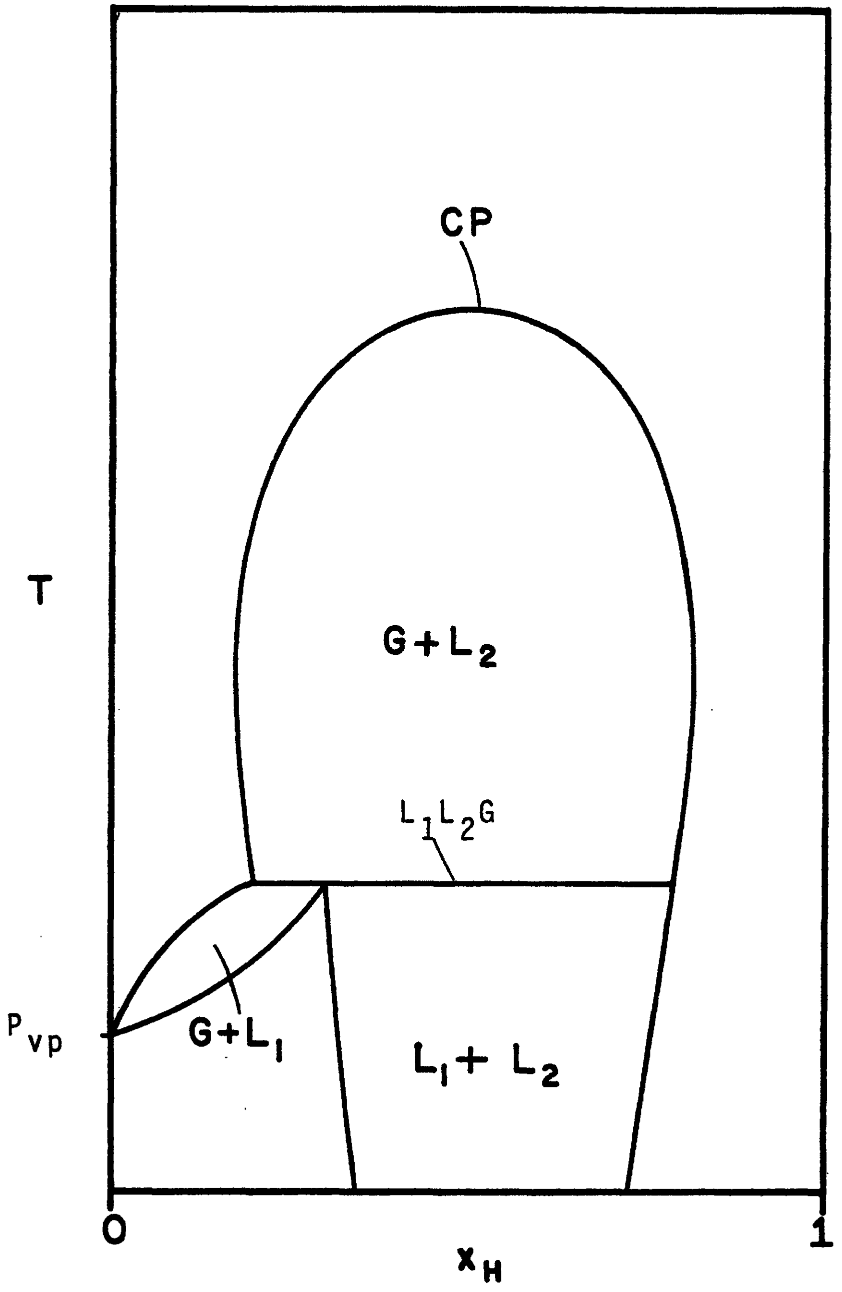

Figure 1.8. A qualitative T-x section for C_{16}-CO_2 at 70 atm.

Figure 1.9 gives the P-R prediction for the T-x section at temperatures near the three-phase line. The concentration axis is given on a logarithmic scale to allow the very small G-L_1 region to be visible. Three-phase equilibrium is predicted at 304 K. Although the predicted diagram is qualitatively correct, it is incomplete, because the P-R equation generates metastable and unstable phase equilibrium solutions in addition to the stable solutions which are shown.

Figure 1.10 gives the T-x section when all phase equilibrium solutions from the P-R equation are drawn in. The binodal curves are labelled by number pairs which refer to particular monotonic segments of the f-x curve from which the equilibrium arises. Figure 1.11 gives a typical f-x plot for this region showing the numbering of the monotonic segments. Comparison of Figure 1.10 with Figure 1.9 indicates that the G-L_2 region is represented by the (1,7) binodals, the G-L_1 region by the (1,5) binodals, and the L_1-L_2 region by the (5,7) binodals. Note that a significant portion of the stable (1,5) binodals falls in a region bounded by two spinodal curves. Stable solutions appear in this nominally unstable region because of the existence of multiple roots to the cubic. Each of the stable binodals (1,5), (1,7), and (5,7) continue in a metastable fashion past the three-phase line to reach a maximum or minimum

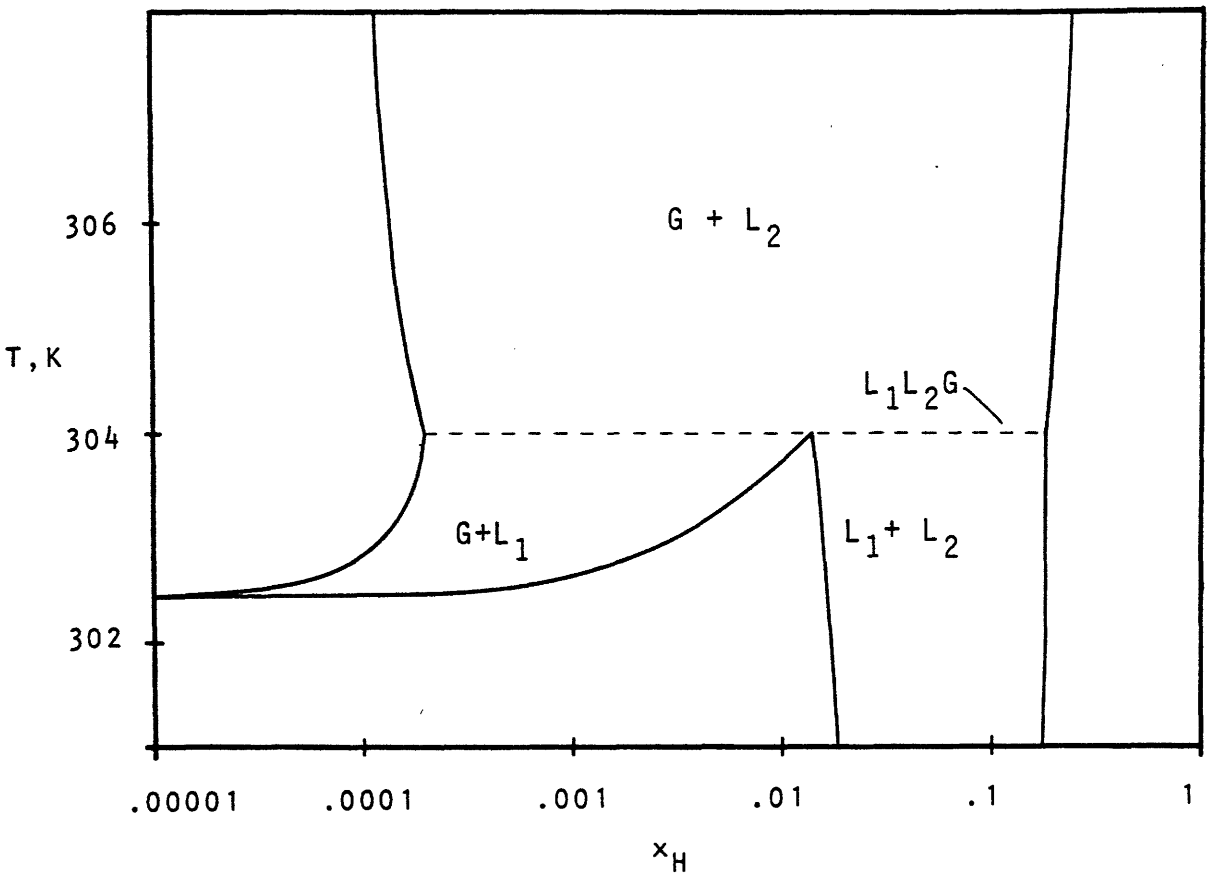

Figure 1.9. The predicted T-x section for C_{16}-CO_2 at 70 atm, in the vicinity of the three-phase line.

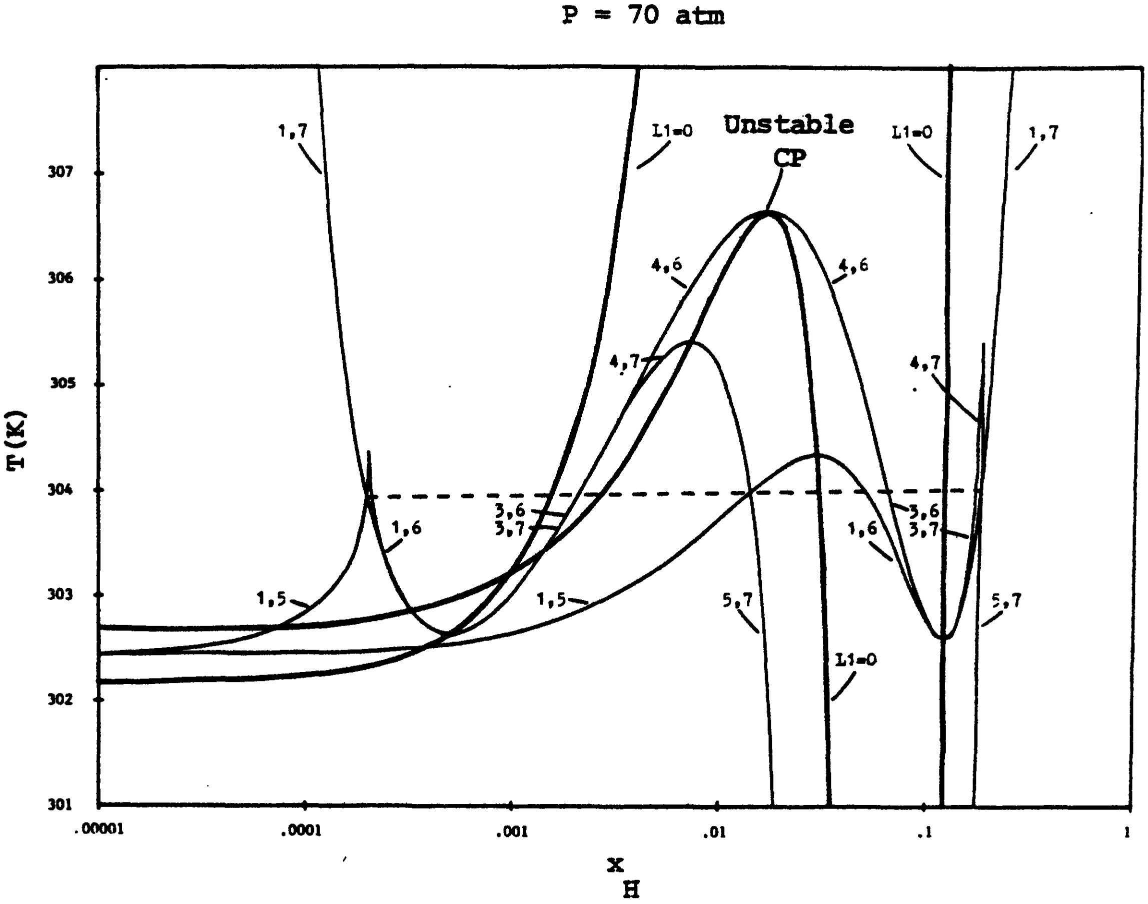

Figure 1.10. The T-x section at 70 atm showing the continuation of the predicted binodal curves. Each binodal is labelled with a number pair to indicate which segments of the f-x curve the equilibrium is derived from. To determine the compositions of coexisting phases, a tieline is drawn at constant temperature joining binodals labelled with the same number pair. Note that the three-phase tieline (dashed) joins the two curves labelled (1,7), the two curves labelled (1,5), and the two curves labelled (5,7). The spinodal curve (L1=0) is given by the heavy lines. At the unstable critical point, both $\left(\frac{\partial(L1=0)}{\partial x}\right)_{T,P}$ and $\left(\frac{\partial L1}{\partial x}\right)_{T,P}$ are zero.

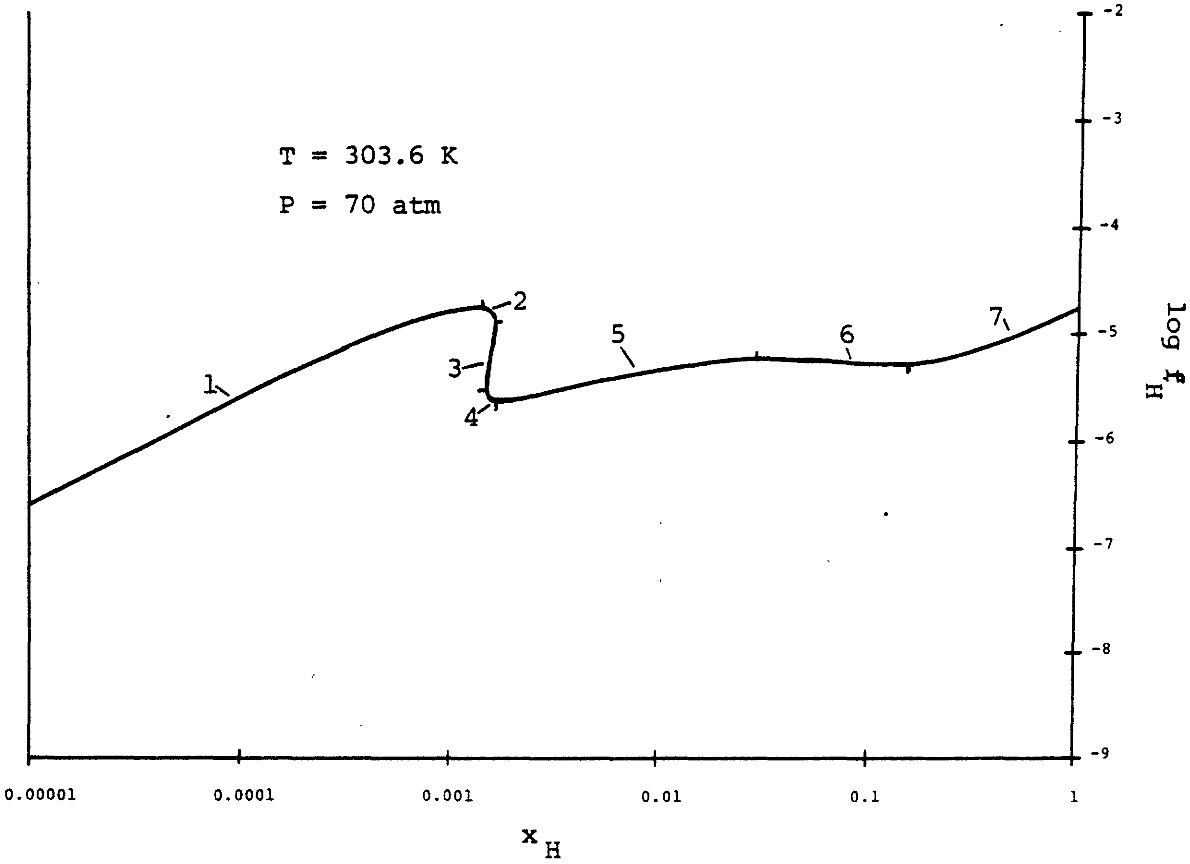

Figure 1.11. An f-x plot in the three-phase region, showing the numbering of the seven monotonic segments.

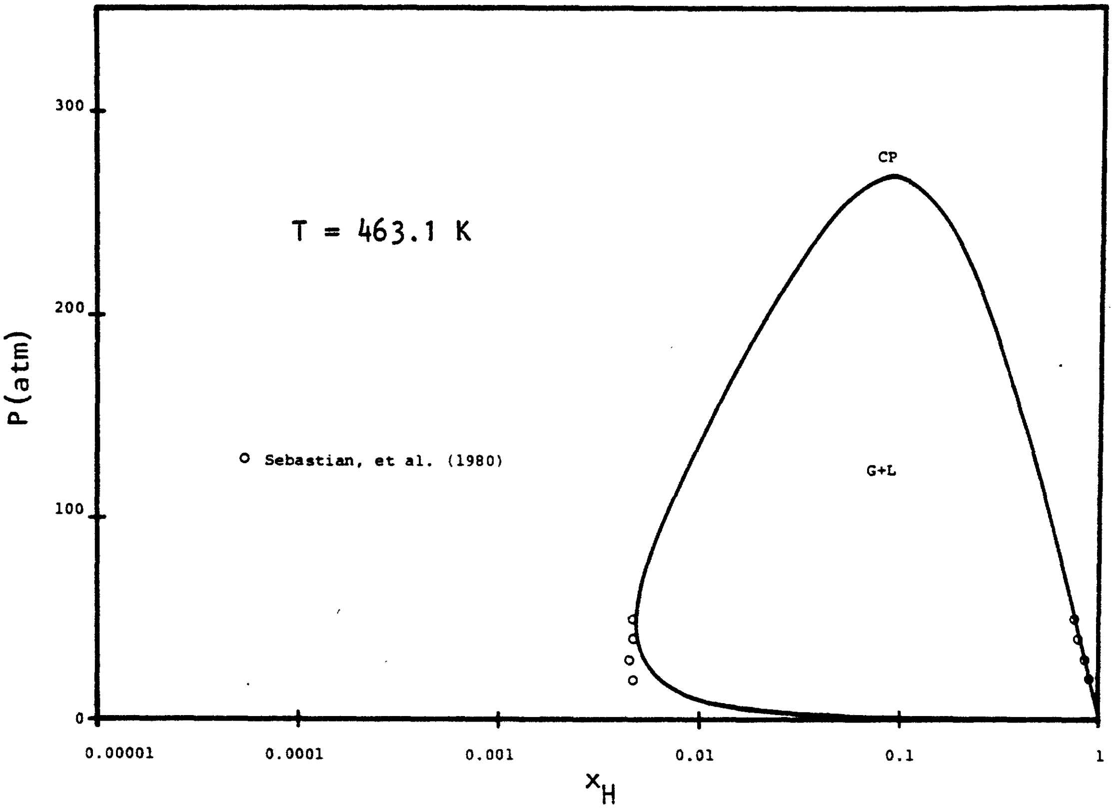

Figure 1.12. The P-x section at 463.1 K.

temperature. At a temperature extremum, the metastable binodal joins an unstable binodal locus. There are three separate continuous curves in Figure 1.9. The first two follow the course (1,7)-(3,7)-(4,7)-(5,7), and the third the course (1,5)-(1,6)-(3,6)-(4,6)-(4,6)-(3,6)-(1,6)-(1,5). This last curve exhibits an unstable critical point where the two (4,6) branches join. Reference to Figure 1.11 shows that both segments 4 and 6 are materially unstable.

A small amount of low pressure P-T-x data is available for the C_{16} - CO_2 system. Figure 1.12 gives a typical comparison between this data and predictions with $\delta_{12} = 0.081$. On the basis of the lean component, errors in the CO_2-rich phase are less than fifteen percent, while those in the C_{16}-rich phase are less than twenty-five percent. On the basis of the rich component, the errors are less than 1 and 5 percent, respectively. This agreement is quite good considering that no composition data was used in the determination of the interaction parameter.

1.7. The Naphthalene - Carbon Dioxide System

The naphthalene (N) - carbon dioxide system adds the complication of pure solid formation to the phase diagrams.

Predictions were carried out using an interaction parameter determined from solubility data in the supercritical fluid region, the same data used in the construction of Figure 1.1. Figure 1.13 gives some of the supercritical solubility data, and shows predictions for four values of the interaction parameter. The predicted curves all have the correct general shape and for the most part are within a factor of two of the experimental values. It is evident that a pressure dependent interaction parameter is needed for quantitative agreement. Figure 1.14 shows the comparison of predictions and experiment at 55°C. The three lowest values of the interaction parameter predict a sudden jump in the solubility of naphthalene and thus show a large discrepancy with the measurements. The solubility jump occurs because the P-R equation predicts a phase transition. Figure 1.15 gives a more complete picture of the P-R predictions at 55°C for a value of $\delta_{12} = 0.11$. The solubility jump is seen to correspond to the S-L-F tieline, as the equilibrium system shifts from solid-fluid to solid-liquid. Note that the data are well correlated by the metastable S-F line to pressures over 300 atm.

The solubility jump of Figure 1.14 is experimentally observed at temperatures above 55°C. Figure 1.16 compares predictions and measurements at 64.9°C. Data taken after the solubility jump exhibited a great deal of scatter due to the presence of more than one phase in the CO_2 stream being

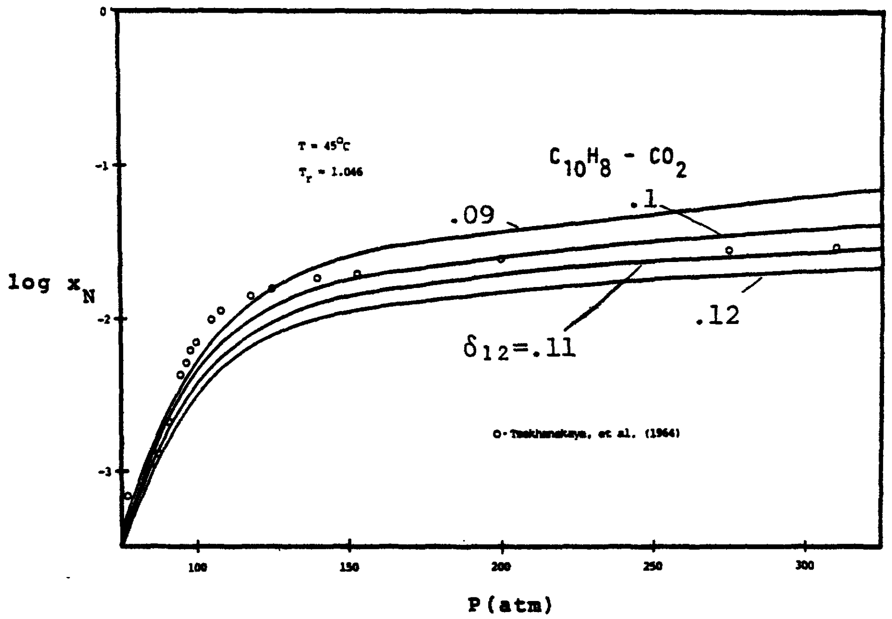

Figure 1.13. The solubility of naphthalene in supercritical CO_2 at 45°C.

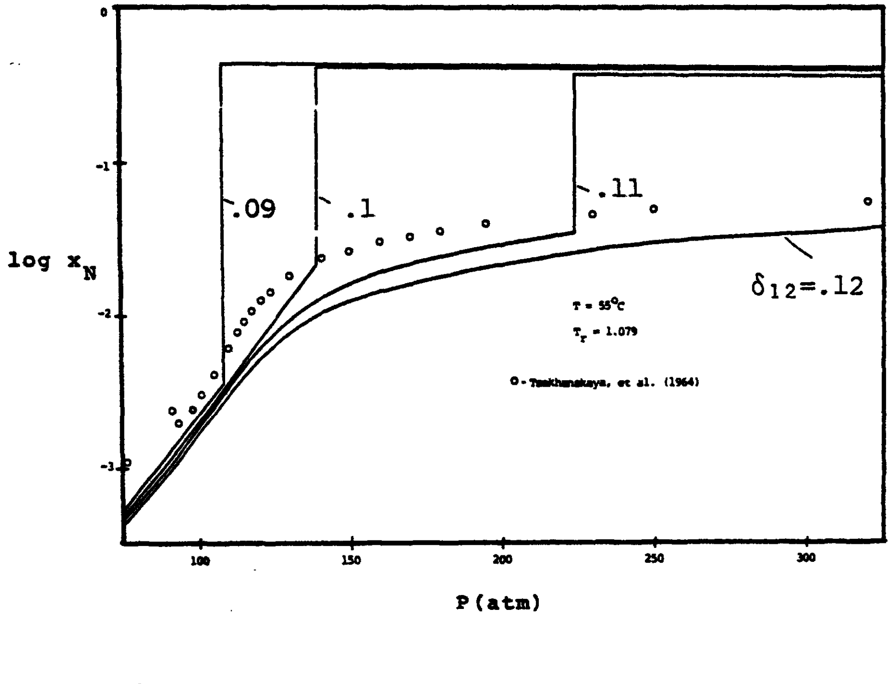

Figure 1.14. The solubility of naphthalene in supercritical CO_2 at 55°C. For δ_{12}= 0.09, 0.10, and 0.11, a solubility jump is predicted by the P-R equation.

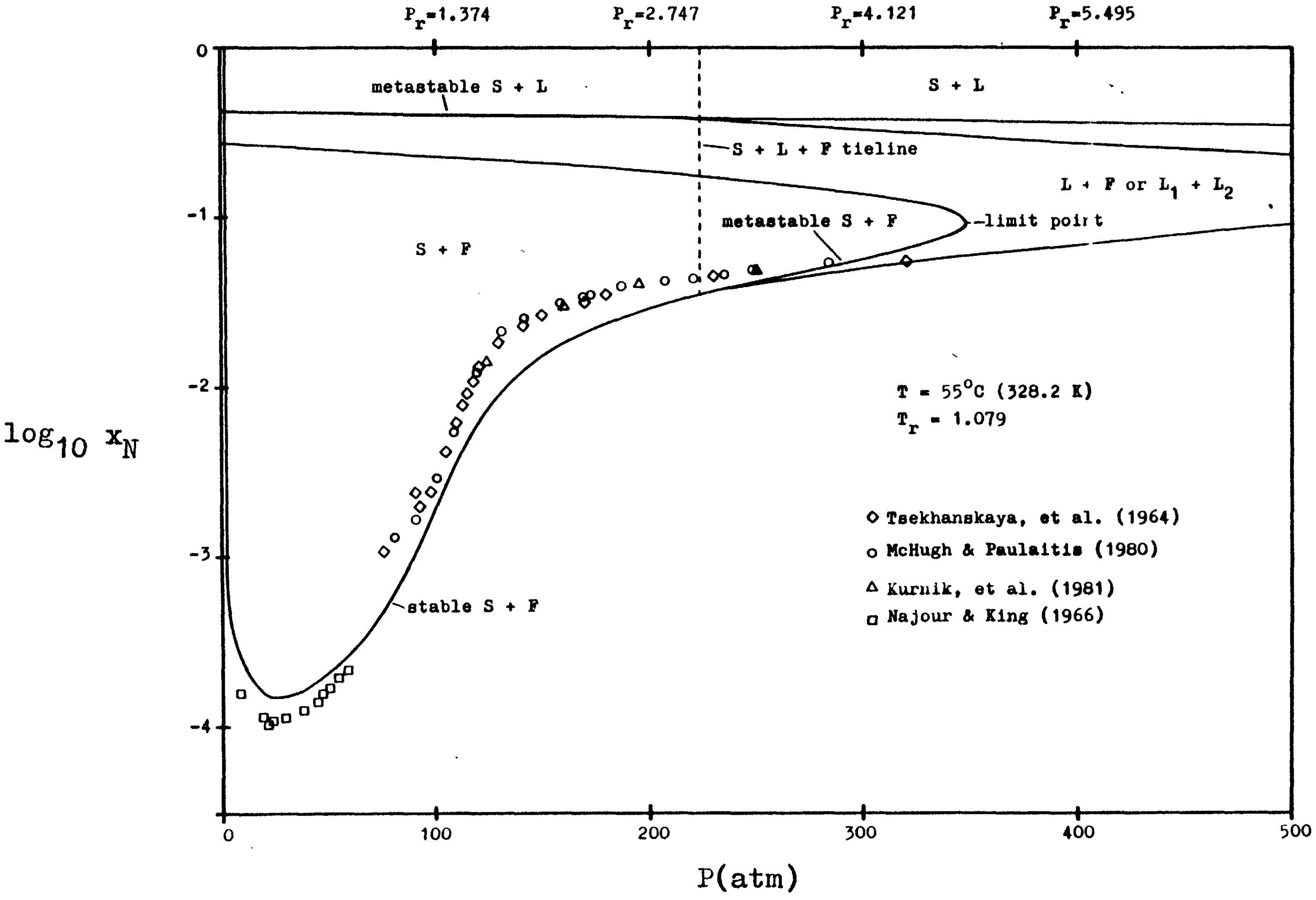

Figure 1.15. The solubility of naphthalene in CO_2 at 55°C. All predicted solid-fluid binodals, and the stable liquid-fluid binodals, are shown.

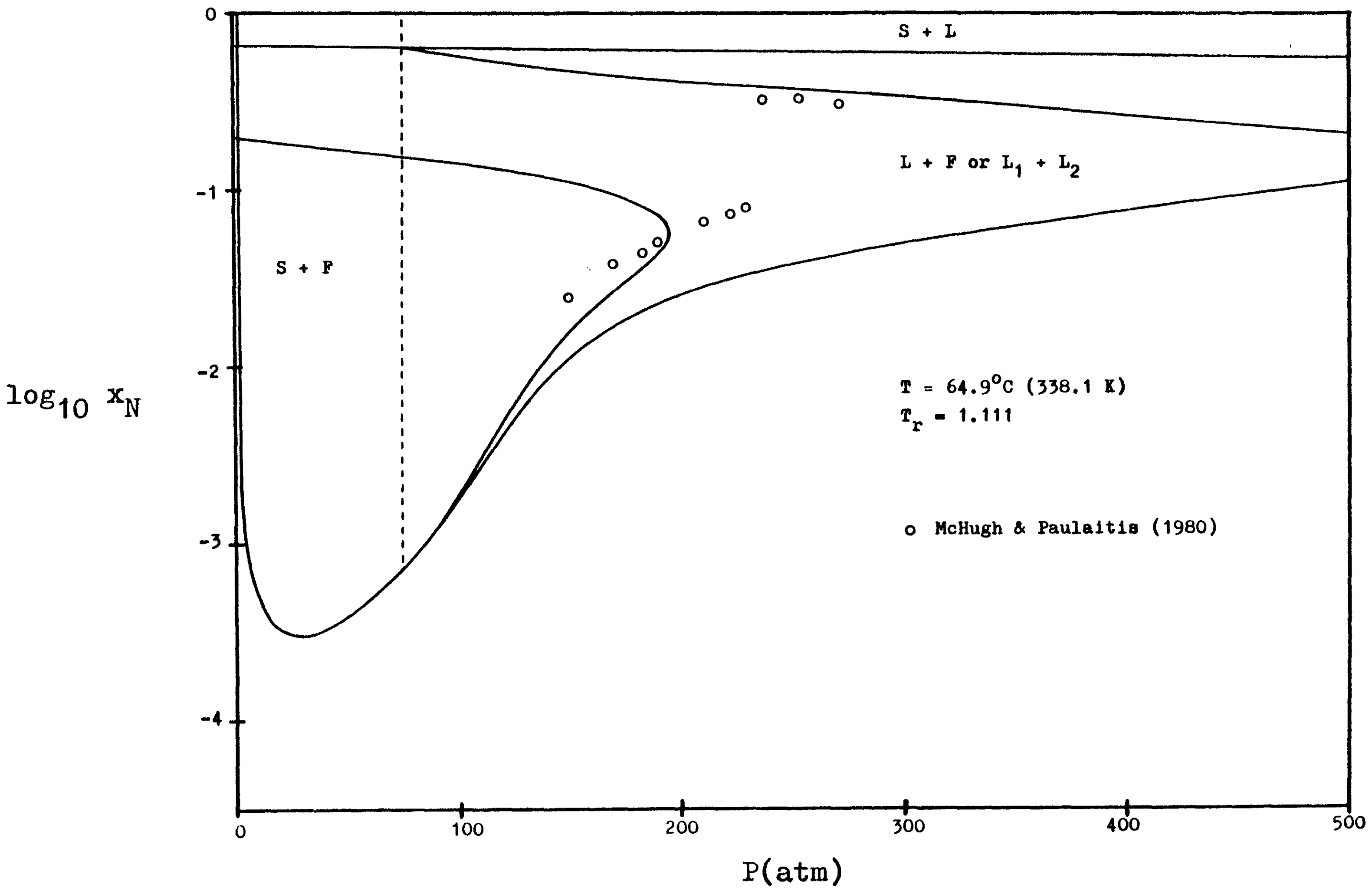

Figure 1.16. The solubility of naphthalene in CO_2 at 64.9°C.

measured; the three points shown represent a maximum of the observed solubilities. Nevertheless, they probably still represent a mixture of stable saturated liquid and metastable unsaturated liquid. The true liquid phase solubility should thus be higher, and quite close to the predicted value.

With the same interaction parameter, the P-R equation generates the solubility map shown in Figure 1.17 This is to be compared with Figure 1.1. The qualitative picture of phase behavior in the S-L-G and supercritical fluid regions is excellent. The P-R prediction of an S-L-F three-phase region terminated by an upper critical end point (cf. Figure 1.3) has been included. The UCEP pressure and mole fraction of naphthalene are both much higher than for the LCEP.

Figure 1.18 shows the naphthalene - CO_2 P-T projection, which is to be compared with Figure 1.3. For naphthalene - CO_2, the critical line is tending toward higher pressures at the UCEP. This indicates that, even had the solid phase not precipitated out, liquid-liquid immiscibility would preclude the occurrence of a continuous critical line between the two pure component critical points. The inset shows the course of the lower critical line (dashed) which terminates at the LCEP. This is the LCEP which appears in Figures 1.1 and 1.17. Unfortunately, there is no data available over most of the pressure and temperature range covered by Figure 1.18. To allow some judgment of its

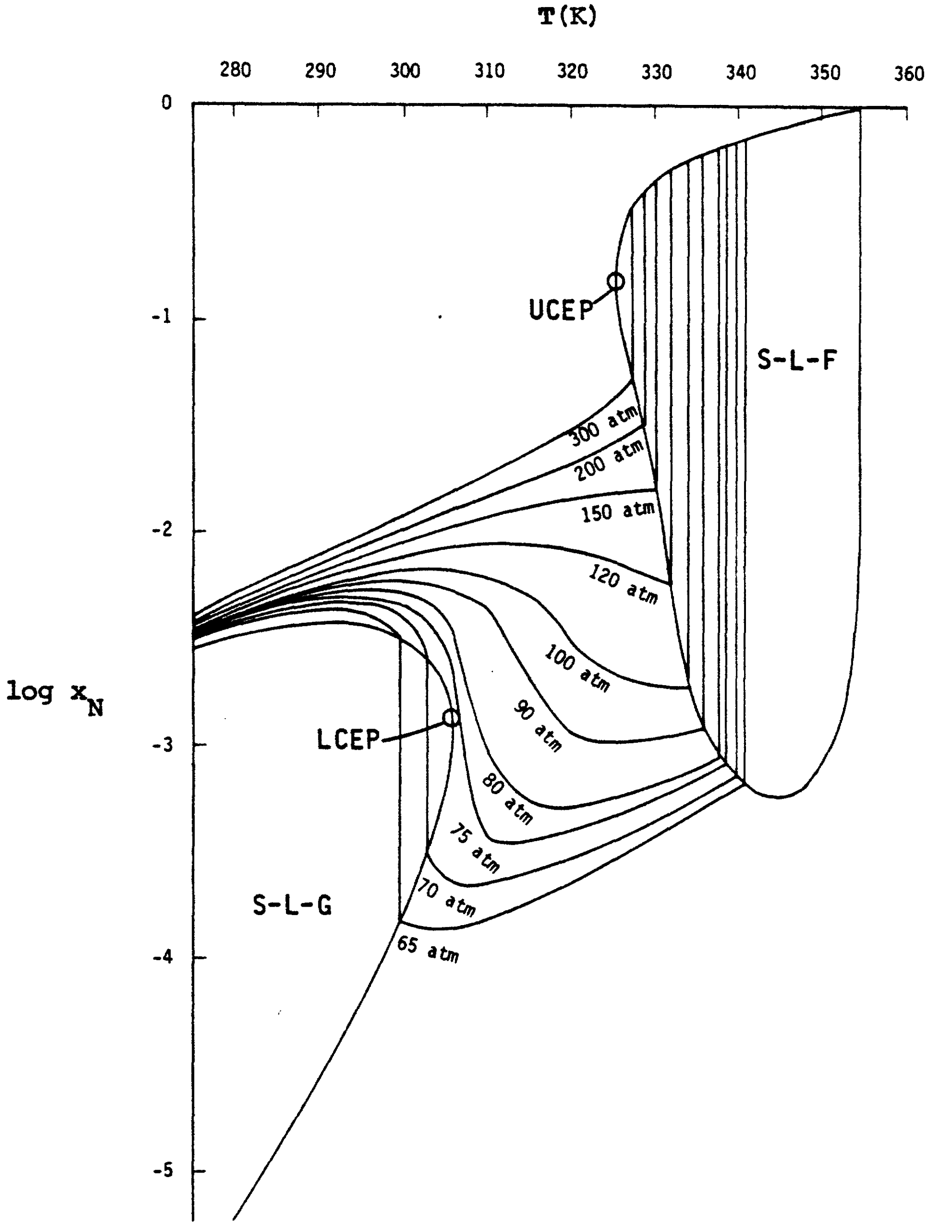

Figure 1.17. The predicted solubility map for naphthalene - CO_2.

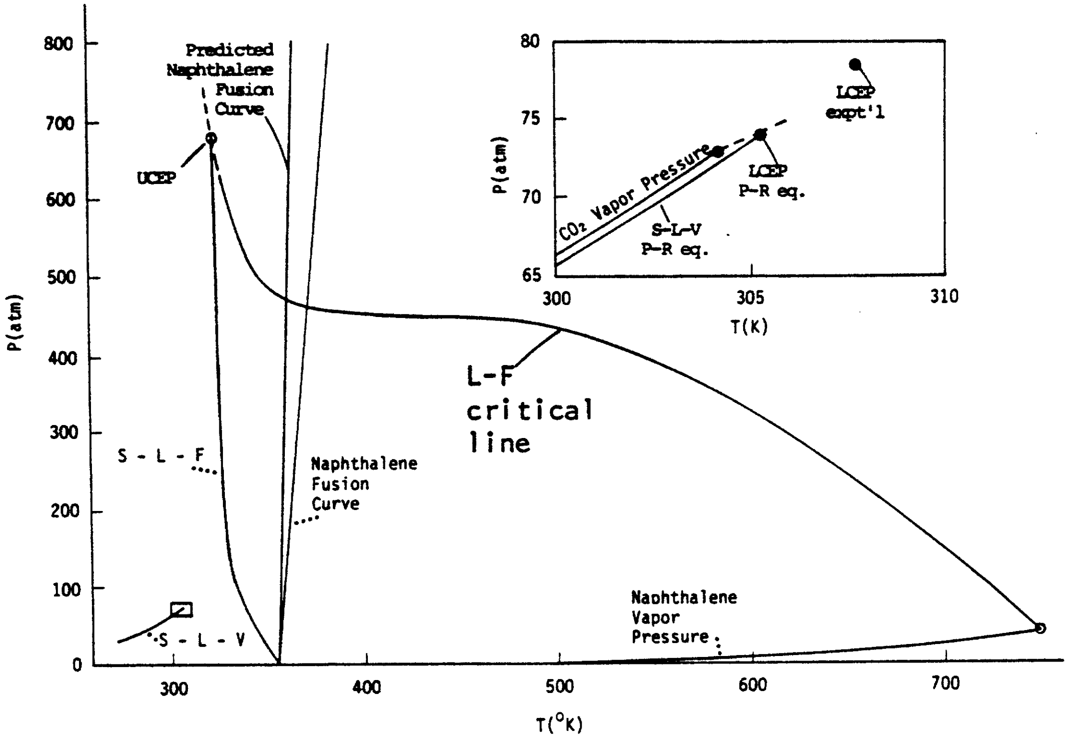

Figure 1.18. The P-T projection for the naphthalene - carbon dioxide system. The range of temperatures between the LCEP and the UCEP is the supercritical fluid region.

accuracy, the naphthalene-ethylene system was studied.

1.8. The Naphthalene - Ethylene System

Considerably more experimental data is available for naphthalene - ethylene than for naphthalene - CO_2, allowing a better evaluation of the correctness of the predicted P-T-x space. In order to draw an analogy between the predictions for naphthalene - ethylene and those for naphthalene - CO_2, the interaction parameter for this system was selected on the basis of data in the supercritical fluid region. A value of $\delta_{12} = 0$ is found to give predictions and agreement similar to Figures 1.13 and 1.14. Figure 1.19, generated with $\delta_{12} = 0$, shows that qualitative agreement is quite good over the entire range of temperatures and pressures. Unlike the naphthalene - CO_2 system, at the UCEP the upper critical line is tending toward lower pressures. As shown by the metastable continuation of this line, however, there again would be liquid-liquid immiscibility if the solid were not present. The qualitative accuracy of Figure 1.19 is an indication of the qualitative accuracy of Figure 1.18. Figure 1.20, the P-x projection for naphthalene-ethylene, shows the semiquantitative agreement of predicted and experimental phase compositions for the S-L-F three-phase line and the L-F critical line.

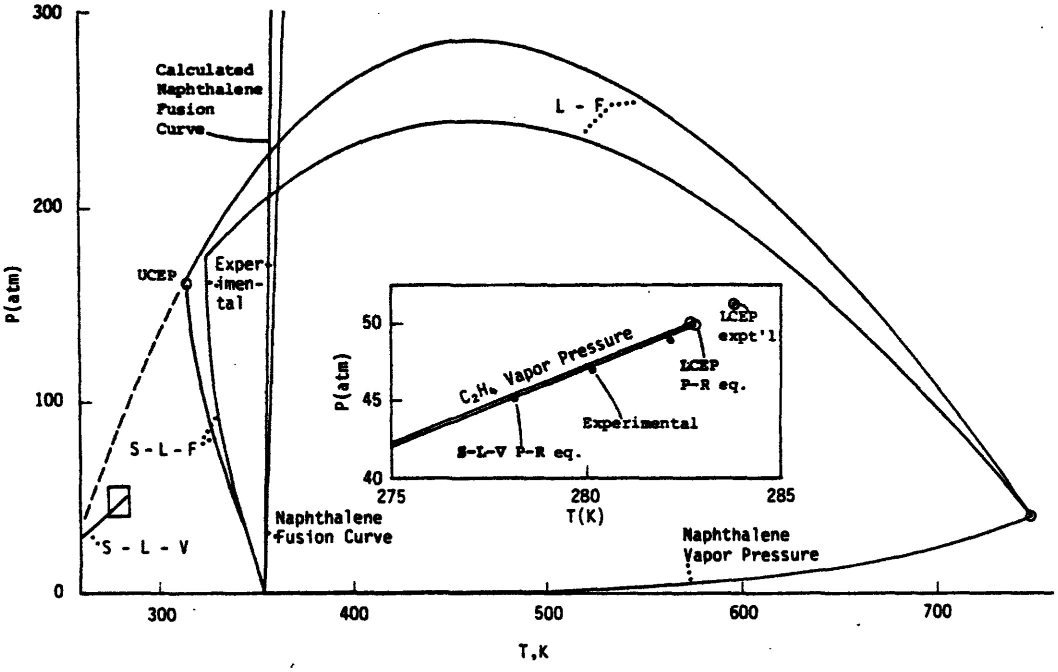

Figure 1.19. The P-T projection of the naphthalene - ethylene system. The inset shows the region near ethylene's critical point (see also Figure 1.21). Experimental curves are from van Welie and Diepen (1961).

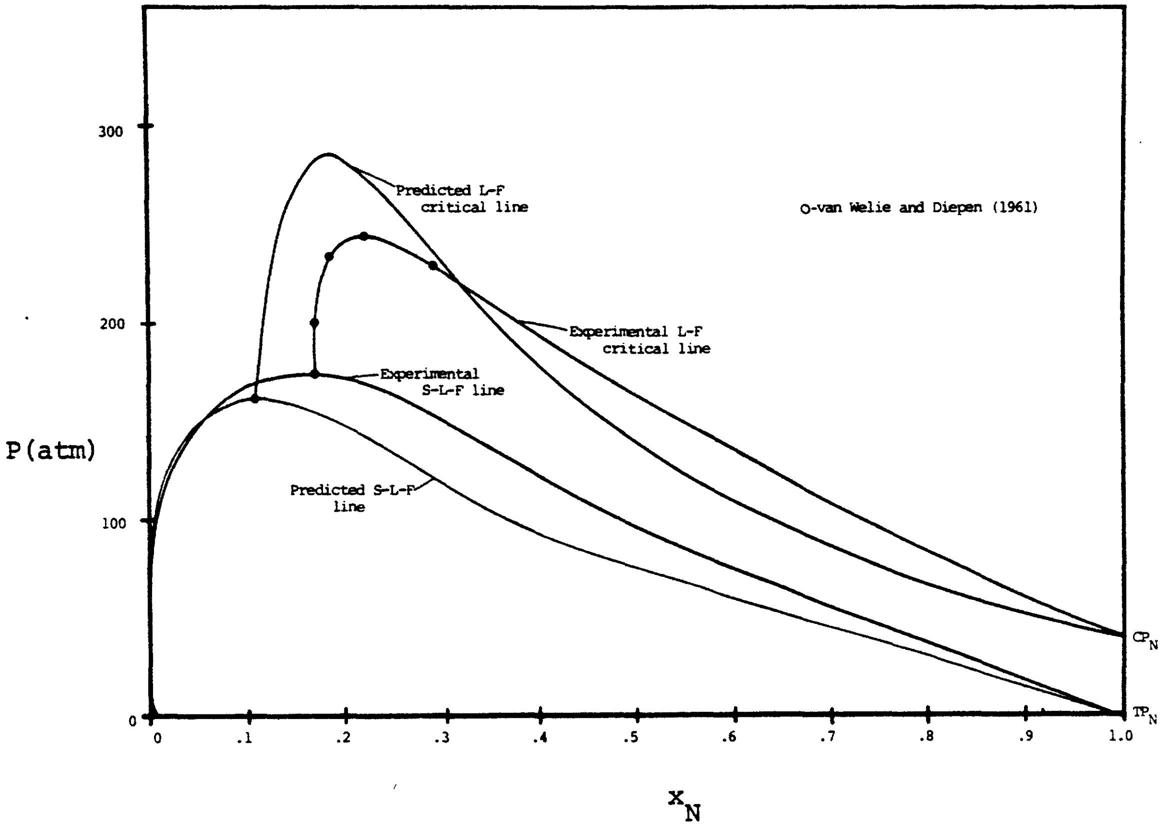

Figure 1.20. The P-x projection of the upper critical line and the SLF region for naphthalene - ethylene.

Figure 1.21 is an enlargement of the naphthalene-ethylene P-T projection in the vicinity of ethylene's critical point. Agreement with experimental S-L-G data is excellent. As with C_{16} - CO_2, the lower critical line starts at the solvent critical point and is terminated when it meets the unstable critical line at a cusp. The diagram also depicts the metastable LLG line and metastable L-F critical line. The metastable LLG line terminates at a metastable CEP at either end.

Figure 1.22 illustrates a P-x section for this system at a temperature between the UCEP and naphthalene's triple point. The S-L-F tieline corresponds to a point along the three-phase S-L-F line in Figure 1.19. Note that the solid-liquid and solid-fluid binodals are part of a single curve with metastable and unstable portions. The L-F binodal has a stable critical point, but is metastable below the tieline. At the UCEP the L-F binodal falls entirely within the S-F binodal, except for the critical point, which intersects the S-F binodal at a point of horizontal inflection. This is shown in Figure 1.23. The horizontal inflection point in the stable binodal is a necessary and sufficient criterion for the occurrence of a critical end point. This is true not only for SLF or SLG critical end points, but also for LLG critical end points in the C_{16} - CO_2 system.

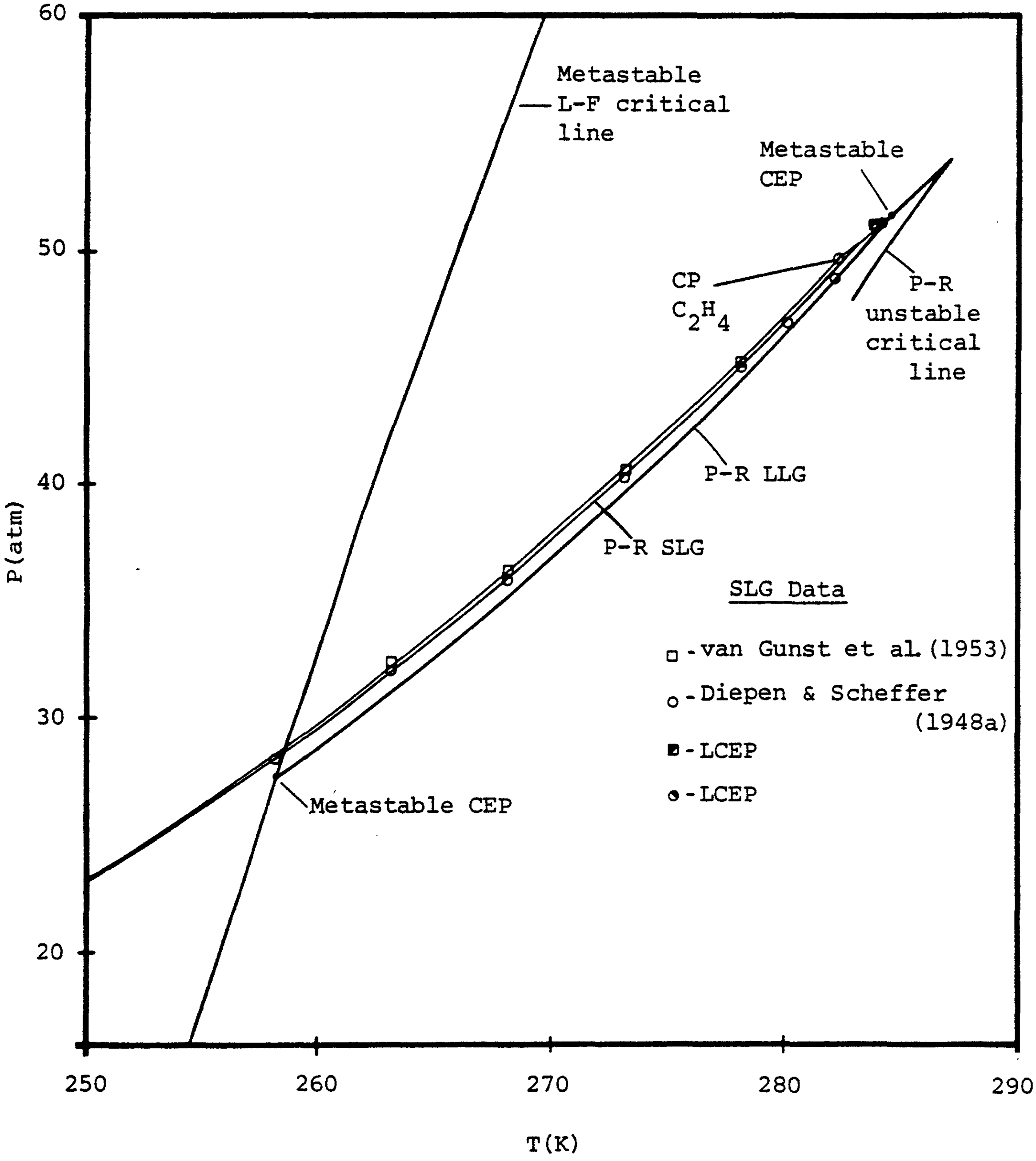

Figure 1.21. The P-T projection of the naphthalene - ethylene system in the vicinity of ethylene's critical point.

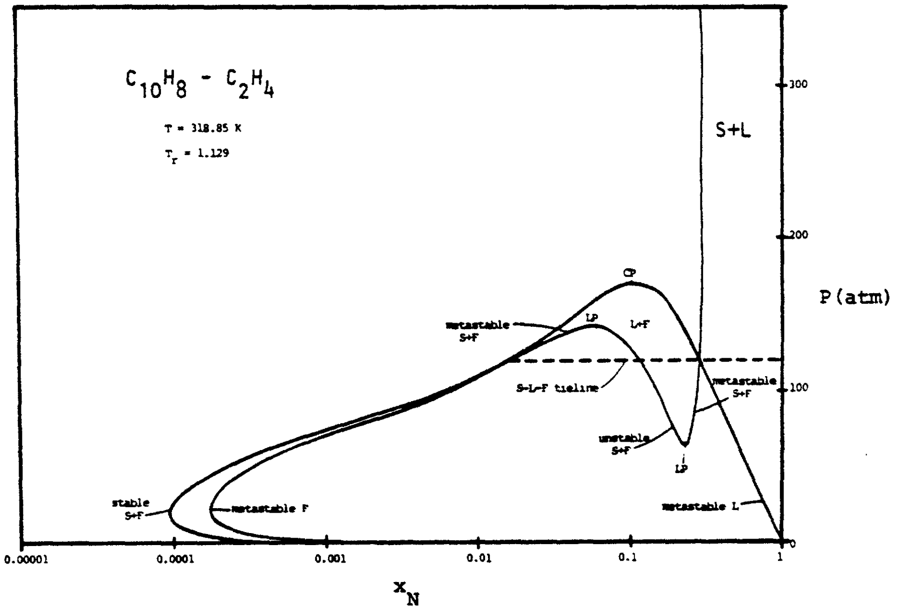

Figure 1.22. A P-x section between the UCEP and naphthalene's triple point.

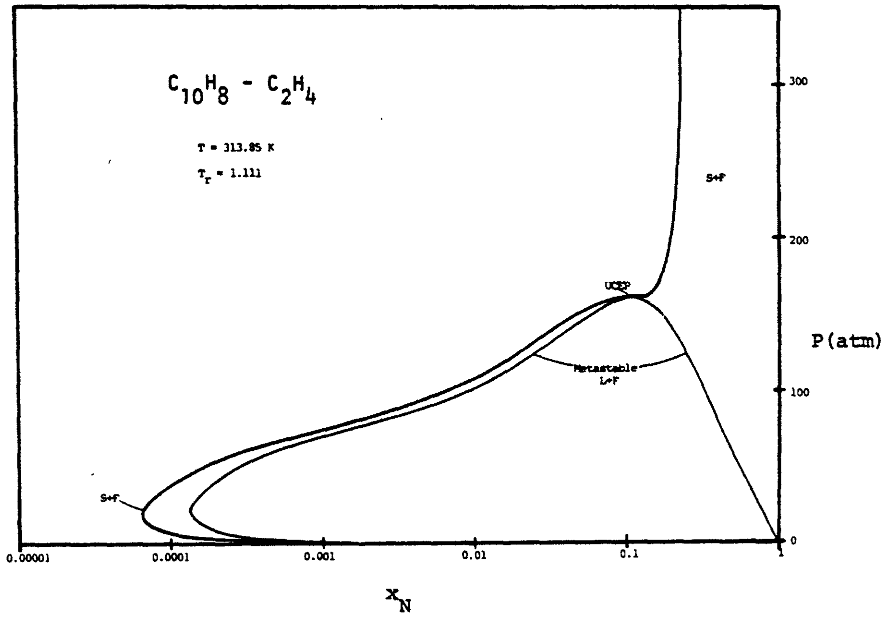

Figure 1.23. The P-x section at the upper critical end point temperature (approximately). The S+F binodal exhibits a point of horizontal inflection.

The presence of the LLG line in Figure 1.21 and the liquid-fluid binodals in Figure 1.22 emphasize the fact that the P-R equation predicts a complete fluid phase diagram for the system, and does not indicate the formation of solid. Solid phase equilibrium lines only result when the expression for solid fugacity is introduced, and these lines are in essence superimposed on the fluid phase diagram.

1.9. The Benzene - Water System

An interaction parameter for the benzene - water system was determined by matching the P-T coordinates of a single point along the experimental upper critical line. Figure 1.24 shows the critical line predicted for two different values of δ_{12}; the value chosen was $\delta_{12} = 0.052$. Although the upper critical line apparently exhibits the correct behavior, some qualitative discrepancies are encountered in the region of the lower critical line. Figure 1.25 shows the experimental P-T projection in the vicinity of benzene's critical point. The lower critical line begins at the benzene critical point, reaches a minimum temperature, and shortly thereafter intersects the LLG line at a critical end point. The dashed line represents the metastable continuation of the critical line. This "hypothetical"

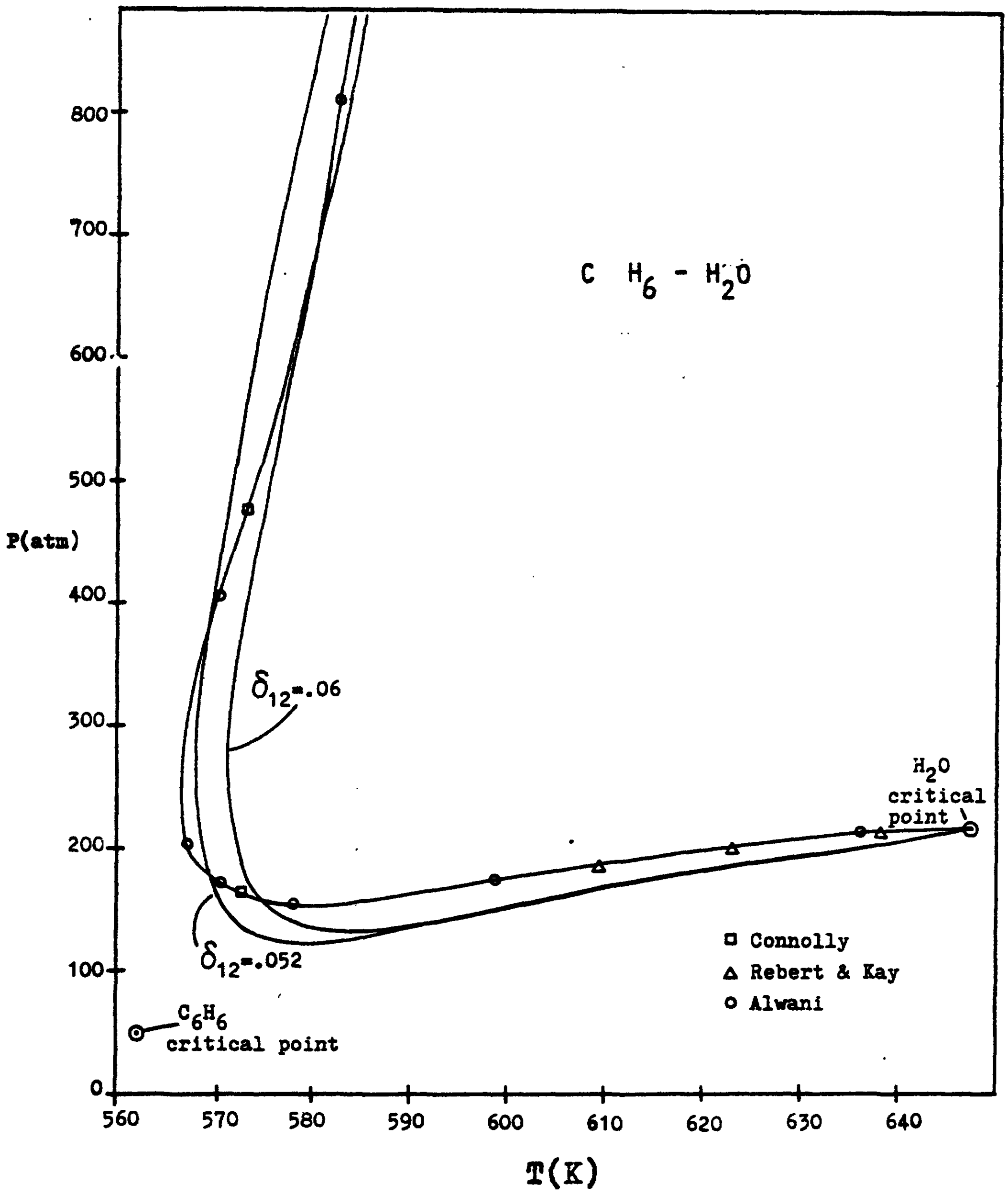

Figure 1.24. The P-T projection of the upper critical locus for benzene - water. The predicted curves are actually two separate segments (see Figures 1.25 and 1.27).

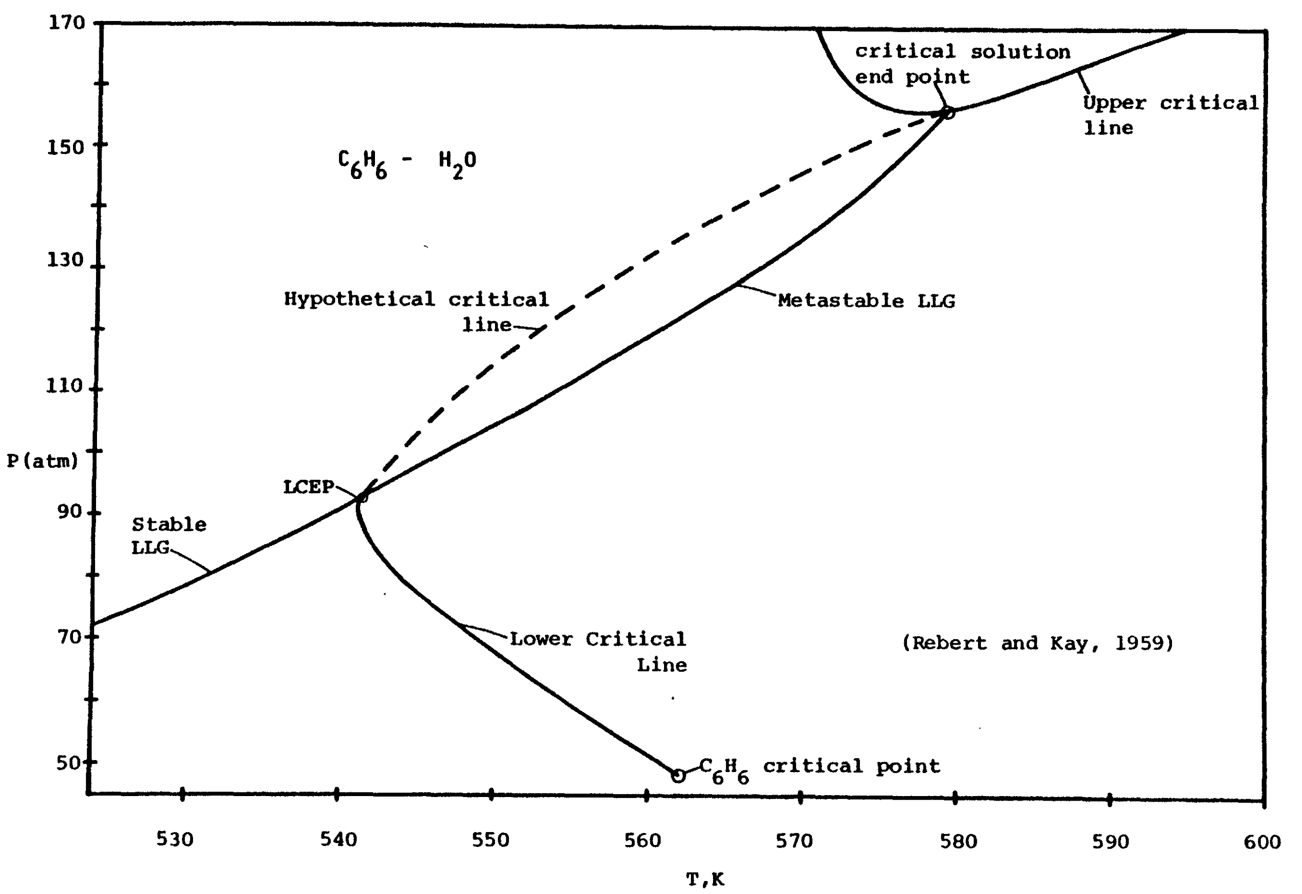

Figure 1.25. The experimental P-T projection of the benzene-water system in the vicinity of the pure benzene critical point. A small portion of the upper critical line of Figure 9.1 appears in this diagram.

critical line has been suggested by experimental work, but has not actually been measured. For this system, a "metastable" continuation of the LLG line past the LCEP has been determined. As shown in Figure 1.26, this line is reported to represent the intersection of two binodal regions, rather than three binodal regions as in Figure 1.8. As such, three phases would not coexist along this line. However, the line is continuous with the stable LLG line, and represents the course of that line had the critical phenomenon not intervened. The metastable LLG line terminates at a critical solution end point, simultaneously intersecting the L-L and L-G critical lines. The transition between the L-L and L-G critical lines has been drawn as smooth, although experimental measurements indicate that this is not actually true. No measurements of the L-L critical line are available in this region to indicate its correct shape, however.

Figure 1.27 gives the calculated P-T projection in the vicinity of benzene's critical point. The critical curve starting from the pure water critical point (cf. Figure 1.24) does not intersect the liquid-liquid critical line, but rather reaches a minimum in temperature and then returns to the benzene critical point. The liquid-liquid critical line on the other hand reaches a minimum in pressure shortly before being terminated by an unstable critical line. The figure also shows the three-phase LLG line which terminates

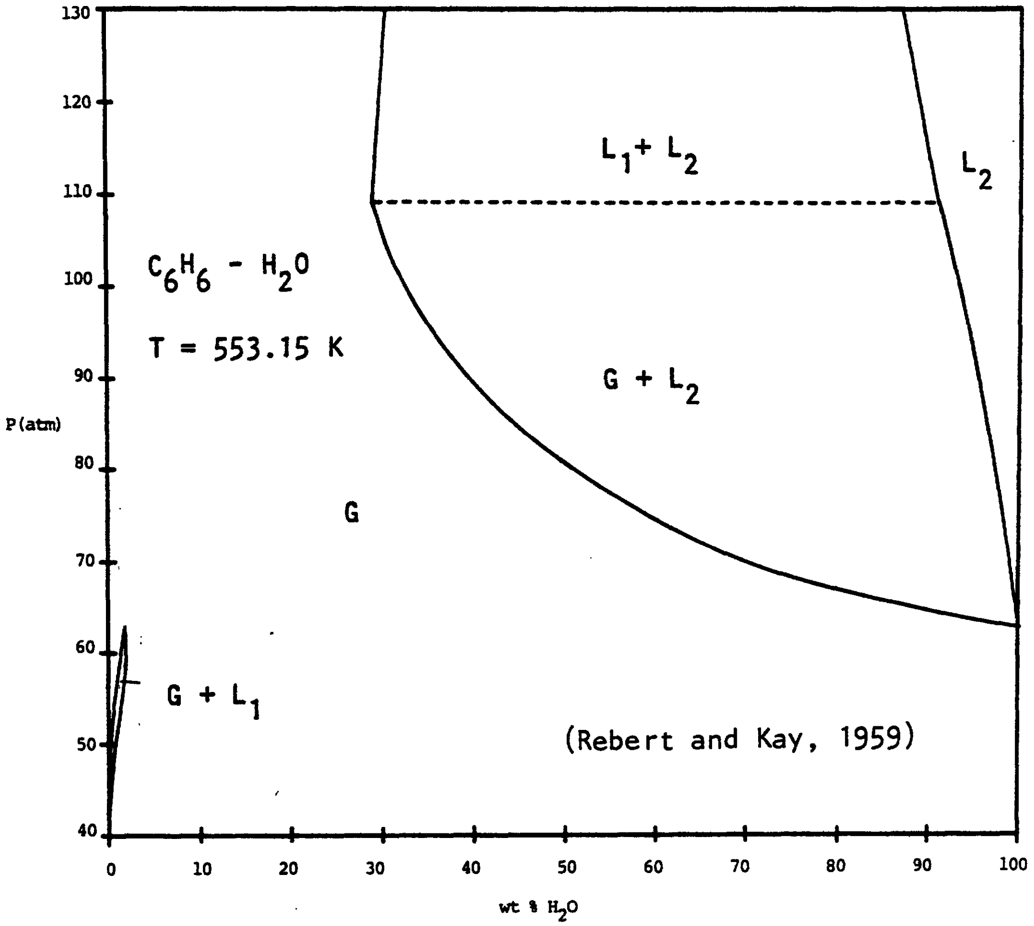

Figure 1.26. A P-x section between the LCEP and benzene's critical point.

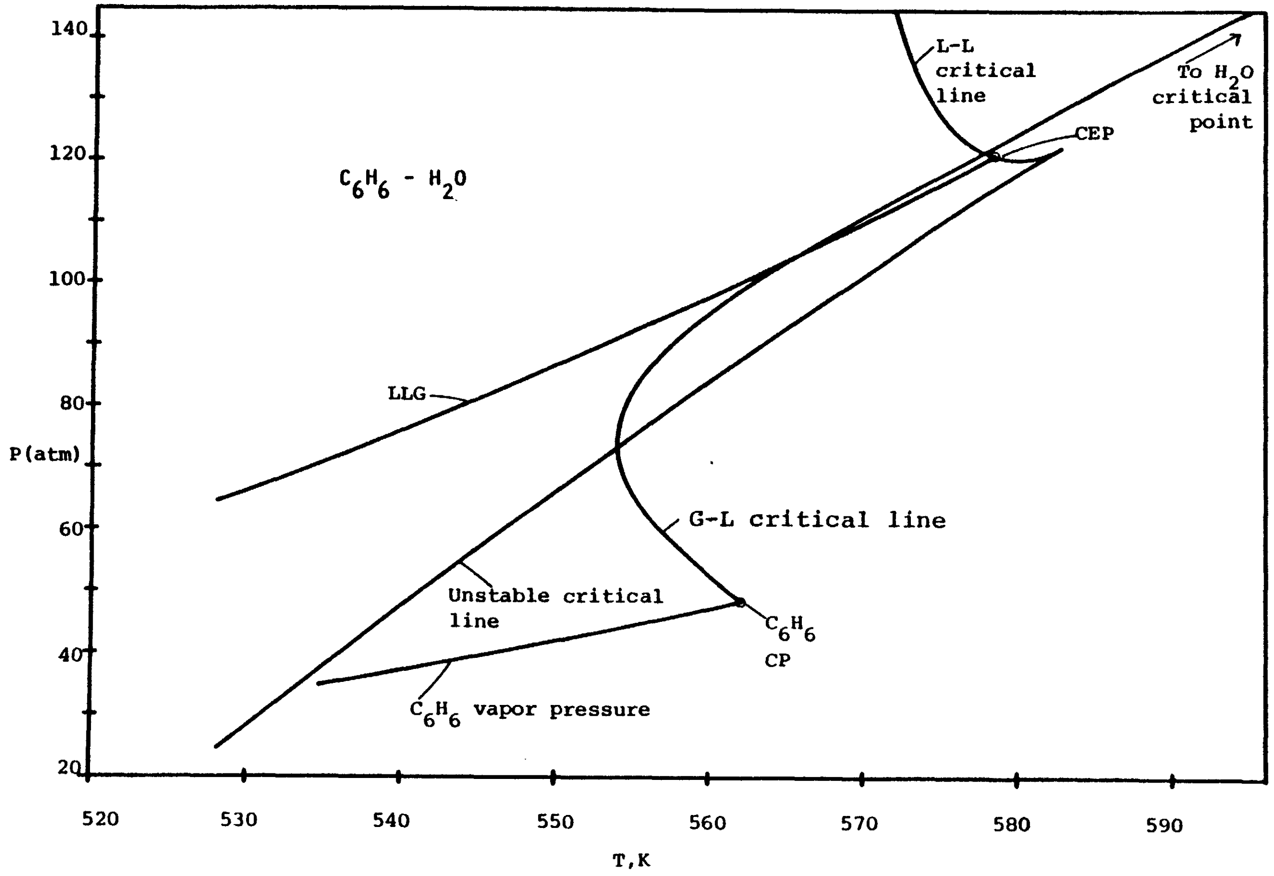

Figure 1.27. The predicted P-T projection of the benzene - water system in the vicinity of the pure benzene critical point.

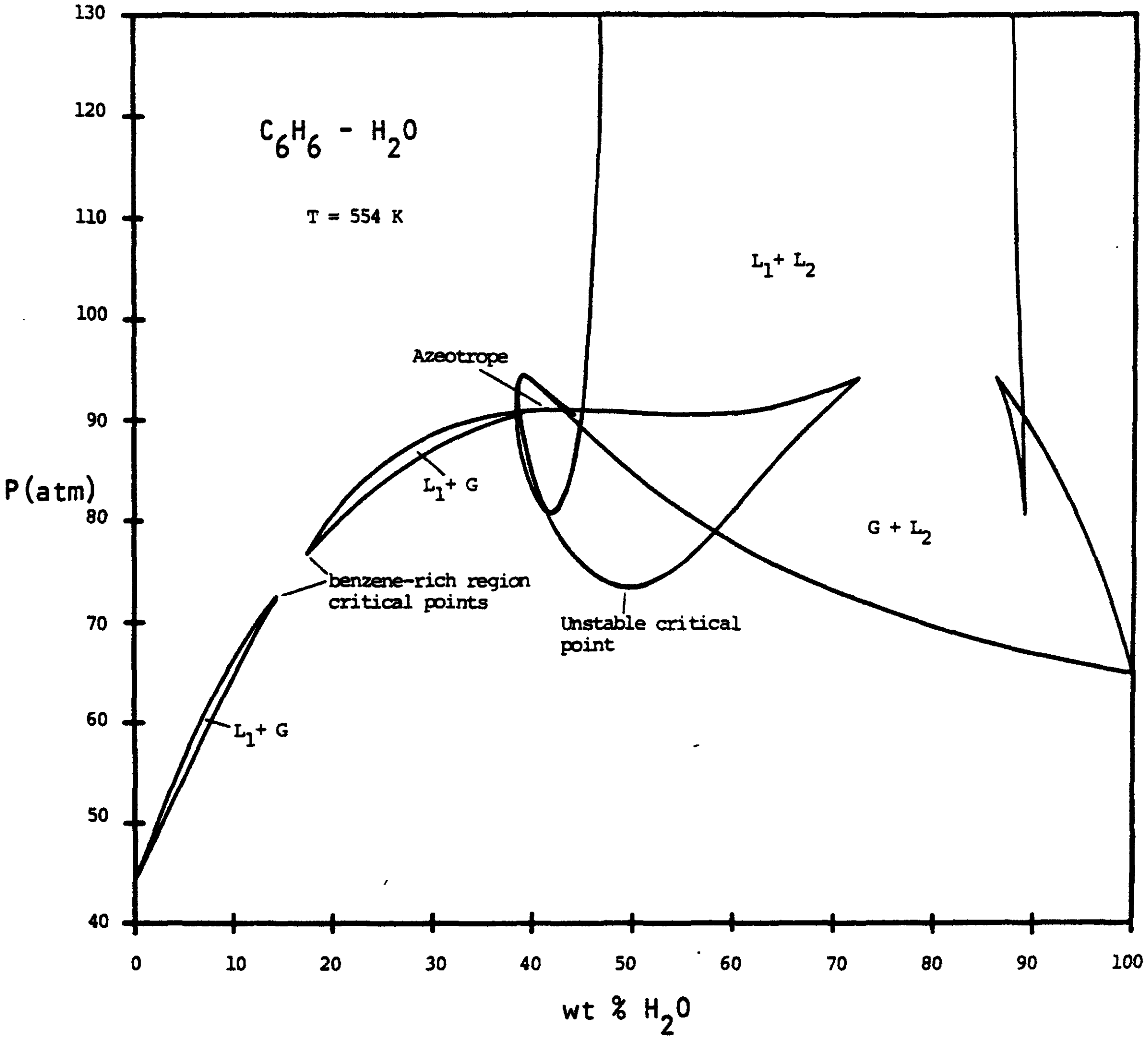

Figure 1.28. A P-x section slightly above the temperature minimum in the G-L critical line of Figure 1.27.

at a critical end point on the LL critical line. The short segment of the LL critical line between the CEP and the point of the cusp where the unstable critical line is joined is metastable.

The experimental and predicted P-T projections differ in that the former depicts a metastable portion of the LLG line, corresponding to the intersection of two binodal regions. However, data were taken on a fairly coarse grid, and a third binodal region of limited extent may well have gone undetected. The equation of state predictions indicate that very careful measurements are necessary to determine the stability or metastability of the LLG line up to the critical solution end point. At present it is not possible to say which of the two P-T projections is correct.

Figure 1.28 gives a predicted P-x section for this system, at a temperature slightly above the temperature minimum in the G-L critical line of Figure 1.27. Note the prediction of a stable azeotrope. Although the experiments were not detailed enough to verify this, a stable azeotrope necessarily exists in this system.

1.10. Conclusions

Knowledge of the overall phase behavior of systems is of importance in process design, since it indicates under what conditions a phase equilibrium process is most favorably carried out. For example, supercritical extraction of naphthalene with ethylene should probably be carried out near the UCEP rather than the LCEP. Although the pressures required are 3.5 times as high (174 atm versus 51 atm), the solubility of naphthalene is 85 times as high (0.17 versus 0.002 mole fraction). As a further example, suppose it was desired to dissolve benzene in water. The shape of the upper critical line for this system shows that conditions of about 300°C and 170 atm are sufficient to yield complete miscibility of these two substances.

In developing a methodology to predict overall P-T-x diagrams, a number of significant results were obtained. These are as follows:

-Fugacity-composition plots provide an excellent means of representing the possible types of stable and metastable phase equilibrium at a given temperature and pressure.

-If the material stability criterion reaches a point of discontinuity in the tracking of a stable system, that point may represent a limit of mechanical stability. This is true even if the material stability criterion is satisfied on either side of the discontinuity.

-Material stability should be considered undefined in a region of mechanical instability, since alternate statements of the material stability criterion may give conflicting information in such a region.

-When the cubic equation has multiple roots, P-x and T-x sections may correctly indicate the existence of stable states within a region bounded by spinodal curves.

-In critical point determinations, the criterion M1=0 may be replaced by the alternate criterion

$$\left(\frac{\partial L1}{\partial x}\right)_{T,P} = 0.$$

-An unstable critical point may be identified as the terminus of an unstable binodal locus. Alternatively, $\left(\frac{\partial^2 L1}{\partial x^2}\right)_{T,P}$ is greater than zero for a stable critical point and less than zero for an unstable critical point.

-A necessary and sufficient criterion for the existence of a critical end point is the occurrence of a horizontal inflection point in the stable binodal locus in a P-x or T-x section.

-Solution of the two-phase equilibrium problem is sufficient for the determination of three-phase equilibrium, since three-phase equilibrium results from the intersection of binodal loci.

From the systems investigated, the following conclusions have been drawn:

-The Peng-Robinson equation, with a single, constant interaction parameter, gives a qualitatively correct representation of phase behavior over the entire fluid region for nonpolar binary systems. The system may be nonideal with respect to molecular size of the components.

-The Peng-Robinson equation, with a single, constant interaction parameter, gives a reasonably correct representation of phase behavior over the entire fluid region for binary systems with one polar component. The qualitative picture may be incorrect in certain minor details.

-Semiquantitative predictions may be obtained in any region of interest by choosing an appropriate interaction parameter. In particular, the supercritical fluid region is amenable to such treatment.

-Analysis of fugacity-composition plots allows the development of phase equilibrium algorithms suitable for any region of the phase diagram.

-Metastable and unstable solutions to the phase equilibrium equations are always associated with three-phase equilibrium in a binary system. The solutions may exist over a substantial region of the P-T-x space, and if not accounted for can lead to erroneous predictions.

The significance of the last two conclusions for computer calculations of phase equilibrium must be strongly emphasized. Algorithms which fail to account for the behavior of the fugacity functionality are liable to experience convergence problems when this functionality takes on a complex shape. Complex shapes are found in three-phase regions, as well as near azeotropic coordinates and pure vapor pressure curves. Similarly, algorithms which fail to account for all phase equilibrium solutions to an equation of state may converge to an incorrect result. Erroneous prediction of both binodal curves and critical lines may occur. Careful development and application of phase equilibrium algorithms is necessary to avoid these difficulties.

Taken as a whole, the above conclusions indicate that a simple, cubic equation of state is well suited to an orienting or preliminary study of binary phase behavior. The minimal computing time required by these equations makes them an excellent choice for such an application. The preliminary study maps out regions where more detailed investigation, in both the theoretical and experimental sense, is warranted.

From the theoretical standpoint, once these regions have been defined, it may in some cases be desirable to switch to a more accurate equation of state. In other cases the cubic equation will provide sufficient accuracy with only a change in the interaction parameter. From the experimental standpoint, the preliminary study indicates the regions where further data should be taken, and how carefully it need be taken. It also serves as a check on the consistency of experimental results.

Chapter 2 Introduction

This thesis is concerned with the generation of binary phase diagrams from a cubic equation of state over extensive ranges of temperature and pressure. Research on this topic was motivated by the unique solvent properties exhibited by a substance somewhat above its critical temperature and pressure, known as a supercritical fluid. Supercritical fluid technology is a relatively recent development. Effective evaluation and use of the technology is aided by knowledge of a system's overall phase behavior. The generation of phase diagrams requires firstly a familiarity with the diagrams, and secondly, a mathematical model, the equation of state, as a means of prediction. This chapter includes a survey of these topics.

Chapter 2 considers the theoretical basis for phase equilibrium predictions, and Chapter 3 illustrates these as applied to pure component systems. Chapters 4 through 7 present the results of this work, calculated phase diagrams covering the complete range of fluid phase behavior for four binary systems. Chapter 8 sums up the conclusions drawn from these results, and gives recommendations for future work.

2.1 Supercritical Fluids

The first published observation of the solubility of solids in supercritical fluids was given by Hannay and Hogarth in 1879. Working with a number of different solutes and solvents, they noted the high sensitivity of the solubility to changes in temperature and presssure. Geochemists, concerned with the transport of minerals below the earth's surface by pressurized steam, were probably the first to realize the practical importance of supercritical phase behavior. Niggli discussed this topic as early as 1912, and by the 1930s, considerable experimental work had been undertaken.

Table 2.1 lists some proposed uses of supercritical fluids which are of interest to the chemical processing industries. Messmore (1943) was apparently the first to suggest an engineering application of supercritical solvents, a process for the removal of heavy components from crude oil. Since that time a number of other supercritical fluid processes have been proposed, but only within the past two decades have these proposals been economically practicable. A milestone was reached in June of 1978, with the convening of the first symposium on extraction with supercritical fluids (Wilke, 1978). That year also saw the industrial commercialization of a coffee decaffeination process using supercritical carbon dioxide, a process discovered by Zosel

Table 2.1

Proposed Supercritical Fluid Processes

Process	Supercritical Solvent	Reference
Removal of asphaltenes from oil	Hydrocarbons	Messmore (1943)
Removal of asphaltenes from oil	Propane	Zhuse & Kapelyushnikov (1955)
Extraction of lanolin from wool grease	Hydrocarbons	Zhuse, Yushkevic, & Gekker (1958)
Supercritical fluid chromatography	Carbon Dioxide	Sie, et al. (1966)
Decaffeination of coffee	Carbon Dioxide	Zosel (1970)
Extraction of coal	Toluene	Wise (1970)
Enhanced oil recovery	Carbon Dioxide	Huang & Tracht (1974)
Supercritical fluid chromatography	Various solvents, e.g. Pentane, Isopropanol	Klesper (1978)
Removal of nicotine from tobacco	Carbon Dioxide	Hubert & Vitzthum (1978)
Extraction of flavor components from hops, spices & cocoa	Carbon Dioxide	Hubert & Vitzthum (1978)
Extraction of oil seeds	Carbon Dioxide	Hubert & Vitzthum (1978)
Regeneration of activated carbon	Carbon Dioxide	Modell (1978)
Purification of dredge spoils	Water	Modell (1979)
Reforming of forest products	Water	Modell (1980)

in 1970.

In theory, any solvent with a chemically stable critical point may be used as a supercritical solvent. Table 2.1 includes the examples of water, toluene, and other hydrocarbons. However, the class of supercritical solvents also includes substances which are gaseous at normal conditions, such as carbon dioxide and ethylene. Table 2.2 (Klesper, 1978) lists critical data for some of the substances which have been suggested for use as supercritical solvents. The state of each substance at ambient conditions is indicated by its boiling point.

Supercritical solvents possess physical properties ranging between those of gases and liquids, and it is for this reason that the term fluid is used. Table 2.3 (Gouw and Jentoft, 1972) lists some typical physical properties of gases, liquids, and supercritical fluids. Note that the table only gives ranges for the properties of supercritical fluids; an important characteristic of a supercritical fluid is that its properties are highly variable for small changes in temperature and pressure.

Table 2.3 indicates that supercritical solvents have a substantially higher self-diffusivity than normal liquids. Higher rates of mass transfer are to be expected in a supercritical solvent, and such an effect has indeed been

Table 2.2

Physical Constants of Supercritical Solvents[a]

	Boiling Point (°C)	Critical Point Data		
	(at 1 atm)	T_c (°C)	P_c (atm)	ρ_c (kg/m^3)
CO_2	-78.5	31.3	72.9	448
NH_3	-33.4	132.3	111.3	240
H_2O	100.0	374.4	226.8	344
Methanol	64.7	240.5	78.9	272
Ethanol	78.4	243.4	63.0	276
Isopropanol	82.5	253.3	47.0	273
Ethane	-88.0	32.4	48.3	203
n-Propane	-44.5	96.8	42.0	220
n-Butane	- 0.5	152.0	37.5	228
n-Pentane	36.3	196.6	33.3	232
n-Hexane	69.0	234.2	29.6	234
2,3 Dimethylbutane	58.0	226.8	31.0	241
Benzene	80.1	288.9	48.3	302
Dichlorodifluoromethane	-29.8	111.7	39.4	558
Dichlorofluoromethane	8.9	178.5	51.0	522
Trichlorofluoromethane	23.7	196.6	41.7	554
1,2-Dichlorotetrafluoroethane	3.5	146.1	35.5	582
Chlorotrifluoromethane	-81.4	28.8	39.0	580
Nitrous oxide	-89.0	36.5	71.4	457
Diethyl ether	34.6	193.6	36.3	267
Ethyl methyl ether	7.6	164.7	43.4	272

a - Klesper (1978)

Table 2.3

Physical Properties of Gases, Liquids, and Supercritical Fluids

Property	Symbol	Units	Gas	Liquid	Supercritical Fluid Phase
Density	ρ	(kg/m^3)	1	1000	100 - 900
Self-diffusivity	D	(m^2/s)	10^{-5}	5×10^{-10}	$10^{-6} - 10^{-8}$
Dynamic viscosity	η	$(kgm^{-1}s^{-1})$	10^{-5}	10^{-3}	$10^{-4} - 10^{-5}$

measured (Hubert and Vitzthum, 1978). In an extraction process, this leads to a reduced contact time. Likewise, the lower viscosity of supercritical solvents results in a lower pressure drop for continuous flow systems. The most important characteristic of a solvent, though, is its affinity for a given solute, which determines the solubility of the solute. This affinity, a result of intermolecular attractive forces, is highly dependent upon the distance between molecules. Near the critical point, small changes in temperature or pressure lead to sizeable changes in the fluid density, with concomitant changes in solubility characteristics. This phenomenon is best illustrated by an example.

Figure 2.1 (Modell, 1979) is a solubility "map" for the system naphthalene ($C_{10}H_8$) - carbon dioxide (CO_2) near the critical point of CO_2. Tracing a particular isobar in this diagram shows how the concentration of naphthalene in the carbon dioxide fluid phase varies with temperature. The lines in the diagram represent saturated solutions, i.e., there is always a pure solid naphthalene phase present (naphthalene's normal melting point is 80°C). Above about 75 atm an isobar gives the composition of a saturated CO_2 fluid in equilibrium with solid naphthalene. For any lower pressure, there is a temperature at which three phases coexist - pure solid, saturated liquid, and saturated vapor. The composition of the liquid and vapor at 65 atm are shown

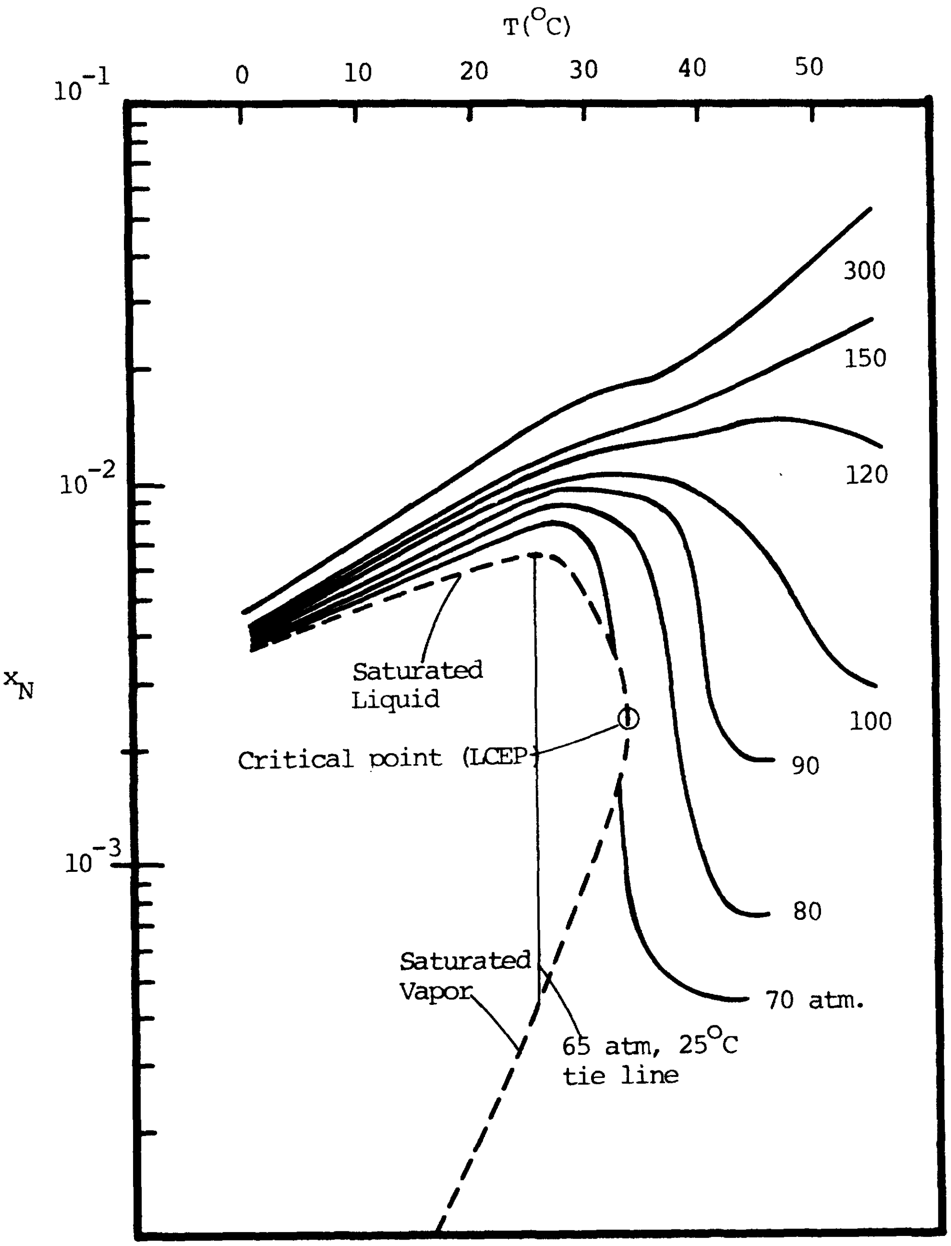

Figure 2.1. The solubility map for the naphthalene (N) - carbon dioxide system. Isobars indicate the mole fraction of naphthalene in solution. The dashed line corresponds to a three-phase solid-liquid-vapor equilibrium. This equilibrium terminates at LCEP, the lower critical end point.

in the figure by a tieline; the locus of all these tieline compositions for various pressures is given by the dashed line. If the solid-liquid-vapor (S+L+V) locus is traced to higher temperatures (and pressures), it is found that the liquid-vapor tielines converge to the critical point labelled in the diagram. At this point the near-critical liquid and near-critical vapor phases become indistinguishable, or, in other words, the vapor-liquid critical phenomenon is observed in the presence of a solid phase. The occurrence of the critical phenomenon between two phases in the presence of a third characterizes a special class of critical points known as critical end points. The critical point in Figure 2.1 is known as a lower critical end point (LCEP), a designation which will become clear in the discussion of phase diagrams (Section 2.2).

The effects of temperature and pressure on solubility may be observed in Figure 2.1. Along the 300 atm isobar, solubility increases continuously with temperature due to the increasing activity of the solid phase. At 55 $^{\circ}$C, the concentration of naphthalene in the supercritical fluid phase is about 5 mole percent, or 15 weight percent. While this compares unfavorably with traditional nonpolar solvents, it is nevertheless a significant quantity of naphthalene.

At 80 atm, solubility decreases sharply with temperature at about 35°C. This is the near critical region, where a slight increase in temperature leads to a large decrease in the density of the fluid. The fluid phase naphthalene concentration drops as the CO_2 loses much of its solvent power. Moving beyond the critical region toward higher temperatures, the density changes again become small and the isobar reverts to a positive slope.

The solubility phenomena in the supercritical fluid region provide the basis for the processes in Table 2.1. With the aid of Figure 2.1, it is easy to imagine how a supercritical fluid extraction process might work. At a supercritical temperature of 45°C, for example, CO_2 is compressed to 150 atm where it dissolves 2 mole percent of naphthalene from an inert substrate. The SCF carries the naphthalene to a collection vessel, at which point the pressure is reduced to 70 atm or less. The naphthalene solubility is lowered by a factor of 50, and it precipitates out as a pure solid. The CO_2 may now be pressurized and recycled. The fact that no distillation or purification step is required for solute recovery often results in an energy savings over conventional extraction operations.

It is important to note the modest pressures and temperatures at which a supercritical CO_2 extraction can be carried out. In the example of Figure 2.1, pressures below 300 atm and temperatures in the range of 30°C to 60°C would be suitable. The low temperature of this process is a main reason why CO_2 is one of the most promising of supercritical fluid solvents. It can be used to extract substances which are unstable at high temperatures. Combined with its nontoxicity and ready availability, supercritical CO_2 is an ideal extracting agent for food and pharmaceutical products. This fact is evidenced in Table 2.1. Availability of CO_2 is also a prime consideration in the enhanced oil recovery process of Table 2.1. The American petroleum companies researching this application intend to utilize CO_2 from natural underground reservoirs (Stalkup, 1978). The CO_2 will be pumped from the reservoir to an oil field, where it is injected into the oil bearing substrate. There it solubilizes and displaces the oil to bring it to the surface.

Water is another supercritical solvent with great promise. Its role in geochemical phenomena has been mentioned. Two applications, which appear in Table 2.1, have recently been suggested by Modell. Table 2.4 also gives a number of literature sources pertaining to the solvent properties of supercritical water. The solubility of a hydrocarbon in water will be investigated in Chapter 7, which deals with the benzene-water system.

The preceding paragraphs have indicated the importance and potential of supercritical fluids for chemical engineering applications. Evaluation of new and existing

Table 2.4

Literature Sources for Supercritical Water

Application	Reference
Solubility of wood	Woerner (1976)
Solubility of glass (silica)	Martynova (1976)
Solubility of hydrocarbons	Connolly (1966)
Solubility of argon	Lentz & Franck (1969)
Solubility of nitrogen	Tsiklis & Maslennikova (1965)
Solubility of salts	Niggli (1912)
Geochemical aspects	Morey (1957)

processes would be greatly facilitated if a means were available to predict supercritical solubility behavior. It is a goal of this thesis to investigate one such method. Before considering predictive methods, however, it is necessary to gain a more complete understanding of phase behavior in the critical region. This is best done graphically through the use of phase diagrams, the topic treated in the next section.

2.2 Phase Diagrams

The term "phase diagram" is generic in nature, being applicable to a graphic depiction of any of the properties of one or more phases in equilibrium. For single component systems, P-T, P-V, and P-ρ diagrams are most common. For binary systems, one of the most informative types of phase diagrams is the P-T-x space diagram, a three-dimensional representation of the relation between pressure, temperature, and composition. While such a diagram gives an excellent overview of the system's phase equilibrium behavior, it is difficult to extract actual P-T-x coordinates from such a diagram, and it is relatively time-consuming to draw. For this reason, two-dimensional slices or sections of the three-dimensional space diagram are most frequently used. These would be T-x (constant P), P-x (constant T), or P-T (constant x) diagrams. Another useful two-dimensional diagram results when lines in the space diagram are projected onto a plane. This results in either a P-T, P-x, or T-x projection, all of which have a particular utility. The term "P-T-x diagram" is used to refer to all two-dimensional projections and sections, as well as the three-dimensional space diagram. For binary systems, V-T-x diagrams are also quite common, but will not be considered in this work.

Phase diagrams may be drawn for various combinations of solid, liquid, or vapor phases. Solid phase diagrams have probably received the most attention, being of primary importance in the field of materials science. A good introduction to these types of diagrams may be found in the books by Reisman (1970) and Gordon (1968). In addition, the journal Calphad is a publication devoted entirely to the computer calculation of solid phase diagrams.

In the chemical processing industries, phase diagrams involving fluids are more often of interest. The term "fluid" includes both gases and liquids, as well as supercritical fluids. A relatively complete survey of fluid phase diagrams for binary mixtures has been given by Rowlinson (1969). Schneider (1970) has also reviewed the literature with emphasis on the critical region, which is of particular interest to this study. The phase diagrams presented by Rowlinson and Schneider are derived from the experimental work of numerous investigators. A study of these diagrams is necessary to obtain a complete understanding of the phase behavior of binary systems, and is indispensible in the interpretation of theoretical phase equilibrium predictions. Most of the phase diagrams in this section have been abstracted from the above references. In all diagrams, species B is the component with the higher critical temperature.

The simplest type of fluid phase behavior for a binary system is depicted in the P-T-x space diagram of Figure 2.2a. The dashed lines indicate the course of the pure component vapor pressure curves. At any given temperature, component A is more volatile (has a higher vapor pressure) than component B. The vapor pressure curves terminate at the pure component critical points CP_A and CP_B. As illustrated, component B has the higher critical temperature, but component A has the higher critical pressure. Systems in which the more volatile component has the lower critical pressure are also common. The two pure component critical points are joined by a continuous curve known as the critical line, which gives the locus of critical points of mixtures of the two components. Since for a given temperature liquid exists at pressures above those at which a vapor exists, it is clear that the region above the P-T-x surface of Figure 2.2a must correspond to a single phase liquid. Likewise, the region below the P-T-x surface represents a single gaseous phase.

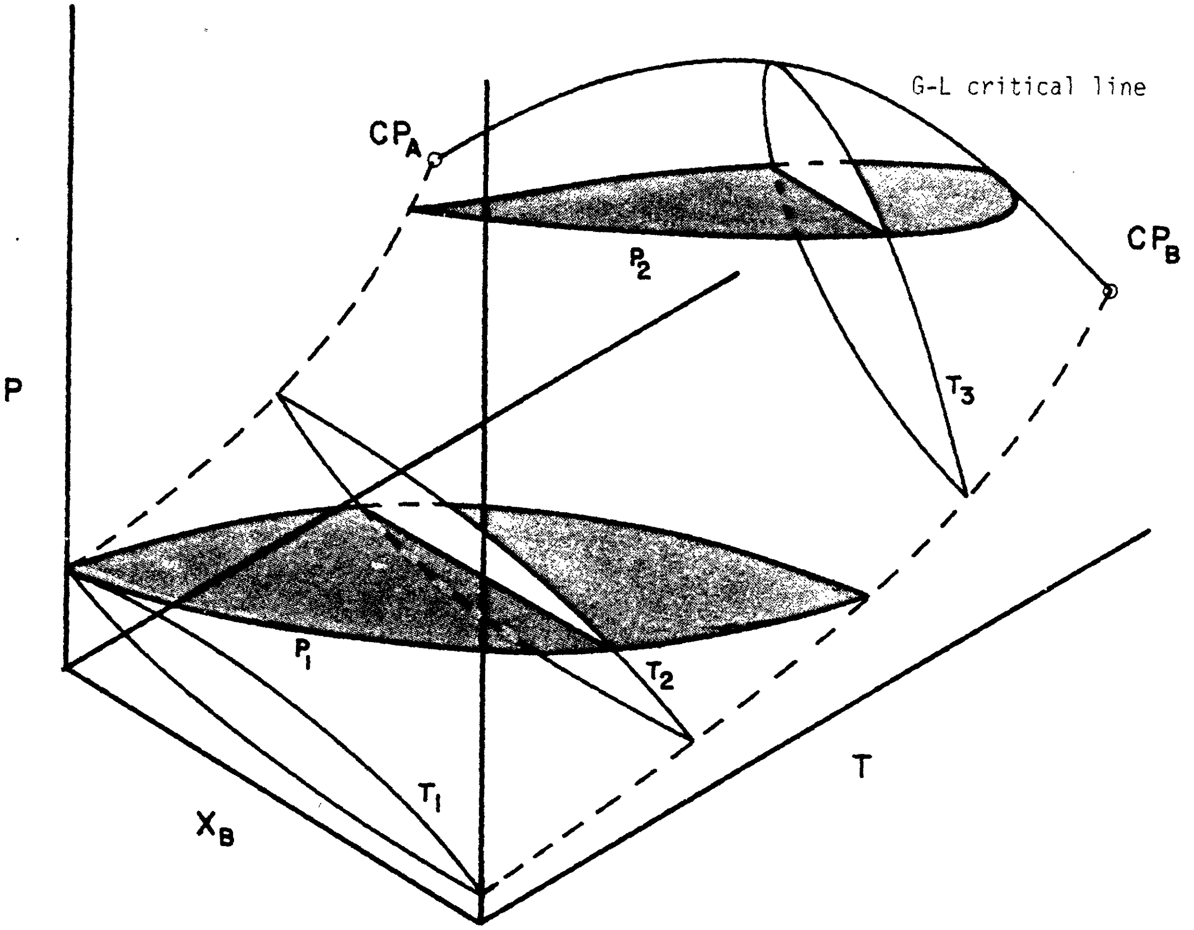

Figure 2.2a. The P-T-x space diagram for a system with completely miscible fluid phases. Vapor pressure curves, shown as dashed lines, terminate at the pure component critical points. These points are joined by the gas-liquid critical line for the mixture. Three unshaded P-x sections and two shaded T-x sections are shown.

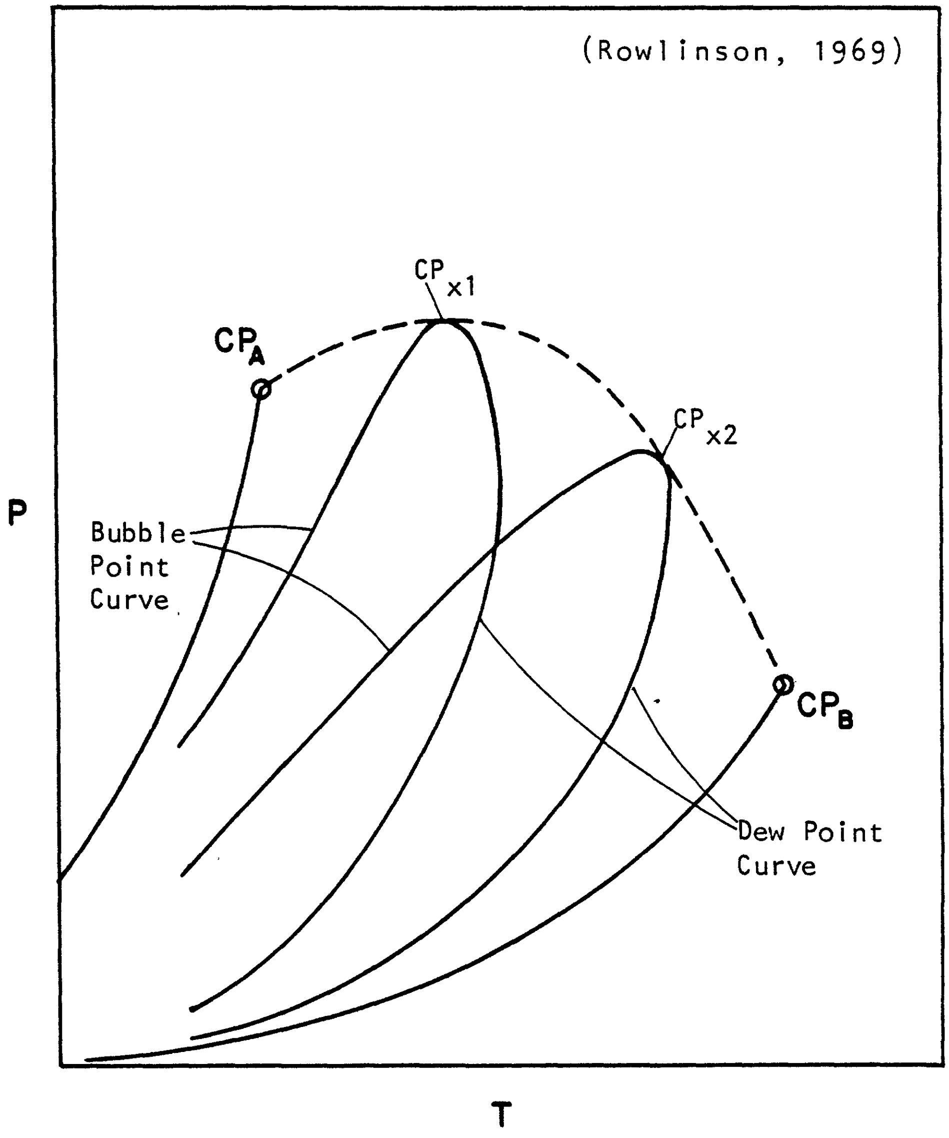

Figure 2.2b. P-T sections for a completely miscible system at compositions x1 and x2. Bubble point curves represent conditions at which the liquid first begins to vaporize. Dew point curves represent the onset of condensation.

Figure 2.2a includes three isothermal P-x sections (unshaded) and two isobaric T-x sections (shaded) to illustrate vapor-liquid equilibrium (VLE). The P-x section at T_1 lies below the critical temperature of both components, and thus terminates at either end along a pure component vapor pressure curve. To determine the compositions of the coexisting liquid and vapor, a tieline is drawn at constant pressure connecting the two branches of the VLE envelope. The points of intersection give the desired compositions. Again, since liquid must lie at higher pressures and gas at lower pressures, it is evident from the figure that the VLE liquid phase contains a greater proportion of component B than the VLE vapor phase. This is consistent with the lower volatility of component B.

At T_3, a temperature above CP_A, the VLE envelope no longer extends to the pure A axis. If at such a temperature tielines are drawn at successively higher pressures, a maximum pressure will be reached where the liquid and vapor legs join and the tieline converges to a point. This is the point on the critical line for the specified temperature. Since it is at a maximum pressure, the smoothness of the VLE envelope requires that it does not fall at a compositional extreme. At temperatures above the critical points of both components, only one phase is present and VLE envelopes no longer exist. For the T-x sections, VLE tielines are drawn at constant T. It follows that for a T-x section above the critical pressure of component B, the critical point falls at a maximum temperature and is not a compositional extreme.

A third possibility is to take a P-T section of the space diagram at constant composition. Figure 2.2b presents two such sections, at compositions x1 and x2. Tielines may not be drawn in a P-T section and, in general, the critical point is not located at either the maximum pressure or the maximum temperature of the VLE loop. As indicated in Figure 2.2b, however, the envelope of these loops does define the critical locus of the mixture. This fact is often used in the experimental determination of critical lines.

The critical curve in Figure 2.2a exhibits a pressure maximum. While such behavior is common, it is by no means universal. Figure 2.3 illustrates six types of P-T projections which have been found for critical lines connecting the pure component critical points. Type 1 corresponds to the critical behavior of Figure 2.2a. Type 2 is a monotonic critical line, found when the two components have fairly similar characteristics such as size, shape, and polarity. If the components are very similar the critical line may be nearly straight as with type 3 in the figure. Types 4 and 5 are critical lines with temperature minima, type 5 possessing as well a pressure maximum. Type 6 exhibits maxima in both temperature and pressure. Analogous

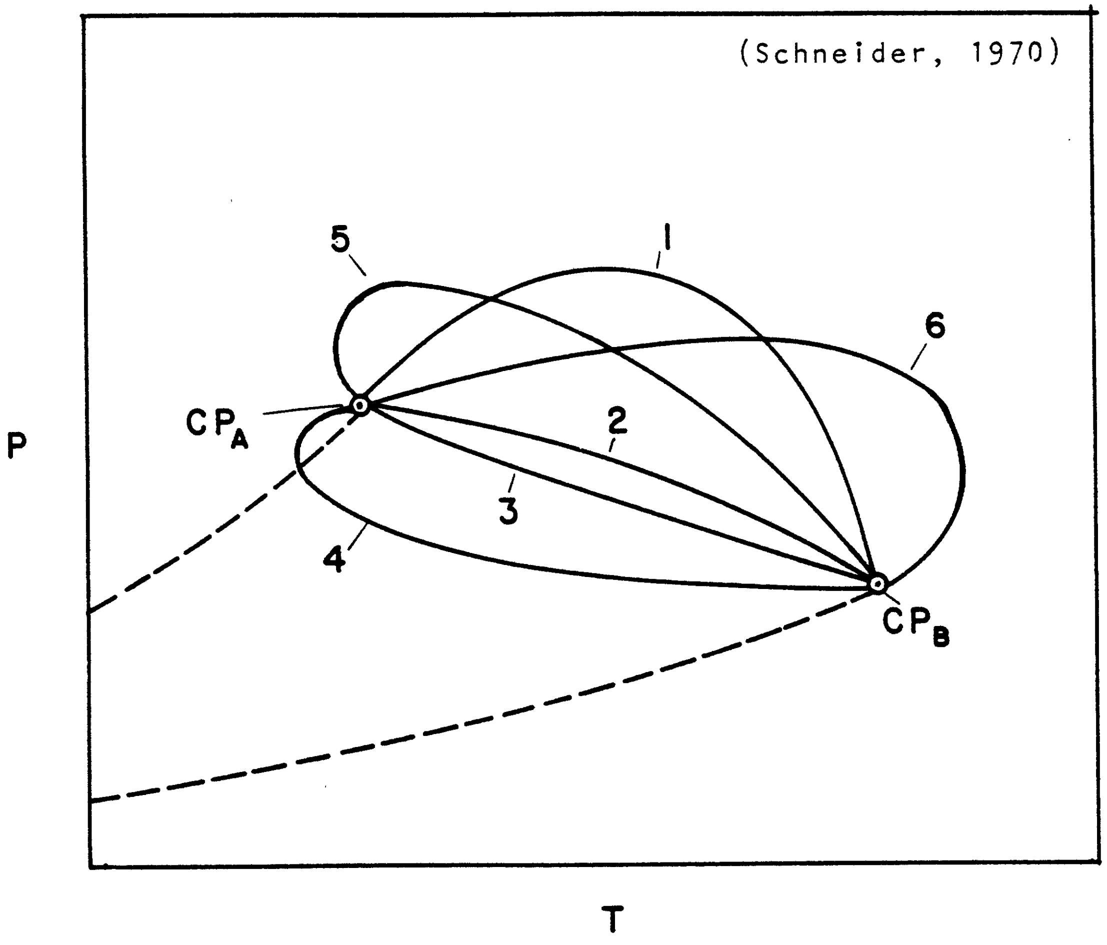

Figure 2.3. P-T projections of six types of critical curves which may connect the two pure component critical points.

critical curves are found when component A has a lower critical pressure than component B.

The systems considered thus far have been simple in that the liquid phases of the two components were completely miscible. Liquid phase immiscibilities may be manifested in a variety of ways. Figures 2.4 - 2.12 illustrate the range of behavior for such cases with both P-T projections and P-T-x space diagrams. The figures are ordered roughly by degree of miscibility.

Figure 2.4 shows the simplest type of liquid-liquid immiscibility, where the region of coexistence is a dome, entirely bounded by the VLE surface and a liquid-liquid critical line. This critical line represents the locus of upper critical solution pressures (at constant T) or upper and lower critical solution temperatures (at constant P). The immiscibility dome meets the VLE surface along a line in the P-T projection; this is the three-phase L-L-G line, which in turn intersects the L-L critical line at two critical end points. At a critical end point (CEP), the three-phase line terminates since two of the phases it represents become identical. The critical locus also terminates in the sense that it becomes metastable, a concept to be discussed in Chapter 2.

The liquid-liquid critical line in Figure 2.4 does not

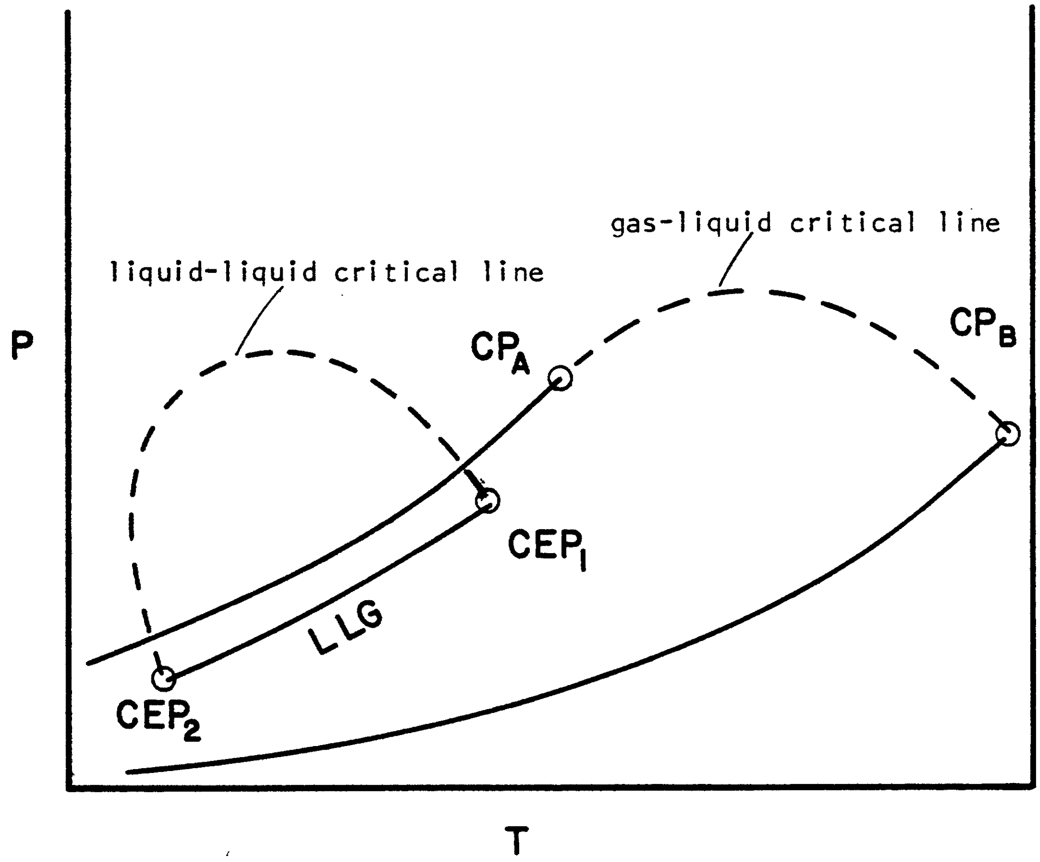

Figure 2.4a. The P-T projection for a liquid-liquid immiscibility dome. The liquid-liquid (L-L) critical line defines the top of the dome. It intersects the bubble point surface at two critical end points (CEPs). Each CEP represents a terminus of both the critical line and the three-phase LLG line.

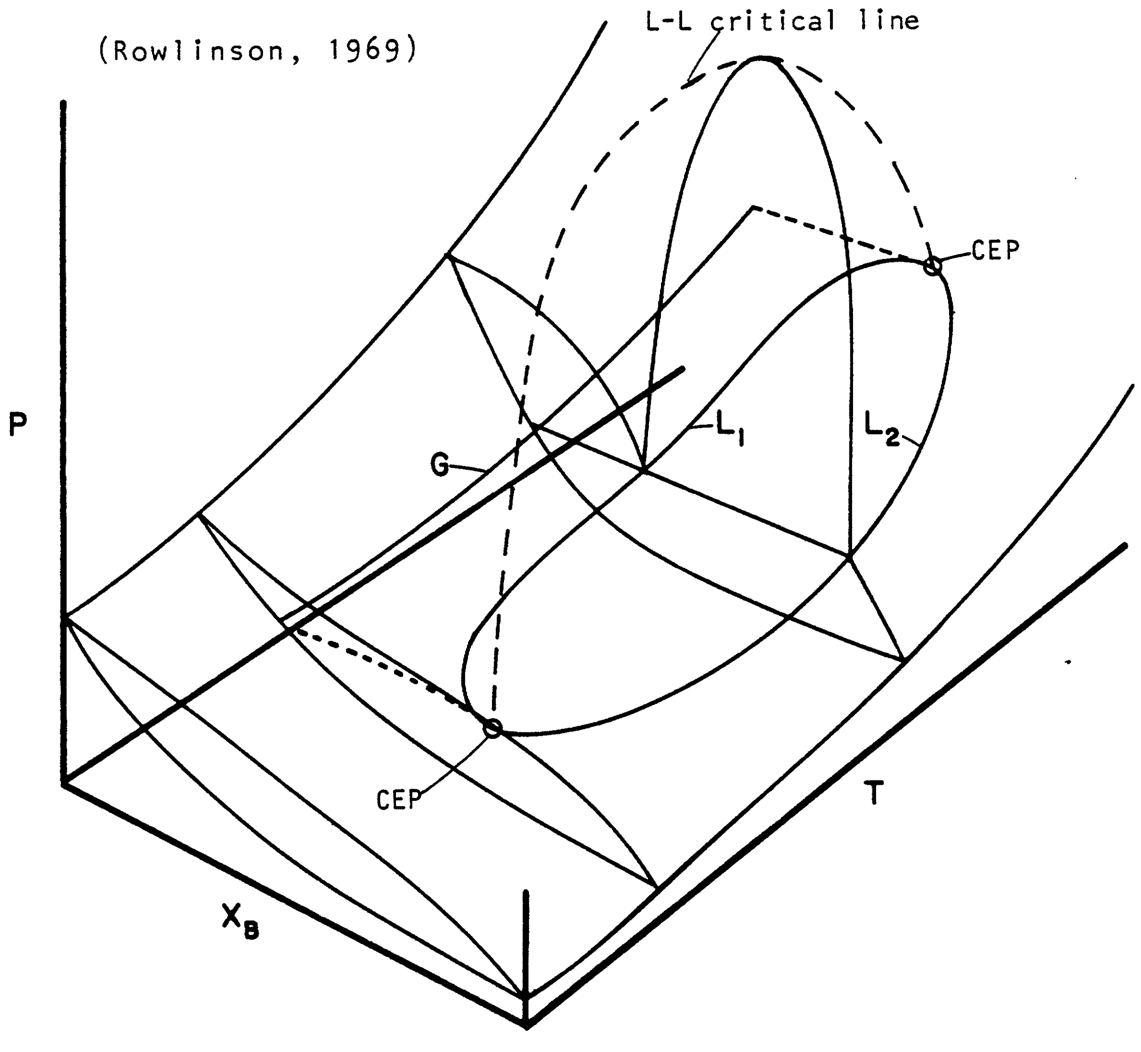

Figure 2.4b. The P-T-x space diagram for Figure 2.4a.

necessarily return to the VLE surface, but may continue to higher pressures as indicated in Figure 2.5. The line may be considered to represent upper critical solution temperatures (UCST's), and these temperatures may either increase or decrease as pressure increases. The figure shows the former case, i.e., $\frac{dP}{dT}$ is positive in the P-T projection, so that the liquid phase immiscibility extends to very high, possibly infinite, pressures. For $\frac{dP}{dT}$ negative, the UCST curve will eventually be terminated by the formation of a solid phase.

Substances less miscible than those just treated will exhibit immiscibility in the critical region of the more volatile component. Figure 2.6 illustrates such a situation. This is the first instance of the L-G critical line not connecting the two pure component critical points. Instead, the lower L-G critical line beginning from CP_A, terminates at the lower critical end point or LCEP. Similarly, the upper critical line starting at CP_B terminates at the upper critical end point or UCEP. Since the CEP's are joined by what is traditionally labelled an L-L-G three phase line, this upper critical line must be designated as liquid-liquid. Near CP_B, however, the upper critical line behaves much as the L-G critical line in a completely miscible system. For this reason, it is most accurate to refer to the upper critical line as a liquid-fluid or L-F critical locus.

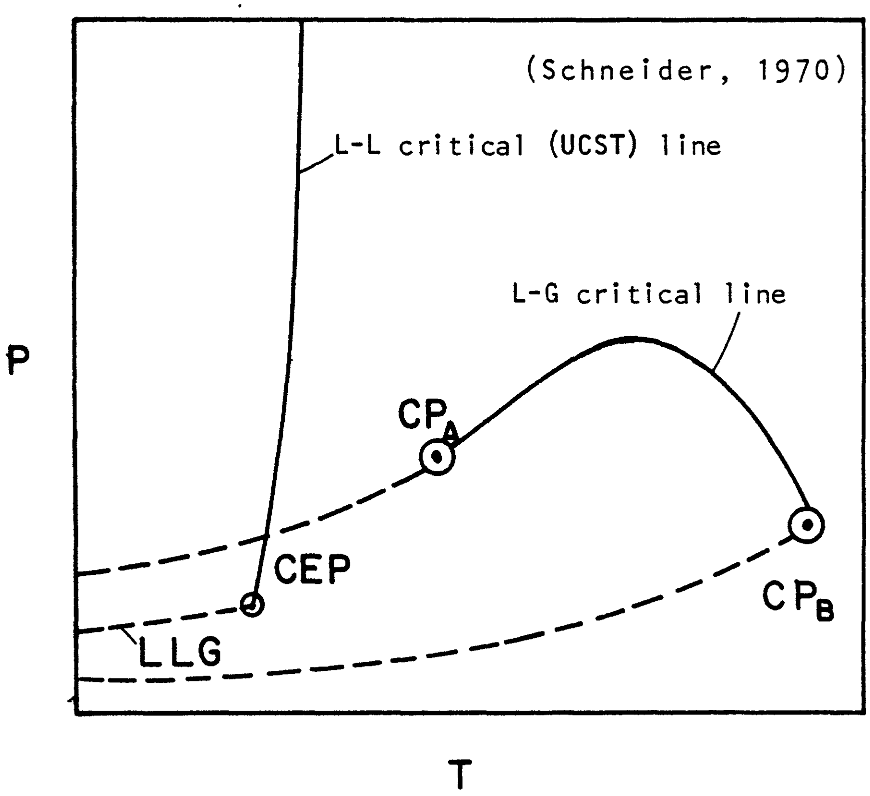

Figure 2.5a. The P-T projection for a system in which the liquid-liquid immiscibility extends to very high pressures.

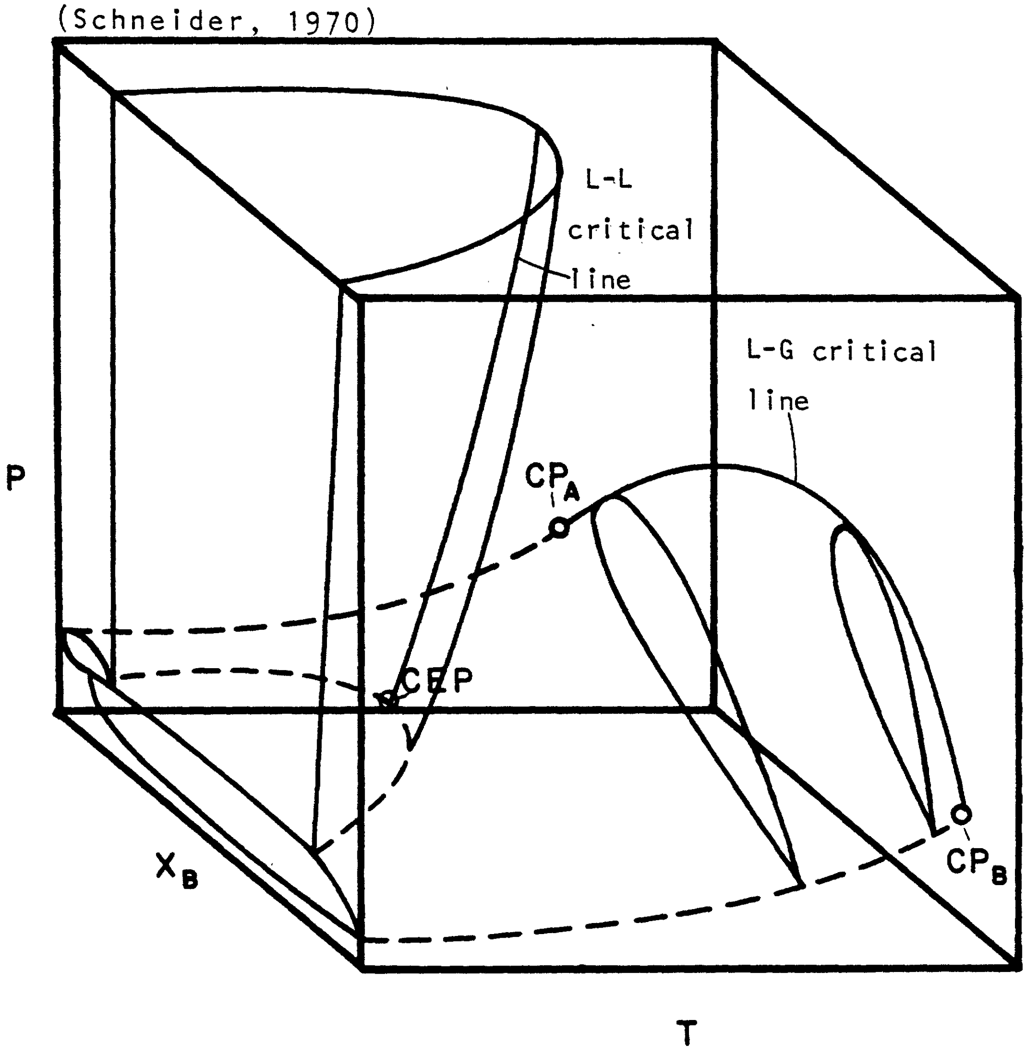

Figure 2.5b. The space diagram for Figure 2.5a.

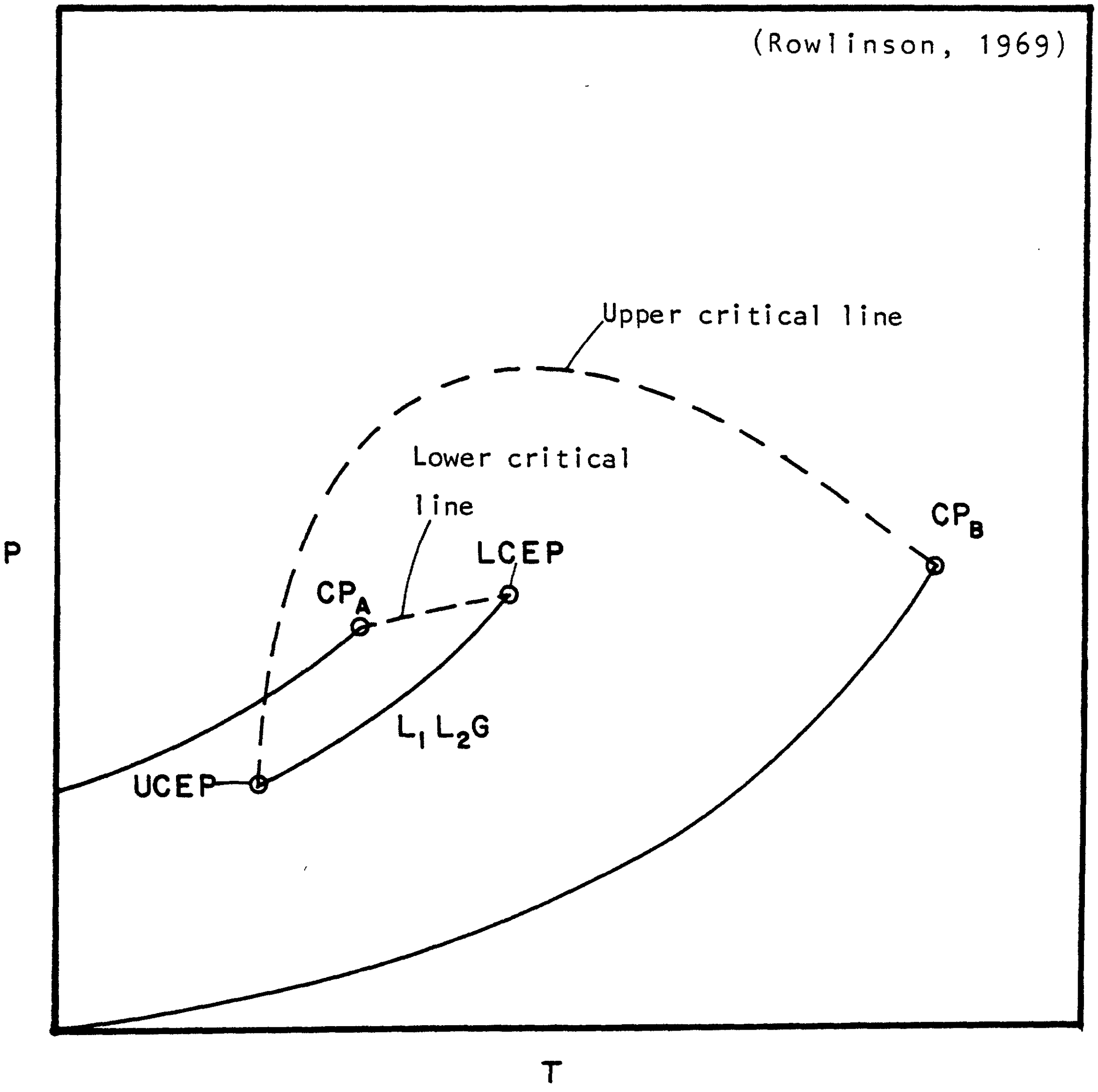

Figure 2.6a. The P-T projection for a system exhibiting immiscibility in the region of CP_A, the critical point of the more volatile component. The upper critical line terminates at the upper critical end point (UCEP), while the lower critical line terminates at the lower critical end point (LCEP). The L-L-G line also terminates at the CEP's. The diagram arbitrarily shows component B with a higher critical pressure than component A.

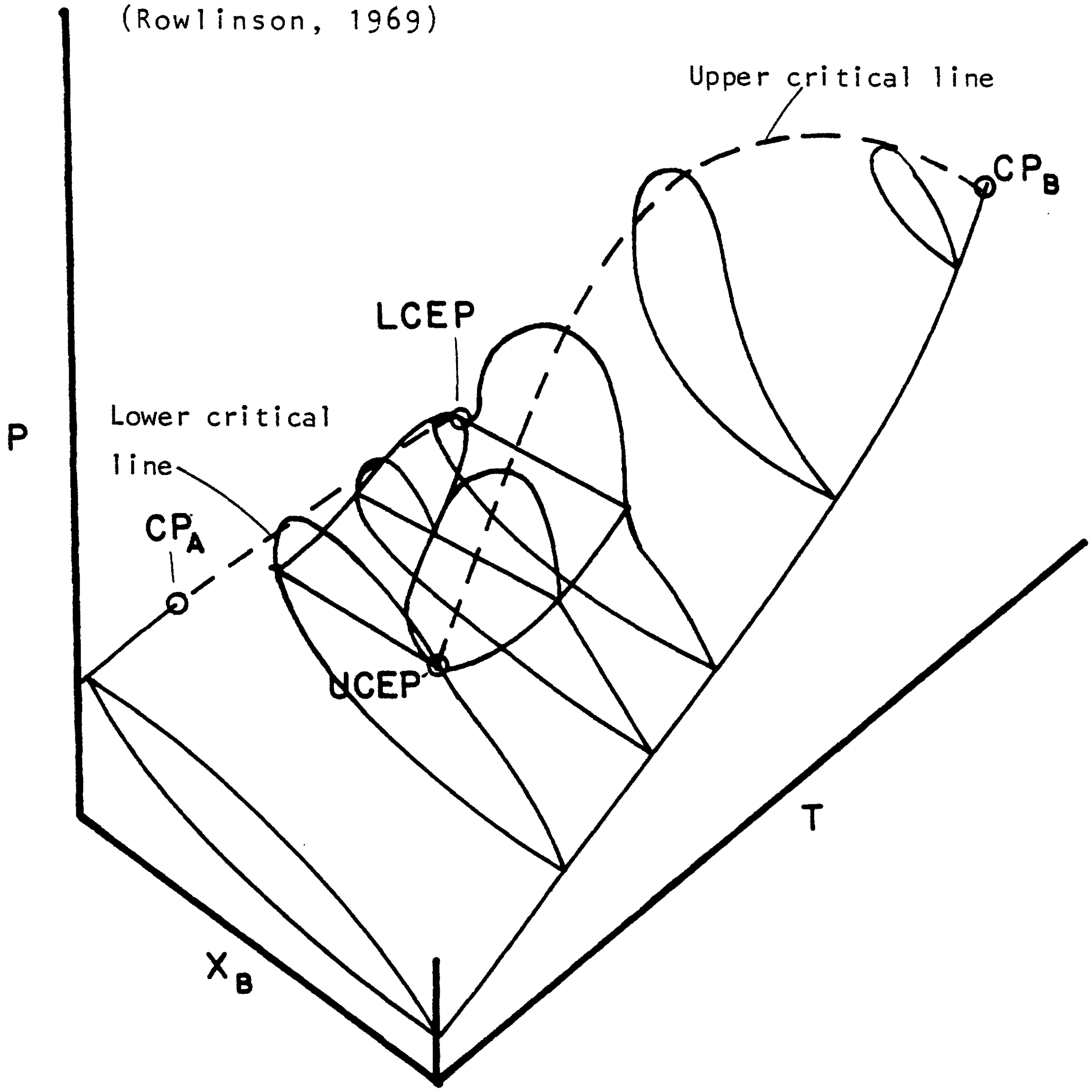

Figure 2.6b. The space diagram for Figure 2.6a.

Figure 2.7 is quite similar to 2.6, but with a second region of liquid-liquid immiscibility of the type illustrated in Figure 2.5. This system exhibits two separate L-L-G curves and three critical end points. As immiscibility increases still further, the UCST line moves to higher temperatures, finally intersecting and forming a smooth continuation to the upper critical locus. This situation is depicted in Figure 2.8. The system again has a single L-L-G curve, but now only one CEP in the fluid region. Figure 2.9 shows the behavior when the high pressure portion of the upper critical curve has a positive slope. The n-hexadecane - carbon dioxide system exhibits features of both Figures 2.8 and 2.9 (see Chapter 5). A further variation of this general type is found when the upper critical line exhibits only a minimum in pressure, rather than both a maximum and a minimum. This case is shown in Figure 2.10, again with the three-phase line at pressures above the pure component vapor pressures. The benzene-water system (see Chapter 8) belongs to this category.

For highly immiscible systems, the region of immiscibility persists up to the vicinity of the critical point of the less volatile component. The upper critical line may exhibit a temperature minimum, as shown in Figure 2.11, or proceed directly to higher temperatures as in Figure 2.12. Both types of upper critical lines have been referred

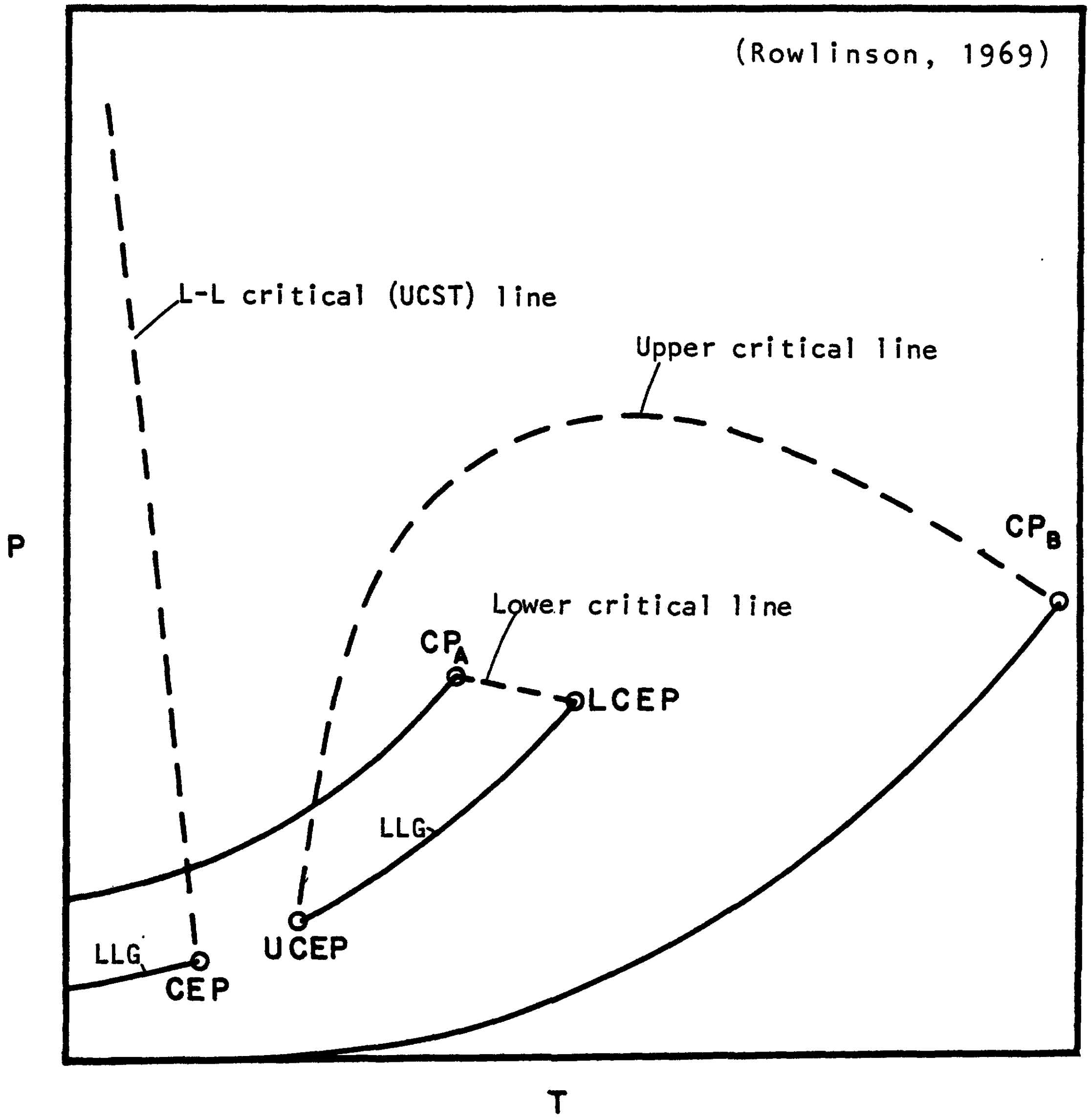

Figure 2.7a. The P-T projection for a system of the type shown in Figure 2.6, but with a separate region of liquid-liquid immiscibility.

(Schneider, 1970)

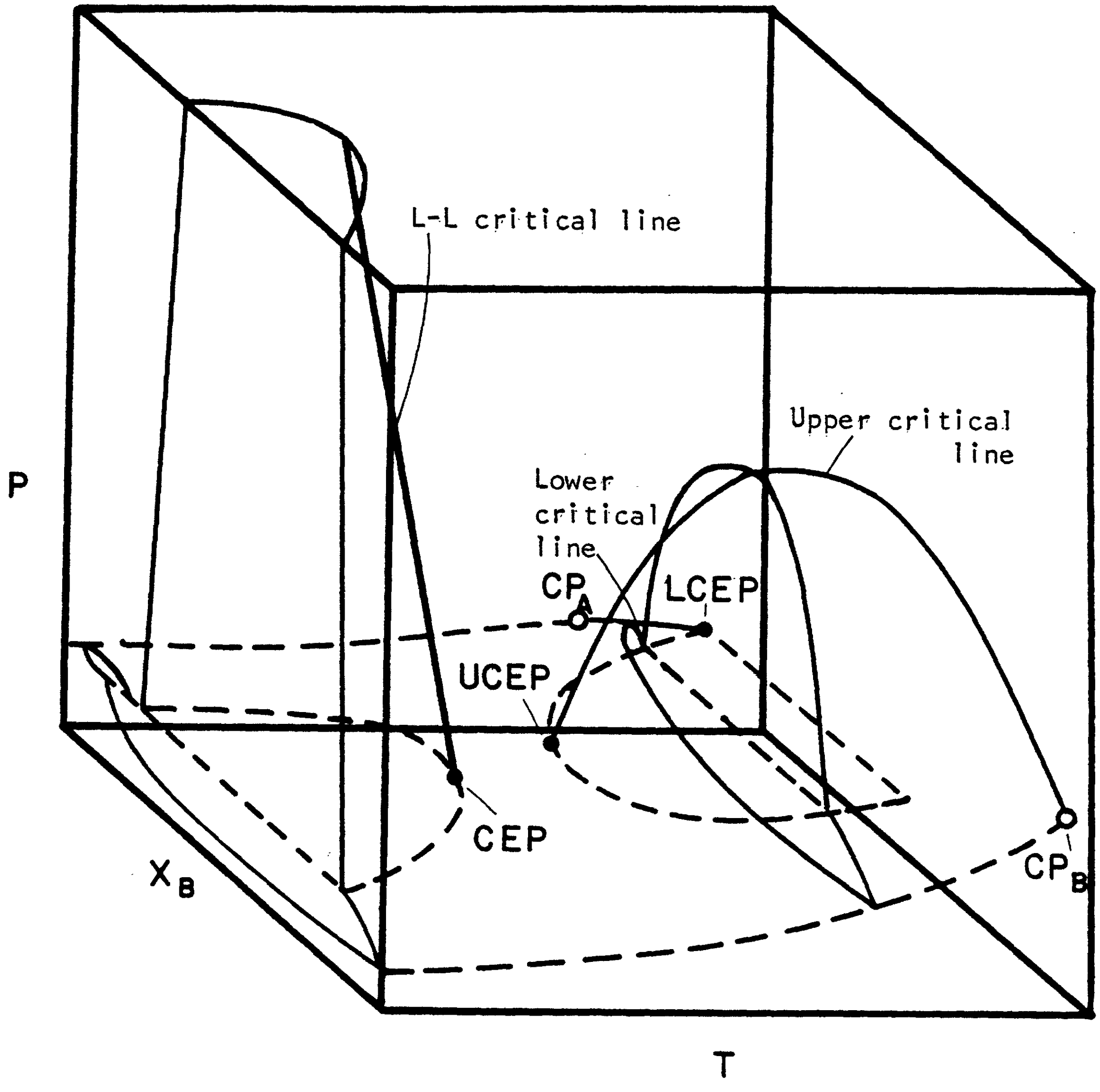

Figure 2.7b. The space diagram for Figure 2.7a.

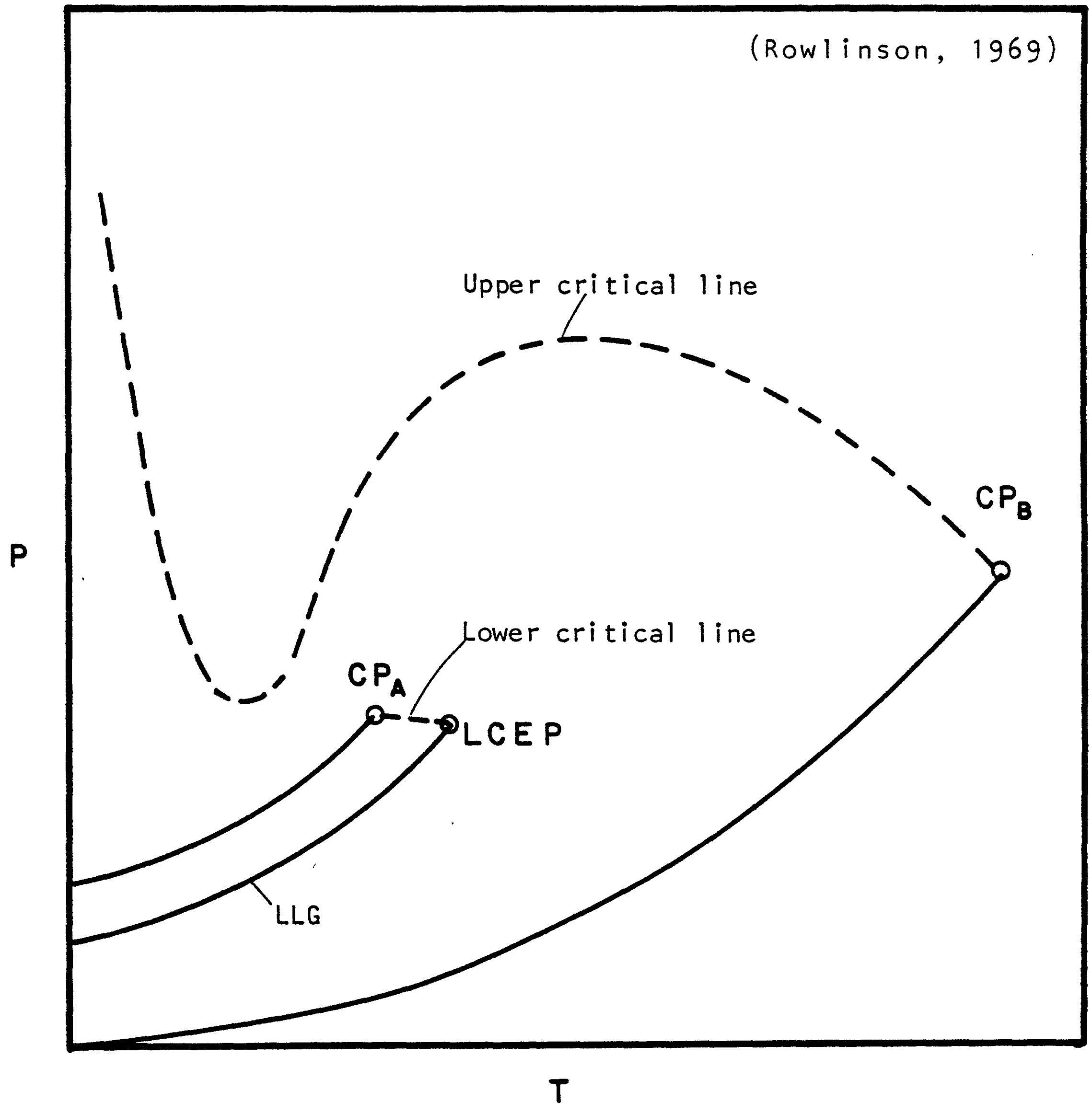

Figure 2.8a. The P-T projection for a system in which the L-L critical line has become part of the upper critical line. The L-L critical line moves to higher pressures as temperature is decreased.

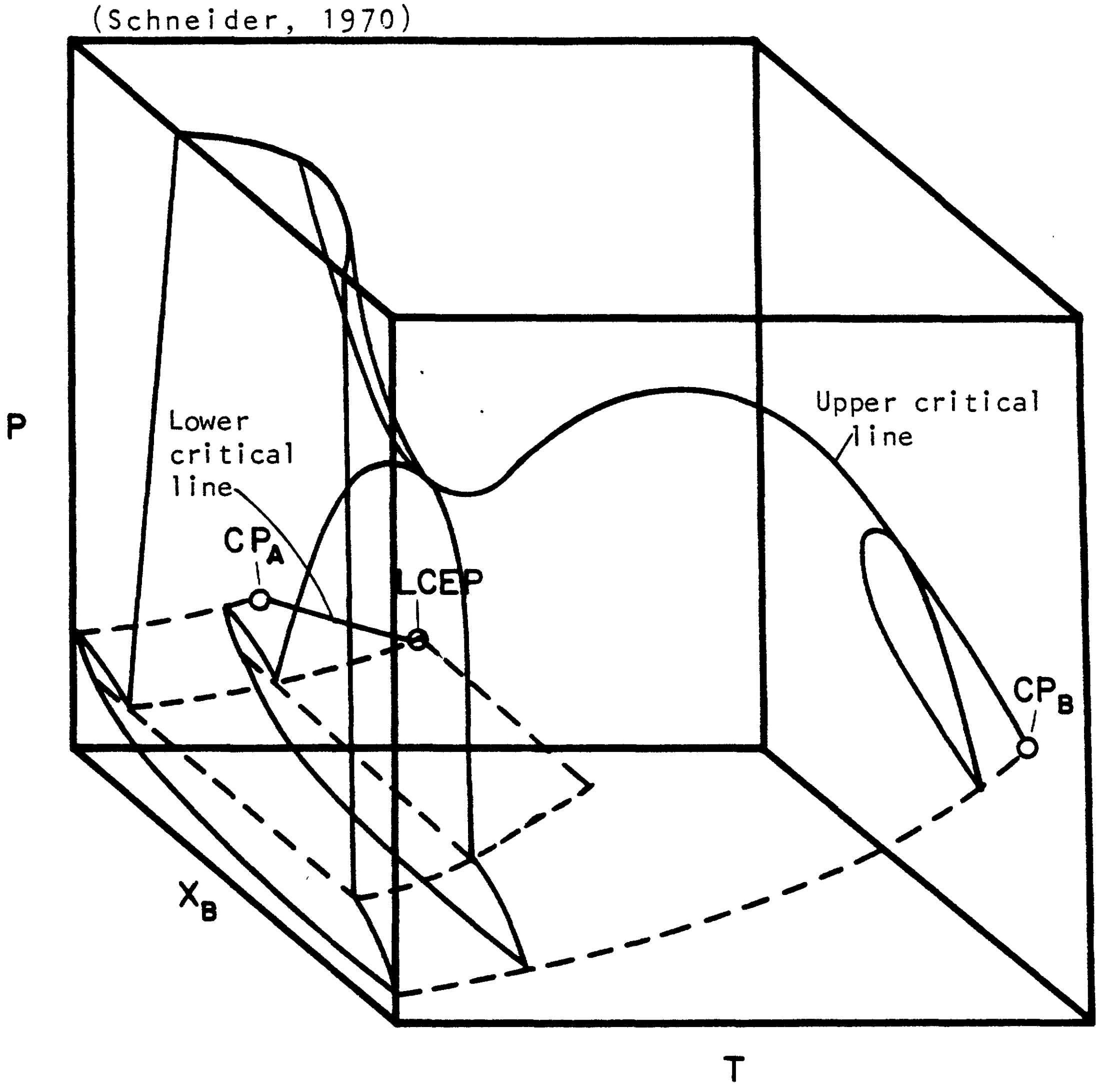

Figure 2.8b. The space diagram for Figure 2.8a.

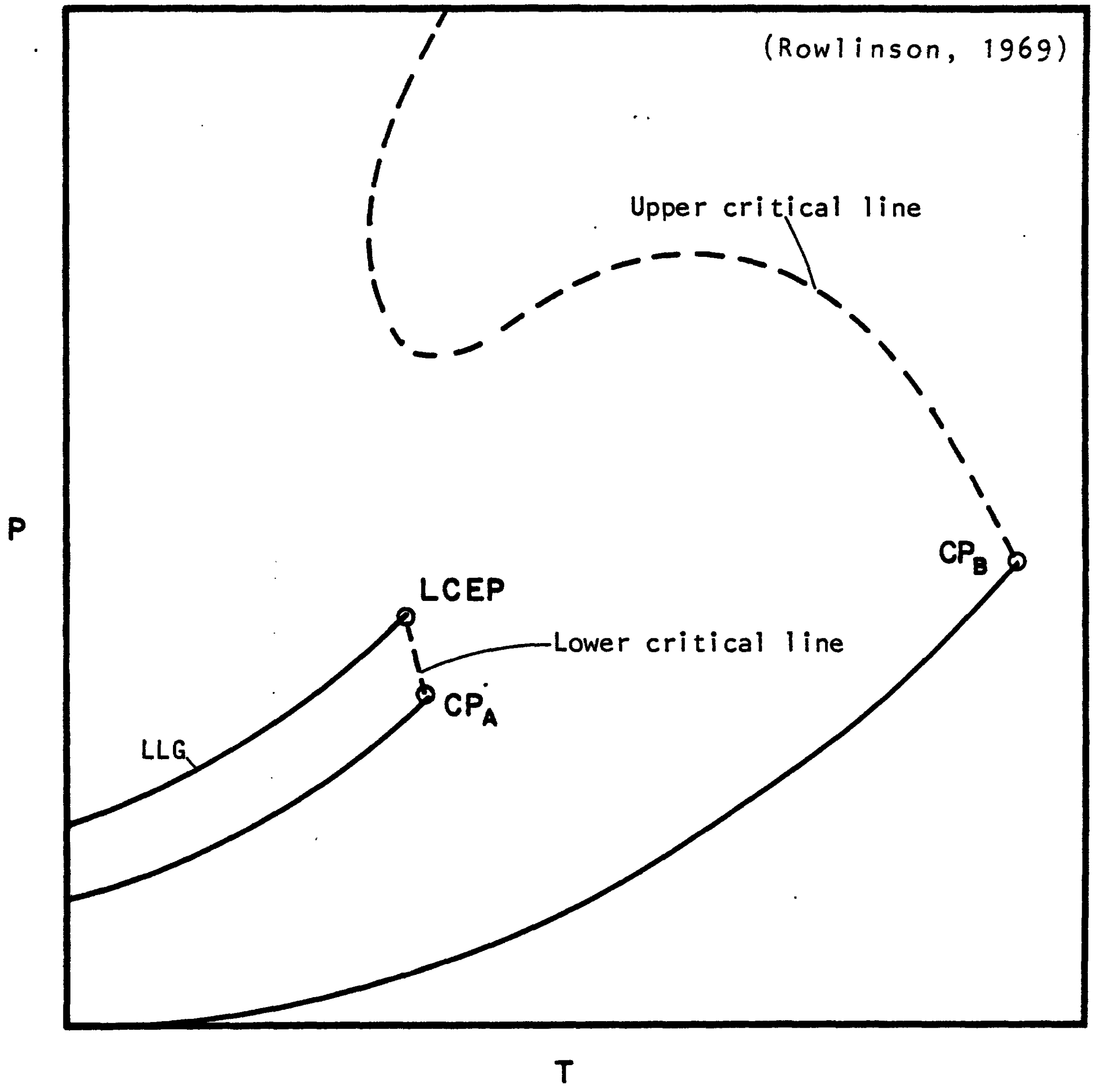

Figure 2.9a. The P-T projection for a system in which the L-L critical line has become part of the upper critical line. The L-L critical line moves to higher pressures as temperature is increased. Unlike previous diagrams, the LLG line now falls at pressures above the vapor pressure curve of A.

(Schneider, 1970)

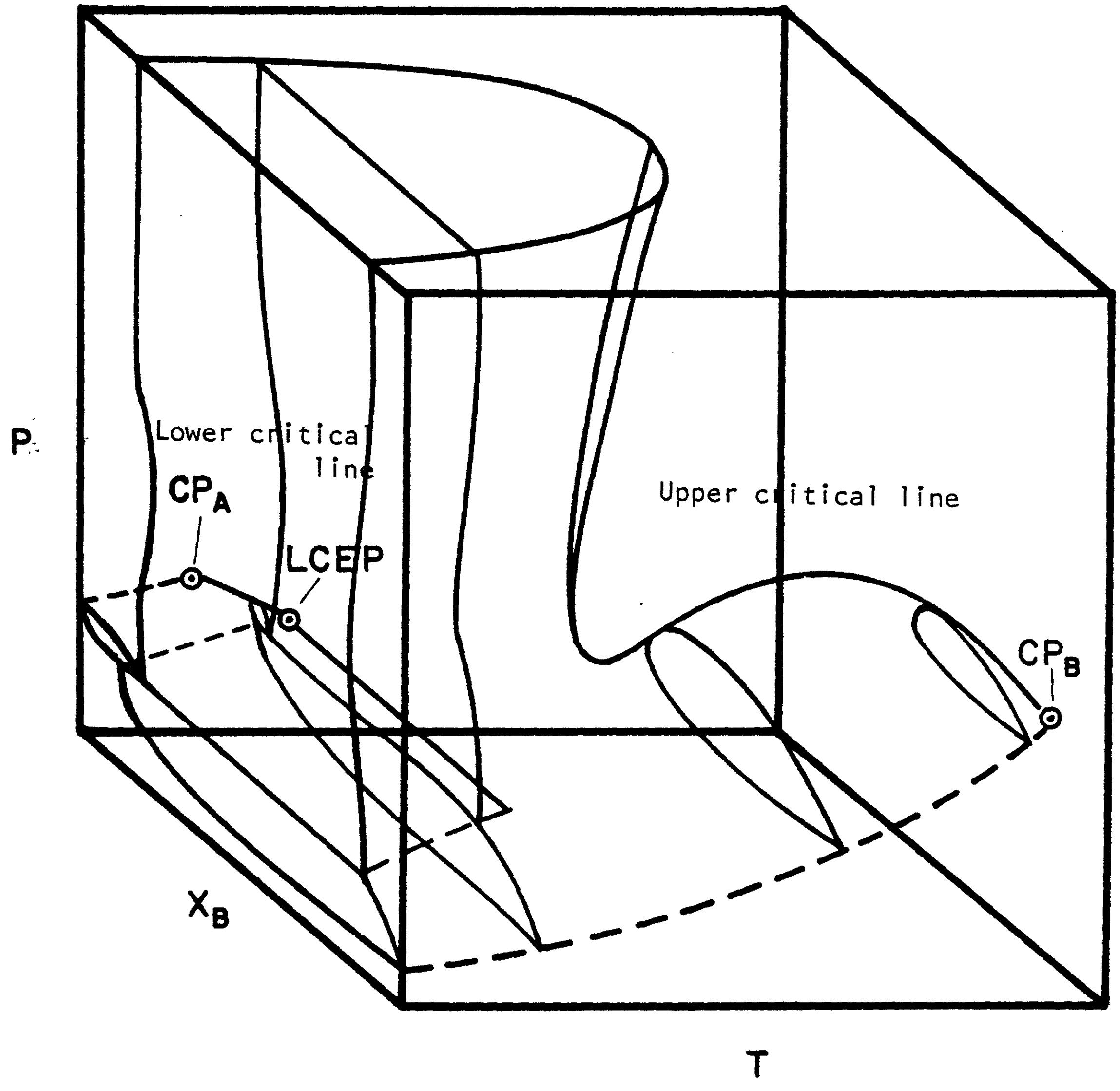

Figure 2.9b. The space diagram for Figure 2.9a.

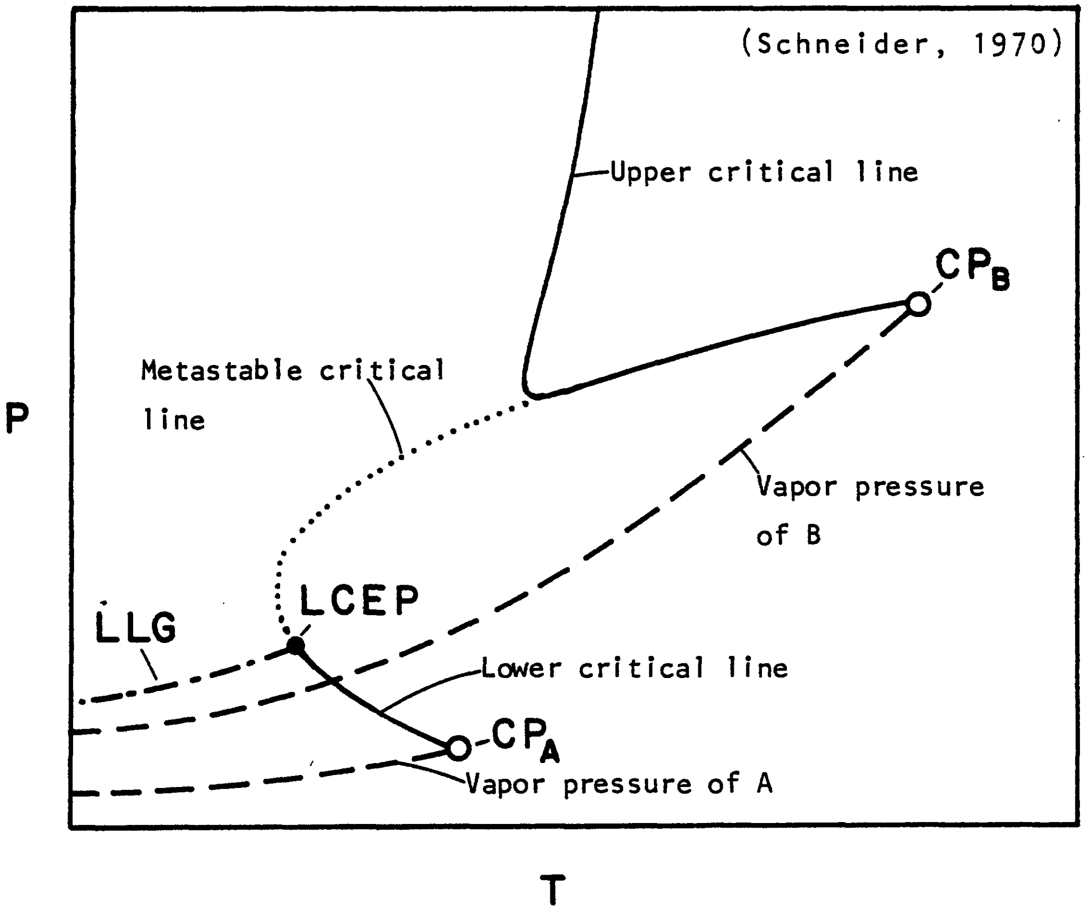

Figure 2.10a. The P-T projection for a system of the type shown in Figure 2.9, but with no pressure maximum in the upper critical line. Once again the LLG equilibrium is found at pressures higher than the vapor pressure of either component. A proposed metastable critical line has been drawn in, showing the course of the lower critical line had liquid-liquid immiscibility not interfered.

(Schneider, 1970)

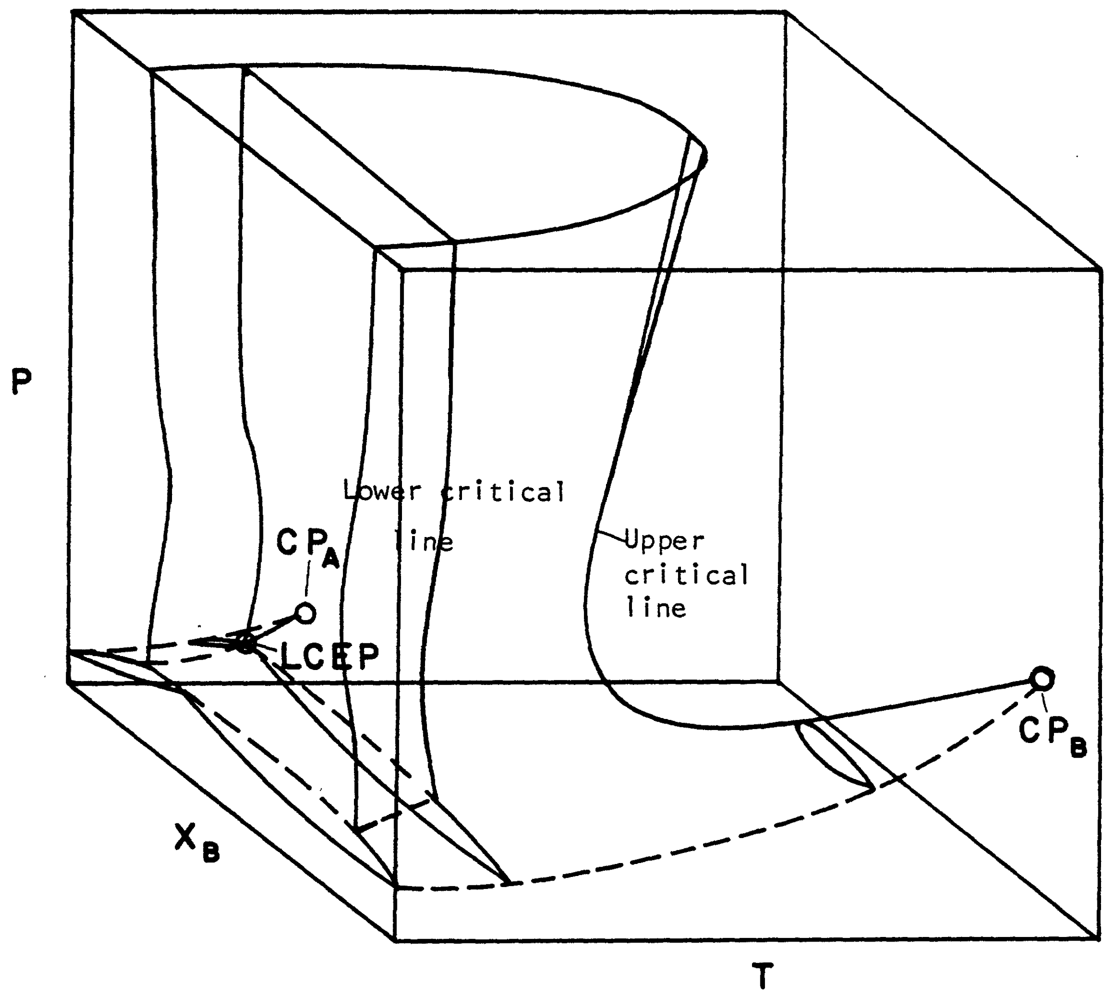

Figure 2.10b. The space diagram for Figure 2.10a.

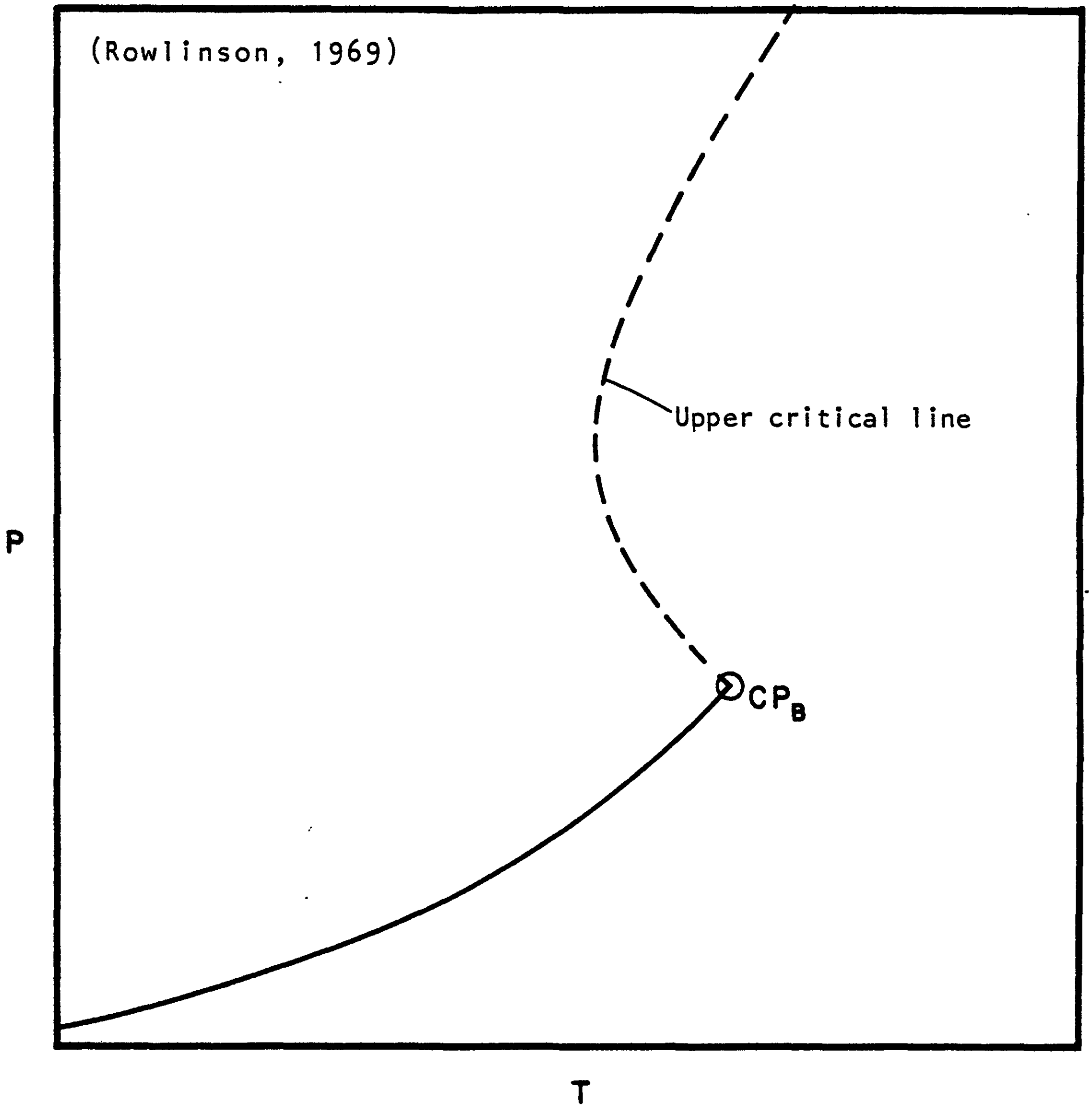

Figure 2.11a. The P-T projection for a system exhibiting gas-gas immiscibility of the first type. Only the upper critical line is shown in this diagram.

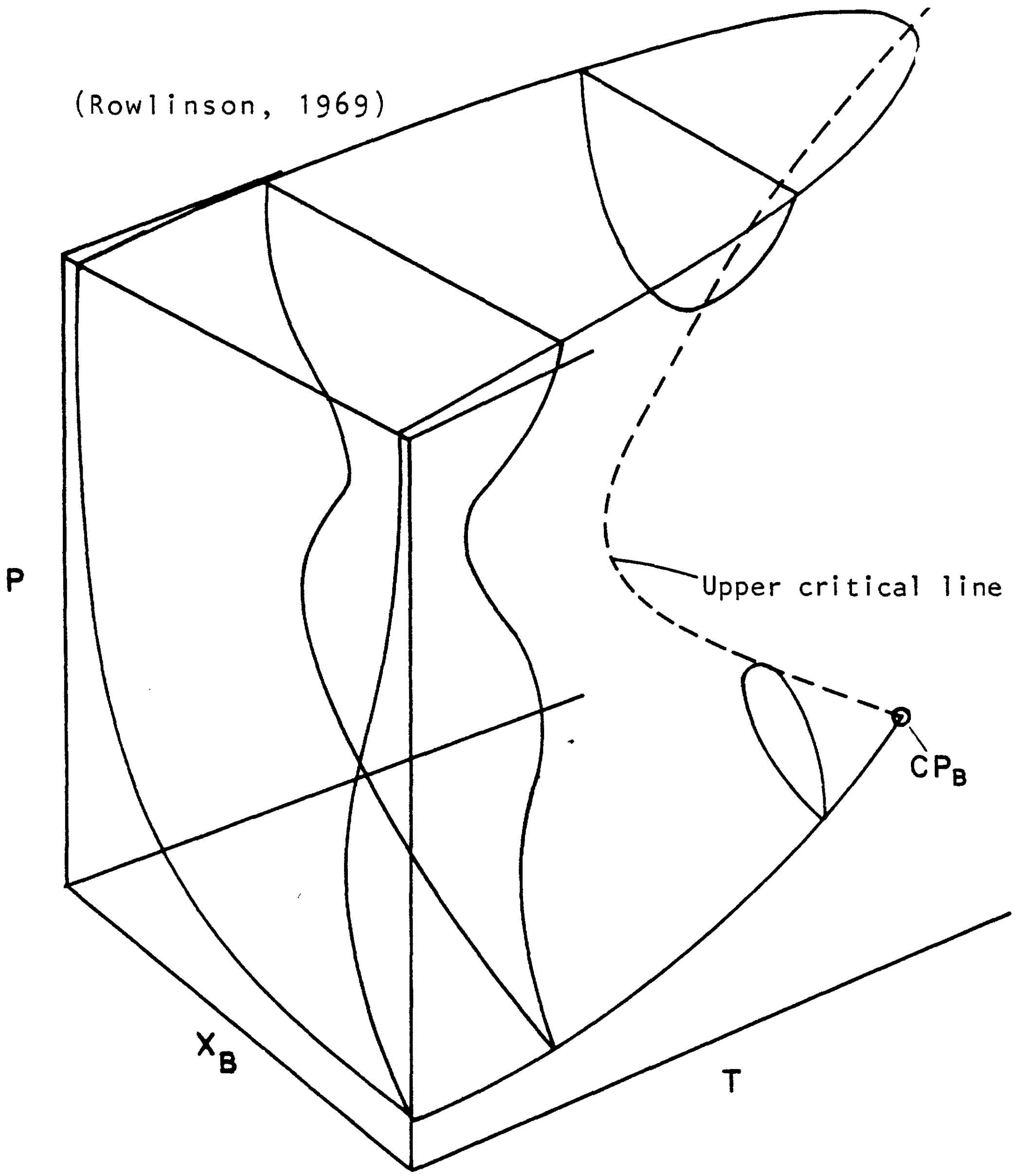

Figure 2.11b. The space diagram for Figure 2.11a.

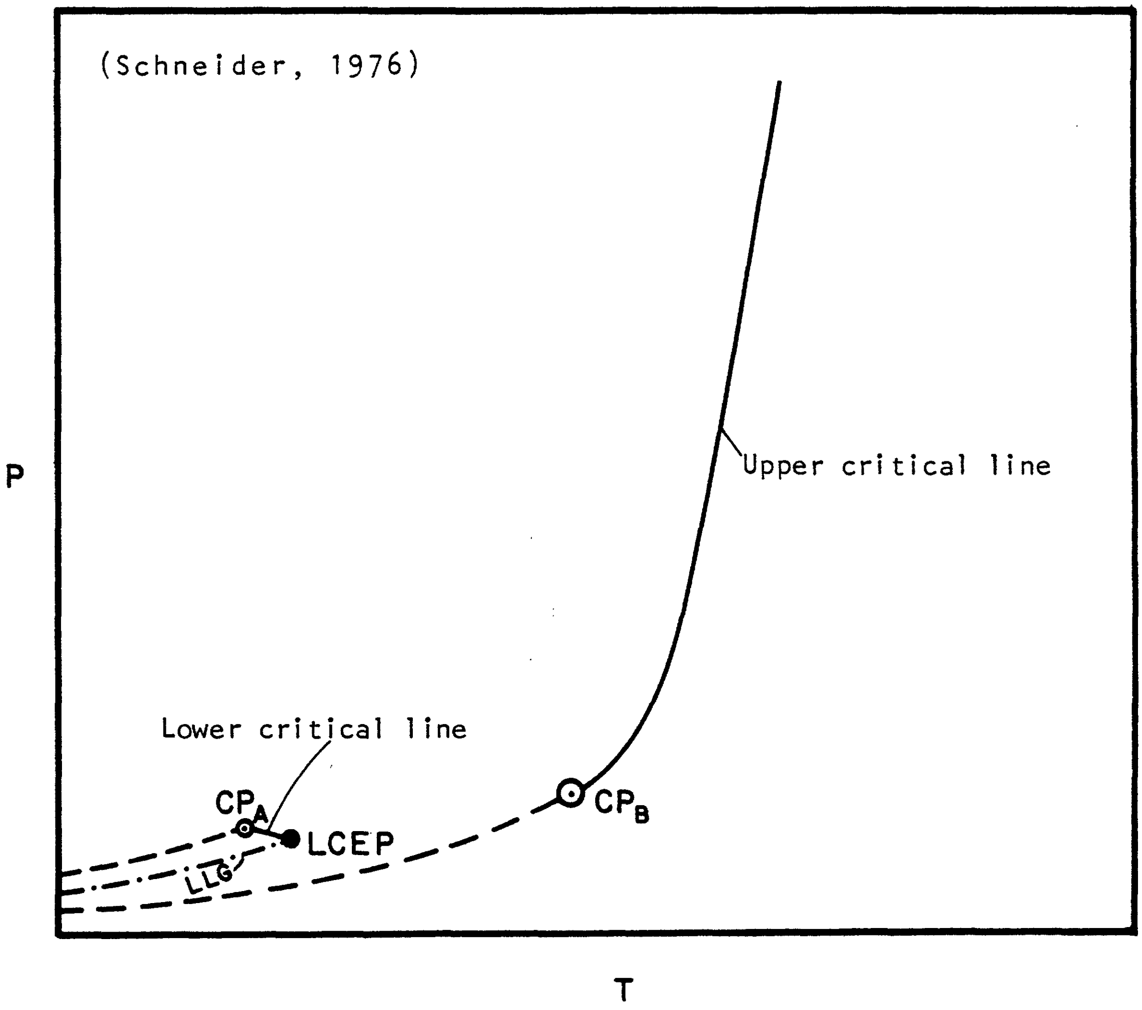

Figure 2.12a. The P-T projection for a system exhibiting gas-gas immiscibility of the second type.

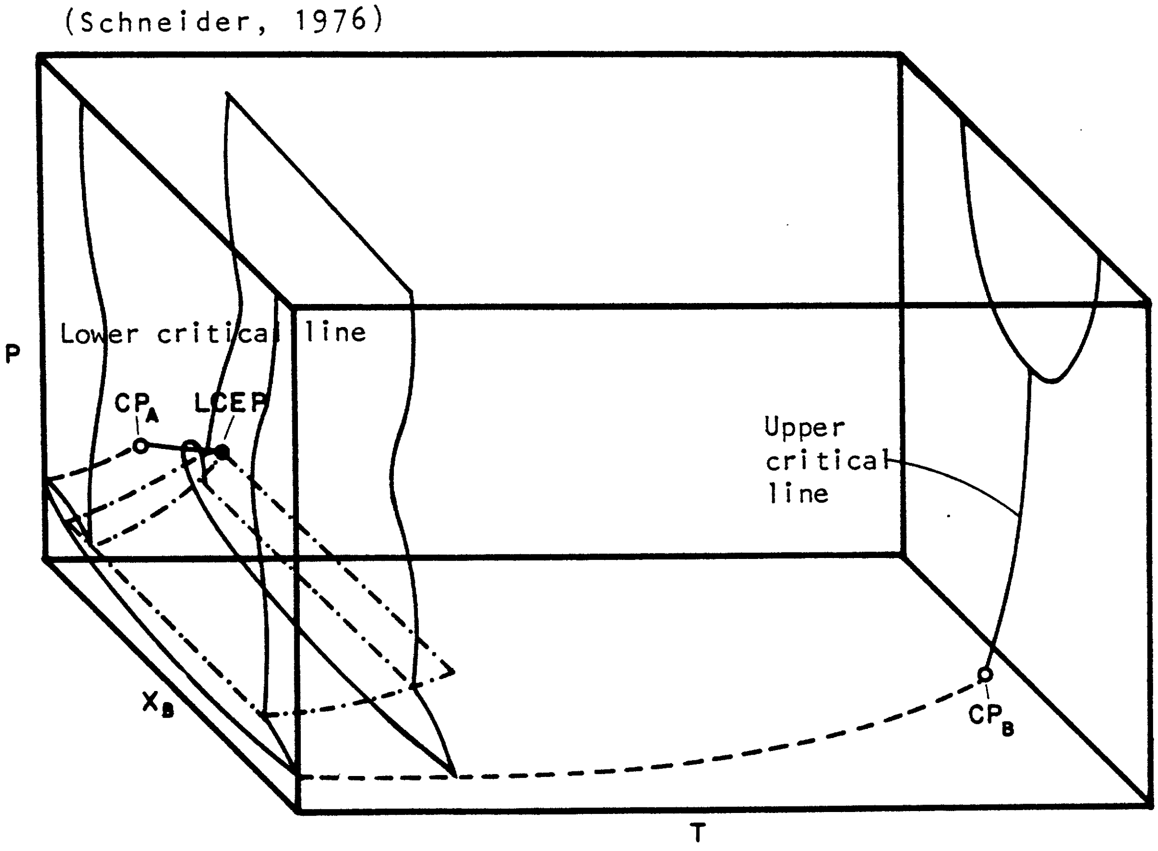

Figure 2.12b. The space diagram for Figure 2.12a.

to as defining gas-gas equilibria (Schneider, 1970), though again the term fluid-fluid is to be preferred.

Another measure of complexity is added to the preceding classification scheme if azeotropic lines are considered. At an azeotropic point, distinguishable liquid and vapor phases coexist, but have identical composition. A locus of azeotropic coordinates has one degree of freedom, and thus forms a line in a P-T-x space diagram. A sequence of P-x sections for an azeotropic system is shown in Figure 2.13a. In this example, component B has the higher critical pressure of the two components. At temperature T_1, below the pure component critical temperatures, the VLE envelope terminates at either extreme at a pure component vapor pressure. The azeotrope which occurs at a pressure maximum divides the VLE envelope into two branches. There exists a range of pressures for which the gaseous phase may be richer or leaner in component B than the coexisting liquid phase, depending upon the overall composition of the system. Whatever the relative compositions of vapor and liquid, the liquid phase is the denser of the two. (The density distinction must be made on a molar basis. In the hydrogen-helium system, for example, the gaseous phase is gravimetrically more dense than the liquid phase.)

At temperature T_2, above the critical point of component A, the A-rich branch of the VLE envelope terminates at a

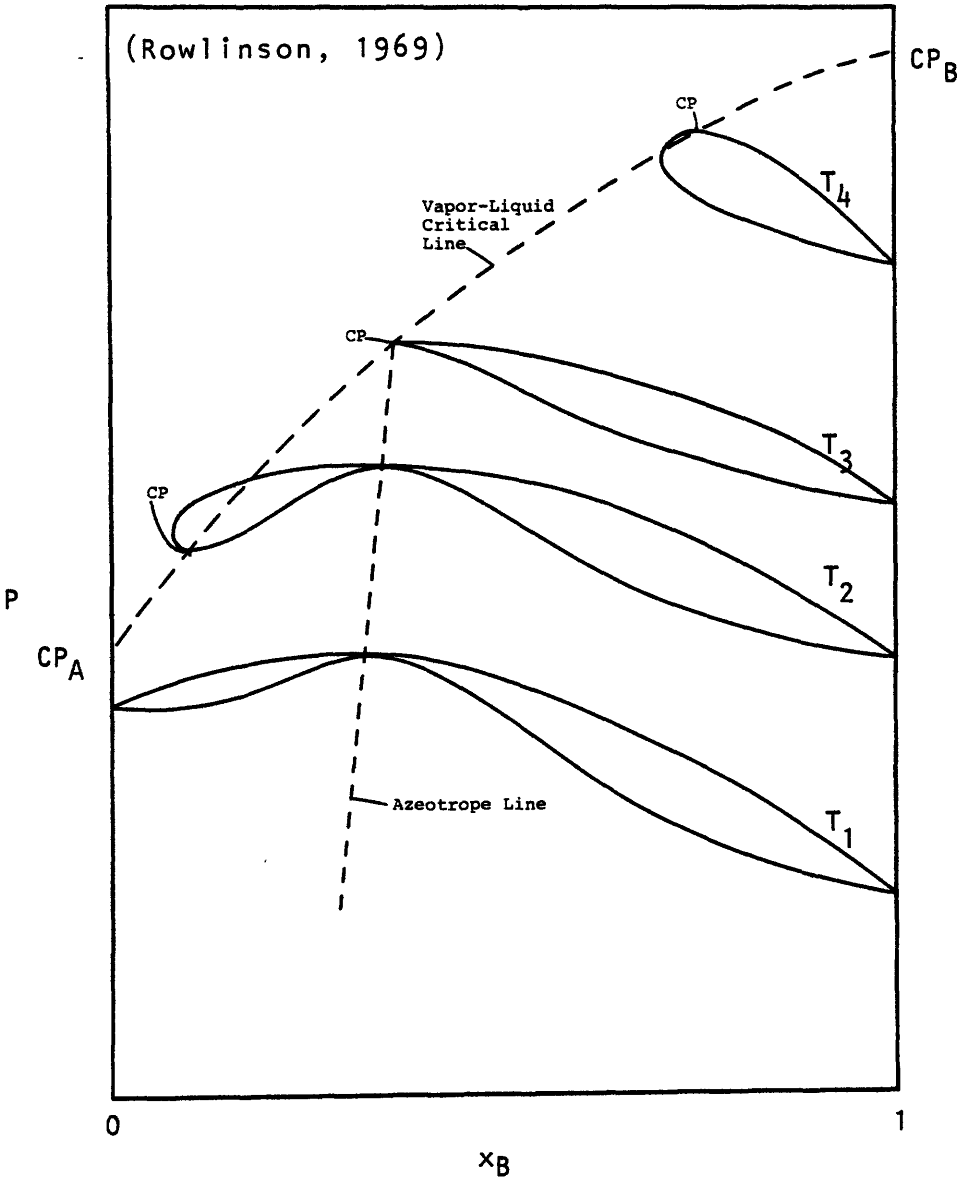

Figure 2.13a. P-x sections for azeotropic behavior in the critical region. This is a maximum pressure or minimum temperature (boiling) azeotrope. A cusp is produced in the VLE envelope when the azeotrope line intersects the critical line.

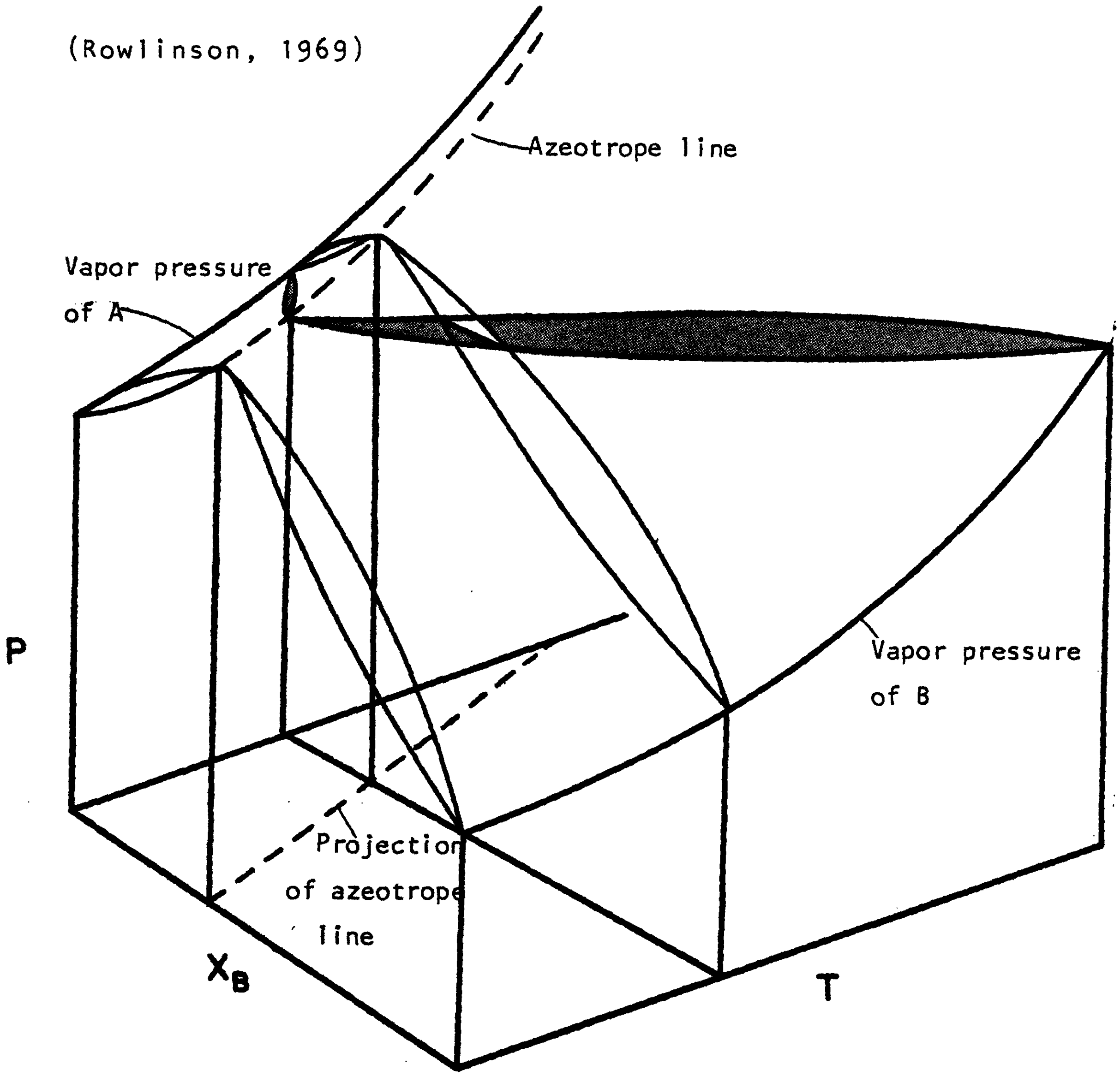

Figure 2.13b. This diagram illustrates the relation between azeotropic P-x and T-x sections. The T-x section is shown shaded. The equivalence of maximum pressure and minimum boiling azeotropes is evident.

point along the critical line. This mixture critical point occurs at a minimum pressure, but not at a compositional extreme. As temperature increases further, the critical line approaches the azeotrope line and the A-rich branch shrinks. At T_3, the lines meet and the VLE envelope terminates in a cusp. The tip of this cusp is the azeotropic critical point, and it occurs at extremes in both pressure and composition. For temperatures above T_3, the cusp reverts to normal behavior, as illustrated by the section at T_4.

Figure 2.13b shows the relationship between P-x and T-x sections in an azeotropic system. It is seen that a pressure maximum in the P-x section corresponds to a temperature minimum in the T-x section. Since azeotropes are often encountered in constant pressure distillations, the T-x behavior of a system serves as the basis for its classification. As the azeotrope in the T-x section occurs at a minimum temperature, the present system is designated a minimum boiling azeotrope.

Other types of azeotropic behavior are presented in Figure 2.14. Figure 2.14a shows the P-x section for a minimum boiling azeotrope where liquid-liquid immiscibility exists over a portion of the compositional range. If the region of immiscibility extends beyond the azeotropic composition, the behavior of Figure 2.14b will result. Figures 2.9 and 2.10 (benzene-water) exhibit this type of

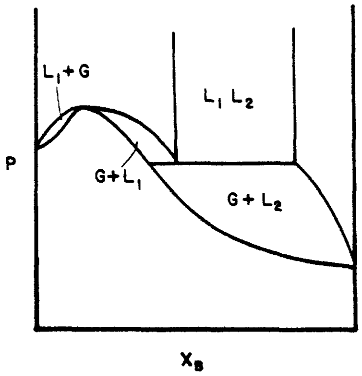

Figure 2.14a. A system with both a minimum boiling azeotrope and liquid-liquid immiscibility at the same temperature.

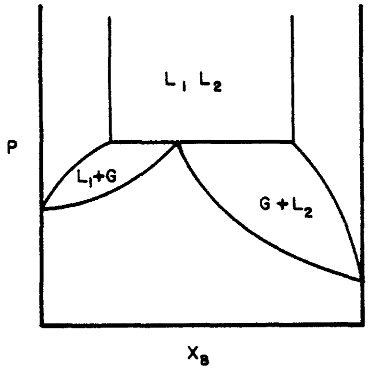

Figure 2.14b. A heteroazeotropic system. The azeotropic composition, which is the composition of the gas phase along the three-phase line, now lies between the compositions of the immiscible liquids. Heteroazeotropes revert to the behavior shown in Figure 2.14a as the UCST is approached and the region of liquid-liquid immiscibility shrinks.

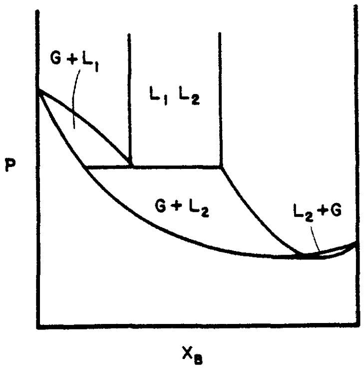

Figure 2.14c. A maximum boiling azeotrope which lies outside the region of liquid-liquid immiscibility. Maximum boiling azeotropes may exist when no immiscibility is present, as well as at the same temperature as a minimum boiling azeotrope.

(Rowlinson, 1969)

behavior, known as heteroazeotropy. Figure 2.14c shows a maximum boiling azeotrope outside the range of immiscibility.

Supercritical fluid extraction processes often involve the dissolution of a solid, as Table 2.1 indicates. P-T-x diagrams for systems in which pure solid phases occur are now considered, with attention directed mainly toward solidification of the less volatile component. These diagrams may be thought of as fluid phase diagrams with the precipitation of a solid phase superimposed.

The simplest case again occurs when the system under consideration does not exhibit any liquid phase immiscibilities. The P-T and P-T-x diagrams in the critical point region have been given in Figure 2.2. Extending the temperature scale to include the triple point region, the diagrams of Figure 2.15 result. In 2.15a, the P-T projection, there are four three-phase lines: S_AS_BG, S_AS_BL, S_ALG, and S_BLG. These lines all intersect at the quadruple point Q, where the four phases S_A, G, L and S_B all coexist. In the P-T-x diagram, these points are labelled Q_A, Q_G, Q_L, and Q_B, respectively, and they all possess the same pressure and temperature coordinates. Q is also the terminus of the S_AS_BL eutectic line.

The S_BLG line in the P-T diagram is a projection of the lines TP_B-Q_G and TP_B-Q_L in the P-T-x diagram. TP_B-Q_G

(Rowlinson, 1969)

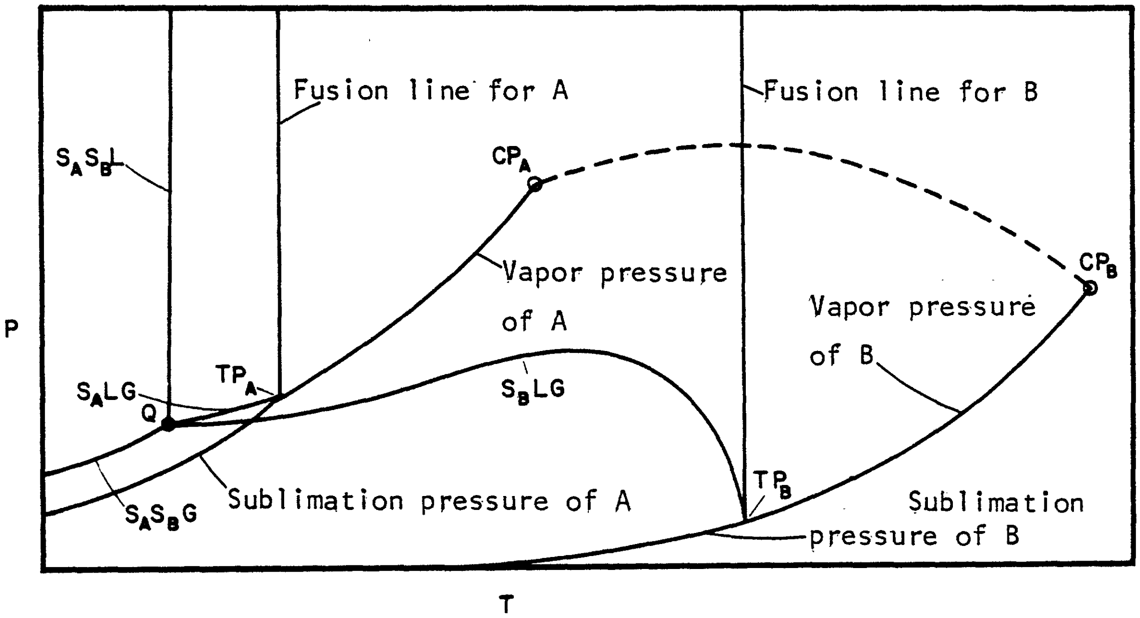

Figure 2.15a. The P-T projection for a system in which the liquid phases are completely miscible, and the solid phases are completely immiscible. Triple points are denoted by TP and the quadruple point by Q. S_A and S_B are the pure solids.

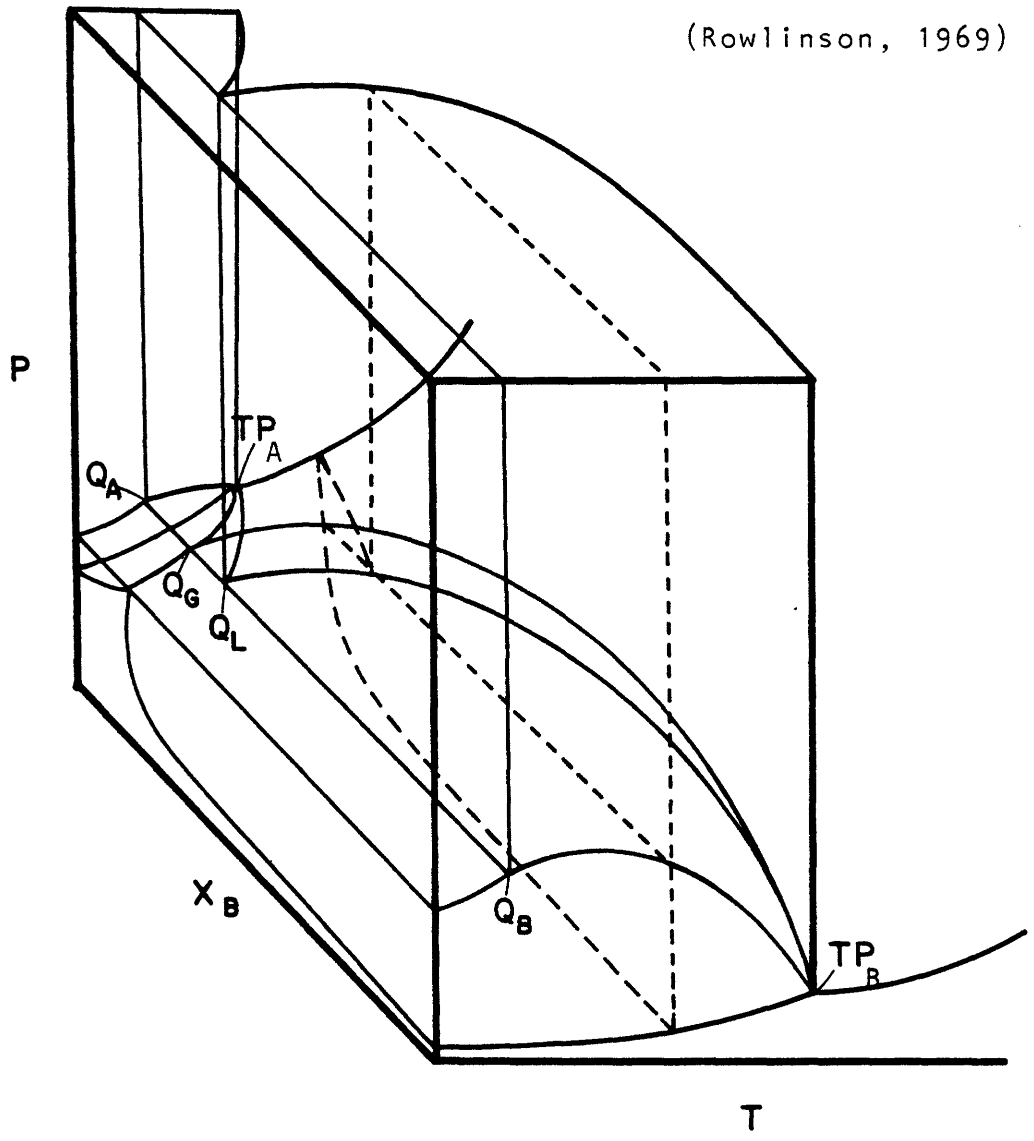

Figure 2.15b. The P-T-x space diagram for Figure 2.15a. The four phases at the quadruple point, Q_A, Q_G, Q_L, and Q_B are now evident. The top face of the diagram is a typical eutectic diagram.

gives the vapor composition and TP_B-Q_L the liquid composition for all S_BLG three-phase systems. The lines TP_A-Q_G and TP_A-Q_L give the corresponding compositions for all S_ALG three-phase systems. An examination of the P-T-x diagram indicates that the TP_A-Q_L and TP_B-Q_G lines cross each other in the composition coordinate. This fact is illustrated more clearly by the P-x sections given in Figure 2.16. Starting at the quadruple point temperature in 2.16a, there exist two regions of gas-solid equilibrium at pressures below the quadruple point tieline. Increasing pressure to that of the quadruple point, four phases coexist as condensation occurs, and the gas-solid equilibrium shifts to one of liquid-solid. Above the quadruple point pressure, for a eutectic line with positive slope, only two pure solids are in equilibrium.

Increasing temperature slightly above the quadruple point, the P-x section takes on the much more complicated shape illustrated in Figure 2.16b. The quadruple point tieline has now been replaced by the three-phase tielines S_ALG and S_BLG and S_AS_BL. As depicted in Figure 2.15a, the first of these tielines falls at a higher pressure than the second. The S_ALG liquid phase is richer in component B than the S_BLG gas phase. For pressures between the S_ALG tieline and the eutectic pressure P_E, liquid may exist as a single phase, or in equilibrium with S_A or S_B according to the overall system composition. Above the three-phase line at

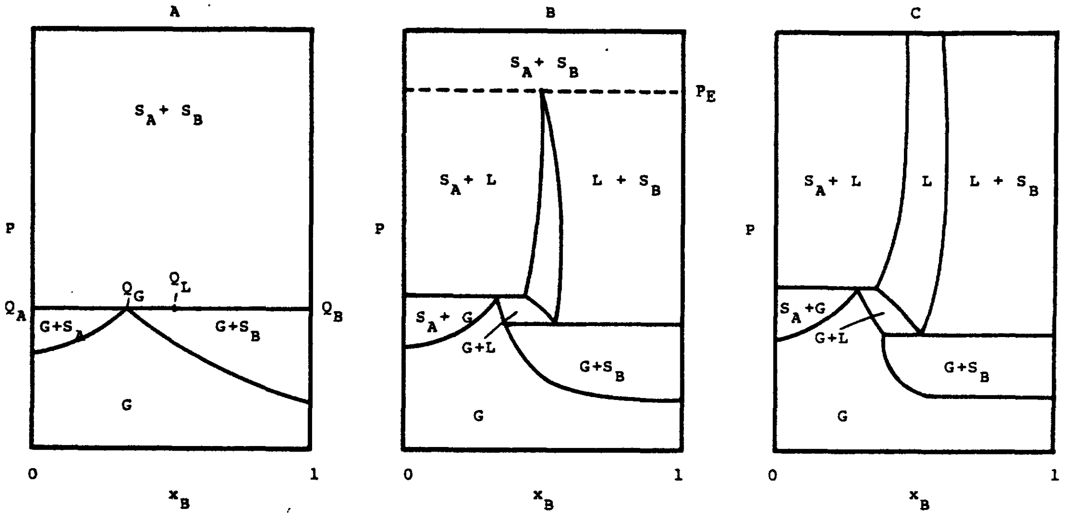

Figure 2.16. P-x sections for Figure 2.15b. T_A is the quadruple point temperature. At T_B, slightly above T_A, the liquid phase in equilibrium with S_A is richer in component B than the gas phase in equilibrium with S_B. At T_C, further above T_A, this relationship has inverted.

P_E, only two pure solid phases coexist.

Increasing the temperature further, but still below TP_A, the P-x section of Figure 2.16c results. At this temperature, the S_ALG liquid phase is leaner in component B than the S_BLG gas phase. Compared to Figure 2.16b, then, the relative composition of these two phases has switched. At T_C, a single liquid phase may persist to much higher pressures than at T_B.

For systems where the solubility of solid B in the liquid phase is very low, and the temperature of TP_B is higher than that of CP_A, the S_BLG liquid phase near the quadruple point is almost pure A. When this low solubility persists to temperatures above the critical point of A, the S_BLG line cuts the LG critical locus to give a lower critical end point. This is shown in Figure 2.17. The segment of the S_BLG line starting from TP_B similarly intersects the LF critical locus at the upper critical end point. At temperatures between the critical end points, the fluid phase critical phenomenon is not observed at any pressure. Consequently, this region is often designated as the supercritical fluid region.

Consider next the case of a liquid immiscibility dome, as shown in Figure 2.4. Precipitation of a solid phase at a temperature in the mid-region of the dome leads to the phase

(Rowlinson, 1969)

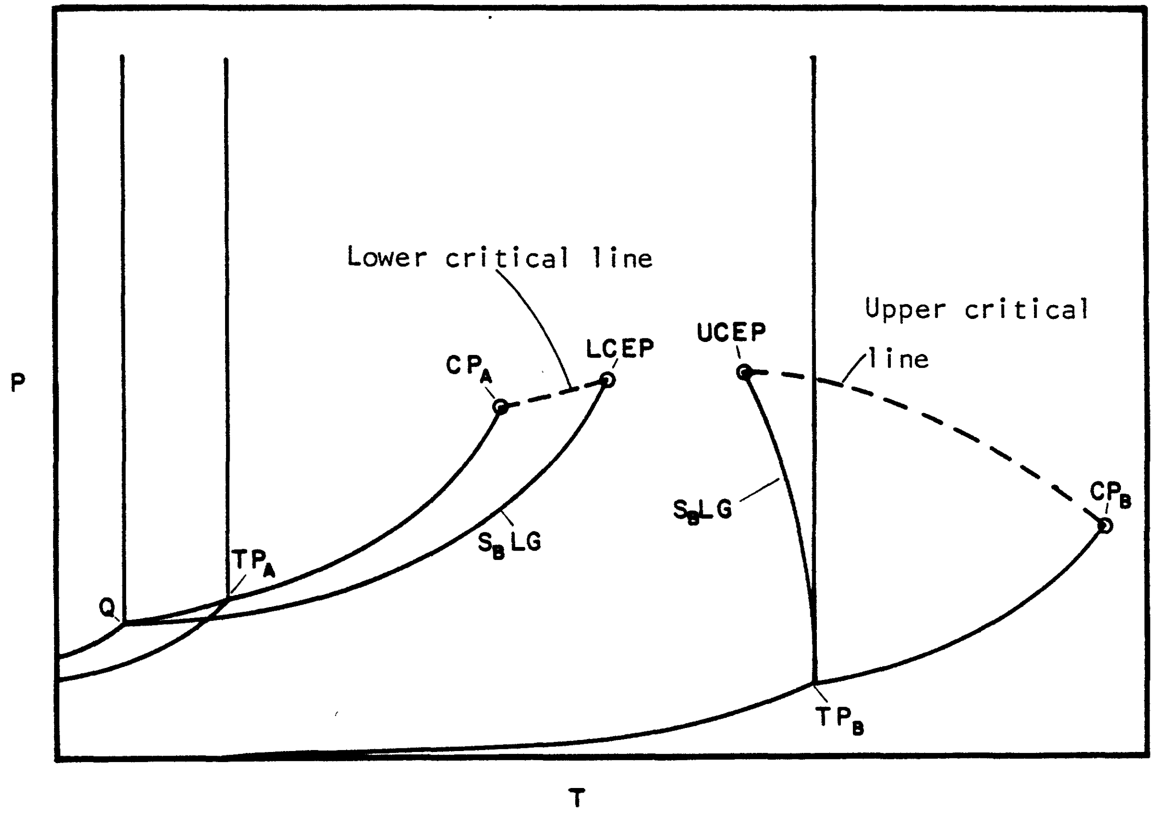

Figure 2.17. The P-T projection of a system in which the gas-liquid critical line is cut by the S_BLG line. The length of the lower critical line has been greatly exaggerated. The LCEP is typically within a few °C of CP_A.

diagrams of Figure 2.18. For temperatures below the $S_BL_1L_2$ line, the behavior is essentially the same as in Figure 2.15, with a eutectic quadruple point. For temperatures above this line, however, phase diagrams of the type shown in Figure 2.18c are encountered. This P-x section has two three-phase tielines, L_1L_2G and S_BL_2G, as required by Figure 2.18a. It is also evident from Figure 2.18a that the L_1L_2G and S_BL_2G lines intersect at a second quadruple point. Here solid B is in equilibrium with two liquid phases and a vapor phase. Figure 2.18a has retained the higher temperature critical end point from Figure 2.4 (CEP_1), and generated a second critical end point where the $S_BL_1L_2$ line meets the liquid-liquid critical locus (CEP_3).

The UCST line of Figure 2.5 will give essentially the same phase diagrams as in Figure 2.18 if the liquid-liquid critical locus has a negative slope in the P-T projection. For a positive slope of this critical line, a CEP along the $S_BL_1L_2$ line still occurs. Now, however, the two liquid phases only coexist at pressures above the CEP, in contrast to Figure 2.18. Below the pressure of the CEP, phase diagrams similar to those shown in Figure 2.15 are found.

Figures 2.6 and 2.7 illustrated the case of liquid-liquid immiscibility causing a relatively minor break in the gas-liquid critical line. When solid precipitates in the critical region, these system types will usually give

(Rowlinson, 1969)

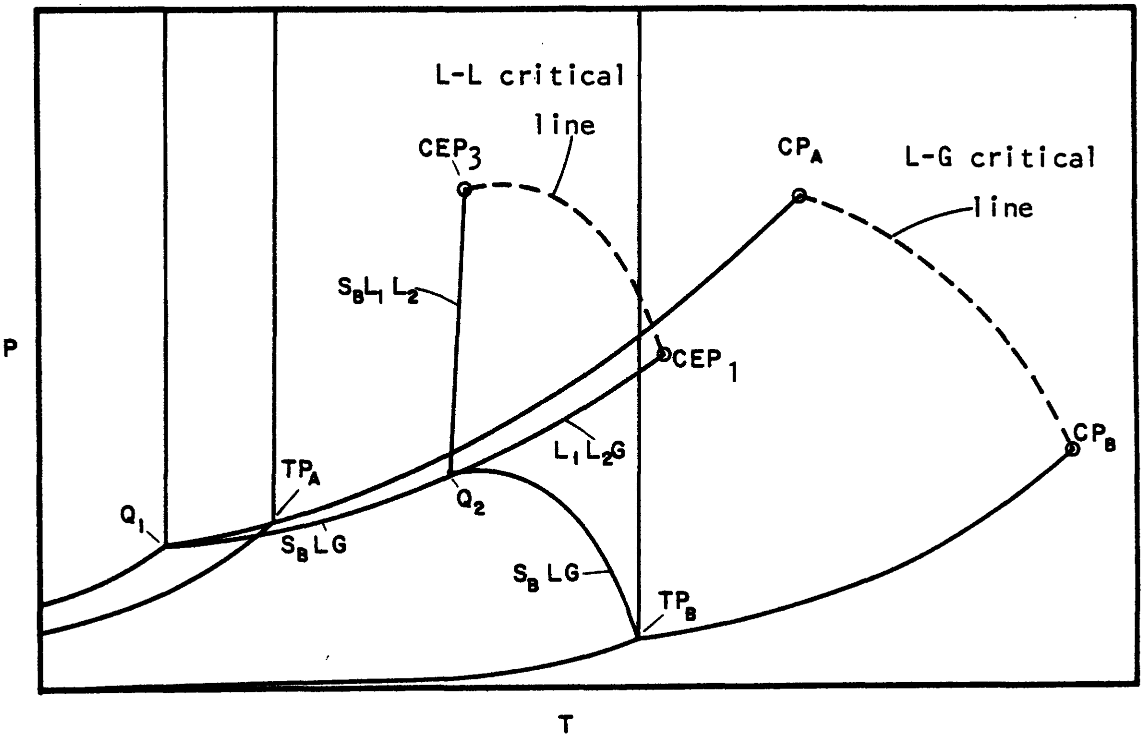

Figure 2.18a. The P-T projection for a system with a liquid immiscibility dome interrupted by formation of a solid phase. This diagram is to be compared with Figure 2.4a. CEP_1 appeared in that figure. The second L_1L_2G critical end point, CEP_2, has become metastable, and no longer appears. A new critical end point, CEP_3, is now the terminus of the L-L critical line. Two quadruple points, Q_1 and Q_2, appear in this diagram.

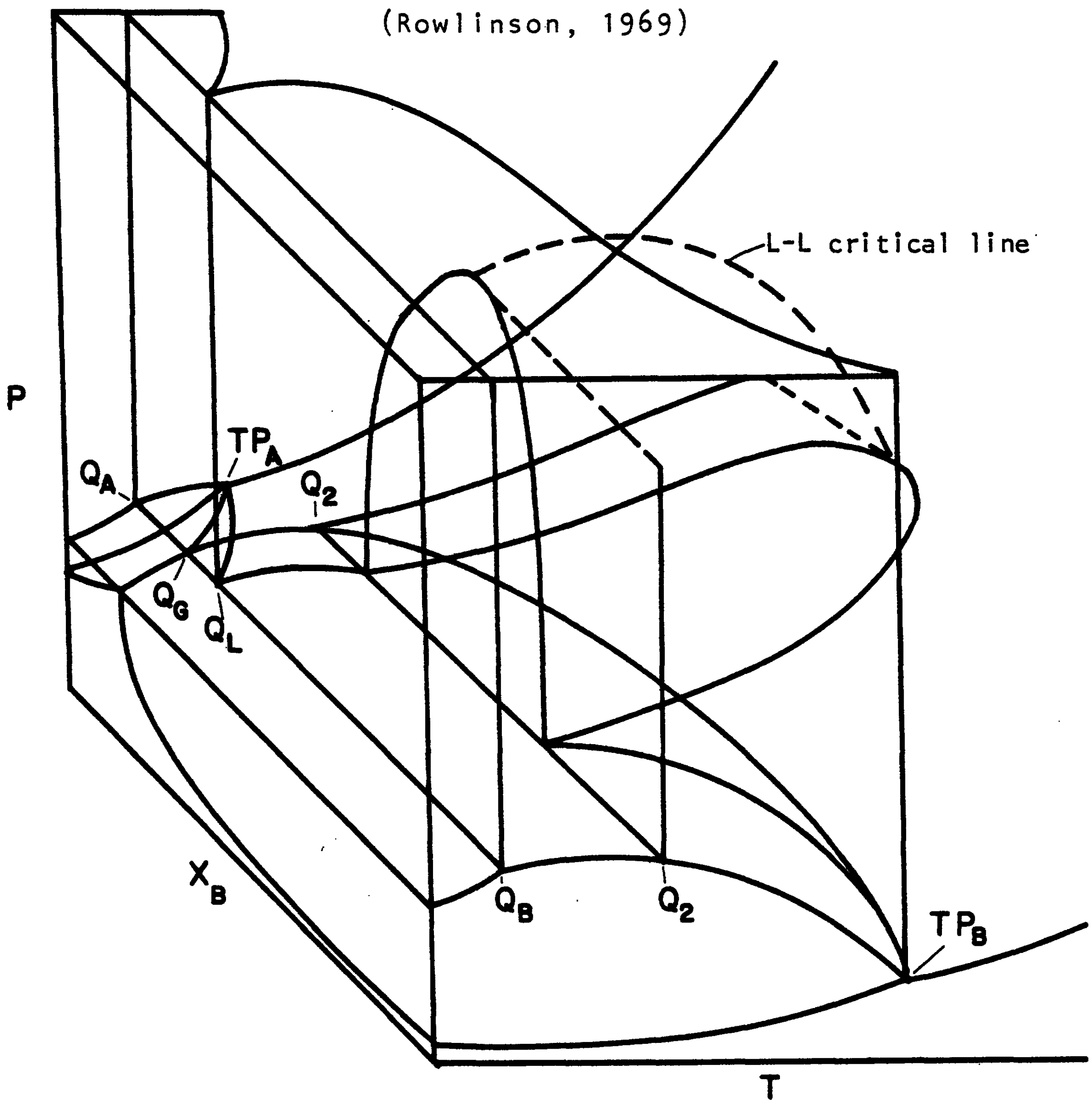

Figure 2.18b. The space diagram of Figure 2.18a. The points Q_A, Q_B, Q_L, and Q_G all coincide with Q_1 in that diagram. The line joining the points labelled Q_2 gives the compositions at the second quadruple point.

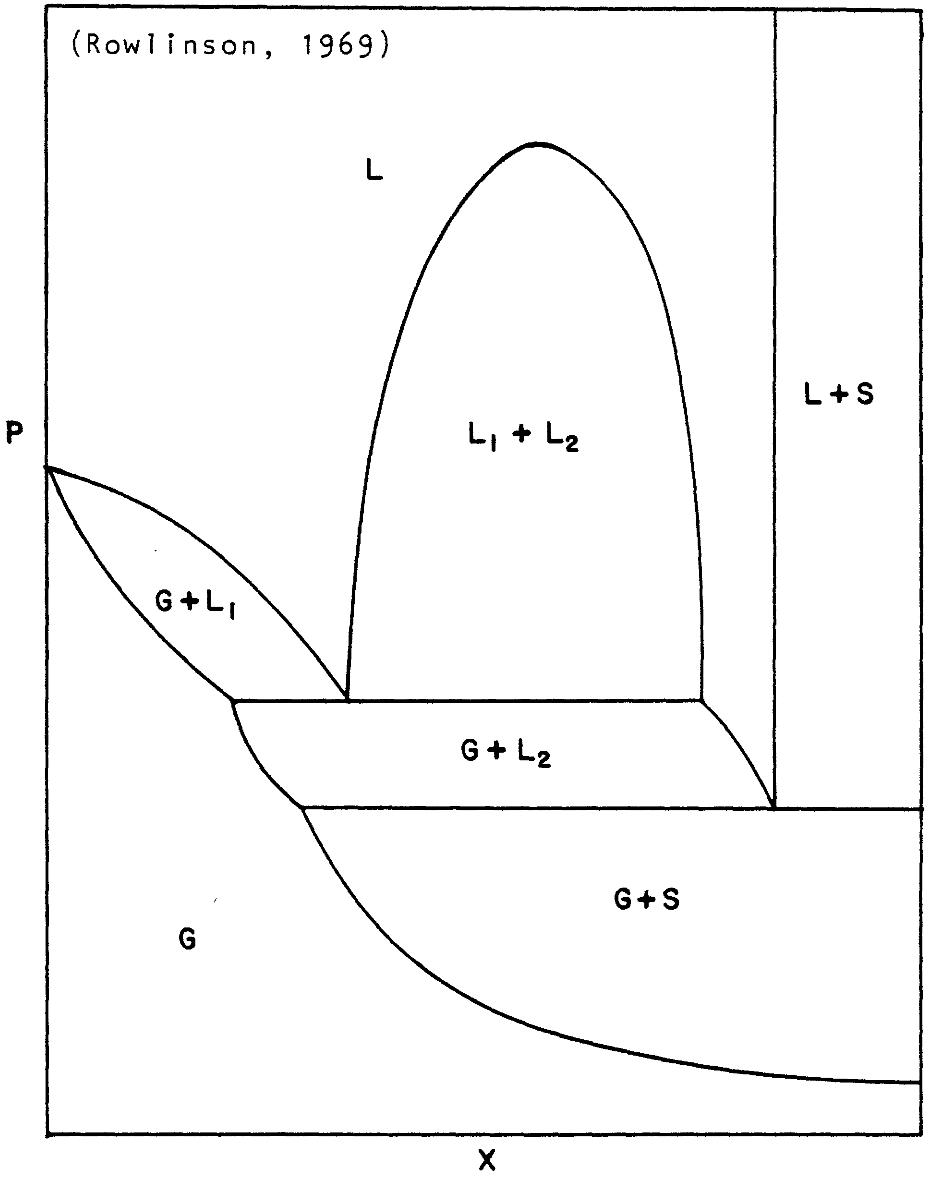

Figure 2.18c. A P-x section of Figure 2.18b, at a temperature above the $S_BL_1L_2$ surface but below TP_B.

similar phase diagrams. In some instances, solid formation occurs below the critical temperature of the light component, in others above this temperature. These possibilities are given by Figures 2.19 and 2.20, respectively. In Figure 2.20a, as in Figure 2.17, there exists a supercritical fluid region within which the critical phenomenon is not observed. Figure 2.20b gives a P-T-x space diagram for a system of the type shown in Figure 2.20a. The space diagram is based on the naphthalene-ethylene system (see Chapter 7), with certain features exaggerated for clarity.

Figure 2.20 would also be valid for solid formation in the phase diagrams of Figures 2.8 through 2.10, if the upper critical line terminates before attaining a steep slope. Frequently, however, the UCEP does fall on the liquid-liquid-like portion of the upper critical line. Examples are given in Figures 2.21, 2.22, and 2.23. The first of these illustrates the possibility that the UCEP falls at a lower temperature than the LCEP, as was the case in Figure 2.19. Figure 2.22a gives the P-T projection for the UCEP at higher temperatures, with the concomitant occurrence of a supercritical fluid region. This diagram is based on theoretical predictions for the naphthalene-carbon dioxide system (see Chapter 6). Figure 2.22b gives the P-T-x space diagram for this case. Finally Figure 2.23 shows the interesting situation of a temperature minimum in the $S_B LF$ line. Although the critical phenomenon is not observed

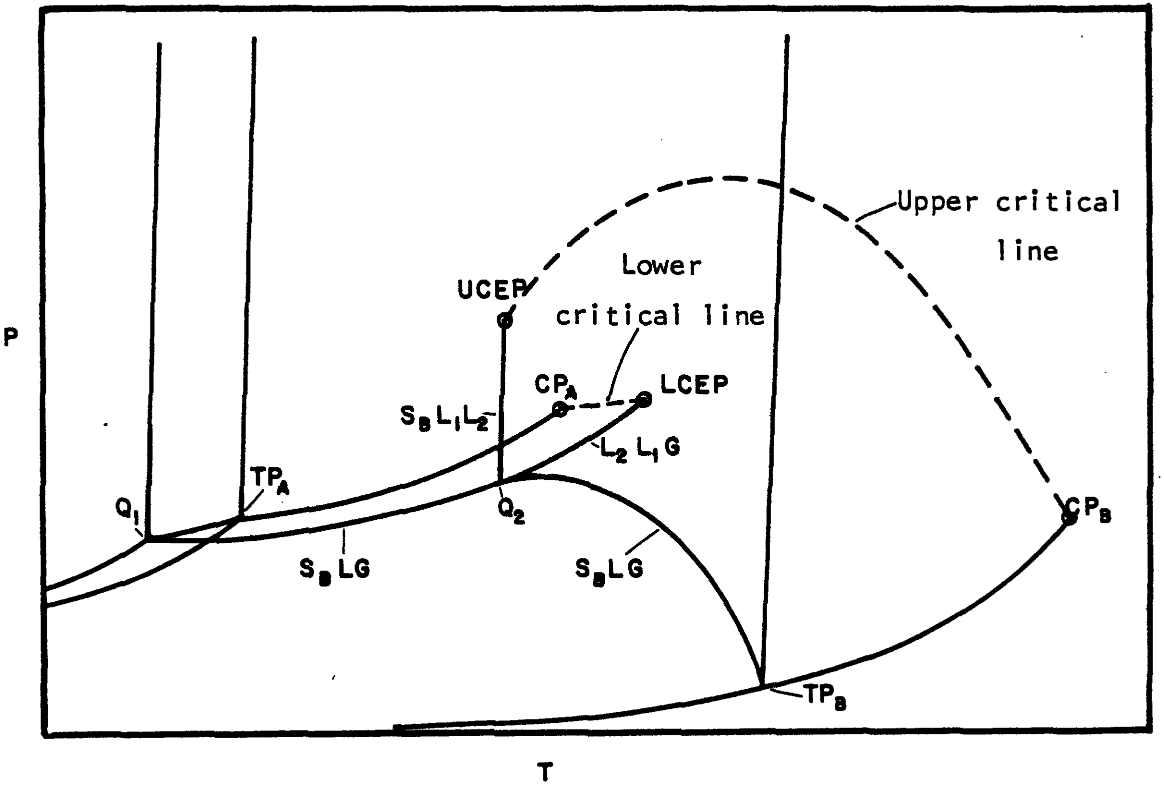

(Rowlinson, 1969)

Figure 2.19. The P-T projection for a system with liquid immiscibility in the vicinity of CP_A. The upper critical line is terminated by the formation of a solid phase at the UCEP. In this example, the UCEP is at a lower temperature than the LCEP and no supercritical fluid region exists. Two quadruple points are found in the diagram.

(Rowlinson, 1969)

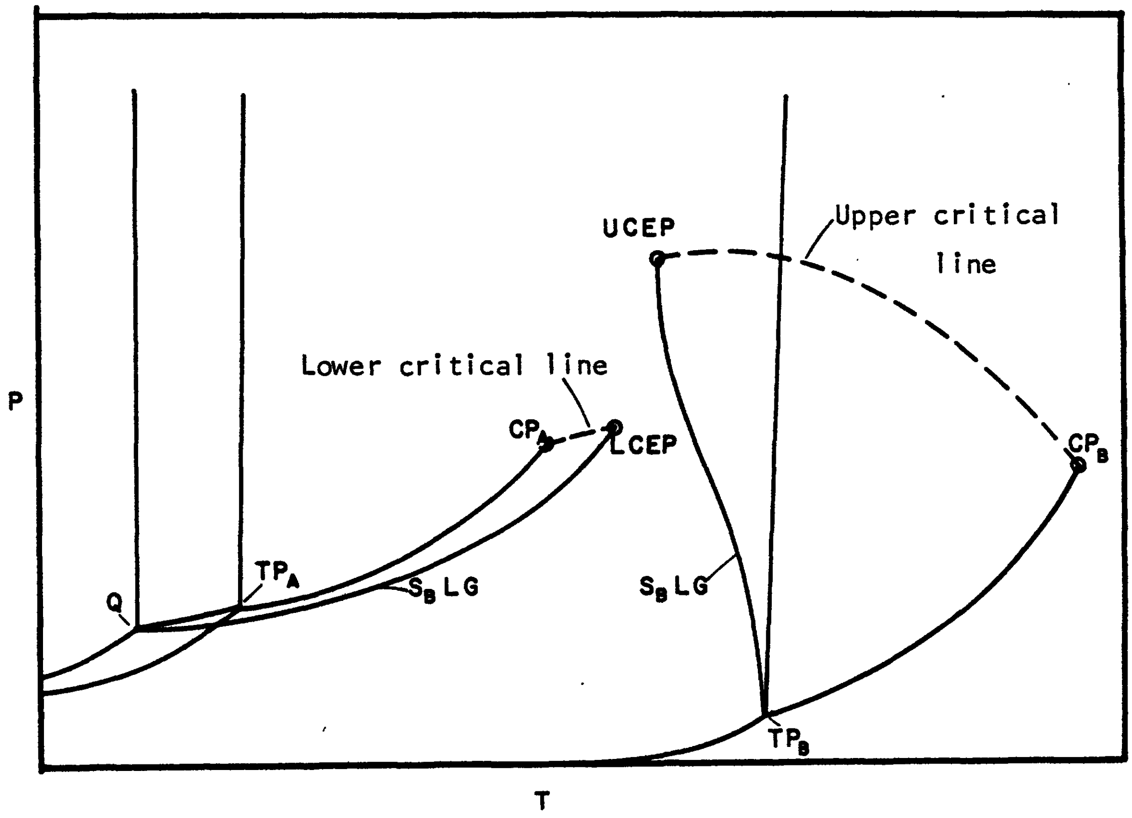

Figure 2.20a. A system similar to that depicted in Figure 2.19, but with the UCEP at a higher temperature than the LCEP. A supercritical fluid region now exists between the LCEP and the UCEP. Only one quadruple point is found in this diagram.

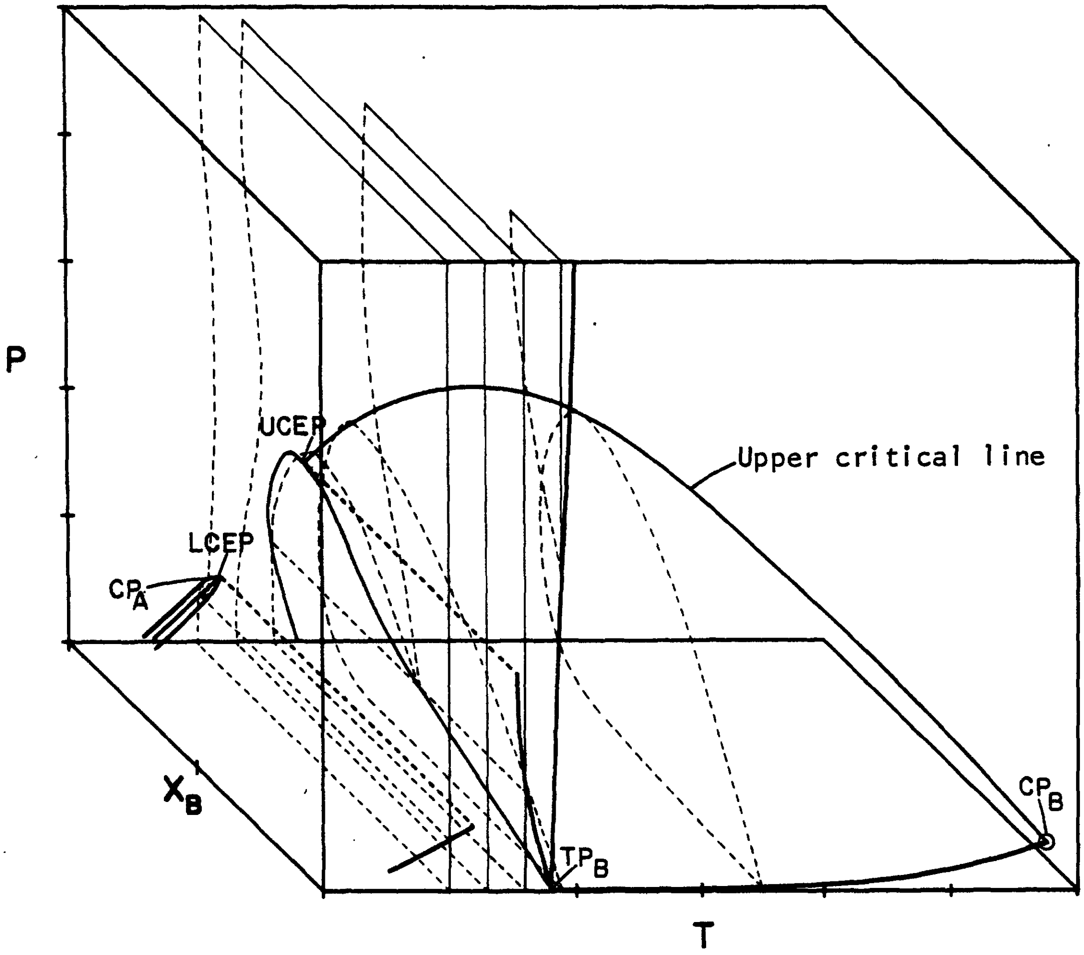

Figure 2.20b. The space diagram for Figure 2.20a. This diagram is based qualitatively on the naphthalene (B) - ethylene (A) system.

(Büchner, 1906b)

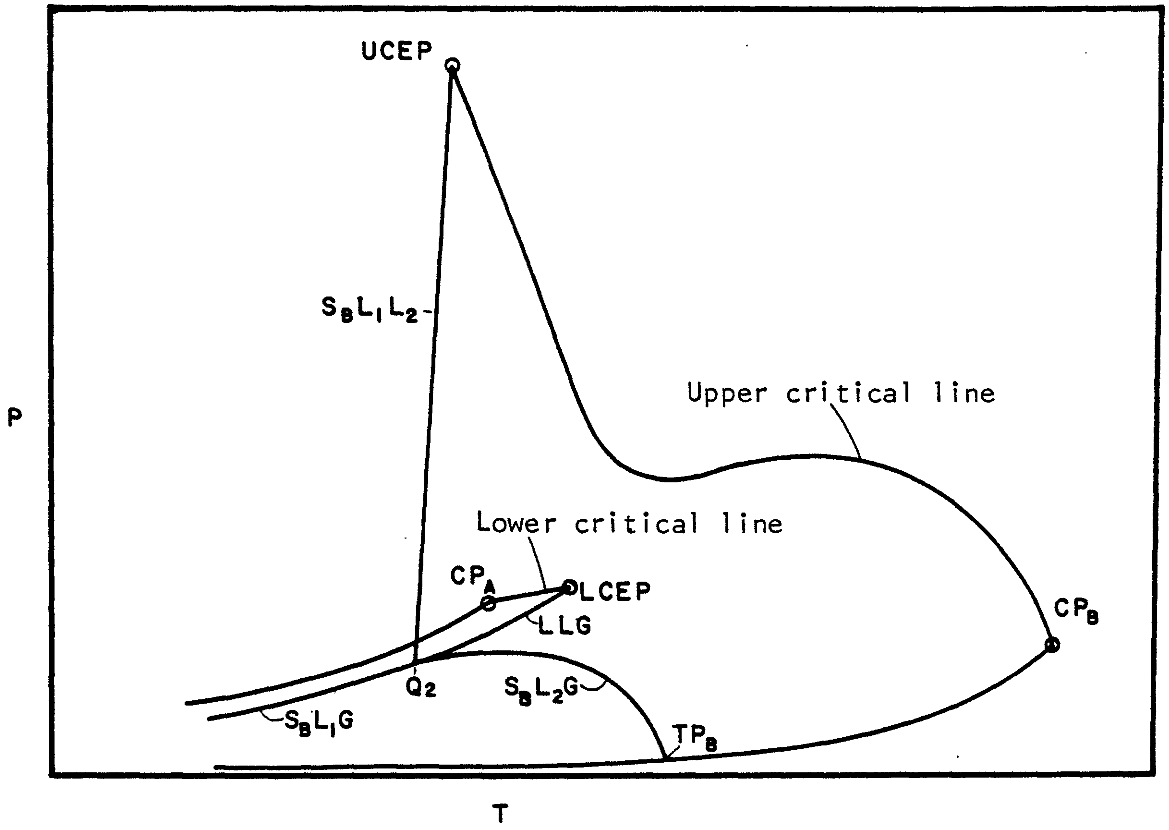

Figure 2.21. A system of the type shown in Figure 2.8, with precipitation of solid at temperatures below the LCEP.

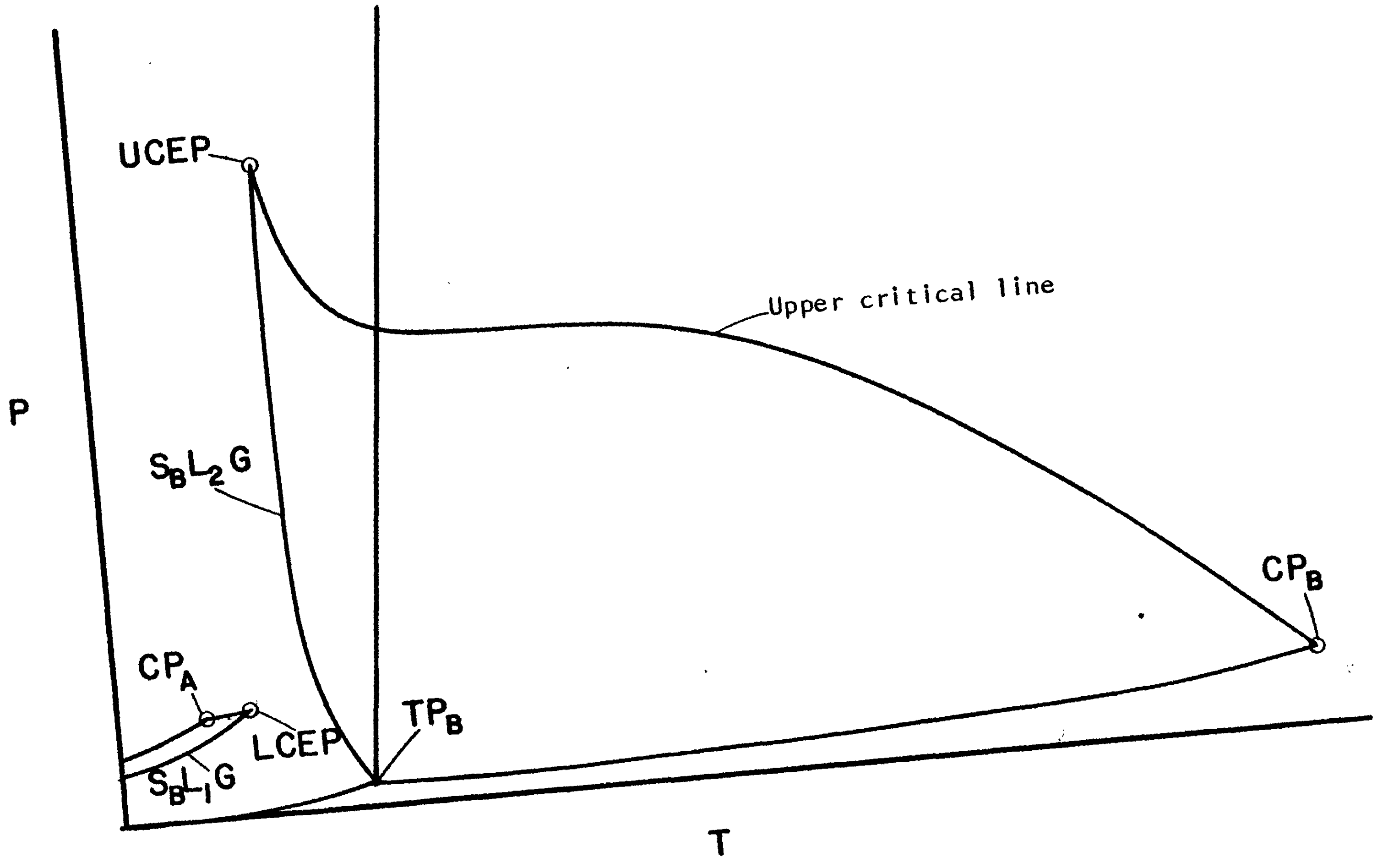

Figure 2.22a. A system similar to the type shown in Figure 2.8, with precipitation of solid B at temperatures above the LCEP.

(Büchner, 1906b)

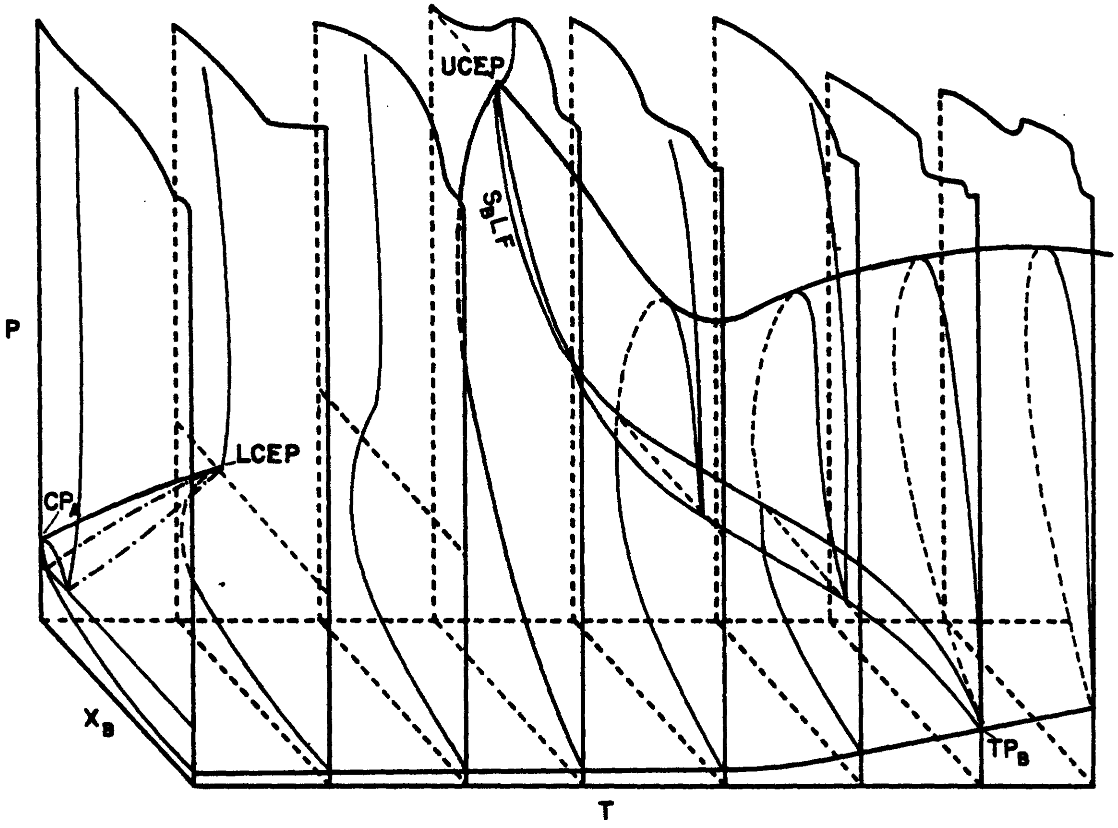

Figure 2.22b. The P-T-x space diagram of Figure 2.22a. Eight P-x sections are shown.

(Büchner, 1906b)

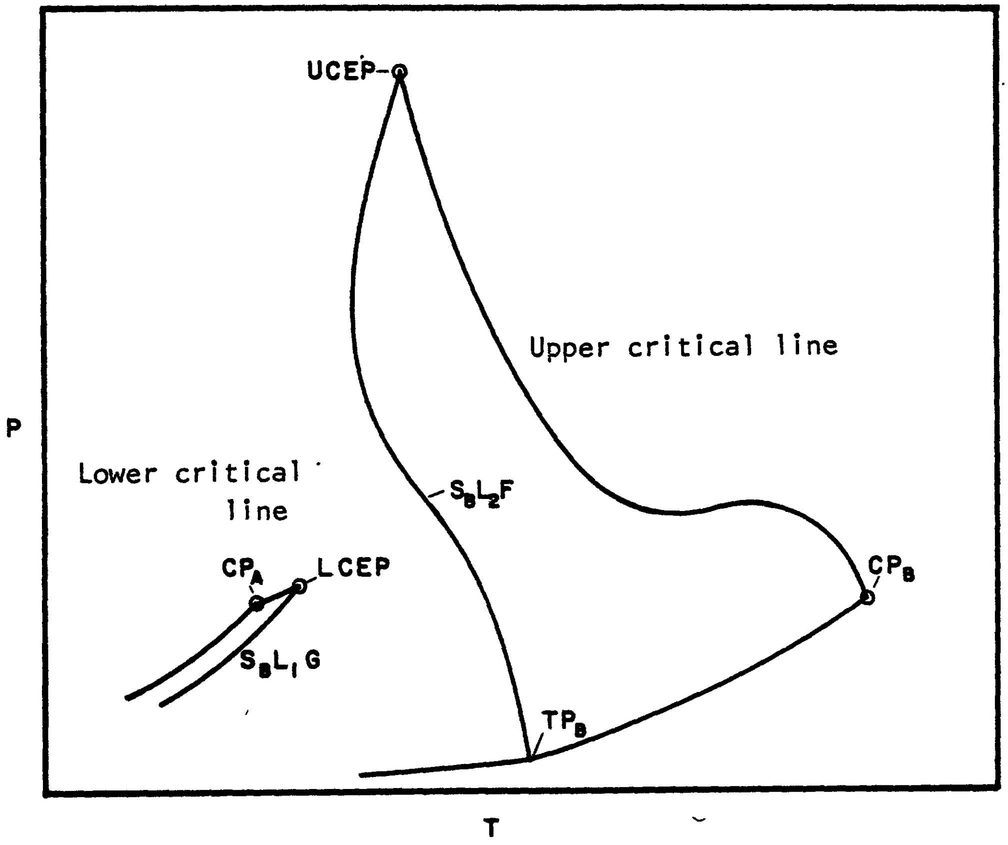

Figure 2.23. A system similar to that of Figure 2.22, but with a temperature minimum in the S_BL_2F curve.

between LCEP and UCEP, it is now possible to encounter two liquids coexisting in this temperature range.

In Figures 2.11 and 2.12, the entire upper critical line is found at temperatures near or above the critical temperature of B. A UCEP due to solid formation is not usually found in these systems. Behavior near the critical point of A is normal, with an LCEP of the type illustrated in previous diagrams.

The preceding classification of binary systems was intended not only to provide an understanding of the types of behavior which exist, but also to emphasize the need for such an understanding. The complexity of the diagrams can easily lead to a misinterpretation of experimental measurements or theoretical predictions. Furthermore, knowledge of a system's overall P-T-x behavior is useful when dealing with phase equilibrium problems. For example, the P-T-x behavior of the naphthalene - carbon dioxide system indicates that the extraction illustrated in Figure 2.1 might be more effectively carried out in a different temperature and pressure regime. For these reasons, it is a goal of this thesis to investigate prediction of the overall phase behavior of binary systems. The means for obtaining these predictions are discussed in the following section.

2.3 Equations of State

A formula relating the temperature, pressure, volume (or density) and composition of a system is known as an equation of state. The accurate correlation of these properties for even a pure component often requires a fairly complex equation. An extreme example is provided by the equation of state for water which has been developed by Keenan, et al. (1978). This equation, used to generate steam table PVT data, contains 50 empirical constants. It is applicable to all fluid phases of water, but contains no information about the solid phase. Furthermore, the equation is solely for use with pure water; it is of no use in determining properties of aqueous mixtures. Prediction of binary phase diagrams requires equations applicable to both pure components and mixtures.

Development of suitable equations of state for gaseous and liquid phases is a problem which has intrigued scientists for several hundred years. The oldest and most well-known of these is the ideal gas law,

$$P\underline{V} = NRT \tag{2.1}$$

which resulted from the work of Boyle in 1662, Charles and Gay-Lussac in the late eighteenth and early nineteenth centuries, and finally Avogadro in 1812. Thus the first equation of state took 150 years to formulate, and was not fully accepted until about 1860. It is only applicable to low density gases.

In his doctoral dissertation of 1873, J.D. van der Waals proposed a semiempirical modification of the ideal gas equation which attempted to account for nonidealities of the pure gaseous state. While not the first model for these nonidealities (see Brush, 1961), it was the first such equation to see widespread usage. This equation is stated in intensive form as

$$\left(P + \frac{a}{v^2}\right)(v-b) = RT \tag{2.2}$$

or

$$P = \frac{RT}{v-b} - \frac{a}{v^2} \tag{2.3}$$

Here a and b are constants, with the term $\frac{a}{v^2}$ accounting for the attractive forces between the molecules and b the finite volume occupied by these molecules. Equation (2.3) provides a good representation of the behavior of gases up to moderate densities, but at higher densities the deviations become quite large. More importantly, though, the nonideal terms introduced by van der Waals cause the equation to predict condensation of the gas at higher densities. As a result, the van der Waals equation may be used to model both gas and liquid phases. In 1890, van der Waals generalized his equation to permit application to multicomponent systems. This step paved the way for great advances in the understanding of fluid phase behavior of mixtures. In the first decade of this century, the Dutch schools at Amsterdam and Leiden experimentally mapped out many of the phase diagrams presented in the previous section. The time required for manual phase equilibrium calculations prohibited the actual prediction of phase diagrams. Mathematical analysis of the van der Waals equation, however, allowed these workers to check the consistency of their results and explain unexpected findings (see e.g., Smits, 1903 and 1905). Van der Waals himself was an active participant in this interpretation. Katz and Rzasa (1946) have prepared a useful bibliography giving references to the work in this period.

Another significant result of the Dutch work was the formulation of the virial equation of state by Kammerlingh Onnes in 1902. This equation is expressed as

$$P = \frac{RT}{v} + \frac{RTB}{v^2} + \frac{RTC}{v^3} + \ldots. \qquad (2.4)$$

Originally proposed on empirical grounds, it has since been derived from statistical mechanical principles (Mason and Spurling, 1969). This fact allows for the development of theoretical expressions for the constants B, C, etc. The virial equation is the only equation of state with a sound theoretical basis for both pure components and mixtures. Unfortunately, it is applicable only to gases of low and moderate density.

Since the time of van der Waals and his colleagues, numerous authors have proposed gas-liquid equations of state. As of 1944, over 100 such equations could be found in the literature (Dodge, 1944). The total at present is undoubtedly several times that number. The large majority of these equations have essentially been modifications of either equation (2.3) or (2.4). Recently, Oellrich, et al. (1977) have surveyed the equations of state most commonly used for VLE calculations. These equations, which all require a single empirical interaction parameter when used for a binary mixture, are given in Table 2.5. The authors used each of these equations to model a variety of binary systems in order to ascertain which gave the most accurate predictions of pressure and gas composition over a wide range of temperatures and pressures. In general, a modified form of the Lee-Kesler equation gave the best results. The Lee-Kesler equation has 24 constants, but this complication is minimal since the constants are the same for all substances. Unfortunately, as with many Benedict-Webb-Rubin type equations, this equation is prone to anomalous behavior in the critical region (Plöcker, et al., 1978; Francis and Paulaitis, 1981).

Table 2.5

Equation of State Comparison by Oellrich, et al. (1977)

Equation	Parent Equations
Soave (1972)	van der Waals (1873); Redlich-Kwong (1949)
Starling (1973)	Virial (1901); Benedict-Webb-Rubin (1940)
Lee-Kesler (1975), modification of Plöcker, Knapp, & Prausnitz (1977)	Virial; Benedict-Webb-Rubin
Peng-Robinson (1976)	van der Waals; Redlich-Kwong
Lu, et al. (1977)	van der Waals; Redlich-Kwong

For the modified van der Waals type equations, the Soave and Lu equations generally provided results nearly as good as the Plöcker-Lee-Kesler correlation. In some cases, most notably CO_2 binaries, the results were superior. The Peng-Robinson equation (Peng and Robinson, 1976) was not as satisfactory as the Soave and Lu equations.

Frequently, van der Waals type equations are used more for their simplicity than their accuracy. The two constants in the equations are always chosen so that the pure component critical point criteria (see Chapter 3) are satisfied. Often this procedure is not followed with the multiconstant virial type equations, leading to difficulties in the critical region. It is also possible with van der Waals type equations to specify temperature and pressure and solve for volume analytically, in contrast to the virial type equations for which a trial and error procedure is required. For mixtures, extension of the two-constant equations is semiempirical and straightforward. The extension involves specifying "mixing rules" which dictate how the pure component constants are to be combined to obtain constants for the mixture. Since the constants do have an approximate physical meaning, these rules are not entirely arbitrary. For more complicated equations, however, constants with no physical significance are often employed. Determining a suitable combination of these constants to obtain mixture parameters is a difficult task.

A weakness of both the van der Waals and virial type equations is that they cannot accurately model behavior in the immediate vicinity of a critical point. Levelt Sengers, et al. (1976) have shown that real substances are nonanalytic at the critical point, a fact not reflected by the previous equations. These authors recommend the use of scaling equations to accurately model critical behavior, equations which are, unfortunately, not very useful over wider temperature and pressure ranges.

The gas-liquid equations of state considered thus far (with the exception of the equation for water) have all viewed the liquid state as a perturbation of the gaseous state. At low densities they simplify to the ideal gas equation. At high densities, on the other hand, there is no common form and errors are more significant. An alternative approach is to use an equation developed specifically for the liquid phase. The higher degree of molecular interaction in the condensed state as compared to the gaseous state does make a theoretical description of liquids substantially more difficult. Equations of state for pure liquids have nevertheless been proposed, most notably those of Yen and Woods (1966) and Chueh and Prausnitz (1967, 1969). Both result from correlations of experimental data rather than a theoretical model of the liquid state, a fact which becomes particularly evident in extending the equations to mixtures.

The Yen and Woods correlation is not suitable for use in the critical region, while the Chueh and Prausnitz correlation is applicable only if the actual mixture critical temperature is already known. The reader is referred to Reid, et al. (1977) for a review of these formulations.

For conditions removed from the gas-liquid critical locus, volume and density are of secondary importance for the liquid state. Phase equilibrium calculations may be carried out without regard to pressure and temperature effects on volume, making an equation of state unnecessary. Prausnitz (1969) has given a review of the various "theories of solution" used for this purpose. These include the regular solution theory of Scatchard and Hildebrand, Guggenheim's lattice theory, and the athermal solution theory of Flory and Huggins, among others. Solution theories give more accurate results for the liquid state than those obtainable from gas-liquid equations of state. They are also useful for liquid-liquid critical phenomena occurring in regions removed from the gas-liquid critical locus.

The lattice theory is a particularly interesting example, as it represents the liquid state as a perturbation of the solid state, in contrast to the approach of the gas-liquid equations discussed previously. Recently, Kleintjens and Koningsveld (1980; see also Trappeniers, et al. (1970) and Schouten, et al. (1974)) have extended the lattice theory to the gaseous region by allowing for the existence of holes or vacancies in the lattice. In this treatment, a pure substance is viewed as a quasi-binary mixture of holes and molecules. Similarly, a binary mixture is considered as a quasi-ternary mixture. The authors have shown that this "lattice-gas model" correctly predicts the occurrence of gas-gas equilibrium (see Section 2.2) in the methane-water system. Beris (1981) has also demonstrated the qualitative correctness of benzene-water phase diagrams generated with this model.

The preceding discussion indicates that the choice of an equation of state for a particular fluid phase application is not always an easy task. In this work, prediction of binary P-T-x diagrams over wide ranges of temperature and pressure, with emphasis on the critical region, was the desired goal. The Peng-Robinson (P-R) equation was selected for this purpose for the following reasons:

a) In an exploratory study of this nature, it is appropriate to use the simplest approach. The P-R equation is a cubic, two-constant equation, the simplest type that can provide realistic results.

b) The critical region is the most difficult region of the P-T-x space to model. In this region, only the scaling equations provide results superior to those of the P-R. As noted, the scaling equations are not applicable for conditions removed from the critical locus.

These reasons do not make the P-R equation an unambiguous choice. In fact, a three constant cubic equation recently proposed by Martin (1979) holds some promise of being at least as good as the P-R equation in all respects. However, the P-R equation is among the simplest, and among the most accurate, of the equations which can be used to attain the stated goal.

The Peng-Robinson equation is expressed as:

$$P = \frac{RT}{v-b} - \frac{a}{v(v+b) + b(v-b)} \tag{2.5}$$

Note the similarity between this equation and the original van der Waals equation (2.3). The parameter b retains the meaning of the van der Waals covolume, while the temperature dependent parameter a = a(T) still represents the attractive forces between molecules. The equation may be rearranged into cubic form to give

$$Z^3 - (1-B)Z^2 + (A-3B^2-2B)Z - (AB-B^2-B^3) = 0 \tag{2.6}$$

where

$$Z = \frac{Pv}{RT} \tag{2.7}$$

$$A = \frac{aP}{R^2T^2} \tag{2.8}$$

$$B = \frac{bP}{RT} \tag{2.9}$$

For further definition of terms, Appendix A should be consulted. The pressure explicit form, equation (2.5) is to be preferred when the quantities T and V are specified, while the cubic form is used to analytically determine V when P and T are specified. The cubic form also indicates that the equation can have one or three real roots. Equation (2.5) predicts a critical compressibility factor of

$$Z_c = \frac{P_c v}{RT_c} = 0.307 \tag{2.10}$$

Note that v is determined from equation (2.5), and does not in general equal v_c, the actual critical volume of the substance. For a real substance,

$$Z_c = \frac{P_c v_c}{RT_c} \tag{2.11}$$

with Z_c being less than 0.307 for most materials. Other van der Waals type equations predict Z_c 's greater than 0.307, which is the major reason for their inferiority to the P-R equation in the critical region. The more realistic Z_c also leads to a better prediction of liquid densities by the P-R equation (Peng and Robinson, 1976a; Martin, 1979). For phase equilibrium calculations, the fugacity of a material is of prime importance. As shown in Appendix A, the P-R equation leads to the following expression for the fugacity of a pure compound:

$$f = P\exp\left[(Z-1) - \ln(Z-B) - \frac{A}{2\sqrt{2}B}\ln\left(\frac{Z + (\sqrt{2}+1)B}{Z - (\sqrt{2}-1)B}\right)\right] \qquad (2.12)$$

In contrast to the equation of state for water which was previously cited, the P-R equation may be applied to any pure substance provided the constants a and b are determined according to that substance's critical temperature, critical pressure, and Pitzer acentric factor ω (see Appendix A). The hypothesis that such a procedure is valid is known as the theory of corresponding states. It is a reasonably accurate assumption for many substances, as Chapter 4 will show.

The corresponding states theory may be applied to mixtures as well as pure components, if the appropriate a and b parameters for the mixture can be determined. It is generally presumed that these parameters can be expressed by a suitable combination of the parameters of the components comprising the mixture. This combination is carried out according to "mixing rules" which have been specified for the system. The mixing rules are necessarily semiempirical, since a and b are themselves semiempirical. The mixing rules used with the P-R equation are:

$$a = \sum_{i}\sum_{j} x_i x_j a_{ij} \tag{2.13}$$

$$b = \sum_{i} x_i b_i \tag{2.14}$$

where $a_{ii} = a_i$, the single subscript referring to the pure component i. The cross terms a_{ij} will be discussed shortly. Equations (2.13) and (2.14) are the mixing rules originally suggested by van der Waals in 1890. Considering a binary system, and keeping in mind the meaning of the parameters, it is easy to see the logic behind these rules. In a binary system of components 1 and 2, a must represent the average attractive force between the molecules. This should be equal to the attractive parameter between any two molecules weighted by the number of times that such a pairing occurs. Thus, for random mixing,

$$a = x_1^2 a_1 + 2x_1 x_2 a_{12} + x_2^2 a_2 \tag{2.15}$$

which is seen to be a special case of equation (2.13). Similarly, b must represent the average volume occupied by a molecule in the mixture, so that

$$b = x_1 b_1 + x_2 b_2 \tag{2.16}$$

in accordance with equation (2.14). Once mixing rules have been specified, it is possible to derive an expression for the fugacity of a component in a mixture (see Appendix A):

$$f_i = x_i P \exp\left[\frac{b_i}{b}(Z-1) - \ln(Z-B) - \frac{A}{2\sqrt{2}B}\left(\frac{2\sum_i x_i a_{ij}}{a} - \frac{b_i}{b}\right) \cdot \ln\left(\frac{Z + (\sqrt{2}+1)B}{Z - (\sqrt{2}-1)B}\right)\right] \tag{2.17}$$

The occurrence of the cross term a_{ij} in equation (2.13) has been noted. This term is defined as

$$a_{ij} = (1-\delta_{ij}) \sqrt{a_i a_j} \tag{2.18}$$

where δ_{ij} is an empirically determined interaction parameter. Equation (2.18) is a modification to the geometric mean rule

$$a_{ij} = \sqrt{a_i a_j} \tag{2.19}$$

which was originally used by van der Waals with little theoretical basis. Some justification for this expression was provided by the work of London in 1937. He showed that, at large distances, the potential energy Γ_{ij} between two spherically symmetric molecules having the same size and ionization potential is given approximately by

$$\Gamma_{ij} = \sqrt{\Gamma_i \Gamma_j} \tag{2.20}$$

Although equation (2.20) is an approximate derivation for the simplest case, equation (2.19) has been applied to many complicated systems. Good results are not always obtained, and it is now common practice to modifiy the geometric mean with an interaction parameter when necessary, as shown in equation (2.18).

The form of equation (2.18) was first suggested by Eckert and Prausnitz in 1965 for a regular solution model. It was based on the premise that mixtures of complicated molecules would exhibit deviations from the geometric mean rule and that the geometric mean would actually represent the maximum value of the interaction energy (Prausnitz had earlier (1959) suggested the form $a_{ij} = k_{ij} \sqrt{a_i a_j}$). In 1967, Chueh and Prausnitz adopted the formula for use with the Redlich-Kwong equation. While on these grounds the interaction parameter δ_{ij} does have some physical significance, and is always between 0 and 1, there are no means of determining how large the deviations from the geometric mean should be. Values for δ_{ij} are always chosen empirically, by determining the best fit of the equation of state to at least one data point. Use of a number of data points is often recommended, since the equations are very sensitive to the value of the parameter. It is also usual to take δ_{ij} as a constant, independent of temperature, composition, and density. This convention is followed in this thesis.

Since the interaction parameter represents a deviation from a mixture of molecules possessing spherically symmetric interactions, one would expect small values of δ_{ij} for systems approaching this ideal. Thus, for the ternary system methane-ethane-propane, Peng and Robinson (1976) found it suitable to use the geometric mean mixing rule, i.e., all $\delta_{ij}=0$. For systems which are asymmetric, polar, or otherwise nonideal, the value of δ_{ij} may be large or small, or even negative, depending on the interplay of the nonidealities. It is usually observed that the optimum value of δ_{ij} is not constant in these systems. Zudkevitch and Joffe (1970) suggest that the interaction parameter be established as a function of temperature and/or pressure for cases in which these conditions vary over a sizeable range. Peng and Robinson (1980) used a temperature dependent δ_{ij} with their equation for the calculation of aqueous-organic equilibria. The interaction parameter, expressed in the form of equation (2.18), was allowed to vary with temperature to give the best fit to the data. Its value increased with temperature, indicating that the attraction energy between unlike molecules decreased with increasing temperature. The authors did not derive an explicit temperature dependence for the parameter. Similarly, Lazalde et al. (1980) have suggested a temperature dependent correction to the geometric mean for systems of polar molecules. This expression has the form

$$\varepsilon_{ij} = \left(1 + \frac{c}{T}\right)\sqrt{\varepsilon_i \varepsilon_j} \qquad (1.21)$$

where ε_{ij} is a characteristic energy. The constant c accounts for orientational effects, and may be identified as an interaction parameter. Lazalde, et al. have proposed this form since orientational effects should be more important at low temperatures than at high temperatures. Energetically stronger interactions would be favored at lower temperatures, so that ε_{ij} should rise as temperature falls.

In contrast to the many choices available for representing fluid phase behavior, thermodynamic analysis of the solid phase is quite standard. For solid-fluid systems, it is often found that very little of the more volatile component dissolves in the solid phase. This is true of the systems considered in this thesis, and leads to the assumption that the solid is present in a pure form. Chapter 4, which deals with pure component phase diagrams, will discuss the treatment of the solid phase.

2.4 Scope and Context of Present Work

The objectives of this thesis are, in order of importance:

a) To illustrate a method for determining the overall phase behavior of binary systems. This capability is important in process design feasibility studies. In experimental phase equilibrium studies, consistency of results may be checked, and regions of the P-T-x space requiring special attention are indicated.

b) To illustrate the application of an algorithm for phase equilibrium calculations and the interpretation of its results. Computational algorithms sometimes experience convergence problems in the critical and azeotropic regions, and can also give erroneous phase equilibrium predictions. A careful examination of these problems should indicate how they might be avoided.

c) To investigate the applicability of the Peng-Robinson equation of state to the supercritical fluid region. If sufficiently accurate results can be obtained, the equation will be useful in process design and correlation of experimental data.

Certain aspects of this study have been treated by other investigators. The work of van Konynenburg (1968; see also Scott and van Konynenburg, 1970) is most closely akin to the first objective. Using the van der Waals equation of state (2.3), van Konynenburg showed that by varying the constants a and b, most known types of binary fluid-fluid equilibria could be qualitatively described. Systems were classified according to the presence and location of critical lines, three-phase lines, and azeotropic lines. Van Konynenburg did not undertake predictions for particular binaries, and did not consider the formation of solid phases.

Predictions of fluid phase equilibria have been carried out since the time of van der Waals by numerous workers. For binary systems, treatment of the critical region is also fairly common. In contrast, prediction of the solubility of solids in supercritical fluids has received limited attention until quite recently. The earliest work on this topic, which used the virial equation of state, has been covered by Rowlinson and Richardson (1959). In 1965, Prausnitz reviewed two standard approaches to the problem. The first of these utilized a modified Redlich-Kwong equation, treating the fluid as a dense gas, while the second treated the fluid as an expanded liquid and was based on regular solution theory. Neither of these methods employed an interaction parameter and, not surprisingly, results were only semiquantitative. Peng and Robinson (1978) used their equation to predict the S-L-G locus up to the critical region of methane in the cryogenic methane - carbon dioxide system. Excellent results were obtained using a constant binary interaction parameter which had been determined at vapor-liquid equilibrium conditions removed from the three-phase line. These authors have also given references to several similar studies.

In 1979, Mackay and Paulaitis proposed a method for solubility predictions which gives reasonable quantitaive accuracy. The fluid is treated as an expanded liquid, although an equation of state (Redlich-Kwong) is still used in the calculations. Two parameters are used in the correlation, a binary interaction parameter and an activity coefficient at infinite dilution, the latter being temperature dependent. Modell, et al. (1979) presented semiquantitative solubility predictions using the dense gas approach with the Peng-Robinson equation of state and a constant binary interaction parameter. That paper summarizes some of the early work on this thesis, and includes several P-T-x diagrams as well as calculations of critical end points.

Within the past year, a number of studies on supercritical fluid solubility have been published. Kurnik, et al. (1981) have shown that reasonably quantitative predictions result with the dense gas approach if the binary interaction parameter is allowed to vary with temperature. Kurnik (1981) has also extended these predictions to systems of two solids in equilibrium with a supercritical fluid. The P-R equation correctly predicts an increase in the solubility of both components over what would be found individually. Francis and Paulaitis (1981) have used the dense gas model, with a modified Lee-Kessler equation, and obtained semiquantitative results with a constant interaction parameter. These authors have also predicted upper critical end points with a fair degree of success. Johnston and Eckert (1981) have used a perturbed hard sphere modification of the van der Waals equation to calculate solubilities. Reasonable results were obtained with a single temperature dependent interaction parameter. The method was limited, however, to fairly low solubilities.

Chapter 3 Theoretical Considerations

Phase equilibrium in chemical systems is most concisely defined by four mathematical relations. The first of these is the criterion of equilibrium, which establishes whether or not phase equilibrium is theoretically possible. The second of these determines if the theoretically possible equilibrium is stable or unstable, and is thus known as the criterion of stability. Stable equilibrium can be realized in practice, while unstable equilibrium cannot. The third relation is the criterion of criticality. This criterion determines if a theoretically possible equilibrium is of a limiting type in which two coexisting phases have become indistinguishable. Such an equilibrium is said to represent a critical point. The final relation, that of critical stability, defines the stability or instability of a critical point.

The phase equilibrium relations result from a consideration of the variations a system in a stable equilibrium state might undergo. The derivations become fairly involved, and are best treated elsewhere. For present purposes, it will suffice to cite the results of previous workers and show how these results apply to one and two component systems.

A typical derivation of the criterion of equilibrium is given by Modell and Reid (1974). These authors consider the Taylor series expansion of a perturbation in the internal energy $\underline{U}$ about an equilibrium state. The internal energy is given by the Fundamental Equation

$$\underline{U} = \underline{U}(\underline{S}, \underline{V}, N_1, \ldots N_n) \tag{3.1}$$

The expansion is written as

$$\Delta\underline{U} = \delta\underline{U} + \frac{1}{2!}\,\delta^2\underline{U} + \;.\;.\;.\;.\; + \frac{1}{m!}\,\delta^m\underline{U} \tag{3.2}$$

where

$$\delta\underline{U} = \sum_{i=1}^{n+2}\left(\frac{\partial\underline{U}}{\partial z_i}\right)\delta z_i \tag{3.3}$$

$$\delta^2\underline{U} = \sum_{i=1}^{n+2}\sum_{j=1}^{n+2}\left(\frac{\partial^2\underline{U}}{\partial z_i\,\partial z_j}\right)\delta z_i\,\delta z_j \tag{3.4}$$

etc.

The symbol δ represents a small but finite change in a quantity, while z_i represents a particular variable of the set $\underline{S}$, $\underline{V}$, N_1, ..., N_n. For a system at equilibrium, it is found that

$$\delta\underline{U} = 0 \tag{3.5}$$

Equilibrium states are therefore extrema in the internal energy functionality.

For a one-component system, equation (3.5) becomes

$$\delta \underline{U} = \left(\frac{\partial \underline{U}}{\partial \underline{S}}\right)_{\underline{V},N} \delta \underline{S} + \left(\frac{\partial \underline{U}}{\partial \underline{V}}\right)_{\underline{S},N} \delta \underline{V} + \left(\frac{\partial \underline{U}}{\partial N}\right)_{\underline{S},\underline{V}} \delta N$$

$$= T\delta \underline{S} - P\delta \underline{V} + \mu \delta N \qquad (3.6)$$

If only one phase is present, the criterion of equilibrium does not lead to any constraints on the system. If two phases are present, however, it is necessary that

$$\delta \underline{V} = \delta \underline{V}^{I} + \delta \underline{V}^{II} = 0 \qquad (3.7)$$

and

$$\delta N = \delta N^{I} + \delta N^{II} = 0 \qquad (3.8)$$

The superscripts I and II denote the two coexisting phases. By equation (3.6), assuming $T \neq 0$,

$$\delta \underline{S} = \delta \underline{S}^{I} + \delta \underline{S}^{II} = 0 \qquad (3.9)$$

as well. Since $\delta \underline{U}^{I} = -\delta \underline{U}^{II}$, equation (3.6) gives

$$T^{I}\delta \underline{S}^{I} - P^{I}\delta \underline{V}^{I} + \mu^{I}\delta N^{I} = -(T^{II}\delta \underline{S}^{II} - P^{II}\delta \underline{V}^{II} + \mu^{II}\delta N^{II}) \qquad (3.10)$$

Rearranging and using equations (3.7) to (3.9), it is found that

$$(T^{I} - T^{II})\delta \underline{S}^{I} - (P^{I} - P^{II})\delta \underline{V}^{I} + (\mu^{I} - \mu^{II})\delta N^{I} = 0 \qquad (3.11)$$

Since $\underline{S}^I$, $\underline{V}^I$, and N^I are independently variable, it follows that the constraints for two-phase equilibrium are

$$T^I = T^{II} \tag{3.12}$$

$$P^I = P^{II} \tag{3.13}$$

$$\mu^I = \mu^{II} \tag{3.14}$$

Were a third phase present, it too would have equal T, P, and chemical potential. (For a pure component, this can only occur at the triple point.) These well-known results are easily extended to a binary system. The temperature and pressure of all phases present are equal, and any particular component must have the same chemical potential in every phase. An equivalent expression for the equality of chemical potentials is the equality of fugacities. From the definition of fugacity, it follows that

$$\mu - \mu^o = RT\ln \frac{f}{f^o} \tag{3.15}$$

where the superscript 0 denotes a reference state at the same temperature as the system. Applying equation (3.14) for a component i in phases I and II, one may write

$$\mu_i^I - \mu_i^o = RT\ln \frac{f_i^I}{f_i^o} = \mu_i^{II} - \mu_i^o = RT\ln \frac{f_i^{II}}{f_i^o} \tag{3.16}$$

Thus,

$$f_i^I = f_i^{II} \tag{3.17}$$

States which satisfy the criterion of equilibrium are said to lie on the binodal locus. A region of the binodal locus may be either stable or unstable. For a stable equilibrium state, the internal energy is a minimum. In addition to equation (3.5), then, it is required that

$$\delta^m \underline{U} > 0 \tag{3.18}$$

where $\delta^m \underline{U}$ is the lowest order nonvanishing variation in equation (3.2) (m>1). Equation (3.18) is the criterion of stability. It is equivalent to the statement:

$$\Delta \underline{U} > 0 \tag{3.19}$$

Excepting the special case of a critical point, the proper form of equation (3.18) is

$$\delta^2 \underline{U} > 0 \tag{3.20}$$

The full expression for the $\delta^2 \underline{U}$ term was given in equation (3.4). Beegle, et al. (1974a,b) have shown that the right hand side of that equation may be expressed as a sum of squares. The condition that the coefficient of each squared term must be positive (to be certain of stability for all possible variations in the z_i) leads to an expression of the criterion of stability in terms of Legendre transform theory:

$$y_{kk}^{(k-1)} > 0, \quad k = 1,\ldots\ldots, n+1 \tag{3.21}$$

Here $y^{(k-1)}$ is the (k - 1) Legendre transform of y ($y = \underline{U}$; see Beegle, et al., 1974b) and the subscript kk denotes a second order partial derivative with respect to the independent varible k in the Fundamental Equation. The limit of stability is reached when any one of the $y^{(k-1)}_{kk}$ becomes equal to zero. The locus of the limit of stability is known as the spinodal (or spinoidal) curve. If one starts with a stable system, the criteria for stability may be simplified to

$$y^{n}_{(n-1)(n-1)} > 0 \qquad (3.22)$$

since the transform $y^{n}_{(n-1)(n-1)}$ is always among the first to become zero. To determine a priori if a system is stable, or if the term $y^{n}_{(n-1)(n-1)}$ has become undefined, it is necessary to evaluate all of the partial derivatives in equation (3.21).

For a pure component, the stability criteria from equation (3.21) are:

$$y^{o}_{11} = \left(\frac{\partial^2 \underline{U}}{\partial \underline{S}^2}\right)_{\underline{V},N} = \left(\frac{\partial T}{\partial \underline{S}}\right)_{\underline{V},N} = \frac{1}{N}\left(\frac{\partial T}{\partial S}\right)_{V} = \frac{T}{NC_{v}} > 0 \qquad (3.23)$$

and

$$y^{1}_{22} = \underline{A}_{VV} = \left(\frac{\partial^2 \underline{A}}{\partial \underline{V}^2}\right)_{T,N} = -\left(\frac{\partial P}{\partial \underline{V}}\right)_{T,N} = -\frac{1}{N}\left(\frac{\partial P}{\partial v}\right)_{T} > 0 \qquad (3.24)$$

where $\underline{A}$ is the total Helmholtz free energy. For a binary system, a third condition must be satisfied:

$$y_{33}^{2} = \underline{G}_{11} = \left(\frac{\partial^{2}\underline{G}}{\partial N_{1}^{2}}\right)_{T,P,N_{2}} = \left(\frac{\partial \mu_{1}}{\partial N_{1}}\right)_{T,P,N_{2}} > 0 \qquad (3.25)$$

where $\underline{G}$ is the total Gibbs free energy. Equation (3.23) is known as the criterion of thermal stability. The heat capacity C_V cannot be determined from an equation of state, and need not be considered further here. Equation (3.24) is the criterion of mechanical stability and equation (3.25) is the criterion of material stability. Equilibrium predictions from an equation of state which satisfy these inequalities are deemed stable. Otherwise, they are unstable.

Two other forms of the material stability criterion are relevant to the present work. For a pressure explicit equation of state, it is more convenient to work with $\underline{A}$ than $\underline{G}$. Beegle, et al. (1974b) have shown that the appropriate stability criterion in this case is

$$L1 = \begin{vmatrix} \underline{A}_{11} & \underline{A}_{1V} \\ \underline{A}_{1V} & \underline{A}_{VV} \end{vmatrix} = \underline{A}_{11}\underline{A}_{VV} - \underline{A}_{1V}^{2} > 0 \qquad (3.26)$$

In this notation, L1 symbolizes a stability criterion in terms of the Legendre transform of the first independent variable in the Fundamental Equation (3.1) ($\underline{S}$ in this case).

Beegle, et al. (1974a) have also shown that by use of a step down operator, equation (3.25) may be transformed directly into an expression in terms of the Helmholtz free energy. This expression is

$$\underline{G}_{11} = \underline{A}_{11} - \frac{\underline{A}_{1V}^{2}}{\underline{A}_{VV}} > 0 \qquad (3.27)$$

Either equation (3.26) or (3.27) is a valid criterion for material stability, provided $\underline{A}_{VV}$ is a positive quantity. If $\underline{A}_{VV}$ is negative, one of the equations will indicate stability and the other instability. Thus, in regions of mechanical instability (i.e., when $\underline{A}_{VV}<0$) it is best to consider material stability as being undefined.

Reid and Beegle (1977) have shown that the mole numbers in equations (3.25) to (3.27) may be replaced by mole fractions. Another equivalent criterion for equation (3.25) therefore is

$$\left(\frac{\partial \mu_1}{\partial x_1}\right)_{T,P} = RT \left(\frac{\partial \ln f_1}{\partial x_1}\right)_{T,P} > 0 \qquad (3.28)$$

At the limit of stability, these derivatives are equal to zero. Thus, at constant T and P, extrema in a plot of partial fugacity versus mole fraction of a component correspond to points on the spinodal curve.

As with the spinodal criteria, critical point criteria may be expressed in a variety of ways. Modell (1977) and Reid and Beegle (1977) have shown that the mathematical conditions for the point at which a stable system reaches criticality are given by:

$$y^{n}_{(n+1)(n+1)} = 0 \tag{3.29}$$

$$y^{n}_{(n+1)(n+1)(n+1)} = 0 \tag{3.30}$$

$$y^{n}_{(n+1)(n+1)(n+1)(n+1)} \geq 0 \tag{3.31}$$

Equation (3.29) is again the material stability criterion (also known as the first criterion of criticality in this context), while equation (3.30) is the critical criterion (or second criterion of criticality) and equation (3.31) is the critical stability criterion. These last two criteria result from considering the third and fourth order variations in equation (3.2), respectively. In equation (3.31), should the equal sign apply, the greater than sign must hold for the next nonvanishing derivative.

For a pure component, it has been shown that equation (3.29) becomes

$$\left(\frac{\partial P}{\partial \underline{V}}\right)_{T,N} = 0 \tag{3.32}$$

Equations (3.30) and (3.31) then become:

$$\left(\frac{\partial^2 P}{\partial \underline{V}^2}\right)_{T,N} = 0 \tag{3.33}$$

$$-\left(\frac{\partial^3 P}{\partial \underline{V}^3}\right)_{T,N} \geq 0 \tag{3.34}$$

For a stable binary system, the criteria become

$$\left(\frac{\partial^2 \underline{G}}{\partial N_1^2}\right)_{T,P,N_2} = \left(\frac{\partial \mu_1}{\partial N_1}\right)_{T,P,N_2} = 0 \tag{3.35}$$

$$\left(\frac{\partial^3 \underline{G}}{\partial N_1^3}\right)_{T,P,N_2} = \left(\frac{\partial^2 \mu_1}{\partial N_1^2}\right)_{T,P,N_2} = 0 \tag{3.36}$$

$$\left(\frac{\partial^4 \underline{G}}{\partial N_1^4}\right)_{T,P,N_2} = \left(\frac{\partial^3 \mu_1}{\partial N_1^3}\right)_{T,P,N_2} \geq 0 \tag{3.37}$$

As implied by the necessity of a critical stability criterion, unstable critical points may exist. Figure 3.1 gives a comparison of stable and unstable critical points (see also discussion of Figure 5.8a). Figure 3.1a shows the derivative $\left(\frac{\partial \mu_1}{\partial N_1}\right)_{T,P,N_2}$ evaluated along the coexistence curve in the region around a stable critical point. The derivative is always positive, except at the critical point where it

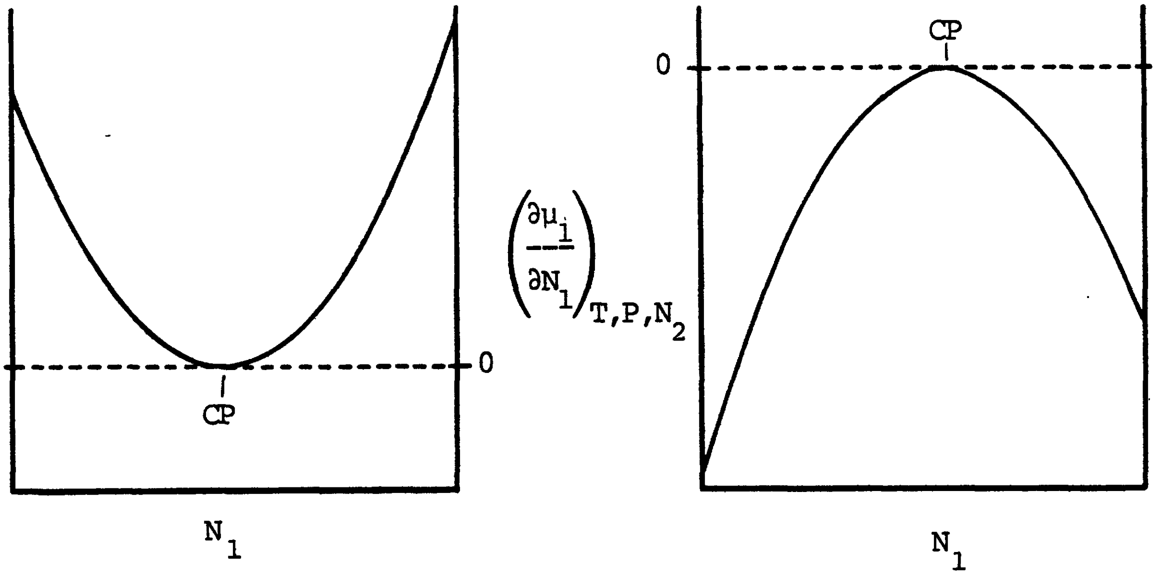

a. Stable critical point b. Unstable critical point

Figure 3.1. The two types of critical points. The ordinate is evaluated along the binodal locus. The stable critical point is a terminus of a stable binodal locus, so that $\frac{\partial \mu_1}{\partial N_1}$ is always ≥ 0. At the critical point, $\frac{\partial \mu_1}{\partial N_1} = 0$, $\frac{\partial}{\partial N_1}\left(\frac{\partial \mu_1}{\partial N_1}\right) = 0$, and $\frac{\partial^2}{\partial N_1^2}\left(\frac{\partial \mu_1}{\partial N_1}\right) > 0$. The unstable critical point is a terminus of an unstable binodal locus, so that $\frac{\partial \mu_1}{\partial N_1}$ is always ≤ 0. At the critical point,

$$\frac{\partial \mu_1}{\partial N_1} = 0, \quad \frac{\partial}{\partial N_1}\left(\frac{\partial \mu_1}{\partial N_1}\right) = 0, \text{ and } \frac{\partial^2}{\partial N_1^2}\left(\frac{\partial \mu_1}{\partial N_1}\right) < 0.$$

equals zero. At the critical point, $\left(\frac{\partial^2 \mu_1}{\partial N_1^2}\right)_{T,P,N_2}$ is zero as well, while $\left(\frac{\partial^3 \mu_1}{\partial N_1^3}\right)_{T,P,N_2}$, the critical stability criterion, is positive. Figure 3.1b shows the spinodal derivative in the region around an unstable critical point. The derivative along the coexistence curve is negative except at the critical point, where it is zero. At the critical point, $\left(\frac{\partial^2 \mu_1}{\partial N_1^2}\right)_{T,P,N_2}$ is zero and $\left(\frac{\partial^3 \mu_1}{\partial N_1^2}\right)_{T,P,N_2}$ is negative.

In equations (3.35) to (3.37), μ_1 may be replaced by f_1 (or $RT\ln f_1$), and N_1 by x_1, without loss of generality. Thus, equation (3.36) corresponds to an inflection point in a plot of f_1 versus x_1. Using the results of Reid and Beegle (1977) equation (3.36) can be written in terms of the Helmholtz free energy, for use with a pressure explicit equation of state, as follows:

$$M1 = \begin{vmatrix} \underline{A}_{VV} & \underline{A}_{1V} \\ \frac{\partial L1}{\partial \underline{V}} & \frac{\partial L1}{\partial N_1} \end{vmatrix} = \underline{A}_{111}\underline{A}_{VV}^{2} - \underline{A}_{VVV}\underline{A}_{11}\underline{A}_{1V} - 3\underline{A}_{VV}\underline{A}_{1V}\underline{A}_{11V}$$

$$+ 2\underline{A}_{1V}^{2} + \underline{A}_{VV}\underline{A}_{1VV}\underline{A}_{11} = 0 \qquad (3.38)$$

M1 symbolizes a critical point criterion in terms of the Legendre transform of the first independent variable in the Fundamental Equation (3.1). Again, the intensive form of this expression is also valid.

There are many ways to use the criteria developed above to achieve a desired goal. In most cases only some of the criteria need be employed. For example, to generate binodal loci, only the criterion of equilibrium need be applied. If critical lines are to be calculated, on the other hand, only the criteria of stability and criticality are necessary. In the generation of binary phase diagrams, it even turns out that the shape of the binodal curves is sufficient to determine regions of instability, as well as stable and unstable critical points. The specific application of the criteria in the present work will now be described.

Pure component, phase equilibrium tielines are conventionally drawn for isotherms in a P-v diagram, as shown in Figure 3.2. The curve has two extrema which define a region of three possible volumes for a given pressure. The lowest of these volumes corresponds to the liquid phase and the highest to the vapor phase. The middle volume is a mechanically unstable solution since $\left(\frac{\partial P}{\partial V}\right)_T > 0$. At the extrema, $\left(\frac{\partial P}{\partial V}\right)_T = 0$, so these must be points on the spinodal curve. The tieline connects the volumes of the coexisting liquid and vapor phases. It is distinguished from the other constant pressure (horizontal) lines which might be drawn between the liquid and vapor segments in that the phases it

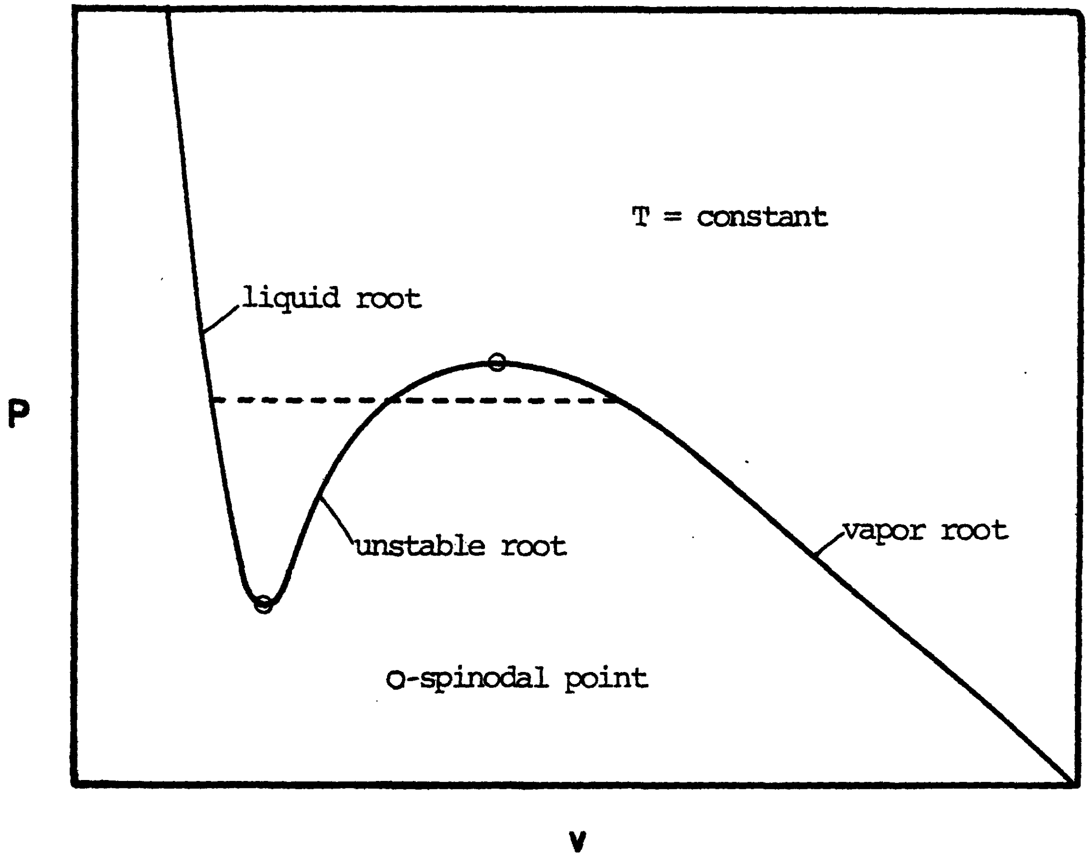

Figure 3.2. A typical P-v isotherm for a pure component. The tieline, which gives the volumes of the coexisting liquid and vapor phases, is shown dashed.

connects have equal fugacity.

For a binary system, an isothermal, isobaric plot of chemical potential or fugacity versus composition is the analog of Figure 3.3. This might be anticipated by comparing the pure component critical point criteria (equations (3.32) to (3.34)) with those for a binary system (equations (3.35) to (3.37)). Fugacity-composition and chemical potential-composition curves contain a great deal of information about the phase behavior of a system. In this thesis, the characteristic shapes of fugacity-composition curves were used to develop a computational algorithm for determining phase equilibrium, as discussed in detail in Appendix C.

At this point, it is instructive to consider some examples of fugacity-composition (f-x) plots. Figure 3.3 gives a plot of n-hexadecane (n-$C_{16}H_{34}$, abbreviated as C_{16} or subscript H) fugacity versus n-hexadecane mole fraction for the n-hexadecane - carbon dioxide system, at a temperature of 300 K and a pressure of 0.1 atm. The systems represented by this diagram are a result of mixing liquid n-C_{16} with gaseous CO_2, and VLE is to be expected if the two components are present in a certain range of proportions. The most striking feature of the plot is that there are actually two separate curves. Segment G is essentially linear over the entire range of composition, with a slope of

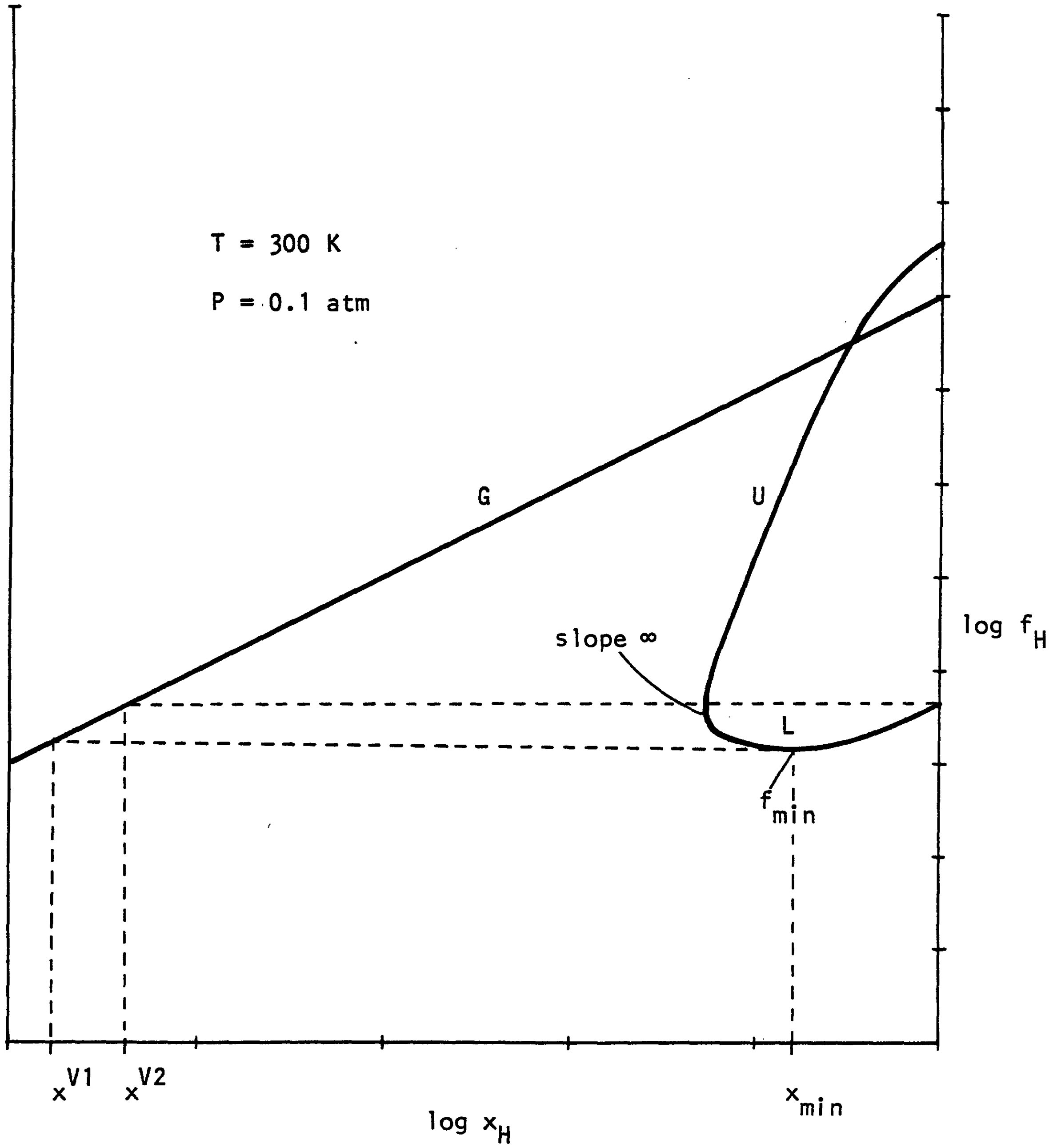

Figure 3.3. An f_H- x_H plot for n-hexadecane - carbon dioxide. Segment G is the gaseous root, segment U is the mechanically unstable root, and segment L is the liquid root. Segments U and L start at the slope infinity and continue to the pure hexadecane axis.

unity and an intercept at the pure C_{16} axis of 0.1 atm. This is the equivalent of ideal gas behavior, since

$$f_H = x_H P = P_H \tag{3.39}$$

where P_H is the partial pressure of C_{16}. The second curve, which is found for compositions greater than the composition of the

infinity in $\frac{df_H}{dx_H}$, gives the mechanically unstable (segment U) and liquid (segment L) fugacities. The existence of this curve corresponds to the existence of three real roots to the cubic equation (2.6). The partial fugacity expression, equation (2.17), is evaluated at a given x_H for each of the three volumes resulting from the cubic equation. As usual, the highest volume root gives the gas phase fugacity, the middle volume root the mechanically unstable fugacity, and the lowest volume root the liquid phase fugacity. As indicated by the crossing of segments G and U in the graph, the middle volume root does not always give the middle fugacity root.

The mechanically unstable root may be recognized in f-x plots since it is associated with the joining of the gas and liquid roots. This will become more evident at higher pressures (as in Figure 3.4). The actual violation of the mechanical stability criterion, i.e., that $\frac{\partial P}{\partial V}_T > 0$, may not be determined from the plot. On the other hand, material stability is readily apparent in the f-x plots. When $\frac{df_H}{dx_H} > 0$, the system is materially stable, and when $\frac{df_H}{dx_H} < 0$, the system is materially unstable. At 0.1 atm, the portion of segment L between the infinity and the minimum is materially unstable. Note that the mechanically unstable segment U appears as materially stable in this plot.

Suppose now that suitable quantities of C_{16} and CO_2 are present in the system so that two phases exist with compositions x^V and x^L, and fugacity f_H^E. The f-x plot shows that x^L must lie between $x_{min} = 0.15$ and $x_H = 1$, and furthermore, that f_H^E is between $f_H(x_{min})$ and $f_H(x_H = 1)$. For the coexisting vapor phase, which must lie on the straight line segment, equality of fugacities requires that

$$x^{V1} \leq x^V \leq x^{V2} \tag{3.40}$$

This limiting procedure illustrates the usefulness of the f-x plots in determining two phase equlibrium, and is one of the steps in the phase equilibrium algorithm detailed in Appendix C. To find the actual compositions for VLE, it is of course necessary to match partial fugacities of carbon dioxide as well.

Consider now Figure 3.4, which gives f-x plots in a series of 16 pressures at 300 K. The first of these, at 0.1 atm, has just been discussed. If pressure is increased to 0.5 atm, the fugacity of the vapor phase (segment G) has increased accordingly. The fugacity of segments U and L (mechanically unstable and liquid phase solutions, respectively) has also increased slightly. One effect of these circumstances is that the unstable and vapor phase solutions now terminate at nearly the same fugacity on the pure C_{16} axis. A second effect is that the composition of the vapor phase is at a lower x_H than it was at 0.1 atm. This must be so because the liquid phase fugacity can only be matched if the vapor phase composition is less than $x_H = 10^{-5}$.

At 1 atm, the vapor and unstable solutions have joined at a peak, so that the region of three roots for a given x_H no longer extends all the way to $x_H = 1$. The curve is continuous, and a second infinity and second zero appear in $\frac{df_H}{dx_H}$. The two zeroes, i.e., the maximum and the minimum, give two points on the spinodal curve at this T and P. The vapor phase solution is no longer a straight line, indicating deviations from ideal gas behavior.

At 5 atm, the peak has rounded substantially, and the trend toward lower C_{16} mole fraction in the VLE vapor phase

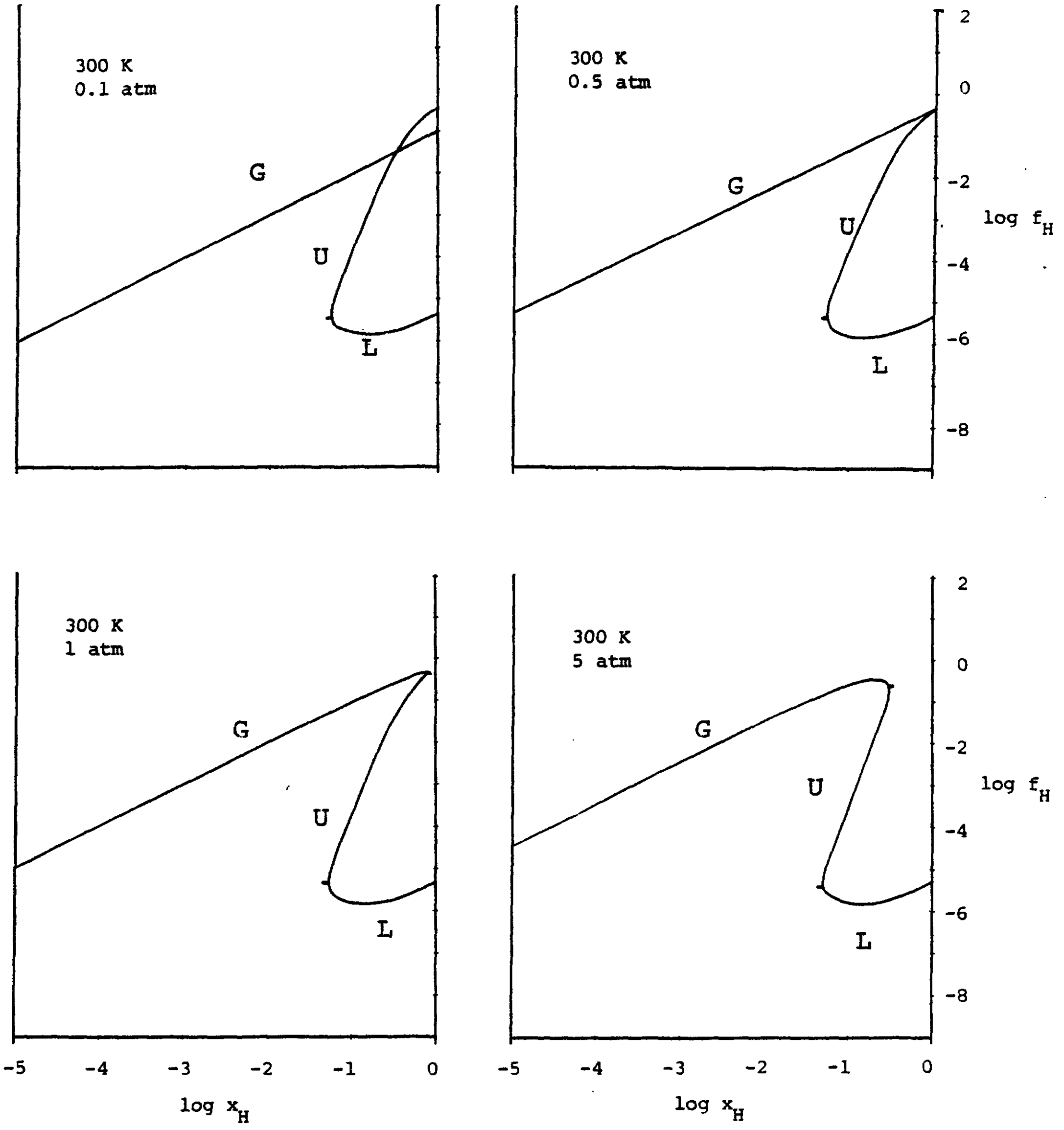

Figure 3.4. (First of four pages) $f_H - x_H$ plots for the n-hexadecane-carbon dioxide system. The curves are calculated from the P-R equation with δ_{12}=0.081. Segments labelled G represent gas fugacities. Segments labelled U are mechanically unstable. Segments labelled L are liquid phase fugacities.

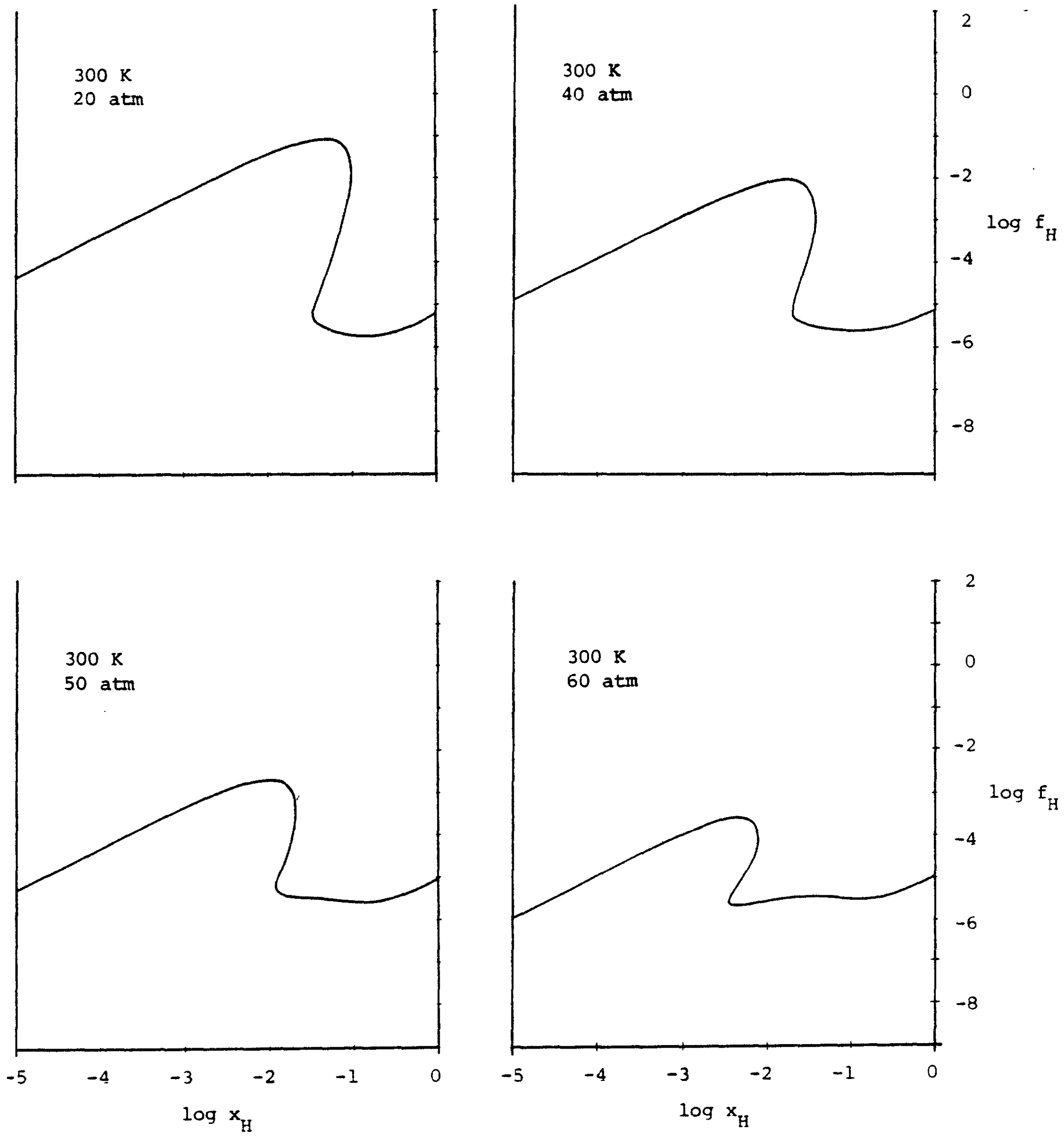

Figure 3.4. (Second of four pages) f-x plots for the n-hexadecane - carbon dioxide system.

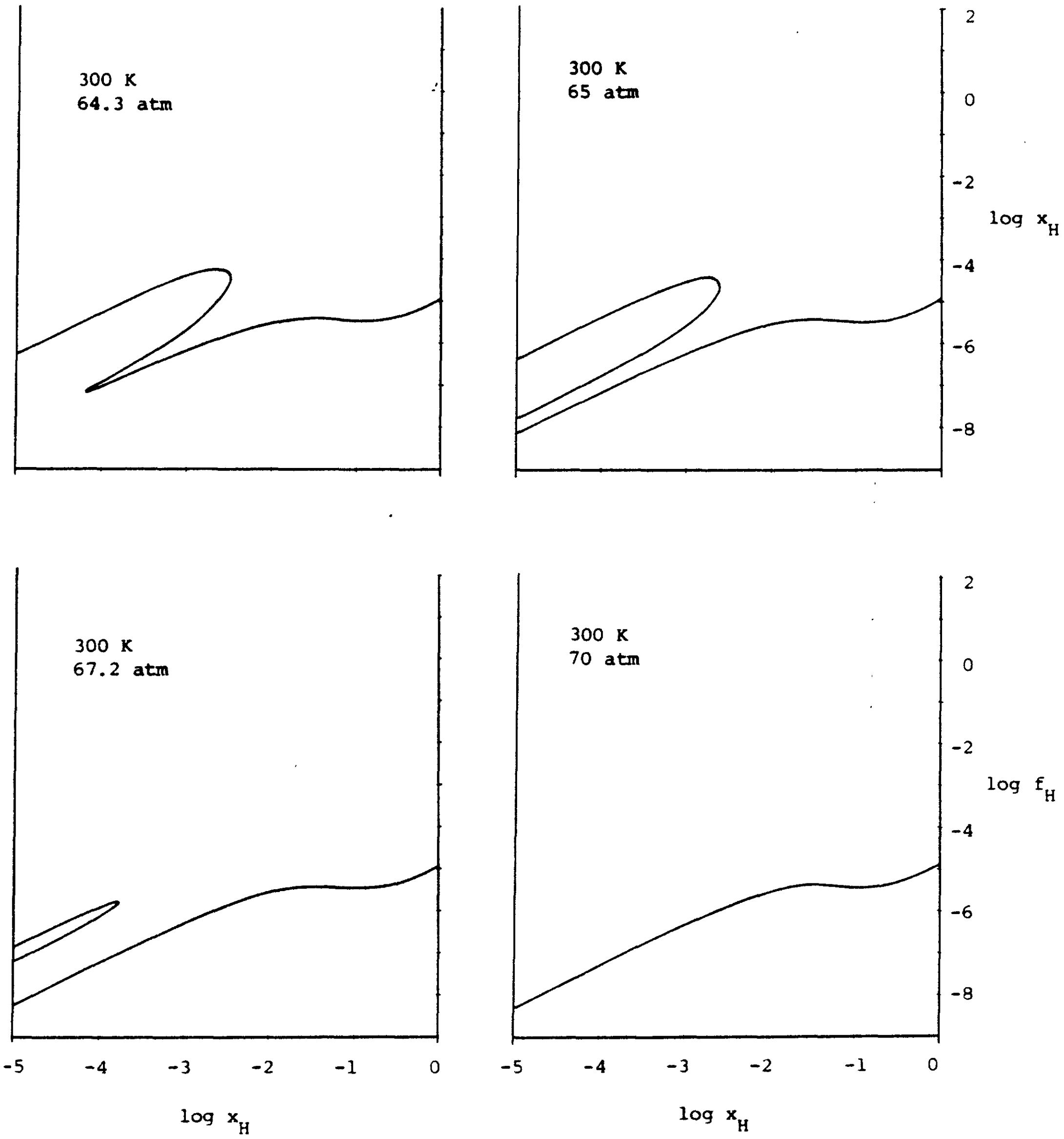

Figure 3.4. (Third of four pages) f-x plots for the n-hexadecane - carbon dioxide system.

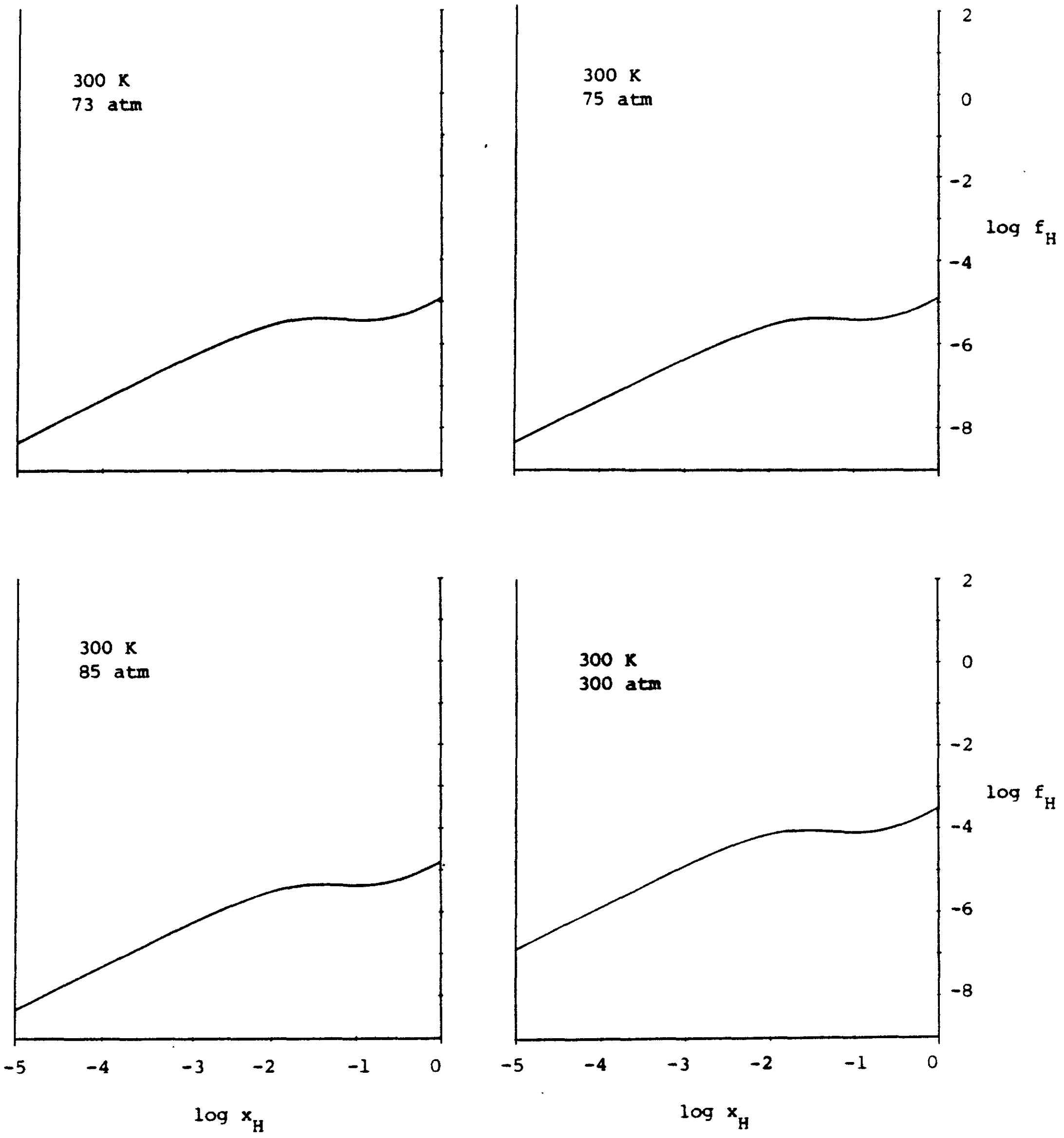

Figure 3.4. (Fourth of four pages) f-x plots for the n-hexadecane - carbon dioxide system.

continues. By the time 20 atm is reached, however, this trend has begun to reverse itself. This is an indication that, for a P - x phase diagram at 300 K, there is a minimum with respect to x_H in the vapor branch of the VLE curve. At 20 atm, it might also be noticed that the materially unstable liquid segment is beginning to show a plateau. This is more evident at 40 and 50 atm. At these pressures the VLE vapor phase x_H is coming back into the range covered by the concentration axis.

It is worthwhile at this point to consider the interpretation of the f-x plot over the entire composition range. For illustrative purposes, the plot for 50 atm has been redrawn in Figure 3.5 with a hypothetical VLE tieline. (The actual VLE tieline would extend off the graph on the vapor side, but this does not affect the validity of the present discussion). The two - phase equilibrium VLE compositions are denoted by x^V and x^L. For an overall system composition of $x_H < x^V$, only one phase is present - a vapor, with a fugacity as given on the f-x plot (extended to lower x_H as need be). For an overall system composition between x^V and x^L, the stable system is two phases of these compositions. Varying composition between x^V and x^L only affects the proportion of the two phases. Increasing x_H beyond x^L, there would again be a single phase system, a liquid with the fugacity shown on the plot.

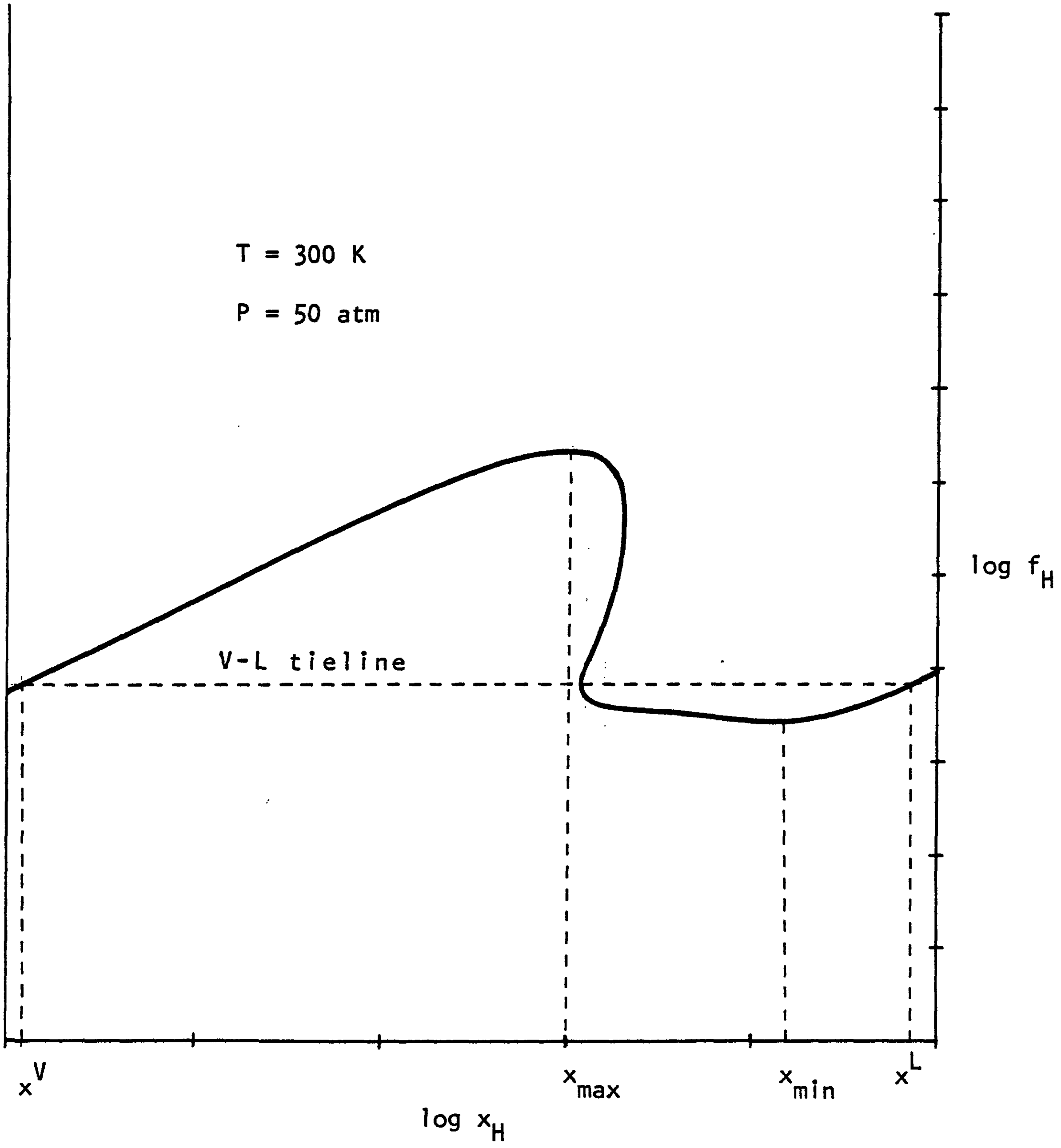

Figure 3.5. An f-x plot illustrating the possibility of metastable phases. Between x^V and x_{max}, a metastable vapor phase may exist. Between x_{min} and x^L, a metastable liquid phase may exist.

The f - x plot, however, indicates all possibilities for phase behavior, not only the stable states just considered. For example, increasing x_H beyond x^V will not invariably lead to the formation of two phases. It is possible that a single, metastable vapor phase will instead persist, with the fugacity given by the f-x curve. A metastable vapor phase is possible for compositions up to x_{max}. At this point, the vapor becomes intrinsically unstable and reverts to a two-phase system. At x_{max} it is the material stability criterion which is violated, rather than the mechanical stability criterion. This is an example of the stability criterion as stated by Beegle, et al. (1974b) - if one starts with a stable system (metastable vapor in this case) and moves toward a region of instability, the highest order criterion is always the first, or among the first, to become zero. As has been seen, the region of mechanical instability does not begin until the infinity is reached.

An argument similar to that above may be applied to the liquid phase compositions in Figure 3.5. Starting at x^L with only a single liquid phase, it is possible to decrease x_H to x_{min}, all the while maintaining a single liquid phase. At x_{min} the system becomes intrinsically unstable and must revert to two-phase behavior.

At 60 atm, two interesting developments have taken place (see Figure 3.4). The plateau after the low fugacity infinity has given rise to a minimum and maximum, making a total of four spinodal points at this T and P. There is now one region of mechanical instability, three regions of material instability, and three regions of stability. The latter indicate the possibility of having three phases simultaneously in equilibrium, as the range of fugacities for each segment overlap to some degree. It is by no means required, though, that three phases coexist at this T and P. For this binary, there is only one pressure at 300 K for which liquid-liquid-vapor equilibrium can occur (see Figures 2.8 and 2.9). Other possibilities at this pressure are a single phase, two-phase equilibrium, or two sets of two-phase equilibrium (i.e., liquid-liquid and liquid-vapor). Which of these in fact occurs depends on the overall system composition. It is also seen at this pressure that the VLE vapor phase composition is now constrained to a minimum composition of about $x_H = 2 \times 10^{-5}$, due partly to a rising liquid phase fugacity, but mostly to the depressed vapor phase fugacity. A system of lower x_H would be a single vapor phase, with a fugacity as given by the f-x plot. Considering the series of f-x plots from 20 to 60 atm, it is evident that the rising pressure has led to an increased solubility of C_{16} in CO_2.

Between 64.3 and 65 atm, a closed loop develops in the f-x plot. The closed loop does not show up in log-log coordinates, so the 65 atm section has been replotted in

Cartesian coordinates in Figure 3.6. All three roots of the fugacity equation converge at the origin, as required by the form of equation (2.17) as $x_H \rightarrow 0$. (A plot of f_{CO_2} versus x_H would have three different real roots at $x_H = 0$, as was true for f_H at 0.1 atm and $x_H = 1$). With the collapse onto the origin, the curve loses an infinity and a minimum, and is no longer continuously differentiable. In this case the statement of the stability criterion by Beegle, et al. (1974b), as given in conjunction with Figure 3.5, must be applied carefully. Conceivably, one could track a stable vapor phase or metastable liquid phase back to $x_H = 0$ and then continue, with increasing x_H, along the middle fugacity solution without violating a criterion of material stability. Using Beegle's definition, it might be thought that the mechanical stability criterion could not yet be violated, when in fact it has been. It is therefore important that a non-differentiable point encountered in the tracking procedure be treated as a violation of the stability criterion.

Returning to the sequence of f-x plots in Figure 3.4, it is seen that the loop shrinks considerably in moving from 65 to 67.2 atm. Upon reaching 70 atm, the loop has disappeared entirely, and there are no longer mole fractions at which three solutions to the cubic form exist. In general, a loop is found if and only if the P and T coordinates of the f-x plot are near the vapor pressure curve of a pure component.

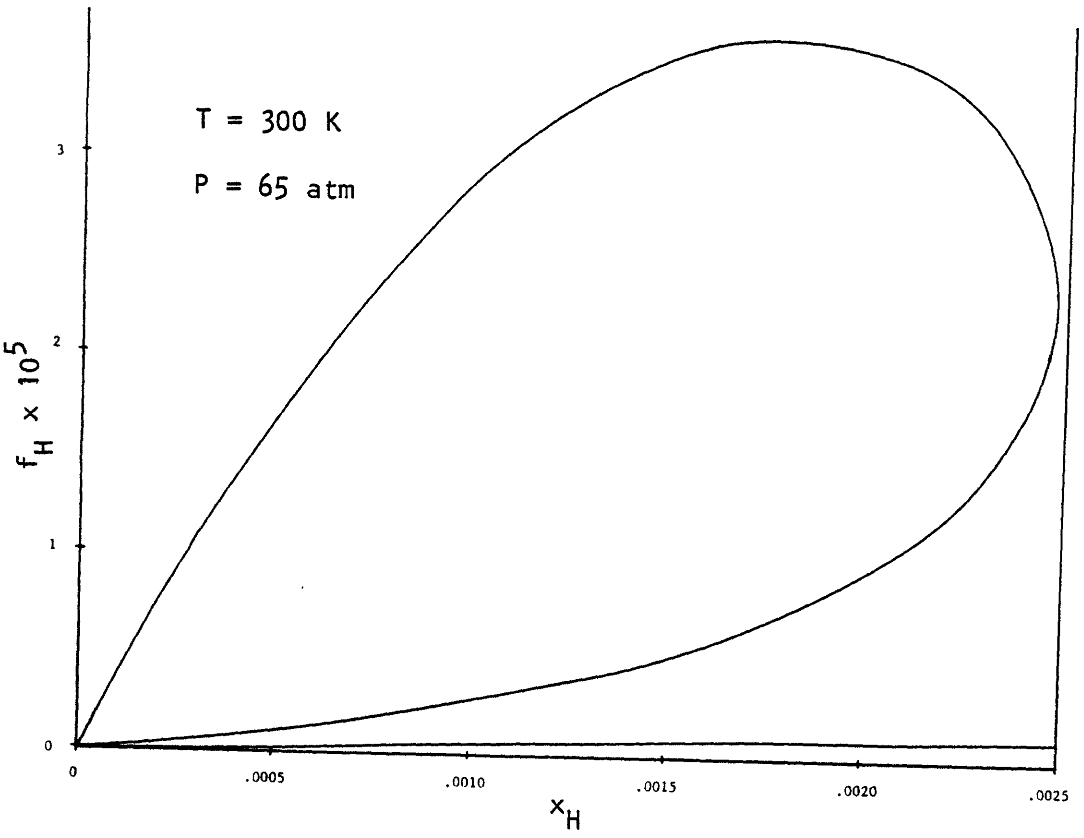

Figure 3.6. A Cartesian plot illustrating the closed loop behavior of the f_H- x_H curve at conditions near CO_2's vapor pressure.

At 300 K, the vapor pressure of n-hexadecane is 4 x 10^{-6} atm, and that of carbon dioxide is 66.3 atm. Thus, an open loop bounded by the pure hexadecane axis was found at 0.1 atm, while a closed loop terminating at the pure CO_2 axis was found between 64.3 and 70 atm. After a vapor pressure line terminates at a pure component critical point, loops terminating at that axis will not occur.

From 70 atm on up, the f-x curves are all qualitatively the same, possessing only one maximum and one minimum. Simple fugacity-composition curves with two extrema, and those which are monotonic in composition, comprise the large majority of curves at the various temperatures and pressures. This is not entirely evident from Figure 3.4, where temperature and pressures were carefully chosen to illustrate the various shapes that are encountered. A more realistic, though still somewhat biased, picture may be obtained by studying the f-x curves in Appendix B. The f-x plots for a matrix of seven temperatures and sixteen pressures are given there, the large majority of which have at most two extrema. As might be expected, the simpler curves are the easiest to analyze and solve for VLE.

Until now only the shapes of hexadecane fugacity curves have been considered. Figure 3.7 shows how carbon dioxide fugacity compares with hexadecane fugacity for the pressure series at 300 K. It is not possible to show all details with

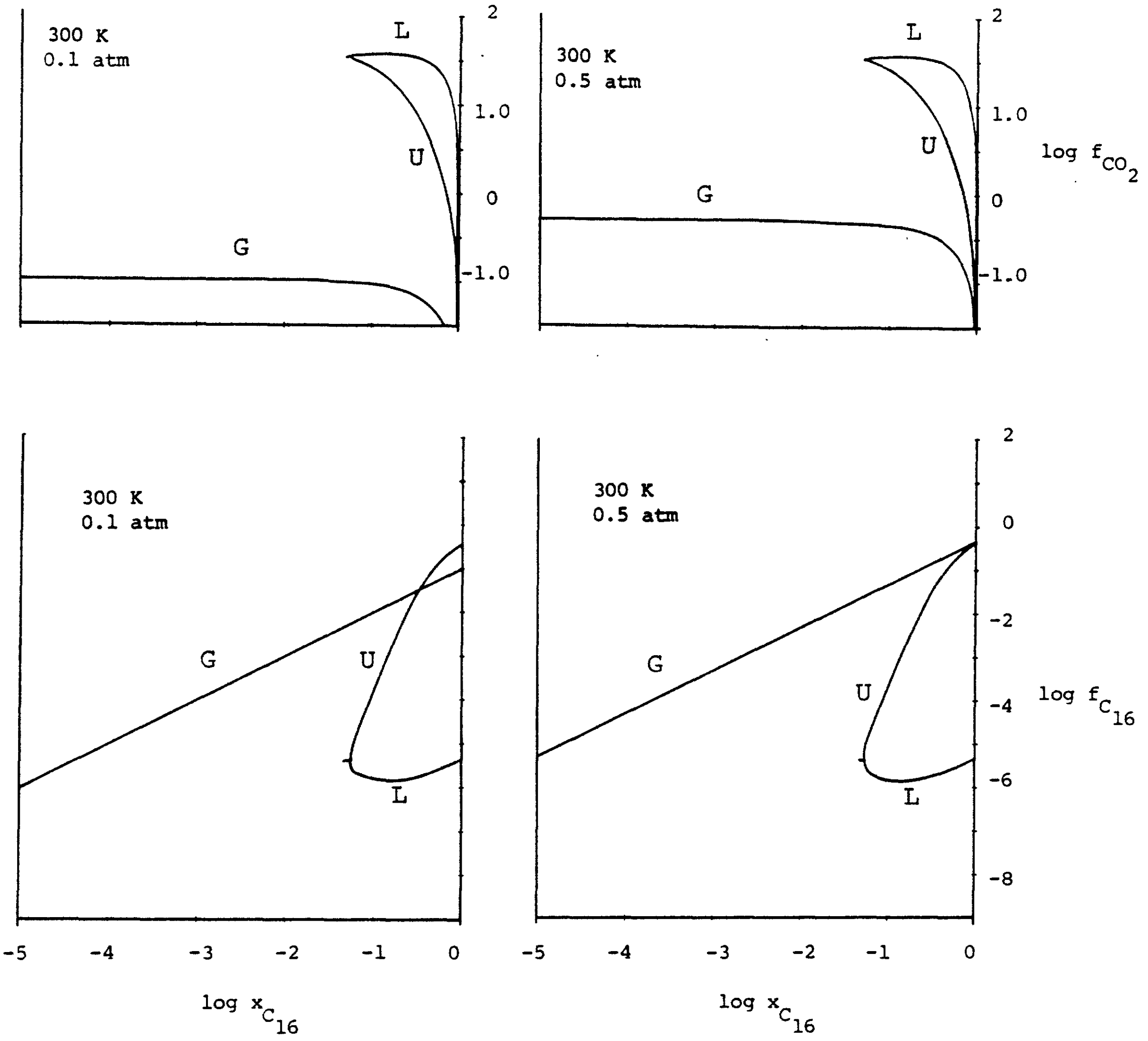

Figure 3.7. (First of eight pages) f_{CO_2}-x_H plots for the n-hexadecane - carbon dioxide system. Note the one-to-one correspondence between slope infinities and extrema. Segments are numbered as in Figure 3.4.

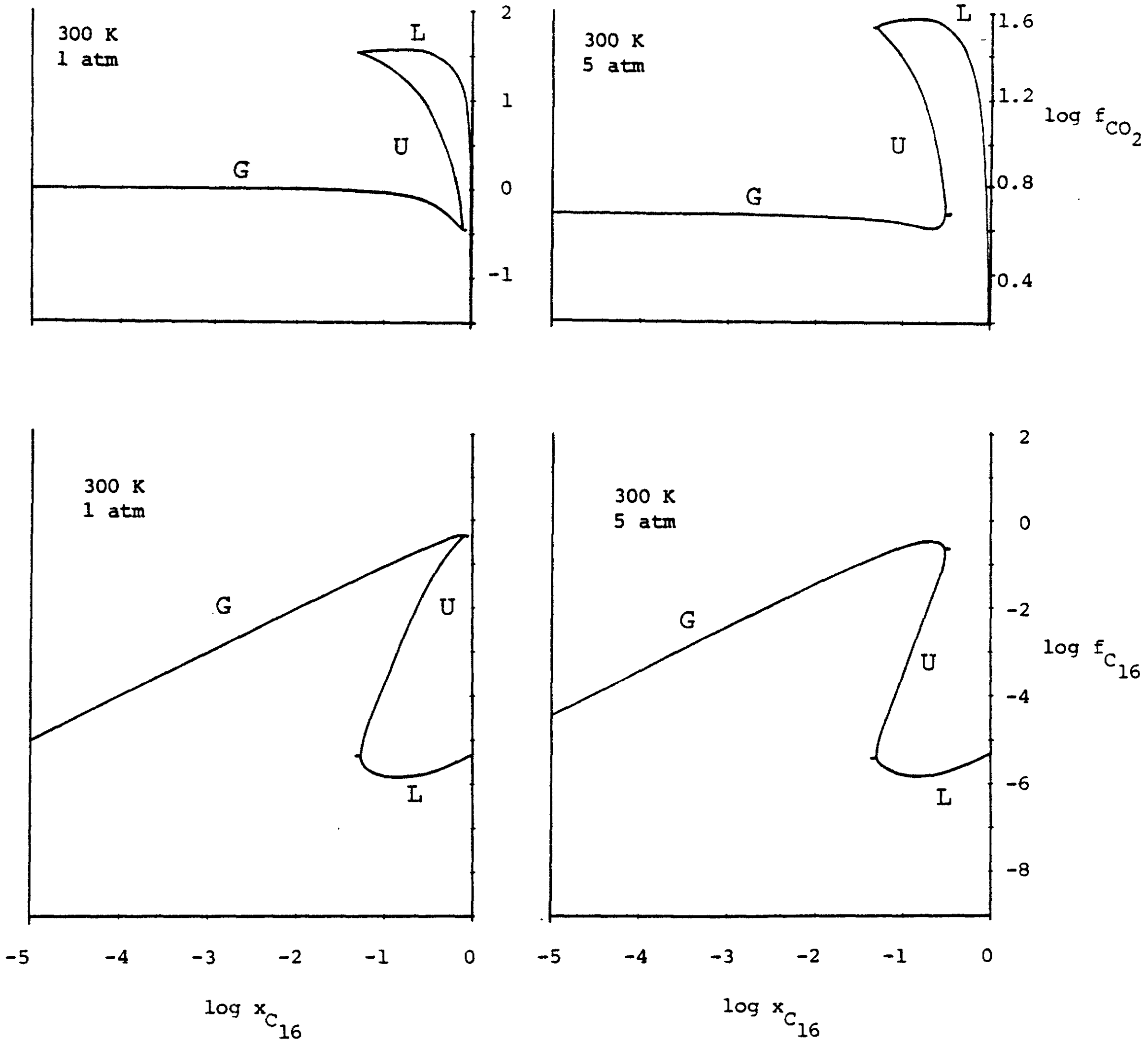

Figure 3.7. (Second of eight pages)

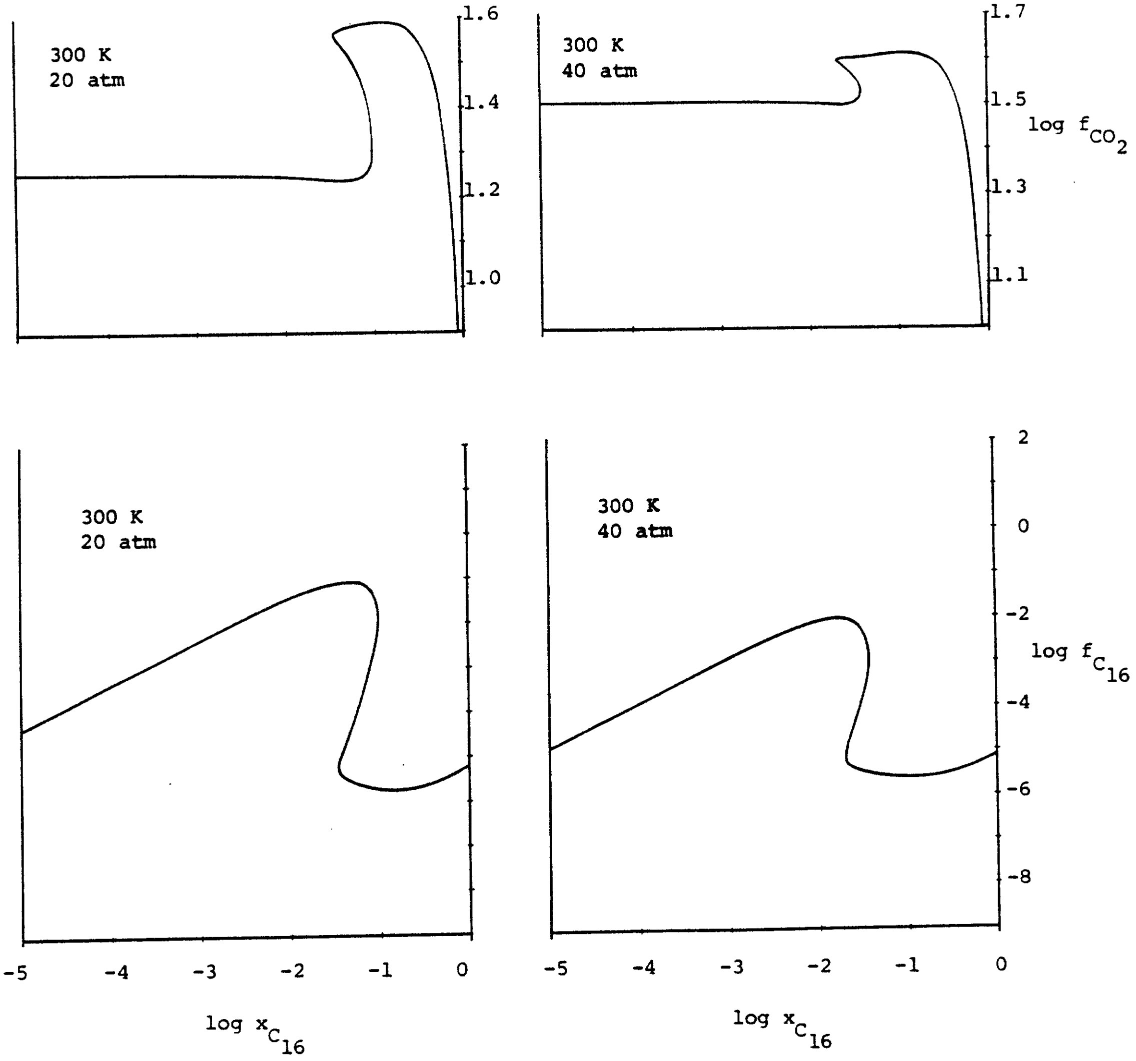

Figure 3.7. (Third of eight pages).

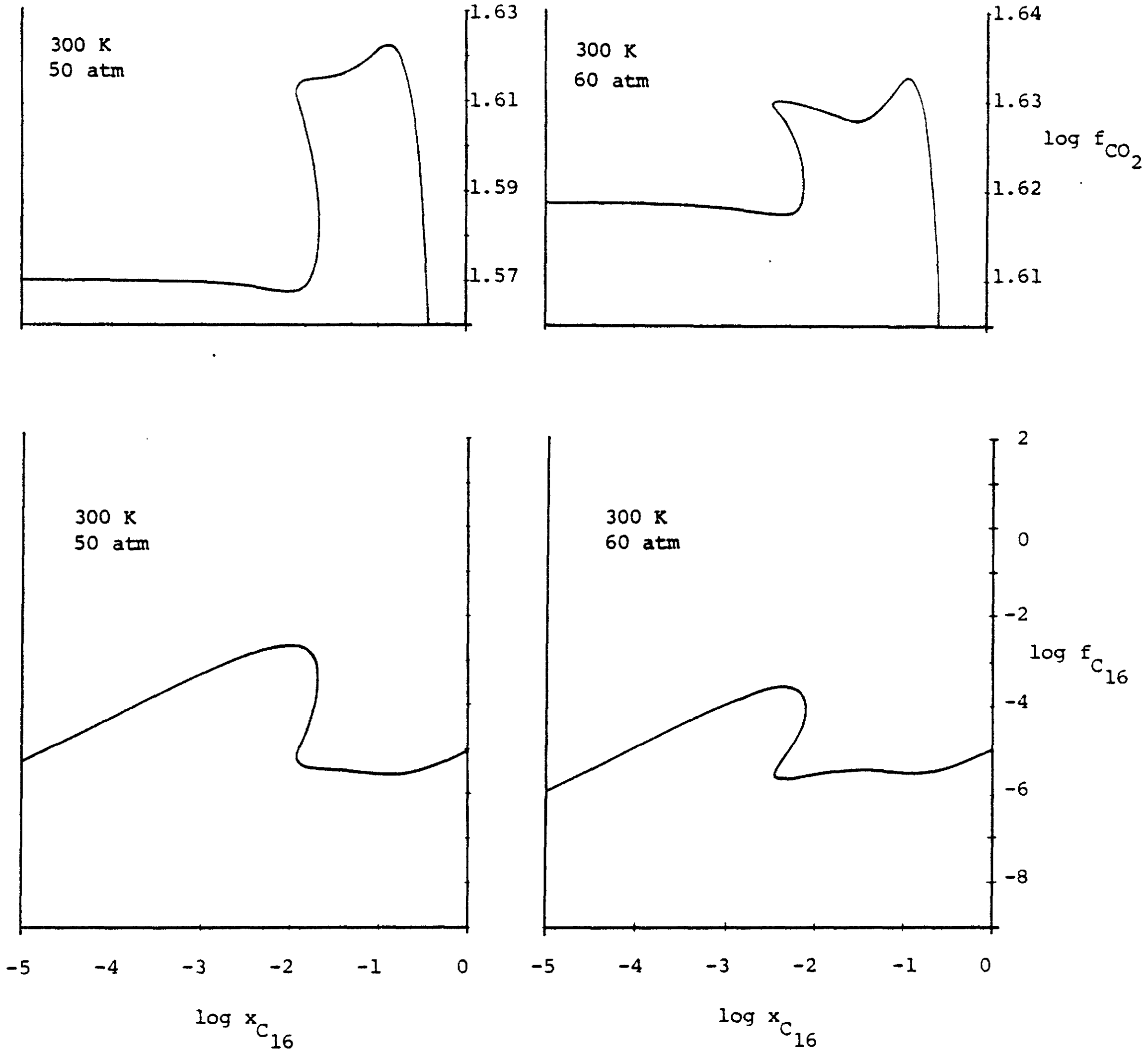

Figure 3.7. (Fourth of eight pages)

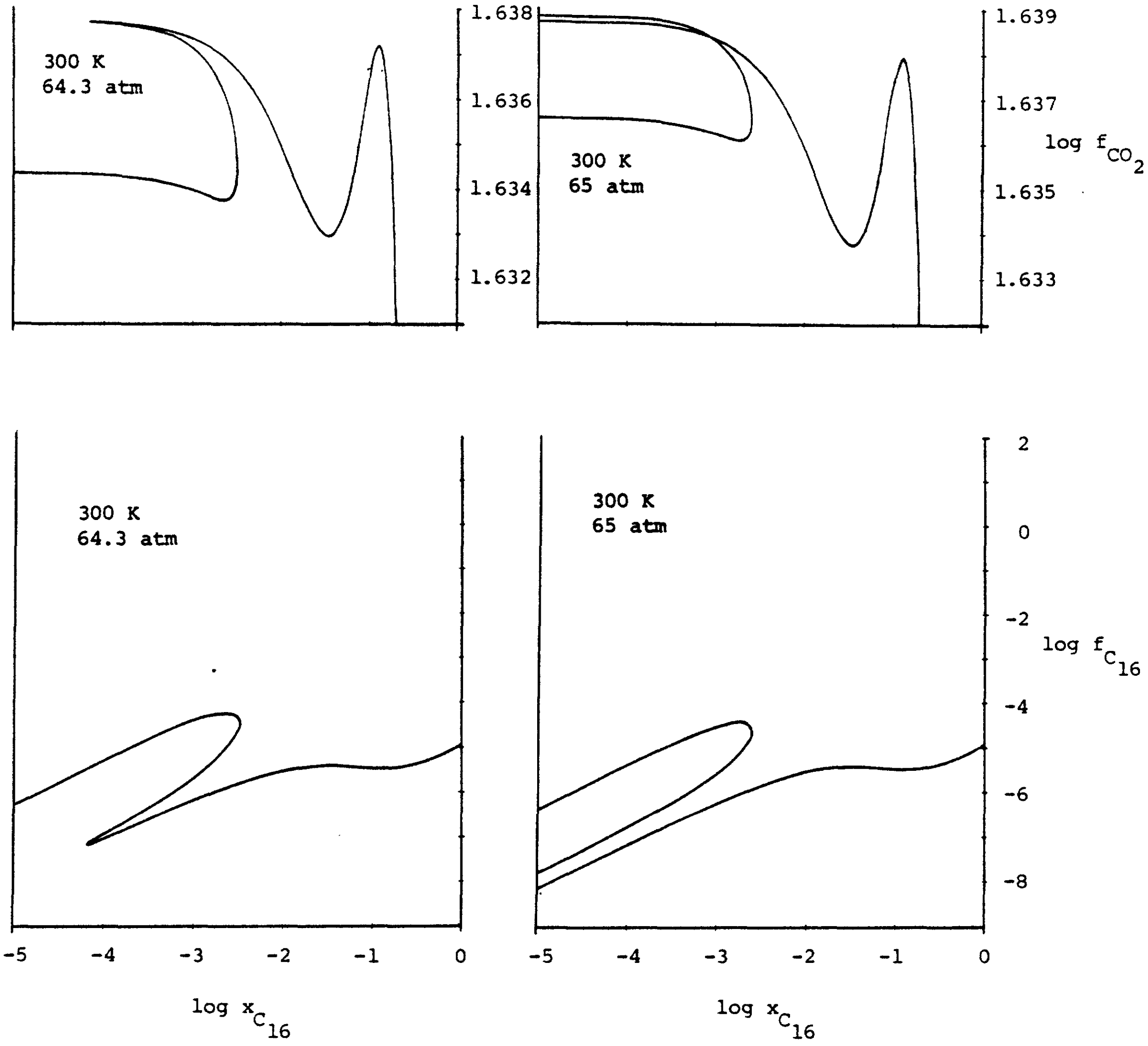

Figure 3.7. (Fifth of eight pages)

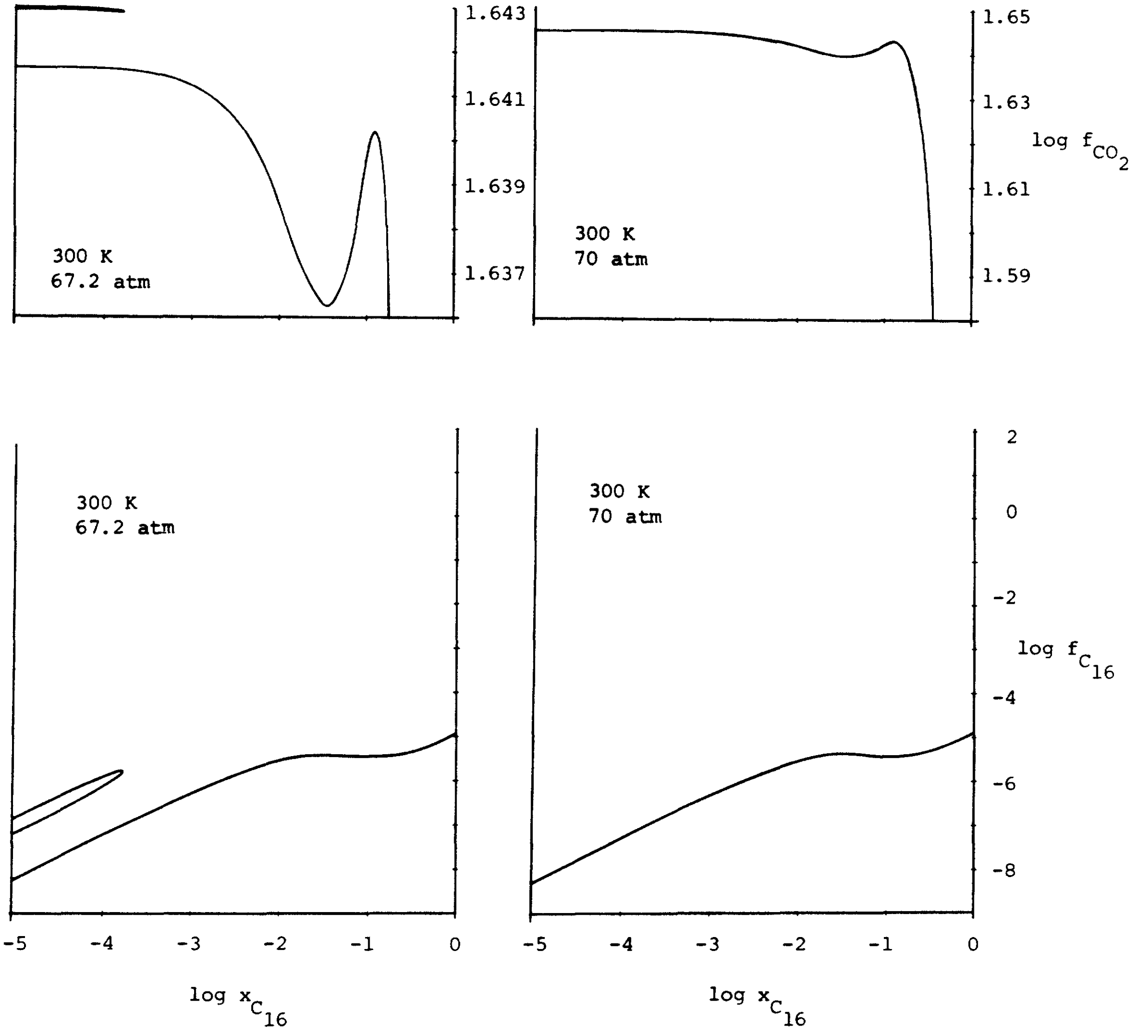

Figure 3.7. (Sixth of eight pages)

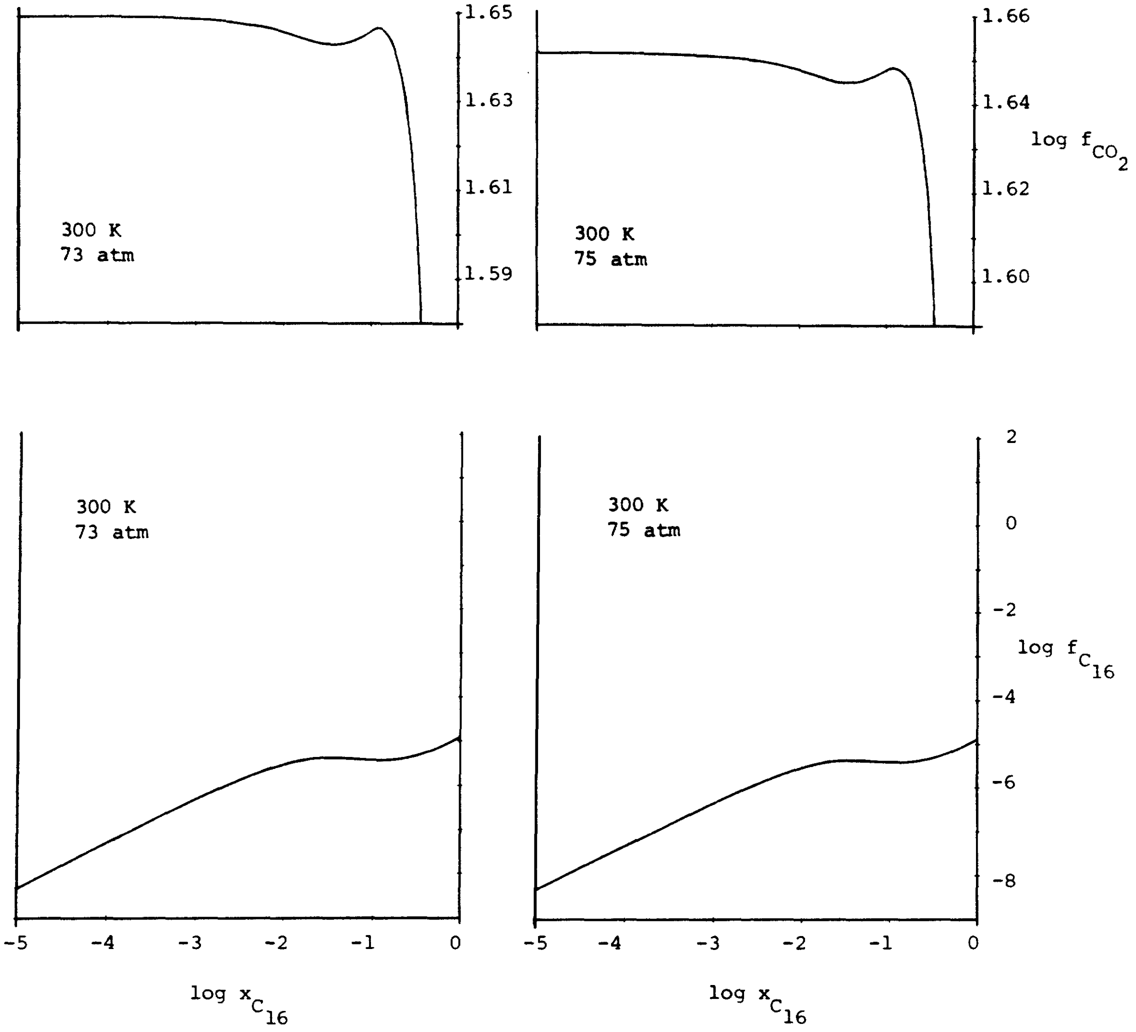

Figure 3.7. (Seventh of eight pages).

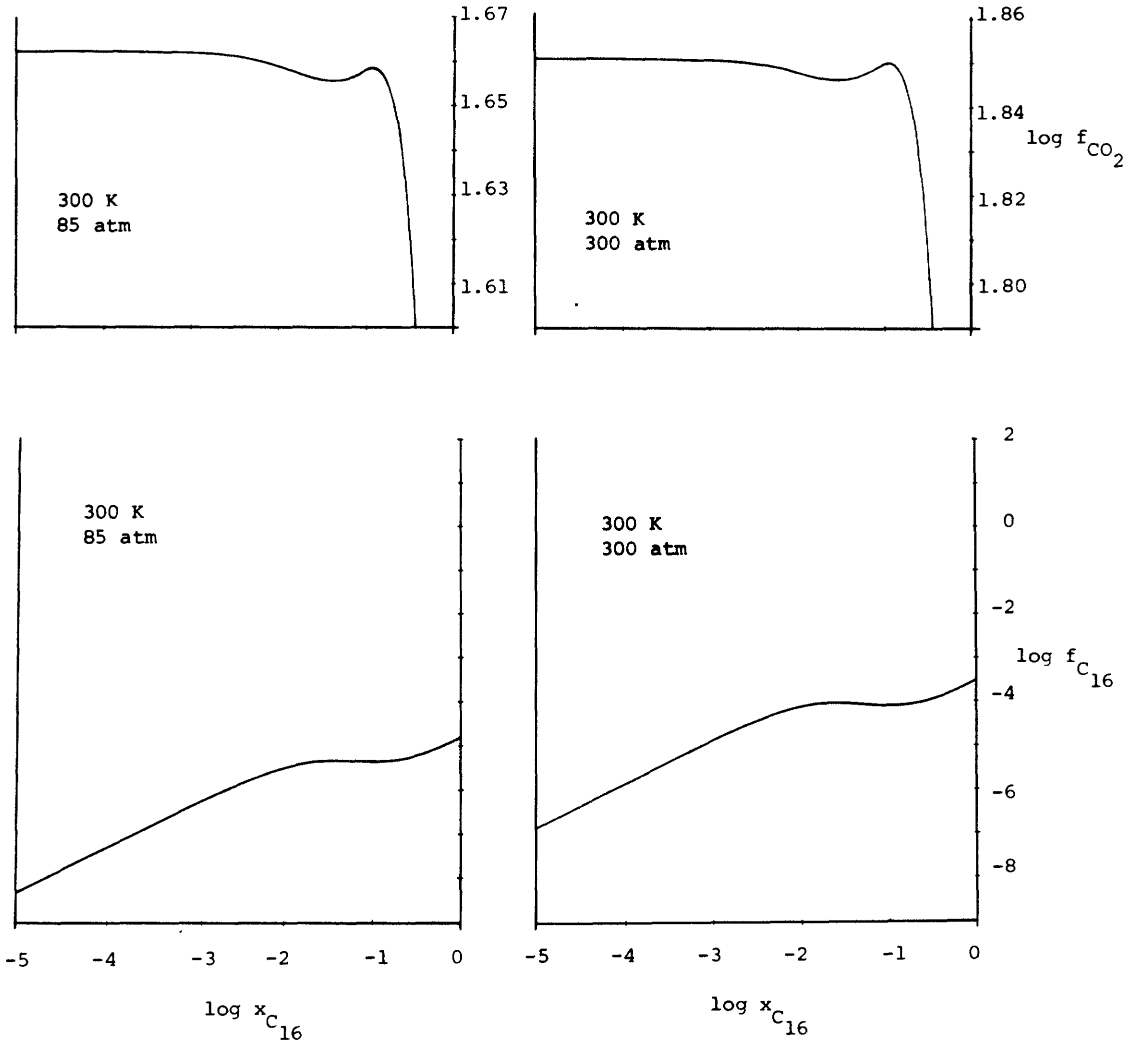

Figure 3.7. (Eighth of eight pages).

a uniform fugacity axis for the CO_2 plots, so scale changes there must be noted. In a region of three solutions, the lower C_{16} fugacity root is associated with the higher CO_2 fugacity root, and vice versa, while the mechanically unstable root connects the two. As expected, the f_H curves and the f_{CO_2} curves have a one-to-one correspondence in extrema and infinities. That this must be so is evident upon writing the Gibbs-Duhem equation for the partial fugacities in a binary system at constant T and P:

$$x_1 d\ln f_1 + x_2 d\ln f_2 = 0 \qquad (3.41)$$

Rearranging and dividing by dx_2, one has

$$x_1 \frac{d\ln f_1}{dx_2} = -x_2 \frac{d\ln f_2}{dx_2} \qquad (3.42)$$

Clearly, if

$$\frac{d\ln f_1}{dx_2} \longrightarrow \infty \quad \text{then} \quad \frac{d\ln f_2}{dx_2} \longrightarrow -\infty$$

and if

$$\frac{d\ln f_1}{dx_2} \longrightarrow 0, \quad \text{then} \quad \frac{d\ln f_2}{dx_2} \longrightarrow 0$$

as well, unless $x_2 \longrightarrow 0$. If $x_2 \longrightarrow 0$, then either

$$\frac{d\ln f_1}{dx_2} \longrightarrow 0 \quad \text{or} \quad \frac{d\ln f_2}{dx_2} \longrightarrow \infty$$

The latter possibility is exemplified by the f_H versus x_H plots. For the plot at 1 atm

$$\frac{d\ln f_H}{d\ln x_H} \longrightarrow 1 \quad \text{as} \quad x_H \longrightarrow 0.$$

Since

$$\frac{d\ln f_H}{d\ln x_H} = x_H \frac{d\ln f_H}{dx_H}$$

it is required that

$$\frac{d\ln f_H}{dx_H} \longrightarrow \infty \quad \text{as} \quad x_H \longrightarrow 0$$

to obtain the finite limit of 1.

The one-to-one correspondence between f_H and f_{CO_2} curves implies that they may be analyzed in virtually identical fashion, so that only a few comments are in order. At the lower pressures, the presence of the ideal gas regime where $f_i = x_i P$ is again noted. Since x_{CO_2} is near 1 in the left hand portion of the plots, this reduces approximately to $f_{CO_2} = P$, or a horizontal line at the system pressure. It was previously mentioned that at 65 atm, three distinct values would be found for f_{CO_2} at the pure CO_2 axis. The logarithmic plot of Figure 3.7 has been redrawn in Cartesian coordinates in Figure 3.8 to illustrate this behavior.

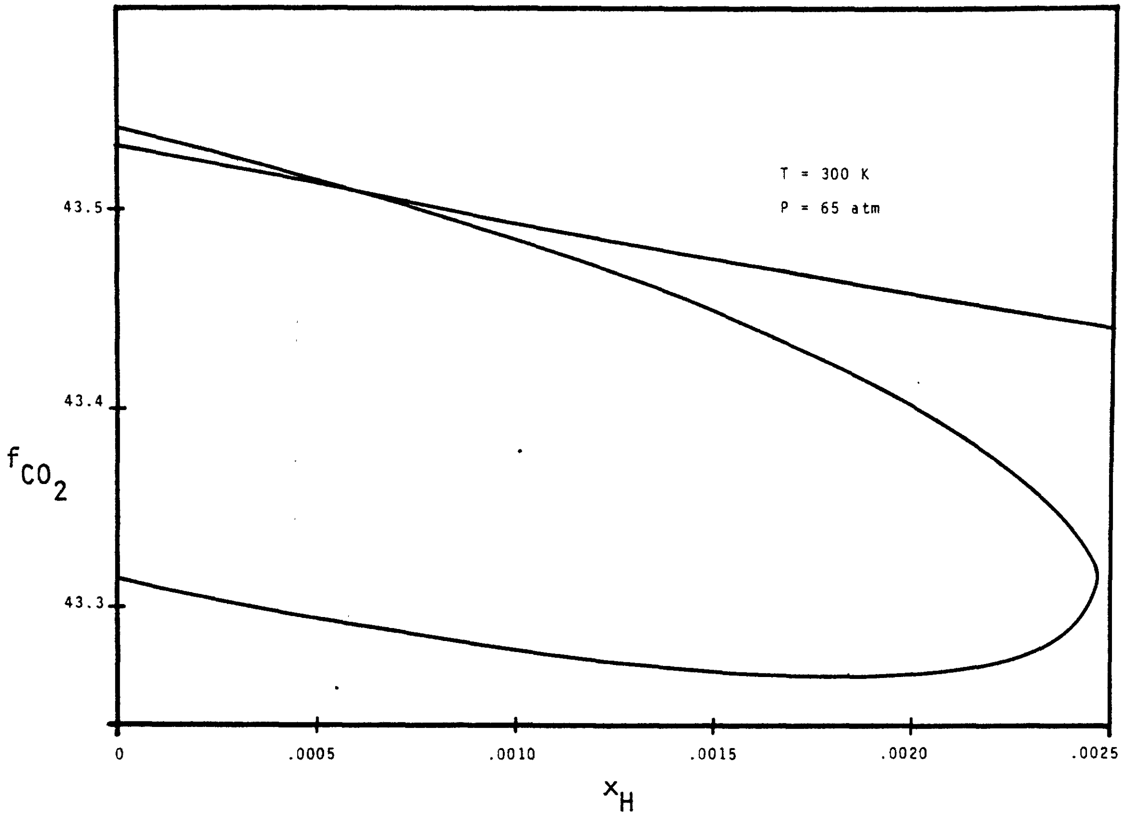

Figure 3.8. A Cartesian plot illustrating the loop in f_{CO_2} at conditions near CO_2's vapor pressure.

Attention is now turned to the shape of the L1 versus x curves at constant T and P, L1 being the determinant defined by equation (3.26). This stability criterion, in its intensive (mole fraction) form, is used in the determination of spinodal curves and critical points in Chapters 5-8. Figure 3.9 shows L1 versus x_H curves for the pressure series at 300 K. Whenever L1 crosses the zero axis, a point on the spinodal surface has been located. As L1 is related to the derivative $\frac{d\ln f_H}{d\ln x_H}$, the f-x plots have also been included in the figure. For the L1 curves, the vertical scale changes between 64.3 and 65 atm.

For the determination of the spinodal curve, The L1-x and f-x curves are equivalent. In mathematical terms,

$$\frac{d\ln f_H}{dx_H} = 0 \quad \text{when} \quad L1 = 0.$$

As long as

$$\left(\frac{\partial P}{\partial v}\right)_T < 0,$$

these two quantities agree in sign as well. This may be seen, for example, at P = 0.1 atm. The L1 curve for the ideal gas solution (segment G) is essentially a horizontal line across the entire range of composition. It is always slightly above the zero axis, i.e., positive, but at this

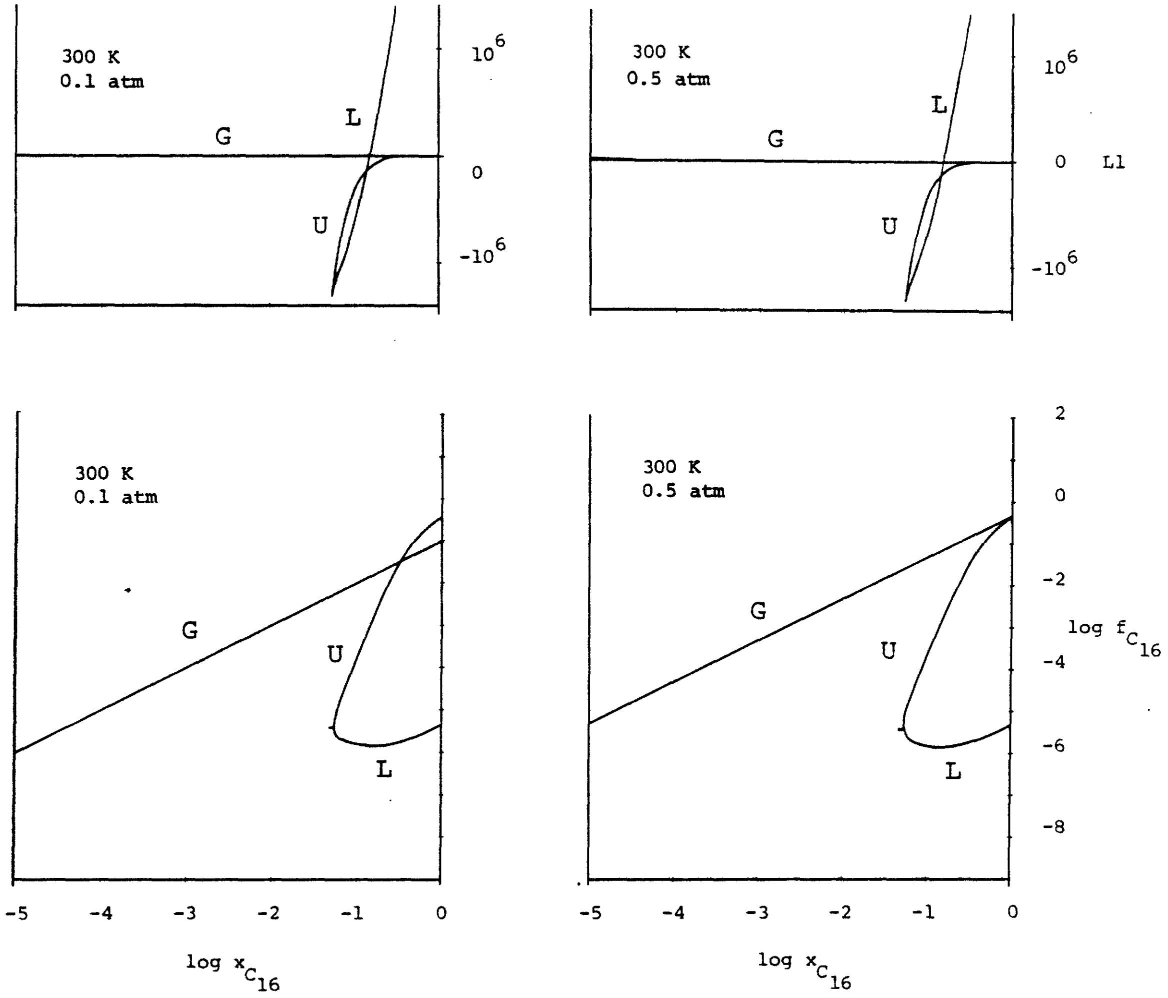

Figure 3.9. (First of eight pages) Plots of the stability criterion matrix, L1, versus mole fraction of n-hexadecane. In the calculation of L1, compositional derivatives of the Helmholtz free energy are taken with respect to n-hexadecane. Segments are labelled as in Figure 3.4.

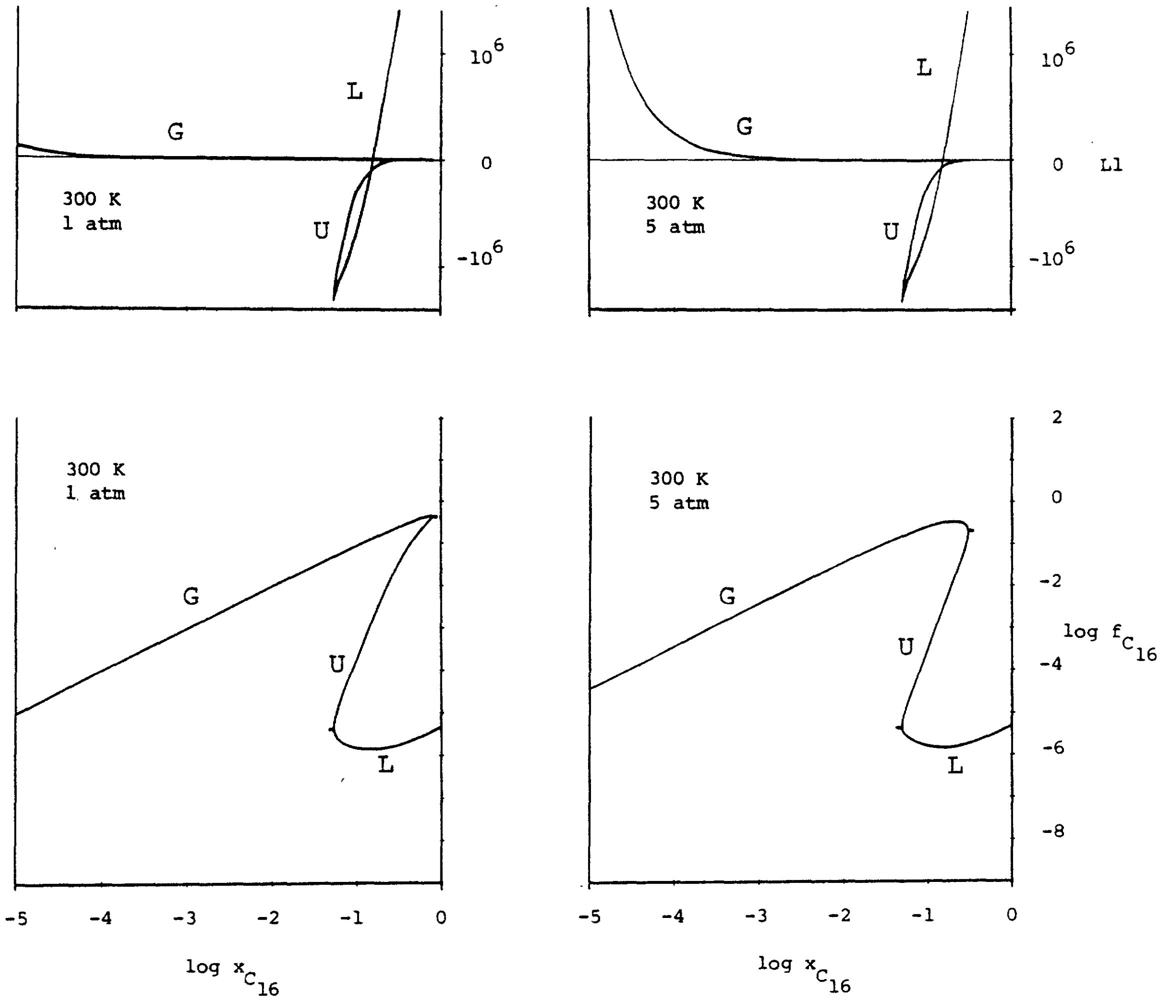

Figure 3.9. (Second of eight pages).

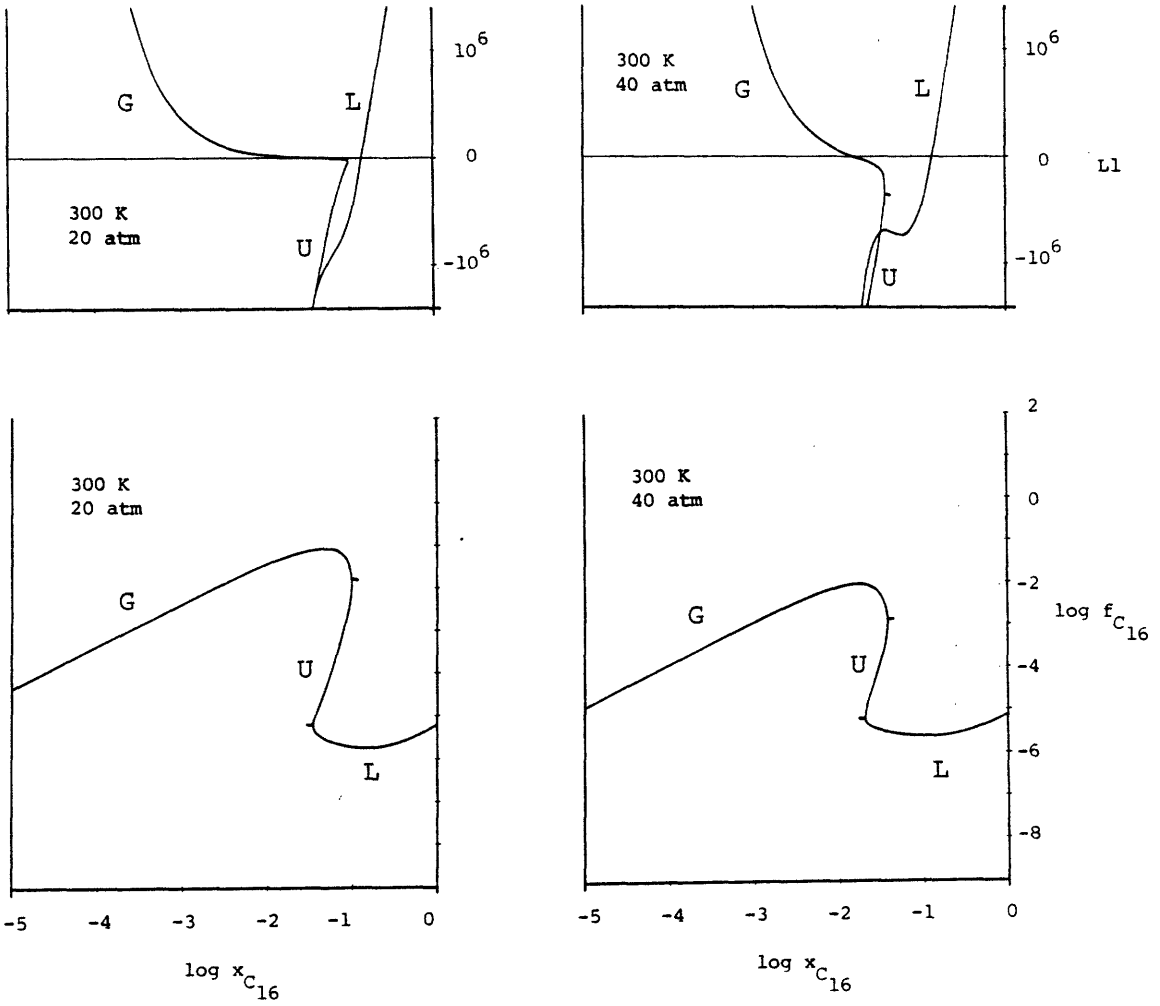

Figure 3.9. (Third of eight pages).

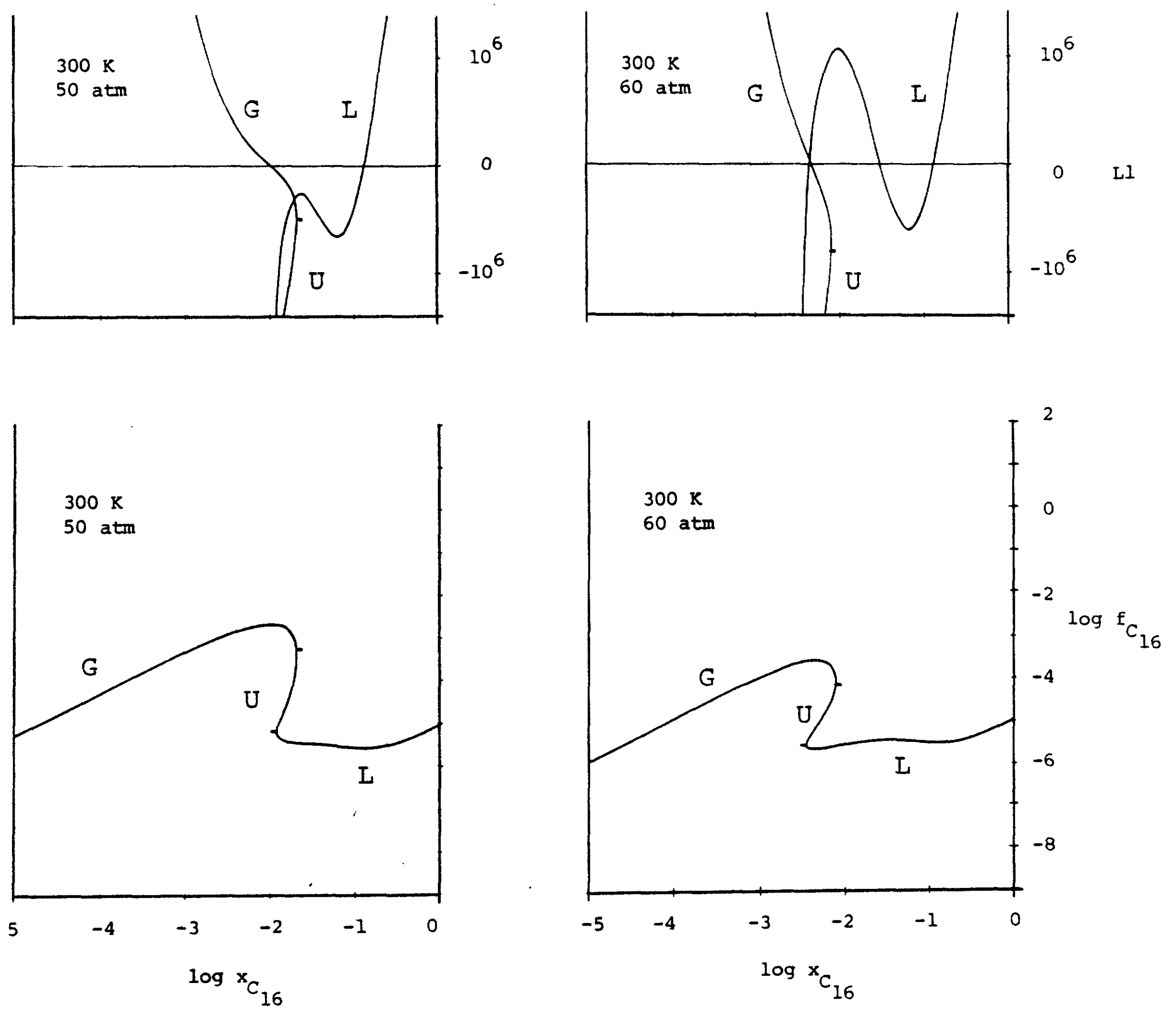

Figure 3.9. (Fourth of eight pages).

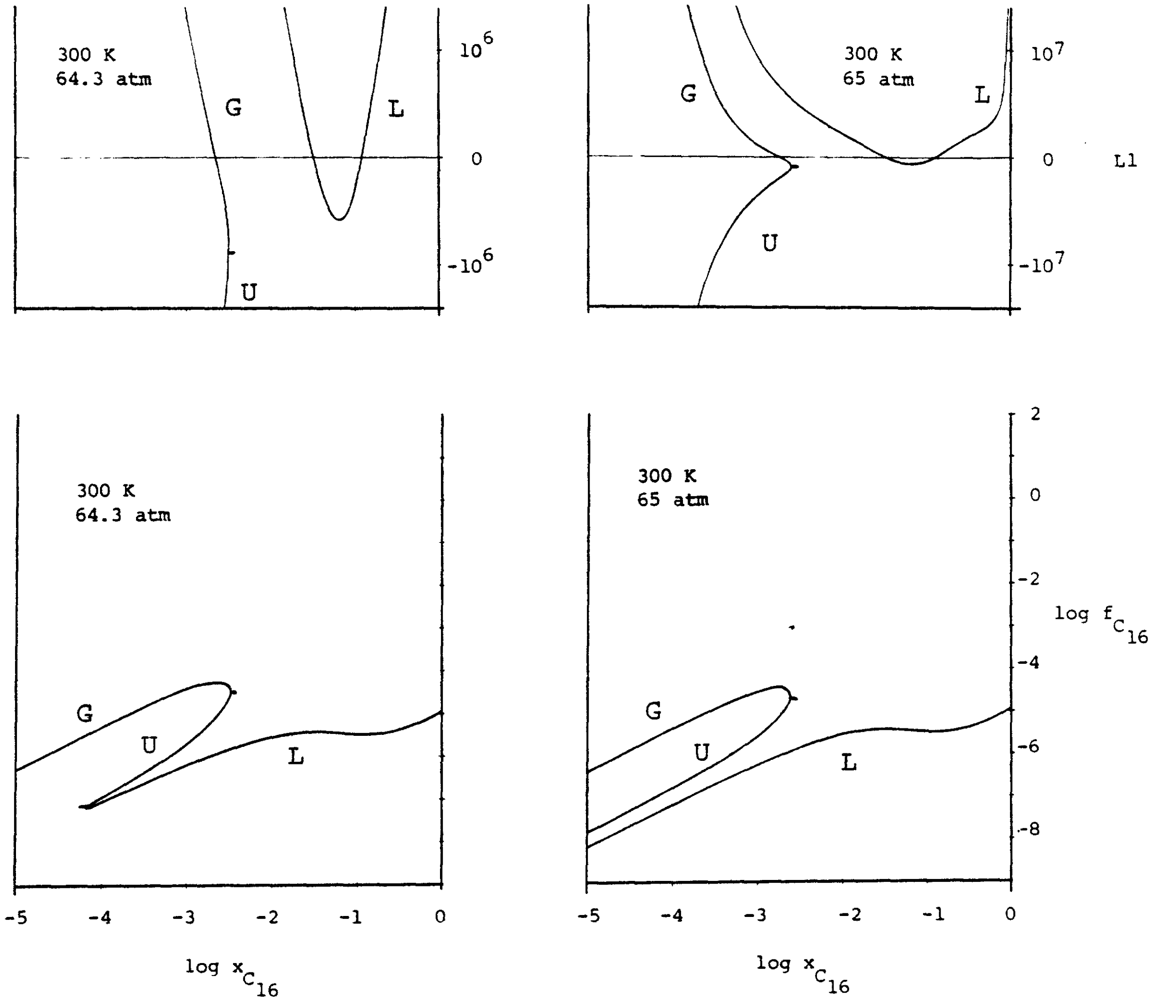

Figure 3.9. (Fifth of eight pages). Note change of scale in the L-x plots between 64.3 and 65 atm.

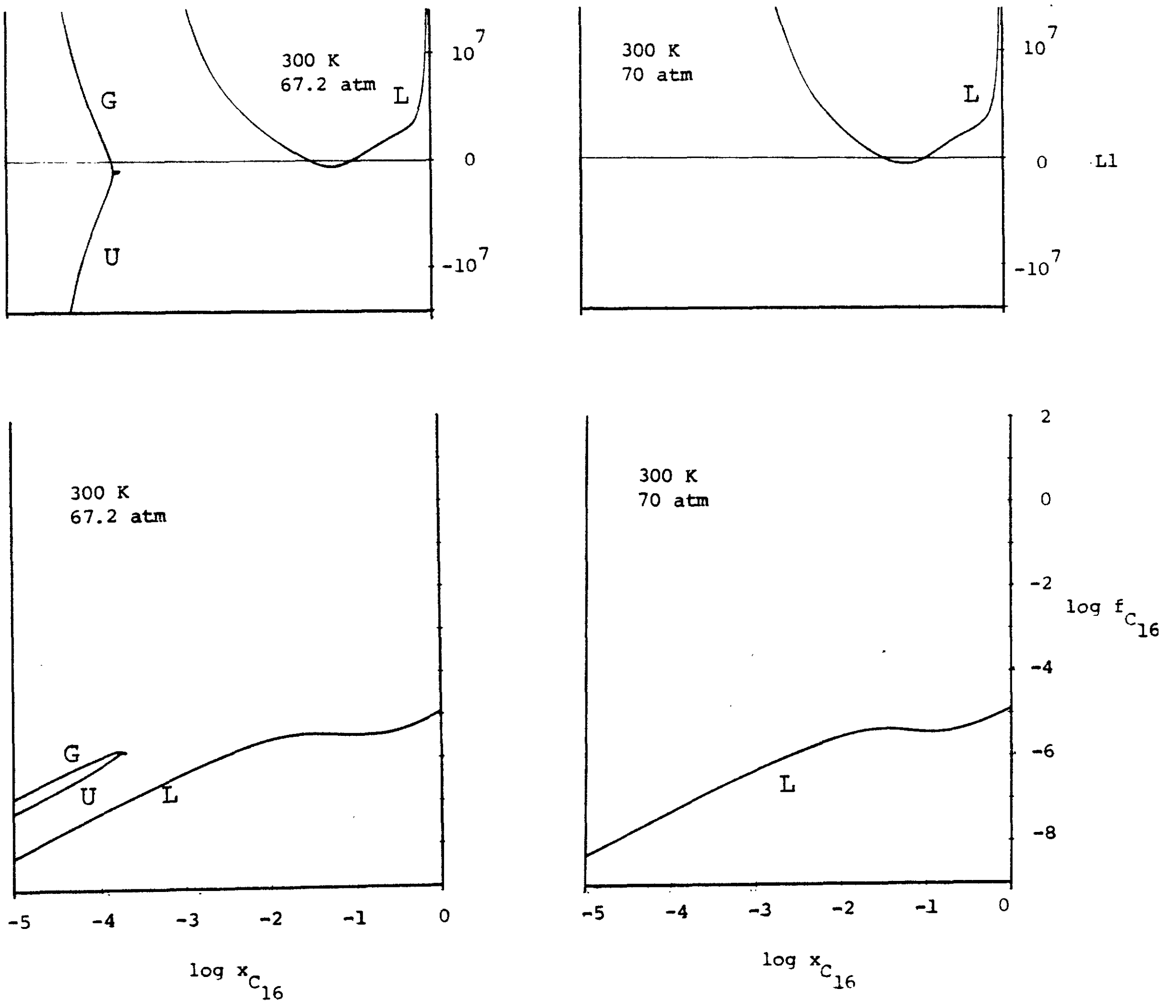

Figure 3.9. (Sixth of eight pages).

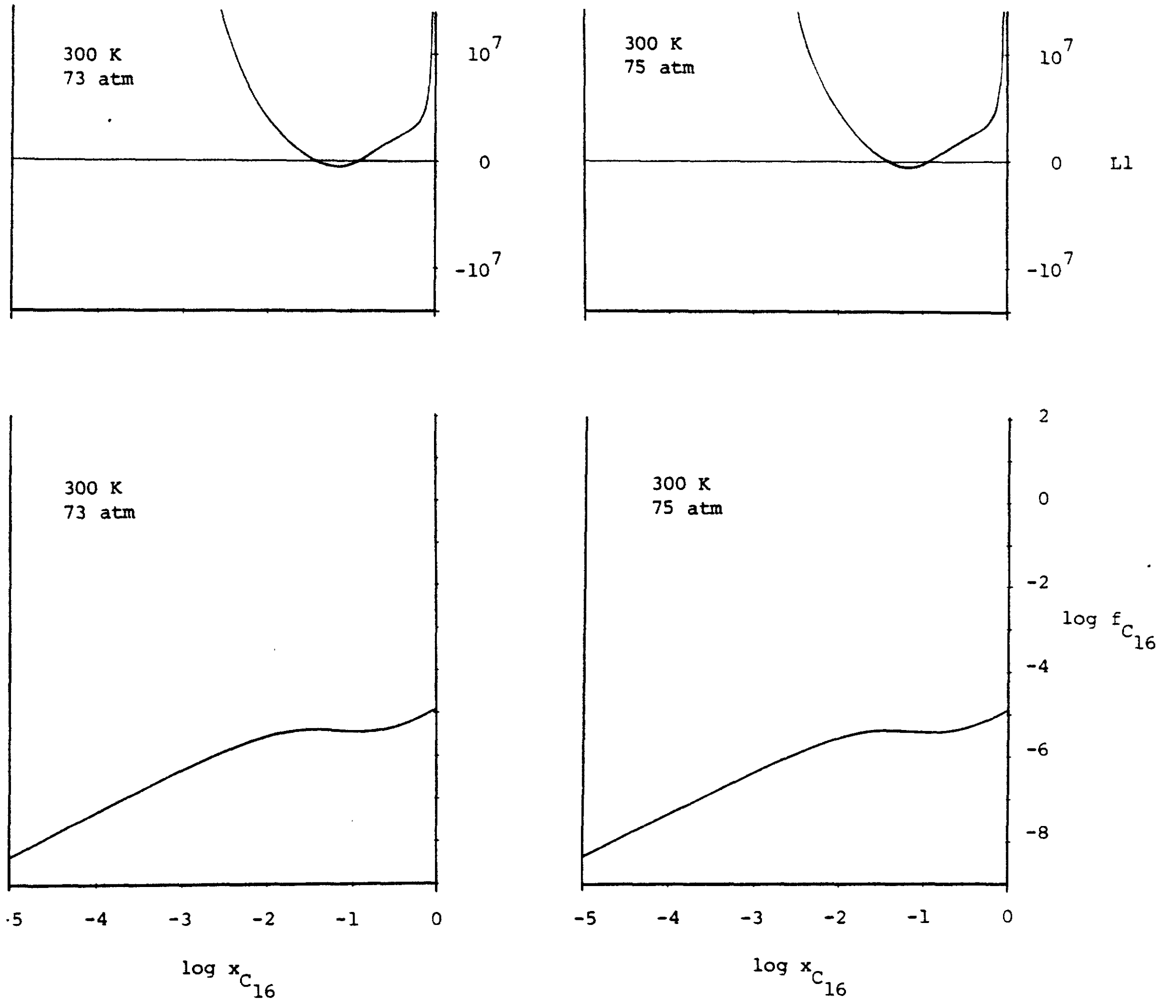

Figure 3.9. (Seventh of eight pages).

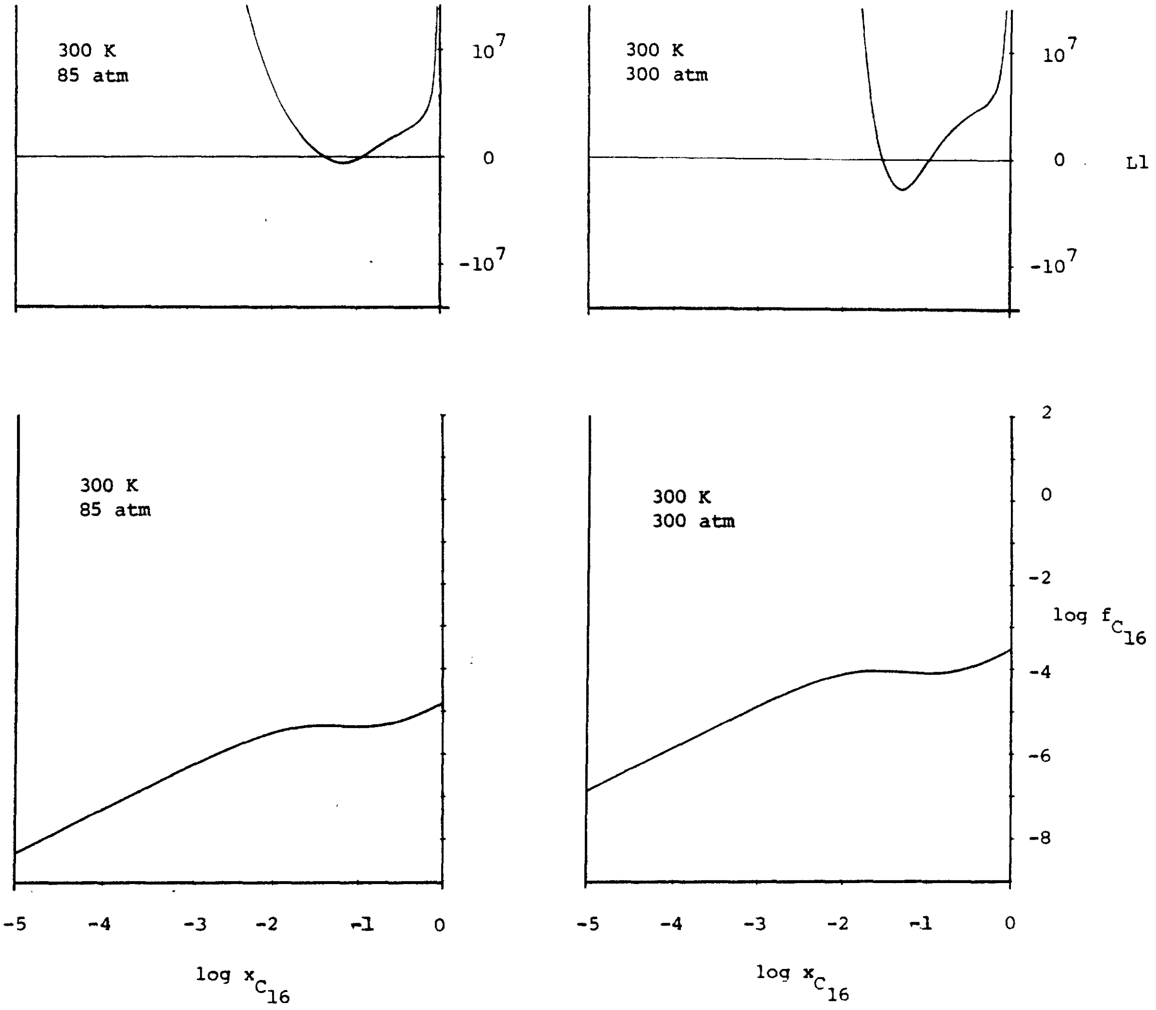

Figure 3.9. (Eighth of eight pages).

scale is indistinguishable from the axis. The liquid root (segment L) starts out at a negative value, crosses the zero axis, and continues on to more positive values. The mechanically unstable root (segment U) meanwhile starts out at a negative value and closely approaches, but never crosses, the zero axis. In this case,

$$\frac{d\ln f_H}{d\ln x_H} < 0 \quad \text{while} \quad L1 > 0.$$

The mechanically unstable root and the liquid root join smoothly at a minimum value of x_H, although this is not readily visible at the scale of this plot. The minimum in x_H, which corresponds with the infinity on the f-x plot, does not coincide with the minimum in L1, which appears to be a cusp (not continuously differentiable). In fact, the minimum in L1 is smooth, and formed entirely by the liquid root.

At 1 atm, a second apparent cusp is formed as the region of three solutions moves away from the pure C_{16} axis. The vapor root now crosses the zero axis to give a spinodal point, and smoothly joins the mechanically unstable root at a maximum value of x_H.

A comparison of the L1-x curves at 5 and 20 atm points out an occurrence that is not particularly evident in the f-x curves. While at 5 atm the high f_H infinity fell at higher x_H than the liquid root minimum, at 20 atm it has moved to a lower x_H. Also at 20 atm, the inflection in the liquid root has become quite noticeable. When a pressure of 40 atm is reached, the inflection gives rise to a maximum and minimum. At 60 atm, the maximum has crossed the zero axis to give two more points on the spinodal surface, for a total of four. Although not shown on the graphs, the liquid root and mechanically unstable root continue to join at a minimum in x_H, while the associated minimum in L1 remains smooth.

At 64.3 atm, the L1 maximum in the liquid root has moved off the graph, and at 65 atm it is entirely gone. The region of three roots now extends to the pure CO_2 axis, and only three spinodal points are found. Finally, at 70 atm, the vapor and metastable roots have disappeared and once again there are only two points where L1=0. This behavior persists to very high pressures.

It was stated earlier that the quantity L1 was related to the derivative

$$\frac{d\ln f_H}{d\ln x_H} .$$

It is helpful to define this relationship more precisely. It may be shown that

$$\left(\frac{\partial \mu_1}{\partial x_1}\right)_{T,P} = \frac{1}{A_{VV}} L1 \qquad (3.43)$$

where A_{VV} and L1 are in intensive form. The relationship between slope in the logarithmic f-x plots and L1 can now be stated:

$$\frac{d\ln f_H}{d\ln x_H} = \frac{x_H}{RT}\frac{RTd\ln f_H}{dx_H} = \frac{x_H}{RT}\frac{d\mu_H}{dx_H} = \frac{x_H}{RTA_{VV}} L1 \tag{3.44}$$

Thus, if the dimensionless quantity $\frac{x_H}{RTA_{VV}} L1$ were plotted versus log x_H for a set of conditions in Figure 3.4, a diagram showing the derivative of the f-x curve would result.

M1, the determinant defined in equation (3.38), was used for the second criterion of criticality in this work. It is not convenient to plot this quantity since its value ranges over many orders of magnitude. No difficulties are encountered in its evaluation, however. It may be shown, for M1 expressed in intensive form, that

$$\left(\frac{\partial^2\mu_1}{\partial x_1^2}\right)_{T,P} = \frac{1}{A_{VV}^2} M1 \tag{3.45}$$

Together equations (3.43) and (3.45) imply that, at a critical point (i.e., when L1 = M1 = 0),

$$\left(\frac{\partial L1}{\partial x_1}\right)_{T,P} = 0 \tag{3.46}$$

Table 3.1 summarizes the features of the phase diagrams generated in this thesis, and the criterion applied to identify each feature. Note that the critical stability criterion was not used in an explicit form, since the stability of a critical point was apparent from its associated binodal locus (see Figure 3.1). As mentioned earlier, the shape of the binodal locus alone can be used to determine critical points. This is a reasonable approach if the shape of the binodal locus is desired. If one is interested only in locating a critical point, however, it is more efficient to use the L1 and M1 criteria. Table 3.1 also lists three features of binary phase diagrams which result indirectly from the criteria discussed in this chapter. Azeotropy, three phase lines, and critical end points have been introduced in Chapter 2, and will be treated more thoroughly in Chapters 5-8 as the need arises.

Table 3.1

Criteria Used in the Calculation of P-T-x Diagrams

Feature	Criterion
Binodal points	Equality of component fugacities
Spinodal points	L1 = 0
Critical points	L1 = 0 and M1 = 0
Critical stability	Stability of the binodal locus which terminates at the given critical point.
Azeotropic points	Shape of the binodal locus. Zero length tieline, but not a critical point.
Three-phase equilibrium points	Intersection of three binodal regions at a single temperature and pressure.
Critical end points	Intersection of three phase line and critical line or point of horizontal inflection in the binodal locus not terminated at the critical end point.

Chapter 4 Pure Component Phase Diagrams

In the generation of binary phase diagrams, pure component diagrams become of interest in two respects. Firstly, the pure component diagrams are an integral part of the binary P-T-x space, giving the P-T sections at compositional extremes. These sections define termini of regions of phase equilibrium. For example, VLE envelopes terminate at points along a pure component vapor pressure curve. The second reason for the importance of pure component predictions is that equations of state are in most cases derived on the basis of pure component behavior. Extension to mixtures is effected through the application of mixing rules which describe the system in terms of the pure components which comprise the system. For most multicomponent systems the proper form of these rules is unknown, and simple approximations are used. The prediction of mixture properties is therefore unlikely to be more accurate than the prediction of pure component properties. It thus becomes important to know how well a chosen equation of state mimics the pure component properties of concern. Fortunately, thermodynamic data for pure components is usually available.

Table 4.1 lists the critical temperatures and pressures of the six components dealt with in this thesis, and compares

Table 4.1

Constants of Pure Components

Substance	T_c(K)	P_c(atm)	actual v_c(m^3/kgmol)	predicted v_c(m^3/kgmol)	actual ρ_c(kg/m^3)	predicted ρ_c(kg/m^3)	actual Z_c	ω
Ethylene (C_2H_4)	282.4	49.7	0.129	0.143	217	196	0.276	0.085
Carbon dioxide (CO_2)	304.2	72.8	0.094	0.105	468	419	0.274	0.225
Benzene (C_6H_6)	562.1	48.3	0.259	0.293	301	266	0.271	0.212
Water (H_2O)	647.3	217.6	0.056	0.075	321	240	0.229	0.344
n-Hexadecane ($C_{16}H_{34}$)	717.0	14.0	-	1.290	-	175	-	0.742
Naphthalene ($C_{10}H_8$)	748.4	40.0	0.410	0.471	312	272	0.267	0.302

Note - The P-R equation predicts a universal Z_c of 0.307.

the calculated and measured critical volumes and compressibility factors. Pure component P-v-T data is easily and concisely expressed by plotting isotherms in a P-v diagram. These diagrams have been drawn up in Figure 4.1 for the species in Table 4.1. Figure 4.1a gives the P-v diagram for carbon dioxide as determined from the Peng-Robinson equation. The isotherms at 200, 250, and 298 K illustrate the fact that for a range of pressures, three different volumes are predicted. The low volume root is the liquid phase solution, the high volume root is the gas phase solution, and the middle root is mechanically unstable.

At each temperature, a horizontal tieline may be drawn between the liquid and gas phase solutions, giving the volumes of the coexisting phases. The tielines are found by determining the pressure at which liquid and gas phase solutions yield equal fugacities. As evidenced by the isotherm at 298 K, the liquid and gas phase solutions are actually joined by the unstable root to form a smooth curve. The minimum and maximum in this curve are points on the stability limit or spinodal curve. Tracing the 298 K isotherm from high pressures, the liquid will normally begin to vaporize (boil) when the binodal curve is intersected. This occurs at about 63 atm. It is possible under certain conditions, however, to reduce pressure below 63 atm without a transition to the vapor phase. In this case, a superheated liquid is formed. This metastable phase may persist until

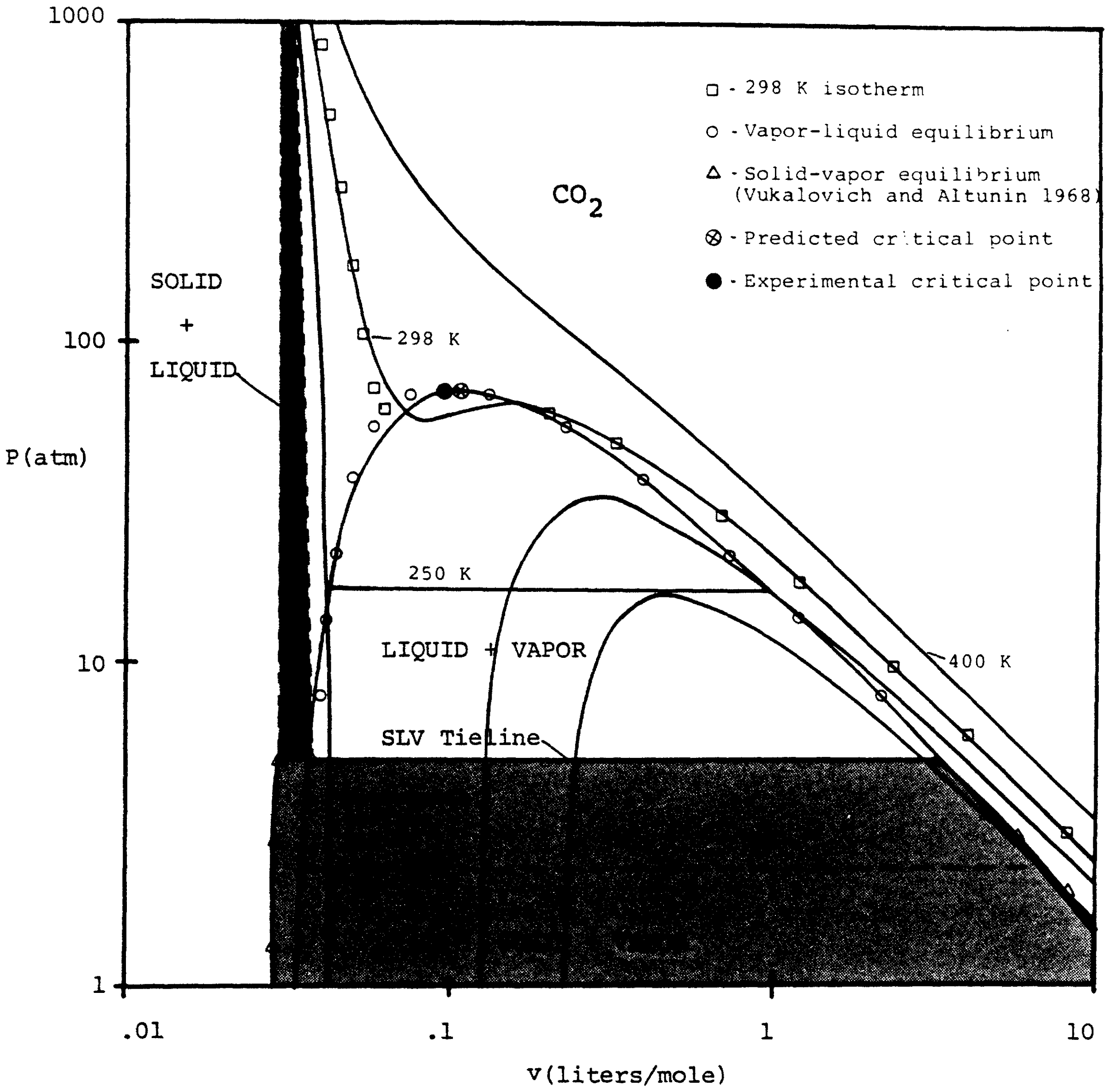

Figure 4.1a. P-v diagram for carbon dioxide. Between the critical point and the SLV (triple point) tieline, liquid and vapor coexist. Below the SLV tieline (light shading) solid and vapor coexist, although the P-R equation continues to predict (metastable) vapor-liquid equilibrium. The darker shaded region gives approximate boundaries for solid-liquid equilibrium.

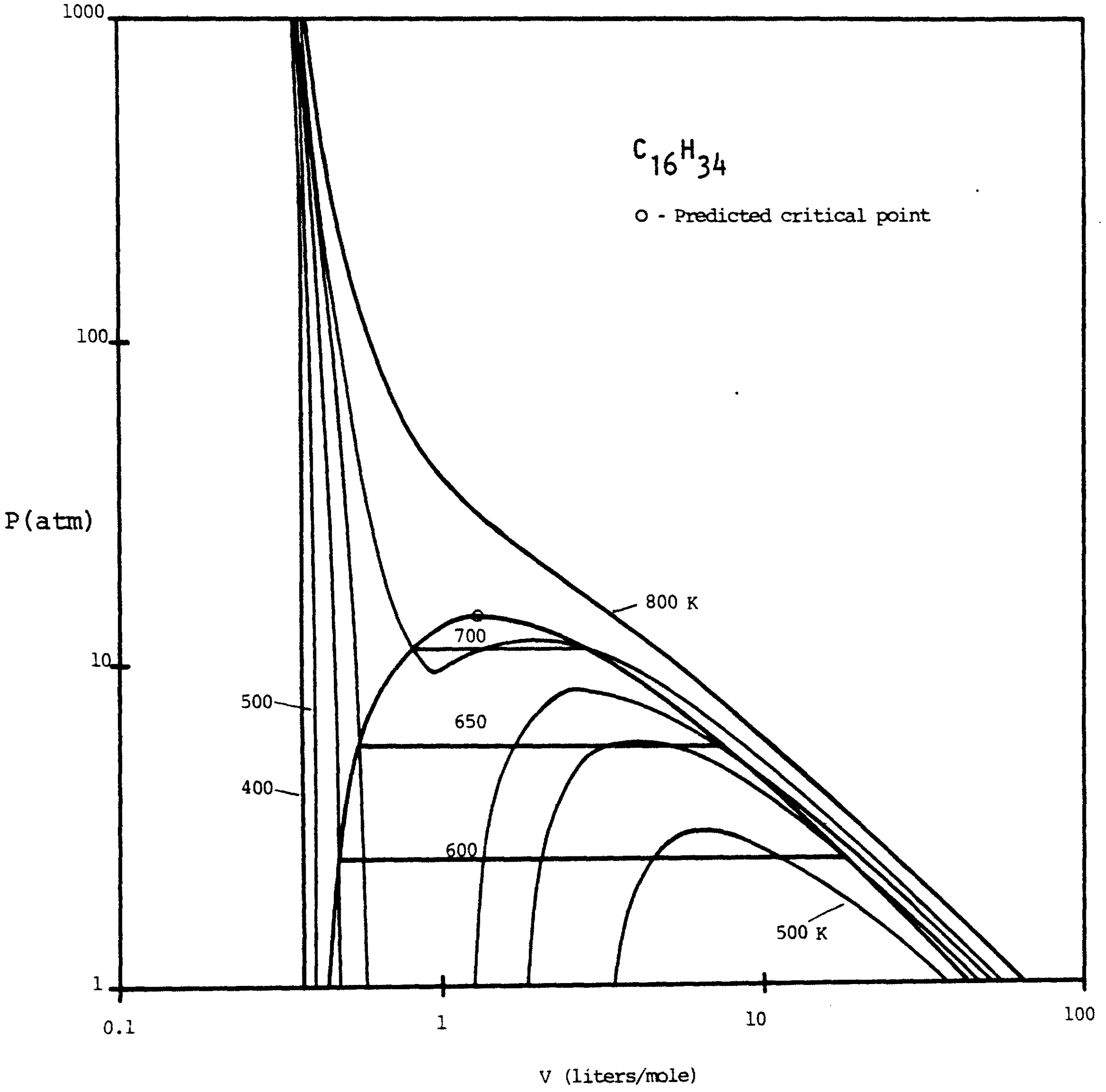

Figure 4 .1b. P-v diagram for n-hexadecane.

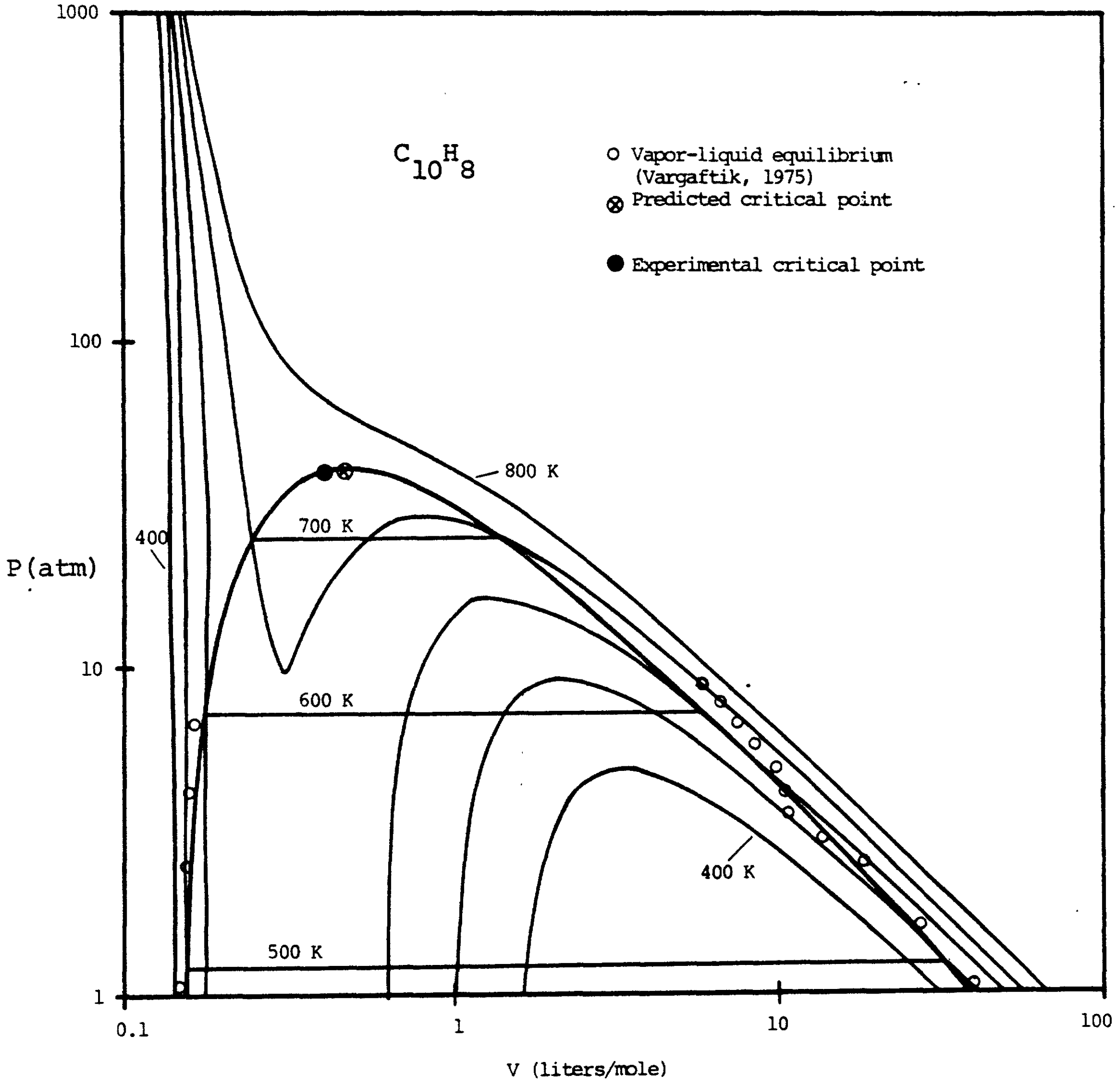

Figure 4.1c. P-v diagram for naphthalene. Note the anomalous behavior of the experimental data for the saturated vapor.

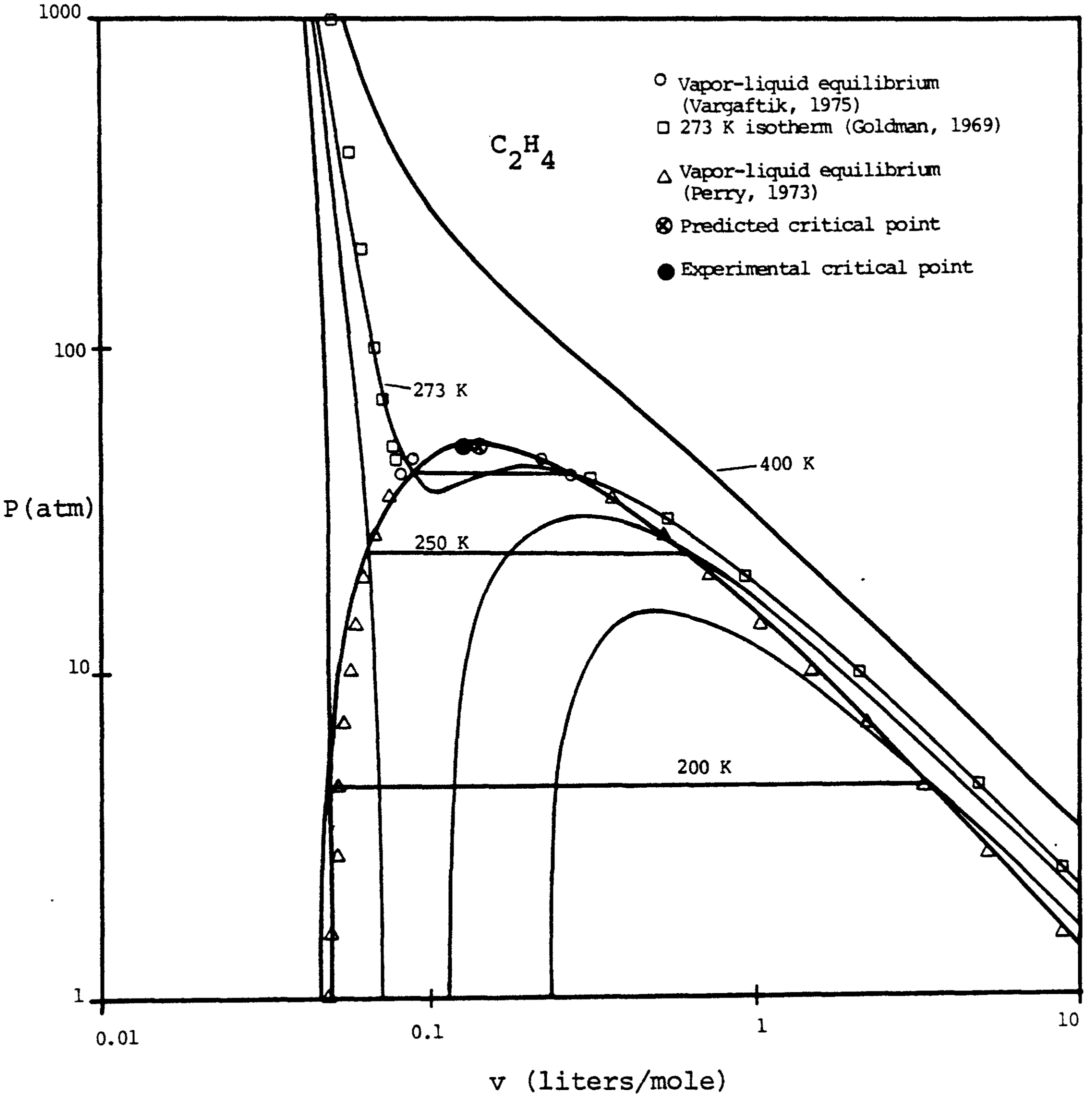

Figure 4.1d. P-v diagram for ethylene.

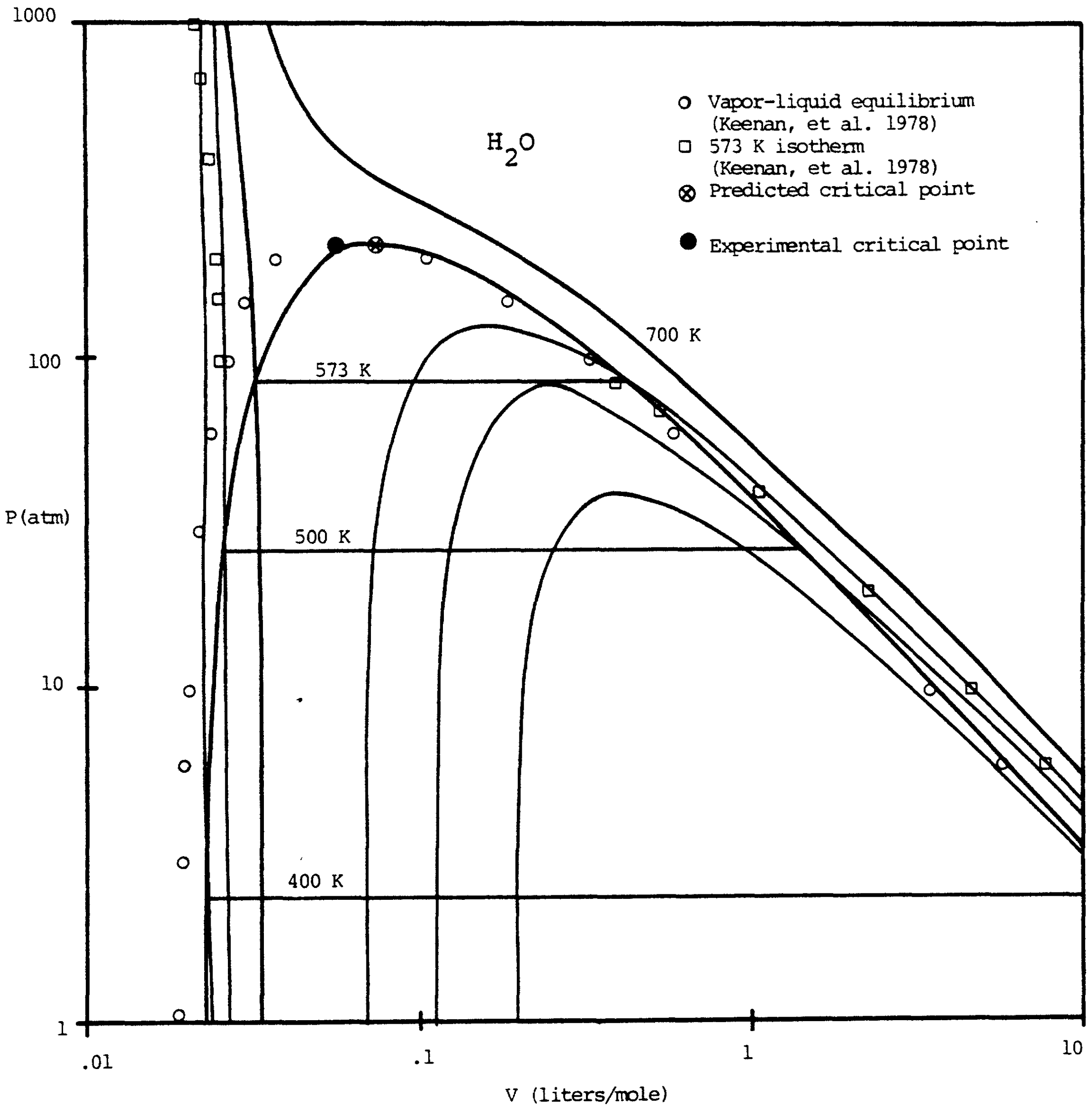

Figure 4.1e. P-v diagram for water.

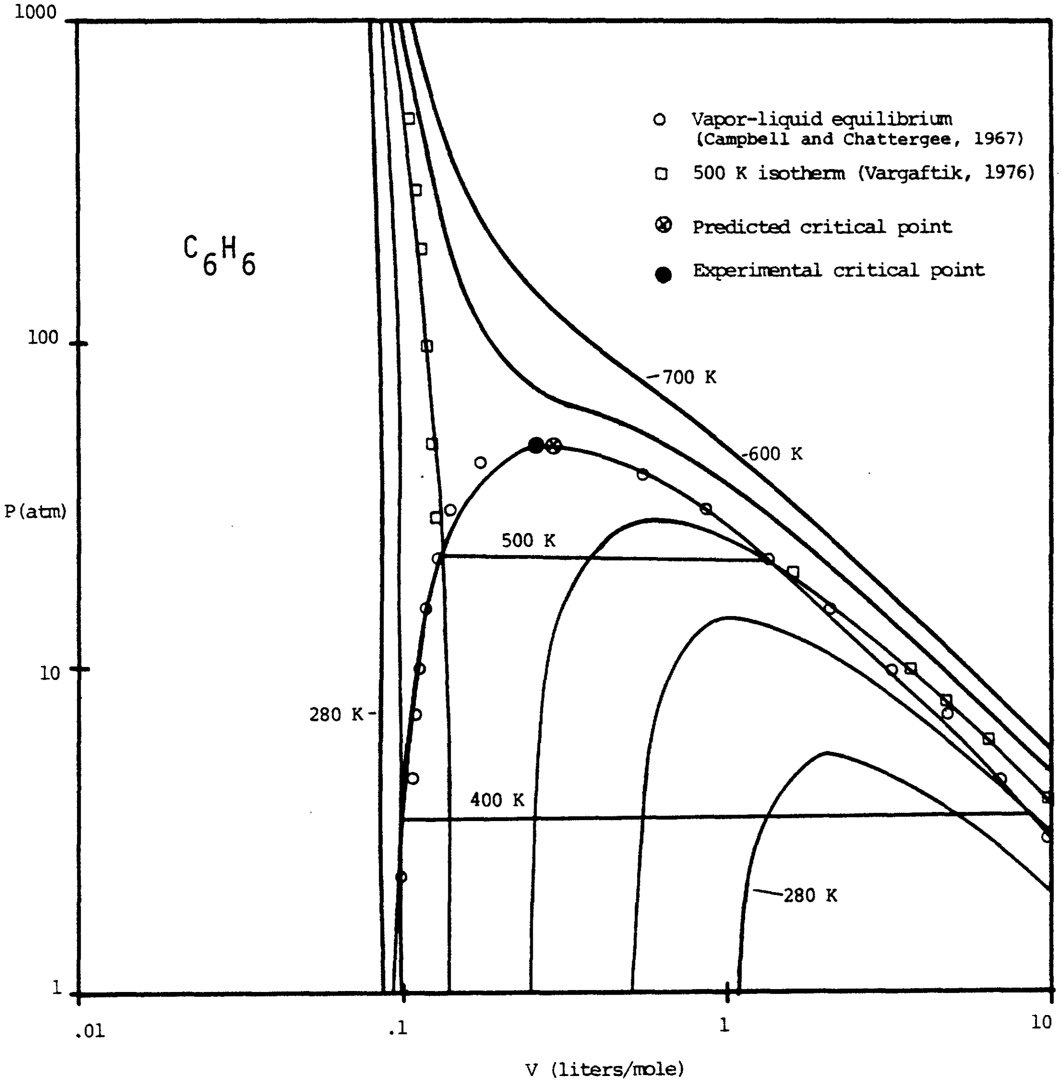

Figure 4.1f. P-v diagram for benzene.

the isotherm intersects the spinodal curve at about 59 atm, at which point there must occur a spontaneous transition to the gaseous state.

At 200 and 250 K, the three roots still form a single curve as they did at 298 K. At these temperatures, however, the stability limit for the liquid is located below 1 atm, and so is not shown on the plot. The maxima and minima in the isotherms converge at the critical point, which thus represents the terminus of the spinodal locus. Above the critical temperature, the isotherms no longer exhibit extrema (see, however, Gomez-Nieto, 1979). Similarly the critical point represents the terminus of the binodal locus, and the liquid-vapor tielines converge to zero length.

Figure 4.1a also includes some experimental data for comparison. The binodal VLE curve is represented very well by the equation of state, except for liquid volumes above a reduced pressure of about 0.5. The prediction for the critical volume is in error by about 10 percent. Similarly, the 298 K isotherm agrees with experimental gas phase volumes quite closely. In the liquid region, though, the slope of the isotherm is not steep enough and significant deviations are found.

At low temperatures, and pressures below the triple point tieline (about 5 atm), experimental data indicate the formation of a solid phase in equilibrium with a vapor phase. Points on the solid-vapor binodal have been given in the figure. An approximate representation of the solid-liquid coexistence region has been included as well. The Peng-Robinson equation has no means for predicting solid phase boundaries, so the predicted VLE dome has been extended into the solid-vapor region. Metastable VLE below the triple point is actually possible, however, as indicated by the labelling of the 200 K tieline. The limit to which VLE metastability may persist is unknown.

Figure 4.1b shows the P-v diagram for n-hexadecane. There is no data available for comparison in the region shown and, in fact, even the critical volume has not been measured. The naphthalene diagram in Figure 4.1c shows the limited amount of data available for this system. The data does not seem particularly reliable in view of the inconsistent vapor phase measurements. The quantitative accuracy of the predictions for naphthalene and n-hexadecane is uncertain, but it is probably comparable to that of Figure 4.1a. For ethylene, water, and benzene, Figures 4.1d, e, and f, data is available for comparison. Except for the absence of solid formation, the diagrams are quite similar to Figure 4.1a.

For the actual construction of binary P-T-x diagrams, pure component P-T diagrams are more useful than the P-v diagrams just considered. As mentioned previously, P-T diagrams are actually part of the binary P-T-x space diagram, falling at either end of the composition axis. Figure 4.2 gives these P-T diagrams for the compounds of interest in this work, along with experimental vapor pressure measurements. Except for naphthalene, quantitative accuracy is quite good. As was true with Figure 4.1c, the naphthalene data are of questionable validity.

The P-T-x diagrams which are covered in Chapters 6 and 7 include a region of formation of solid naphthalene. The solid is to an excellent approximation a pure phase, and its fugacity is thus simply expressed. Knowledge of the solid phase fugacity in turn allows calculation of the desired phase equilibria.

To derive an expression for the pure solid fugacity, one starts with the Gibbs-Duhem equation written for the coexisting solid and vapor phases:

$$d\mu^c = -s^c dT + v^c dP \tag{4.1}$$

$$d\mu^g = -s^g dT + v^g dP \tag{4.2}$$

Here the supercript c denotes the pure solid (crystalline) phase and the superscript g the pure vapor (gaseous) phase. At equilibrium, $d\mu^c = d\mu^g$, so the two equations may be equated and rearranged to yield

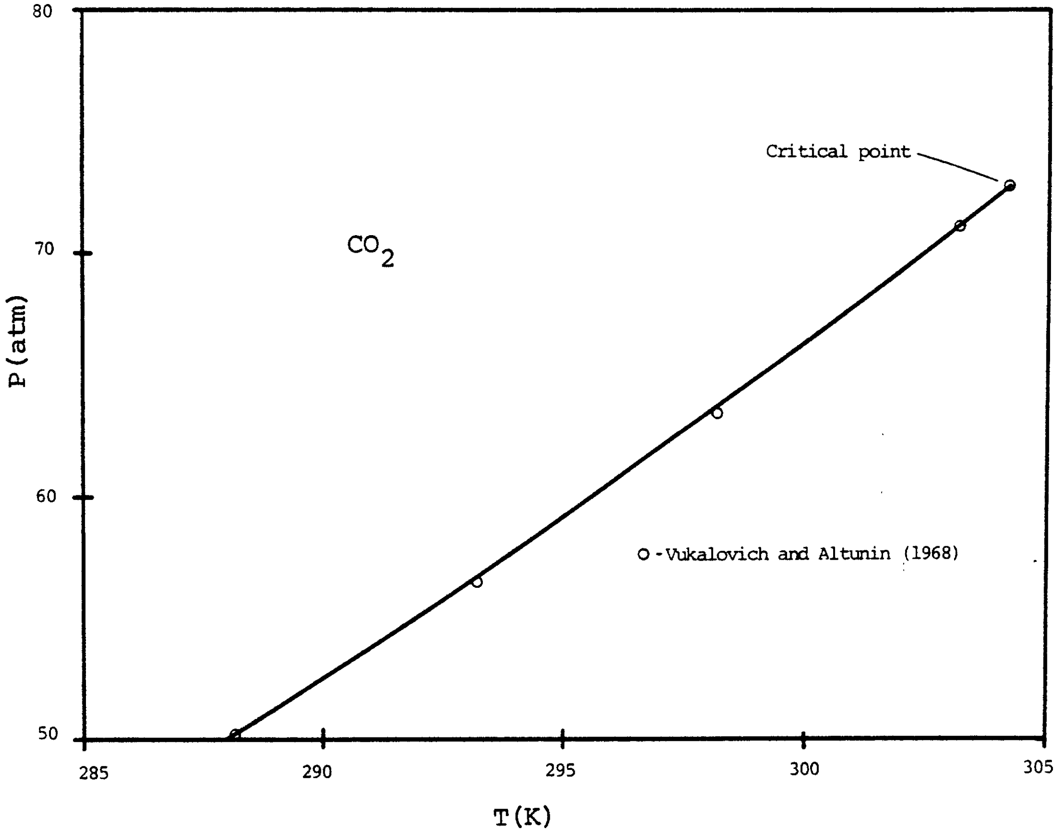

Figure 4.2a. P-T diagram for carbon dioxide.

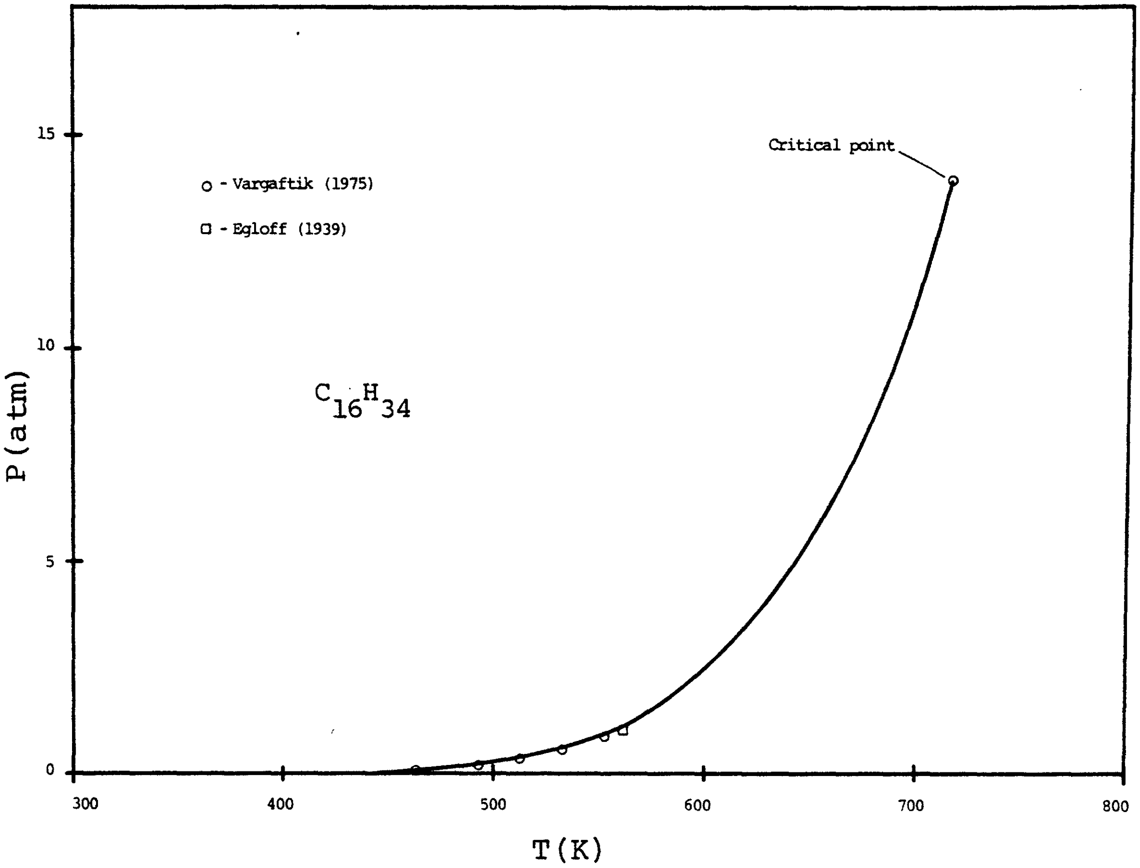

Figure 4.2b. P-T diagram for n-hexadecane.

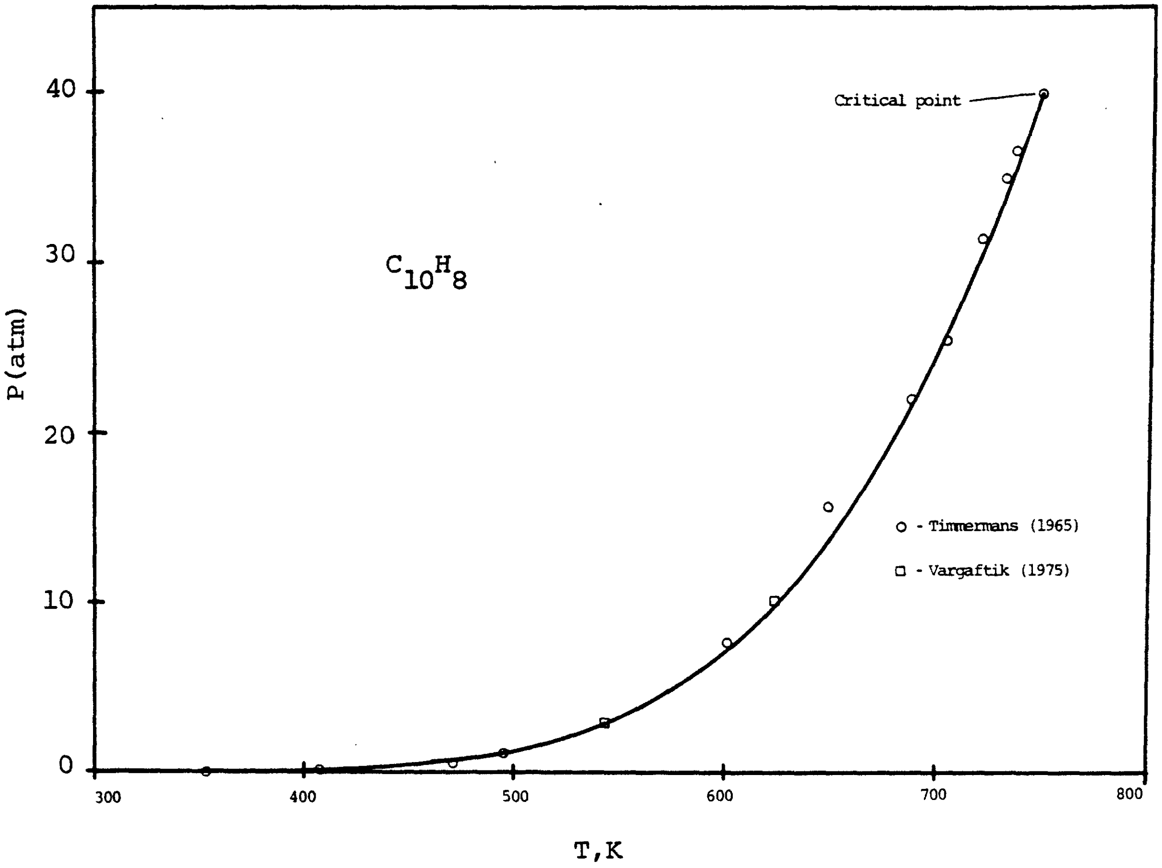

Figure 4.2c. P-T diagram for naphthalene.

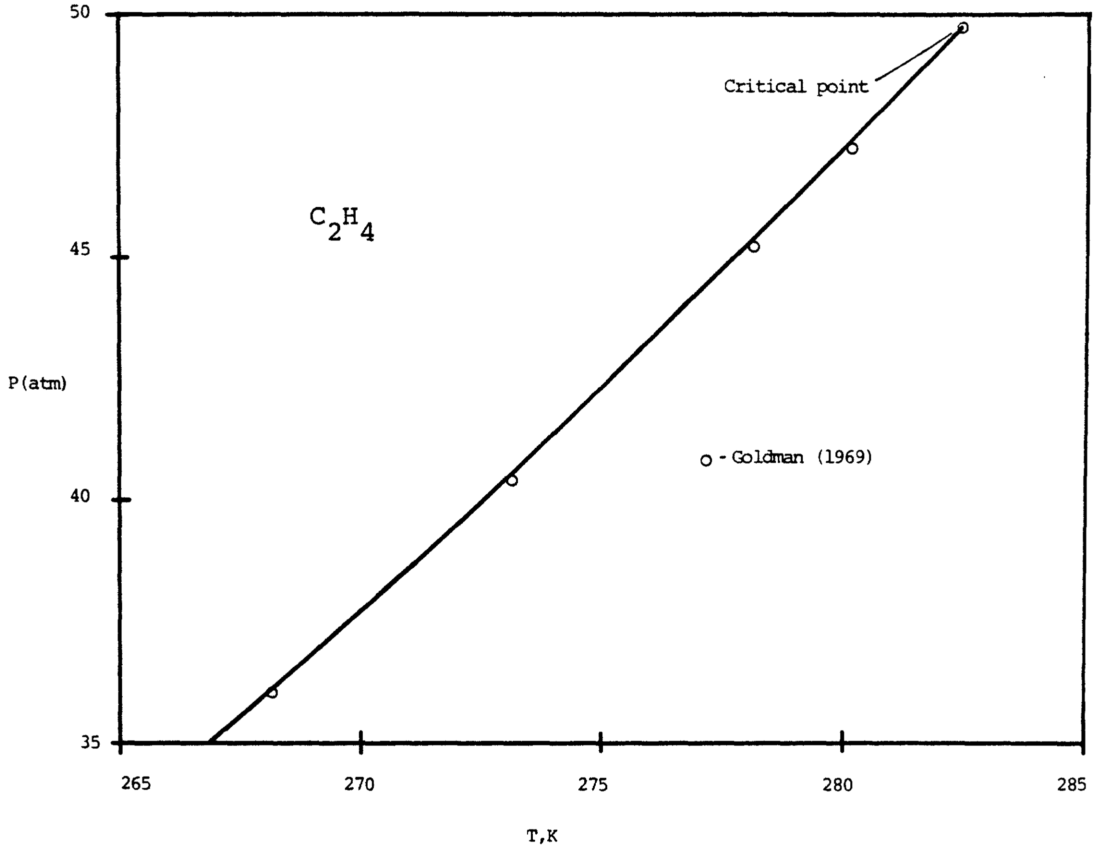

Figure 4.2d. P-T diagram for ethylene.

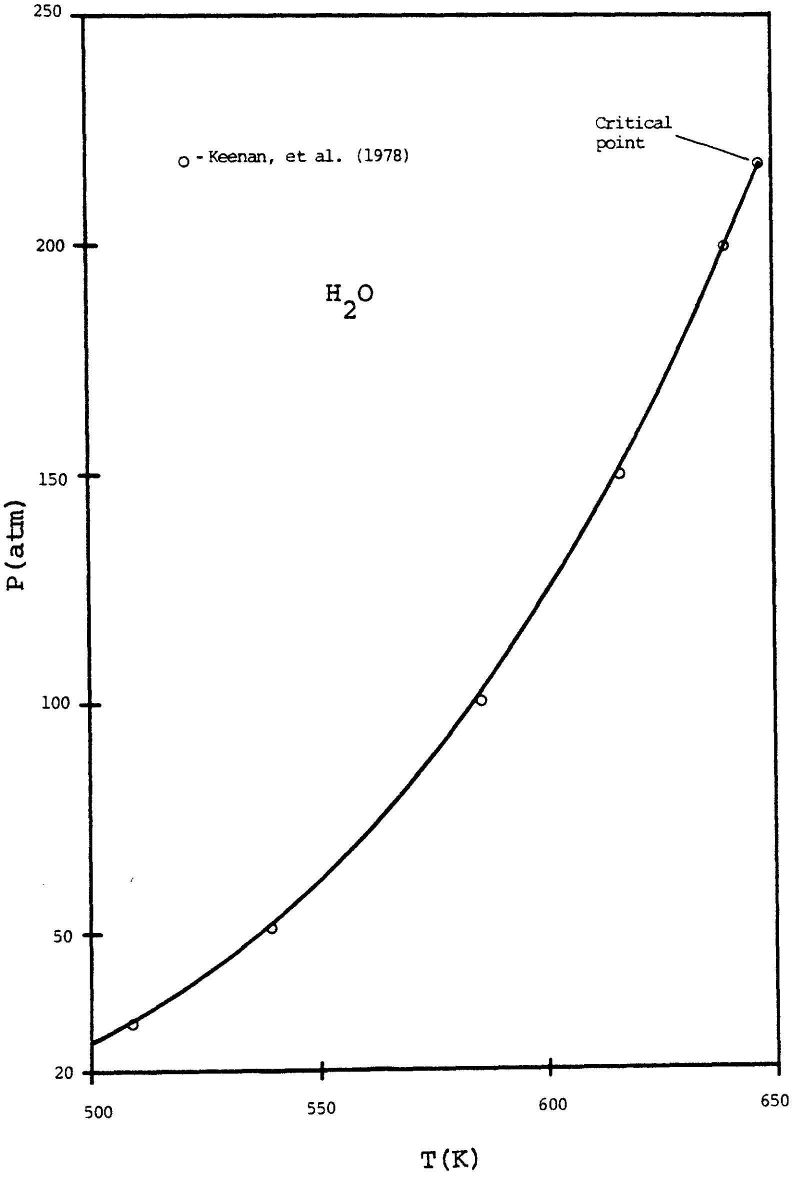

Figure 4.2e. P-T diagram for water.

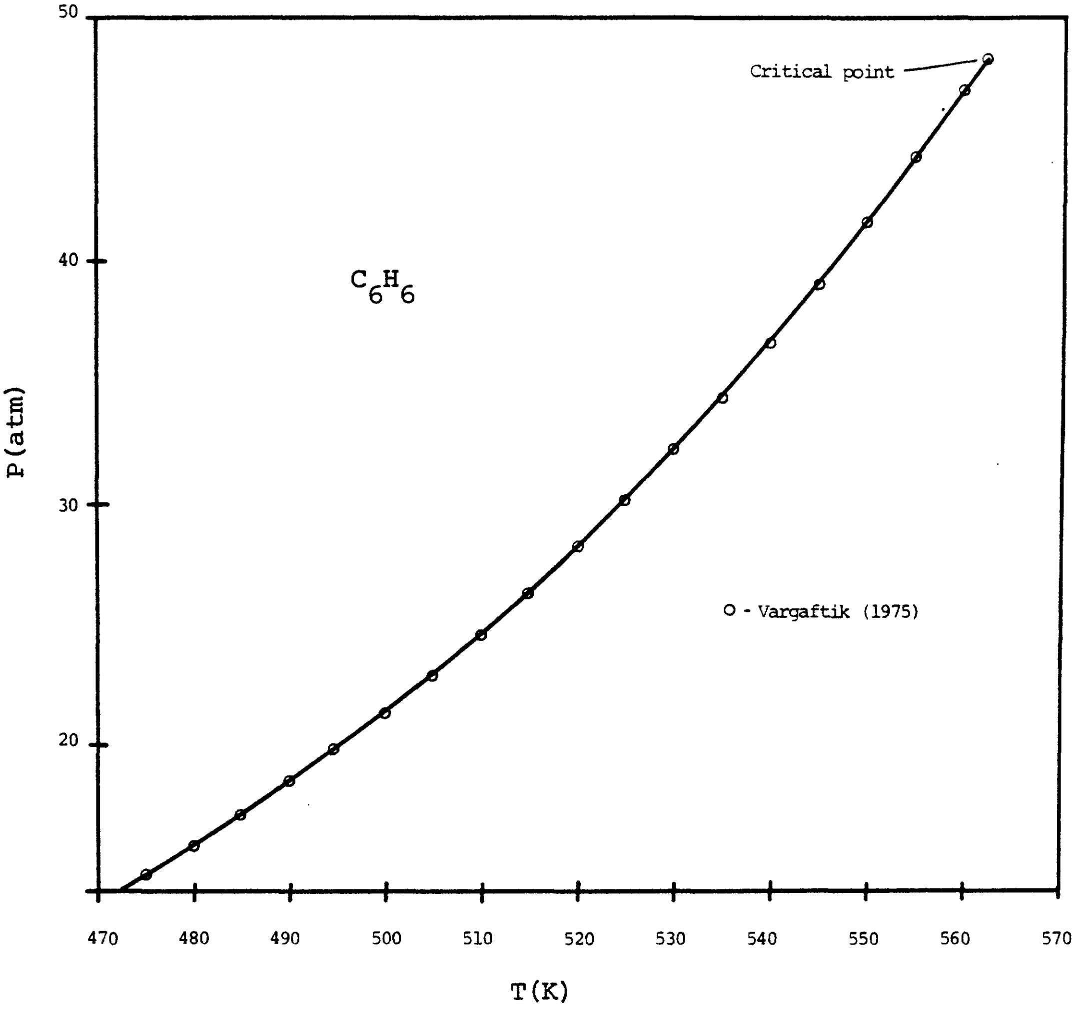

Figure 4.2f. P-T diagram for benzene.

$$\frac{dP}{dT} = \frac{S^g - S^c}{v^g - v^c} \qquad (4.3)$$

Applying the identity G=H-TS to both phases allows equation (4.3) to be rewritten as

$$\frac{dP}{dT} = \frac{H^g - H^c}{T(v^g - v^c)} = \frac{\Delta H^{sub}}{T\Delta v^{sub}} \qquad (4.4)$$

the superscript sub indicating conditions along the sublimation curve. Under sublimation conditions, the ideal gas equation is usually applicable to the vapor phase. Furthermore, the crystalline volume is negligible compared to that of the gas. Incorporating these two assumptions, one finds

$$\frac{d\ln P}{d(1/T)} = - \frac{\Delta H^{sub}}{R} \qquad (4.5)$$

The quantity ΔH^{sub} is relatively constant over a moderate temperature range, so that equation (4.5) is readily integrated to give

$$\ln P^{sub} = - \frac{\Delta H^{sub}}{RT} + C \qquad (4.6)$$

This equation expresses the relationship between temperature and pressure along the sublimation curve. The values of $\frac{\Delta H^{sub}}{R}$

and C are usually evaluated by fitting experimental data. Since some approximations are involved in deriving equation (4.6), ΔH^{sub} will be slightly different than the true heat of sublimation.

Prausnitz (1969) has shown that the fugacity of a pure solid at a given temperature and pressure may be stated as

$$f^c = P^{sub} \phi^{sat} \exp\left[\int_{P^{sub}}^{P} \frac{v^c dP}{RT}\right] \qquad (4.7)$$

Here ϕ^{sat} is the fugacity coefficient of the saturated vapor phase. For the low pressures associated with solid-vapor equilibrium, it is almost always very close to 1. v^c is the molar volume of the solid, and is essentially constant over wide ranges of pressure. Incorporating these two simplifications, equation (4.7) becomes

$$f^c = P^{sub} \exp\left[\frac{v^c (P - P^{sub})}{RT}\right] \qquad (4.8)$$

Equation (4.8) is used in the calculation of solid-fluid equilibria.

Application of equation (4.6) in conjunction with the P-R equation for a pure substance allows the prediction of naphthalene's triple point. Figure 4.3 gives a detailed picture of the $C_{10}H_8$ triple point region, in comparison with

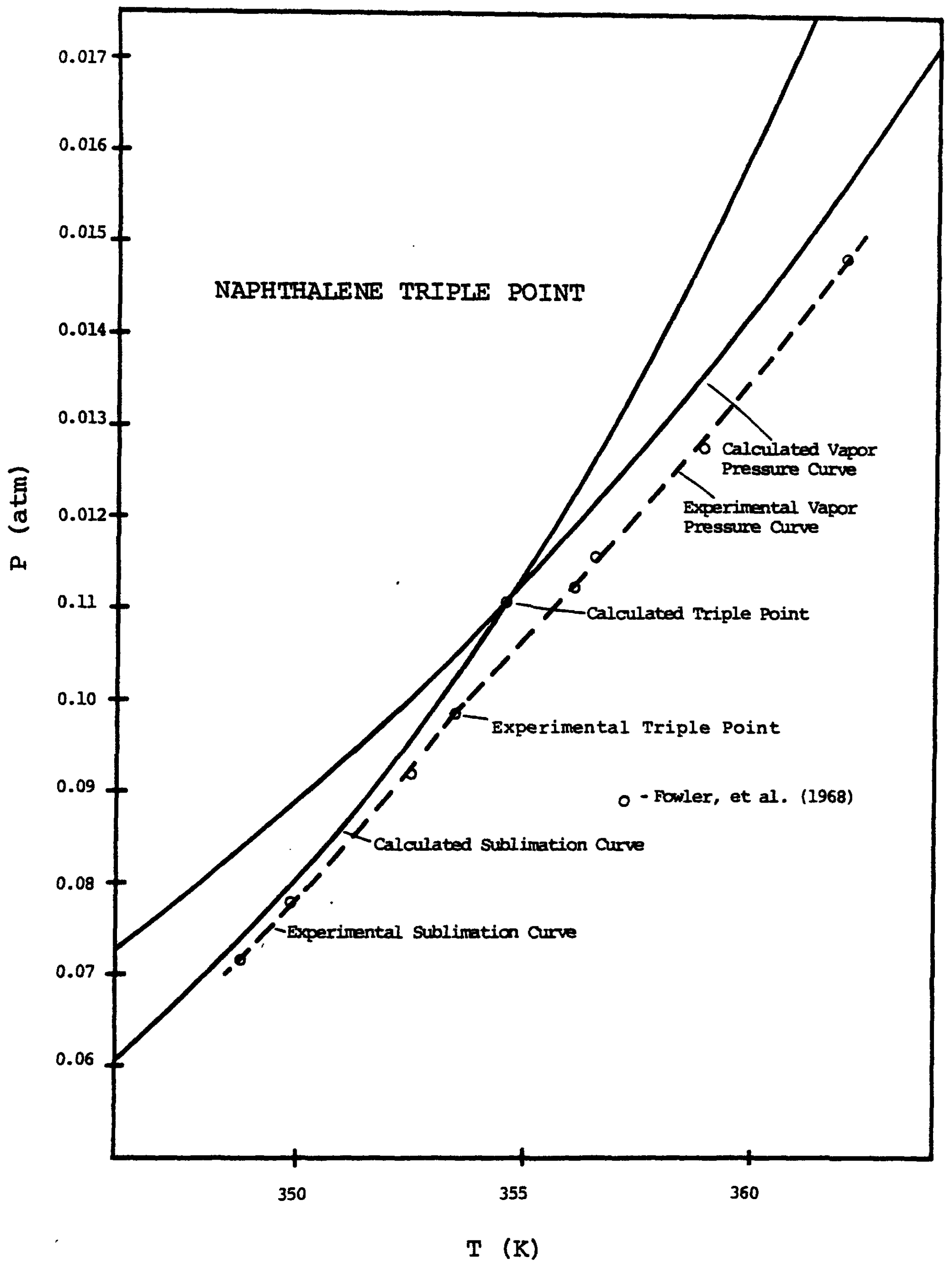

Figure 4.3. A comparison of experimental and predicted triple points for naphthalene. The vapor pressure curve is calculated using the P-R equation, the sublimation curve is calculated using equation (4.9).

experimental data. The calculated vapor pressure curve is in error by about 0.0006 atm over the range of temperatures shown. The triple point is predicted when the calculated vapor pressure curve intersects the calculated sublimation pressure curve for the solid. The expression for the sublimation curve is given by

$$P^{sub} = 0.0001 \exp\left[-8719/T + 29.3\right] \qquad (4.9)$$

which stems from a reduction of data taken at 273 to 333 K (Ambrose, et al., 1975). Equation (4.9) deviates from the experimental curve by as much as 0.0004 atm at the temperatures covered in Figure 4.4. More accurate expressions are available (see Ambrose, et al. (1975) or Fowler, et al. (1968)) but they do not yield significant differences in the binary phase diagrams. In fact, since the P-R vapor pressure curve is somewhat inaccurate, equation (4.9) gives a better prediction of the triple point than these other expressions.

To summarize, a consideration of the pure component phase diagrams gives every indication that the Peng-Robinson equation should be suitable for the generation of binary P-T-x diagrams.

Chapter 5 The n-Hexadecane - Carbon Dioxide System

The n-hexadecane (C_{16}) - carbon dioxide (CO_2) system is similar to the types shown in Figures 2.8 and 2.9. The upper critical line starts at the critical point of C_{16}, rises to a pressure maximum, falls to a pressure minimum, and thereafter runs to very high pressures with a slightly positive dP/dT. The lower critical line starts at the CO_2 critical point with a positive dP/dT, and after a short distance intersects the three-phase LLG line. For ease of reference, physical constants for C_{16} and CO_2 are given in Table 5.1.

The first step in the prediction of P-T-x diagrams is the determination of a value for the interaction parameter δ_{12}. For this system, the pressure-temperature coordinates of the upper critical line have been measured (Schneider, et al., 1967) and provide a basis for this determination. Figure 5.1 shows the upper critical lines generated for various values of δ_{12}, and illustrates the marked effect of this parameter on the predictions. It is possible to fit the data precisely by allowing the interaction parameter to vary with temperature (and possibly pressure). Figure 5.2 shows the values of δ_{12} needed to match the data in Figure 5.1 as a function of temperature. Peng and Robinson (1980) have found similar results in working with aqueous-organic systems. Although δ_{12} increases monotonically with T, the

Table 5.1

Physical Constants of n-Hexadecane and Carbon Dioxide

	$n\text{-}C_{16}H_{34}$	CO_2
T_c(K)	717	304.2
P_c(atm)	14	72.8
ω(acentric factor)	0.746	0.225
Melting Point (K)	291	216.6 (at 5.2 atm)

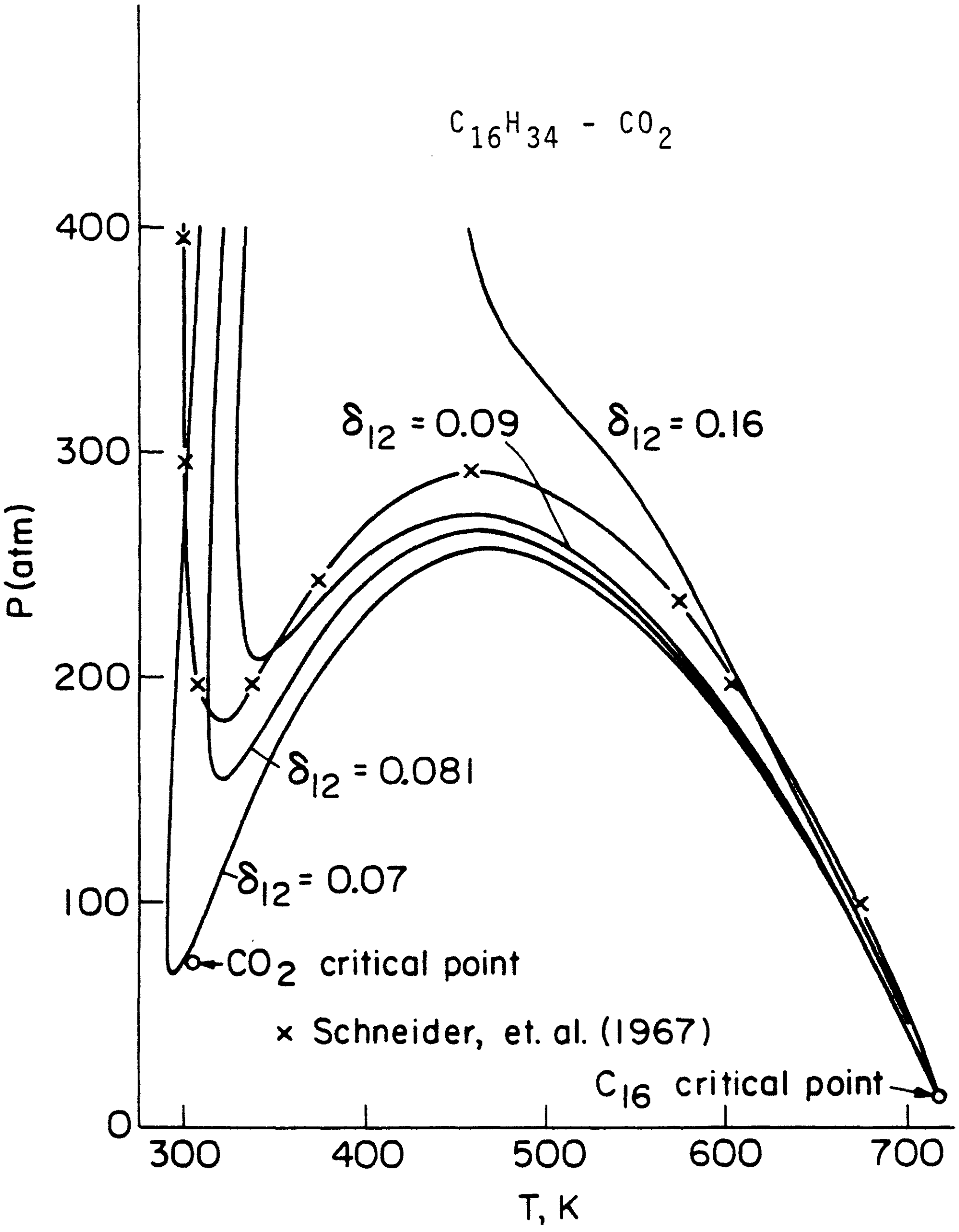

Figure 5.1. P-T projection for the C_{16}- CO_2 system showing the effect of δ_{12} on the predicted upper critical line. The pure CO_2 critical point has also been included, although it is not a part of this line.

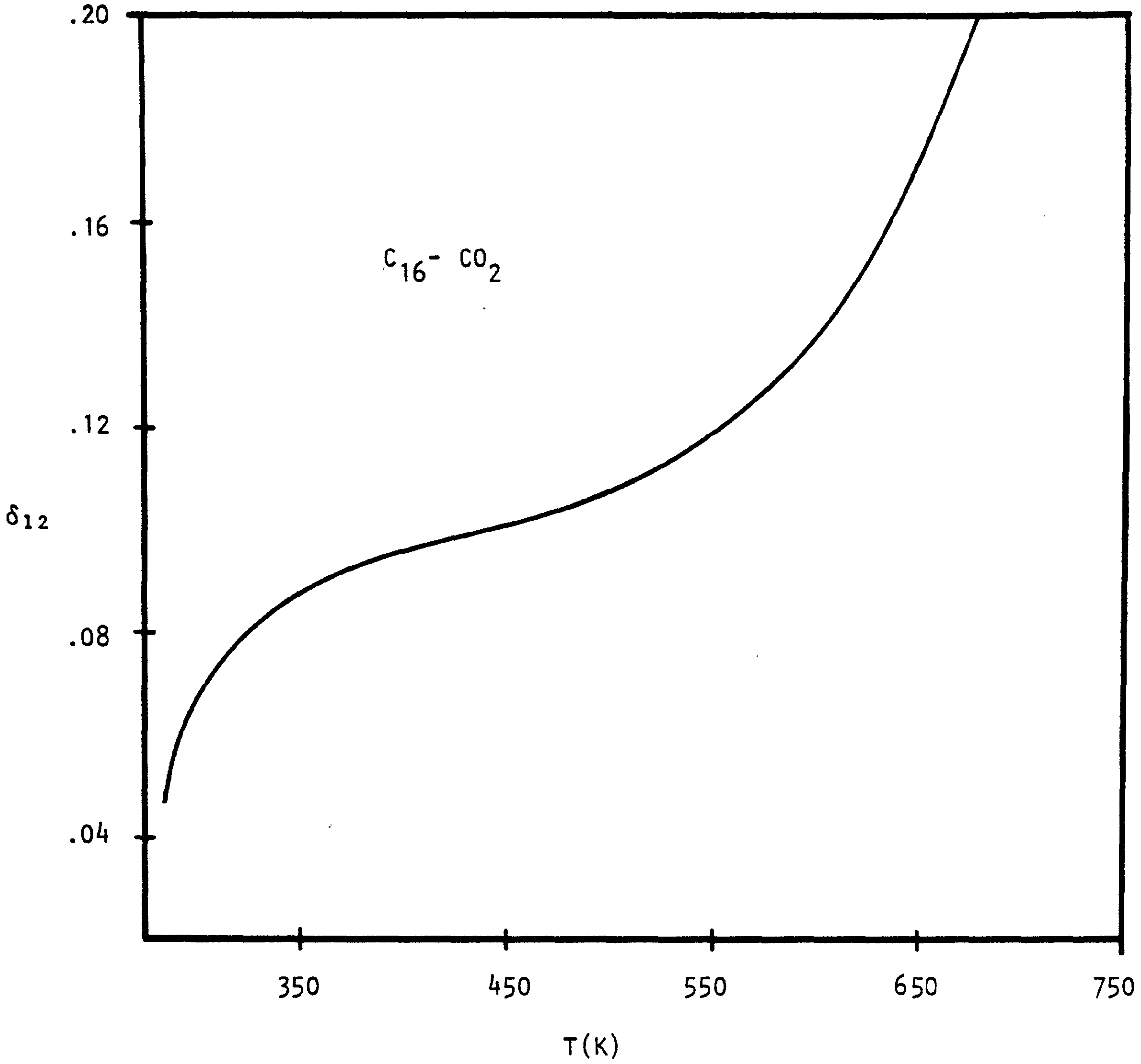

Figure 5.2. The temperature dependence of the interaction parameter δ_{12}. Allowing δ_{12} to vary with temperature along the curve shown, an accurate matching of the data in Figure 5.1 is obtained.

functionality is not simple in shape. More than one numerical constant would be required to express this function analytically. The pressure functionality of the interaction parameter is more complicated than the temperature functionality.

It was not considered desirable in this thesis to introduce more than one empirical parameter into the equation of state. For this reason, the conventional approach of using a constant interaction parameter was followed. A value of δ_{12}=0.081 was selected, and is seen from Figure 5.1 to be a reasonably optimal choice. It should be noted that composition data along the upper critical line is not available, and thus is not a factor in this determination.

Having selected an appropriate interaction parameter, it is helpful to backtrack a bit and see how the critical points in Figure 5.1 are predicted. Figure 5.3 presents a sequence of T-x sections which illustrate the shape of the spinodal (L1=0) and second critical criterion (M1=0) curves. Critical points are located at the intersections of these two curves.

Starting at 300 atm, Figure 5.3a, the curves have relatively simple shapes. The spinodal curve is dome shaped, and is actually composed of two branches which meet at the critical point. The right hand branch gives the limit of intrinsic stability for liquid phases, and the left hand

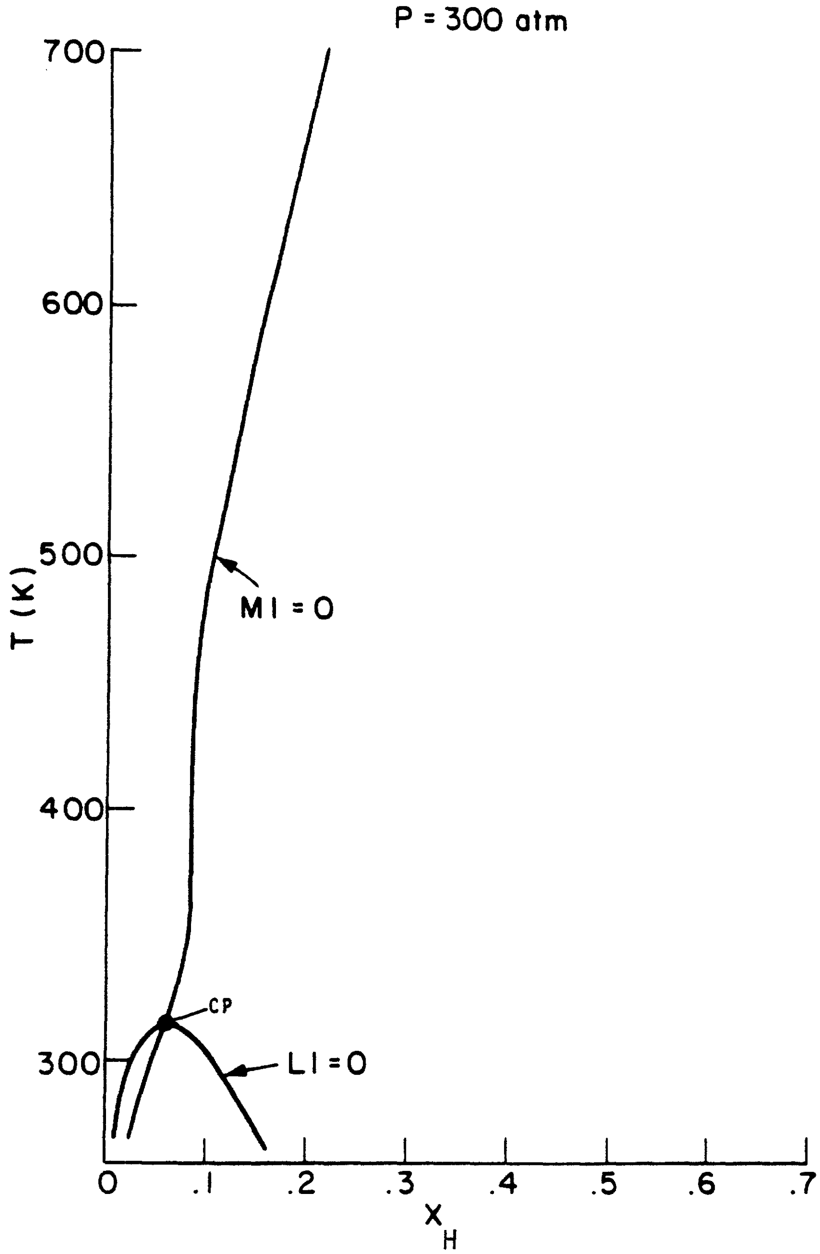

Figure 5.3a. The T-x section at 300 atm showing the L1=0 and M1=0 curves. There is one critical point at this pressure.

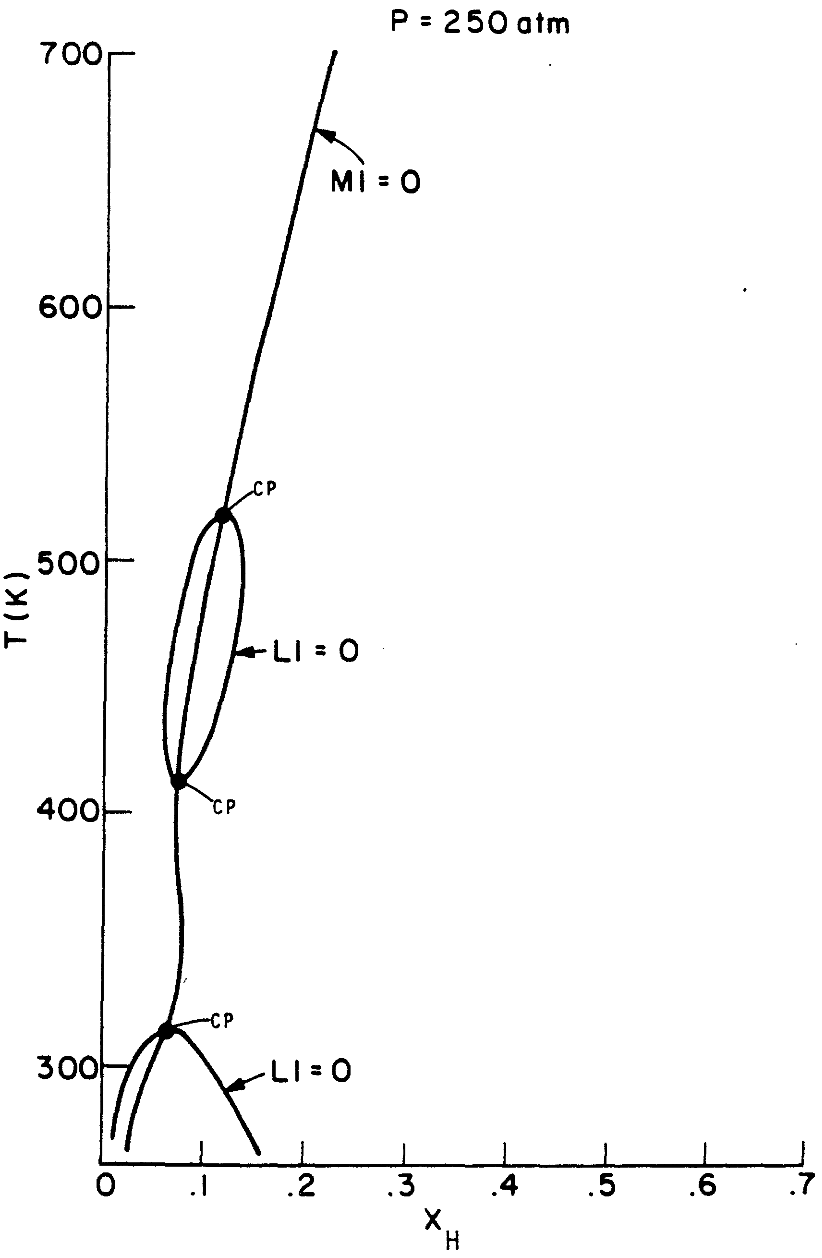

Figure 5.3b. The T-x section at 250 atm showing the L1=0 and M1=0 curves. There are three critical points at this pressure.

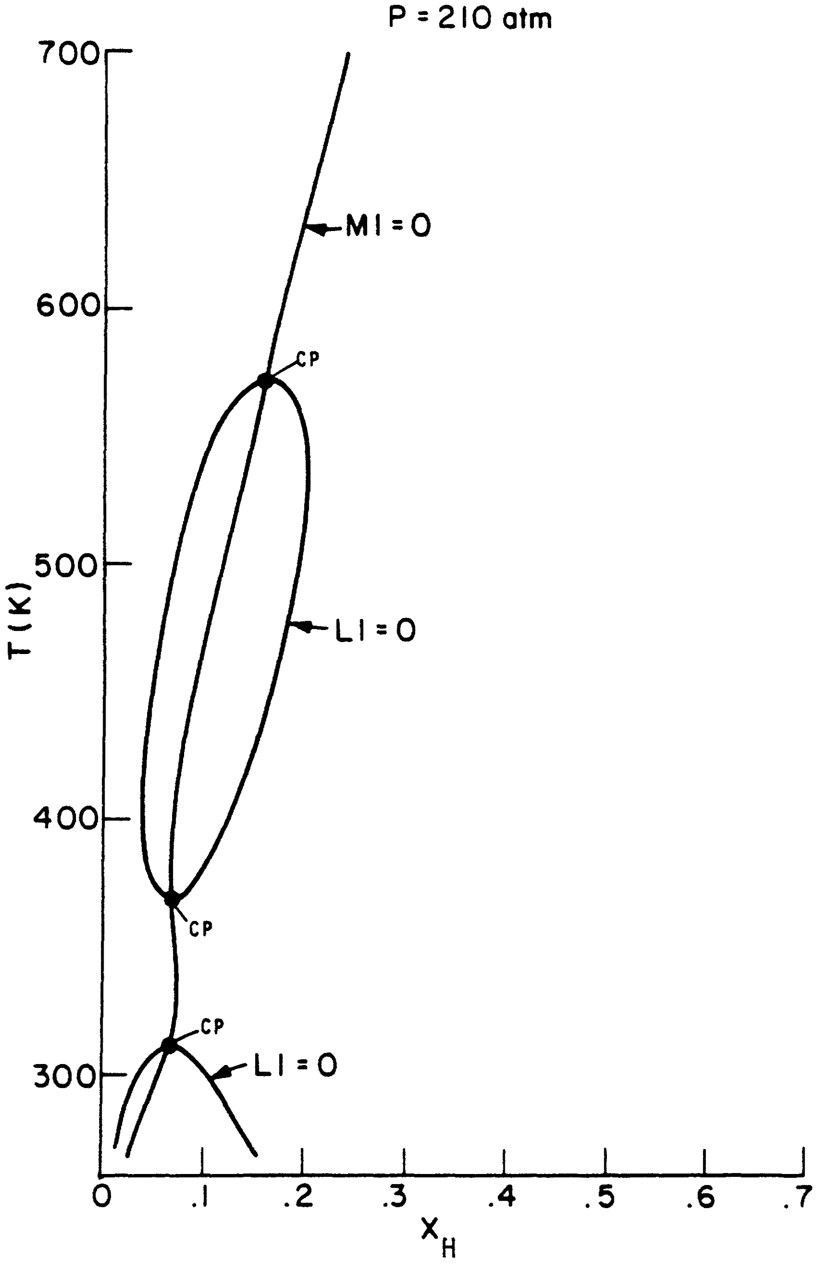

Figure 5.3c. The T-x section at 210 atm showing the L1=0 and M1=0 curves.

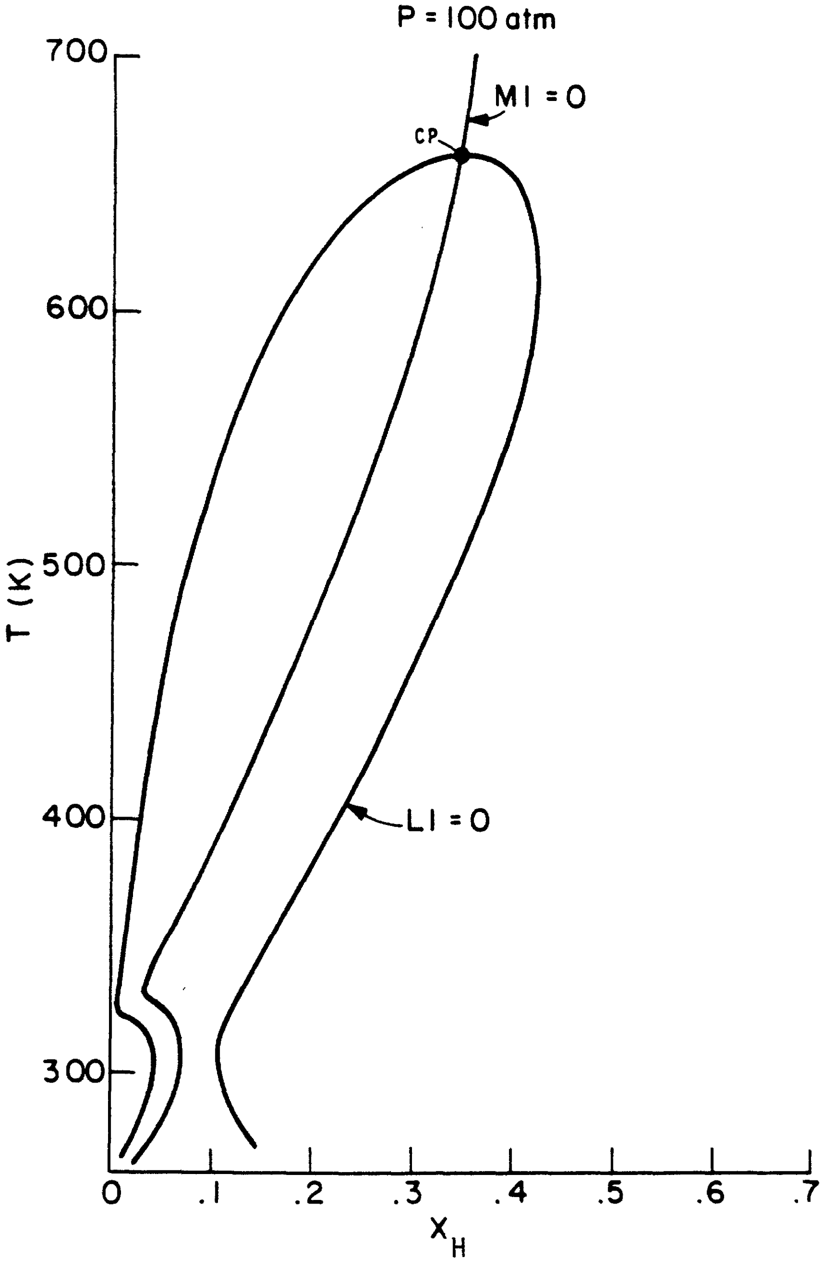

Figure 5.3d. The T-x section at 100 atm showing the L1=0 and M1=0 curves. The two separate L1=0 curves present at higher pressures have merged.

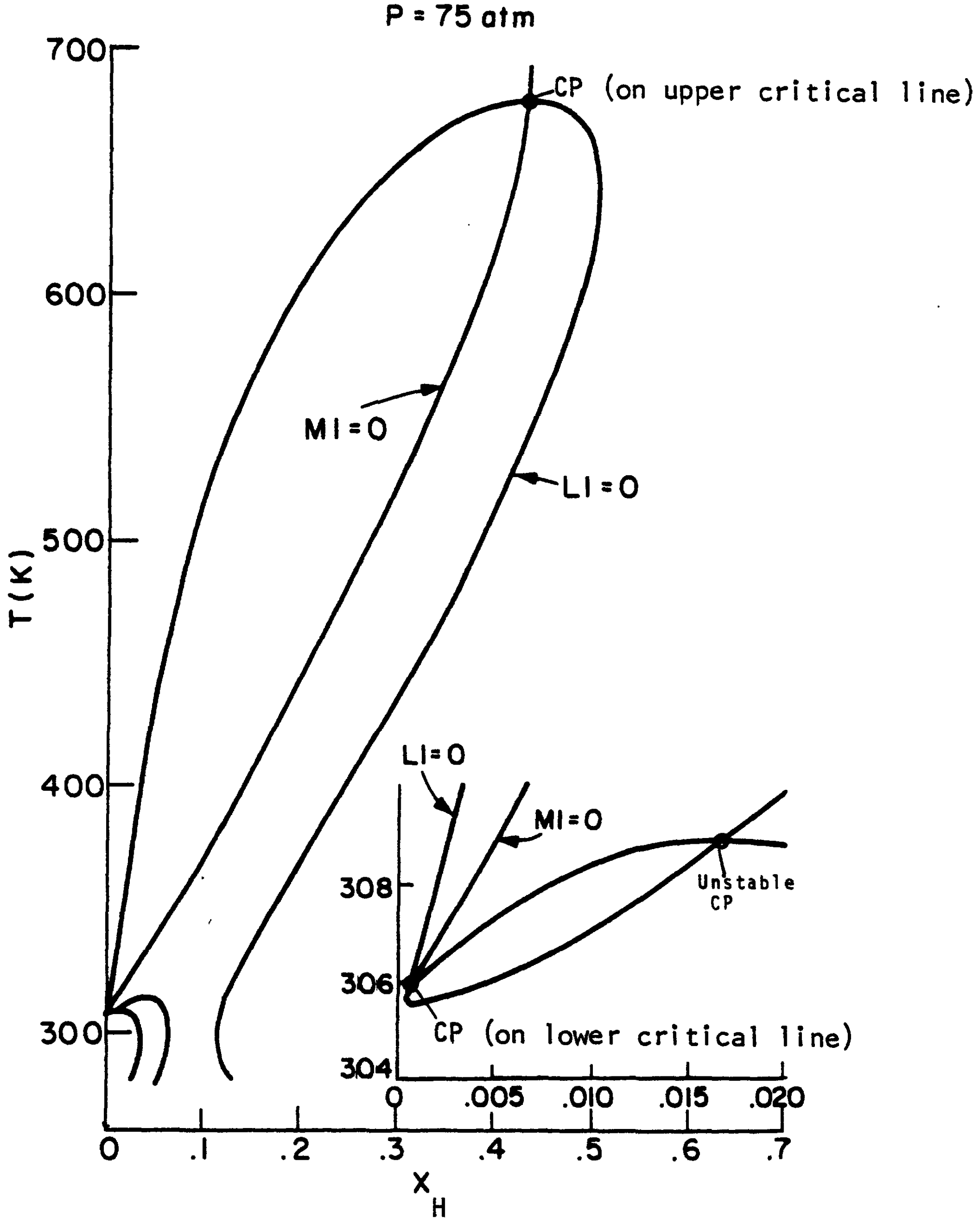

Figure 5.3e. The T-x section at 75 atm showing the L1=0 and M1=0 curves. Once again three critical points are present. The two low temperature critical points in this figure, however, are not related to the two low temperature critical points present at 210 and 250 atm.

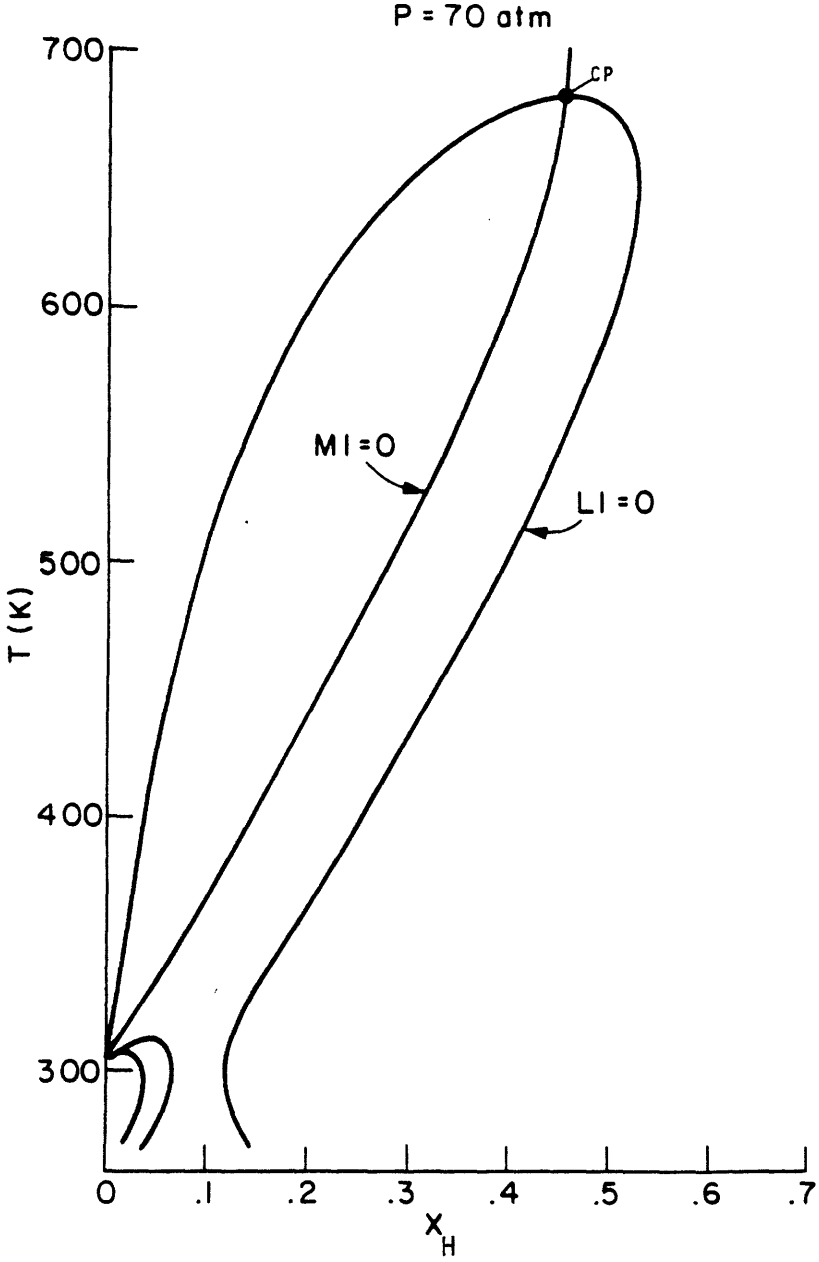

Figure 5.3f. The T-x section at 70 atm showing the L1=0 and M1=0 curves. Only one critical point is visible at this scale.

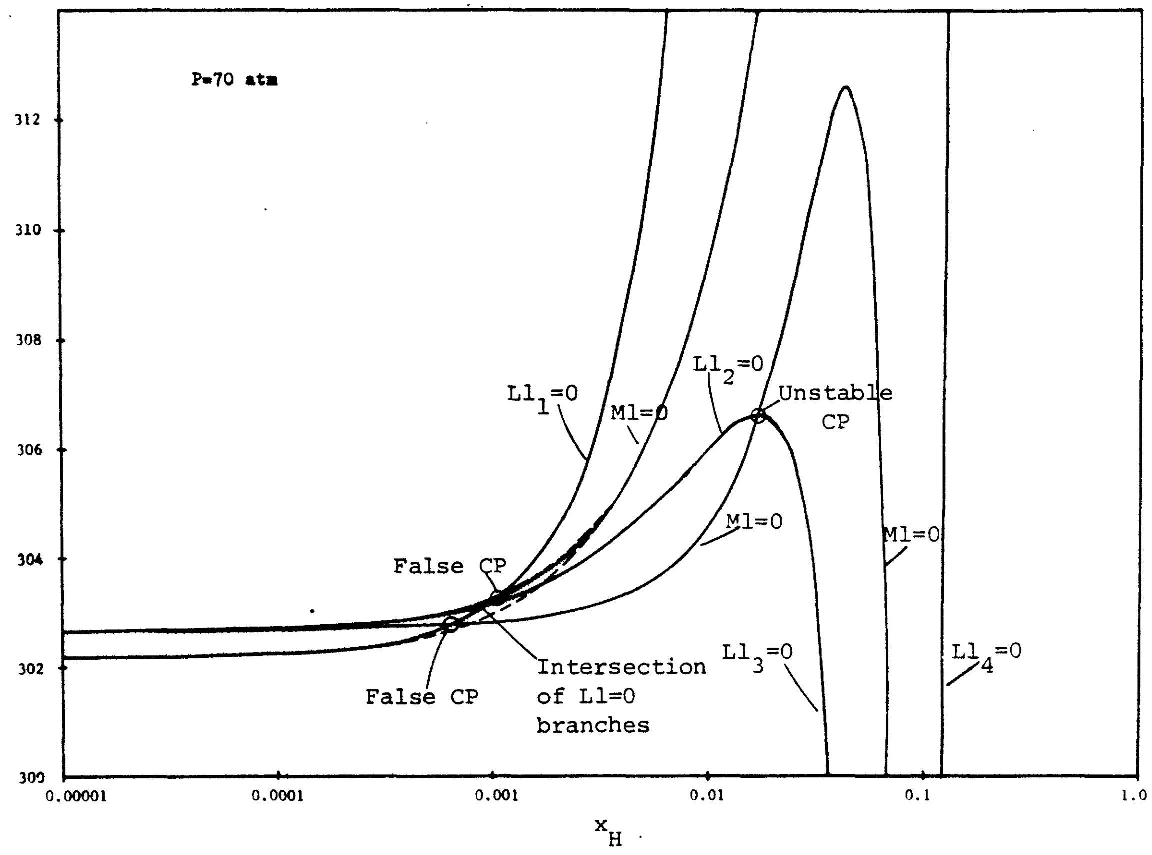

Figure 5.3g. A T-x section at 70 atm showing the L1=0 and M1=0 curves. The four separate branches of the spinodal (L1=0) curve have been labelled with subscripts. The shaded area indicates the region of three roots. Of the three intersections of the L1 and M1 curves, only one, the unstable CP, actually satisfies the criteria of criticality.

branch the limit of intrinsic stability for gaseous phases. A homogeneous system cannot exist at points within the spinodal dome. At the critical point, both L1 and M1 are zero. Also, as discussed in Chapter 3, $\frac{dL1}{dx} = 0$. The critical point in this diagram corresponds to the critical point at 300 atm in Figure 5.1.

At 250 atm, Figure 5.3b, a second spinodal curve has appeared in the form of a closed loop. The closed loop spinodal is crossed by the M1 = 0 curve twice, to give a total of three critical points at this pressure. By tracing a constant pressure line at 250 atm in Figure 5.1, the position of these critical points along the upper critical line is evident. At 210 atm (Figure 5.3c), the closed loop spinodal has increased in size, and finally, at 100 atm (Figure 5.3d), the two spinodals have merged. There is again but one critical point at this pressure, as confirmed by Figure 5.1.

The course of the L1 = 0 and M1 = 0 curves at 75 atm is shown in Figure 5.3e. Behavior for the critical point on the upper critical locus is similar to that at the higher pressures. At lower temperatures, though, a sharp but differentiable point has developed in the L1 curve. The region of this point has been enlarged in the inset to show its two intersections with the M1 = 0 curve. As labelled in the figure, one of these critical points is on the lower critical locus, which starts from CO_2's critical point. The second of these is the terminus of an unstable binodal surface, i.e., it is an unstable critical point. The shape of the unstable binodal surface will be presented later in this chapter.

Figure 5.3f illustrates the L1=0 and M1=0 curves at 70 atm. This pressure is below the critical pressure of CO_2. Figure 5.3g gives the enlargement for the region near the CO_2 axis, with a logarithmic concentration scale. The four segments of the spinodal curve have been labelled separately. Once again, there is an unstable critical point. There are also two more points of L1-M1 intersection, noted on the graph as false critical points. These false intersection points lie within a region of three real roots to the cubic equation of state, as indicated by the shaded portion of the figure. They are not true critical points because the L1=0 criterion is satisfied for one root while the M1=0 criterion is satisfied for another root. For a true critical point (e.g., the unstable CP in the figure) the L1=0 and M1=0 criteria must be simultaneously satisfied for the same root of the cubic.

The occurrence of 3 roots leads also to an intersection of two branches of the L1=0 curve. It is no longer accurate to define the intrinsically unstable region as the region between the two branches of the spinodal curve. The stable and unstable regions in Figure 5.3g are not readily apparent, and it is best to return to the fugacity-composition plots to gain a proper understanding. Figure 5.4 shows a temperature sequence of f-x plots at 70 atm. In light of the discussion in Chapter 3, the general shape of these curves should be familiar. Consider first Figure 5.4a, drawn for T = 303.6 K, which is above the temperature at which the Ll = 0 curves cross in Figure 5.3g. Although there is a small composition range of three roots, all mole fractions between Ll_1 and Ll_2 give unstable solutions. This will continue to be so until Ll_2 moves to a lower mole fraction than Ll_1, i.e., until the two branches in Figure 5.3g cross. Once they have crossed, the behavior shown at 302.8 K (Figure 5.4b) is valid, and a stable solution may be found for any mole fraction between Ll_1 and Ll_2, provided the proper leg of the f-x curve is chosen. This also holds true after Ll_2 has moved to $x_H=0$ and formed a closed loop, as at 302.6 K (Figure 5.4c; cf. Figure 3.4). In a region of multiple roots then, as previously implied, a T-x section must be interpreted separately for each root. With respect to Figure 5.3g, the vapor phase solution is stable for x_H less than $Ll_1=0$, while for x_H greater than $Ll_1= 0$, the vapor phase solution is unstable. Likewise, for x_H less than $Ll_2=0$, the liquid phase solution is unstable, and for x_H greater than $Ll_2=0$, the liquid phase solution is stable.

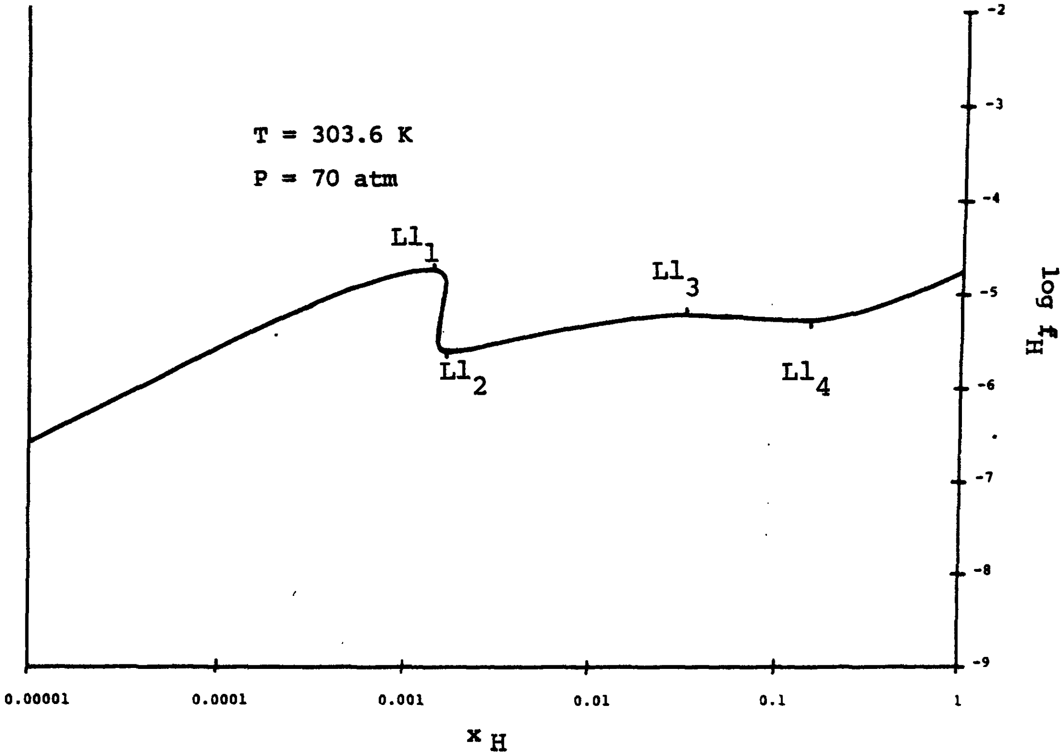

Figure 5.4a. f-x plot. The labelled extrema indicate points where Ll = 0. A single phase system with a composition between Ll_1 and Ll_2 would be either materially or mechanically unstable.

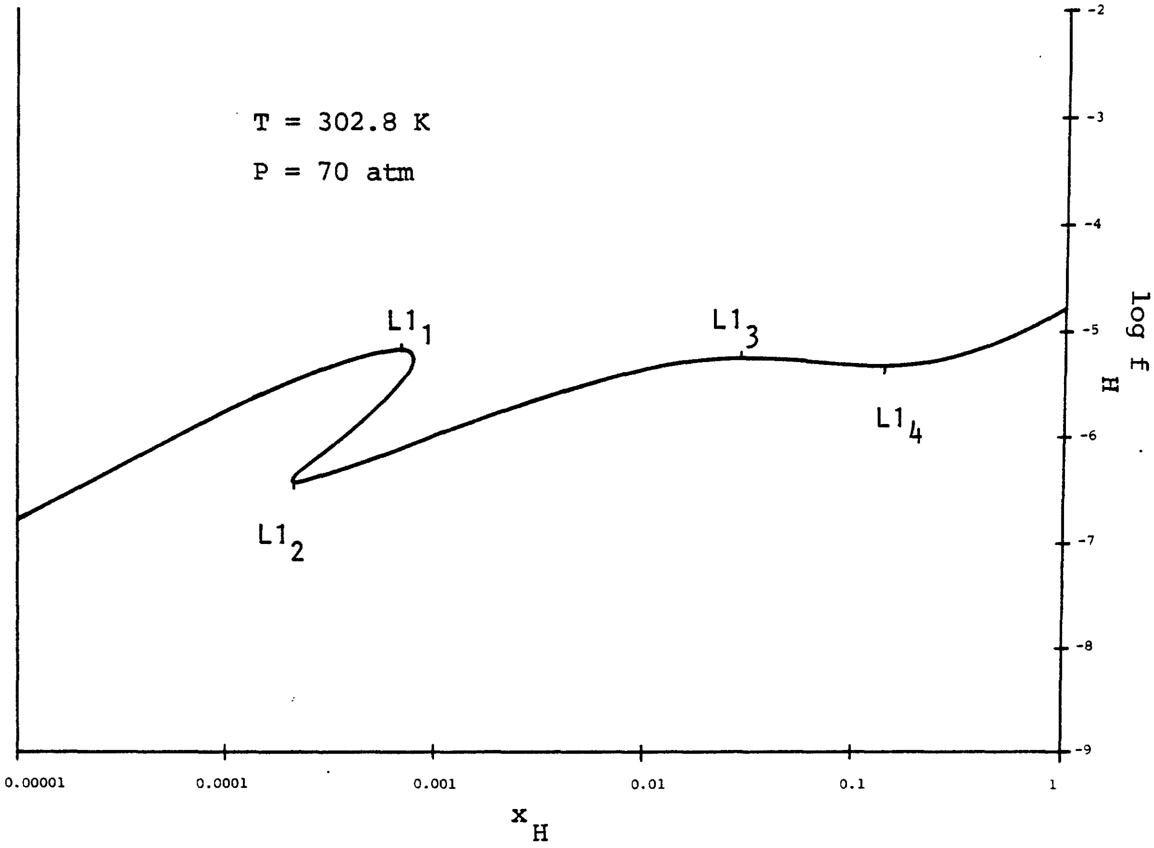

Figure 5.4b. f-x plot. A single phase vapor is stable or metastable at compositions up to Ll_1. A single phase liquid is stable or metastable between Ll_2 and Ll_3. The only composition range in which a single phase system cannot exist is from Ll_3 to Ll_4.

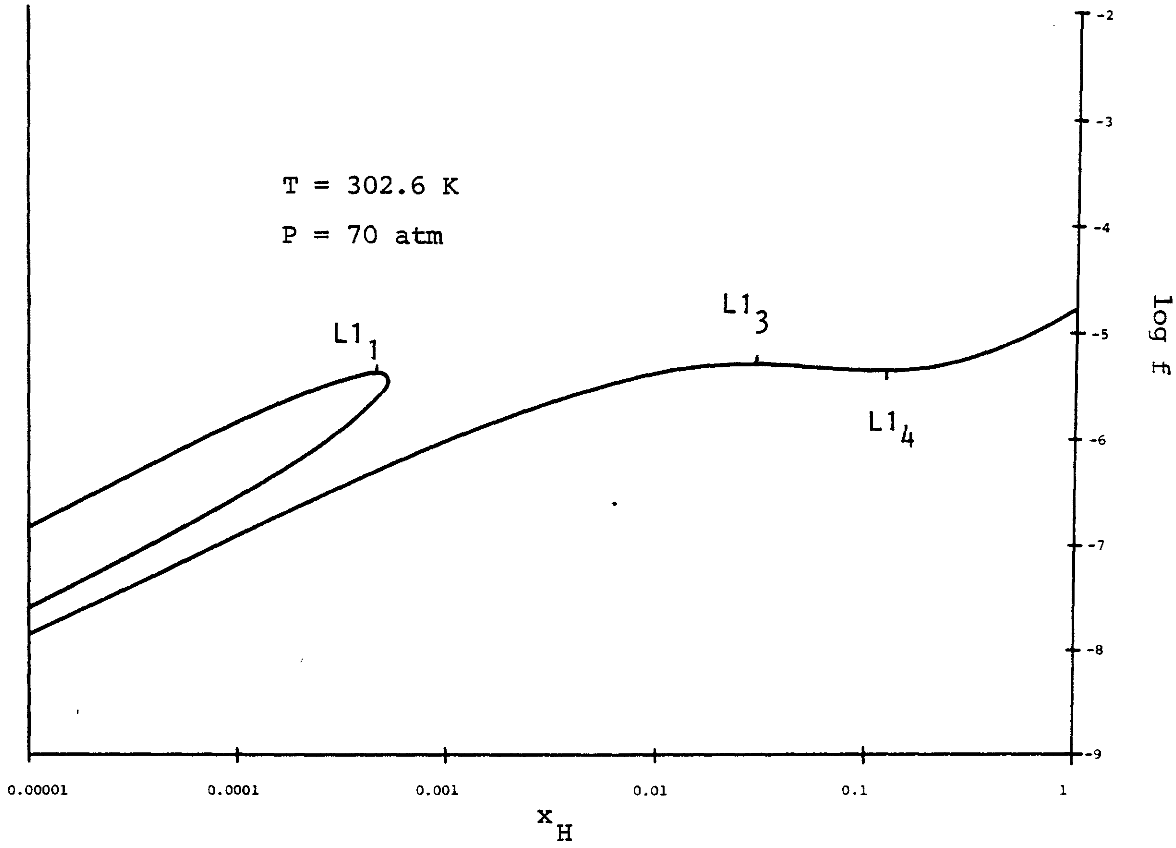

Figure 5.4c. f-x plot. $L1_2$ has moved to $x_H=0$. Behavior is otherwise the same as in Figure 5.4b.

With the interpretation of the critical point criteria now clarified, prediction of the lower critical locus is possible. The P-T projection for this locus is shown in Figure 5.5. Here the dashed line indicates the vapor pressure curve of CO_2, which terminates at the CO_2 critical point. From this point, the lower critical locus begins, and in conjunction with the unstable critical locus forms a cusp terminating at about 86 atm and 315 K. As indicated by the T-x section at 70 atm (Figure 5.3g), the unstable critical locus extends to pressures and temperatures below the pure CO_2 critical point. Also shown in Figure 5.5 is the three phase L_1-L_2-G line, the calculation of which will be considered shortly. It intersects the lower critical locus at the lower critical end point, and stops there since the vapor phase and one of the liquid phases become identical. Beyond the intersection point, the critical locus is metastable with respect to the formation of two liquid phases. The lower critical locus for this system has not been experimentally determined, but its behavior is of the type expected from the discussion of Chapter 2 (see Figure 2.8).

The correct shape of the critical lines predicted with δ_{12}=0.081 indicates that a qualitatively accurate picture of the P-T-x space for this system may be obtained through the use of the P-R equation. A complete definition of the P-T-x space requires the calculation of the binodal surfaces. The

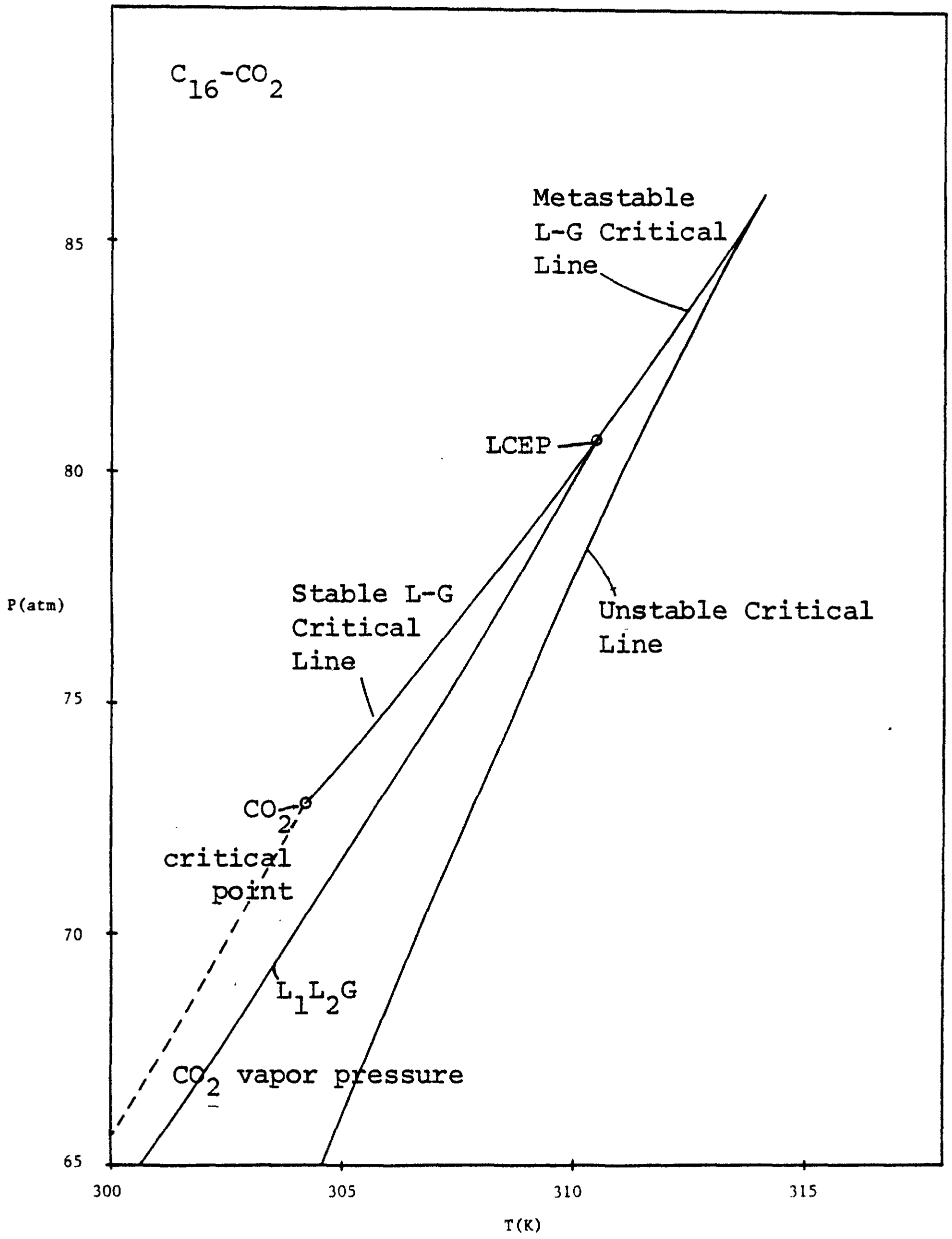

Figure 5.5. The P-T projection of the lower critical locus for C_{16}- CO_2. The stable critical line is metastable between LCEP and the cusp.

algorithm used for this purpose is explained in detail in Appendix C. Briefly, for a given T and P, a search in composition is carried out to locate all extrema and slope infinities in the f-x curve. The f-x curve may then be broken up into monotonic sections which are easily searched for points satisfying the criterion of equilibrium. As mentioned in Chapter 3, curves which have no slope infinities, and either no extrema or two extrema, are found for the large majority of P-T coordinates in the space diagram. Figure 5.6, the T-x section at 210 atm, exemplifies this fact. The spinodal curves in this diagram have already been seen in Figure 5.3c. Since a point of L1=0 corresponds to a maximum or a minimum in an f-x curve, it is clear that, for any given T, there are either two extrema or none. It is clear as well that there cannot be phase equilibrium for a monotonic f-x function, since every mole fraction has a different fugacity. Thus it is required that the binodal curve intersect the spinodal curve tangentially at a critical point. Figure 5.6 also indicates that either the spinodal or binodal curve alone could be used to predict a critical point, since $\left(\frac{\partial T}{\partial x}\right)_P = 0$ for both at such a point. Alternatively, for the binodal curve, one could determine when the compositions of the coexisting phases became equal, i.e., when the tielines became of zero length, to locate the critical point. These two procedures emphasize the fact that the criterion M1 = 0 is not so much a prerequisite for

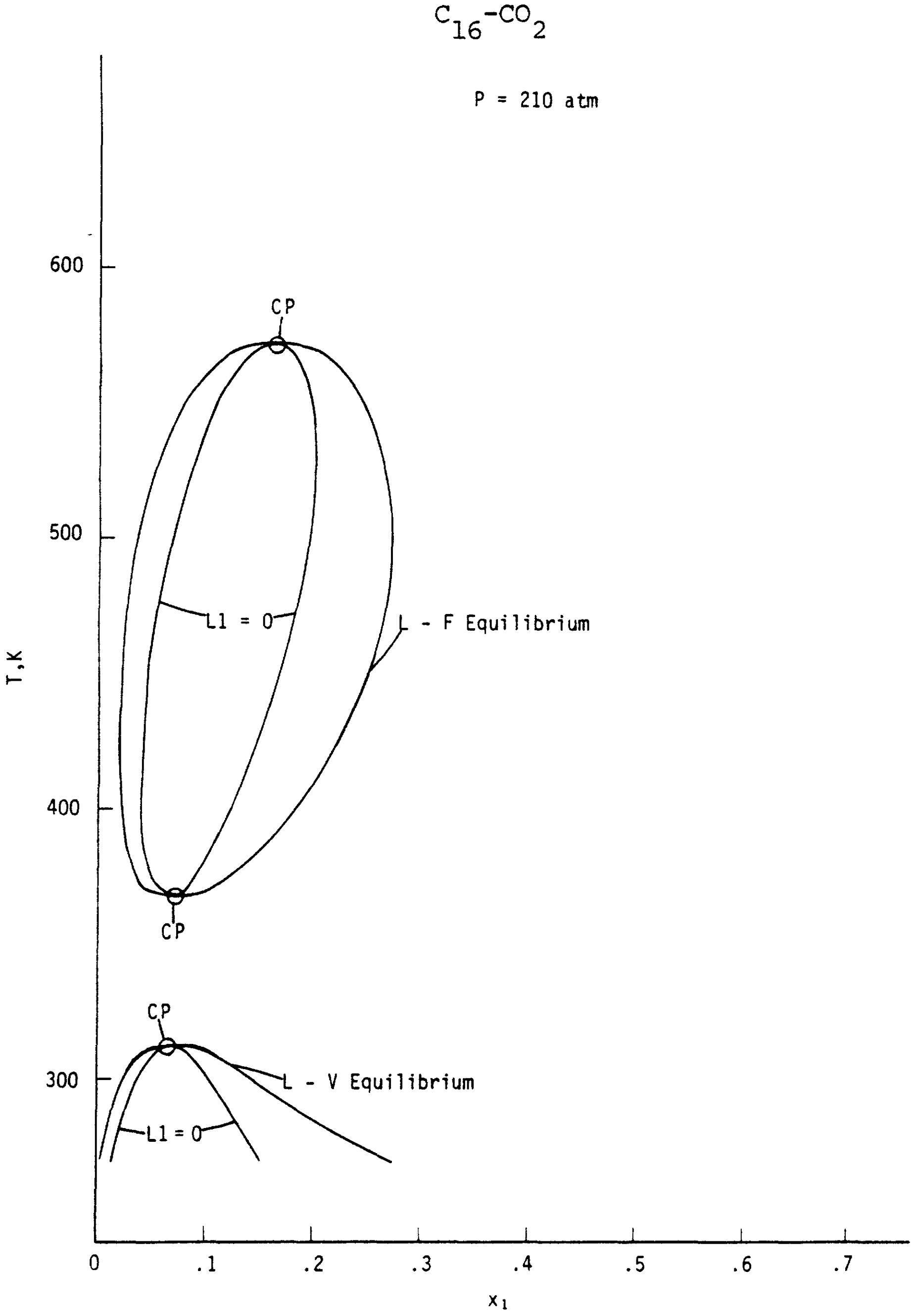

Figure 5.6. A T-x section at 210 atm showing the binodal and spinodal curves. Areas enclosed by the spinodals are unstable. Areas between the spinodals and binodals are metastable.

criticality as a consequence of criticality.

At 70 atm, the behavior of the binodal curves is much more complicated. Figure 5.7a illustrates qualitatively the shape of the T-x section expected on the basis of the measured critical loci. The three binodal regions intersect at a common temperature to give a three-phase L_1-L_2-G tieline. At the high temperature end, the G+L_2 region terminates at a point along the upper critical line. The G+L_1 region, on the other hand, terminates at the CO_2 vapor pressure point (i.e., the boiling point of CO_2 at 70 atm). The L_1+L_2 region extends off the plot to lower temperatures, where it will eventually terminate due to solid formation.

Figure 5.7b gives the P-R prediction for the T-x section at temperatures near the three-phase line. The concentration axis is given on a logarithmic scale to allow the very small G+L_1 region to be visible. Three-phase equilibrium is predicted at 304 K. Although the predicted diagram is qualitatively correct, it is incomplete, because the P-R equation generates metastable and unstable phase equilibrium solutions in addition to the stable solutions which are shown.

Figure 5.8a shows the T-x section when all phase equilibrium solutions from the P-R equation are drawn in. The spinodal curves, which were already given in Figure 5.3g,

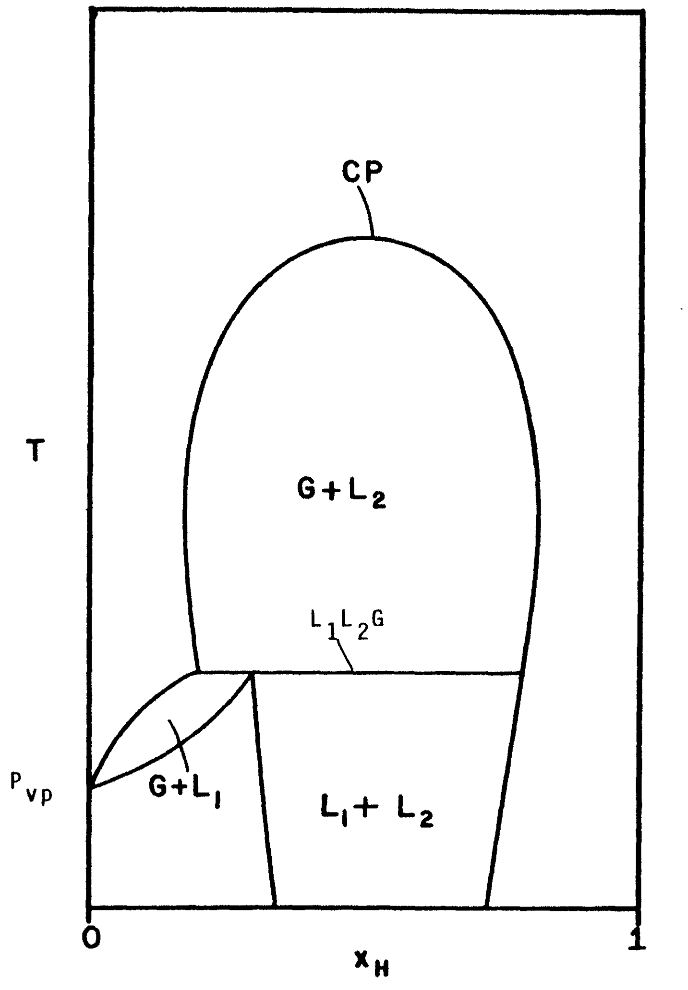

Figure 5.7a. A qualitative T-x section for C_{16} - CO_2 at 70 atm.

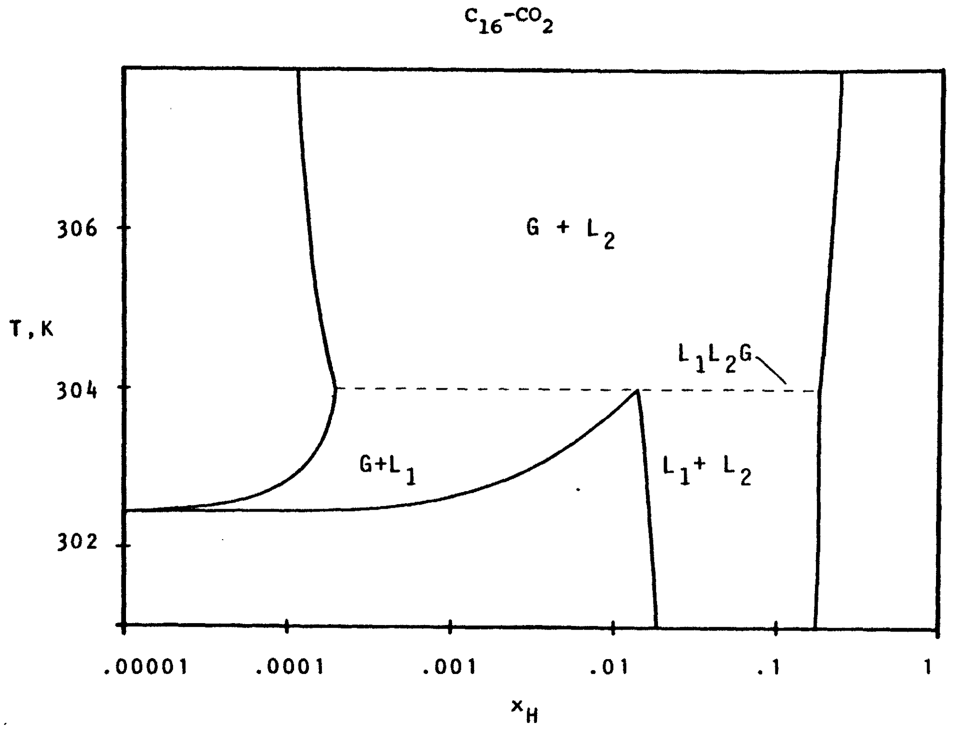

Figure 5.7b. The predicted T-x section in the vicinity of the three phase line.

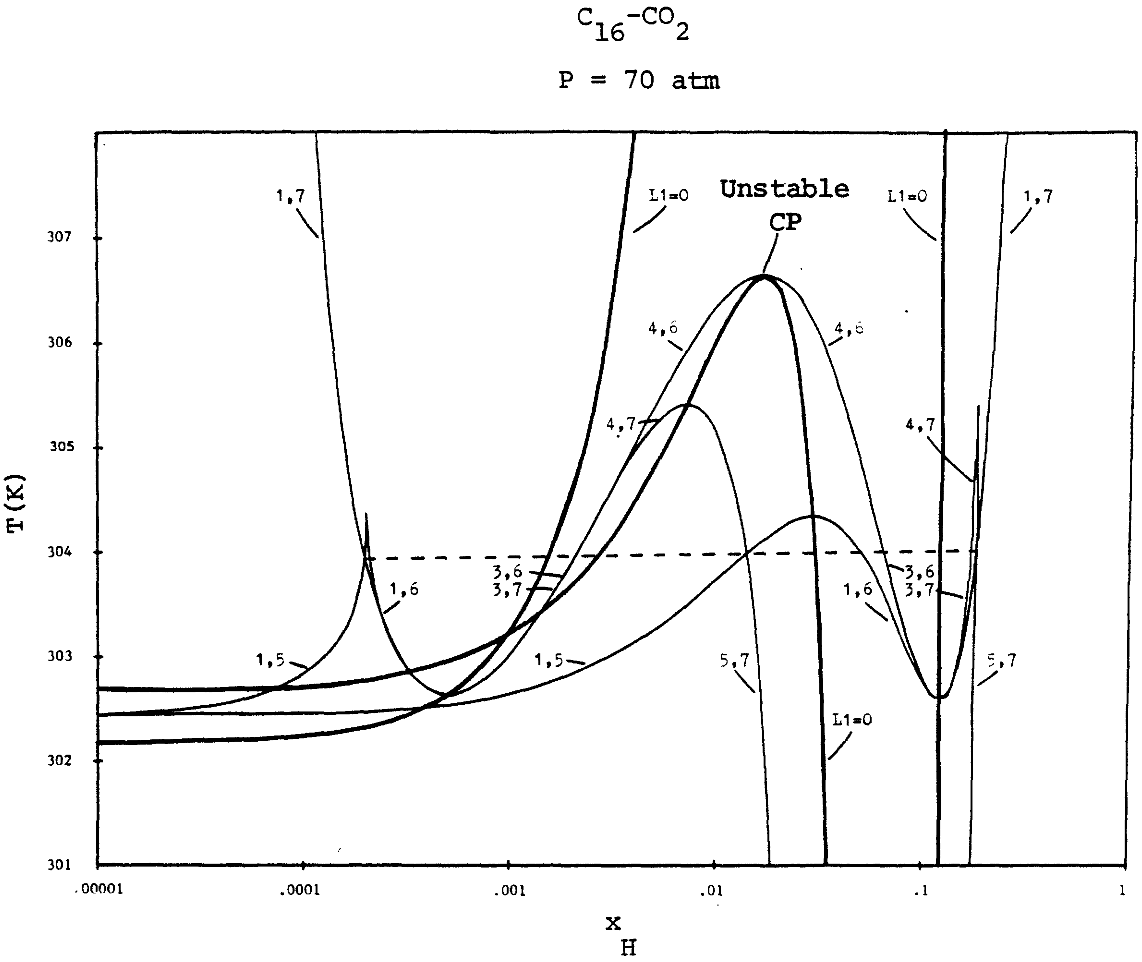

Figure 5.8a. A T-x section at 70 atm showing the continuation of the predicted binodal curves. Each binodal is labelled with a number pair to indicate which segments of the f-x curve the equilibrium is derived from. To determine the compositions of coexisting phases, a tieline is drawn at constant temperature joining binodals labelled with the same number pair. Note that the three phase tieline, given by the dashed line, joins the two curves labelled (1,7), the two curves labelled (1,5), and the two curves labelled (5,7). The spinodal curve (L1=0) is given by the heavy lines.

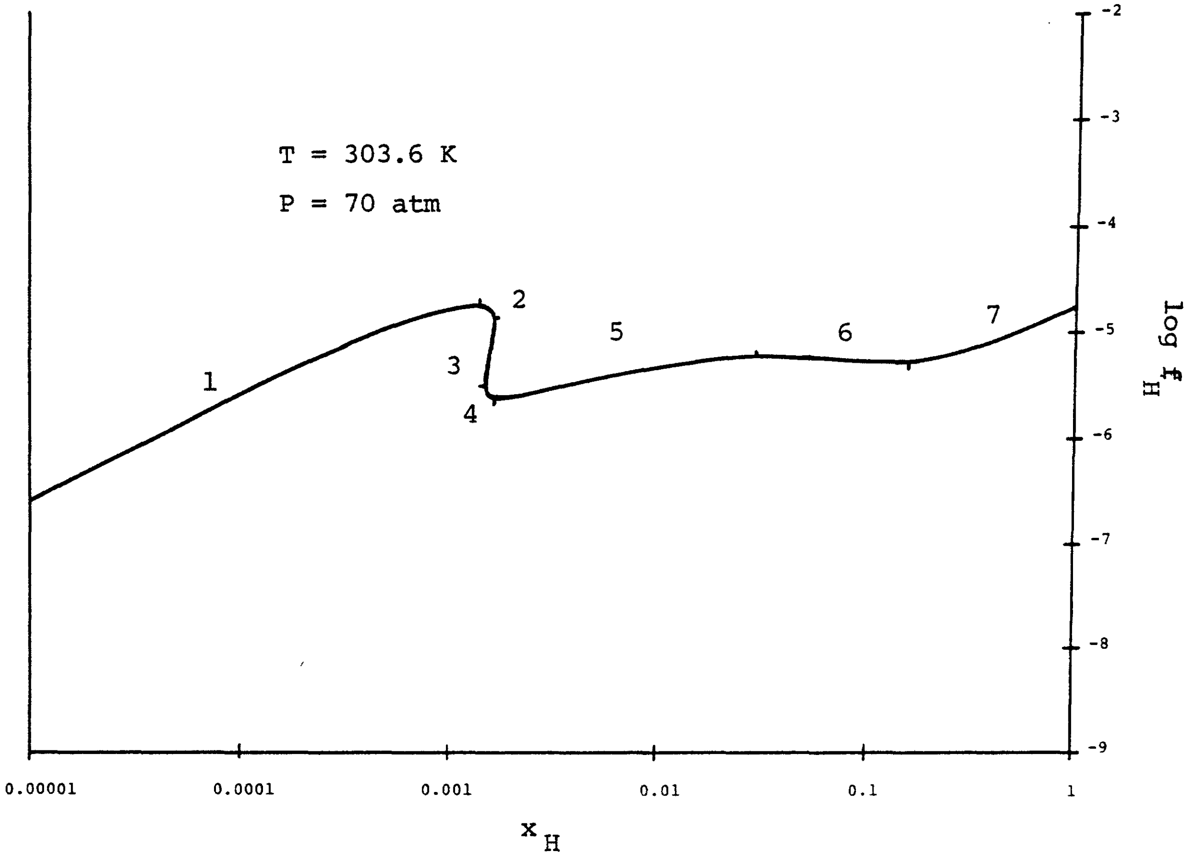

Figure 5.8b. An f-x plot in the three-phase region, showing the numbering of the seven monotonic segments.

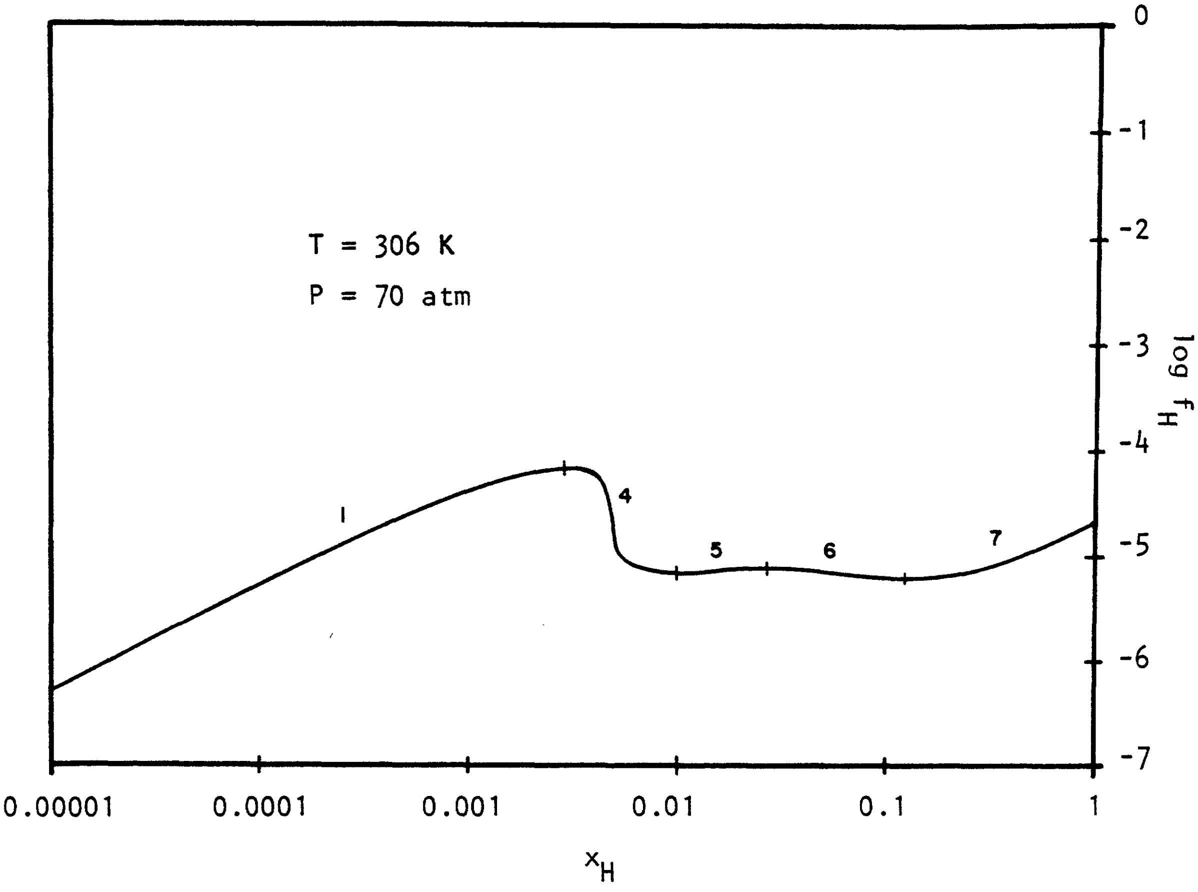

Figure 5.8c. f-x plot. At this temperature, only five monotonic segments are present. Comparison with Figure 5.8b shows that segment 2 (or, alternatively, segment 4) and segment 3 no longer exist.

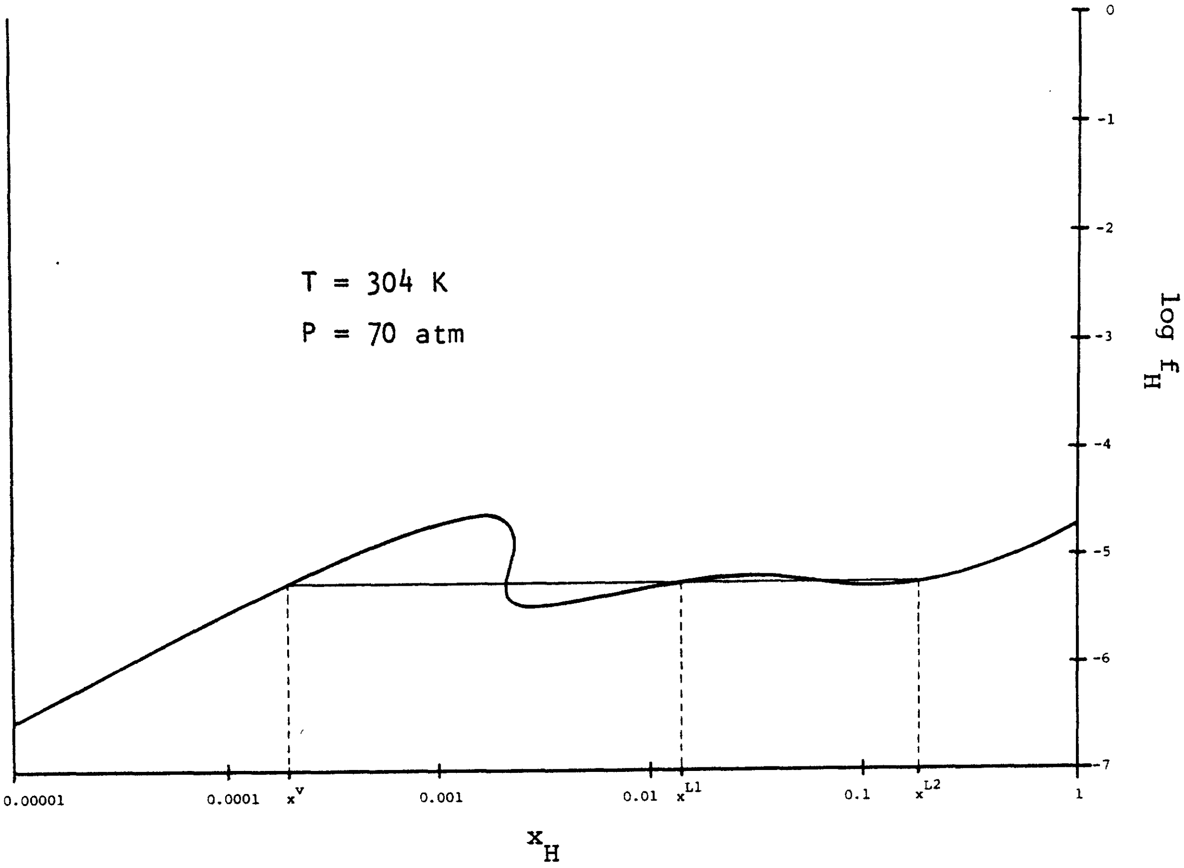

Figure 5.8d. f-x plot at the three-phase temperature. The three-phase tieline is shown connecting the compositions of the coexisting phases in segments 1, 5, and 7. These are denoted as x^V, x^{L1}, and x^{L2}, respectively. Although the tieline crosses segments 3 and 6, these compositions are not in equilibrium. This would be shown by the different partial CO_2 fugacities of these points in an f_{CO_2} - x plot.

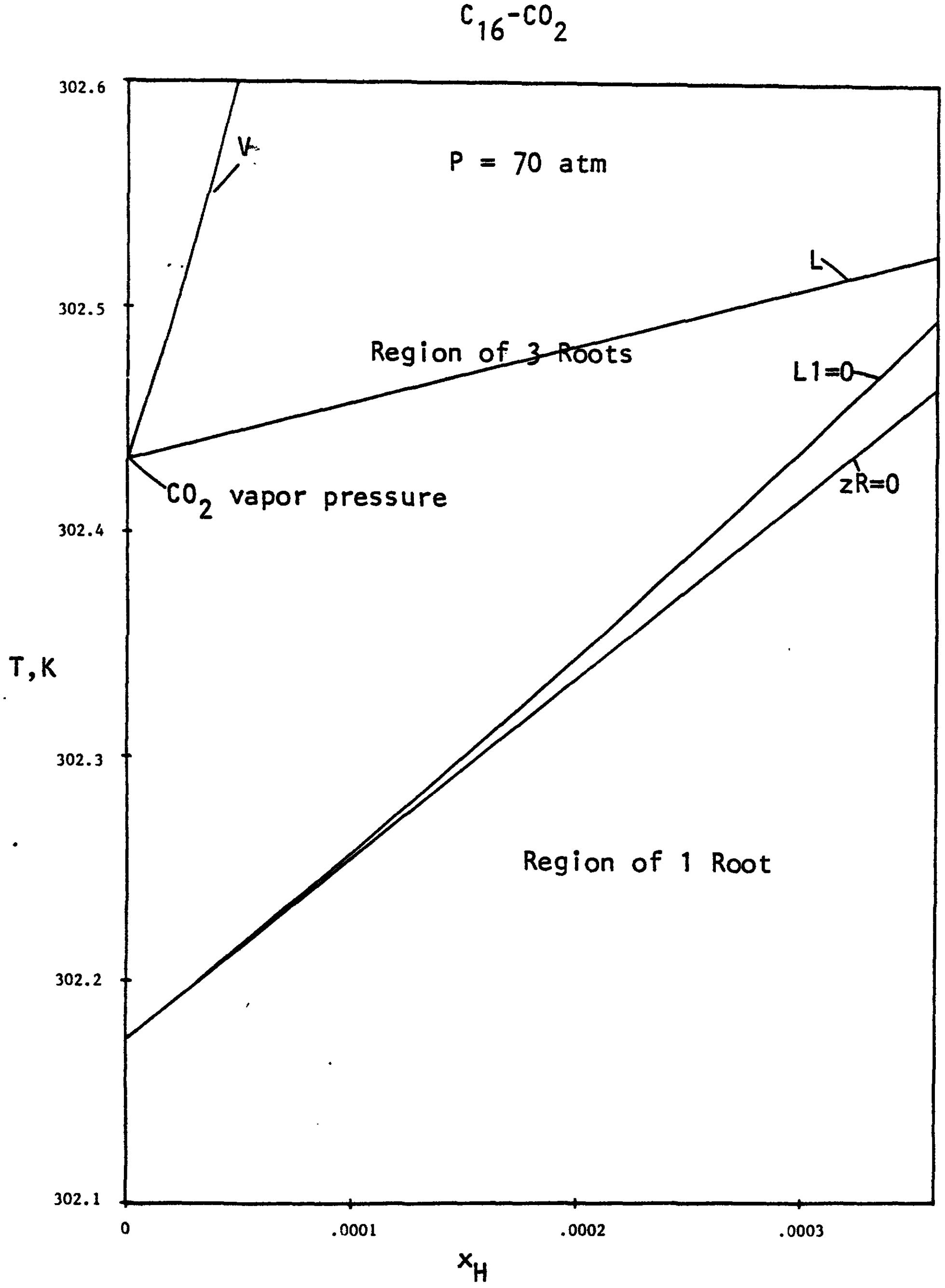

Figure 5.8e. A T-x section at 70 atm in Cartesian coordinates. The VLE region terminates at the CO_2 vapor pressure. The zR=0 line is the boundary between the regions of one and three roots.

are also displayed in the figure. The binodal curves are labelled by number pairs, which refer to the particular monotonic segments of the f-x curve from which the equilibrium arises. Figure 5.8b gives a typical f-x plot for the three-phase region, showing the numbering of the seven segments. Not all of the f-x curves in the three-phase region are comprised of seven segments since some segments may appear or disappear as temperature is varied. It is possible, though, to assign each binodal curve a consistent number pair by following the evolution of a particular segment. This is illustrated by the f-x curve at 306 K in Figure 5.8c. Figure 5.8d shows the f-x plot at the three-phase temperature, 304 K, with the tieline drawn in. The three-phase equlibrium is seen to be between segments 1, 5, and 7. This is also evident from the intersection of the binodal curves (1,7), (1,5), and (5,7) in Figure 5.8a. These binodal curves do not terminate at the three-phase line, but continue beyond it. Upon crossing the three-phase line, however, a Gibbs free energy analysis will show that the binodal represents a metastable equilibrium (see Baker, et al., 1981). Thus, at temperatures below 304 K (the three-phase temperature) the (1,7) binodal is metastable. At its minimum temperature, the metastable (1,7) binodal joins the unstable (3,7) binodal.

There are three separate continuous curves in Figure 5.8a. The first two follow the course (1,7)-(3,7)-(4,7)-

(5,7). Of these two, the one at low x_H crosses the spinodal between (1,7) and (2,7) while the one at high x_H reaches a cusp at the spinodal and turns back. The third curve follows the course (1,5)-(1,6)-(3,6)-(4,6)-(4,6)-(3,6)-(1,6)-(1,5). This curve crosses the spinodal between (1,6) and (3,6) at low x_H, but not at high x_H. The two branches of the (4,6) binodal meet at the unstable critical point. Reference to Figure 5.8c shows that both segments 4 and 6 are materially unstable, in accordance with Figure 3.1. Figure 5.8a also shows that, in tracing the three curves, the occurrence of a cusp is accompanied by the occurrence of a smooth extremum. For example, following the two branches of the VLE binodal (1,5), it is seen that the vapor leg ends in a cusp while the liquid leg ends in a smooth maximum.

A significant portion of the G+L_1 region (see Figure 5.7b) defined by the (1,5) binodal falls within the "apparently unstable" region between two spinodal curves. As previously discussed, the (1,5) binodal is stable in this region. The termination of the (1,5) binodal at the pure CO_2 axis is shown in Figure 5.8e in Cartesian coordinates. The vapor and liquid roots converge at the vaporization temperature of CO_2 at 70 atm, and remain within the region of three roots.

As evidenced by the phase diagrams in Chapter 2, it is more common to define the binodal surfaces in a P-T-x space diagram by P-x sections, rather than by T-x or P-T sections. A sequence of P-x diagrams will now be considered. Figure 5.9a shows the P-x section at 300 K, a temperature below the critical points of both components. Thus, the very narrow $G+L_1$ region terminates at the vapor pressure of CO_2 along the pure CO_2 axis. Likewise, the $G+L_2$ region terminates at C_{16}'s vapor pressure along the pure C_{16} axis. At low pressures, the gaseous branch of the $G+L_2$ binodal has a very low concentration of hexadecane, and does not appear on the plot. The L_1+L_2 region extends to very high pressures without reaching a critical point, in agreement with Figure 5.1. The three binodal regions all intersect simultaneously to give a three-phase L_1-L_2-G line at about 64 atm. The pressure and temperature of this three-phase equilibrium are seen to be on the L_1-L_2-G line in Figure 5.5. As in the P-x section at 70 atm, metastable and unstable binodals connect the stable binodals shown in Figure 5.9a, and these may be seen in the enlargement of Figure 5.9b. The $G+L_1$ and $G+L_2$ binodals are both part of the same continuous curve, while the L_1+L_2 binodal is separate, terminating at low pressure at an unstable critical point.

Figure 5.10a gives the P-x section at 305 K, a temperature above the critical point of CO_2. The $G+L_1$ region has now detached from the pure CO_2 axis, a fact which is more evident in the enlargement, Figure 5.10b. The inclusion of the metastable and unstable phase equilibrium

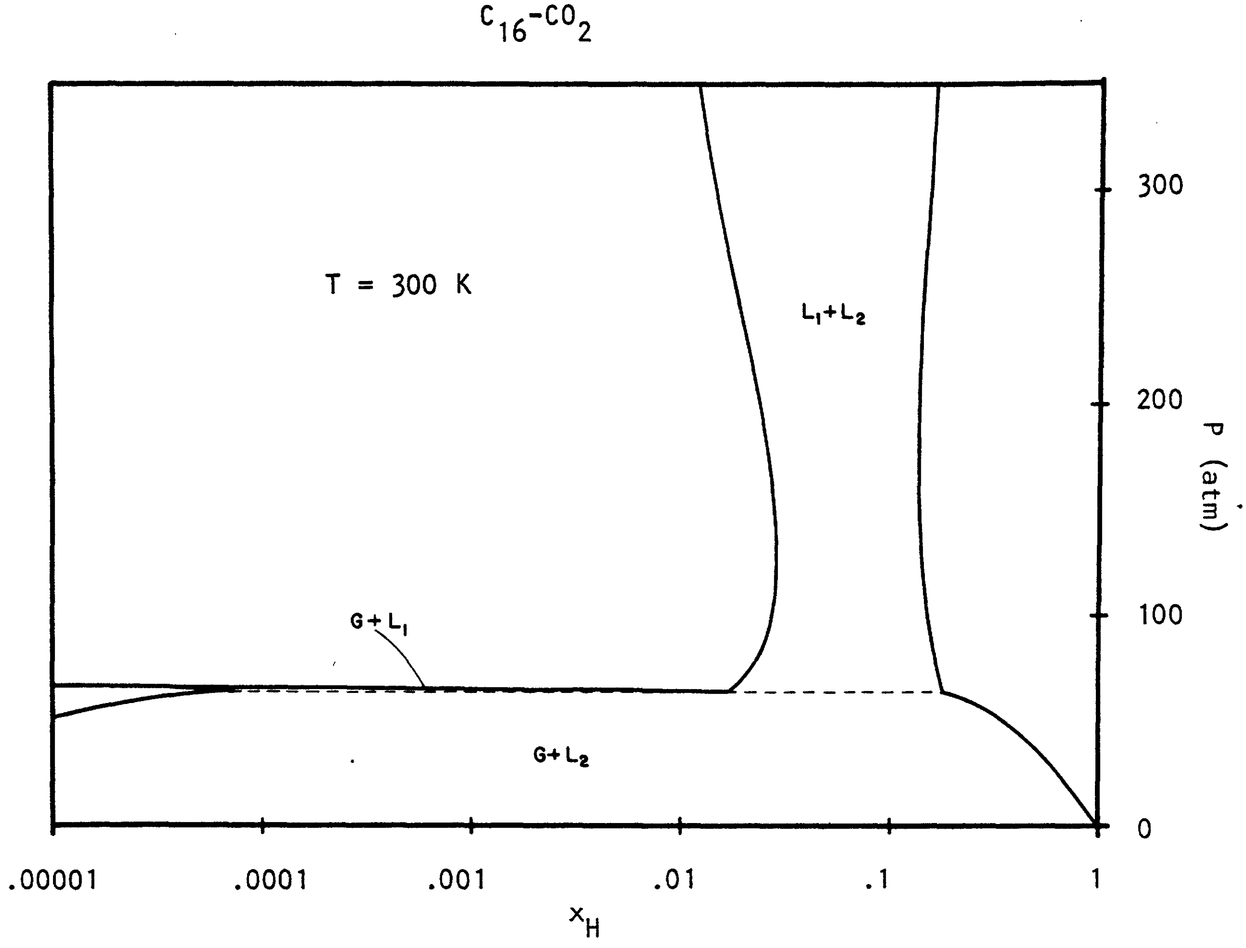

Figure 5.9a. The P-x section below CO_2's critical point.

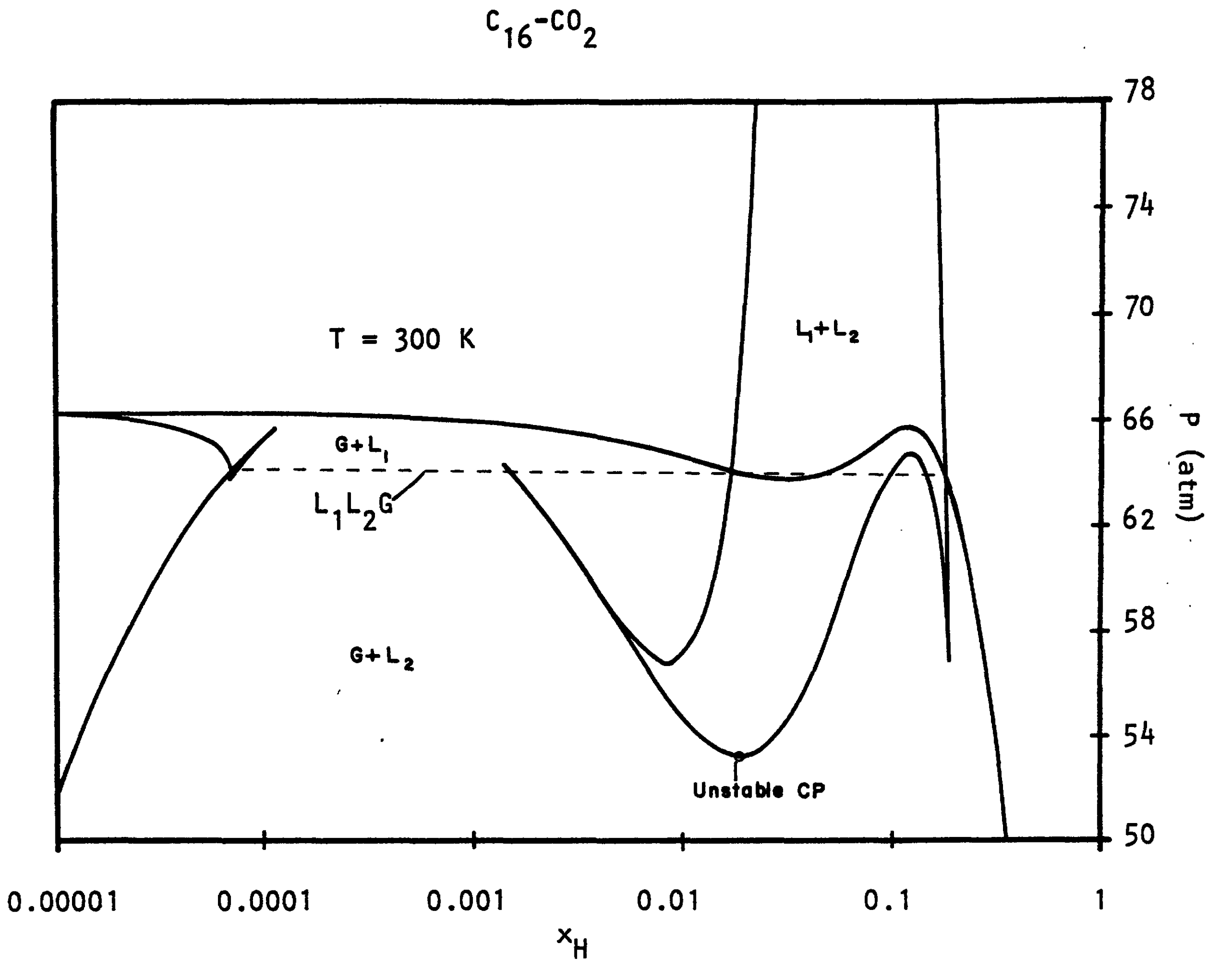

Figure 5.9b. The P-x section at 300 K in the region of the three-phase line (dashed) showing all metastable and unstable binodals. The stable regions in this graph are essentially what would result if the T-x section at 70 atm (Figure 5.8a) were flipped over. In the present case, however, the L_1+ L_2 binodal is a separate curve, rather than the L_1+ G binodal.

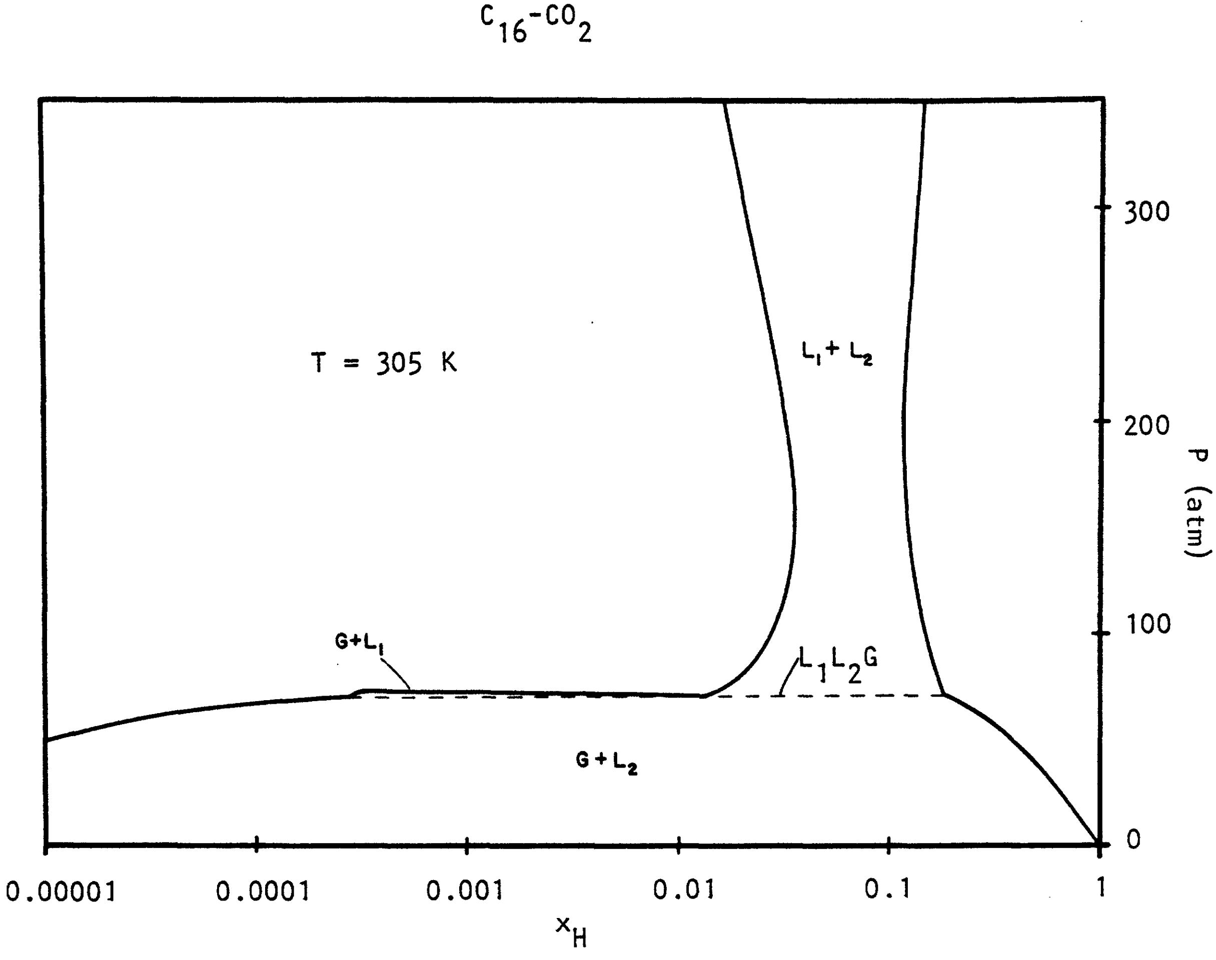

Figure 5.10a. The P-x section between CO_2's critical point and the LCEP.

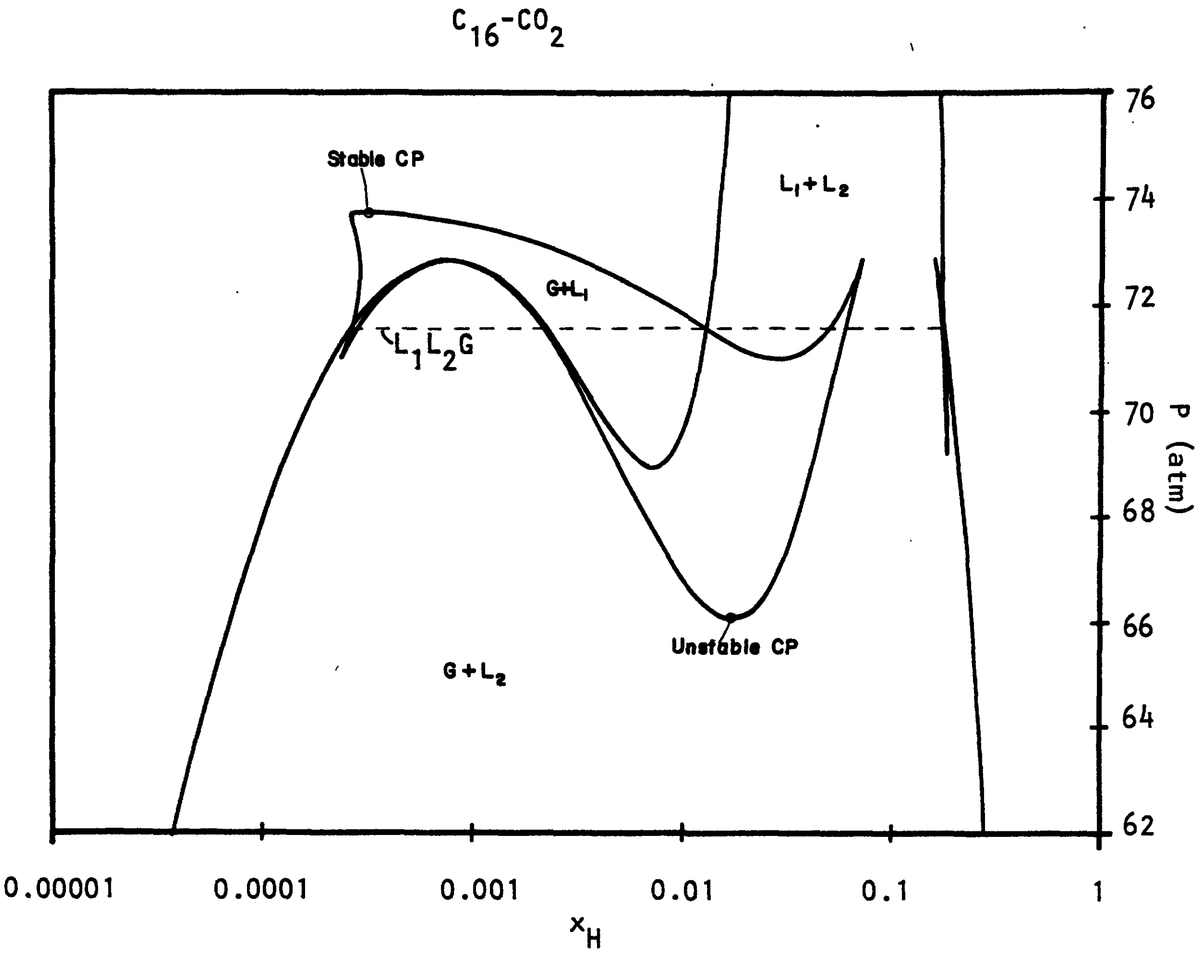

Figure 5.10b. The P-x section at 305 K in the region of the three-phase line. The G + L_1 binodal is now a separate curve, exhibiting both a stable and an unstable critical point.

solutions shows that the $G+L_1$ binodal is now a separate curve. This binodal exhibits both a stable and an unstable critical point, in accordance with Figure 5.5.

With reference to Figure 5.5, the presence of a metastable critical line between the LCEP and the cusp is noted. The meaning of this metastability is clarified upon generating a P-x section at a temperature in this range. This is done in Figure 5.11, at 311 K. Figure 5.11a shows the large scale P-x section, including stable binodal curves, spinodal curves, and the region of three roots. At about 80 atm, the binodal curve at low x_H displays a nearly horizontal segment. This might be regarded as the influence of the lower critical end point, which occurs a few tenths of a degree below 311 K. At the LCEP, the binodal curve exhibits a horizontal point of inflection. Enlarging this region, the diagram of Figure 5.11b results. With the three-phase line no longer present, the $G+L_2$ and L_1+L_2 regions are not clearly distinguishable. These regions have thus collectively been labelled the $F+L_2$ region. As at 305 K, the $G+L_1$ binodal exhibits both a stable and an unstable critical point. Now, however, the entire curve lies within the $F+L_2$ region. Under these conditions, the stable (1,3) segments represent a metastable equilibrium. At the LCEP, the (1,3) critical point would be in a state of incipient metastability, and would just touch the $F+L_2$ binodal at its horizontal inflection point. At 311 K, the

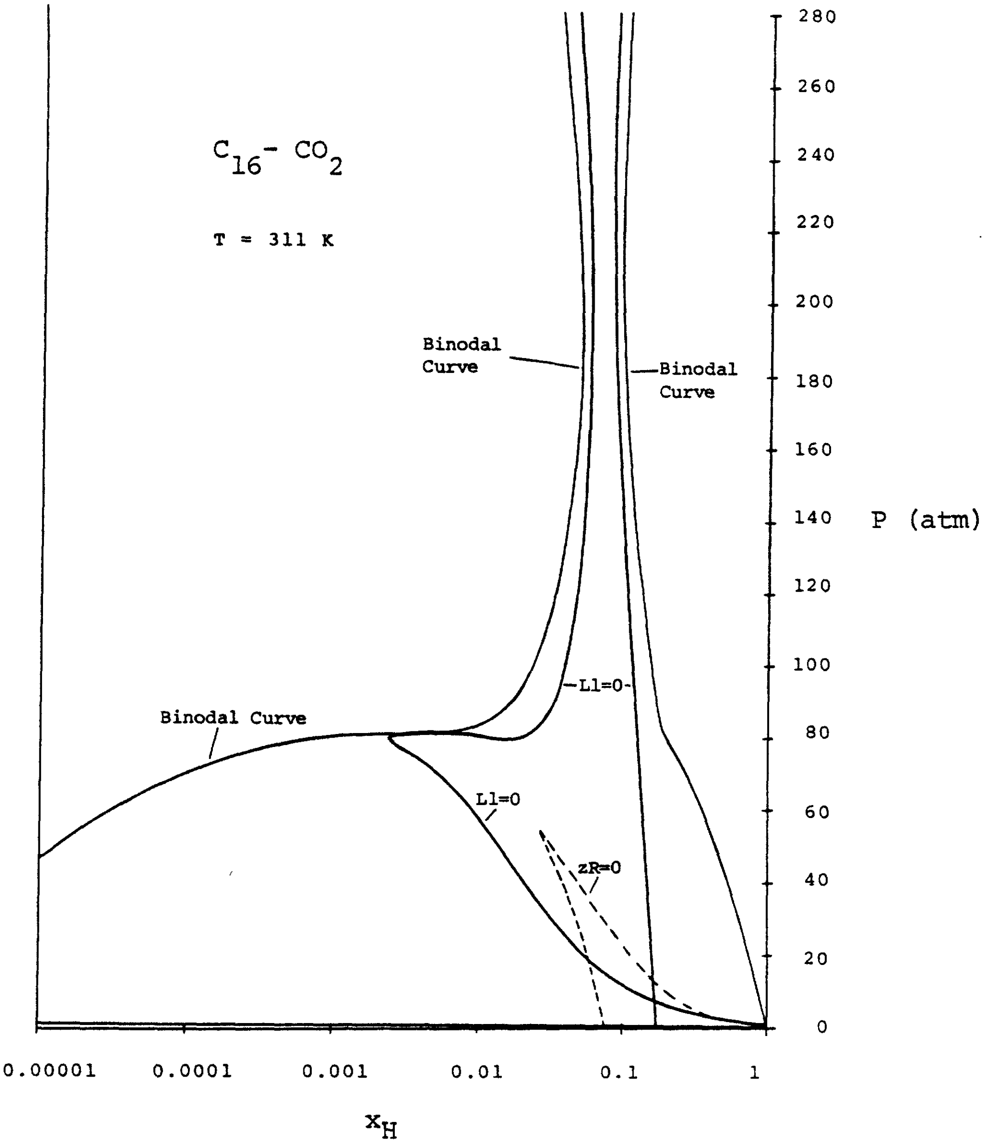

Figure 5.11a. The P-x section at 311 K. The spinodal curve does not actually intersect the binodal curve at 80 atm, although it appears so at the scale of this drawing.

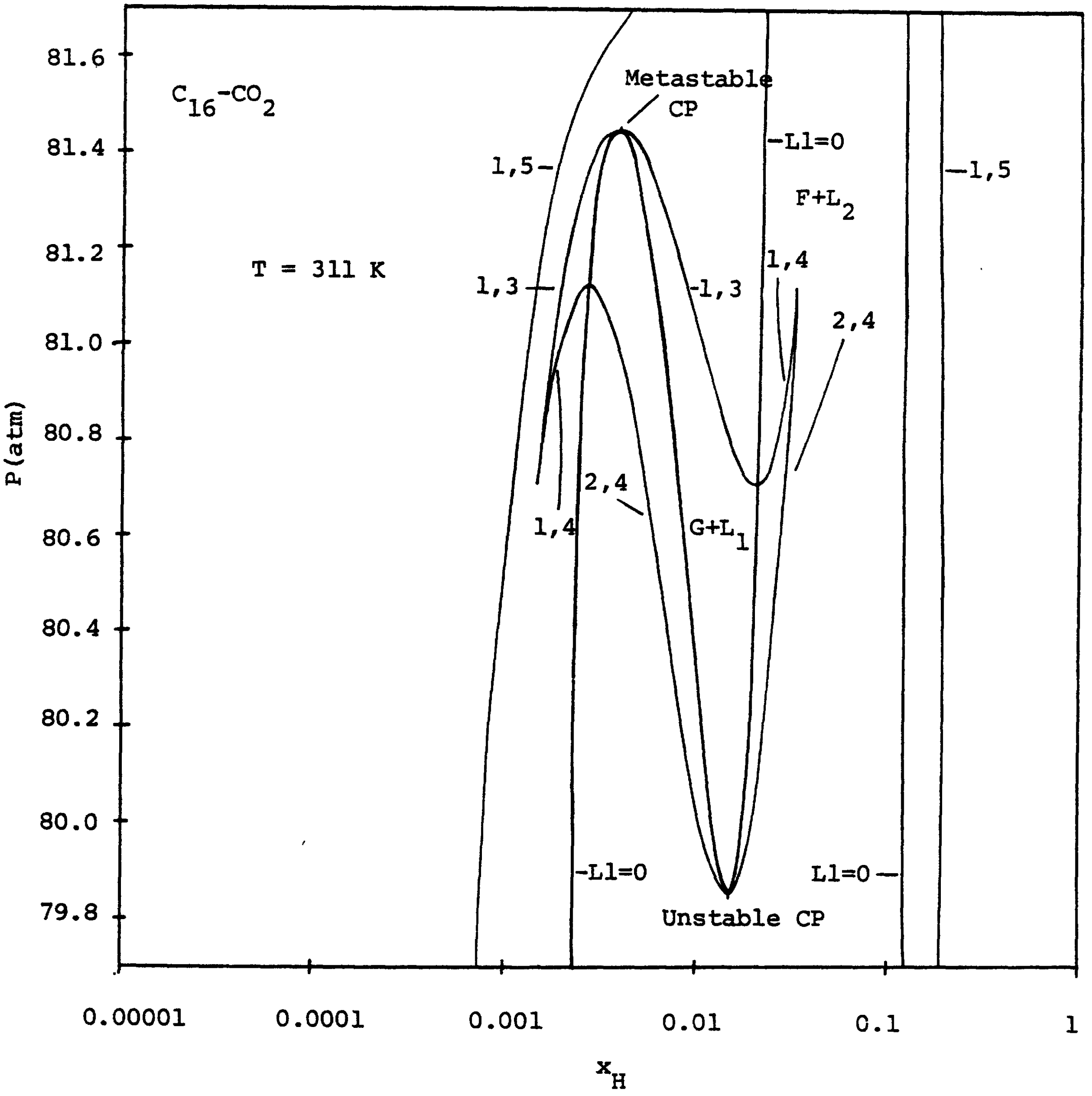

Figure 5.11b. The P-x section at 311 K in the vicinity of 80 atm. The metastable G+L_1 region lies entirely within the F+L_2 region. This diagram shows that the spinodal curve does not intersect the F+L_2 binodal curve.

$G+L_1$ critical points lie much closer together than they did at 305 K. This circumstance is also indicated in Figure 5.5. It is now evident that the cusp in that figure forms as the $G+L_1$ region shrinks to a point where the metastable and unstable critical points coincide.

Figure 5.12 shows the P-x section predicted at 313.5 K. The necked shape of Figures 5.9 through 5.11 has given way to a splitting of the $F+L_2$ region. The high pressure coexistence region may be unambiguously labelled as one of L_1+L_2 equilibrium. The occurrence of the split is necessitated by the temperature minimum in the upper critical line, as shown in Figure 5.1. The existence of a temperature minimum has been experimentally confirmed.

Increasing temperature to 400 K, the P-x section of Figure 5.13 is found. The VLE region no longer extends to very low hexadecane concentrations, and is beginning to look more like a normal VLE envelope in a completely miscible system. This trend continues through Figures 5.14 to 5.16, at temperatures of 463.1 K, 542.9 K, and 623.1 K. At these temperatures, some low pressure phase composition data is available and is included in the diagrams. On the basis of the concentration of the lean component, the liquid phase predictions are within fifteen percent and the vapor phase predictions are within twenty-five percent of the measured values. This agreement is considered quite good in view of

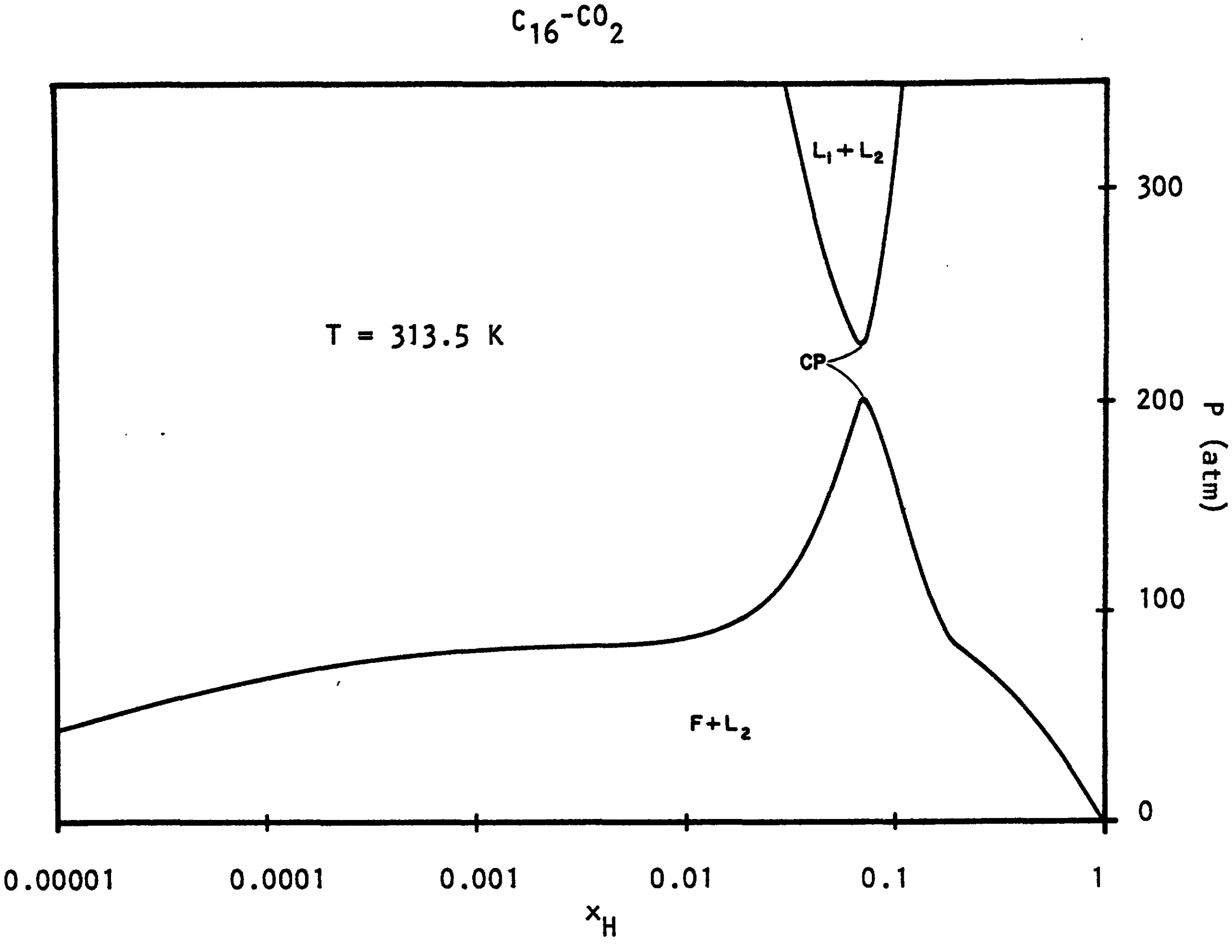

Figure 5.12. The P-x section at 313.5 K. Two separate regions of fluid-fluid equilibrium exist.

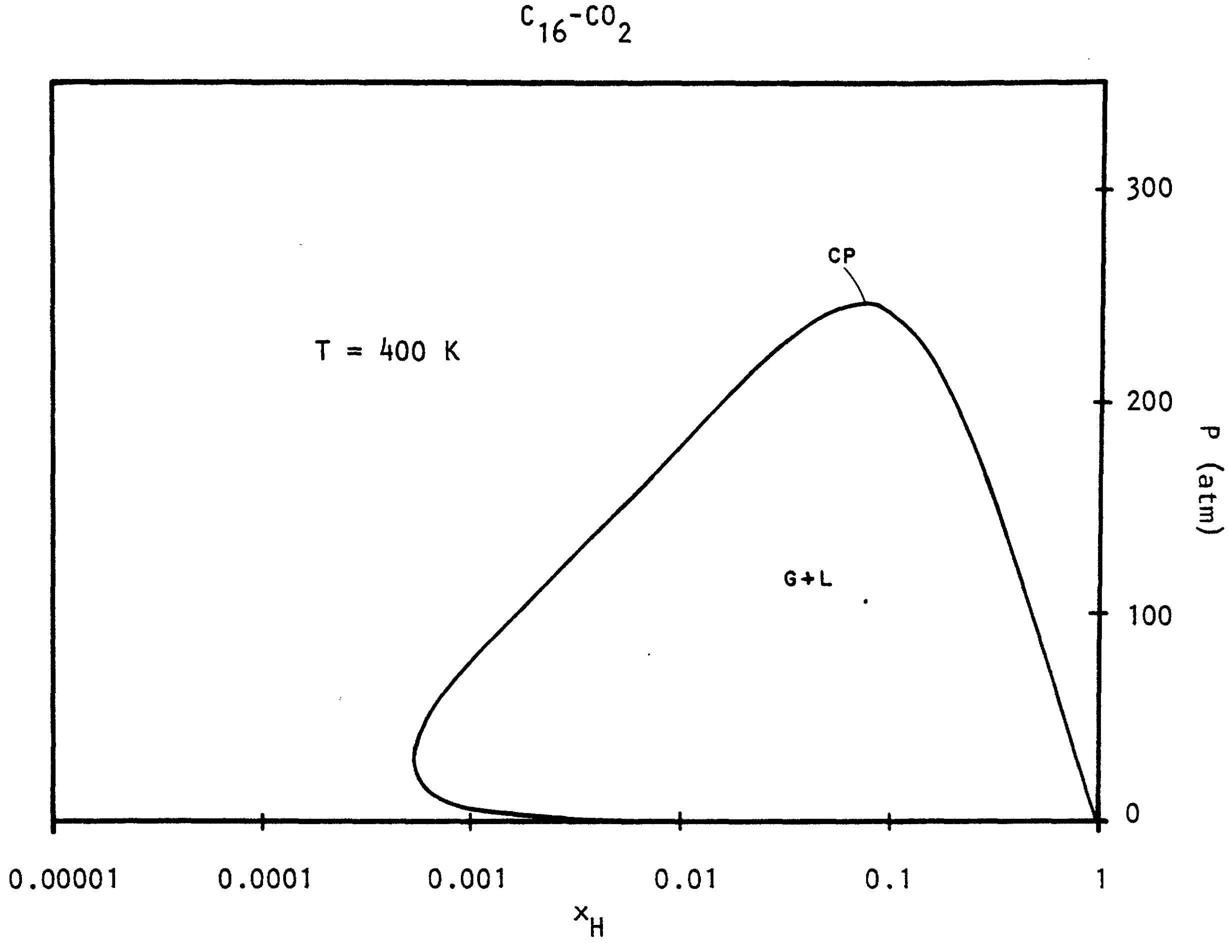

Figure 5.13. The P-x section at 400 K.

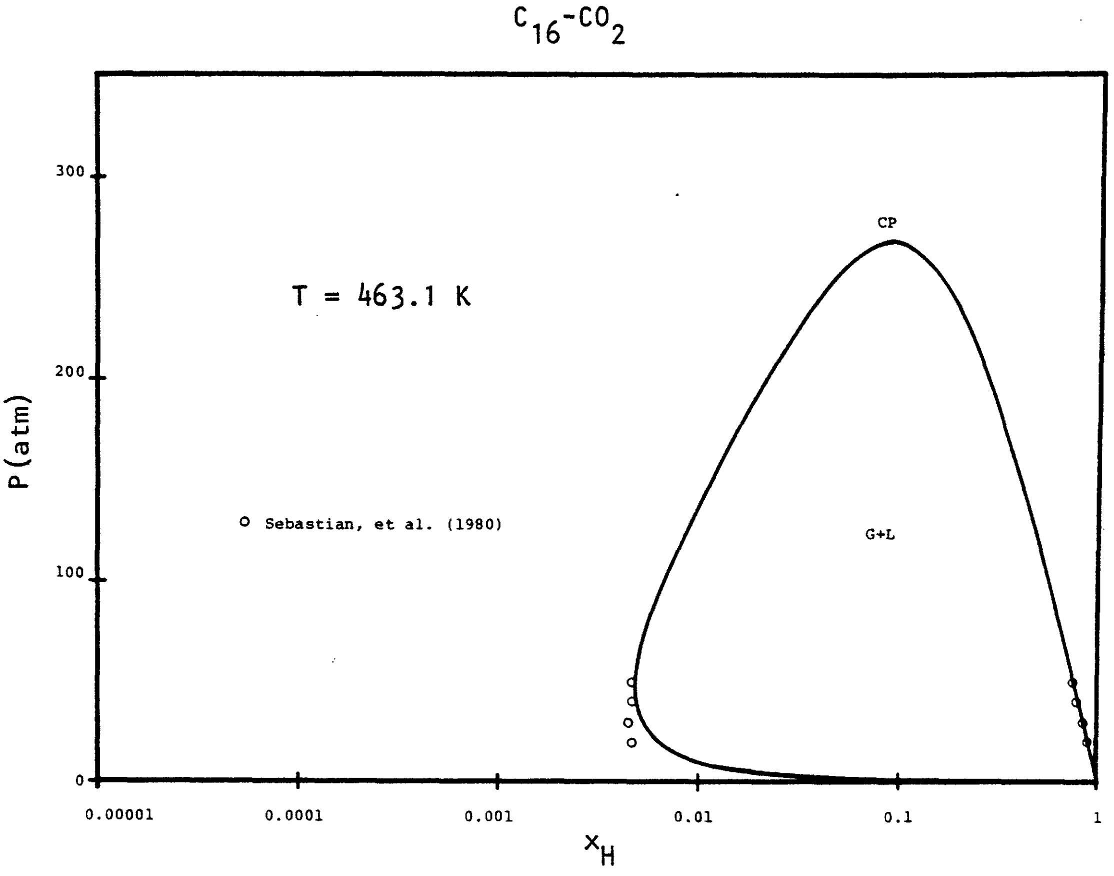

Figure 5.14. The P-x section at 463.1 K.

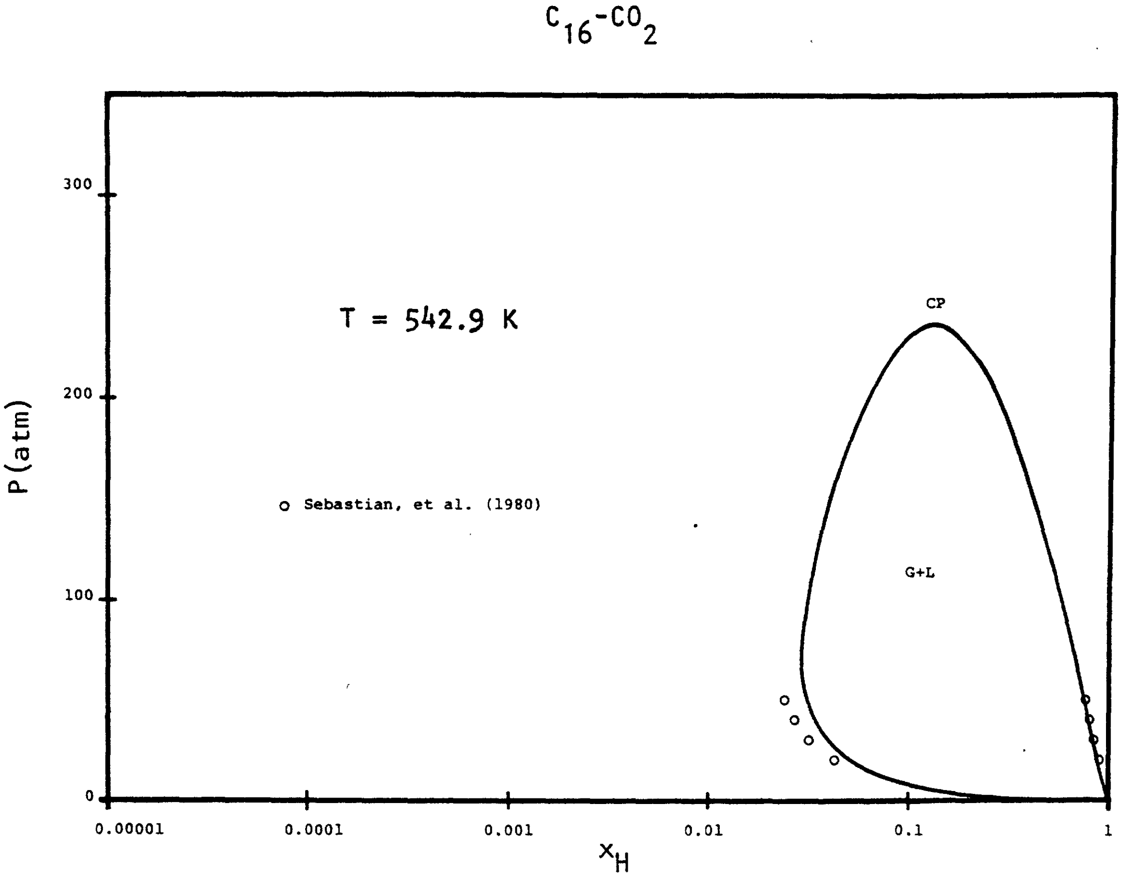

Figure 5.15. The P-x section at 542.9 K.

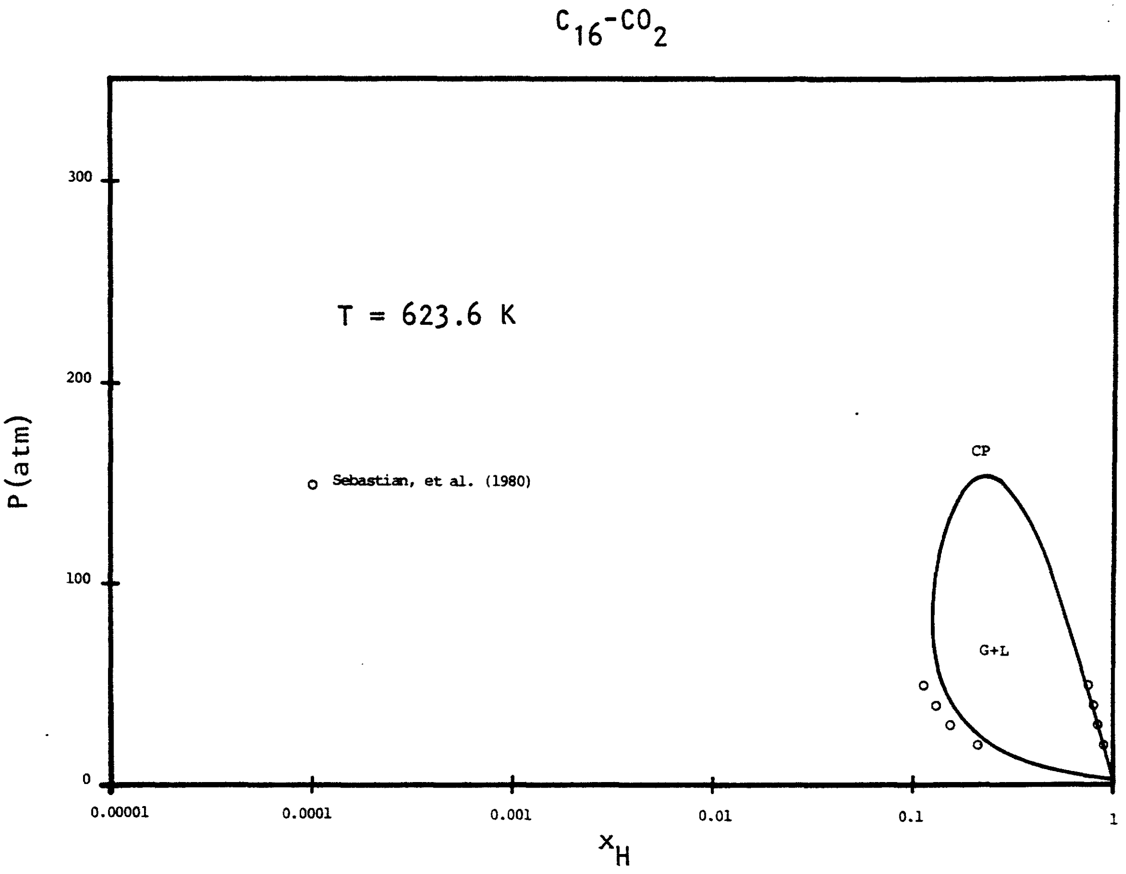

Figure 5.16. The P-x section at 623.6 K.

the fact that no compositional data was used in the determination of the interaction parameter.

Figure 5.17a gives the P-x section at 650 K, and includes the L1=0 and M1=0 curves. The behavior of these curves is quite simple, except at pressures below about 15 atm. Figure 5.17b gives an enlargement of this low pressure region. The shaded area corresponds to the region of three roots. Within this region, two false critical points of the type encountered in Figure 5.3g are found. A consideration of the f-x curves helps clarify the meaning of the various lines in Figure 5.17b. Figure 5.17c shows the Cartesian f-x plot at 9 atm. Referring to Figure 5.17b, if a line of increasing x_H is followed at 9 atm, a region of three roots is entered at the zR=0 line. This composition is the composition of the second infinity point in Figure 5.17c. Shortly thereafter, an L1=0 line is crossed, which corresponds to f_{min} in Figure 5.17c. At a C_{16} mole fraction of about 0.95, a second spinodal point is encountered (f_{max} in 5.17c), and at slightly higher concentrations the equations revert to one root (first infinity point in 5.17c).

Following a constant pressure line at 7 atm, the three root region is entered at a point corresponding to the infinity point in Figure 5.17d. Only one spinodal point (f_{min} in 5.17d) is encountered as x_H is increased at this

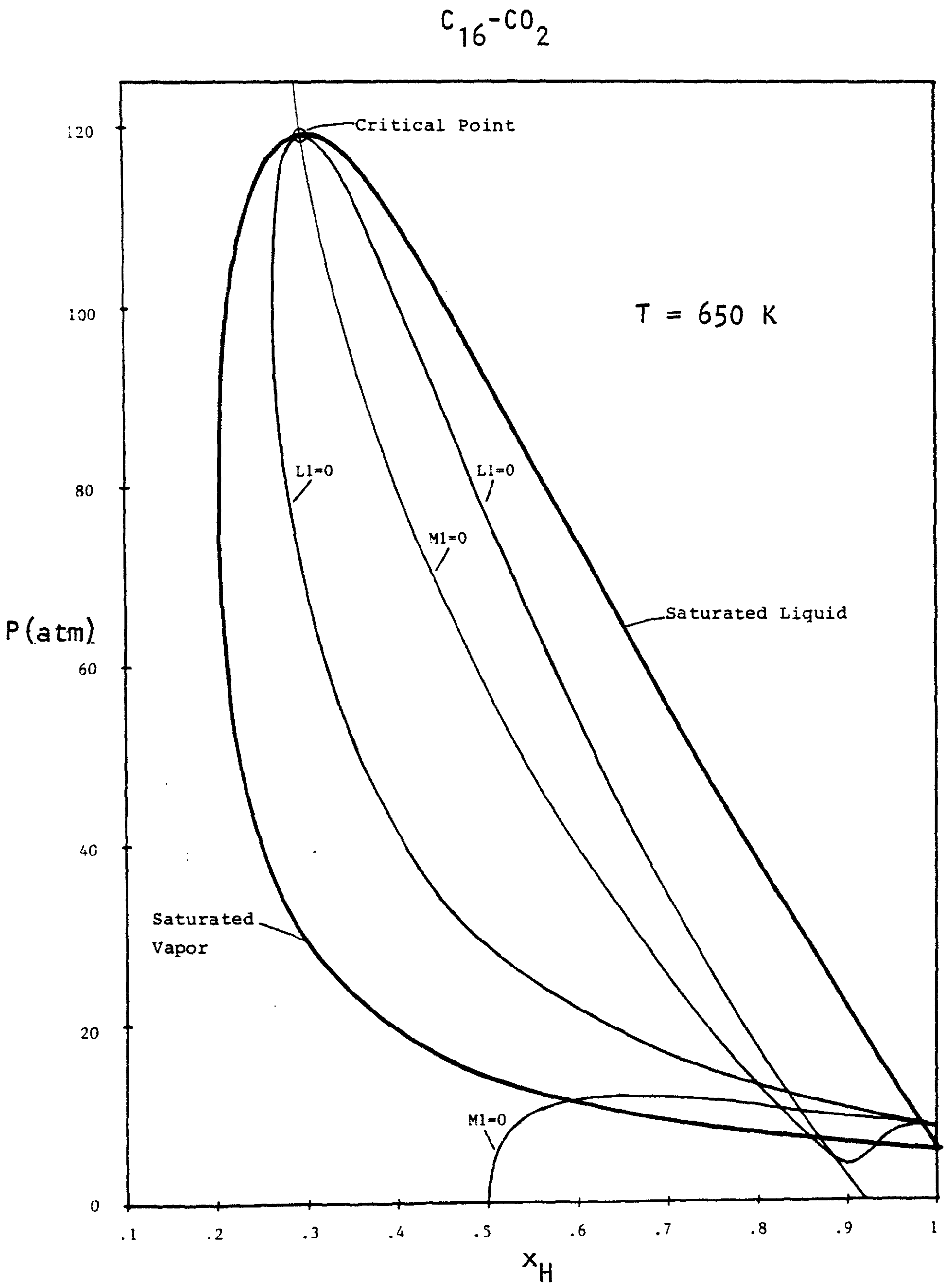

Figure 5.17a. The P-x section at 650 K.

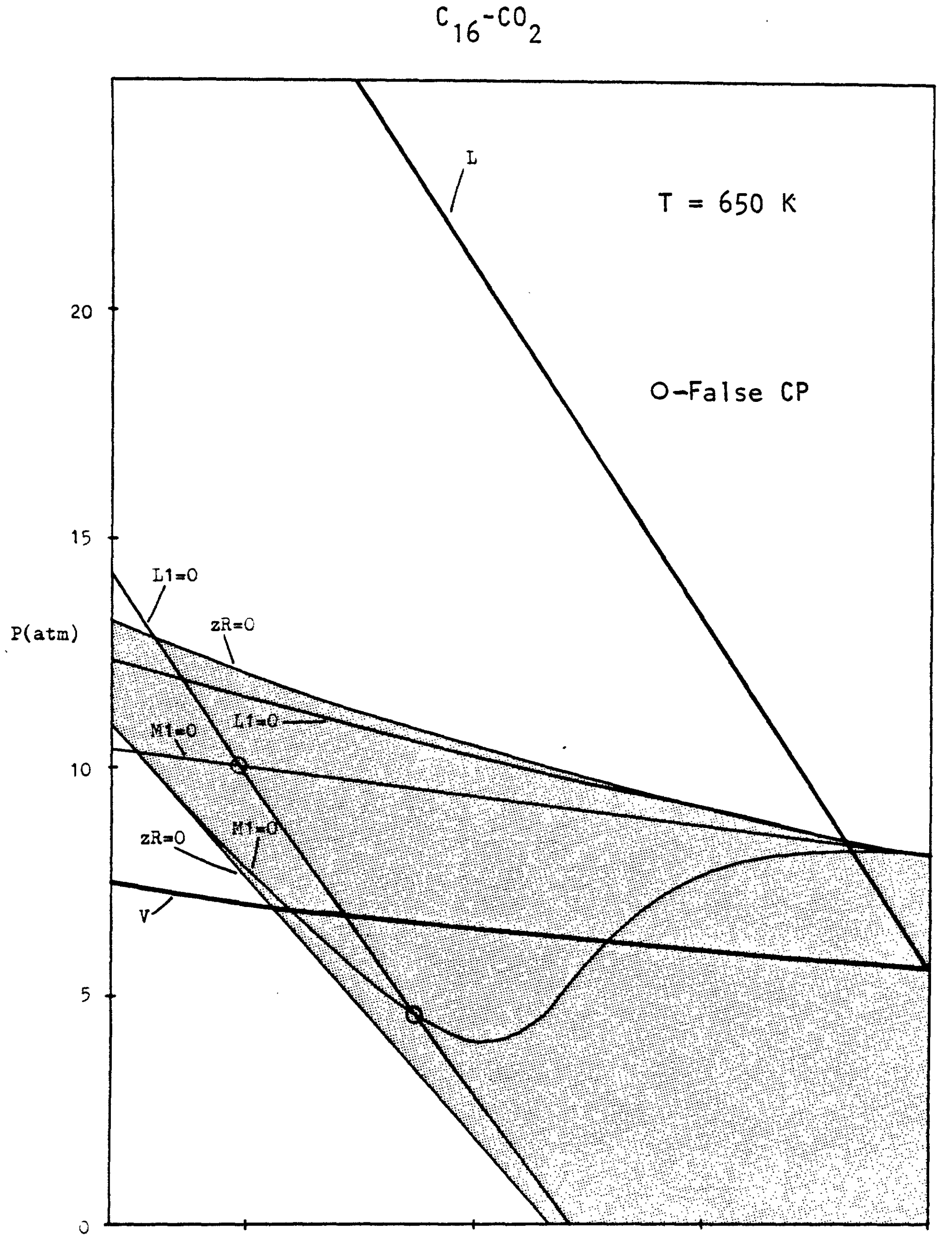

Figure 5.17b. The low pressure P-x section at 650 K. The region of three roots, shown shaded, is bounded by the two zR=0 curves. Within this region, two false critical points are found.

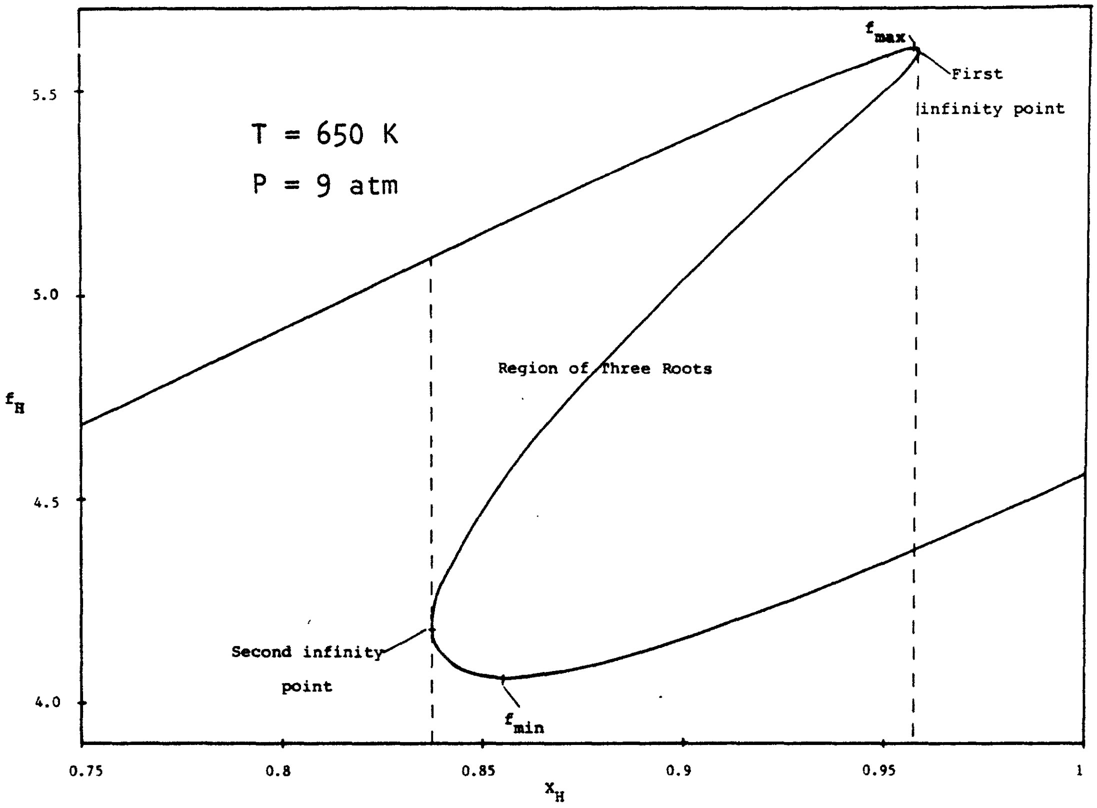

Figure 5.17c. The f-x plot for Figure 5.17b at 9 atm. The region of three roots is bounded at either end by a slope infinity. Two spinodal points, f_{min} and f_{max}, are present.

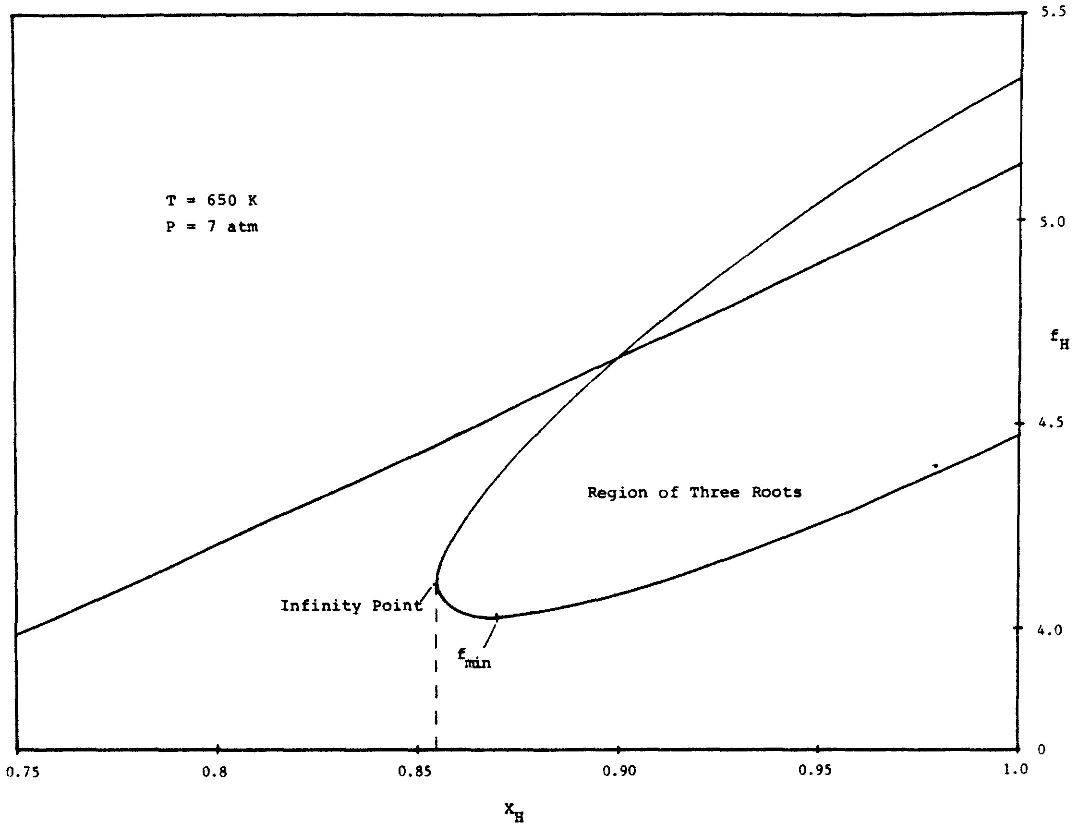

Figure 5.17d. The f-x plot for Figure 5.17b at 7 atm. The region of three roots extends to the pure hexadecane axis. Only one spinodal point is present.

pressure, however, since the region of three roots extends to the pure C_{16} axis.

A final P-x section, at 663.8 K, is given in Figure 5.18. Low pressure data is available, and the accuracy of the predictions is comparable to that at the lower temperatures.

This chapter has shown that the P-R equation with a constant interaction parameter yields an excellent qualitative picture of the overall phase behavior of the n-hexadecane - carbon dioxide system. In some regions, semiquantitative accuracy may be obtained. Of the four binary systems treated in this thesis, the C_{16} - CO_2 system has the simplest phase behavior. Nevertheless, it illustrates many of the characteristics of the more complex diagrams which will be studied. One of these characteristics is the critical end point phenomenon. Analysis of the P-x diagrams has shown that such a point may be located using the criterion of a horizontal inflection point. It has also been indicated that a solution of the two-phase equilibrium problem is sufficient for the determination of three-phase equilibrium, since the binodal curves mutually intersect at the three-phase conditions. Furthermore, the stable binodal curves are interconnected by metastable and unstable binodal curves.

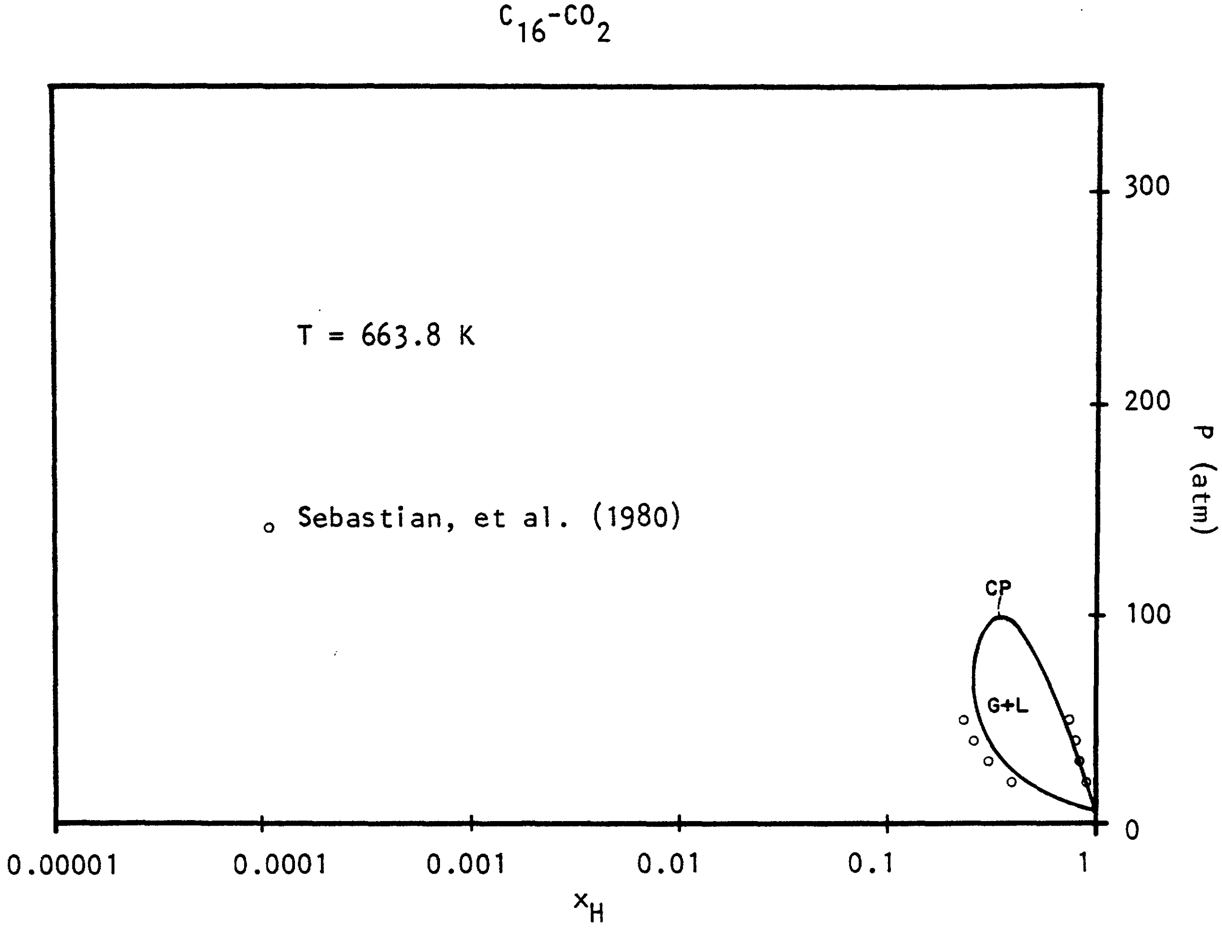

Figure 5.18. The P-x section at 663.8 K.

Chapter 6 The Naphthalene-Carbon Dioxide System

6.1 Qualitative predictions

The naphthalene (N) - carbon dioxide system adds the complication of pure solid formation to the P-T-x space diagram. The physical constants of these two substances are given in Table 6.1. The melting point of naphthalene is nearly 50 K higher than the critical temperature of CO_2, a circumstance which, as pointed out in Chapter 2, often leads to the interruption of the critical lines by three-phase S-L-G lines.

The predictions in this section are carried out using an interaction parameter of δ_{12}=0.11. This value was selected on the basis of data available in the supercritical fluid region, as will be discussed more thoroughly when quantitative predictions are considered. With this interaction parameter, it is possible to generate a fluid phase P-T-x space, as was done in the last chapter with n-hexadecane and carbon dioxide. More specifically, the Peng-Robinson equation represents only the gaseous and liquid phases, and does not indicate the possibility of solid formation. Introduction of solid-fluid equilibria to the P-T-x space requires the use of an equation describing the

Table 6.1

Physical Constants of Naphthalene and Carbon Dioxide

	$C_{10}H_8$	CO_2
T_c(K)	748.4	304.2
P_c(atm)	40.0	72.8
ω(acentric factor)	0.302	0.225
Melting Point (K)	353.3	-

fugacity of the pure solid phase. This relation was developed for naphthalene in Chapter 4. The solid-fluid equilibria may be simply determined by matching the pure solid naphthalene fugacity with the partial fugacity of naphthalene in the fluid phase.

As with C_{16} - CO_2, the first features of interest in the $C_{10}H_8$ - CO_2 P-T-x diagram are the critical loci. These involve only fluid phases, and are thus generated from the equation of state alone. To reiterate, the equation of state has no means of defining under what conditions a solid phase will form, and so predicts fluid phase P-T-x relations as it would for any other all-fluid system. As the critical parameters for $C_{10}H_8$ are not too far removed from those of n-hexadecane (C_{16}), it is not surprising that the phase diagrams have similar attributes. A T-x section at 75 atm for $C_{10}H_8$ - CO_2 is given in Figure 6.1, which is to be compared with Figure 5.3e. Again note the prediction of one unstable and two stable critical points. The high temperature critical point for the $C_{10}H_8$ system occurs at almost twice the solute concentration of the corresponding C_{16} critical point. This is mainly due to the difference in reduced pressure for the two systems - P_r(= P/P_c) for C_{16} is about 5, while P_r for the $C_{10}H_8$ is less than 2. For naphthalene - CO_2, the critical line is still fairly close to its origin at the pure naphthalene critical point. It is also seen in the figure that the M1 = 0 curve has two

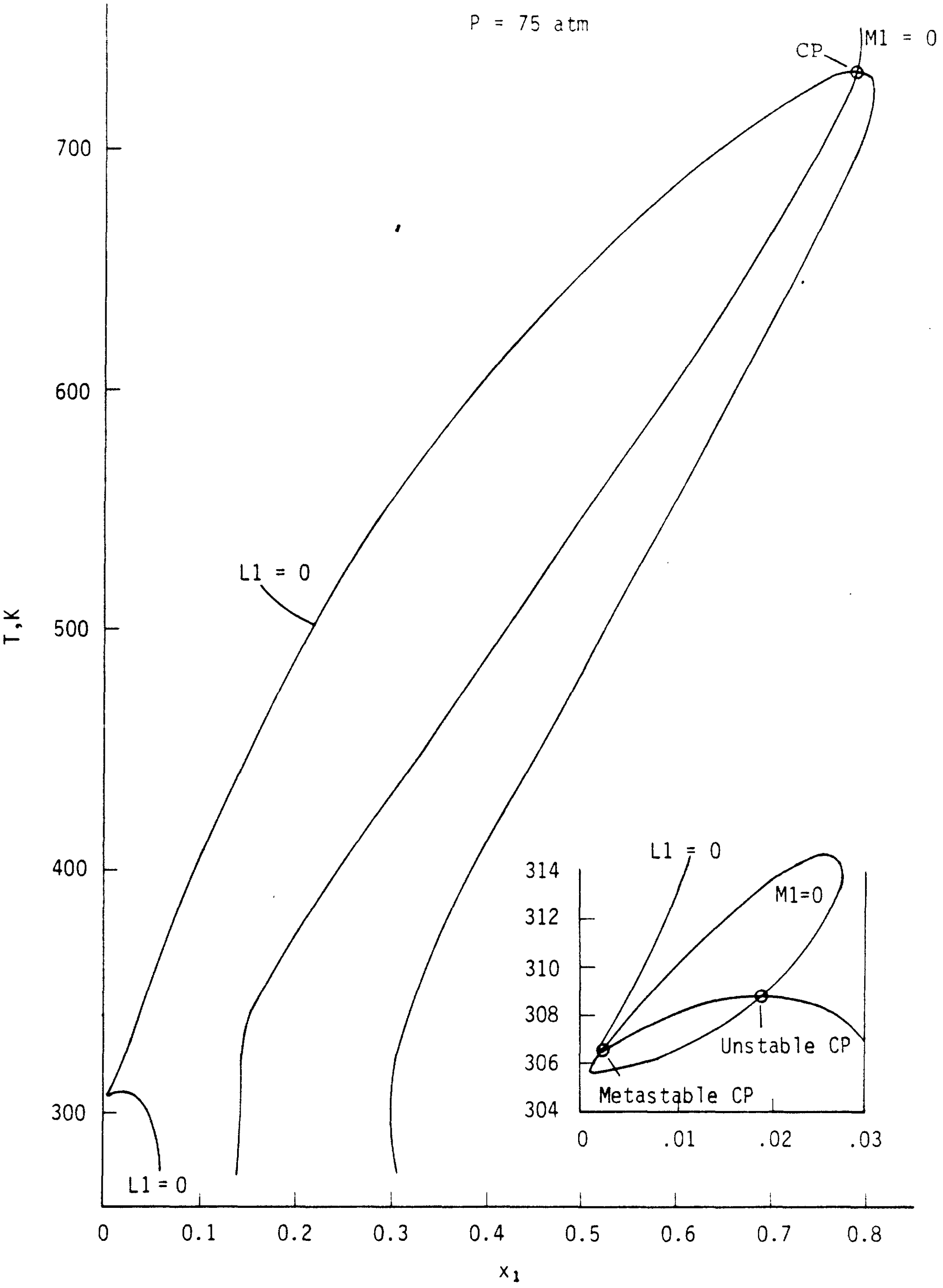

Figure 6.1. The T-x section at 75 atm showing the L1=0 and M1=0 curves. Three critical points are predicted.

separate branches, one of these being the closed loop shown in the inset. This behavior was not found in the T-x sections for C_{16} - CO_2.

Upon predicting critical points for a number of different temperatures and pressures, the P-T projection of the points may be constructed as in Figure 6.2a. As with the hexadecane - CO_2 system, there are two separate critical lines, each beginning at a pure component critical point. The hexadecane - CO_2 system, however, had only one critical end point, where liquid and vapor phases became identical in the presence of a third, liquid phase. There are now two critical end points, where the liquid-vapor or liquid-fluid critical phenomenon occurs in the presence of a solid phase. Another way of stating this is that, while the critical lines in general indicate the critical phenomenon for unsaturated solutions, the critical end points represent the critical phenomenon for saturated solutions.

Figure 6.2a also indicates that the prediction of critical lines does not stop at the critical end points. The upper critical locus continues indefinitely while the lower critical locus, shown in more detail in Figure 6.2b, continues until it meets with an unstable critical locus in a cusp. A continuation of the three-phase lines after the CEP's is not possible, on the other hand, since beyond the critical line the equation of state predicts only one fluid.

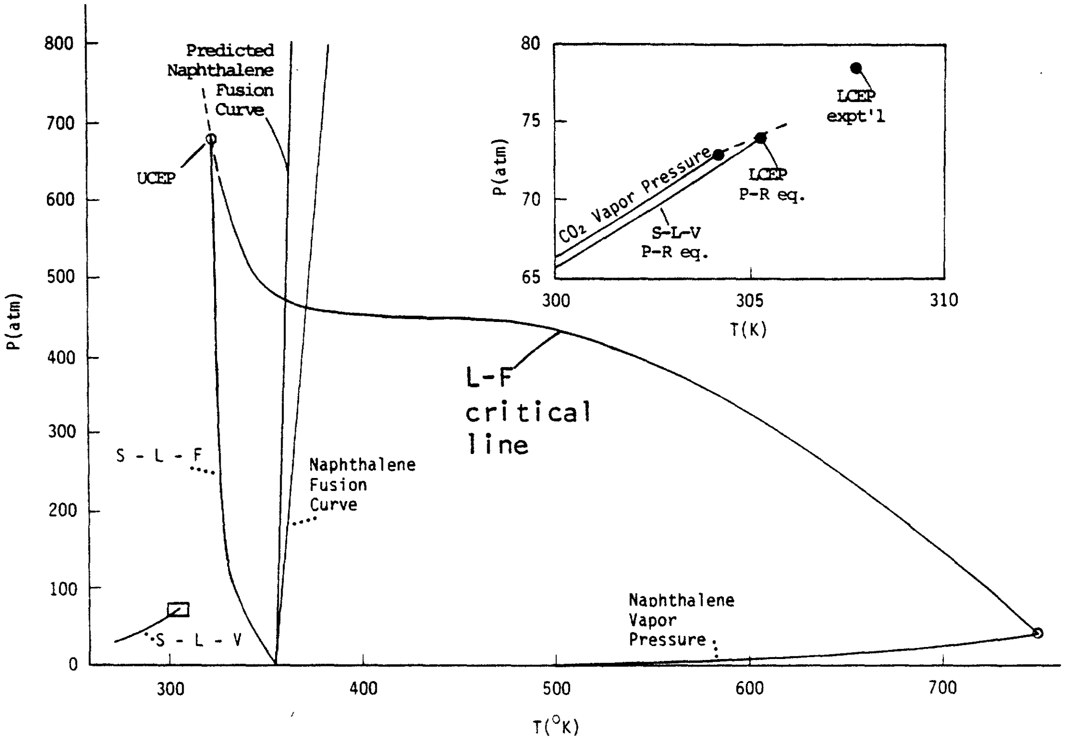

Figure 6.2a. The P-T projection for the naphthalene - carbon dioxide system. A portion of this diagram appeared in Chapter 2 as Figure 2.22a. The range of temperatures between the lower critical end point (LCEP) and the upper critical end point(UCEP) is the supercritical fluid region.

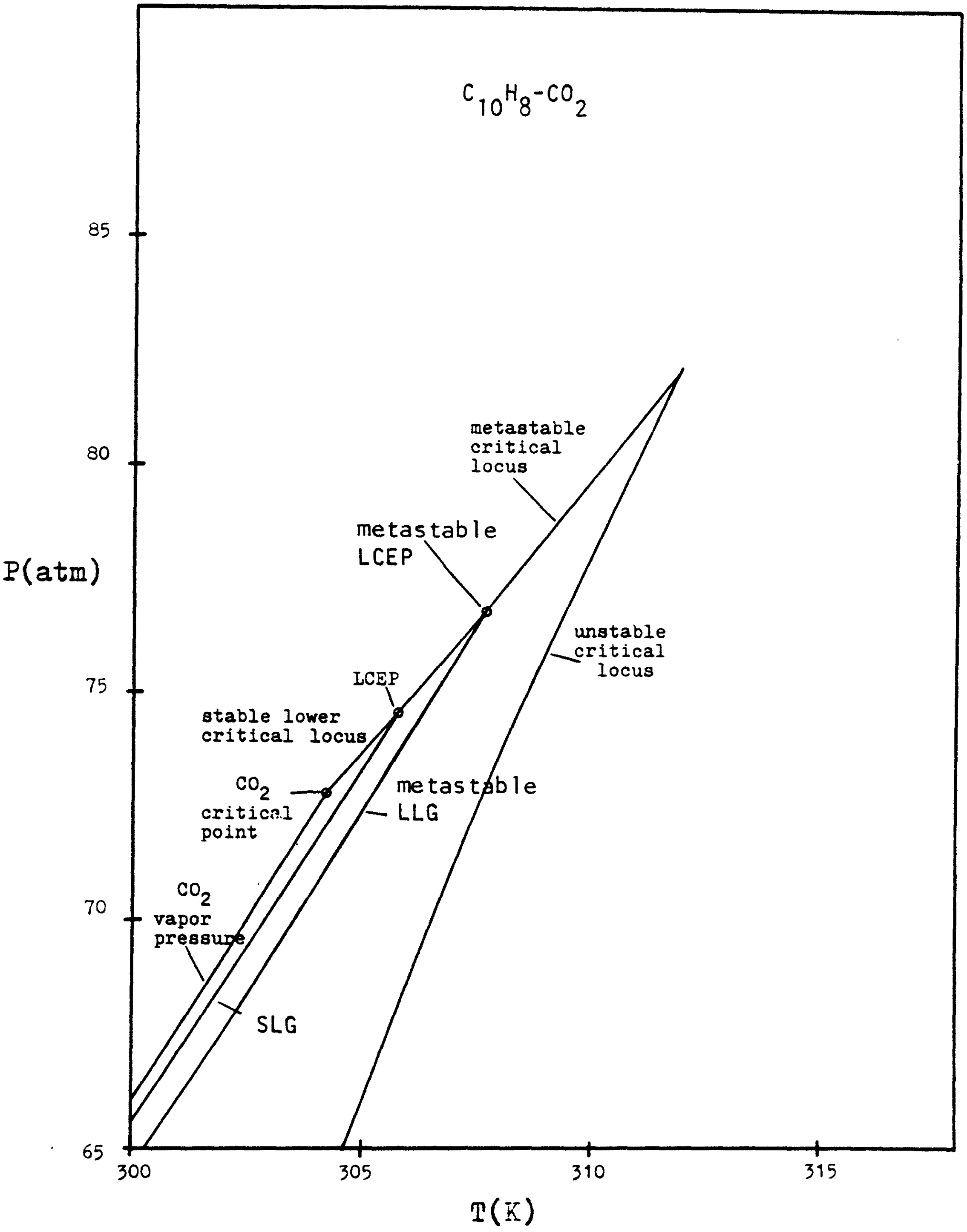

Figure 6.2b. An enlargement of the naphthalene - carbon dioxide P-T projection in the vicinity of the lower critical end point. The stable/metastable critical line meets the unstable critical line at a cusp.

In addition to the critical and three-phase lines, the P-T projection in Figure 6.2a depicts the pure component vaporization curves and the naphthalene fusion curve. The vaporization curves predicted by the P-R equation as in Chapter 4 are at this scale indistinguishable from the experimentally measured curves. The predicted naphthalene fusion curve, on the contrary, shows a significant deviation. This is a result of the poor modelling of liquid phase densities by the P-R equation (see Chapter 4). Figure 6.2b illustrates several other features of the $C_{10}H_8$ - CO_2 system which will be discussed in the context of the P-x sections to be considered next.

Before calculating the P-x sections for the $C_{10}H_8$ - CO_2 system, it is helpful to see what is to be expected. As will be shown in Chapter 7, predictions of phase behavior in the naphthalene-ethylene system (for which considerable experimental data is available) suggest that the critical lines in Figure 6.2 are qualitatively correct. Büchner (1906b) has given a P-T-x space diagram for this case, which was presented in Figure 2.22b. On the basis of this diagram, it is possible to draw up the P-x sections which are expected to be found in the naphthalene - CO_2 system. Figure 6.3 presents a series of eight schematized P-x sections, for temperatures ranging from below CO_2's critical point up to the near critical region of naphthalene. Certain features of these sections have been exaggerated for clarity.

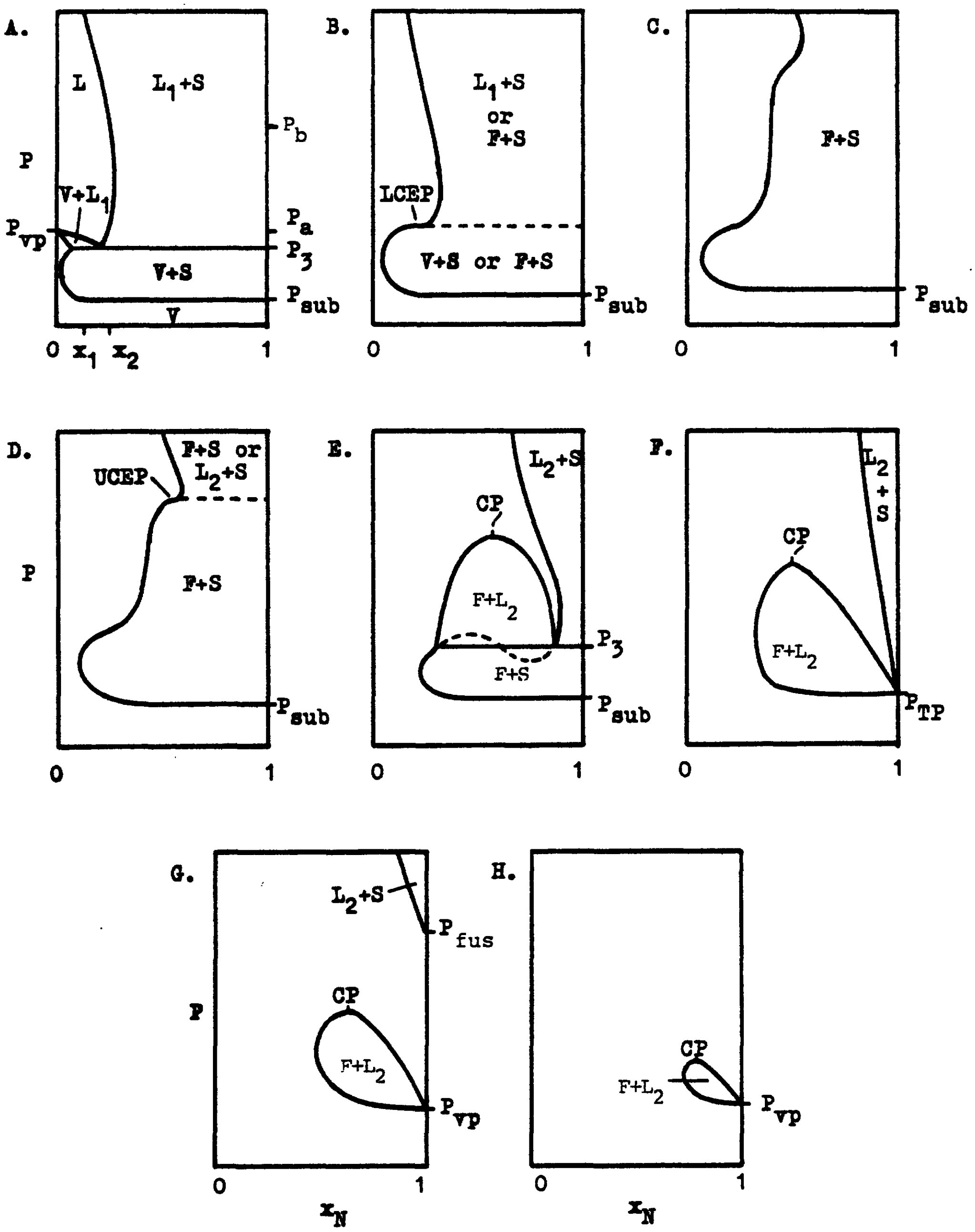

Figure 6.3. A series of qualitative P-x_N diagrams for naphthalene - CO_2. P_{vp} signifies a pure component vapor pressure, P_3 a three-phase pressure, P_{sub} a naphthalene sublimation pressure, P_{fus} a naphthalene fusion pressure, and P_{TP} the naphthalene triple point pressure.

Figure 6.3a is drawn at a temperature below the critical point of the CO_2 solvent. There is a small region of vapor-liquid equilibrium starting at P_{vp}, the vapor pressure of pure CO_2. Adding more $C_{10}H_8$ to the system depresses the vapor pressure of the unsaturated solution until finally, at P_3, the solid no longer dissolves but begins to accumulate. This is the three-phase S-L-V (or S-L-G) pressure at this temperature.

Suppose that instead of varying composition independently, an overall mole fraction of x_1 is chosen, and the system pressure varied. Below P_{sub}, the sublimation pressure of naphthalene, there is only a single vapor phase. Upon increasing the pressure, solid begins to precipitate out and a two-phase system forms, persisting until P_3 is reached. At this pressure, the transformation of solid to liquid occurs. When this transformation is complete only liquid and vapor remain in equilibrium. For a further increase in pressure, the liquid and vapor phases remain in equilibrium until the liquid leg of the VLE section is intersected. At this point, the vapor condenses to a liquid of composition x_1. At higher pressures, only the liquid of composition x_1 remains. If a composition of x_2 rather than x_1 was chosen, the three-phase pressure P_3 would be reached in the same manner. Now, however, the vapor condenses to liquid rather than the solid melting to liquid. Proceeding to higher pressures, the solid is in equilibrium with liquid at first, but dissolves entirely at P_a. The single liquid phase persists until P_b, at which point solid again precipitates out. Thus, the system at x_2 exhibits retrograde solidification.

Figure 6.3b is drawn at the temperature of the lower critical end point. Here the VLE loop, which becomes detached from the pure CO_2 axis at temperatures above the CO_2 critical point, has just disappeared, yielding in the process a horizontal inflection point. The distinction between liquid and vapor is no longer clear in the absence of the three-phase line, so the two-phase equilibrium is now referred to as solid-fluid. The LCEP is the lowest temperature in the supercritical fluid regime, where it is possible to increase pressure indefinitely without observing liquid phase immiscibility. The system is comprised either of a single fluid phase, or is a two-phase solid-fluid system. A P-x section in the middle of the supercritical fluid region is given in Figure 6.3c. There are two regions where a large increase in solubility is observed for a small increase in pressure, a fact which is used to advantage in supercritical fluid extraction processes. The two regions are associated with the critical end points, as is evident upon comparison of Figures 6.3b, c, and d. In Figure 6.3d, the high pressure region of solubility increase has evolved into a horizontal inflection point which is the upper critical end point.

Figure 6.3e illustrates the situation after leaving the supercritical fluid regime on the high temperature side. A three-phase line, the S-L-F line in Figure 6.2a, is now present. There exists a concentration range for which an increase in pressure leads to liquid-liquid or fluid-fluid immiscibility. It is clear, however, that sufficient pressure increase will lead to either complete miscibility of the two components, or a two-phase system of solid in equilibrium with a concentrated solution. In either case one can attain significantly higher solubilities than are possible in the SCF regime. Also shown in Figure 6.3e is a dashed line connecting the two curves defining solid-fluid equilibrium. The portion of this line between the maximum and the minimum represents an unstable solid-fluid equilibrium, while the remaining portions represent metastable conditions. The connection of the solid-fluid equilibrium lines is analogous to the connection or continuation of the fluid-fluid equilibrium lines in the hexadecane-carbon dioxide system. The shape of the dashed curve in Figure 6.3e was suggested by the work of Büchner (1906b). It is not an experimentally measured line.

Increasing temperature to the $C_{10}H_8$ triple point, Figure 6.3f, the terminus of the S-L-F three-phase line is reached. This is a result of the melting of the solid naphthalene. Above the triple point temperature, a solid phase is encountered only at elevated pressures. This is shown in Figure 6.3g. The L_2+S region moves quickly to higher pressures as temperature is raised, due to the steep slope of the naphthalene fusion curve. At the temperature of Figure 6.3h, the L_2+S region no longer appears in the diagram. The phase diagram has reverted to the familiar and more simple form found for vapor-liquid systems.

A sequence of P-x sections calculated from the P-R equation will now be presented, again starting at temperatures below the CO_2 critical point. The predicted sections must be plotted on a logarithmic concentration axis for the region of gas-liquid equilibrium to be visible. Figure 6.4a shows the P-x section at 300 K, and corresponds to Figure 6.3a. Except for a small region at about 70 atm, the S+F binodal represents the stable equilibrium state. The fluid-fluid binodal falls largely within the S+F region, where it represents metastable equilibrium. The metastable L_1L_2G tieline has been shown in the figure. This tieline represents a point on the metastable L_1L_2G line in Figure 6.2b. The SLG tieline, also indicated in Figure 6.2b, is not easily drawn until the 70 atm region is enlarged. Figure 6.4b gives this enlargement, and shows both three-phase tielines. This diagram also includes the region of three roots, the spinodal curves, and the labelling of the fluid-fluid binodals. The L_1+G binodals, which were not

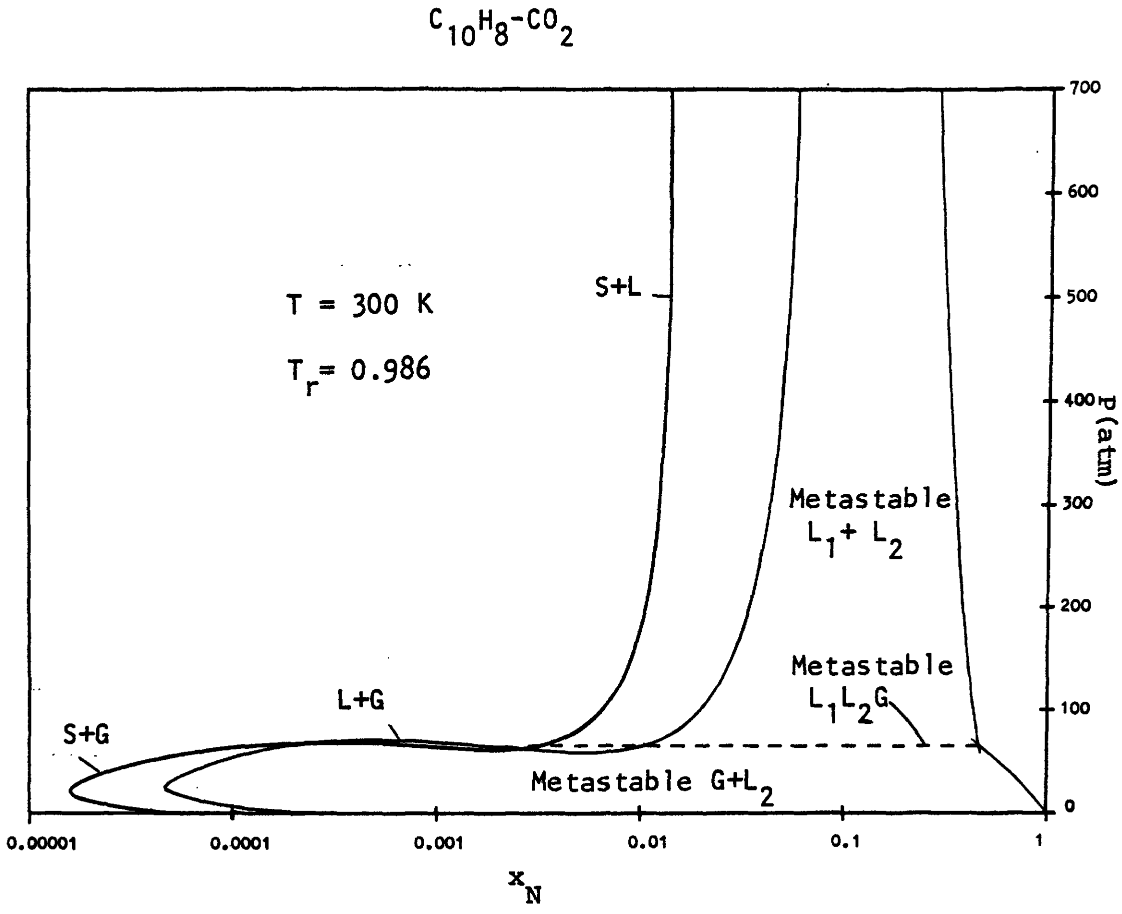

Figure 6.4a. A P-x section below CO_2's critical point. This figure corresponds to Figure 6.3a. Retrograde solidification does not occur until around 1000 atm. T_r in this and all following figures is given with respect to CO_2. The L_1+G region does not appear at this scale.

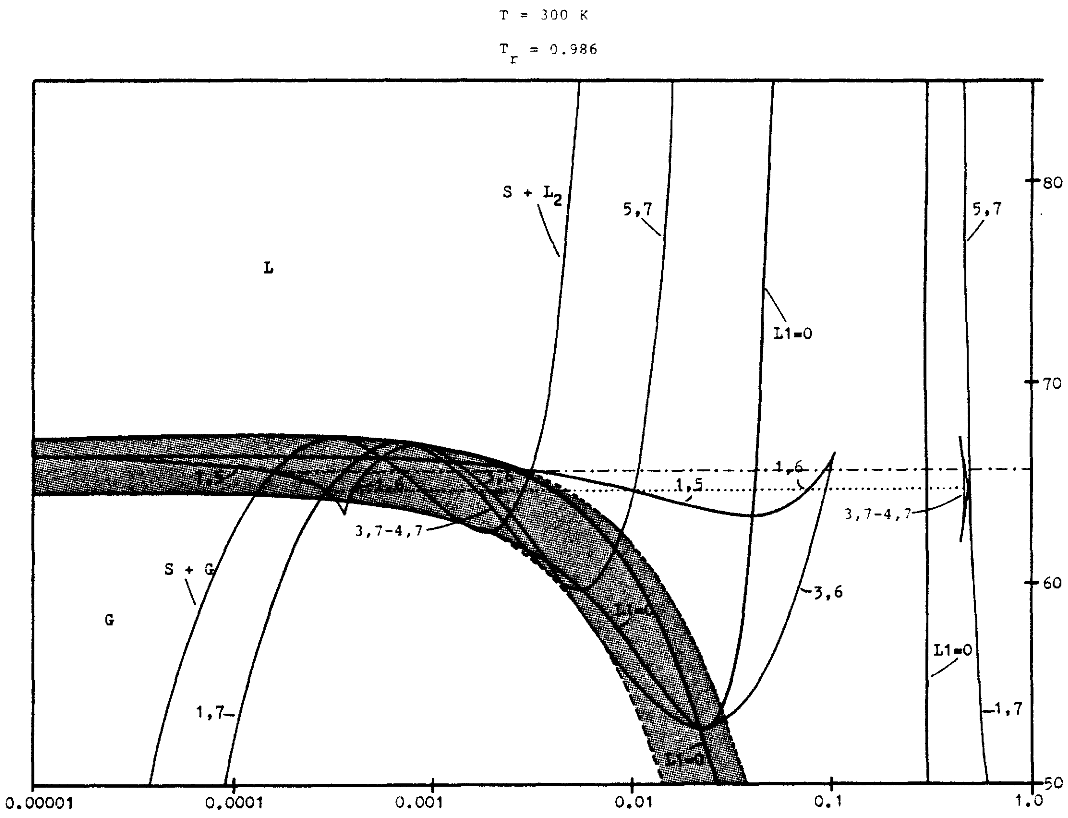

Figure 6.4b. The P-x section at 300 K in the vicinity of 70 atm. The dot-dash line is the SLG tieline, while the dotted line is the metastable LLG tieline. Limit points along the solid-fluid binodal have been circled. The region of three roots is shaded.

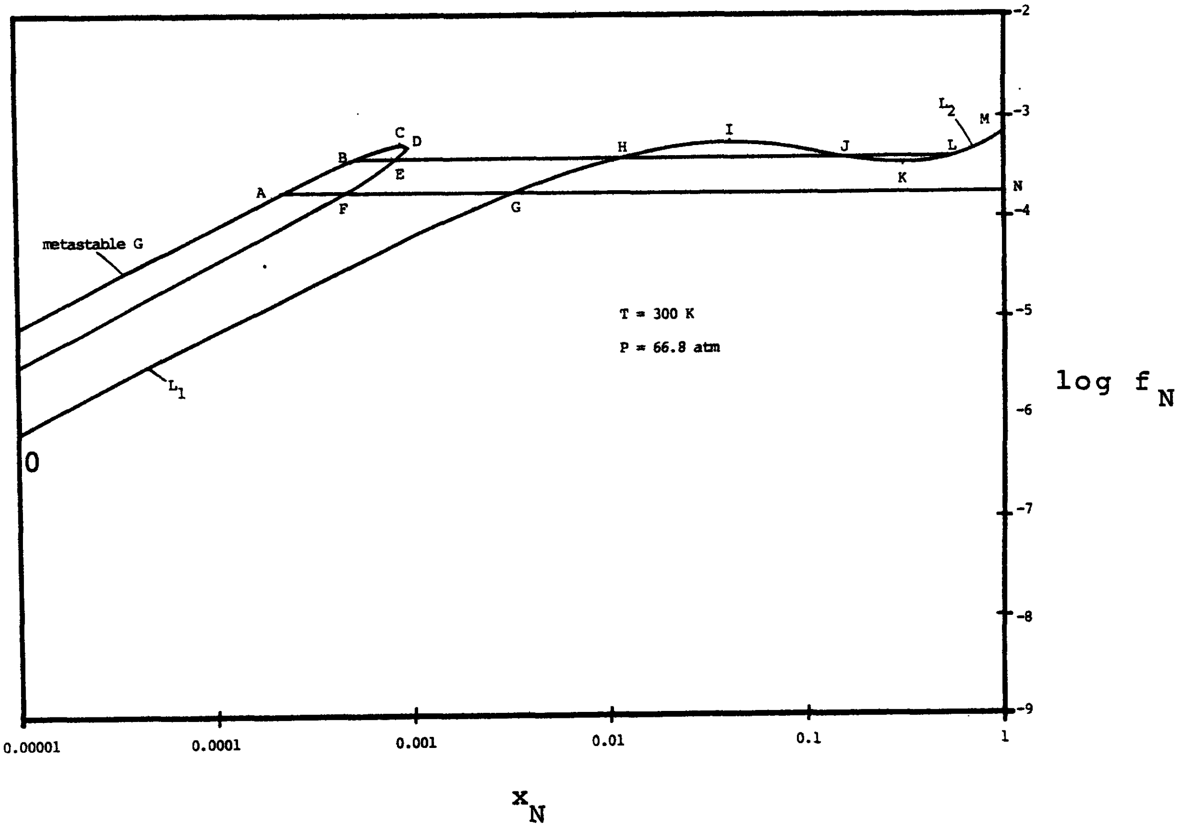

Figure 6.4c. An f-x plot illustrating various metastable states (see text). AN is a metastable S+G tieline and BL is a metastable G+L_2 tieline. GN is the stable S+L tieline.

visible in Figure 6.4a, form a closed loop which follows the path (1,5)-(1,6)-(3,6)-(3,6)-(1,6)-(1,5). Since 300 K is below CO_2's critical temperature, the stable L_1+G binodal (1,5) would extend to the pure CO_2 axis on a Cartesian plot, as in Figure 6.3a. The metastable L_2+G binodals are represented by the (1,7) segments, and are joined to the metastable L_1+L_2 binodals, (5,7), by the unstable (3,7) and (4,7) segments.

Solid-fluid equilibria are represented in Figure 6.4b by a single curve. The S+G binodal starts at low pressures and rises to a smooth maximum in pressure. This point is designated as a limit point, and is circled in the figure. The curve then enters an unstable region, reaches a smooth pressure minimum, and finally proceeds to higher pressures along the S+L binodal. The pressure minimum is also designated as a limit point.

An interesting feature of this diagram is noted upon following the S+G binodal more carefully. Starting at low pressure, the three-phase S-L-G pressure is reached at about 66.6 atm. In continuing to higher pressures, the metastable S+G curve passes entirely through the G+L_1 region before becoming intrinsically unstable at the limit point. Examples have previously been given where a single phase could exist in a metastable state, with a two-phase system representing the true stable equilibrium. The present case demonstrates that the opposite can also occur, i.e., that two phases may exist in a metastable state in a stable one-phase region. It is instructive to consider how the S+G metastable state is defined in an f-x plot. Figure 6.4c gives an f-x plot at 66.8 atm, which is slightly above CO_2's vapor pressure (i.e., above the G+L_1 region), and below the maximum pressure limit point (see Figure 6.4b). This pressure is also below the pressure maximum in the gaseous branch of the (1,7) binodal, so that the fugacity plot must also indicate a metastable L_1+G region. Referring now to Figure 6.4c, the segment from low x_N to A represents a metastable vapor phase system since the pressure is above the G+L_1 region. At A, the partial fugacity of naphthalene in the vapor phase reaches the fugacity of the pure solid, and the system may split into two phases, S+G, as indicated by tieline AN. The points F and G are not in equilibrium with A since they do not have matching CO_2 fugacities. Alternatively, the vapor may persist as a single phase to point B. Again at B, the system may split into two phases, this time G+L_2 with compositions given by points B and L. If the system at B does not split into two phases, it may continue as a single phase until point C, when it must revert to the metastable G+L_2 state, the metastable S+G state, or the stable, single liquid phase system found along segment OG. The stable system for x_N greater than composition G is given by the tieline GN, representing S+L. It has already been shown that metastable S+G and G+L systems could exist for this range of compositions as well.

These are not the only possibilities, however. Between G and H, metastable L_1 might persist. At a composition slightly beyond H, L_1 is in metastable equilibrium with L_2 of a composition slightly greater than L. This tieline has not been drawn since it would be indistinguishable from tieline B-L. If L_1 does not split to an L_1+L_2 system at H (approximately), it may exist until composition I is reached, at which point it reverts to a two-phase system. Finally, for compositions greater than K, a single phase metastable L_2 is possible. Analysis of the f-x plot thus demonstrates the complexity of the phase equilibrium predictions when metastable states are accounted for. Between compositions of H and I, either the stable system L+S or one of the four metastable systems L_1, L_1+L_2, L_2+G, and S+G could exist. The f-x plot also makes clear how each of the different metastable states arises.

The metastable S+G and L_2+G regions present at 300 K increase in size as temperature is decreased. This is illustrated in Figure 6.5a, at 290 K. On the other hand, at 304 K, these regions no longer protrude into the single phase liquid region. This is shown in Figure 6.5b. Since 304 K is still below CO_2's critical temperature, the L_1+G region extends to the pure CO_2 axis.

Figure 6.6a depicts the overall P-x section at 306.3 K. This is very nearly the LCEP temperature, so the diagram may

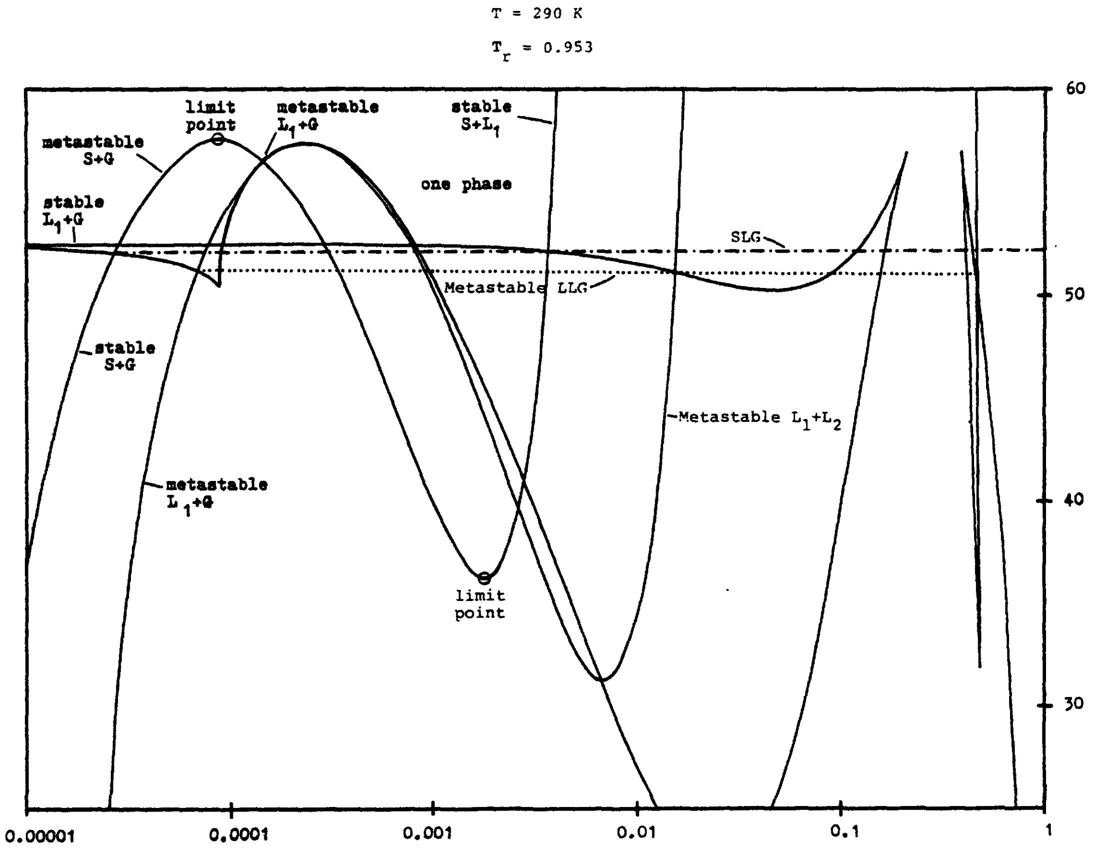

Figure 6.5a. The P-x section at 290 K in the vicinity of the three-phase lines. The metastable S+G and L_2+G binodals extend about 5 atm into the single phase liquid region.

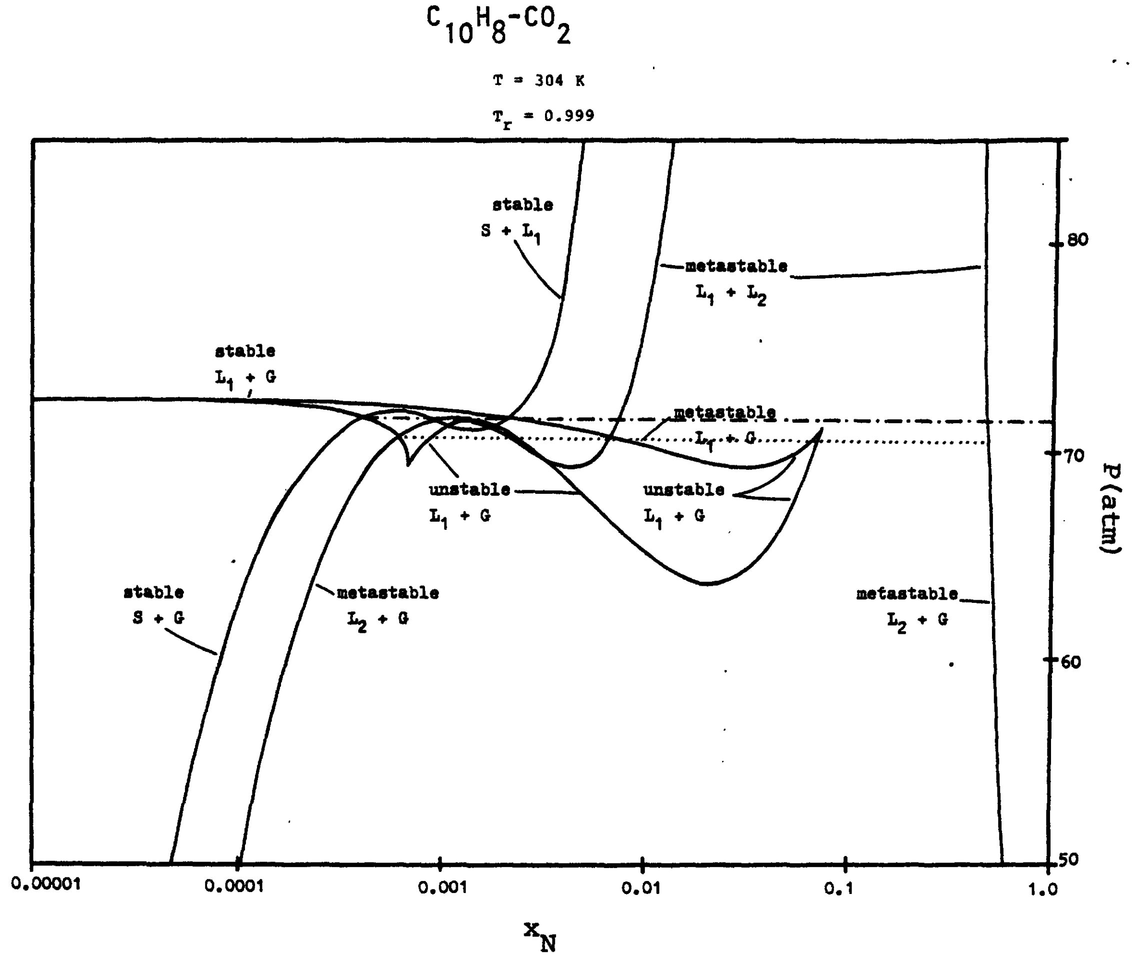

Figure 6.5b. The P-x section at 304 K in the vicinity of the three-phase lines (not shown). The metastable S+G and L_2+ G binodals do not extend into the single phase liquid region.

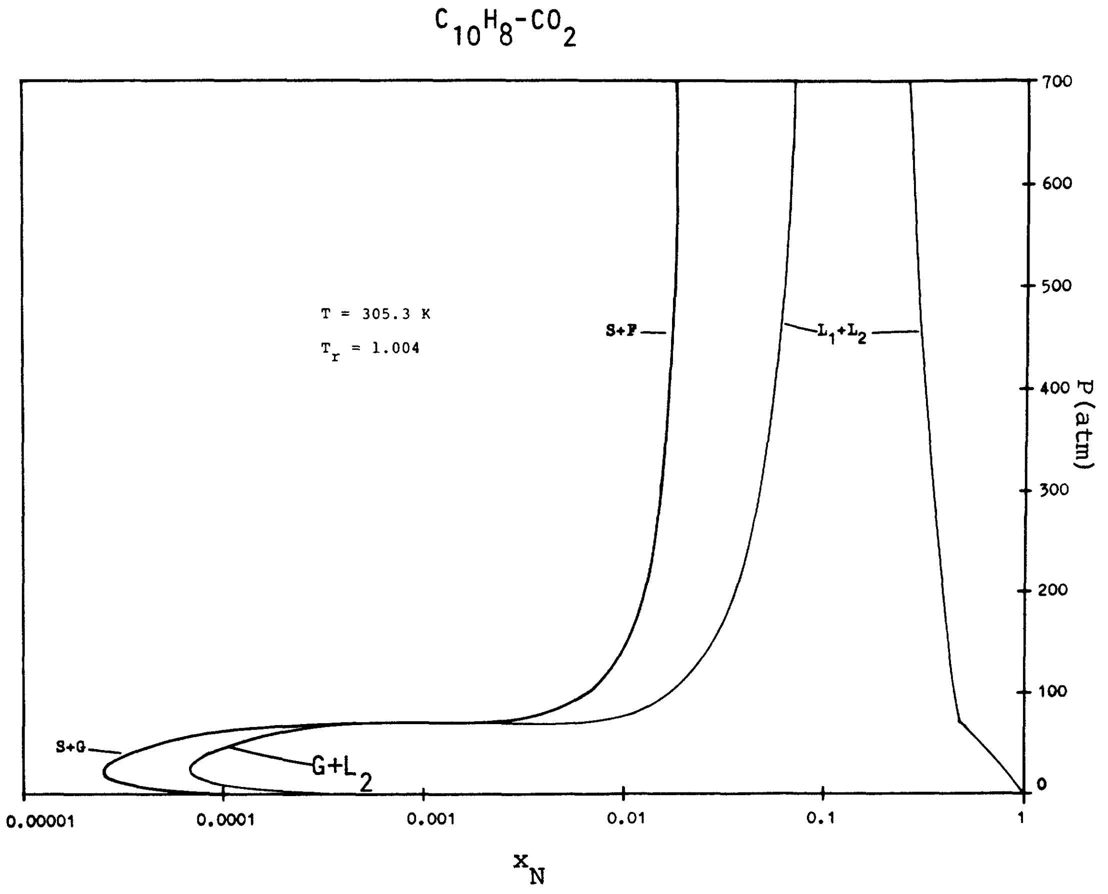

Figure 6.6a. A P-x section between CO_2's critical point and the LCEP. The fluid-fluid binodal (corresponding to L_1+ L_2 at high pressures and G+L_2at low pressures) no longer crosses the solid-fluid binodal.

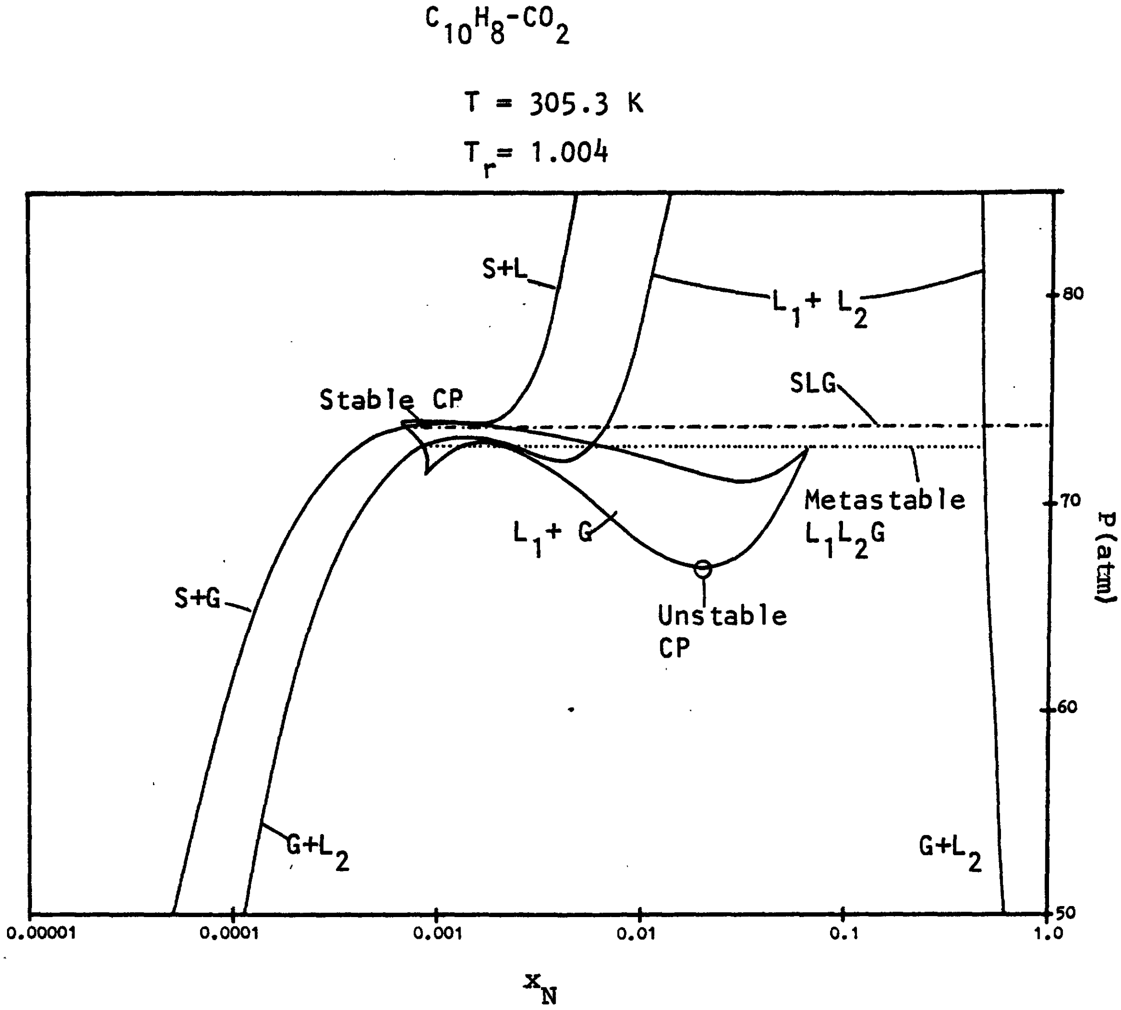

Figure 6.6b. The P-x section at 305.3 K in the vicinity of the three-phase region. The L_1+ G binodal crosses the solid-fluid binodal to yield a three-phase SLG tieline. The L_1+ G binodals exhibit two critical points. This temperature is slightly below the lower critical end point temperature.

be compared with Figure 6.3b. The section is similar to that at 300 K (Figure 6.4a), except that the fluid-fluid binodal no longer crosses the solid-fluid binodal. The L_1+G binodal still intersects the solid-fluid binodal, though, as shown in the enlargement of Figure 6.6b. Having detached from the pure CO_2 axis, the L_1+G region now terminates in a stable critical point. At a temperature slightly above 306.3 K, the stable critical point will remain as the last point of contact between the L_1+G binodal and the solid-fluid binodal. This is the lower critical end point. At this point, the solid-fluid binodal exhibits a horizontal point of inflection. It is also evident from the figure that, as temperature is raised further, a metastable LCEP will be predicted as the metastable critical point meets the metastable L_1L_2G line. The meaning of the two critical end points in Figure 6.2b should now be clear.

Figure 6.7 gives a P-x section in the supercritical fluid region, at 311 K. This diagram corresponds to Figure 6.3c. The solid-fluid binodal is now the stable two-phase system throughout the entire pressure range. The solubility increase between about 40 and 80 atm is actually not as dramatic as it was at lower temperatures (see Figure 6.4a and 6.6a), although at higher pressures the solubility is somewhat greater than previously. The solubility increase associated with the upper critical end point is not visible in this diagram since it occurs above 700 atm.

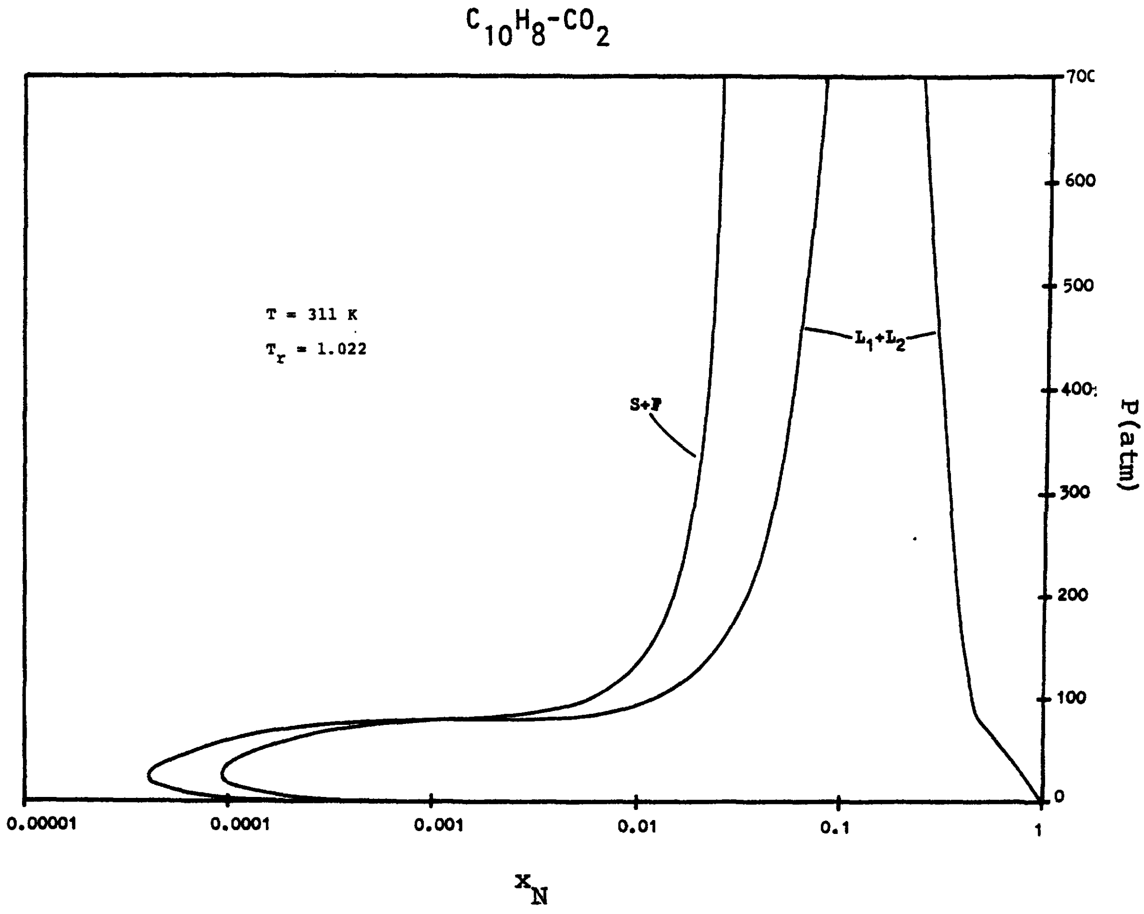

Figure 6.7. A P-x section in the supercritical fluid region. The S+F binodal represents the stable two-phase equilibrium at all pressures.

Increasing temperature to 326.3 K, the P-x section of Figure 6.8 is found. This is slightly above the upper critical end point temperature, and the diagram is thus similar to Figure 6.3d. A region of liquid-liquid equilibrium now exists between 650 and 680 atm. It intersects the solid-fluid binodal in two places to form the three-phase SLF line. Note that the solid-fluid binodal is again a single curve with two extrema. As the diagram suggests, at the UCEP temperature the L-L critical point intersects the solid-fluid binodal at a horizontal inflection point. Figure 6.8 also illustrates the course of the spinodal curve and the region of three roots.

The P-x section at 340 K is given in Figure 6.9a. This diagram is the equivalent of Figure 6.3e. A three-phase S-L-F line is predicted at about 65 atm. Above this pressure, depending upon overall system composition, liquid-liquid or solid-liquid are the stable two-phase systems. Below this pressure, the S+F binodal represents the stable two-phase system. Consequently, the low pressure portion of the L+F envelope is metastable.

The connection of the S+F and S+L binodals, shown as a hypothetical curve in Figure 6.3e, is not at all apparent in 6.9a. In this case, the continuation is discernable only at very low pressures, as depicted in Figure 6.9b. As is seen,

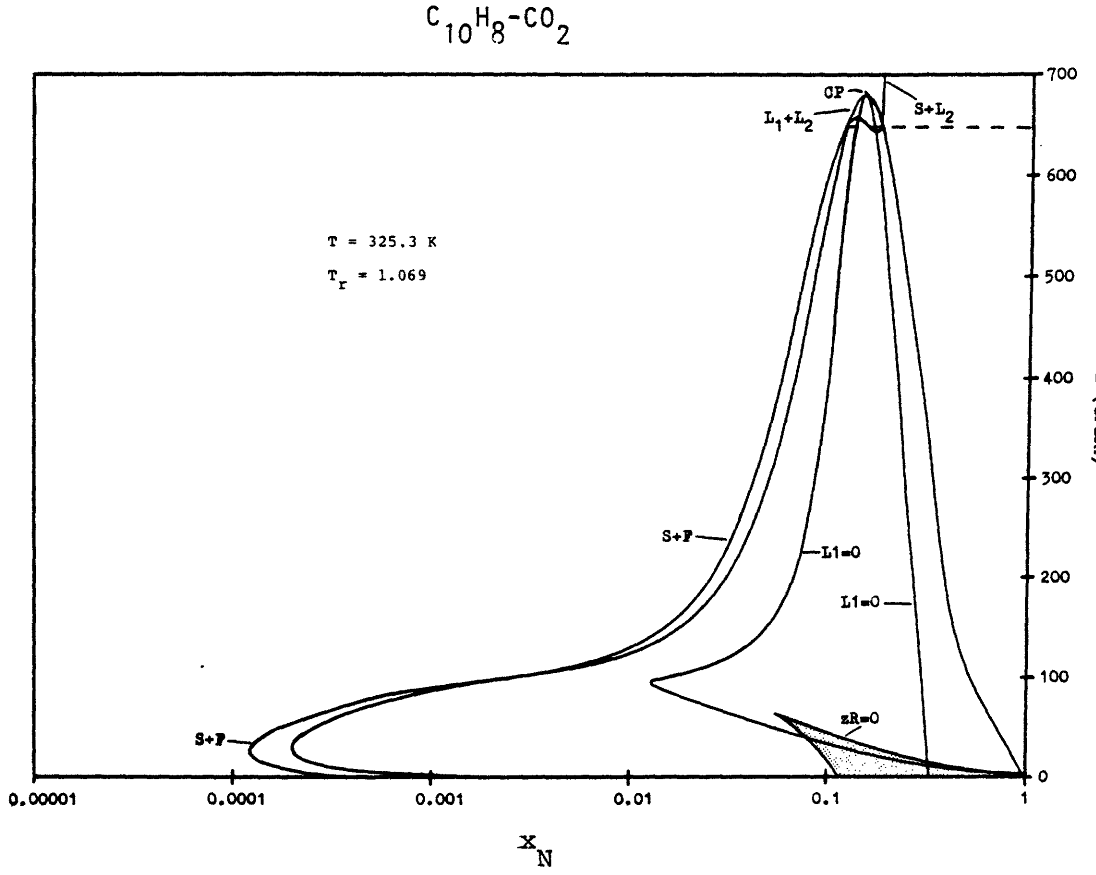

Figure 6.8. A P-x section at a temperature slightly above the upper critical end point. The SLF tieline is shown dashed. The region of three roots is shaded.

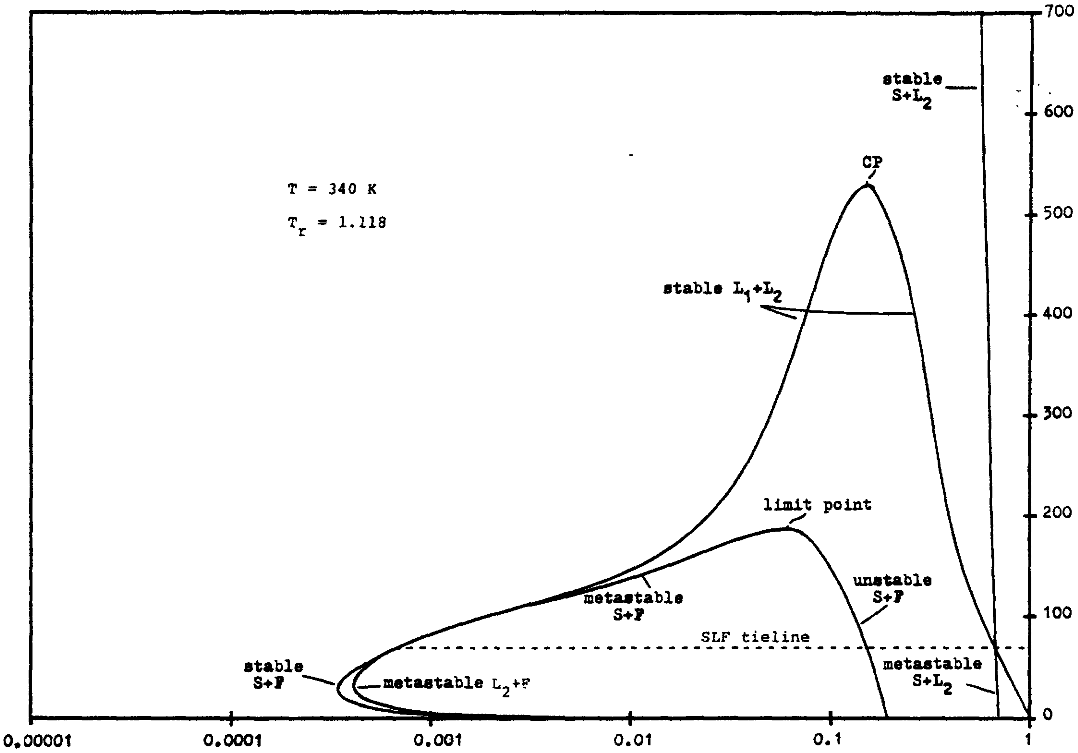

Figure 6.9a. A P-x section between the UCEP and naphthalene's triple point. The SLF tieline is shown dashed.

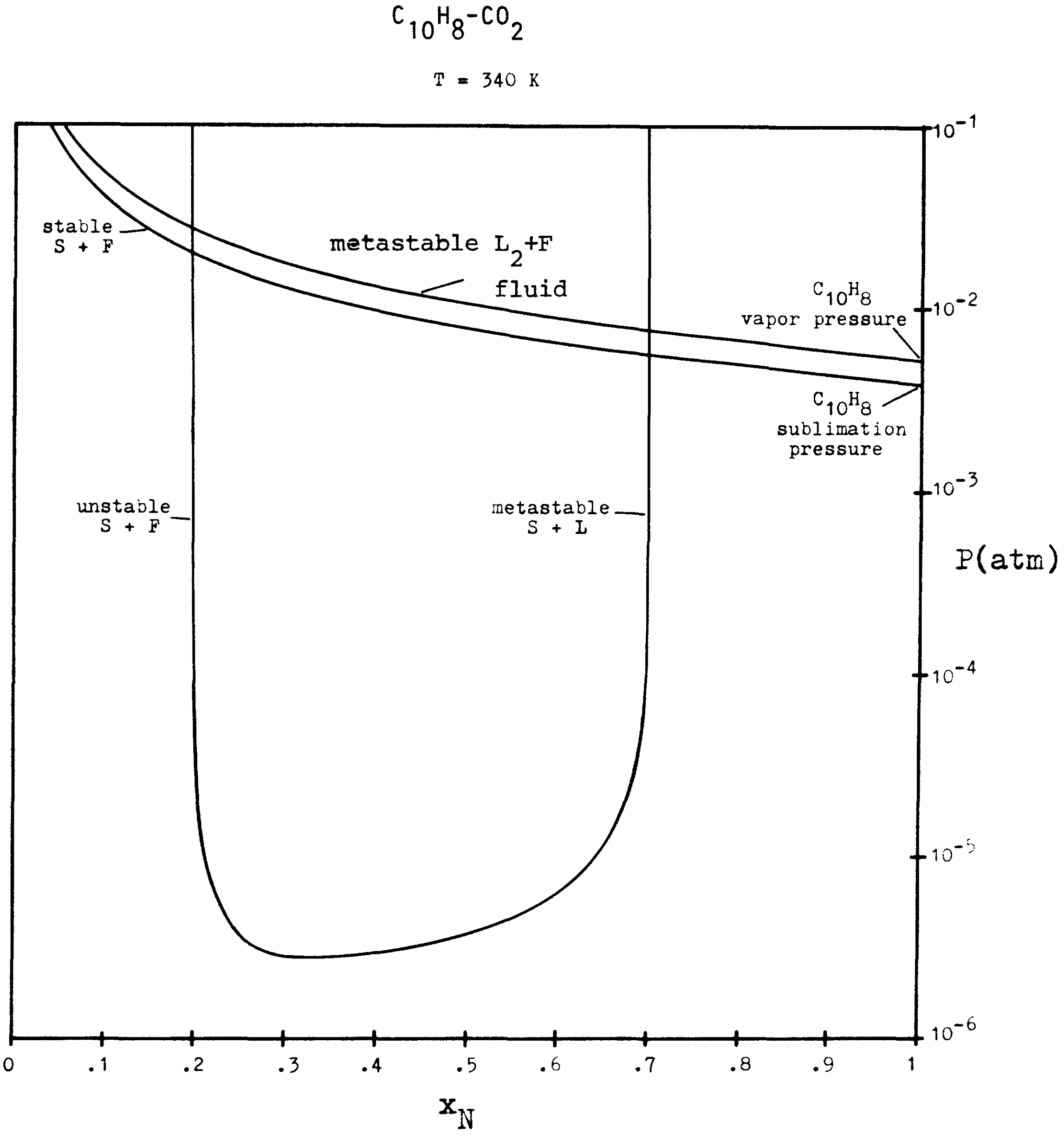

Figure 6.9b. The low pressure P-x section at 340 K.

the metastable S+L line connects to the unstable S+F line at about 3 x 10^{-6} atm. The unstable S+F line then proceeds to the limit point where it joins the metastable S+F line (see Figure 6.9a). The metastable S+F segment in turn continues to lower pressures, crossing the fluid branch of the L+F curve at the three-phase pressure, thus becoming stable, and attaining a minimum naphthalene concentration at about 30 atm. Thereafter, naphthalene concentration in the fluid increases with decreasing pressure, crossing both the unstable S+F and metastable S+L lines before intersecting the pure naphthalene axis at the sublimation pressure. It is seen that the metastable S+L line extends to pressures below the $C_{10}H_8$ sublimation pressure. Such a metastable region has not been experimentally observed. The metastable L+F binodal is also shown in the diagram, and terminates at a metastable naphthalene vapor pressure.

Figure 6.10 gives the calculated P-x section at 354.5 K, the predicted triple point temperature of naphthalene. This diagram corresponds to Figure 6.3f. The L-F envelope and the $S+L_2$ binodal meet at the triple point. In contrast to the situation at 340 K, the S+F binodal now represents only a metastable equilibrium.

Figure 6.11 gives the predicted P-x section at 360 K, somewhat above naphthalene's triple point temperature. It is to be compared with Figure 6.3g. At sufficiently high

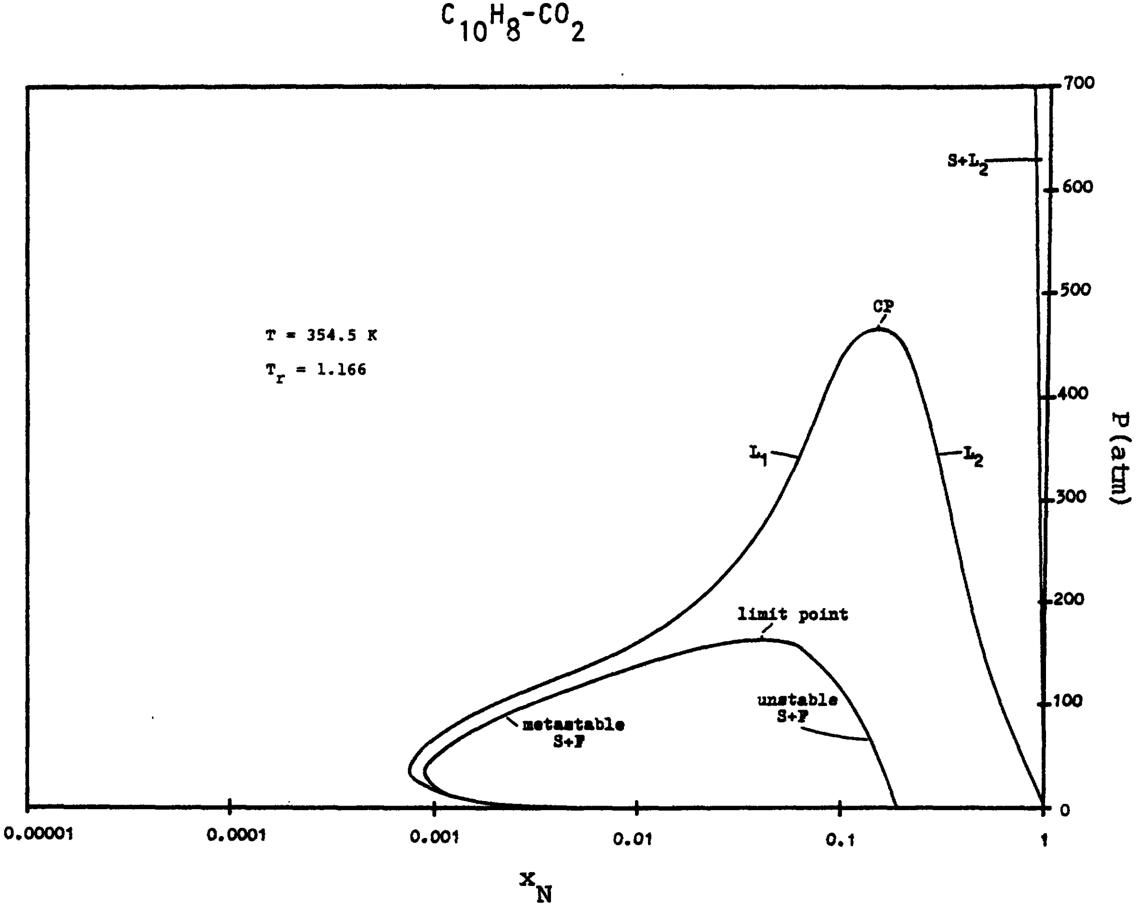

Figure 6.10. The P-x section at the triple point temperature. Each of the binodal curves terminates at the triple point.

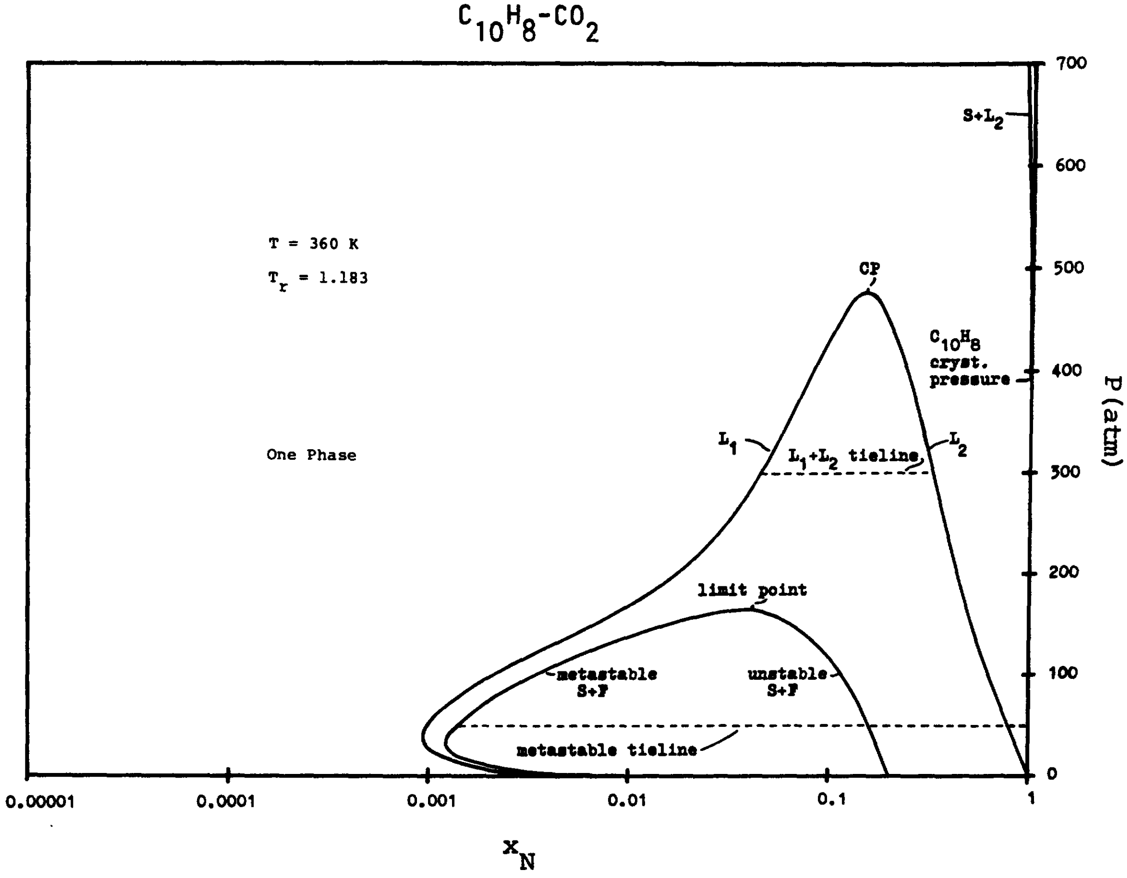

Figure 6.11. A P-x section above naphthalene's triple point temperature.

pressures, it is still possible to have solid present in the system, in equilibrium with a very concentrated solution. This two-phase region begins at a point along the naphthalene fusion curve, labelled as the $C_{10}H_8$ crystallization pressure in the figure. Such a point is found by determining the pressure at which $f_N^L = f_N^C$ when $x_N=1$. Knowledge of the crystallization pressure at several temperatures allows one to plot the predicted naphthalene fusion curve depicted in Figure 6.2a. As at 354.5 K, the S+F binodal is metastable. A metastable S+F tieline has been included in this diagram to emphasize that the limit point is not a critical point. Although two S+F binodals meet at the limit point, the two phases in equilibrium (solid and fluid) do not become identical. At low pressure, the S+F loci cross, with the metastable segment intersecting the pure naphthalene axis at a metastable sublimation pressure.

The preceding sequence of P-x sections covers the important features of the naphthalene - carbon dioxide system. It is convenient to summarize some of the compositional information contained in these sections through P-x and T-x projections. These projections are given in Figures 6.12a and b for the upper critical line and the SLF three-phase region. The P-x and T-x projections of the lower critical line and the SLG region are very similar to those for the naphthalene - ethylene system, which will be shown in Chapter 7 (Figure 7.3).

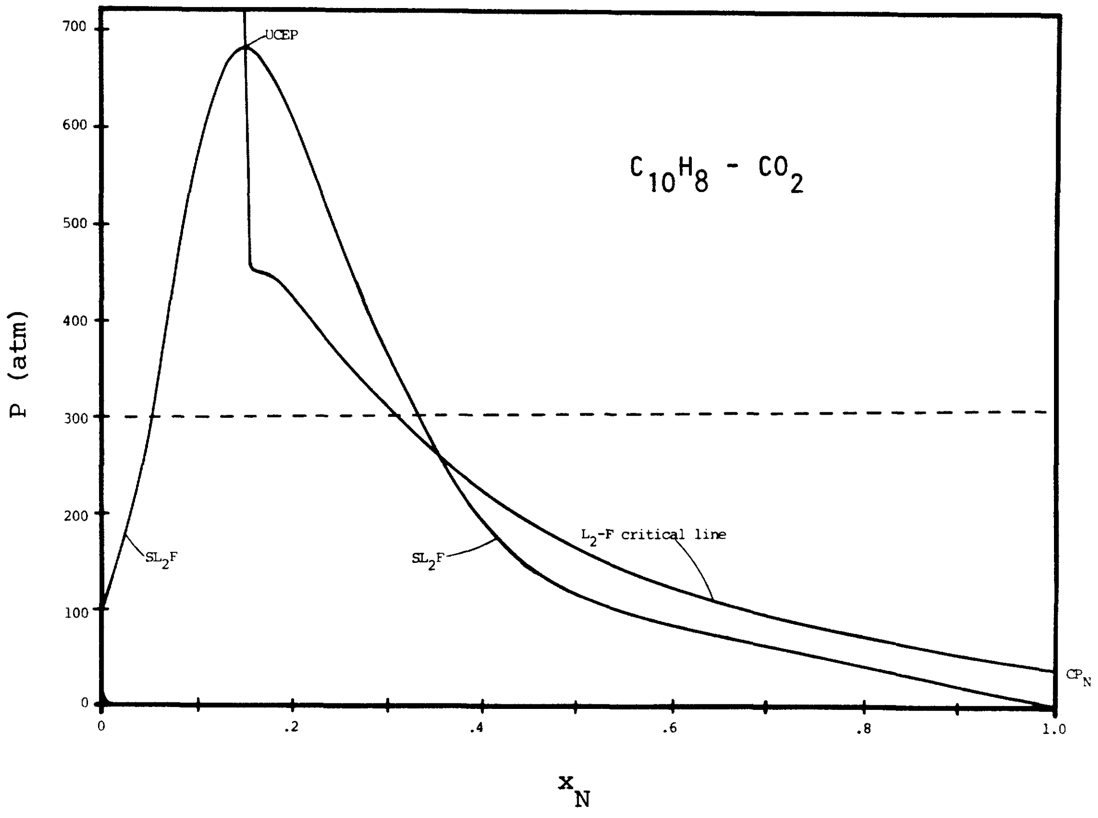

Figure 6.12a. The P-x projection of the upper critical line and the SLF region. A sample SLF tieline is shown dashed.

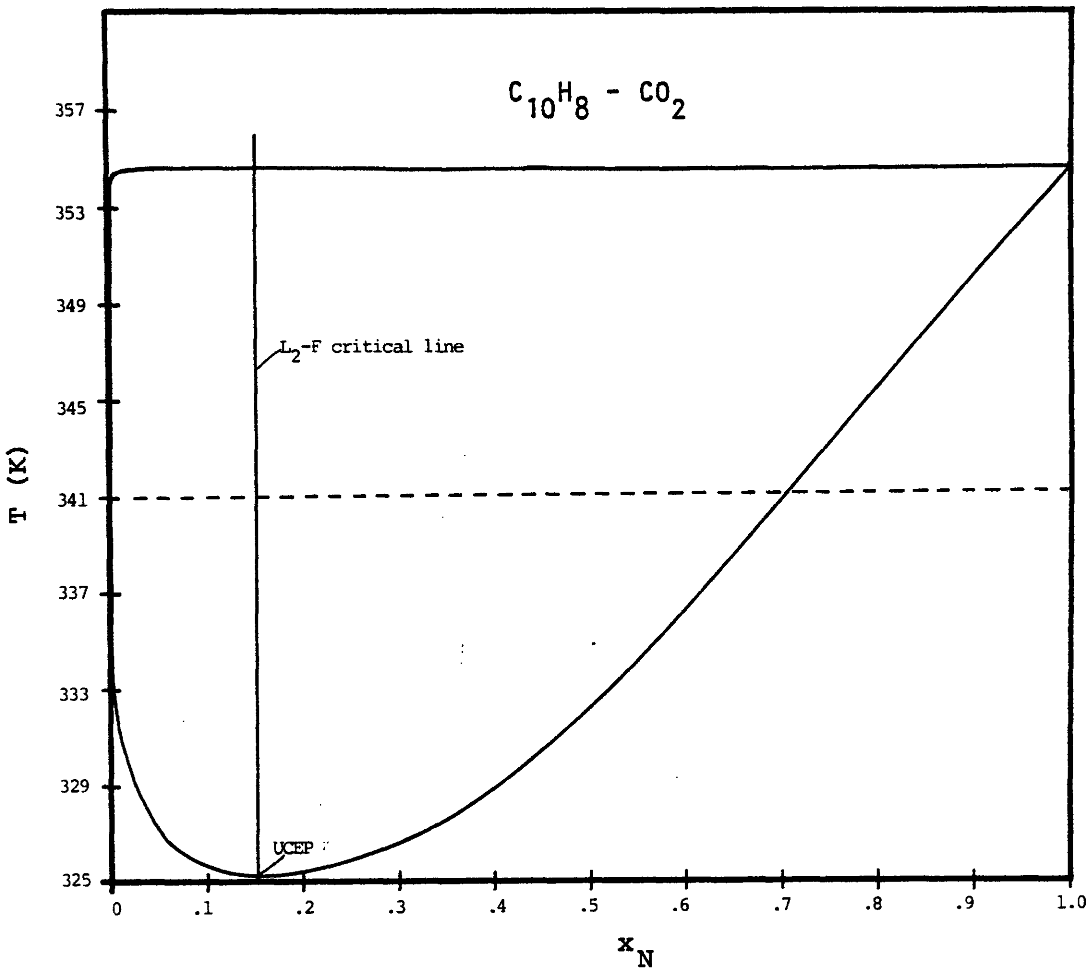

Figure 6.12b. The T-x projection of the upper critical line and the SLF region. A sample SLF tieline is shown dashed.

6.2 Quantitative Predictions

A limited amount of actual phase equilibrium data is available for the naphthalene - CO_2 system. The most frequently cited measurements are those of Russian origin, by Tsekhanskaya, et al. (1964), whose observations have recently been confirmed by the work of McHugh and Paulaitis (1980) and Kurnik, et al. (1981). The Russian data, which fall within the supercritical fluid region, are typically plotted as shown in Figure 6.13. Also illustrated there is the effect of the value of the interaction parameter. At 35°C and 45°C, Figures 6.13a and b, the curves all have the correct general shape, and for the most part give the solubility to within a factor of two. The predicted solubility increase with pressure due to the proximity of the lower critical end point is not quite rapid enough, which is particularly evident at 35°C and about 80 atm where the calculated values are off by a factor of 4 or 6. The largest discrepancy, however, arises at 55°C (Figure 6.13c), when the Peng-Robinson equation predicts entry into the three-phase S+L+F region for the three lowest δ_{12} values. The vertical lines in Figure 6.13c represent SLF tielines of the type seen in Figures 6.3e and 6.9a. After predicting a solubility jump due to the phase change of fluid to liquid, the calculated solubility for $\delta_{12} = 0.11$ is eight times too high. According

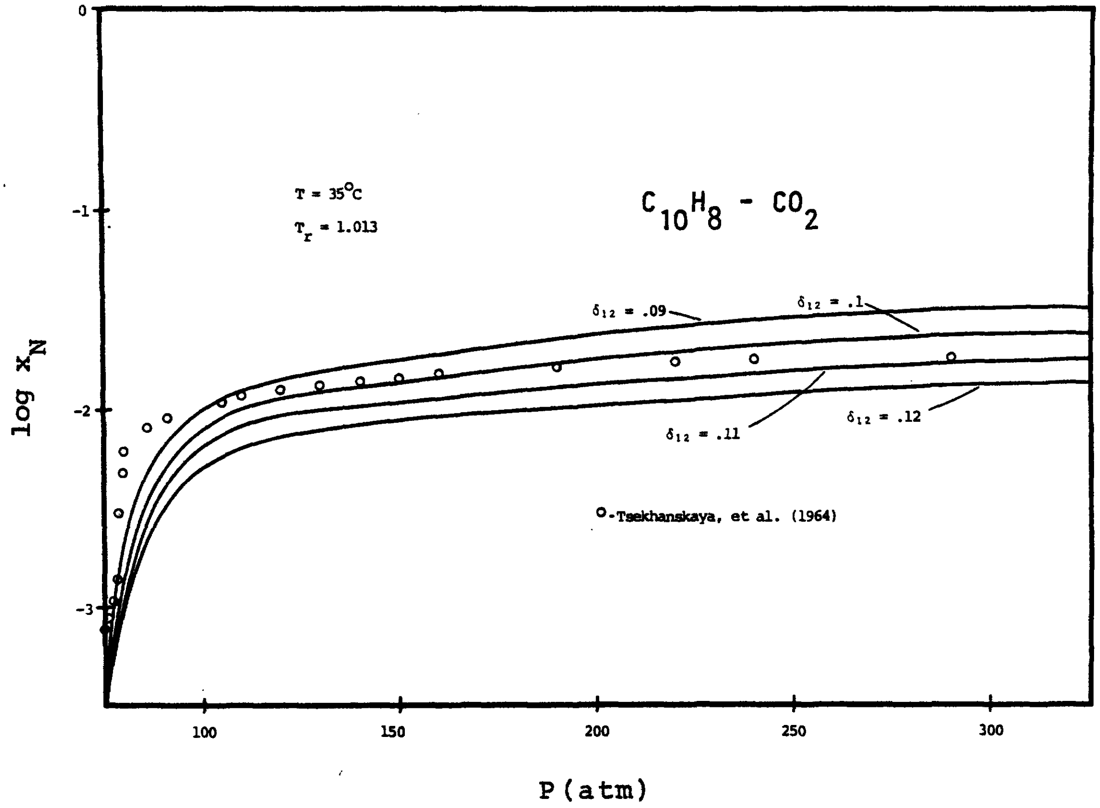

Figure 6.13a. The solubility of naphthalene in supercritical CO_2 at 35°C. Predicted solubilities for four different values of the interaction parameter are shown.

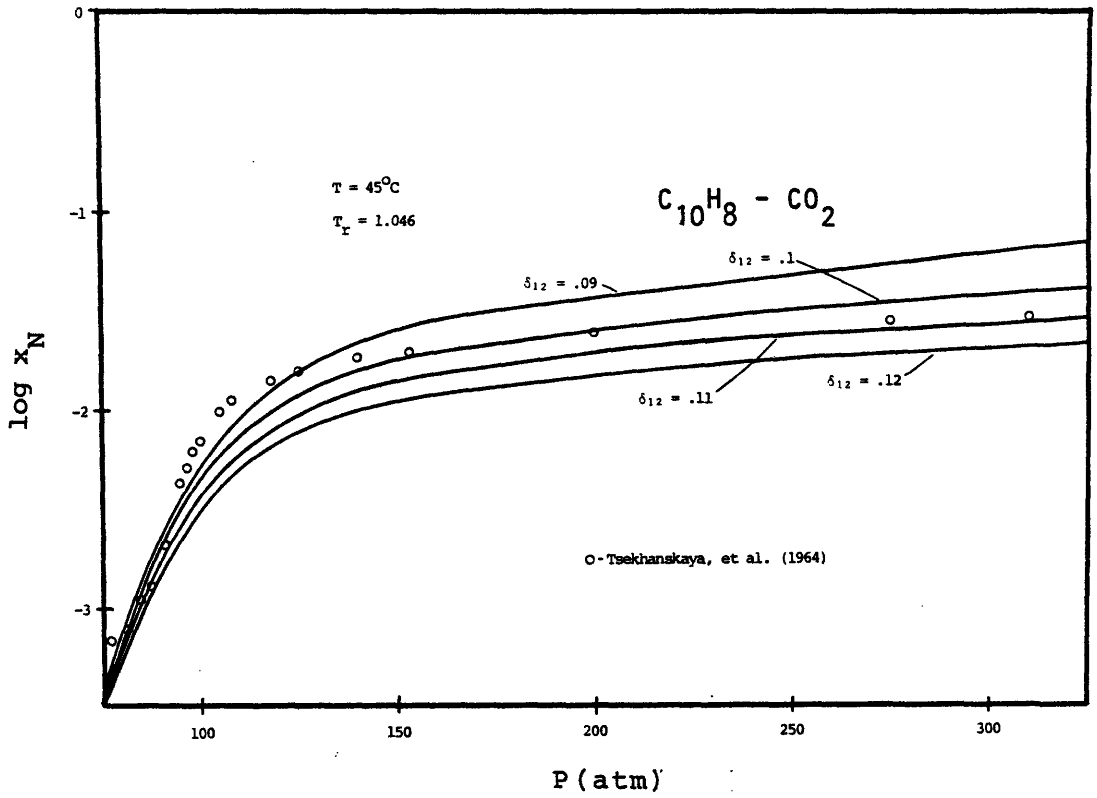

Figure 6.13b. The solubility of naphthalene in supercritical CO_2 at 45°C.

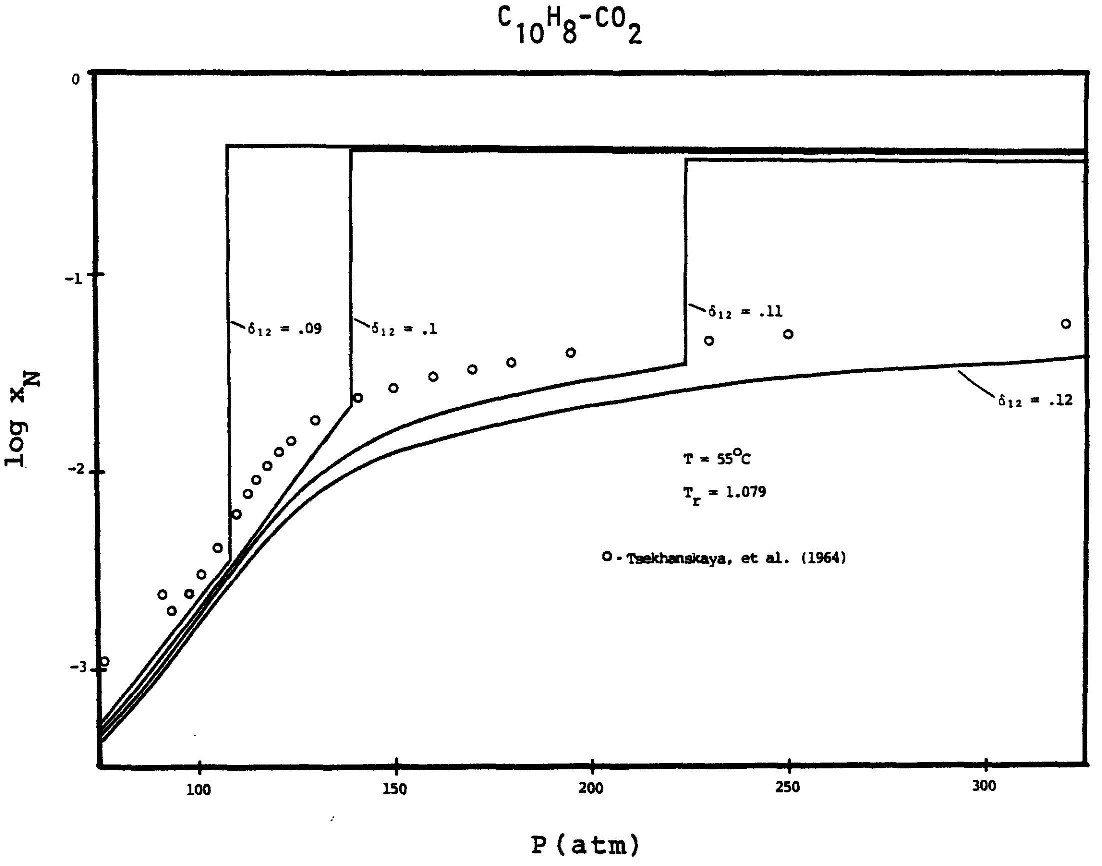

Figure 6.13c. The solubility of naphthalene in supercritical CO_2 at 55°C. For δ_{12}= 0.09, 0.10, and 0.11, a solubility jump is predicted by the P-R equation.

to experimental observations, a three-phase pressure will not be encountered until somewhat higher temperatures. Although predicting the three-phase line and the UCEP at too low a temperature, a δ_{12} of 0.11 gives better agreement over most of the SCF region than a δ_{12} of 0.12, and was therefore used for all further calculations.

Saturated liquid solubilities in the SLG region have been measured by Quinn (1928). A measurement made by Francis (1954) is in close agreement with Quinn's observations. These data are plotted in Figure 6.14 along with the lower critical end point as determined by Tsekhanskaya, et al. (1964). The Peng-Robinson solubilities are again largely within a factor of 2, except near the LCEP. If the data point at 25^{o}C is used as the sole basis for selecting an appropriate interaction parameter, a value of $\delta_{12} = 0.09$ is found.

Using the data of Quinn and Tsekhanskaya, Modell, et al. (1979) have developed the "solubility map" for $C_{10}H_8 - CO_2$ which was presented in Chapter 2. This diagram, shown again in Figure 6.15, is essentially a projection of solubility isobars on the T-x plane, and is a particularly concise means for summarizing the data in the SCF region. The three-phase region represented by the dashed line (saturated liquid + saturated vapor + solid) corresponds to the SLG line in Figure 6.2. Figure 6.16 gives the solubility map as

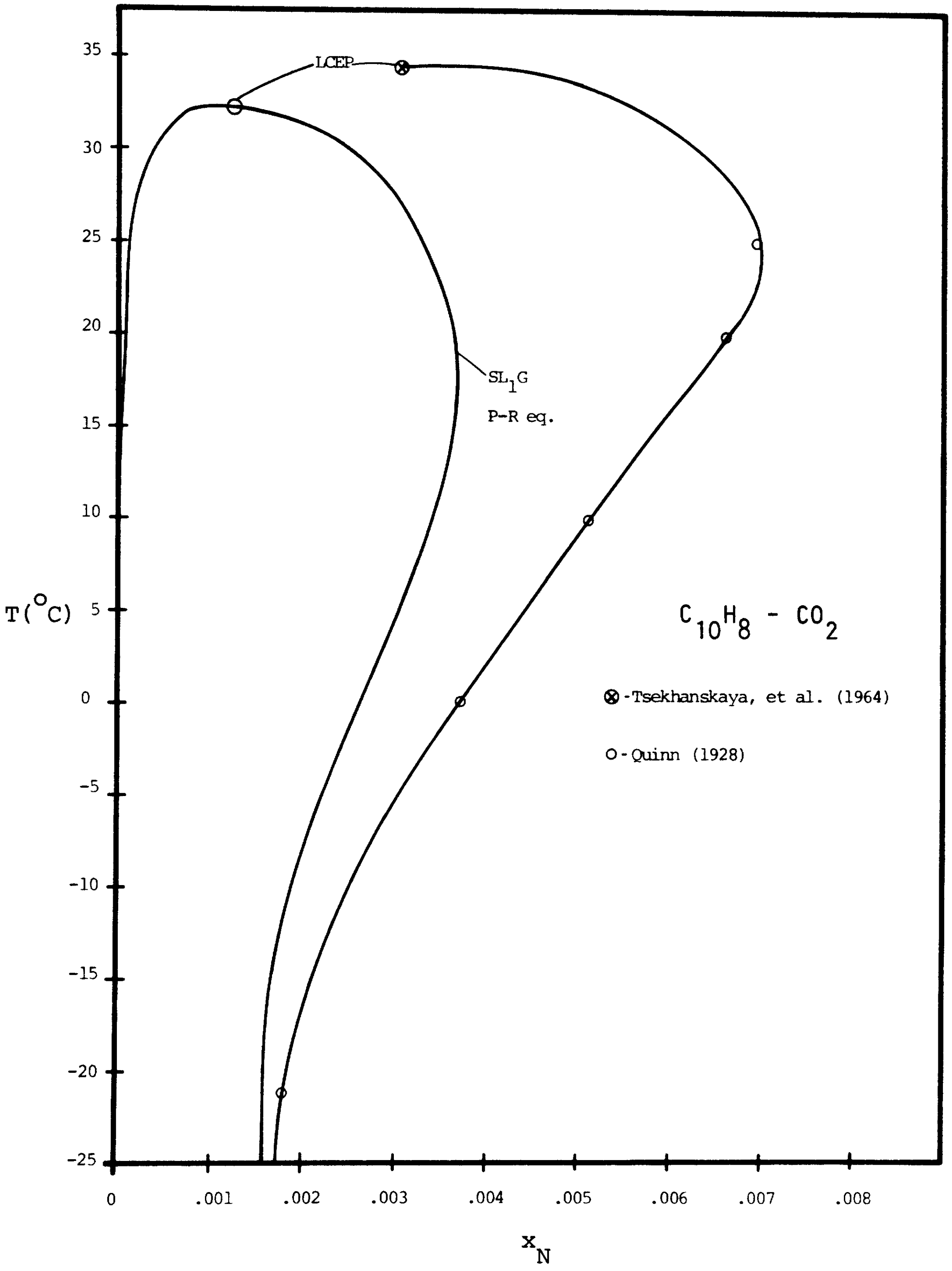

Figure 6.14. The T-x projection of the SLG region.

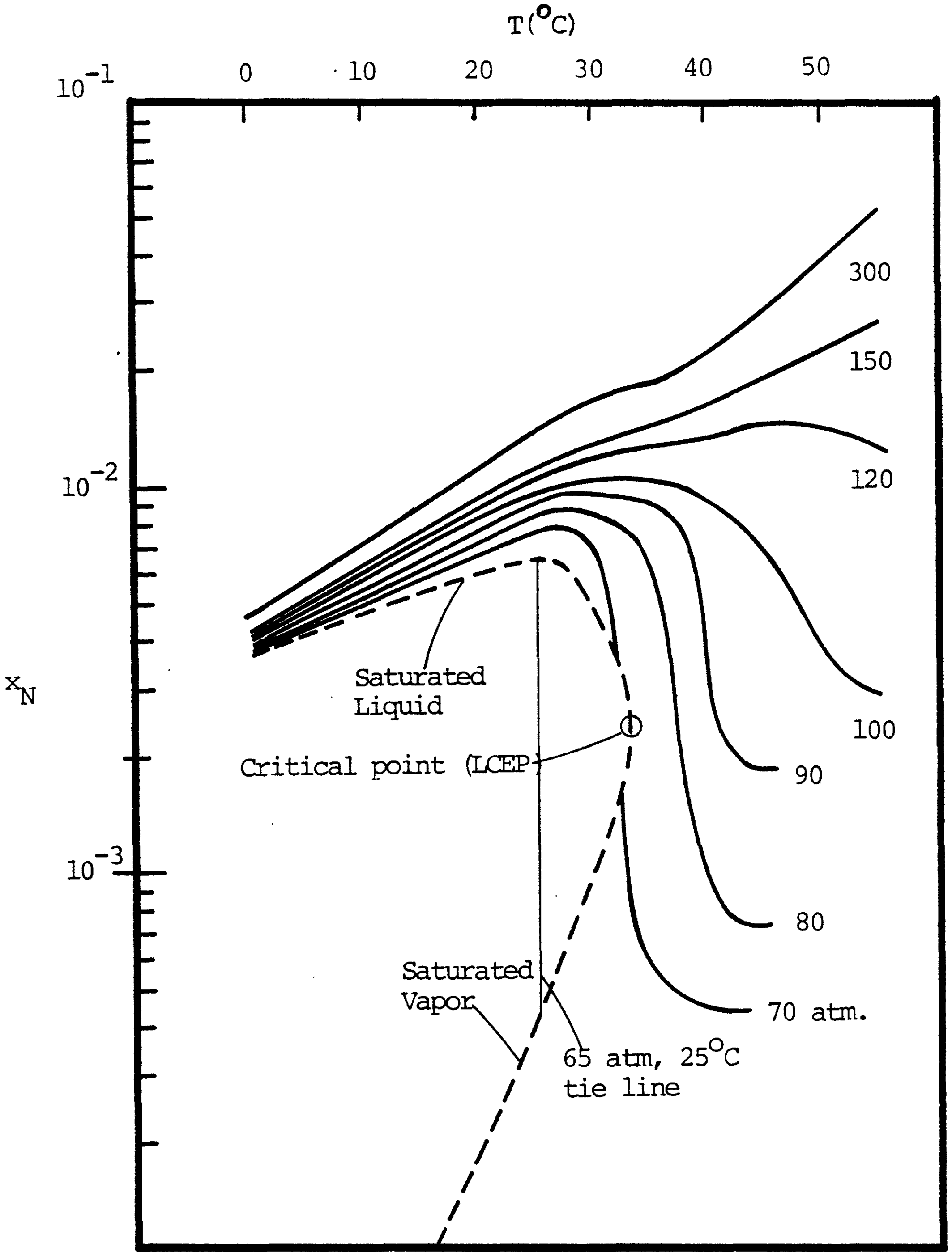

Figure 6.15. The solubility map for the naphthalene (N) - carbon dioxide system. Isobars indicate the mole fraction of naphthalene in solution. The dashed line corresponds to a three-phase solid-liquid-vapor equilibrium. This equilibrium terminates at LCEP, the lower critical end point.

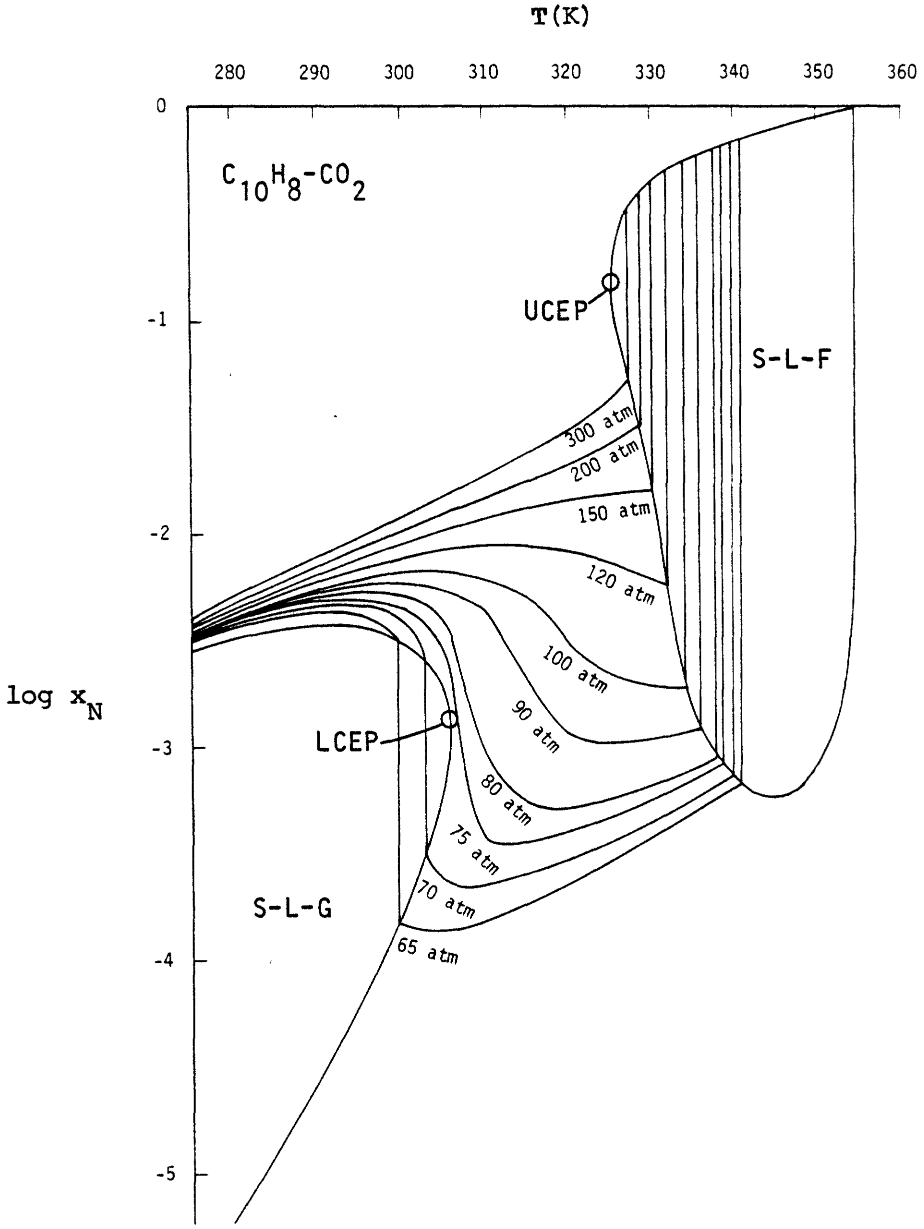

Figure 6.16. The predicted solubility map for naphthalene - CO_2.

predicted by the P-R equation, with the SLF region and UCEP now appearing. It has already been noted that the UCEP seems to occur in practice at somewhat higher temperatures, and that the solubilities in the SCF region may be off by a factor of 2. It is nevertheless clear that the equation of state gives an excellent qualitative description of the phase behavior in this region. As a further aid to the interpretation of the solubility map, a T-x section at 65 atm has been included in Figure 6.17. Portions of the 65 atm isobar which appear in Figure 6.11 have been denoted by the heavy line. Figure 6.17 also corresponds to a horizontal plane at 65 atm in Figure 6.2a.

Recently, McHugh and Paulaitis (1980) have experimentally determined naphthalene solubilities in (or near) the SCF region at 60.4^{O}C and 64.9^{O}C and estimated the coordinates of the UCEP. Their data, and its comparison with the P-R predictions for δ_{12}=0.11, is shown in Figure 6.18. In both cases the predicted solubilities are too high, with large errors when the equation of state predicts a phase change. The data at 64.9^{O}C is particularly interesting, as the temperature is high enough to intersect the SLF line at the pressures studied. The solubility jump, occurring between 230 and 236 atm, still falls significantly short of the predicted solubility level. A possible reason for this discrepancy will be considered shortly. In any event, the data allows estimation of the coordinates of the upper

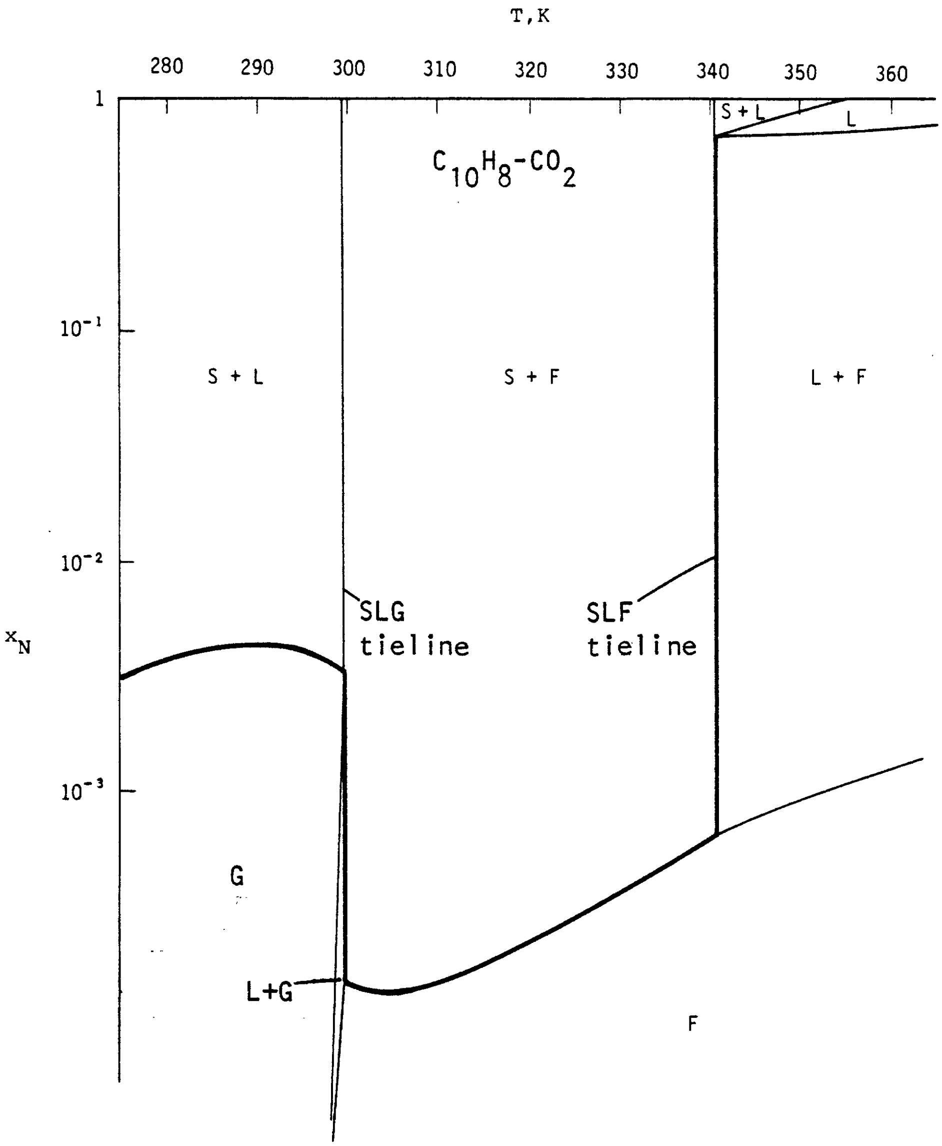

Figure 6.17. A T-x section at 65 atm. Phase equilibrium lines which appear as the isobar in Figure 6.16 have been accentuated.

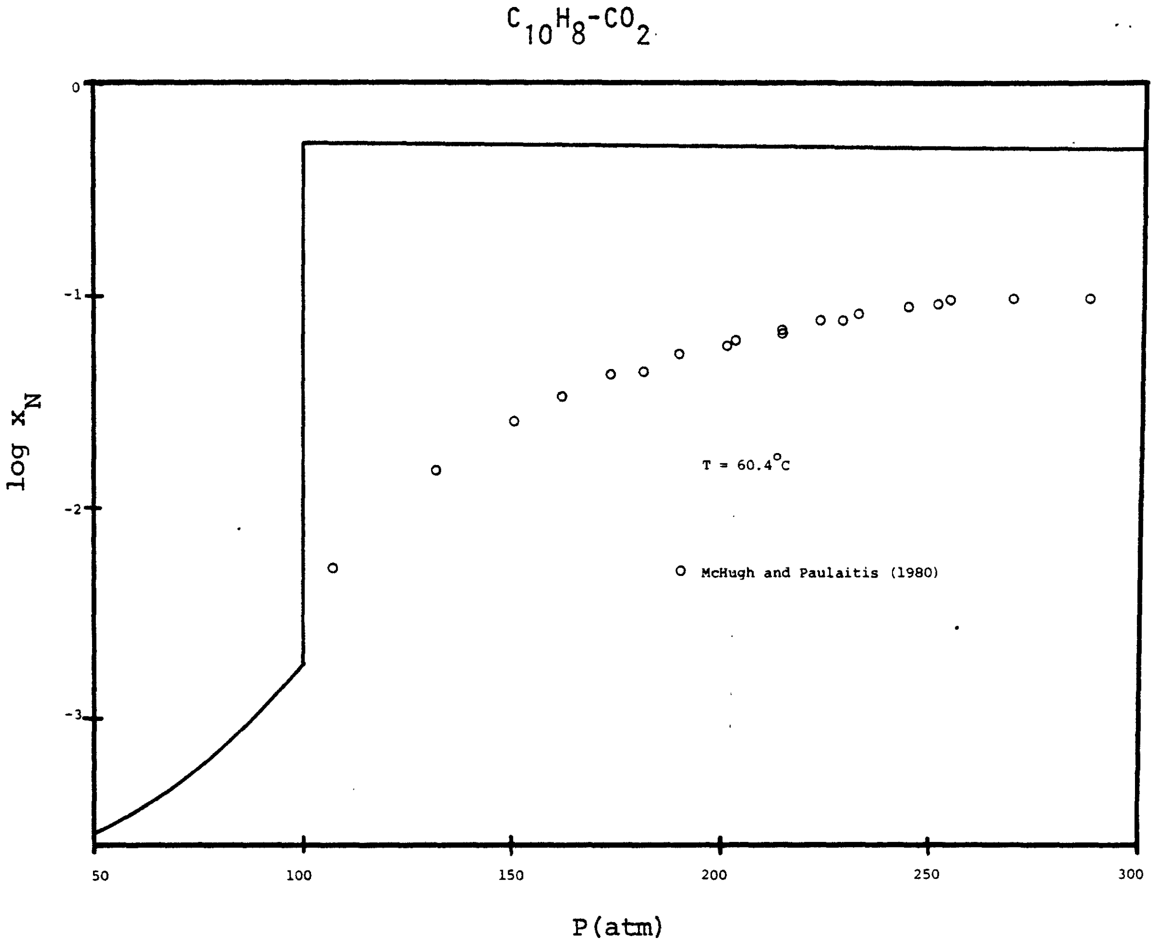

Figure 6.18a. The solubility of naphthalene in CO_2 at 60.4°C. For the predicted curve, δ_{12}= 0.11.

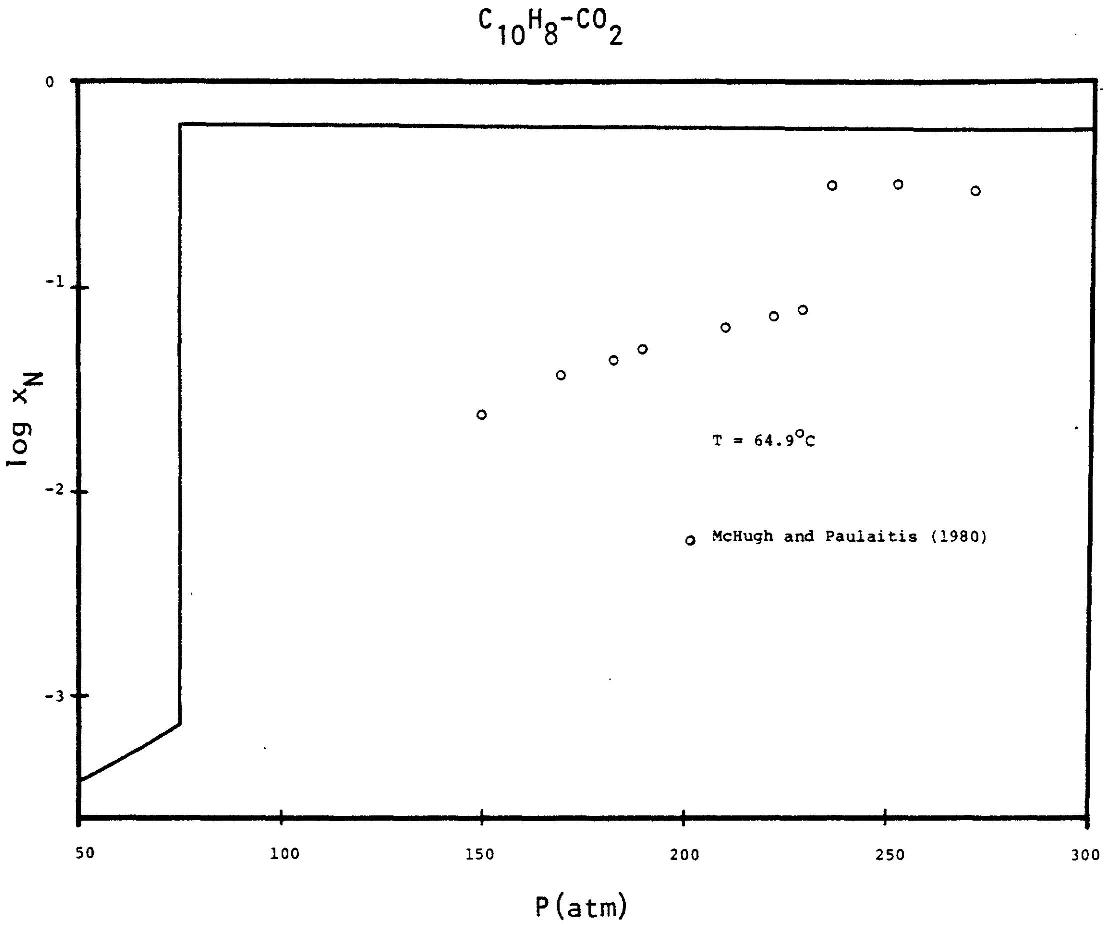

Figure 6.18b. The solubility of naphthalene in CO_2 at 64.9°C. For the predicted curve, δ_{12}= 0.11.

critical end point. Since a solubility jump was not observed at 60.4 °C, but was at 64.9 °C, the UCEP must lie between these two temperatures (assuming that the UCEP falls below 290 atm, the highest pressure investigated). Since Büchner (1906a) has observed the formation of a liquid phase in the presence of solid and vapor at 64 °C, the estimate should actually fall below this temperature. McHugh and Paulaitis' estimate of the UCEP temperature is shown in Table 6.2, which compares calculated and experimental critical end points. These authors have also estimated the UCEP pressure on the basis of the shape of the solubility isotherms. This method can only provide a very rough estimate. It is seen in Table 6.2 that the estimated UCEP composition agrees well with the calculated value, in marked contrast to the temperature, and especially the pressure, coördinates. The situation at the LCEP is just the opposite, with reasonable agreement between pressure and temperature and a predicted composition 2.5 times too small.

Up to this point, it has been presumed that the experimental data available represent true stable equilibrium conditions. There is little reason to question this assumption at the lower temperatures, where agreement between prediction and experiment is relatively satisfactory. At 55 °C and above, however, when the equation of state predicts a phase change, there are some grounds for contending that the calculated values may be closer to the truth than at

Table 6.2

Naphthalene - Carbon Dioxide Critical End Points

	T(°C)	P(atm)	$C_{10}H_8$	T(°C)	P(atm)	$C_{10}H_8$
Experimental	34.5^a	78.5^b	0.0031^c	63^d	240^d	0.16^d
P-R, δ_{12}= 0.11	32.5	74.5	0.0012	52.1	682	0.149

a - Büchner (1906a) and Tsekhanskaya, et al. (1962).

b - Estimated from data of Tsekhanskaya, et al. (1966).

c - Tsekhanskaya, et al. (1962).

d - Estimate of McHugh and Paulaitis (1980).

first appears. A comparison of Figure 6.9a (66.8°C, 340 K) and 6.13c (55°C, 328 K), which give qualitatively identical P-x sections, shows that the solubility jump corresponds to the three-phase SLF line, and that Figure 6.13c is not a complete picture. Figure 6.19 shows again the predicted and experimental solubilities for cases where the P-R equation gives a solubility jump. Now, however, all solid-fluid binodals are included, as well as the stable fluid-fluid binodals.

Consider Figure 6.19a, at 55°C, ignoring for the moment the L+F equilibrium. It is seen that the metastable S+F solution matches the data quite well, even at the highest pressure of 320 atm. At 60.4°C (Figure 6.19b) and 64.9°C (Figure 6.19c), on the other hand, the metastable S+F line does not extend to high enough pressures to match the data. It is nonetheless plausible, given the limited accuracy of the P-R equation of state, that the experimental points do in actuality represent metastable, subsaturated S+F equilibrium. The likelihood of the existence of such metastable states is uncertain, but it should be pointed out that examples of metastable supersaturated solutions are quite common.

Some evidence for the existence of metastable equilibrium may be supplied by the solubility jump observed at 64.9°C. McHugh and Paulaitis (1980) indicate that considerable uncertainty was involved in the determination of

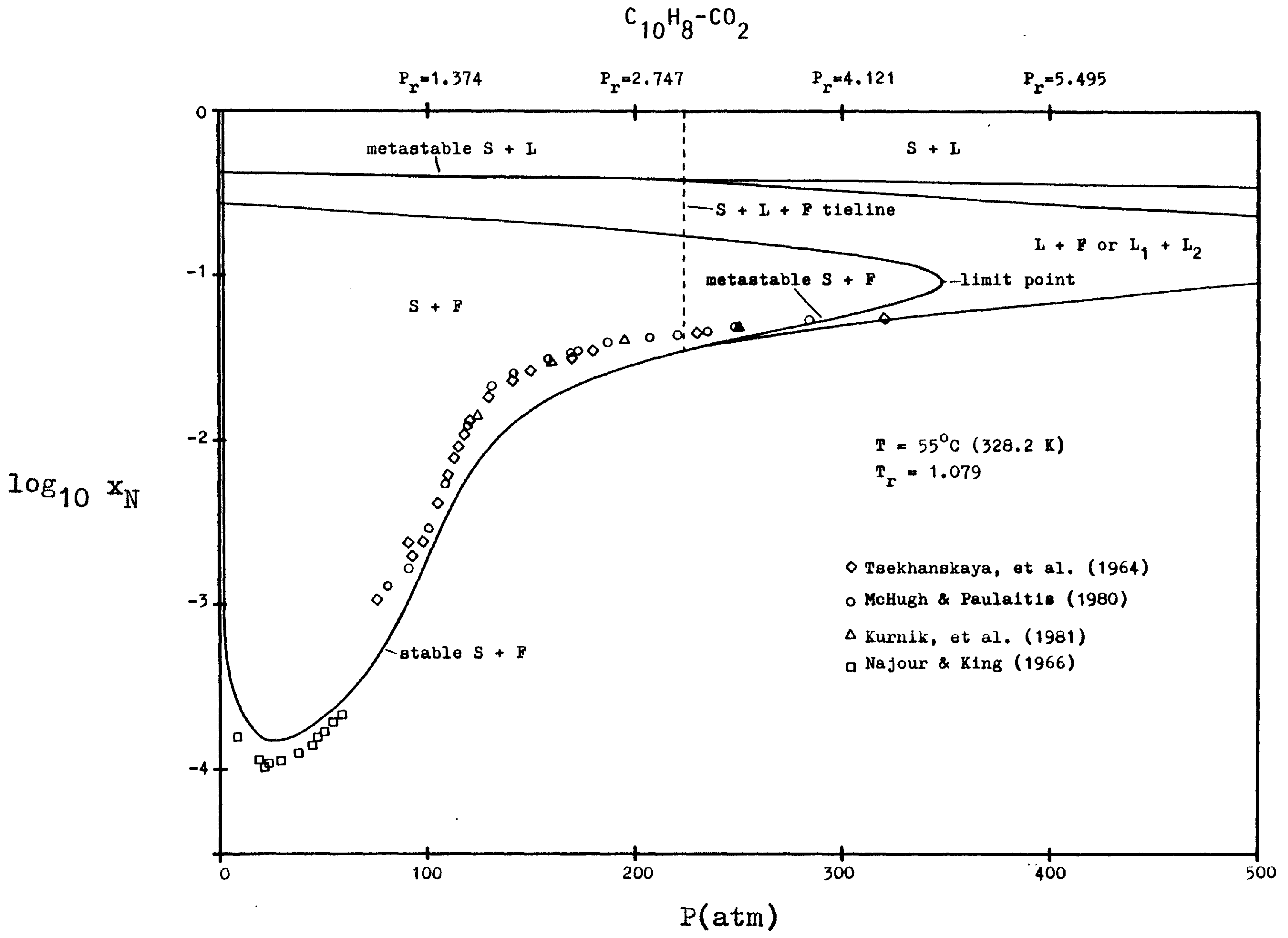

Figure 6.19a. The solubility of naphthalene in CO_2 at 55°C. All predicted solid-fluid binodals, and the stable liquid-fluid binodals, are shown.

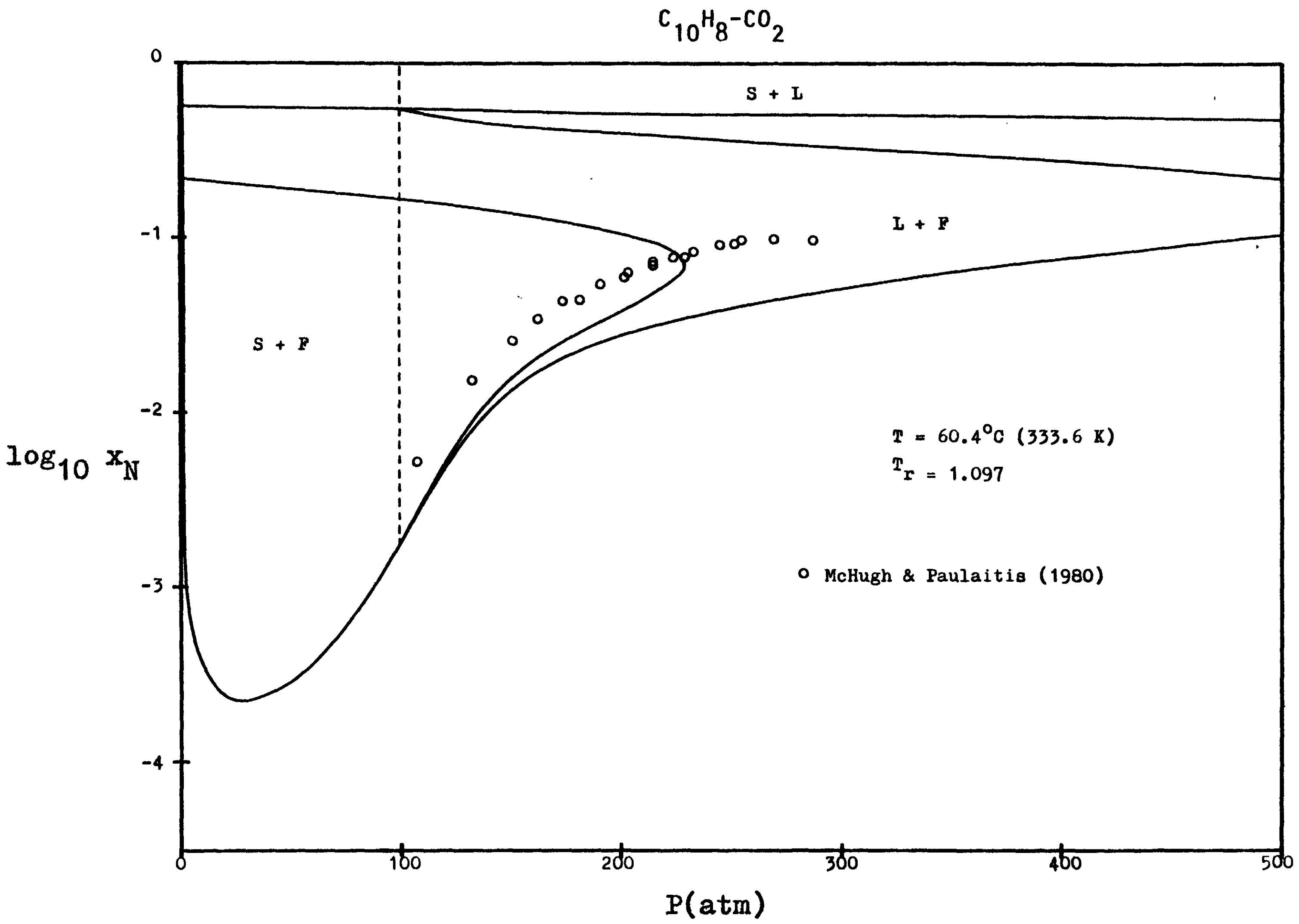

Figure 6.19b. The solubility of naphthalene in CO_2 at 60.4°C.

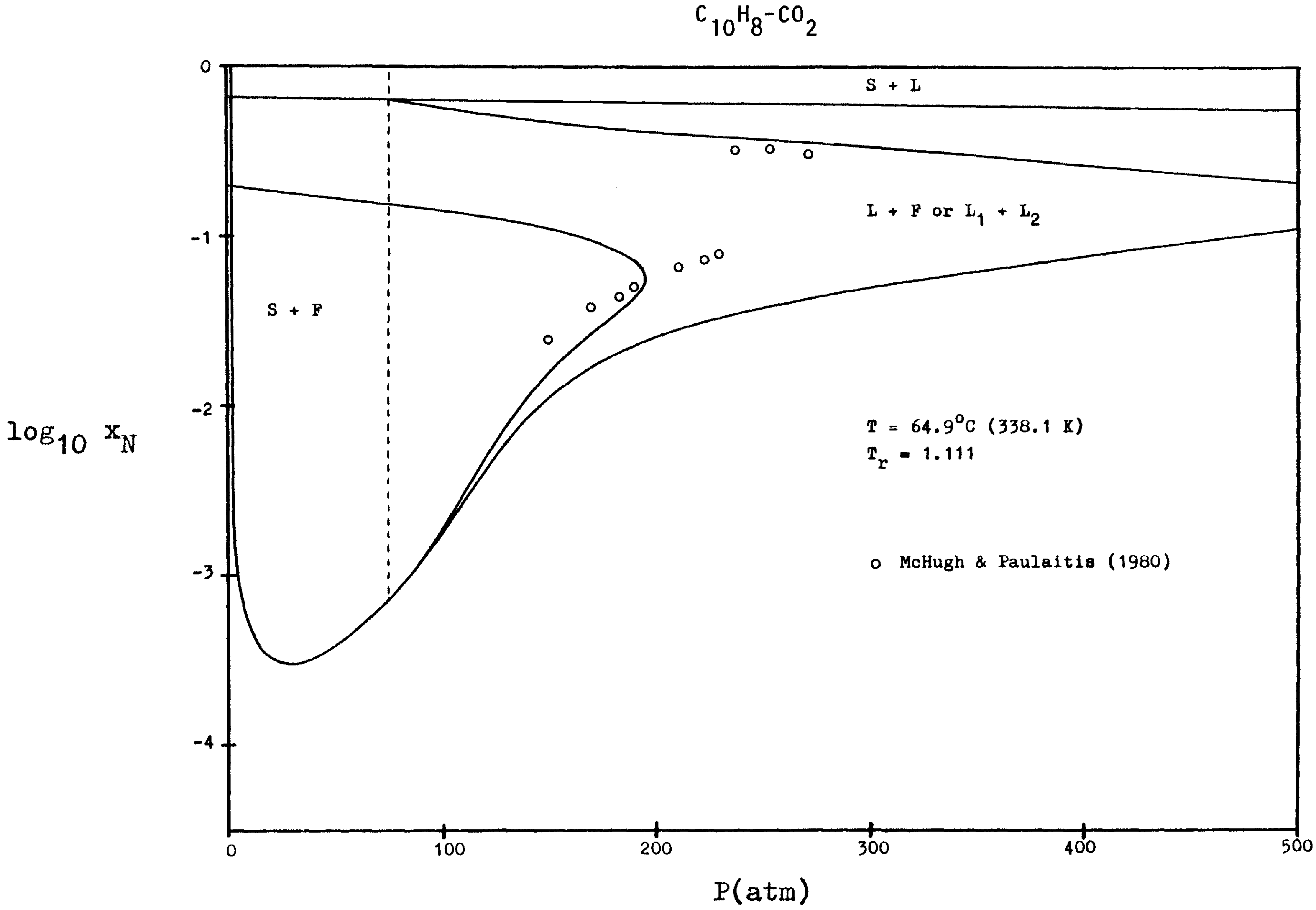

Figure 6.19c. The solubility of naphthalene in CO_2 at 64.9°C.

the solubility points at pressures above the solubility jump. One possible explanation of this scattering is that more than one phase was present in the CO_2 stream being measured. It is easiest to imagine that the three-phase pressure occurs between 230 and 236 atm, and that the scattered measurements represent the combined solubility of naphthalene in a stable liquid and a metastable fluid phase. The proportion of these phases in the CO_2 stream would be variable. For this reason, McHugh and Paulaitis have chosen the maximum of the solubilities obtained at a particular pressure as representative of the true liquid phase solubility. If metastable fluid was still present in these cases, however, the true liquid solubility is actually higher than the reported values, and closer to the predicted values.

The existence of metastable phases in this system could be readily ascertained by approaching the SLF line from pressures above the limit point (i.e., 400 atm or more). The experiments of Figure 6.19 were most likely carried out entirely below the limit point, as 320 atm was the highest pressure attained. In light of the uncertainty in the experimentally measured solubility jump, the question of the actual UCEP temperature and pressure must be considered unresolved until more data becomes available. Most probably they lie somewhere between the experimental estimates and the predicted coordinates.

One other region of the $C_{10}H_8$ - CO_2 phase diagram has been experimentally investigated. Najour and King (1966) have taken measurements at 9 temperatures from 24°C to 73° C, with pressures ranging between 2 and 60 atm, yielding what might be called compressed gas solubilities (some of this data appeared in Figure 6.19a). A sampling of their results in comparison with predictions is given in Figures 6.20a, b, and c. Although the interaction parameter of 0.11 was chosen for compatibility with the SCF region data, agreement is actually better in the compressed gas region. Predictions are well within a factor of two in all cases (note the use of a linear concentration axis). Also shown in the figures are the solubilities which would be found in the ideal case, when Dalton's law would apply, i.e.,

$$x_N = \frac{P_N^{sub}}{P} \tag{5.1}$$

Deviations from the ideal case are significant even below 10 atm.

This chapter has indicated that the Peng-Robinson equation, with a constant binary interaction parameter, gives at best semiquantitative solubilities in the supercritical fluid region of naphthalene - CO_2. If the interaction parameter is allowed to vary with temperature, a review of Figure 6.13 shows that predicted solubilities may be kept within approximately a factor of 2. A pressure functionality

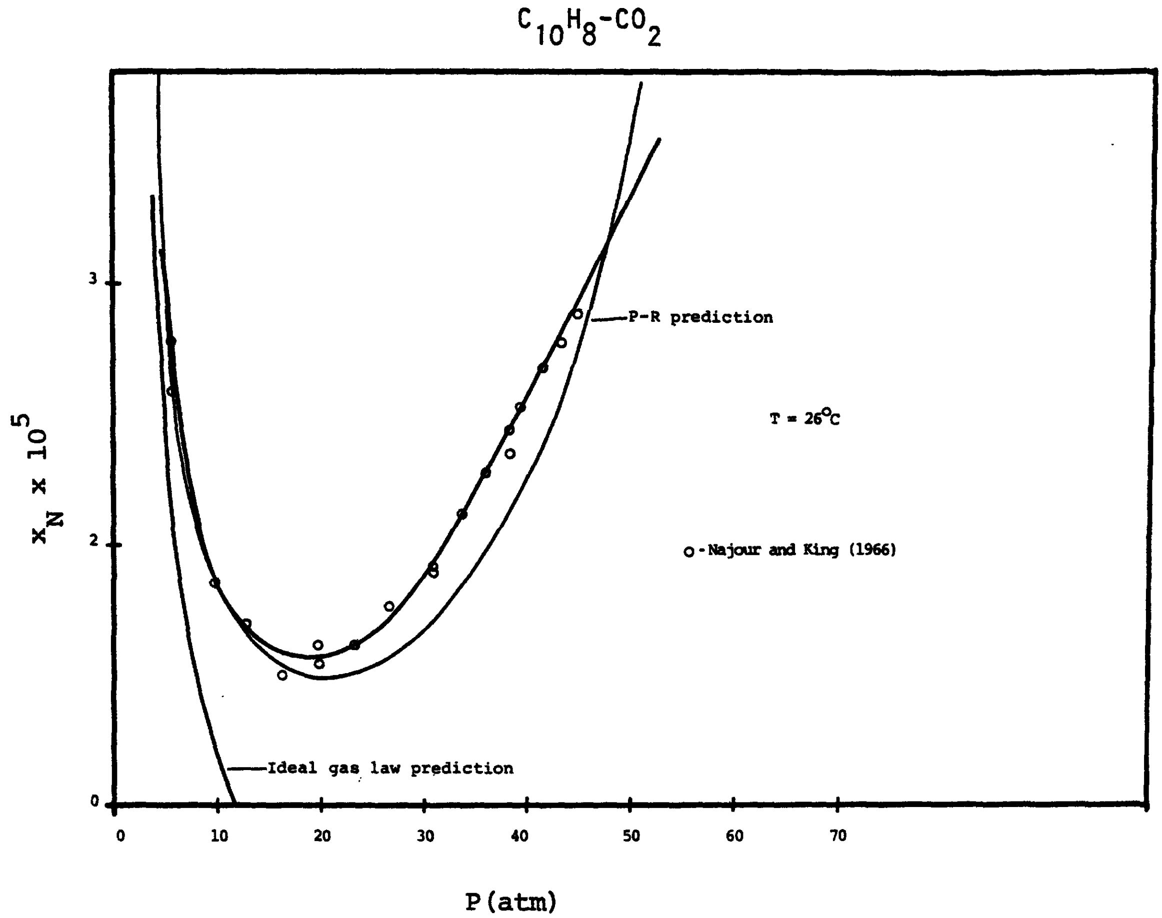

Figure 6.20a. The solubility of naphthalene in CO_2 at 26°C.

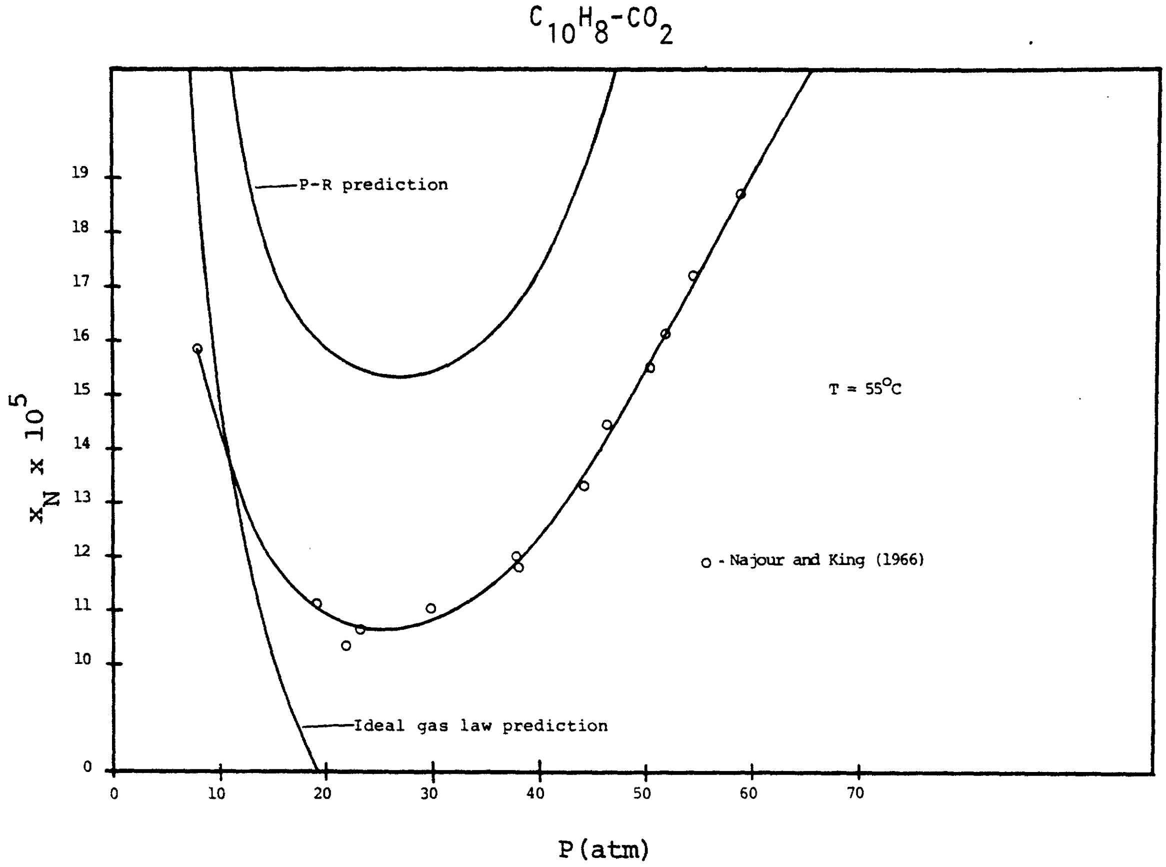

Figure 6.20b. The solubility of naphthalene in CO_2 at 55°C.

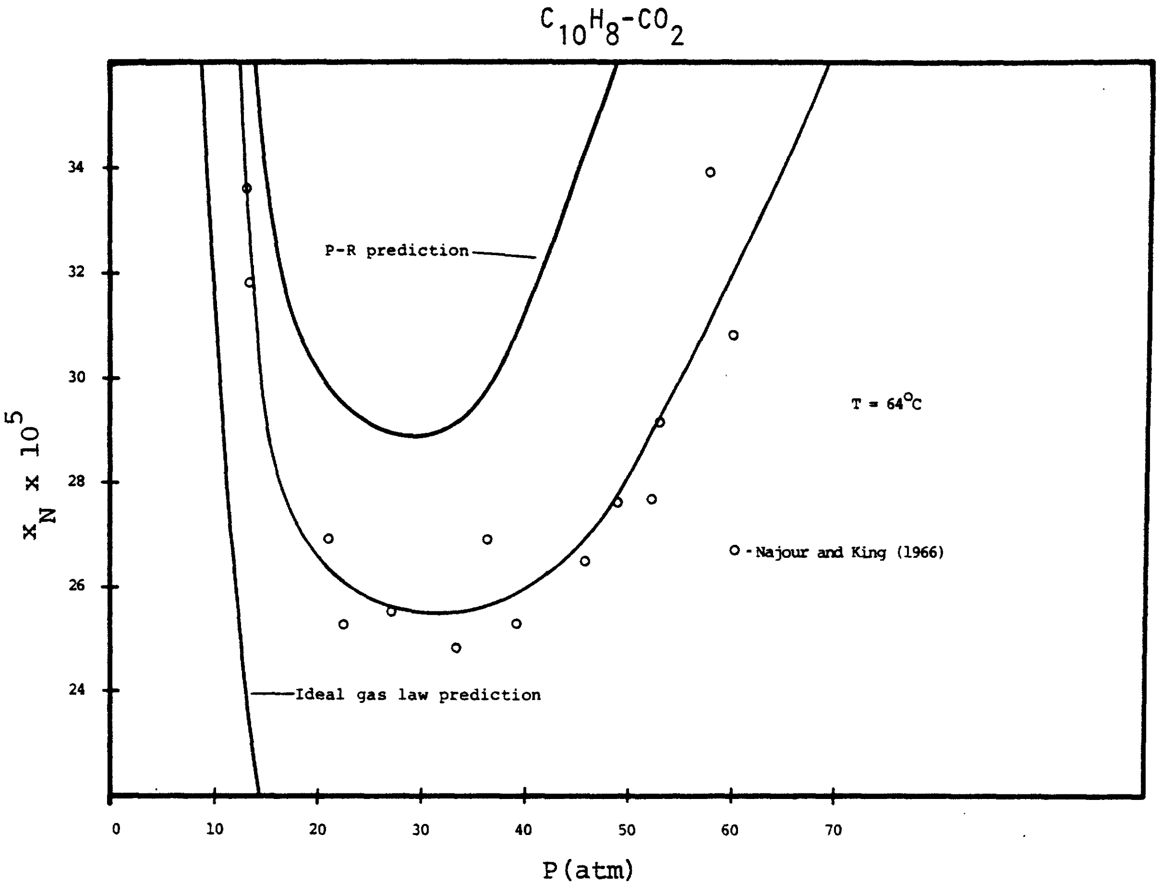

Figure 6.20c. The solubility of naphthalene in CO_2 at 64°C.

of δ_{12} would be necessary to obtain quantitative predictions. Kurnik (1981) has reported similar results using the P-R equation.

More importantly, though, the equation of state has allowed the construction of what is believed to be a qualitatively correct P-T-x space for the $C_{10}H_8$ - CO_2 system. Knowledge of the overall P-T-x behavior is of substantial value in process design. The P-T-x diagrams show, for example, that a supercritical fluid extraction process run near the UCEP rather than near the LCEP has the advantage of much higher solute solubilities. The diagrams also suggest that a two-phase extraction process might be desirable (see Figure 6.16). Furthermore, the predicted phase diagrams indicate regions where experimental data must be interpreted with care, and in what regions further data may be necessary.

Chapter 7 The Naphthalene - Ethylene System

A drawback to the modelling of the naphthalene-carbon dioxide system is that data are available over only a small range of pressures and temperatures. A portion of the S-L-F line, and the entire L-F critical locus, fall at some distance from the region which can be used in the determination of the interaction parameter. The only basis for judging the accuracy or qualitative correctness of such extrapolated predictions is by analogy with similar systems. One such system is that of naphthalene-ethylene, for which a fairly complete set of experimental results have been reported. These include accurate measurements of the critical end points, as well as data along the S-L-F line and L-F critical line. For these reasons the naphthalene-ethylene system was chosen for study. Physical constants for naphthalene and ethylene are given in Table 7.1.

In order to gauge the reliability of the naphthalene-CO_2 predictions by the reliability of the naphthalene-C_2H_4 predictions, only data in the supercritical fluid regime were used in the determination of the interaction parameter (as was done with $C_{10}H_8$-CO_2). A value of $\delta_{12}=0$ was found to give reasonably good fit, as shown in Figure 7.1. The behavior is essentially the same as in Figures 6.13 and 6.19 which gave the analogous plots for $C_{10}H_8$ - CO_2. In that system, a

Table 7.1

Physical Constants of Naphthalene and Ethylene

	$C_{10}H_8$	CO_2
T_c(K)	748.4	282.4
P_c(atm)	40.0	49.7
ω(acentric factor)	0.302	0.085
Melting Point (K)	353.3	-

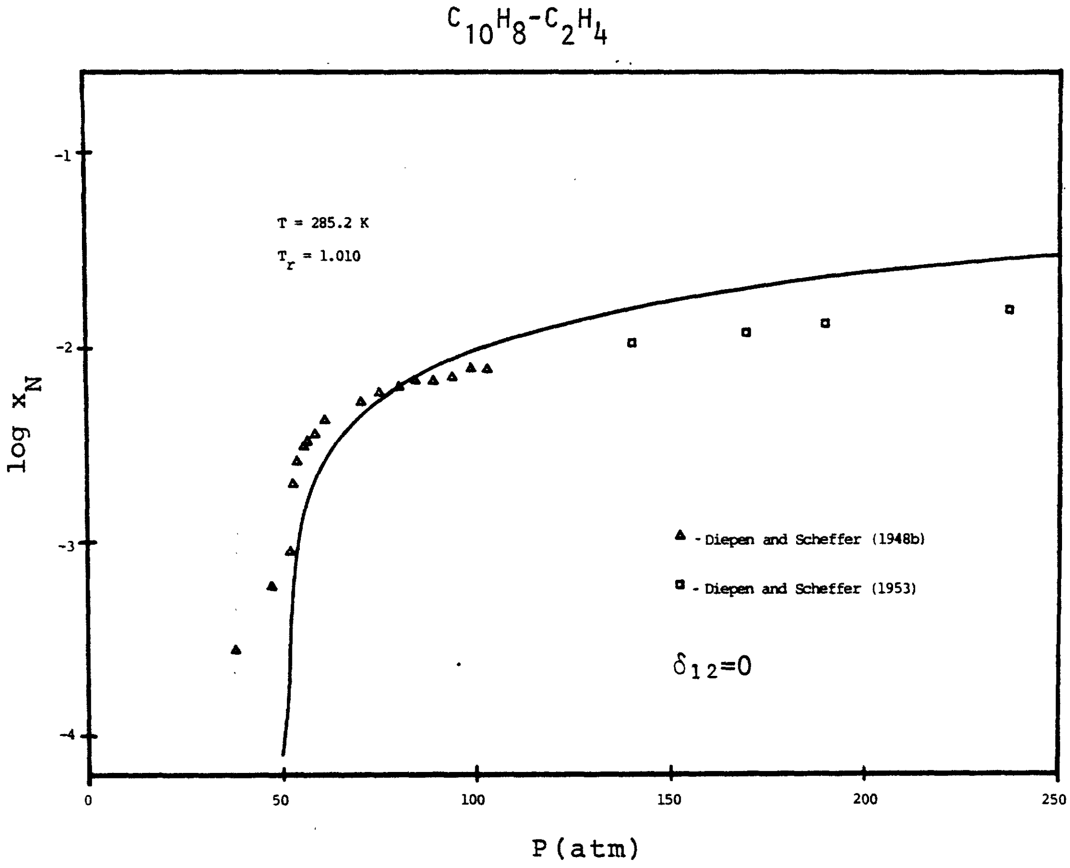

Figure 7.1a. The solubility of naphthalene in ethylene at 285.2 K (12°C). For the predicted curve, δ_{12}= 0. The reduced temperature in this and all following figures is given with respect to ethylene.

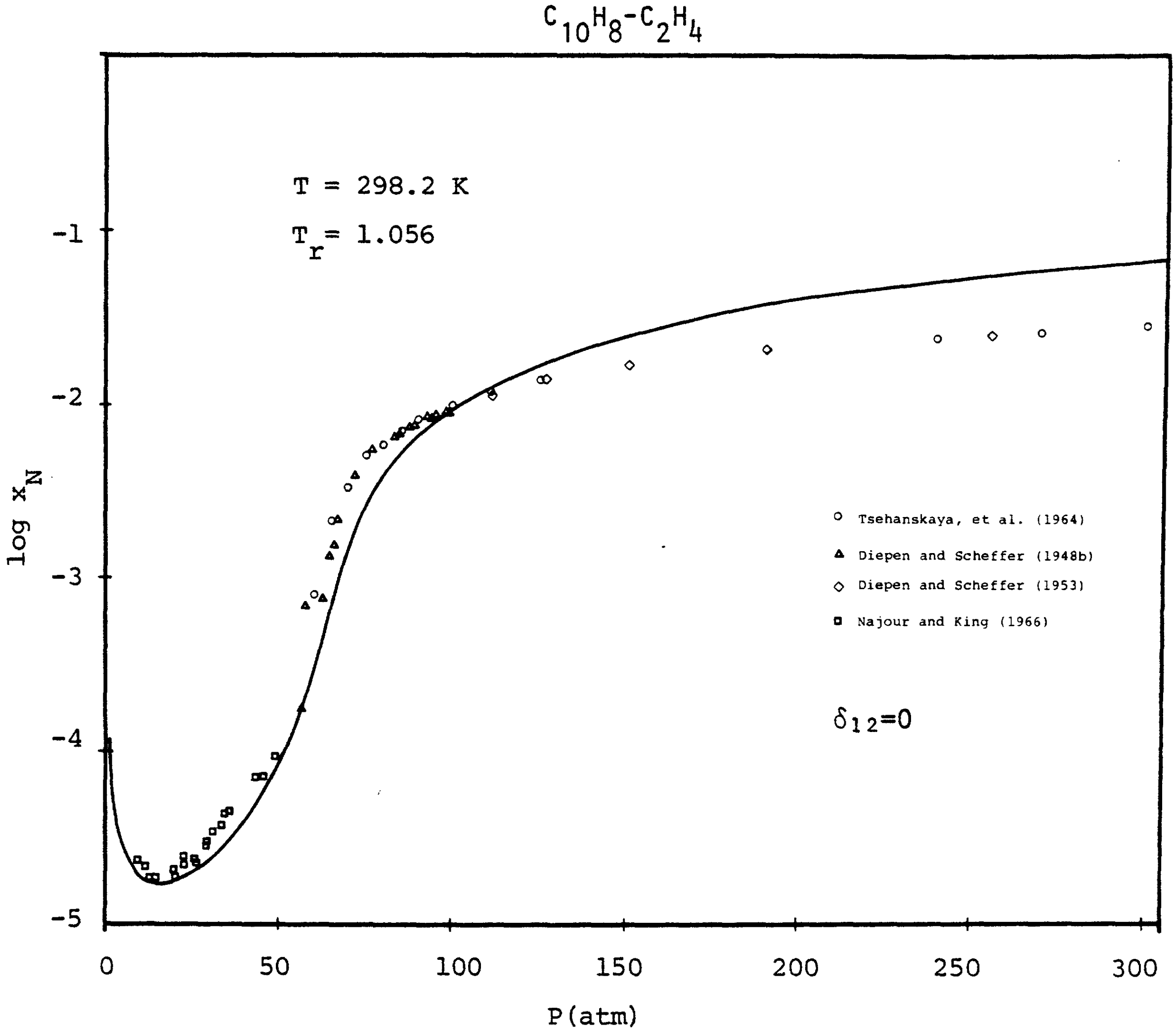

Figure 7.1b. The solubility of naphthalene in ethylene at 298.2 K (25°C).

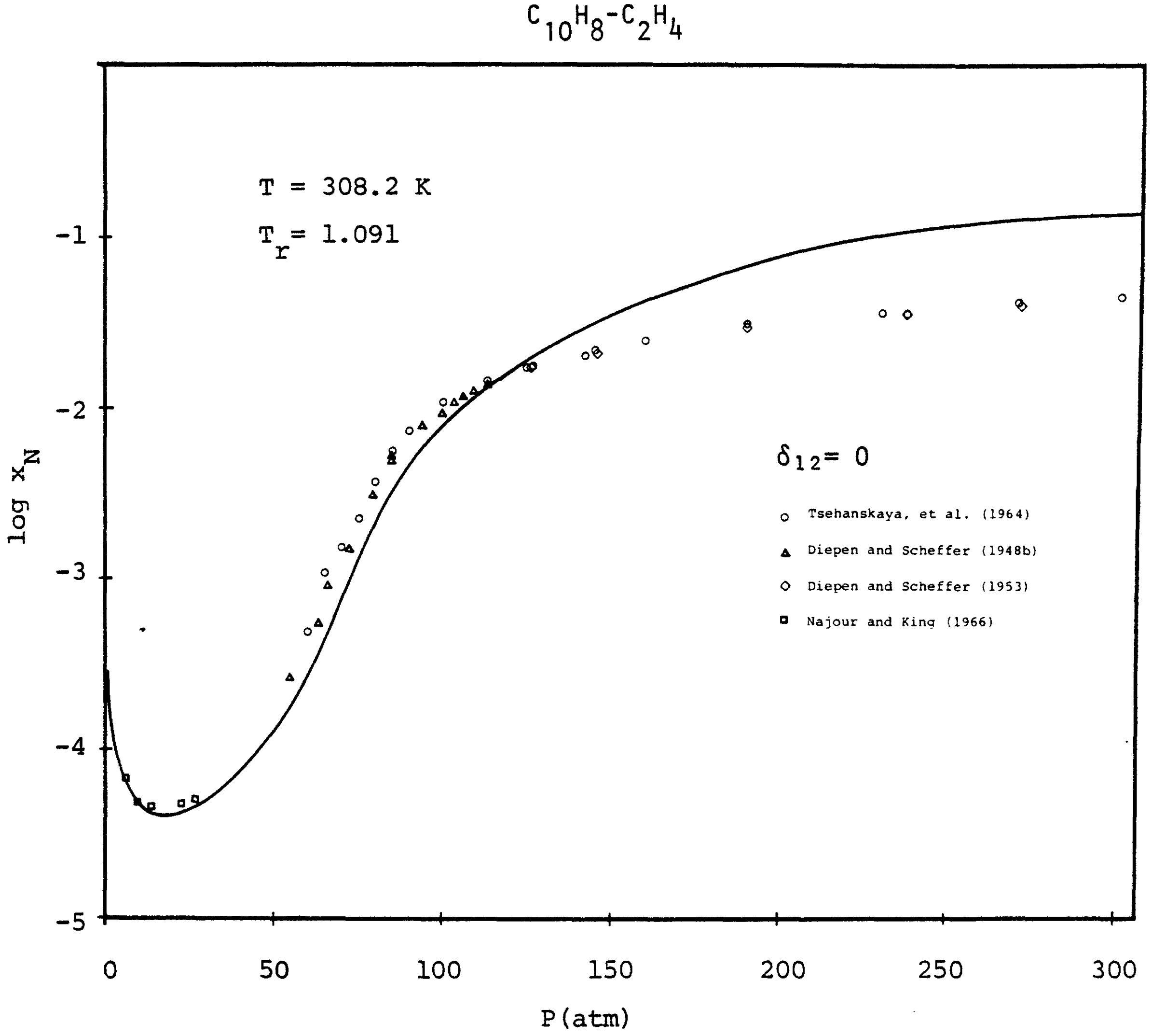

Figure 7.1c. The solubility of naphthalene in ethylene at 308.2 K (35°C).

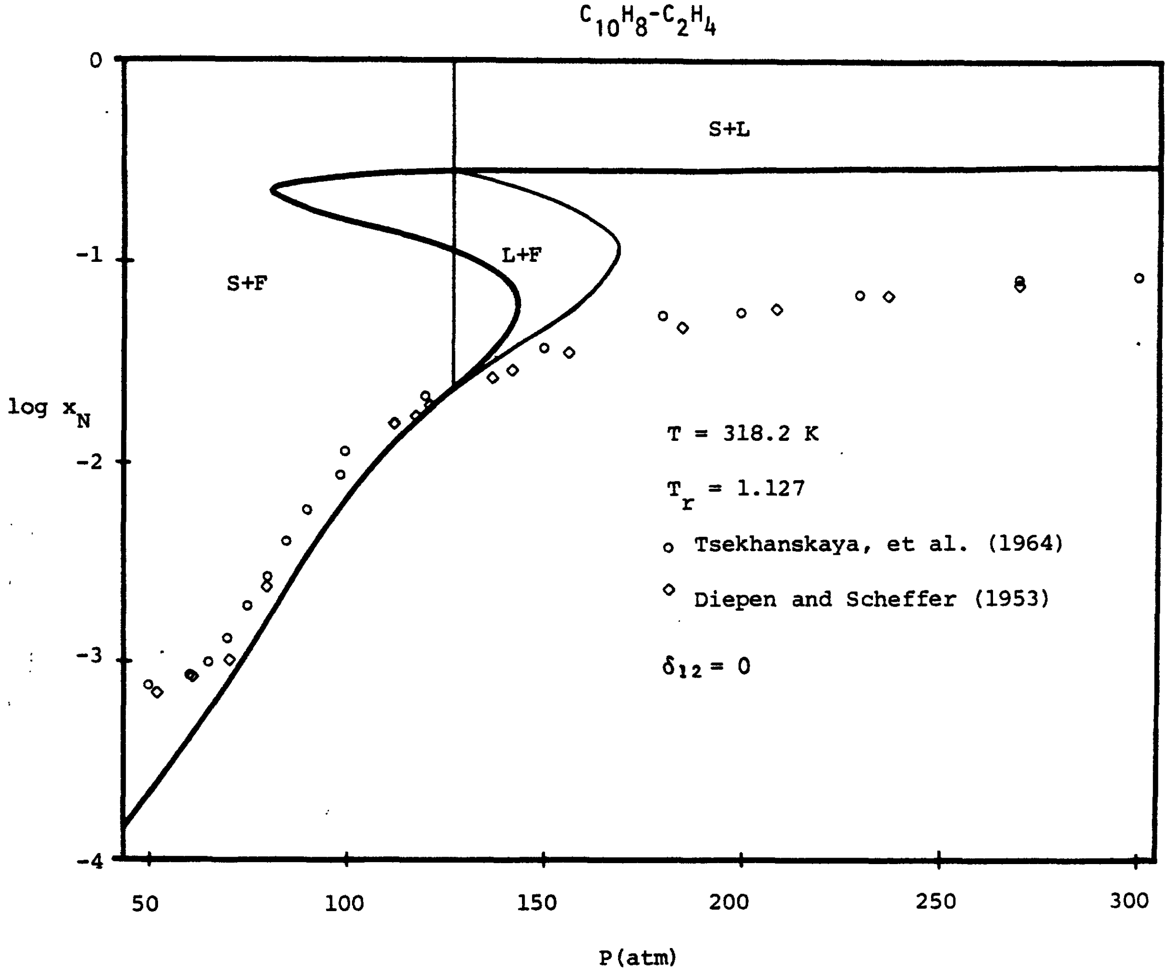

Figure 7.1d. The solubility of naphthalene in ethylene at 318.2 K (45°C). A solubility jump is predicted, so the complete solid-fluid binodal and the stable L+F binodals have been included.

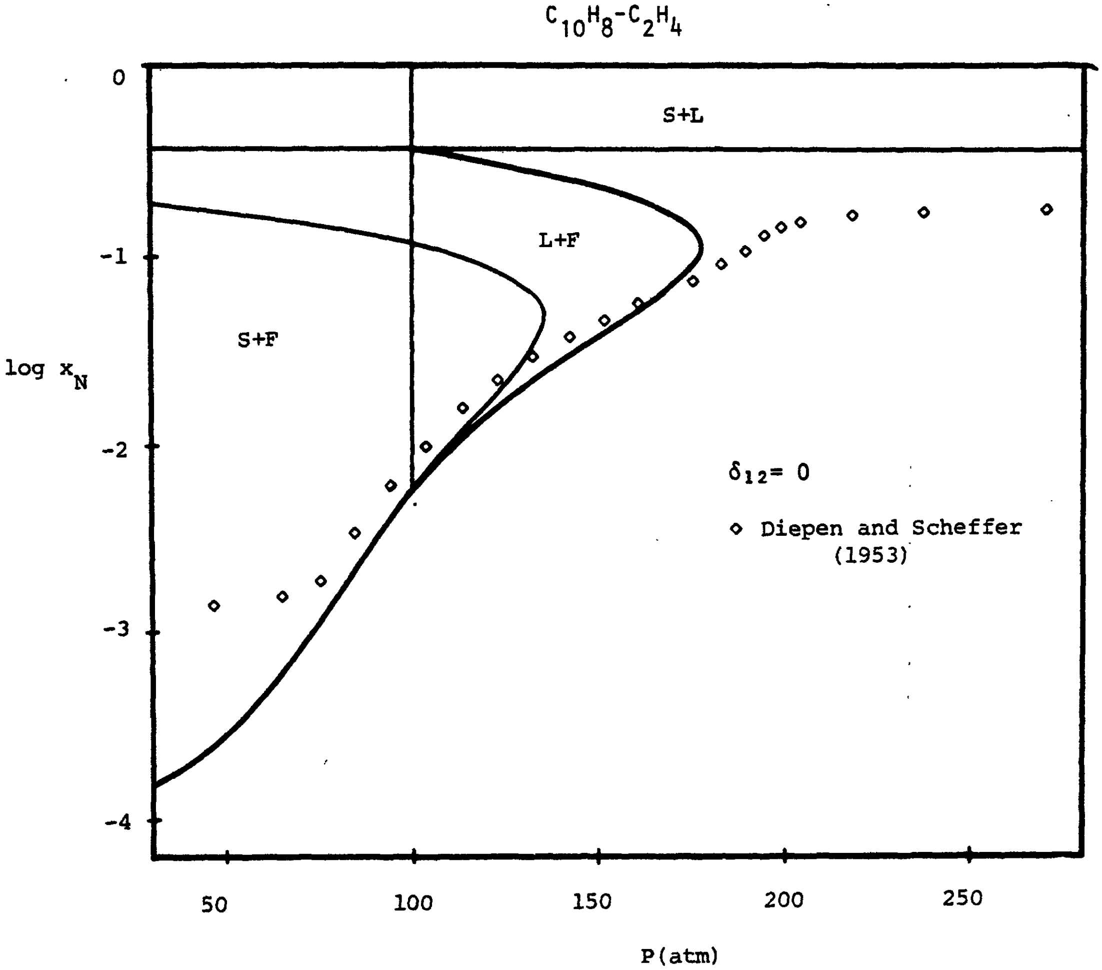

Figure 7.1e. The solubility of naphthalene in ethylene at 323.2 K (50°C). A solubility jump is again predicted at this temperature.

solublity jump was predicted at 55°C. For naphthalene-ethylene a solubility jump is predicted at 45°C, as shown in Figure 7.1d. With respect to ethylene, the data extend to around $P_r=6$, as compared to a P_r of about 4 with respect to CO_2 in Figure 6.8. Even with this extensive pressure range, no solubility jump is evidenced by the experimental points, an indication that 45°C is truly below the UCEP temperature.

With δ_{12} set equal to zero, the P-T projections of Figure 7.2 are generated. Qualitative agreement with the experimental phase diagram is quite good over the entire range of temperatures and pressures. The calculated pure component vapor pressure curves for ethylene and naphthalene are indistinguishable from the experimental curves. The calculated fusion line, however, has a steeper slope than it should. Figure 7.2a differs from Figure 6.2a, the naphthalene-CO_2 P-T projection, in that a maximum is predicted in the L-F critical line. As indicated in Chapter 2, such a maximum is by no means universal. Rather, the qualitative correctness of the naphthalene-ethylene critical line speaks in favor of the qualitative correctness of the naphthalene-CO_2 critical line. The L-F critical line is once again shown continuing past its intersection with the S-L-F line at the UCEP. This metastable portion forms a CEP with the metastable L-L-G locus, as depicted in the enlargement, Figure 7.2b. There is a second CEP formed by

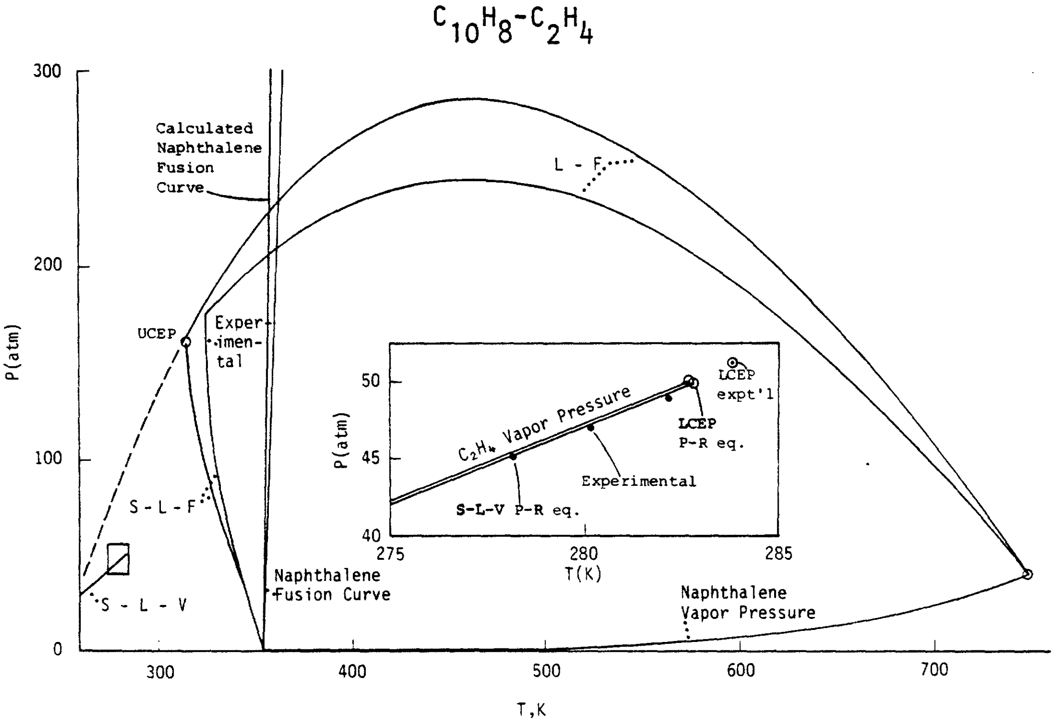

Figure 7.2a. The P-T projection of the naphthalene–ethylene system. The inset shows the region near ethylene's critical point. (See also Figure 7.2b.)

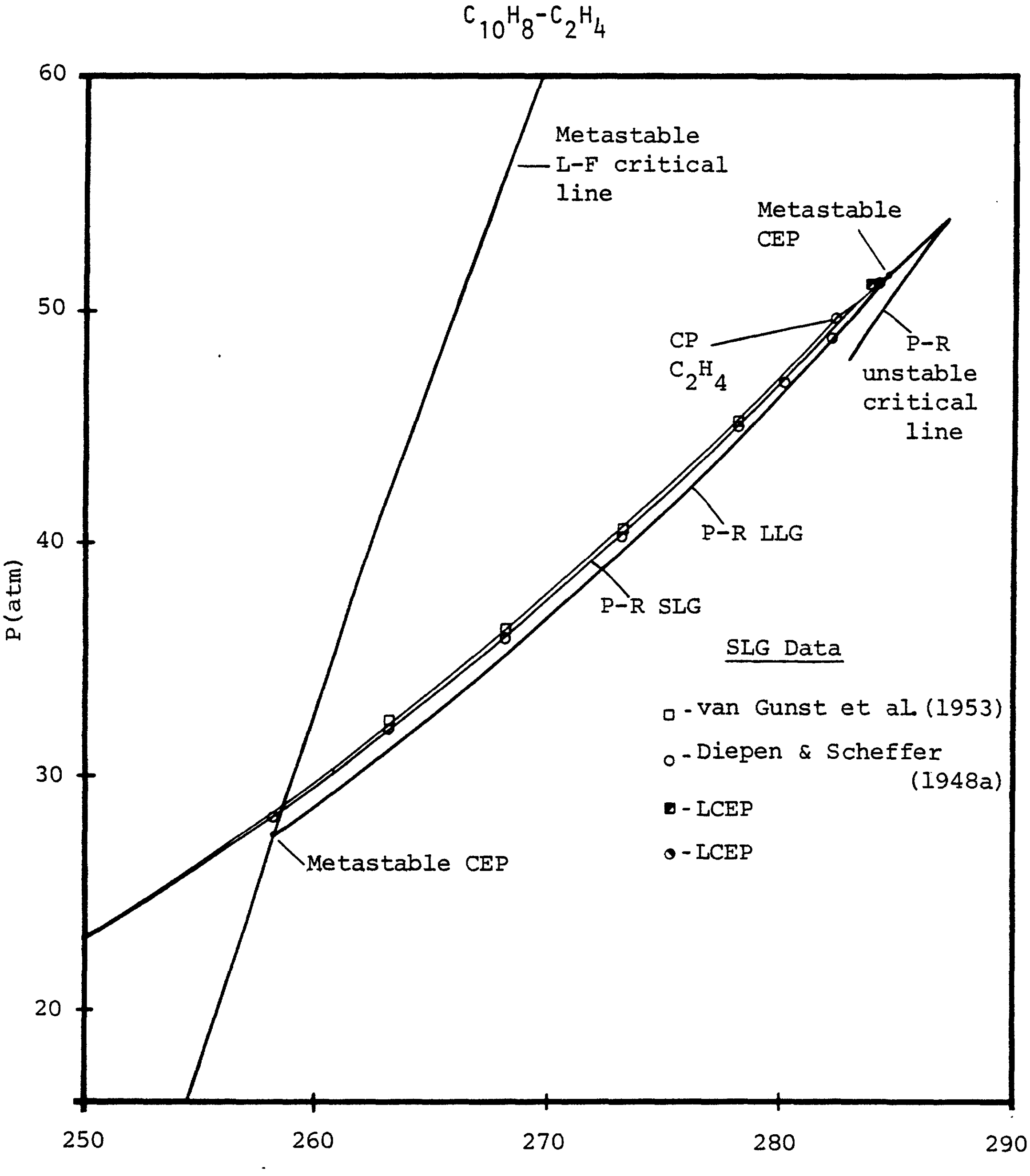

Figure 7.2b. The P-T projection of the naphthalene - ethylene system in the vicinity of ethylene's critical point.

the intersection of the metastable L-L-G locus and the metastable L-G critical line. The figure also shows the generally excellent agreement between calculated and measured S-L-G loci. Note that the S-L-G line is not terminated by the metastable L-F critical line.

A comparison of the stable critical end points for this system is given in Table 7.2. As with naphthalene-CO_2, (Table 6.2), the temperature and pressure coordinates for the LCEP agree quite closely, while the predicted mole fraction is too low, in this instance by a factor of 6 or 7. At the UCEP the predicted temperature is about 20 percent too low, and the predicted naphthalene mole fraction about 35 percent too low. This is similar to what was found for naphthalene-CO_2. The predicted UCEP pressure is only slightly low, which might speak for the reliability of the calculated UCEP pressure in Table 6.2. In that table, however, the calculated UCEP pressure was almost three times the estimated experimental value. This is perhaps due to the steep slopes of the L-F critical line and the S-L-F line in the naphthalene-CO_2 P-T projection (Figure 6.2a) at temperatures near the UCEP. From a calculational standpoint, an inaccuracy of a few degrees in the predicted UCEP could change the predicted pressure by almost one hundred atmospheres. From an experimental point of view, assuming that a region of steep slopes does indeed exist, it will be detected only by measurements at carefully selected

Table 7.2

Naphthalene - Ethylene Critical End Points

	LCEP			UCEP		
	T(°C)	P(atm)	x_N	T(°C)	P(atm)	x_N
Experimental	10.7[a]	51.2[a]	0.002[a]	52.1[b]	174[b]	0.17[b]
P-R, δ_{12}= 0	10.0	50.4	0.000324	40.7	161.0	0.108

a - van Gunst, et al. (1953)

b - van Welie and Diepen (1961)

temperatures and pressures.

For the naphthalene - C_2H_4 system, van Welie and Diepen have also measured composition coordinates of the S-L-F three phase line and part of the L-F critical locus. This allows the plotting of T-x and P-x projections in addition to the P-T projection just considered. Figure 7.3a shows how these data compare with predictions in the P-x projection. The T-x projection of the S-L-F region and a portion of the L-F critical line are given in Figure 7.3b. The T-x projection of the entire stable L-F crtical line is illustrated in Figure 7.3c. For all three diagrams, the results are best described as semiquantitative. Figures 7.3d and e show the P-x and T-x projections of the S-L-G region, for which no data other than the LCEP is available. As evident from the P-T projection of Figure 7.2b, the LCEP lies at the highest temperature and pressure along the S-L-G locus. Figure 7.3 is to be compared with Figure 6.7, which gives P-x and T-x projections for the naphthalene - CO_2 system. The only major difference between the two figures is in the P-x projections. In contrast to the naphthalene - C_2H_4 L-F critical line, the naphthalene - CO_2 L-F critical line has a sharp bend and thereafter runs very steeply to higher pressures. The S-L-F locus, as a result, must extend to fairly high pressures before it can intersect the critical line at the UCEP.

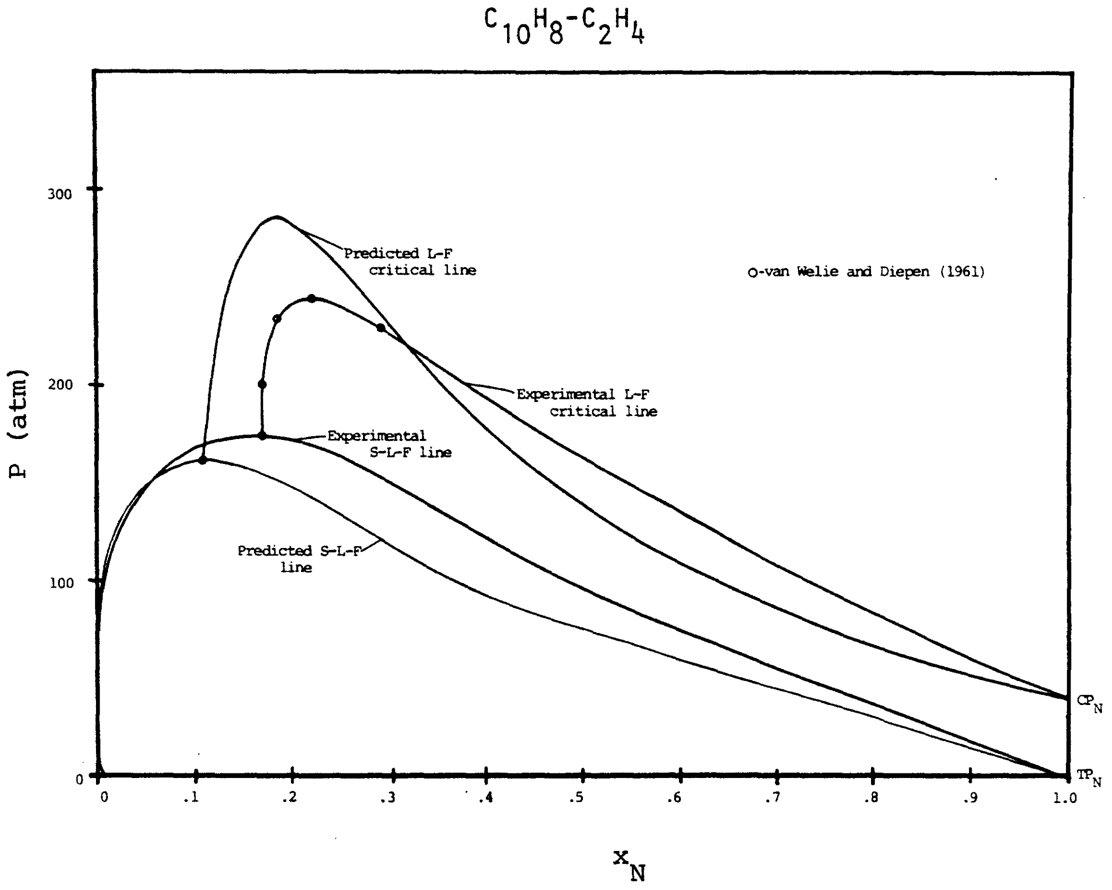

Figure 7.3a. The P-x projection of the upper critical line and the SLF region for naphthalene - ethylene. This diagram is to be compared with Figure 6.12a.

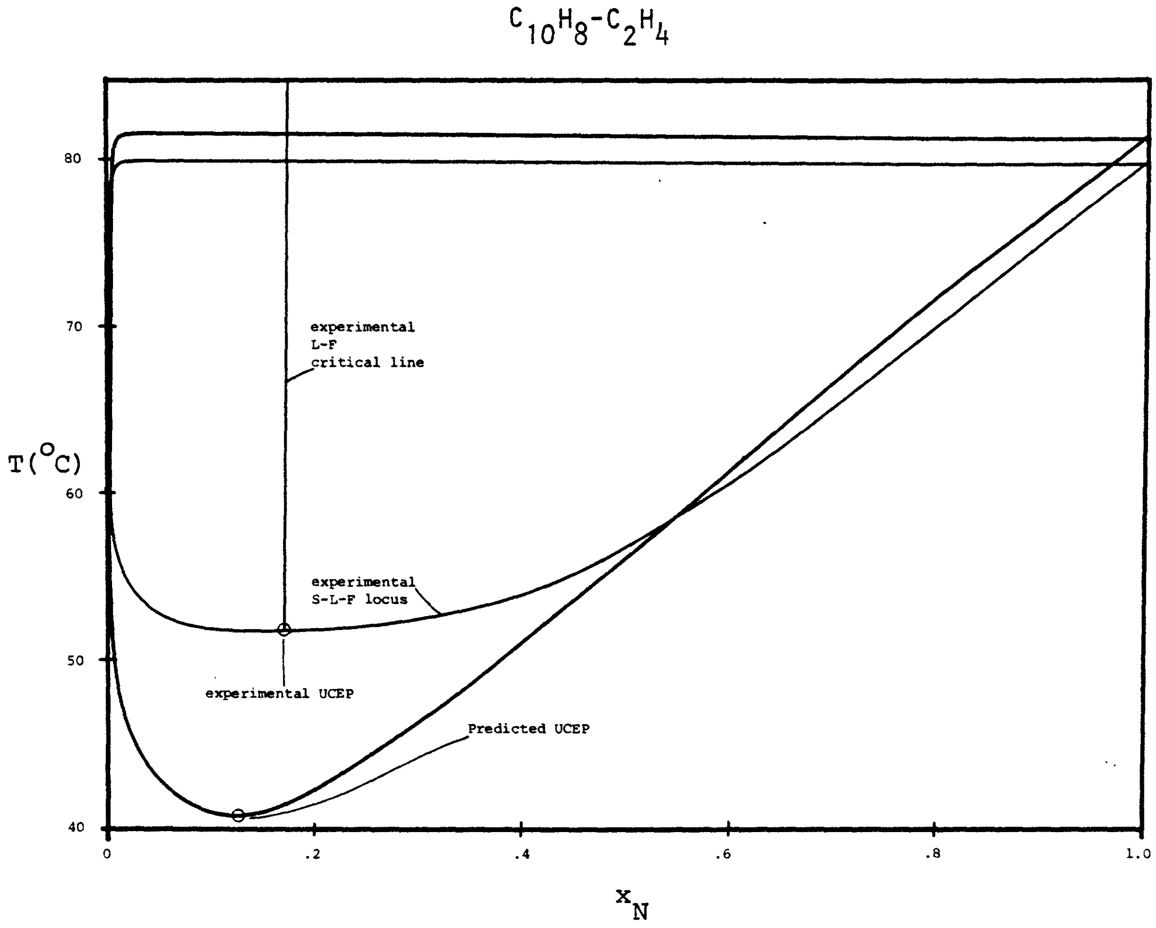

Figure 7.3b. The T-x projection of the SLF region and a portion of the upper critical line for naphthalene - ethylene. This diagram is to be compared with Figure 6.12b.

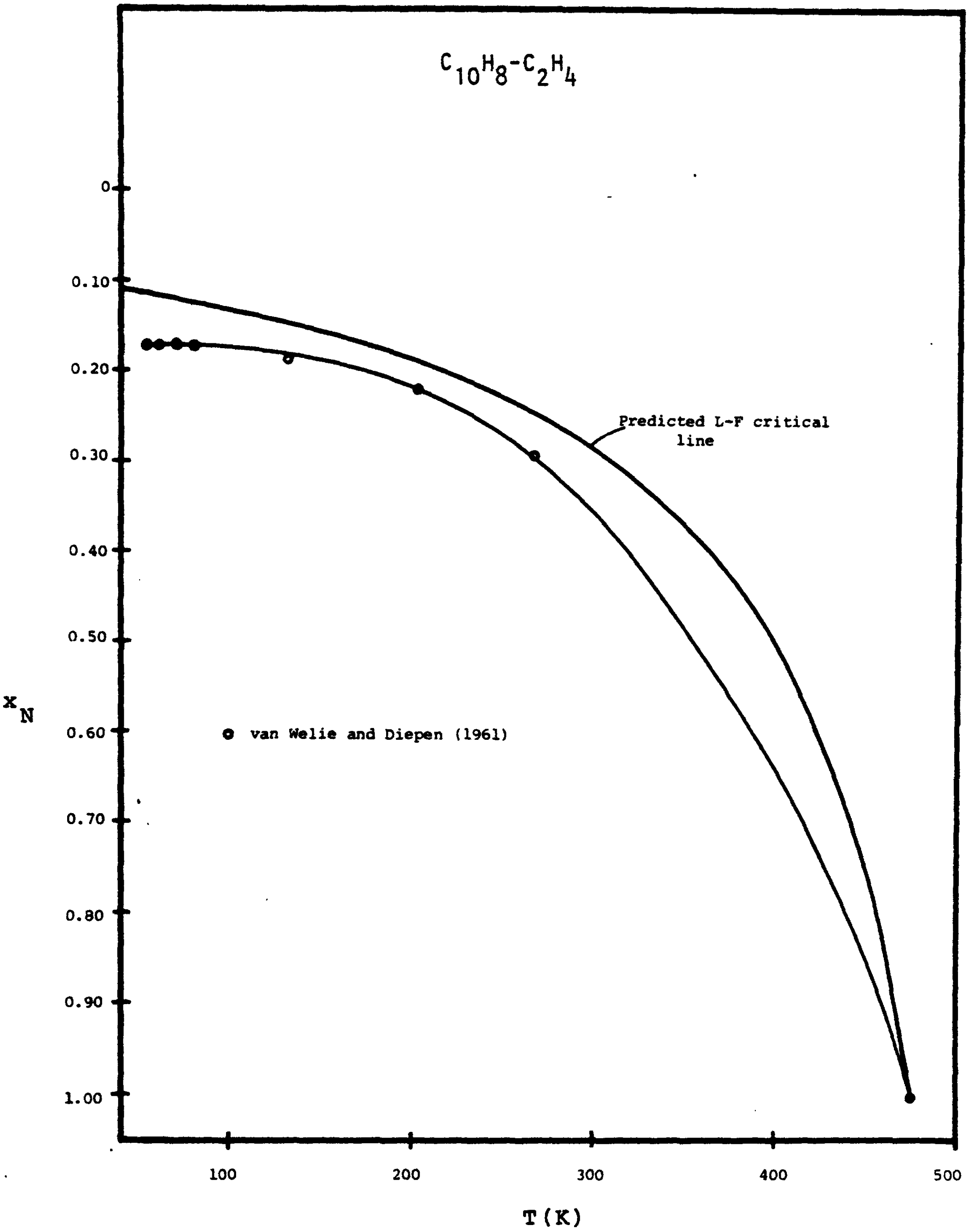

Figure 7.3c. The T-x projection of the upper critical line for naphthalene - ethylene.

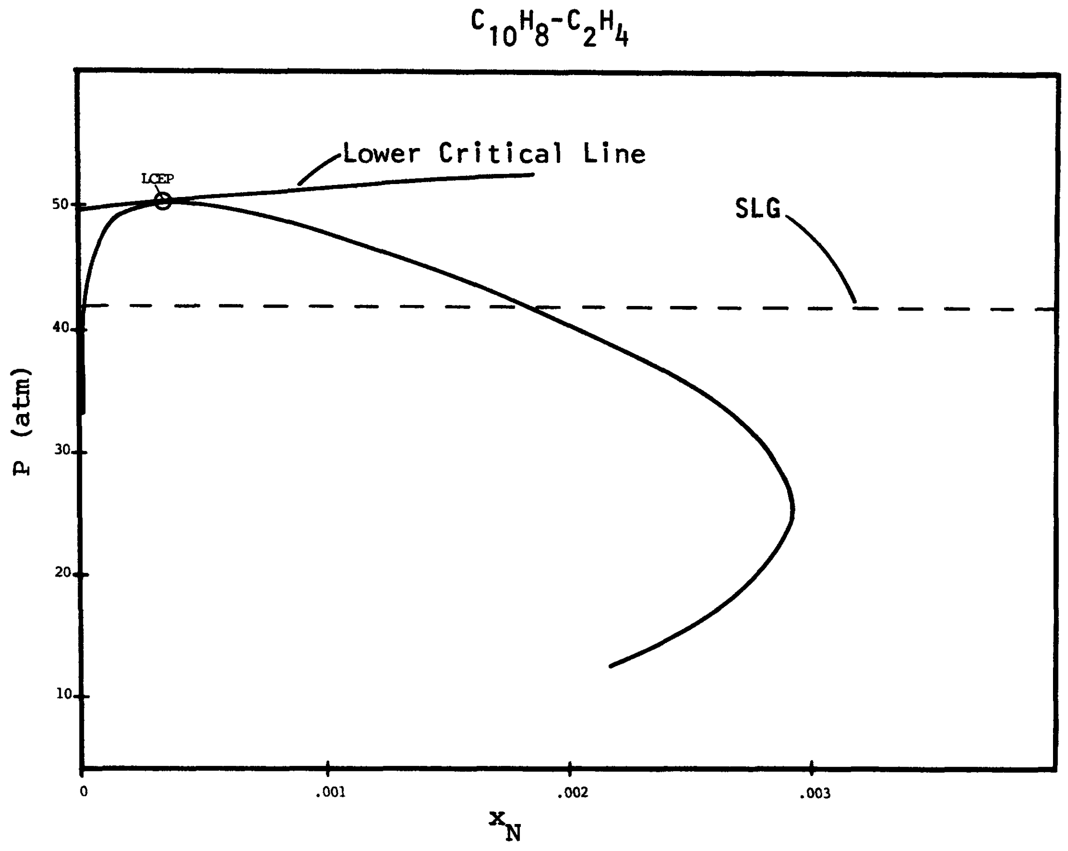

Figure 7.3d. The P-x projection of the SLG region and a portion of the lower critical line for naphthalene - ethylene. A sample SLG tieline, which continues off the graph to the pure naphthalene axis, has been included. The corresponding diagram for naphthalene - CO_2 is qualitatively the same.

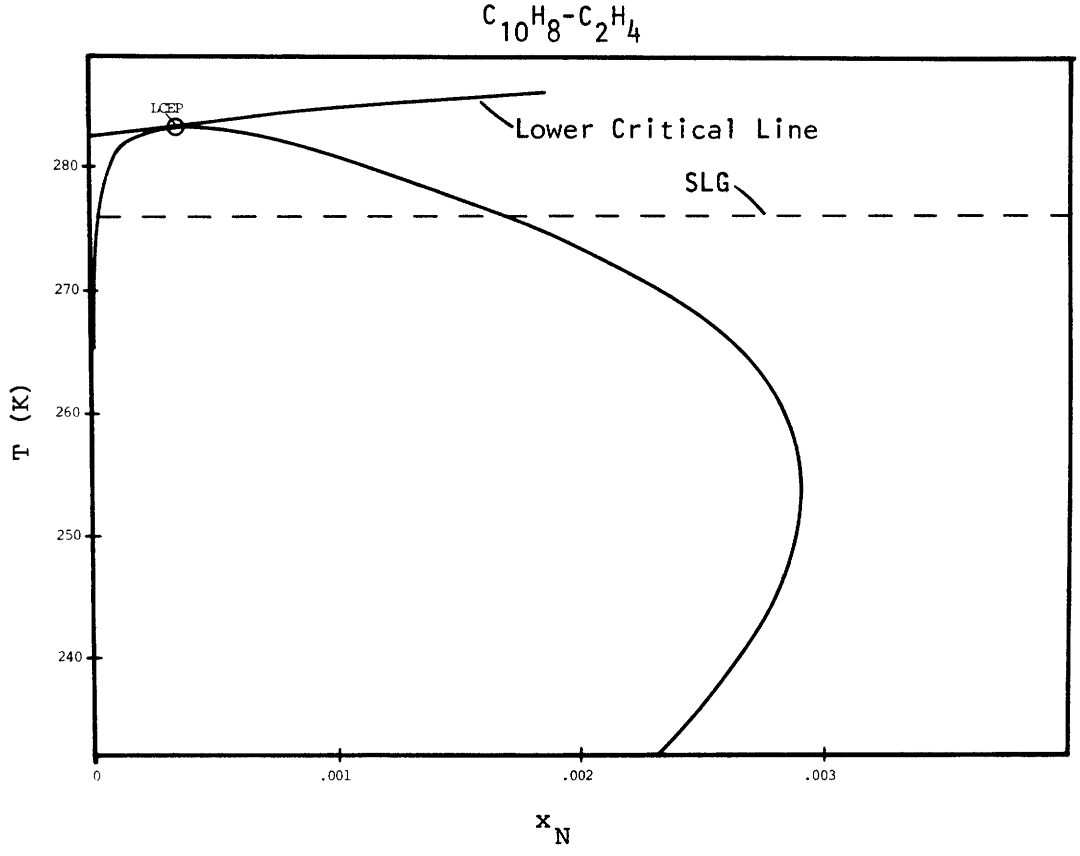

Figure 7.3e. The T-x projection of the SLG region and a portion of the lower critical line for naphthalene - ethylene. A sample SLG tieline, which continues off the graph to the pure naphthalene axis, has been included. The corresponding diagram for naphthalene - CO_2 is qualitatively the same. This diagram is to be compared with Figure 6.14.

In order to provide further comparison between the naphthalene - ethylene and naphthalene - CO_2 systems, P-x sections at nine different temperatures have been drawn up. Some of the sections have been chosen at the same absolute temperature, and some at the same reduced temperature, with respect to the solvent, as their naphthalene - CO_2 counterparts. Experimental data is not available for these diagrams.

Figure 7.4a shows the P-x section at 255 K, a temperature below the low temperature termination of the metastable LLG line (see Figure 7.2b). The connections between the various binodal curves are not evident at this scale. Figure 7.4b expands the low pressure range of Figure 7.4a. The presence of the SL_1G tieline is now evident, along with the stable S+G, L_1+G, and S+L_1 regions. The metastable behavior is in most respects similar to that of Figure 6.5a. The metastable L_1+L_2 critical point is a point along the metastable L-F critical line in Figure 7.2b. In both Figures 7.4a and 7.4b, it appears that the unstable S+F and metastable S+L_1 segments will join in the usual fashion, previously given for very low pressures in Figure 6.9b. An attempt to show this, Figure 7.4c, met with computational difficulties which were not encountered in the generation of Figure 6.9b. Although the stable S+G segment and the metastable L_1+G region terminate normally at the $C_{10}H_8$ sublimation pressure and the metastable $C_{10}H_8$ vapor

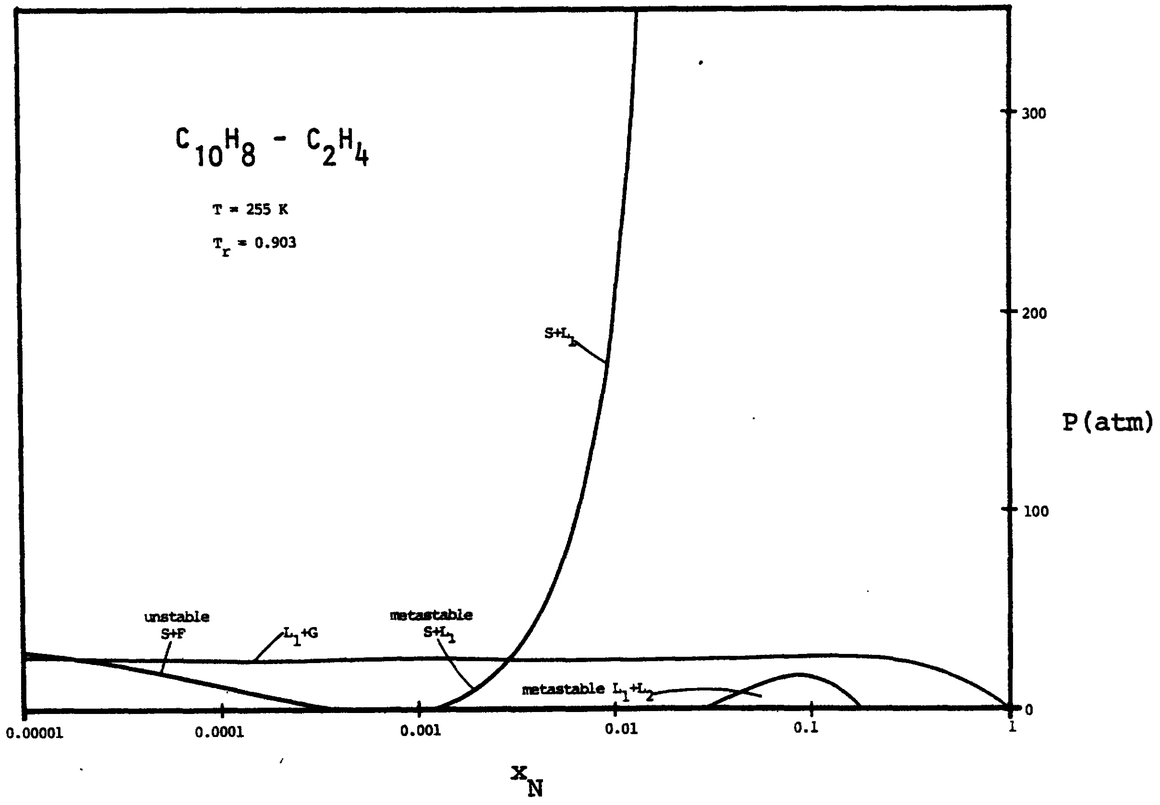

Figure 7.4a. A P-x section below the lower metastable CEP in Figure 7.2b.

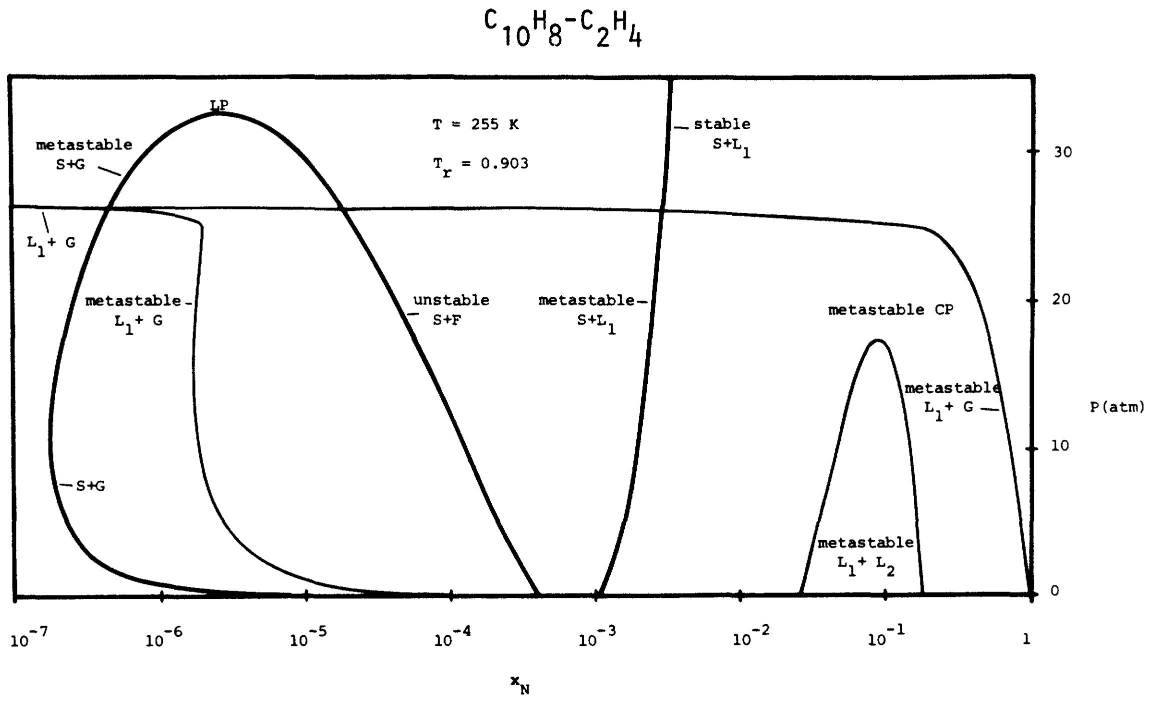

Figure 7.4b. The P-x section at 255 K and low pressures. No $G+L_2$ region is present.

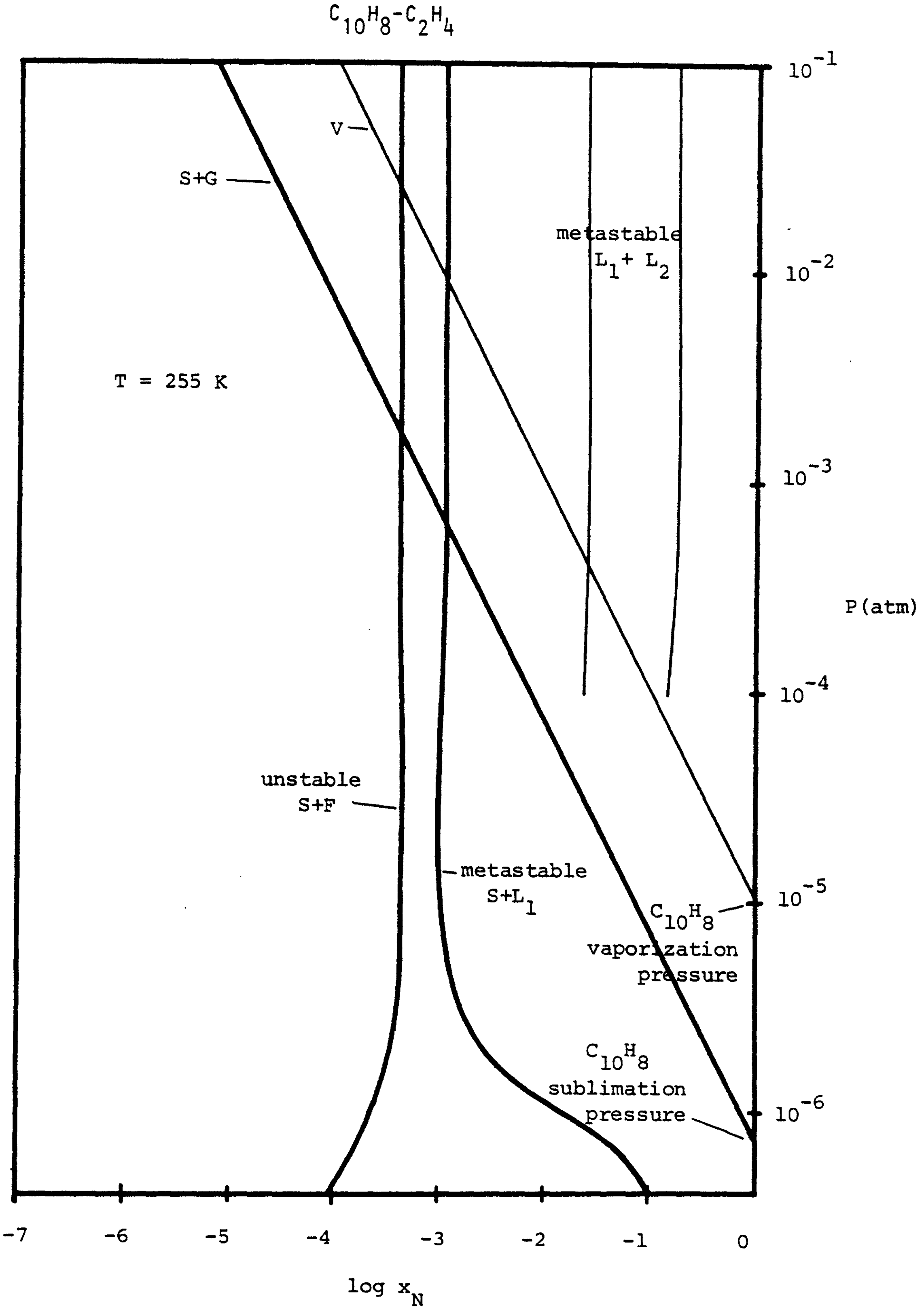

Figure 7.4c. The P-x section at 255 K and very low pressures.

pressure, respectively, the S+F and S+L_1 legs still do not join for pressures as low as 10^{-6} atm. In fact, the two legs are diverging at this point. The metastable L_1+L_2 binodals are traced down to 10^{-4} atm without any significant convergence or divergence. By 10^{-4} atm, certain quantities in the defining equations had become extremely small, resulting in unreliable calculations even in double precision mode. Since this low pressure region is not of practical significance, the problem was not considered further.

In the course of tracing the low pressure solutions in Figure 7.4c, the form of the f-x curves was also investigated. Figure 7.5 illustrates several shapes which have not been previously presented. All of the plots yield three roots across the entire composition range. The high volume, ideal gas root is essentially a straight line, intersecting the pure naphthalene axis at approximately the total system pressure. The low volume, liquid root has two spinodal points and is quite similar to the curves for this root which are presented in Chapter 3 and Appendix B. The liquid solution is affected very little by the small absolute pressure difference between the three figures. The f-x curves shown previously at 0.1 and 1 atm for n-hexadecane-CO_2 showed the unstable root continuous with the liquid root. This behavior will also be found in the naphthalene-ethylene system at temperatures higher than 255 K. It can be seen in Figure 7.5 that when the unstable root does join with the

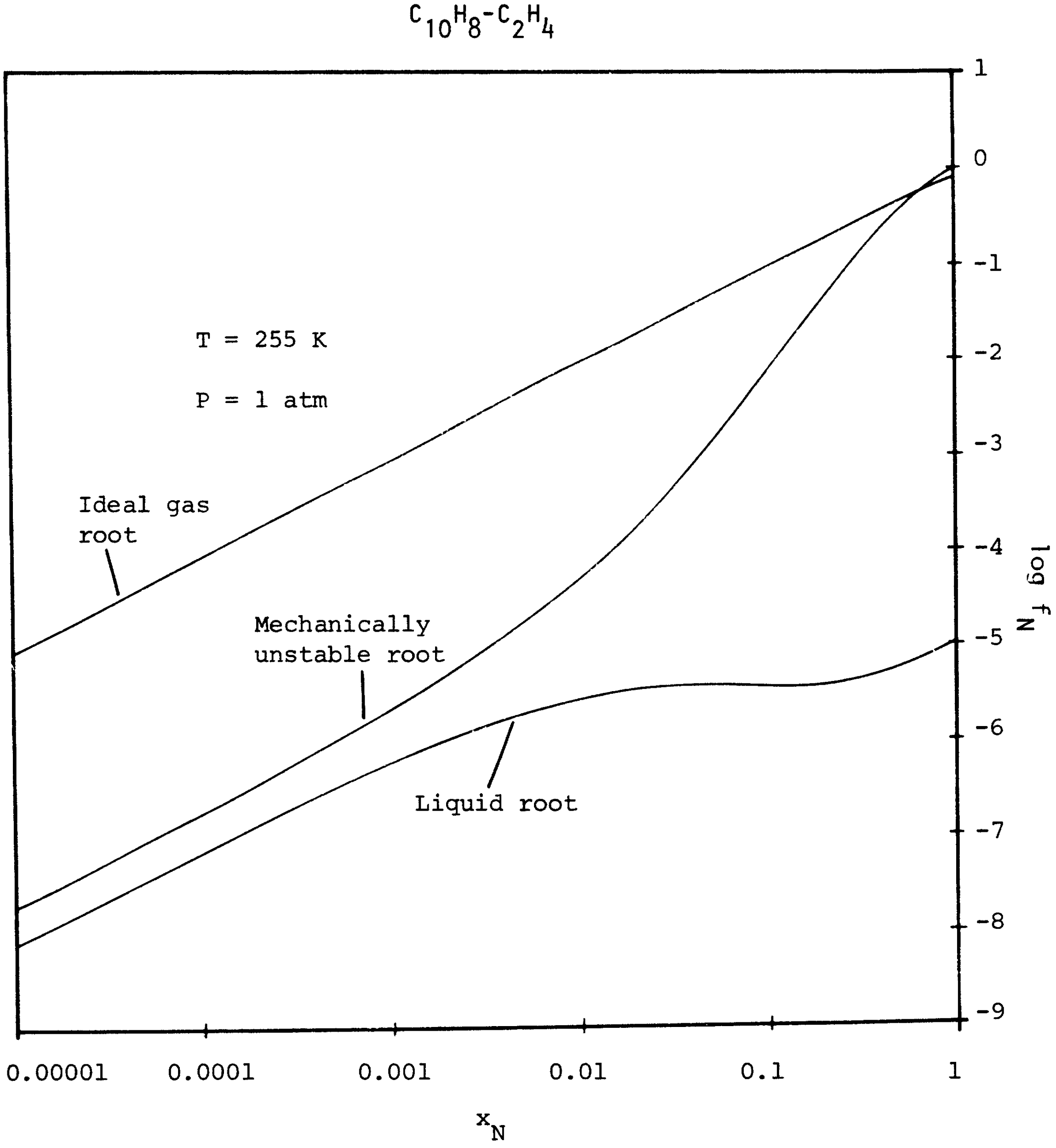

Figure 7.5a. An f-x plot with three roots over the entire composition range. The three roots would converge at x_N= 0 in a Cartesian plot.

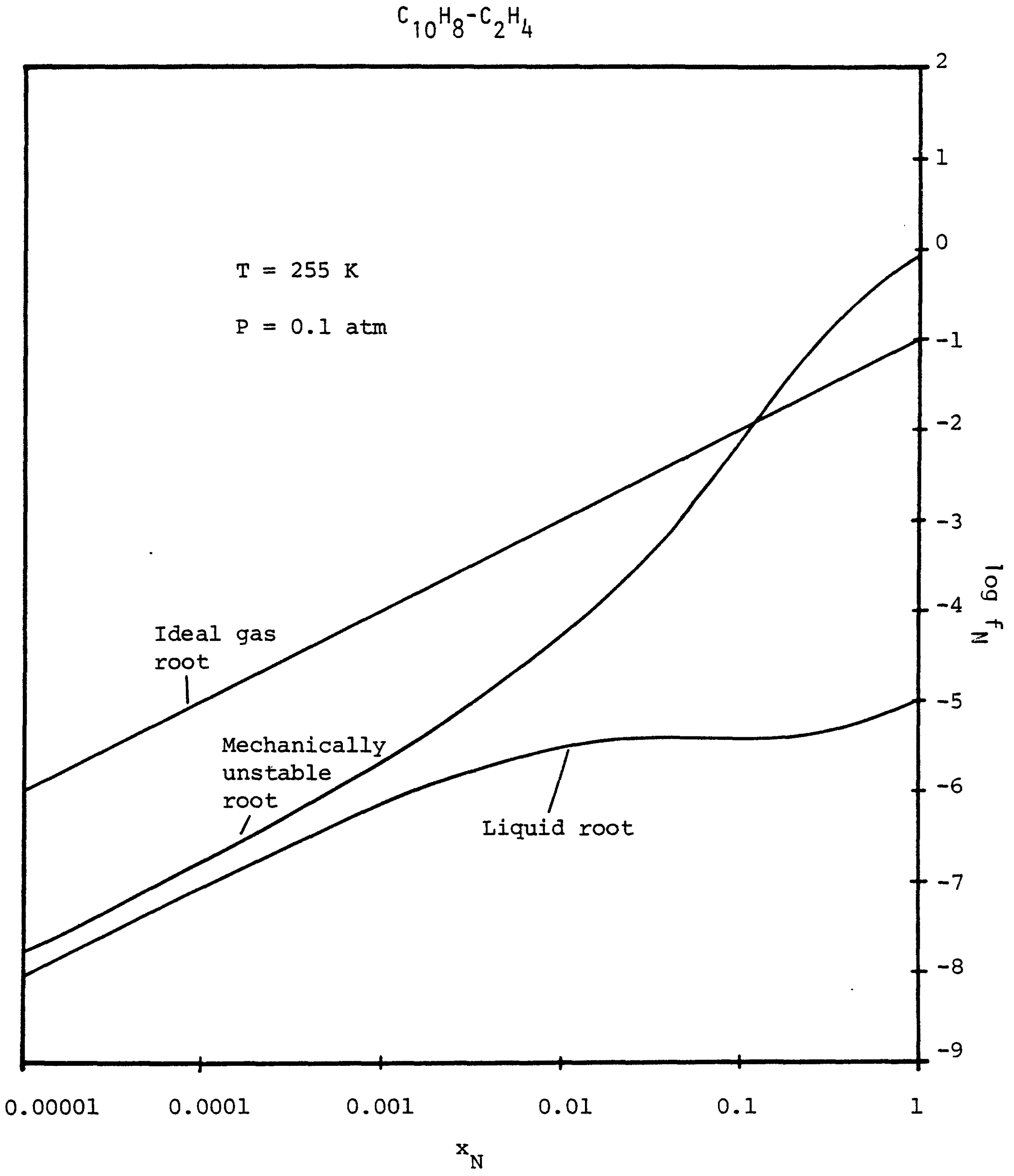

Figure 7.5b. An f-x plot with three roots over the entire composition range.

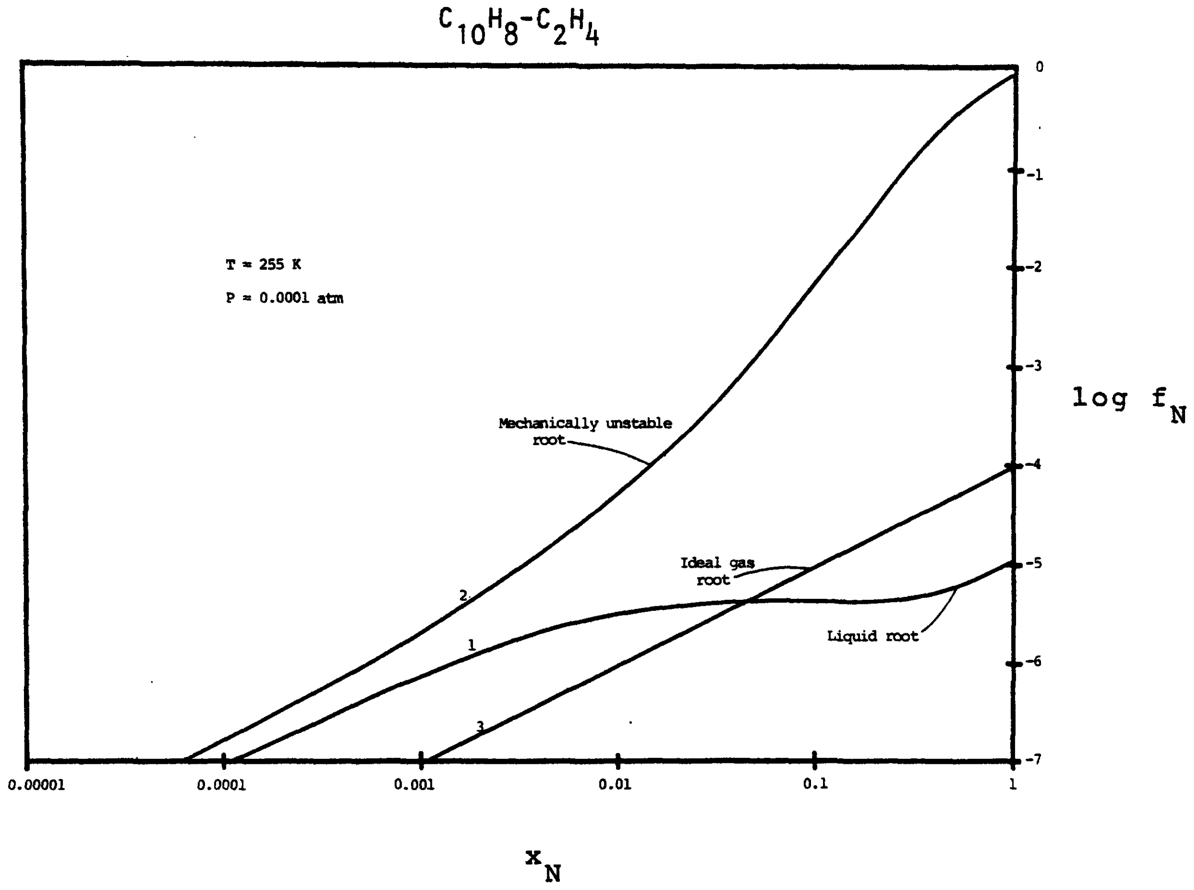

Figure 7.5c. An f-x plot with three roots over the entire composition range. The mechanically unstable root has the highest fugacity over much of this range.

liquid root, it will give a shape similar to the C_{16}-CO_2 plots at these pressures.

Figure 7.6a gives the P-x section at 278.5 K, a temperature below ethylene's critical point. The metastable $G+L_2$ and L_1+L_2 regions are now of a familiar shape, and are completely enclosed by the S+F region. The stable L +G region only shows up on an expanded scale, as depicted in Figure 7.6b. Figures 7.6a and b may be compared with Figures 6.4a and b which have been drawn at the same reduced temperature with respect to the solvent. In Figure 6.4a, the solubility in the S+G region is considerably higher than in Figure 7.6a. This is due to the lower absolute temperature in Figure 7.6a, which leads to a lower naphthalene vapor pressure, and hence a lower solubility.

At 283.2 K, Figure 7.7, the LCEP temperature has been reached. The S+F equilibrium curve exhibits a point of horizontal inflection. Coincident with this point is the stable critical point of the metastable L_1-G region which is, however, too small to appear in the figure. The shape of this region has previously been given in Figure 6.6b.

Increasing temperature further, the supercritical fluid region is entered. Figure 7.8 is drawn at 288.7 K, the same reduced temperature with respect to the solvent as Figure 6.7. The stable two-phase system for the entire pressure

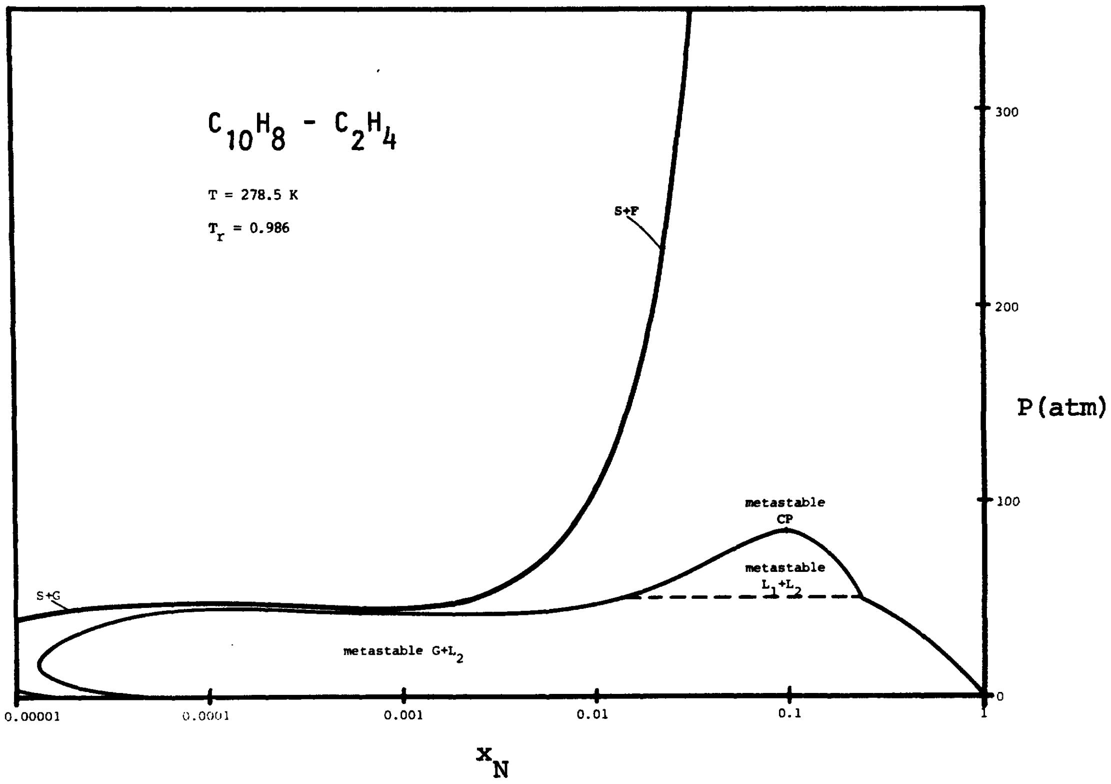

Figure 7.6a. A P-x section below ethylene's critical point. This diagram is at the same reduced temperature, with respect to the solvent, as Figure 6.4.

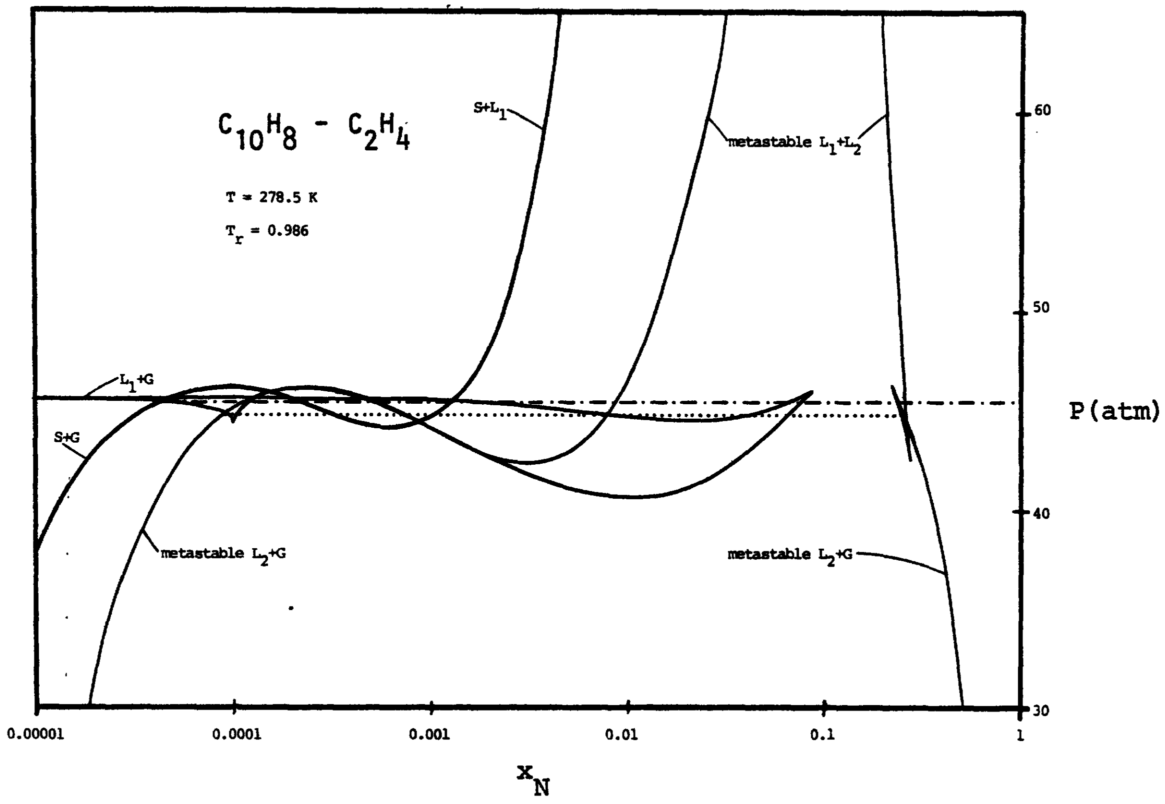

Figure 7.6b. The P-x section at 278.5 K in the vicinity of the three-phase region. This diagram is to be compared with Figure 6.4.

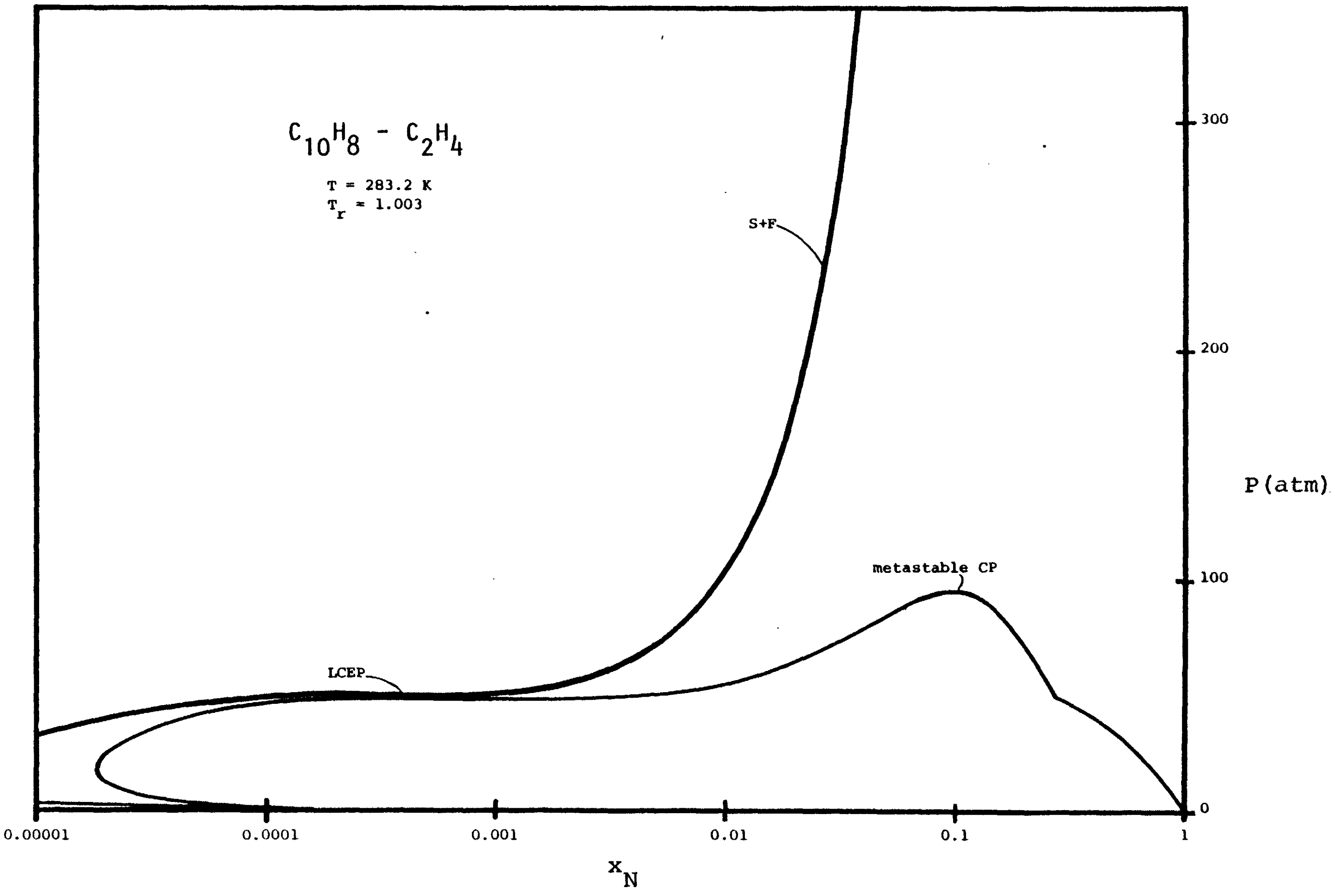

Figure 7.7. The P-x section at the lower critical end point (approximately). The solid-fluid binodal exhibits a point of horizontal inflection.

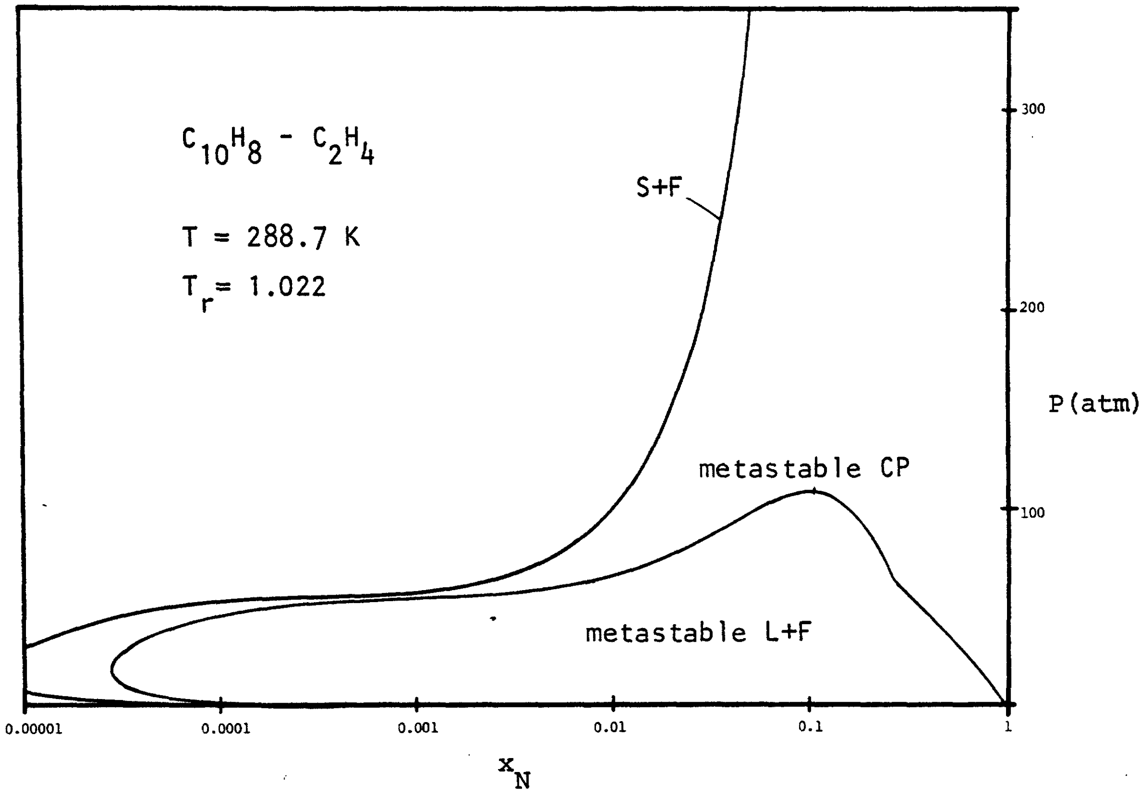

Figure 7.8. A P-x section in the supercritical fluid region of naphthalene - ethylene. The metastable G+L_2 and L_1+L_2 regions have become a single, metastable L+F region.

range is S+F. This temperature is above the upper metastable CEP in Figure 7.2b, so that separate L_2+G and L_1+L_2 regions no longer exist. The L_1+G binodals, though too small to appear in the figure, are still present. They fall entirely within the L+F region, and exhibit the usual stable and unstable critical points (see Figure 6.11b). These critical points persist up to the cusp in Figure 7.2b.

Figure 7.9 is drawn at 313.85 K, which is essentially the upper critical end point temperature. The solid-fluid binodal now exhibits a horizontal inflection point, which is coincident with the stable critical point of the metastable L+F region. This diagram is to be compared with Figure 6.8.

Figure 7.10 gives the P-x section at 318.85 K, somewhat above the UCEP temperature. As in Figure 6.9a, a stable region of L+F is now present, along with the associated SLF tieline. The solid-fluid binodal now possesses two limit points, where the metastable and unstable segments are joined. Below the SLF tieline, S+F is the stable two-phase system. At pressures above the tieline, depending on the overall system composition, the stable two phase system will be L+F or S+L.

Figure 7.11 gives the P-x section at 340 K, the same temperature as Figure 6.9a. As with Figure 7.10, this temperature lies between the UCEP and naphthalene's triple

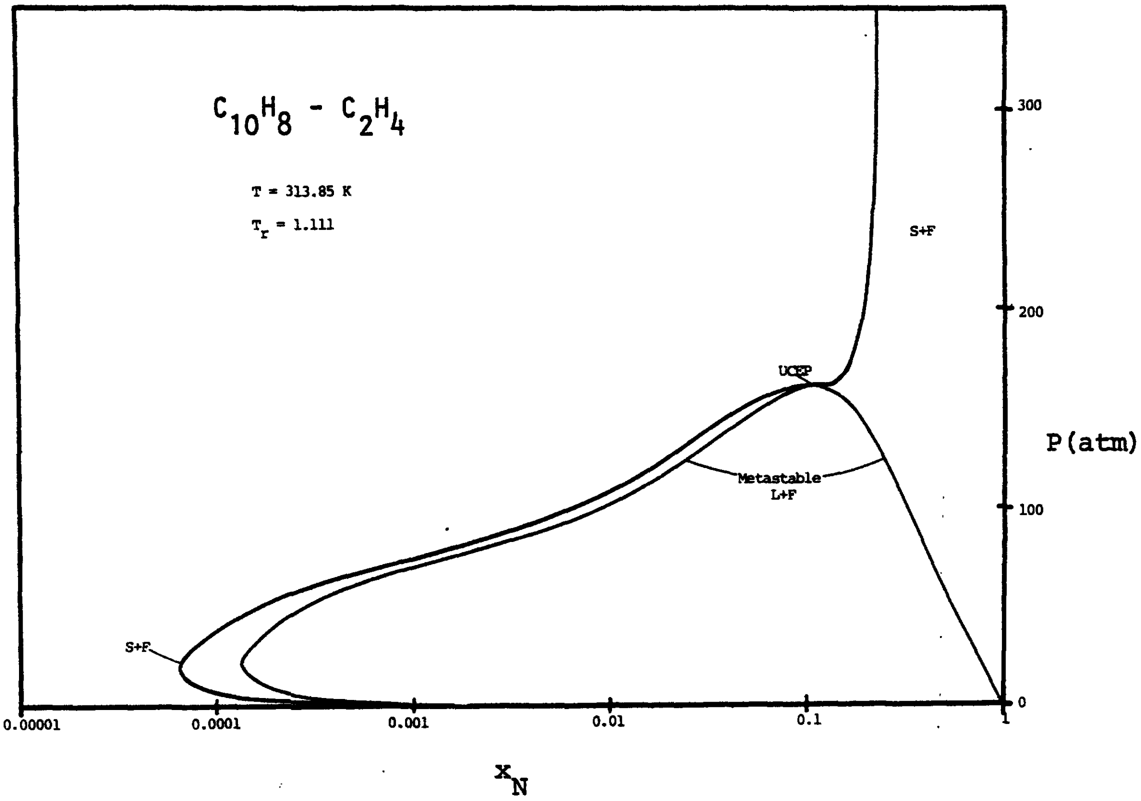

Figure 7.9. The P-x section at the upper critical end point temperature (approximately). The S+F binodal exhibits a point of horizontal inflection.

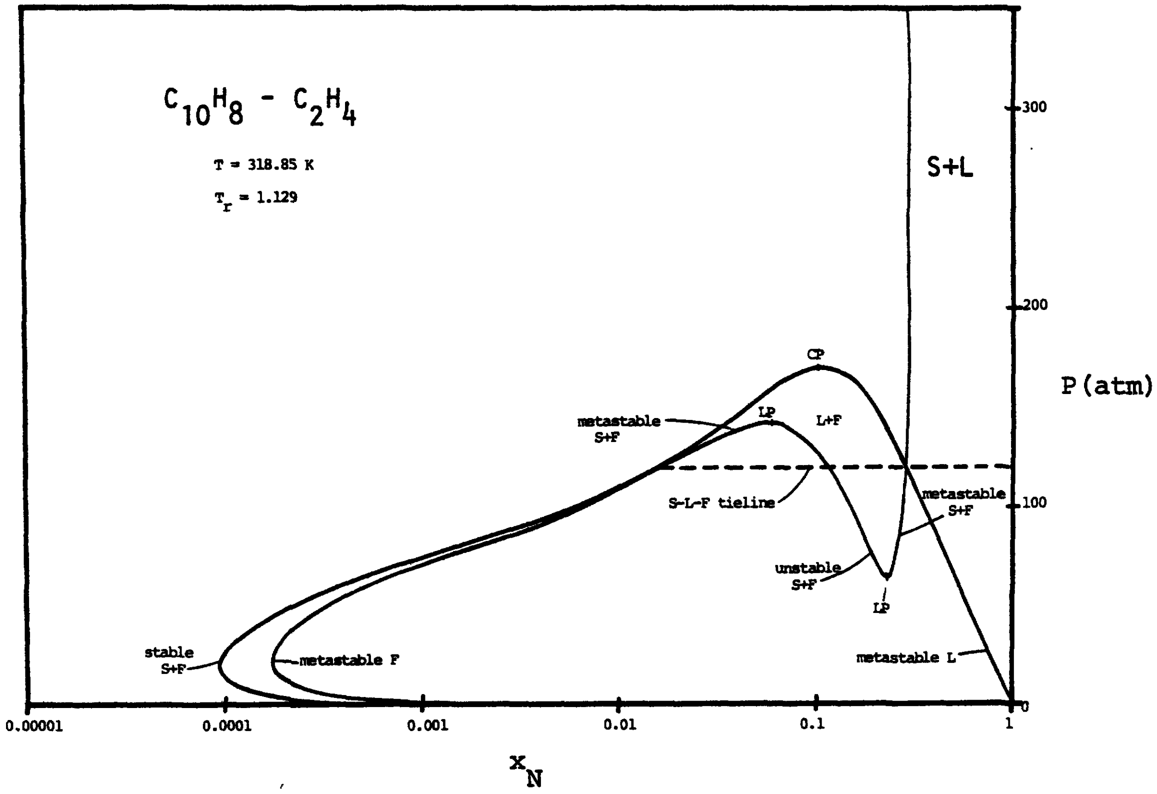

Figure 7.10. A P-x section between the UCEP and naphthalene's triple point.

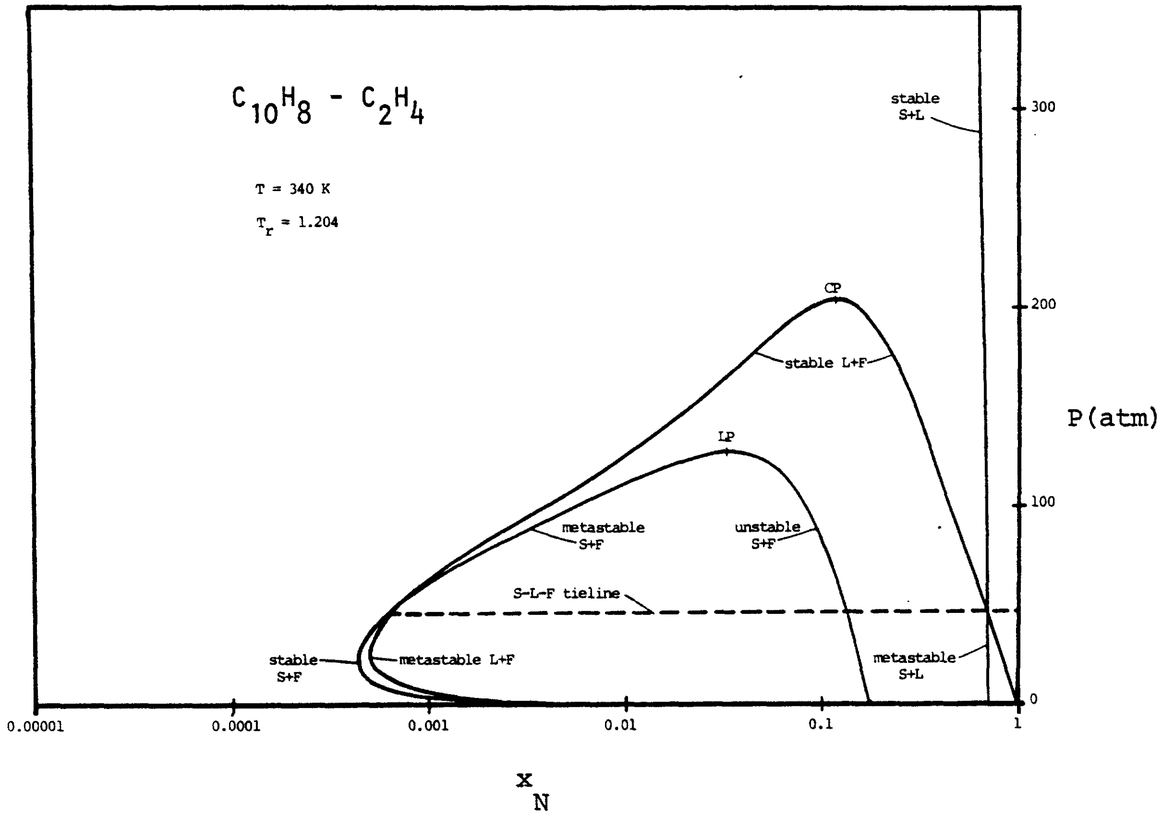

Figure 7.11. A P-x section between the UCEP and naphthalene's triple point.

point, and the features of the phase diagram are qualitatively the same. The S+L and S+F binodal branches are joined at very low pressures, so a second limit point does not appear in the plot. The L+F critical point occurs at a higher pressure than at 318.15 K, in agreement with Figure 7.2a.

At naphthalene's triple point, the P-x section of Figure 7.12 is found. This diagram is to be compared with Figure 6.10. The S+L and L+F binodals meet at the triple point pressure. Upon increasing the temperature to 360 K, Figure 7.13, the S+L region has moved off the graph. As seen in Figure 6.11, naphthalene will not precipitate out until about 390 atm.

The conclusions to be drawn from the study of the naphthalene - ethylene system include those of the previous chapter. The most significant result, however, is that the experimental measurements have proven the qualitative validity of the predicted P-T-x space. This is an indication that the P-T-x predictions for naphthalene - carbon dioxide are qualitatively correct.

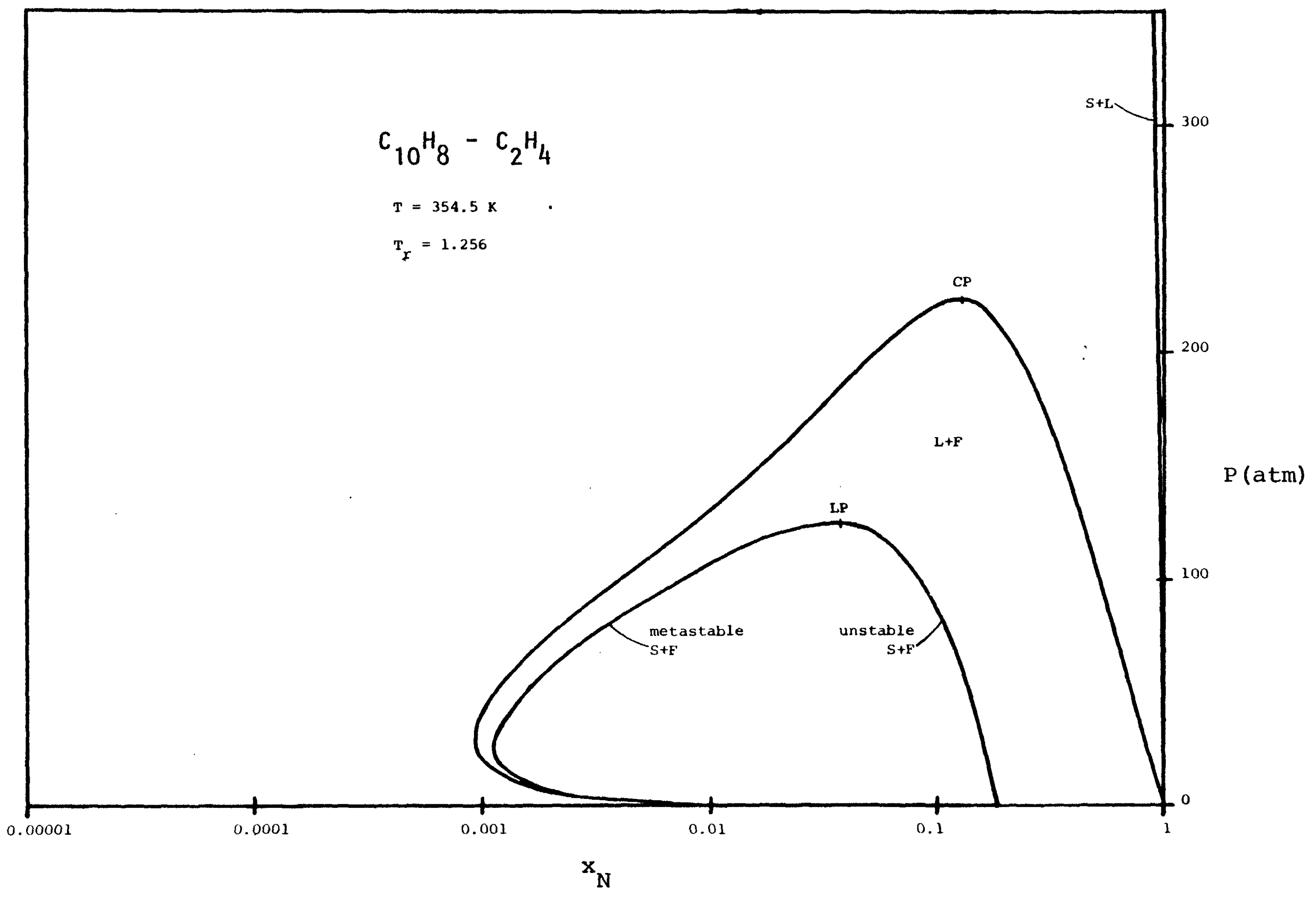

Figure 7.12. The P-x section at naphthalene's triple point.

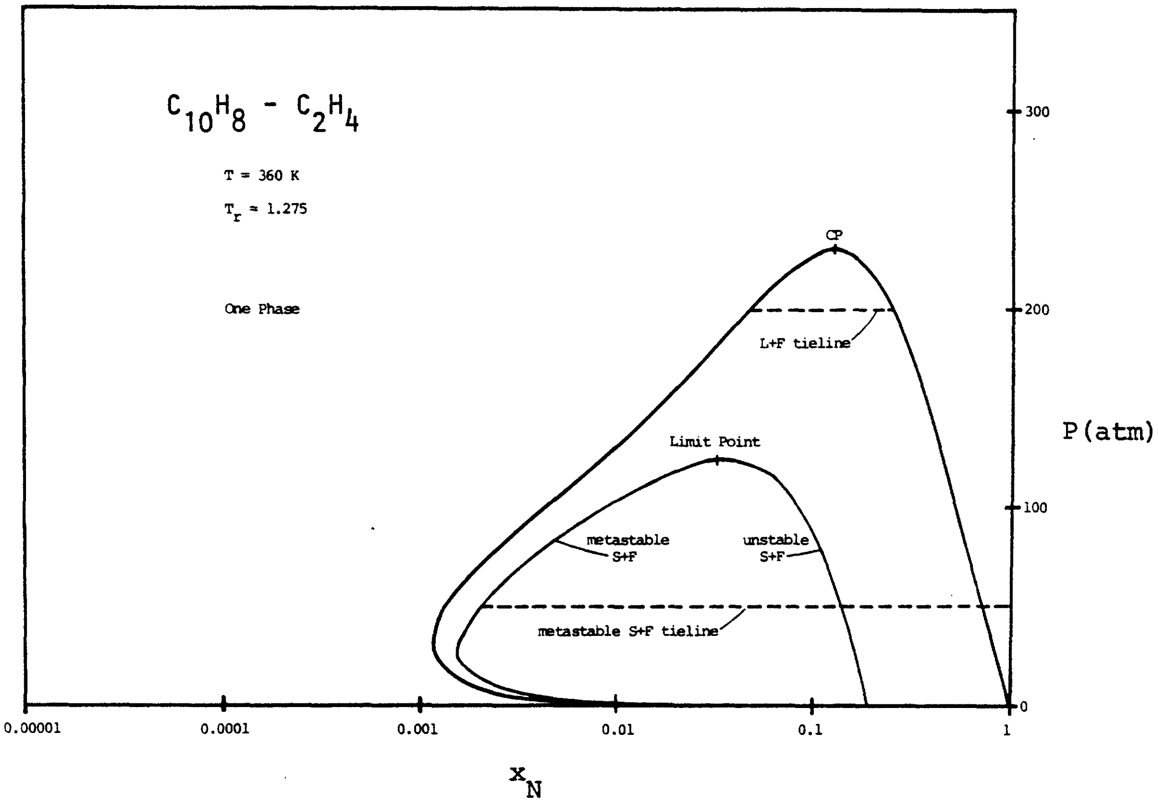

Figure 7.13. A P-x section above naphthalene's triple point.

Chapter 8 The Benzene - Water System

The preceding chapters have demonstrated the utility of the P-R equation in modelling nonpolar systems. In these systems the components were considerably different in molecular size, leading to nonidealities manifested as liquid-liquid immiscibilities. In the present case, nonidealities are a result of both size and polarity differences. The polar compound will have a strong self-affinity, in this instance the hydrogen bonding of water. It is a formidable task to accurately model such polar intermolecular forces - witness the 50 constant equation of Keenan, et al. (1978) - but, as will be seen, the simple cubic equation of state still provides a reasonably accurate qualitative description of the binary system. Peng and Robinson (1976b) have in fact used their equation to predict three-phase equilibrium in multicomponent hydrocarbon - water systems with some degree of success. It was indicated in Chapter 4, as well, that the P-R equation gives a reasonable picture of the phase behavior of pure water.

The physical constants of water and benzene are given in Table 8.1. At 455.2 K, the vapor pressures of benzene and water are equal. Below this temperature, benzene is the more volatile component, while at higher temperatures water is more volatile. The crossing of the vapor pressure curves

Table 8.1

Physical Constants of Benzene and Water

	C_6H_6	H_2O
T_c(K)	562.1	647.3
P_c(atm)	48.3	217.6
ω(acentric factor)	0.212	0.344

requires the occurrence of an azeotrope in the system, although not necessarily a stable one. This is evident upon considering a binary VLE P-x section, which is terminated at compositional extremes by the pure component vapor pressures (see e.g., Figure 2.2). Since the pressures at either end of the envelope are the same, or nearly the same, any deviation from ideality must lead to an envelope with a maximum or minimum pressure, i.e., an azeotrope.

A fairly extensive amount of experimental data has been gathered for the benzene-water system, by a number of investigators. The system belongs to the general class depicted in Figure 2.10. No single study has covered the entire fluid region, but between the work of Rebert and Kay (1959) at low to moderate pressures, the work of Connolly (1966) at moderate to high pressures, and the mapping of the upper critical locus by Alwani and Schneider (1967) a good overall picture of the phase behavior is obtained.

A value of δ_{12} for this system was selected by matching a single point along the P-T projection of the upper critical locus. Since the critical locus is univariant, choice of a temperature fixes one or more sets of pressure and composition along the locus. In using the equation of state, choosing the pressure and temperature of a critical point on the experimental locus fixes the composition and δ_{12}. Figure 8.1 shows the experimental upper critical locus along with

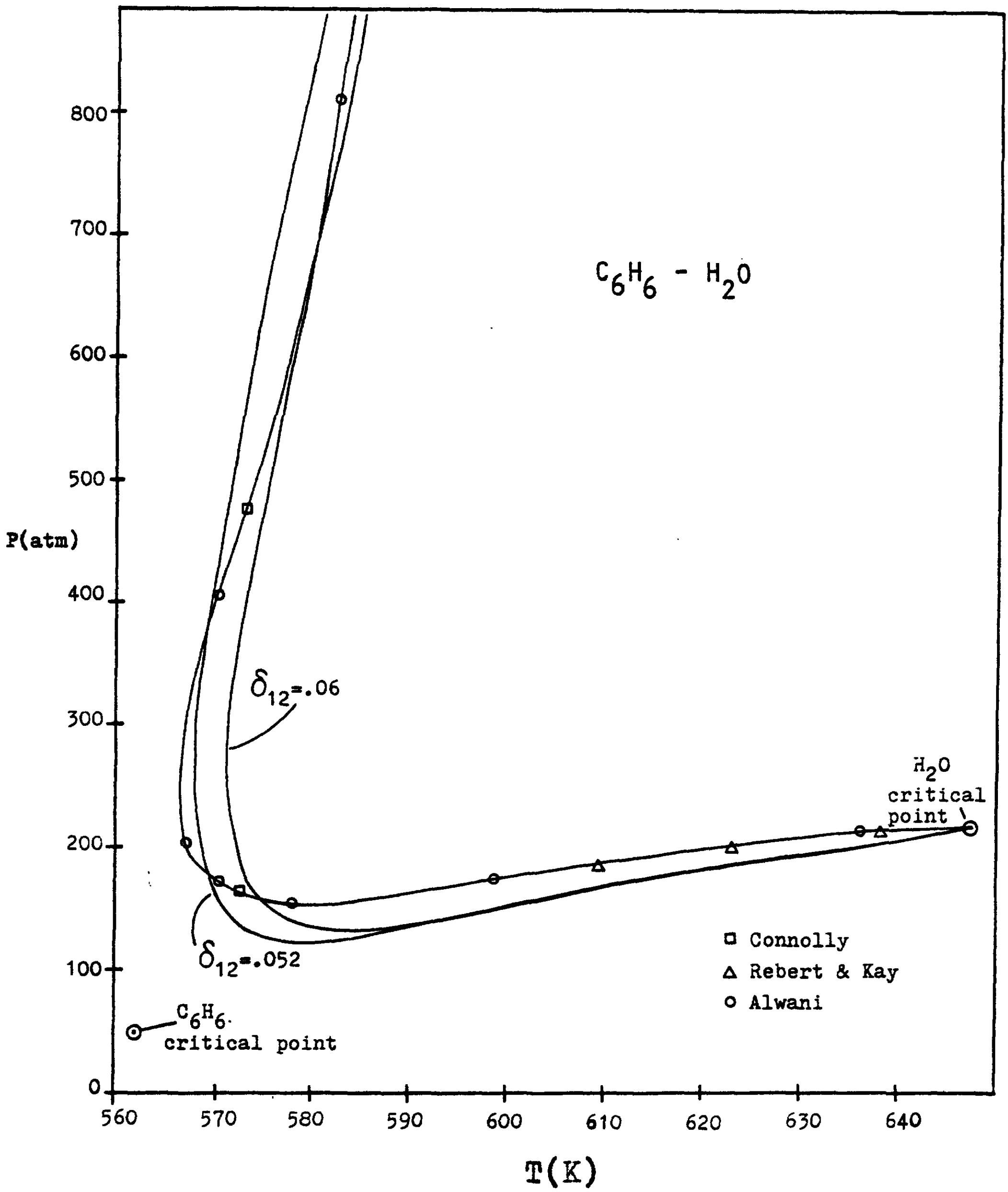

Figure 8.1. The P-T projection of the upper critical locus for benzene - water. The curves are actually composed of two separate segments (see Figures 8.2 and 8.3).

two predicted loci. The value of δ_{12} =0.052 is reasonably optimal in reproducing the course of the critical line, and was used for all further predictions in the benzene-water system.

The critical curves in Figure 8.1 have been depicted as smooth and continuous. It is necessary to examine the region near the benzene critical point more closely to elucidate this behavior. Figure 8.2 illustrates the phase relationships as deduced from experimental measurements. The lower critical locus begins at the benzene critical point and tends toward lower temperatures and higher pressures. It reaches a temperature minimum, turns toward higher temperatures, and shortly thereafter is terminated at the lower critical end point. Alwani and Schneider (1967) have suggested a hypothetical continuation of the lower critical line to indicate its course had a third phase not intervened. This line might be thought of as a metastable critical line. It is presumed to intersect the upper critical line near its pressure minimum.

Rebert and Kay's measurements indicate that the three-phase LLG line also has a metastable continuation beyond the lower critical end point. The meaning of this metastable locus will be discussed shortly, when the P-x sections for the benzene - H_2O system are considered. It terminates at a critical solution end point, simultaneously

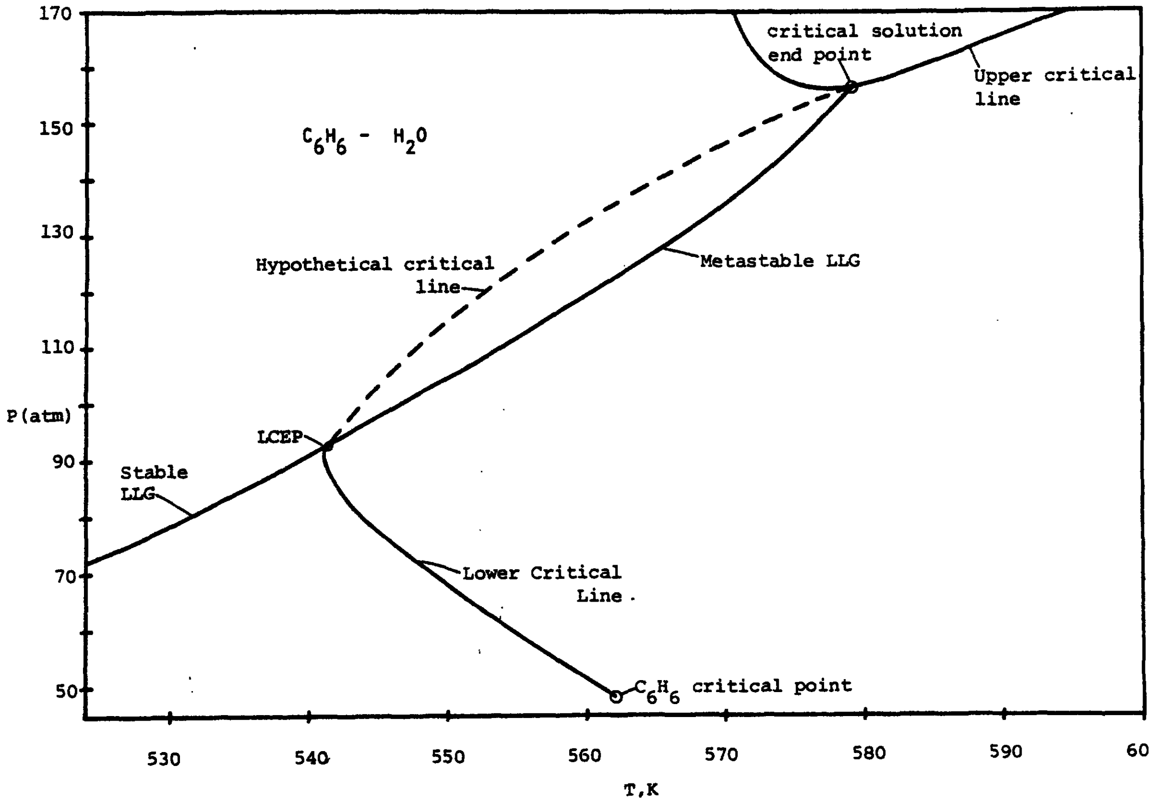

Figure 8.2. The experimental P-T projection of the benzene - water system in the vicinity of the pure benzene critical point.

intersecting the L-L and L-G critical lines. The transition between the L-L and L-G critical lines has been drawn as smooth, although experimental measurements indicate that this is not actually true. No measurements of the L-L critical line are available in this region to indicate its correct shape, however.

Figure 8.3 gives the calculated P-T projection in the vicinity of benzene's critical point. The critical curve starting from the pure water critical point does not transform into the liquid-liquid critical line (see Figure 8.1), but rather reaches a minimum in temperature and then returns to the benzene critical point. The liquid-liquid critical line on the other hand reaches a minimum in pressure shortly before being terminated by an unstable critical line. Figure 8.3 also gives the three-phase LLG line which terminates at a critical end point on the LL critical line. The short segment of the LL critical line between the CEP and the point of the cusp where the unstable critical line is joined is metastable.

The experimental and predicted P-T projections differ in that the former depicts a metastable portion of the LLG line. Rebert and Kay assert that this metastable line corresponds to the intersection of two binodal regions. However, data were taken on a fairly coarse grid, and a third binodal region of limited extent may well have gone undetected. As

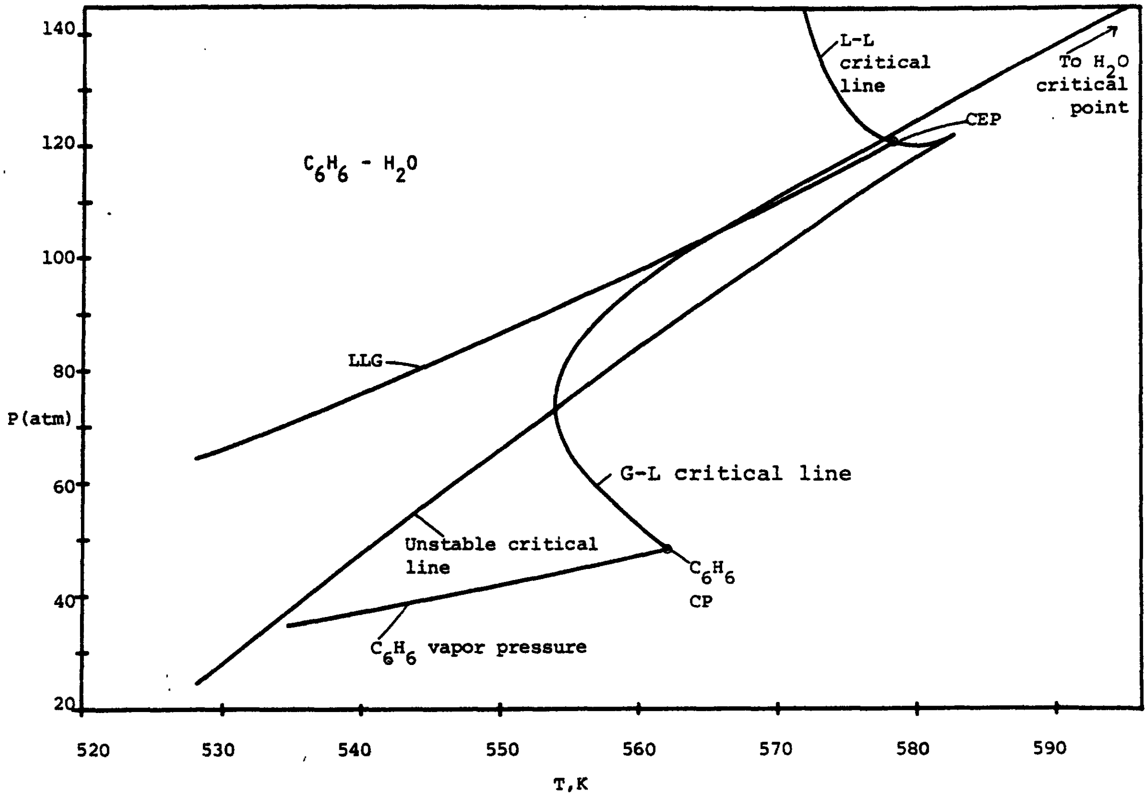

Figure 8.3. The predicted P-T projection of the benzene - water system in the vicinity of the pure benzene critical point.

consideration of the P-x sections will show, the equation of state predictions indicate that a third binodal region does exist, and that very careful measurements will be necessary to determine the stability or metastability of the LLG line up to the critical solution end point. At present it is not possible to say which of the two P-T projections is correct.

The P-x sections for the benzene - water system will now be considered. A fairly complete set of these diagrams has been published by Rebert and Kay (1959). These have been reproduced in Figure 8.4. Some high pressure data from Connolly (1966) has been included in Figures 8.4d and e.

Figure 8.4a shows the P-x section at 528.15 K, a temperature below the critical end point in Figure 8.2. The diagram is typical for systems in which the three-phase LLG line lies at a higher pressure than the vapor pressure of either component. Systems of this type are known as heteroazeotropes (see Figure 2.14). In this instance the azeotropic composition at 528.15 K is given by x. When two coexisting liquid phases of overall composition x are brought to the boiling point, the vapor phase which forms also has a composition x. Thus, as with a normal azeotrope, no separation may be effected by simple distillation. Heteroazeotropes also exhibit the property of vapor phase compositions intermediate to two liquid phase compositions at a given pressure and temperature. Despite this composition

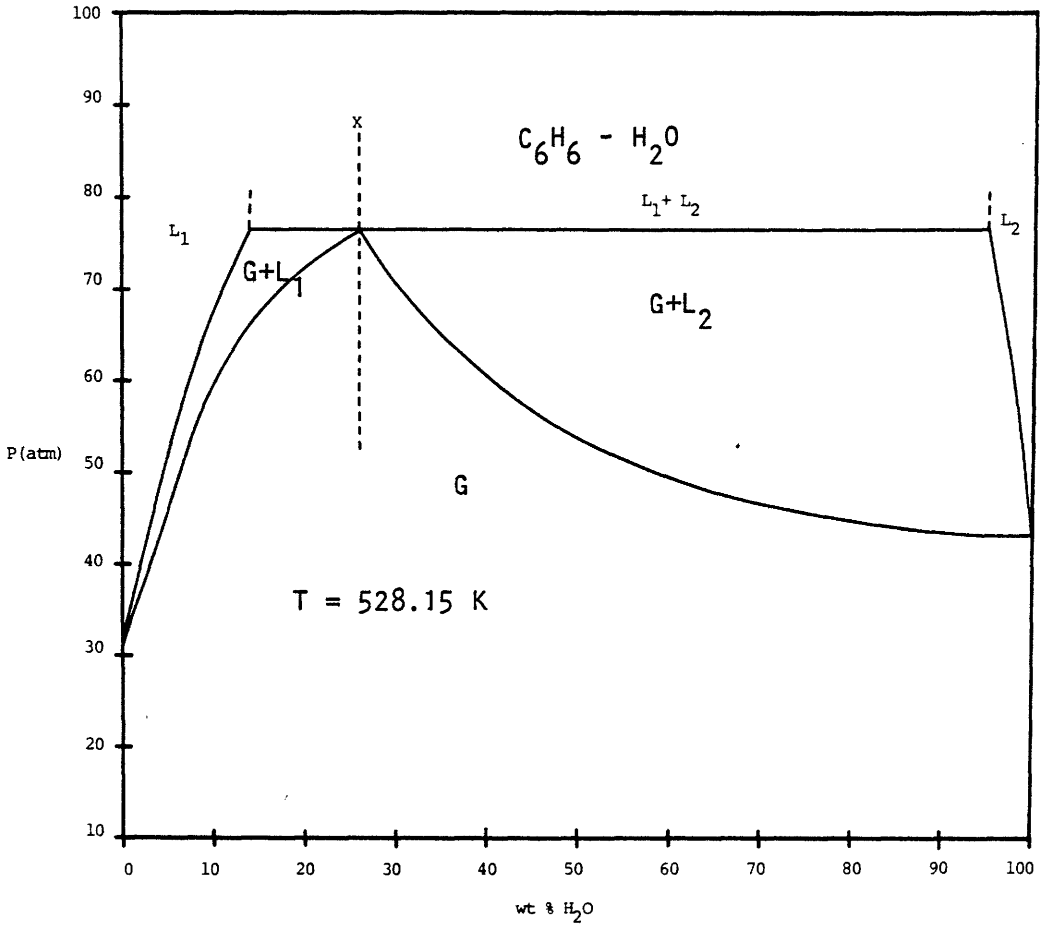

Figure 8.4a. An experimental P-x section below the temperature minimum in the lower critical line (see Figure 8.2).

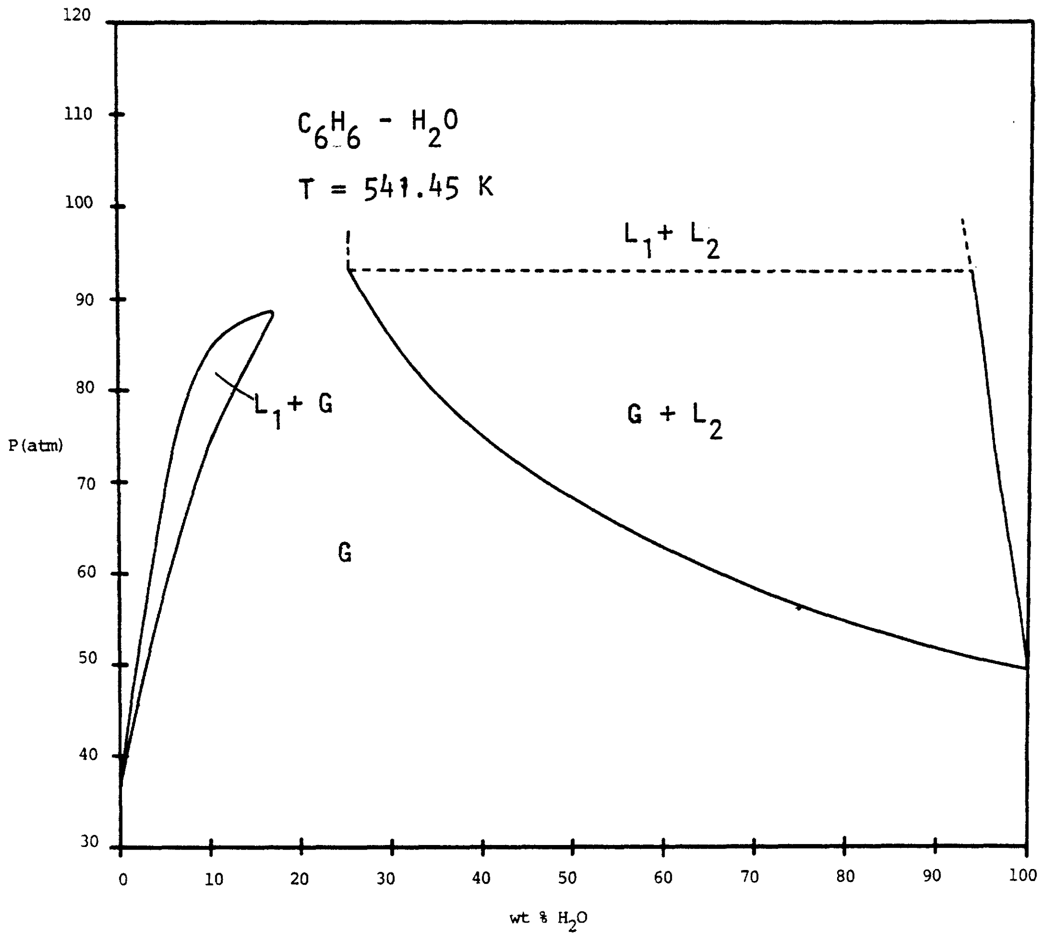

Figure 8.4b. A P-x section slightly above the LCEP in Figure 8.2.

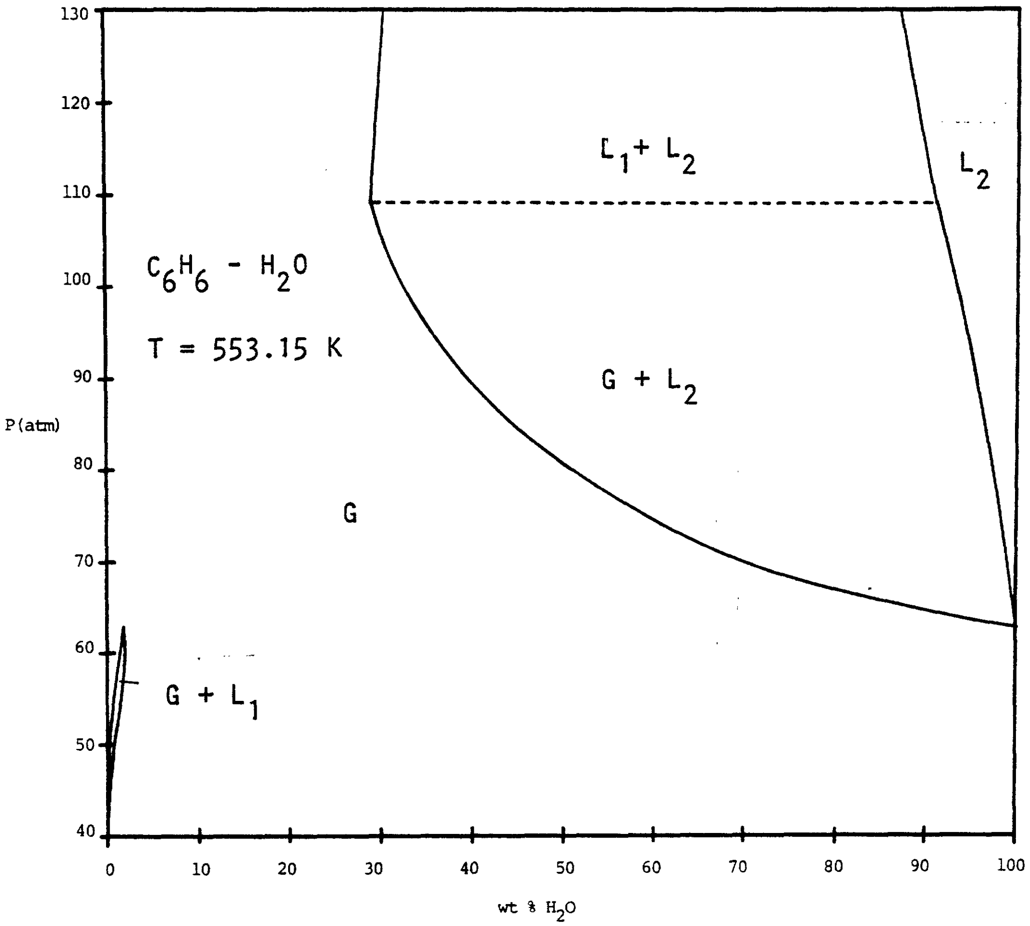

Figure 8.4c. A P-x section between the LCEP and benzene's critical point.

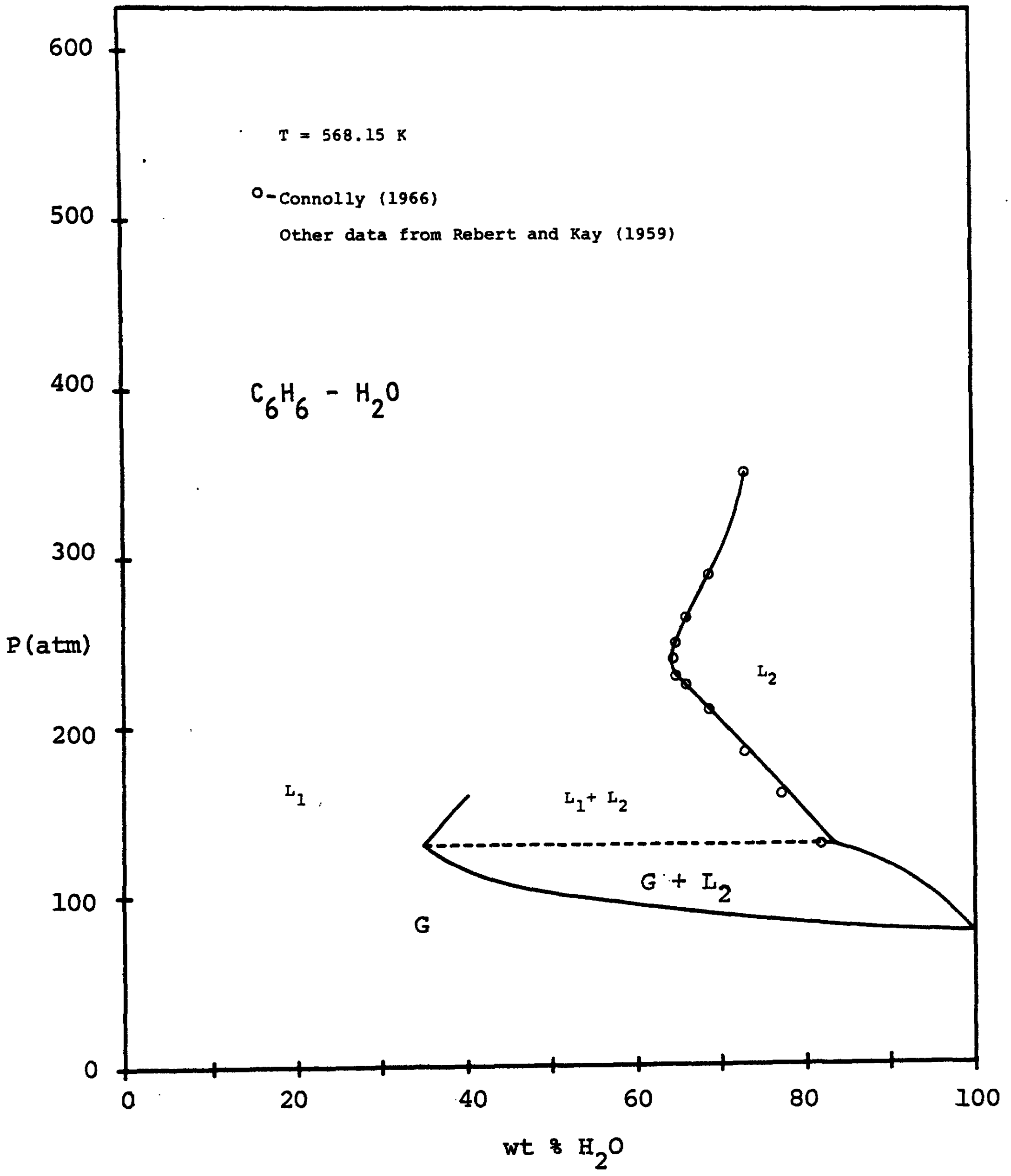

Figure 8.4d. A P-x section between benzene's critical point and the temperature minimum in the upper critical locus.

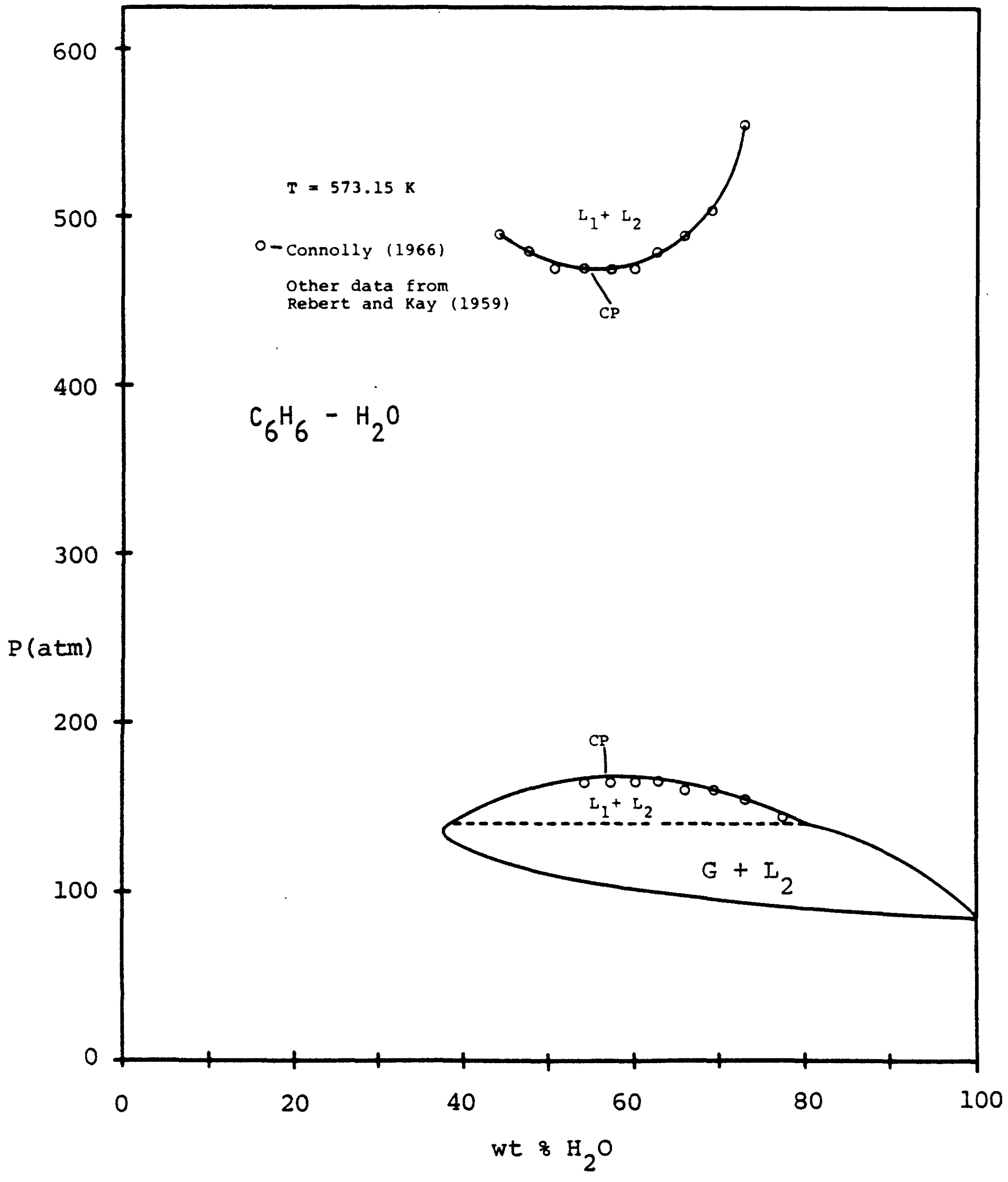

Figure 8.4e. A P-x section between the temperature minimum in the upper critical locus and the critical solution end point.

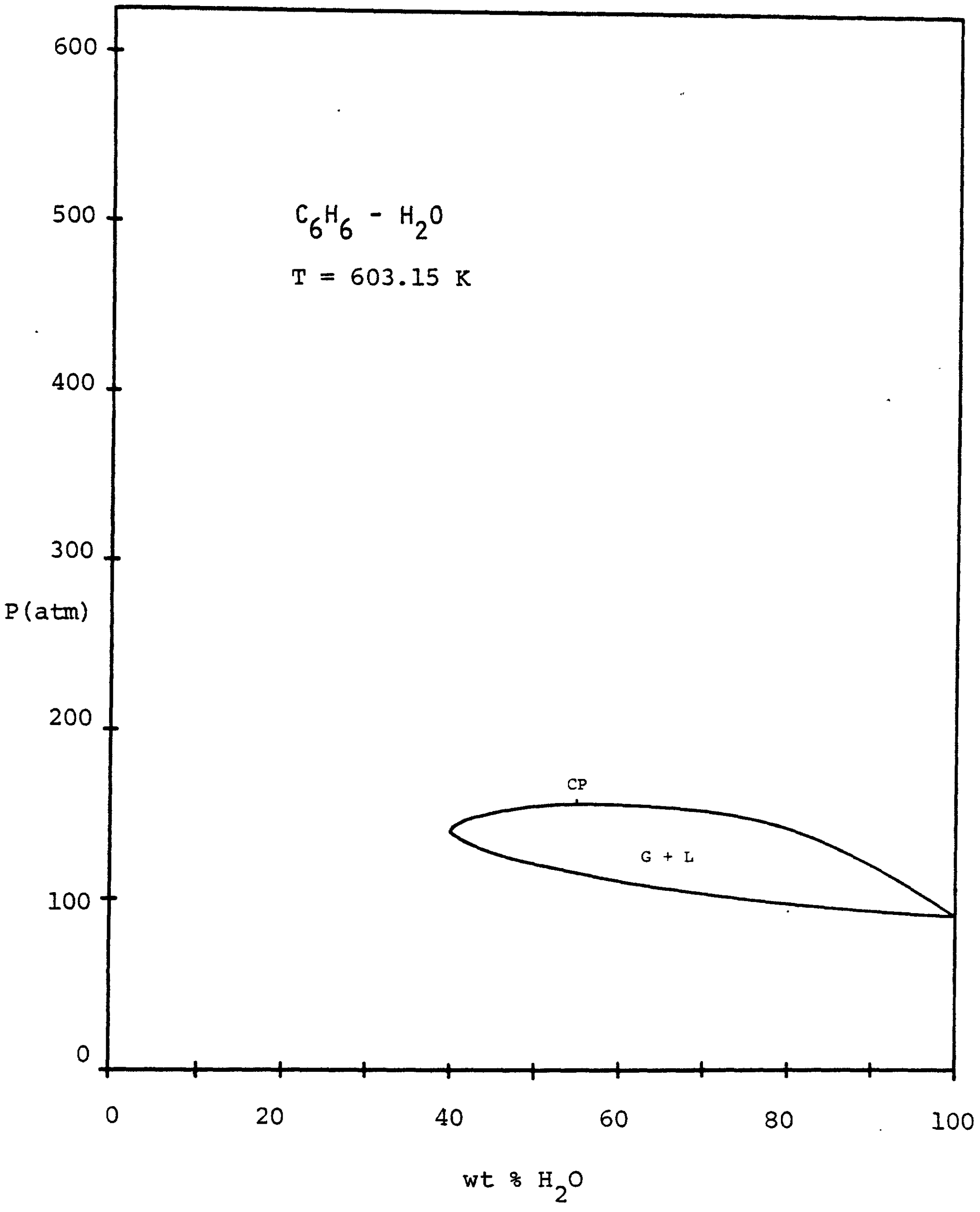

Figure 8.4f. A P-x section above the critical solution end point.

inversion, the liquid is more dense than the coexisting vapor along both branches of the VLE envelope.

Figure 8.4b is drawn at 541.45 K, a temperature slightly above the critical end point. The benzene-rich G+L_1 region has separated from the water-rich G+L_2 and L_1+L_2 regions. This separation occurs at the temperature minimum in the lower critical locus in Figure 8.2, and not at the critical end point as might at first appear. In the few tenths of a degree between the lower critical locus minimum and the critical end point, there is a small region of benzene-rich VLE attached to the three-phase line in addition to the separate "island" stemming from the vapor pressure of pure benzene. This must be so, since at any temperature just above the minimum in the critical locus there must be two critical points. A diagram of this type will be presented in Figure 8.9.

The L_1+L_2 and G+L_2 regions in Figure 8.4b are shown to intersect along a horizontal tieline (dashed) which corresponds to a point on the metastable LLG tieline in Figure 8.2. Thus, this three-phase line represents the intersection of two, rather than three binodal regions, as is normally the case. At the metastable three-phase pressure, a discontinuity in the slope of the binodal locus has been indicated. Rebert and Kay have drawn the section in this manner, although their data are insufficient to prove such a discontinuity. As seen in previous chapters, the equation of state does not yield slope discontinuities when only two binodal regions merge.

Increasing temperature to 553.15 K, the section of Figure 8.4c is found. The benzene-rich island is now quite small. Figure 8.4d is drawn at 568.15 K. This temperature is above benzene's critical point, so that the benzene-rich island no longer exists. The figure also includes some higher pressure data along the L_1+L_2 envelope. Only the water-rich leg of the curve has been measured. As expected from Figure 2.10, it exhibits a pronounced minimum in water composition. The benzene leg would have a corresponding maximum in water composition. At 573.15 K, as shown in Figure 8.4e, the pinching effect created by these extrema has been completed, yielding two distinct L_1+L_2 regions separated by a miscibility gap. As temperature is further increased, the lower L_1+L_2 region shrinks and finally disappears at the critical solution end point. At temperatures above this end point, the VLE envelopes are of the usual shape, as illustrated in Figure 8.4f.

The P-x sections generated from the P-R equation will now be considered. This series of diagrams includes all the temperatures of Figure 8.4 as well as several others. Reference to Figure 8.3 should be made to clarify the relationship between the various sections. To reiterate, the major qualitative difference between the predicted Figure 8.3 and the experimental Figure 8.2 is that the former has no critical end point along the critical locus starting from the pure benzene critical point. This fact leads to the prediction of normal azeotropes because, as Rowlinson (1969) has pointed out, heteroazeotropes must in general revert to normal azeotropes as the critical solution end point is approached. Figure 8.5 illustrates this point.

Figure 8.6a gives the calculated P-x section at 528.15 K. Three stable binodal regions are correctly predicted. As in previous chapters, the stable binodal curves are interconnected by metastable and unstable curves. In this instance the L_1+L_2 and G+L_2 binodals are continuous with one another, while the L_1+G locus forms a closed curve. This fact is more evident in Figure 8.6b, an enlargement of the azeotropic region. A metastable normal azeotropic point is visible in this diagram as well. At 541.45 K, as shown in Figure 8.7, the predicted behavior is essentially the same. A benzene-rich island has not broken off as it did in Figure 8.4b. This will not occur until the temperature minimum in the vapor-liquid critical locus has been reached. Spinodal curves have also been given in this figure, and indicate the location of an unstable critical point. This is a point along the unstable locus in Figure 8.3.

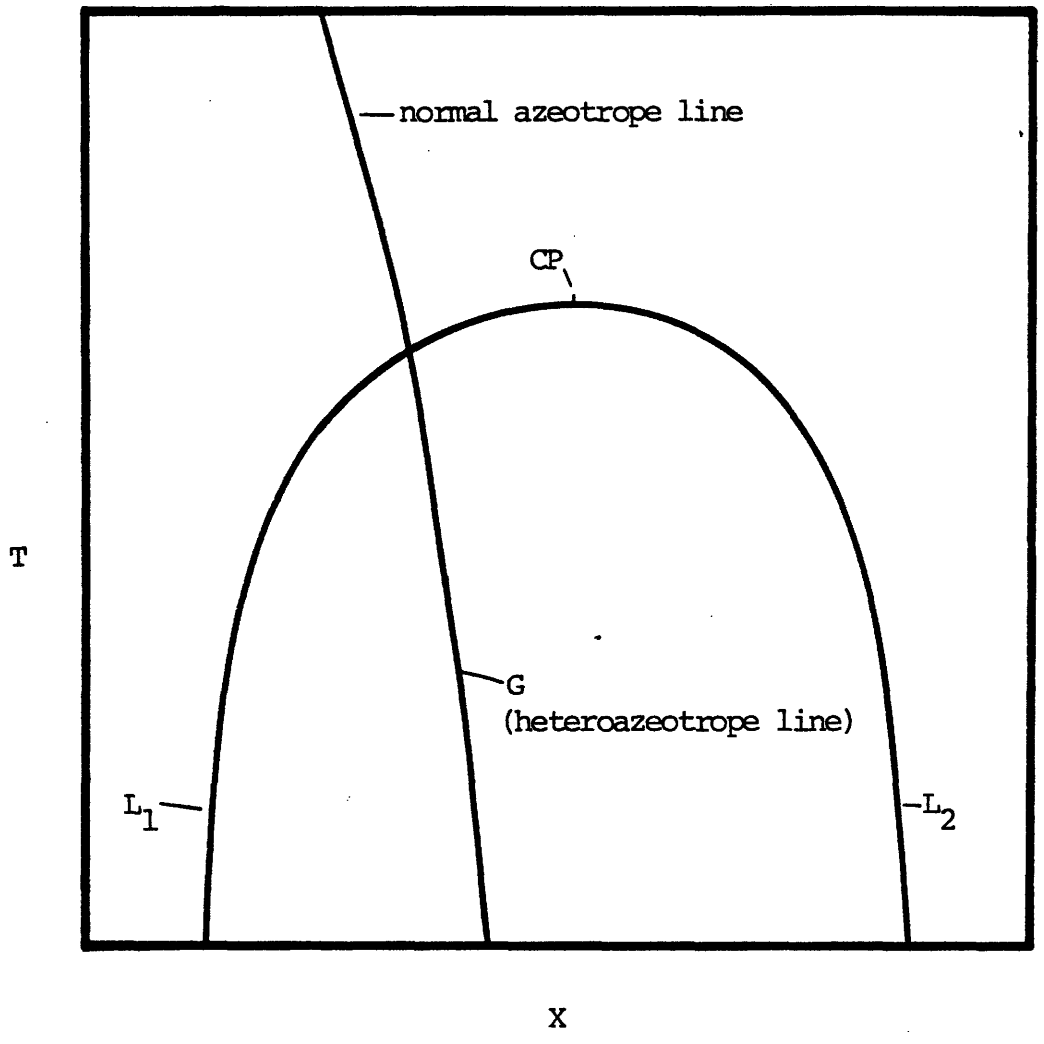

Figure 8.5. The T-x projection for a heteroazeotrope system. Only the compositions of the three coexisting phases at each temperature have been plotted. The azeotropic composition must fall outside the composition range of the coexisting liquids as the critical solution temperature, CP, is approached.

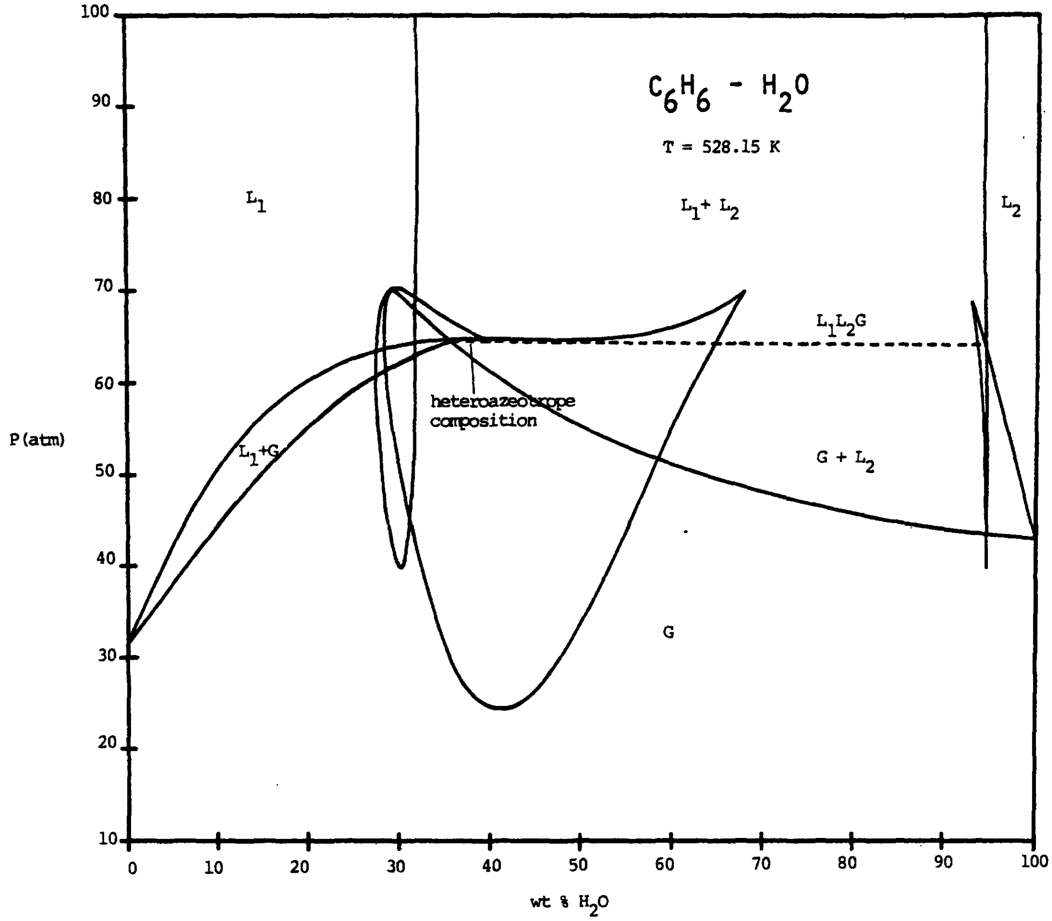

Figure 8.6a. A predicted P-x section below the temperature minimum in the G-L critical line. (See Figure 8.3.)

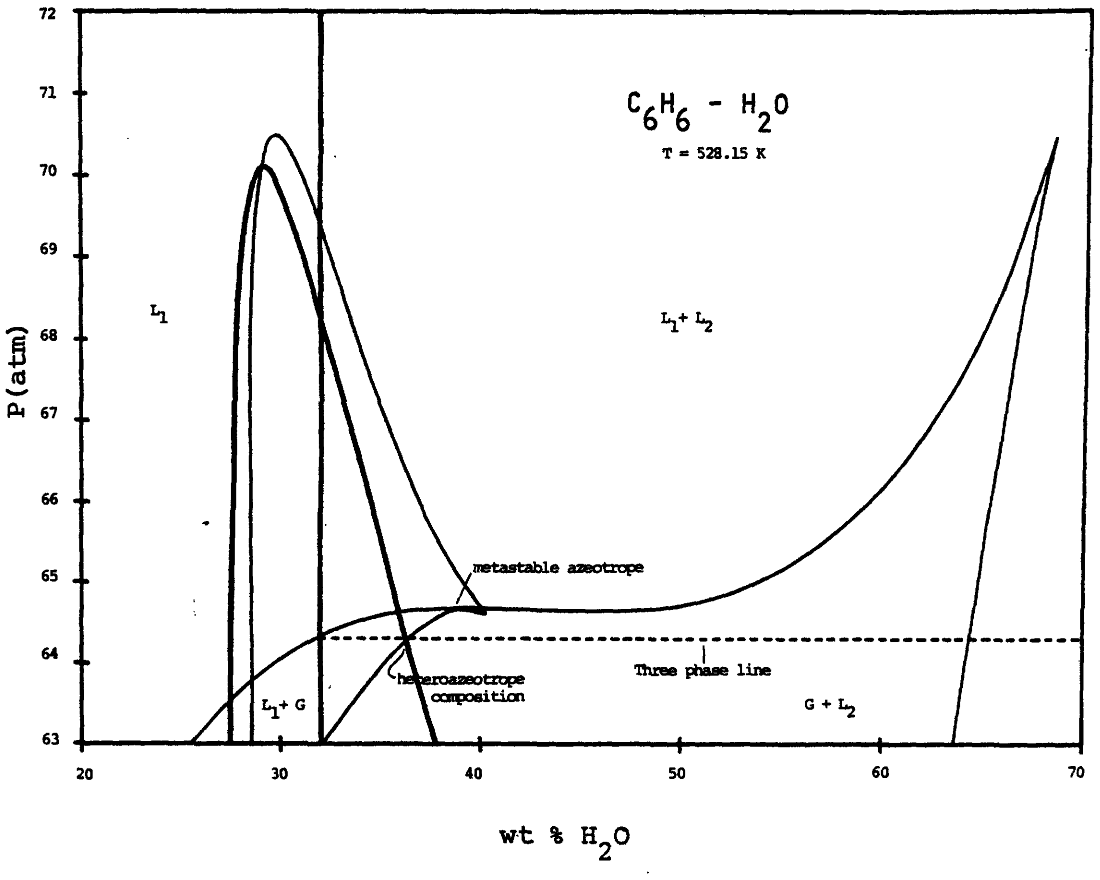

Figure 8.6b. The P-x section at 528.15 K in the vicinity of the azeotrope.

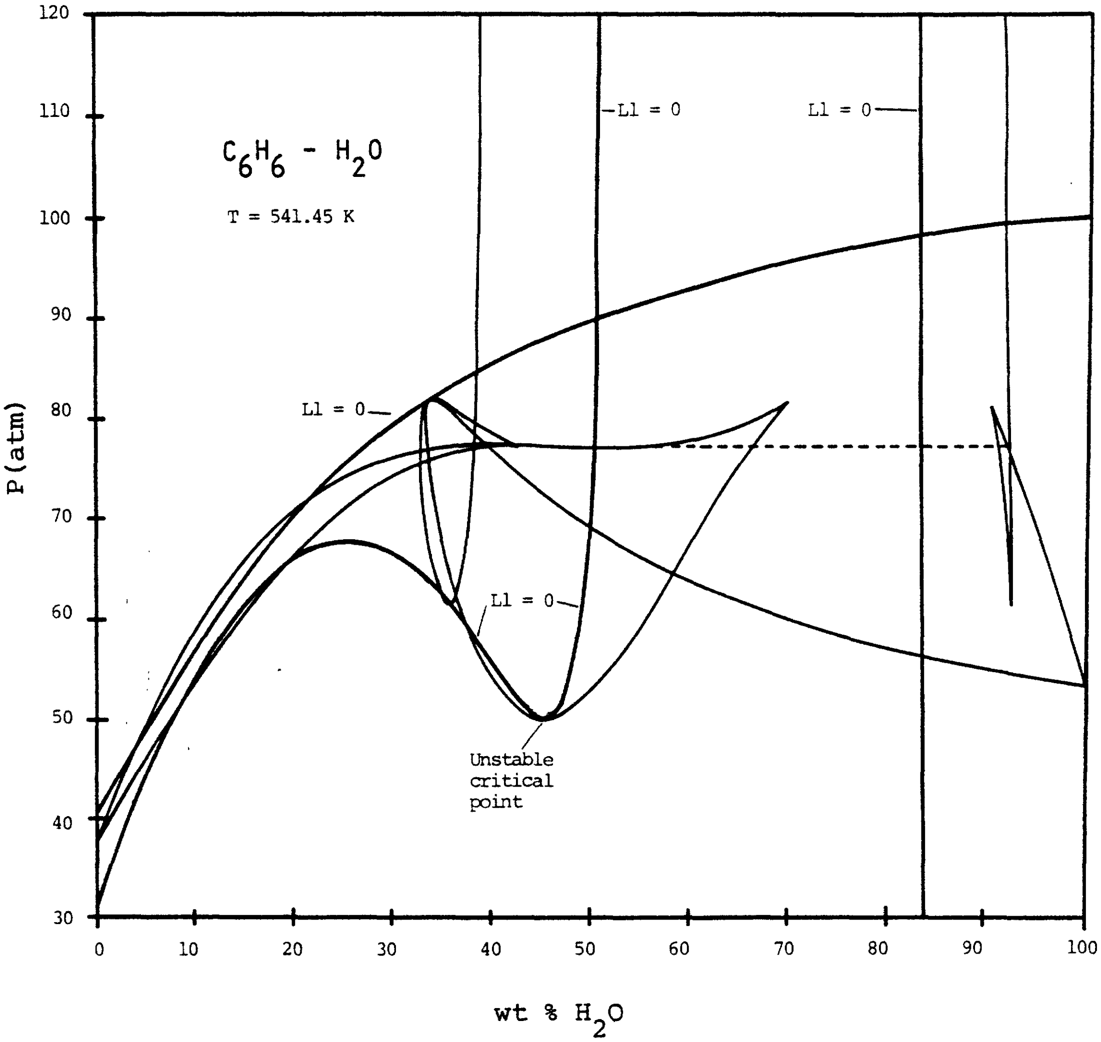

Figure 8.7. A P-x section below the temperature minimum in the G-L critical line.

Figure 8.8a shows the P-x section for 553.15 K. The benzene-rich VLE envelope has continued to narrow. At this temperature, the previously metastable normal azeotropic point has moved into the stable region, as seen in the enlargement of Figure 8.8b. Thus, a normal, minimum boiling azeotrope is now predicted rather than a heteroazeotrope.

Increasing temperature slightly, to 554 K, the temperature minimum in the vapor-liquid critical locus has just been exceeded. From Figure 8.3, it is evident that there must now be a separate benzene-rich region. Figure 8.9 illustrates these features. As mentioned previously, there must be a similar break with the formation of two critical points just above the temperature minimum in Figure 8.2. Experimental measurements have not been detailed enough to verify the presence of a normal azeotrope in this small region. A normal azeotrope must exist, however, unless by chance the lower critical locus is coincident with the heteroazeotrope-normal azeotrope transition point. This situation is analogous to that of Figure 8.5. The equation of state has thus brought out an important feature of the system's phase behavior which was not evident from the experimental results.

Figure 8.10a is the P-x section at 568.15 K. The azeotropic region has diminished in size considerably. An interesting change has also taken place in the continuation

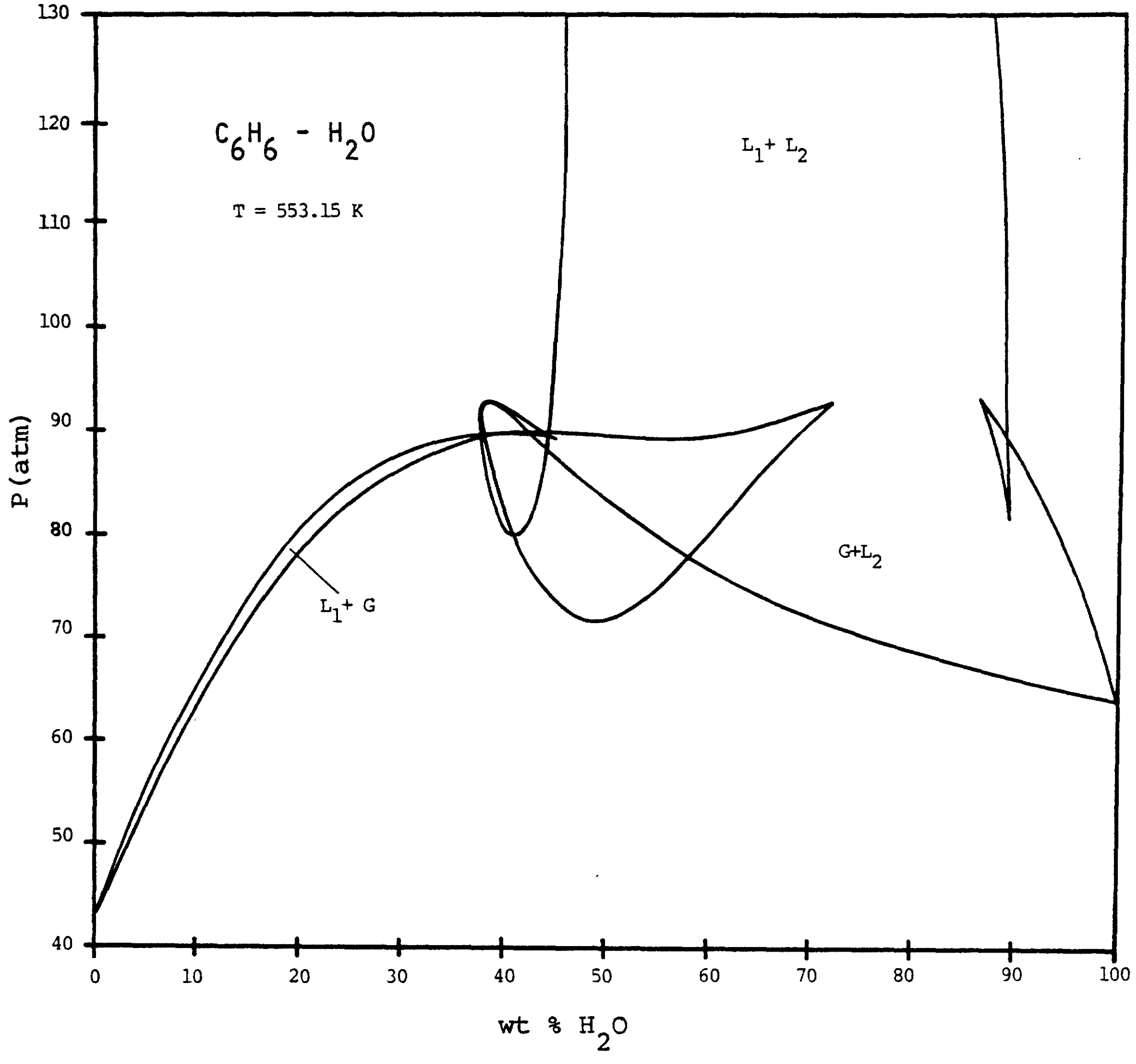

Figure 8.8a. A P-x section below the temperature minimum in the G-L critical line.

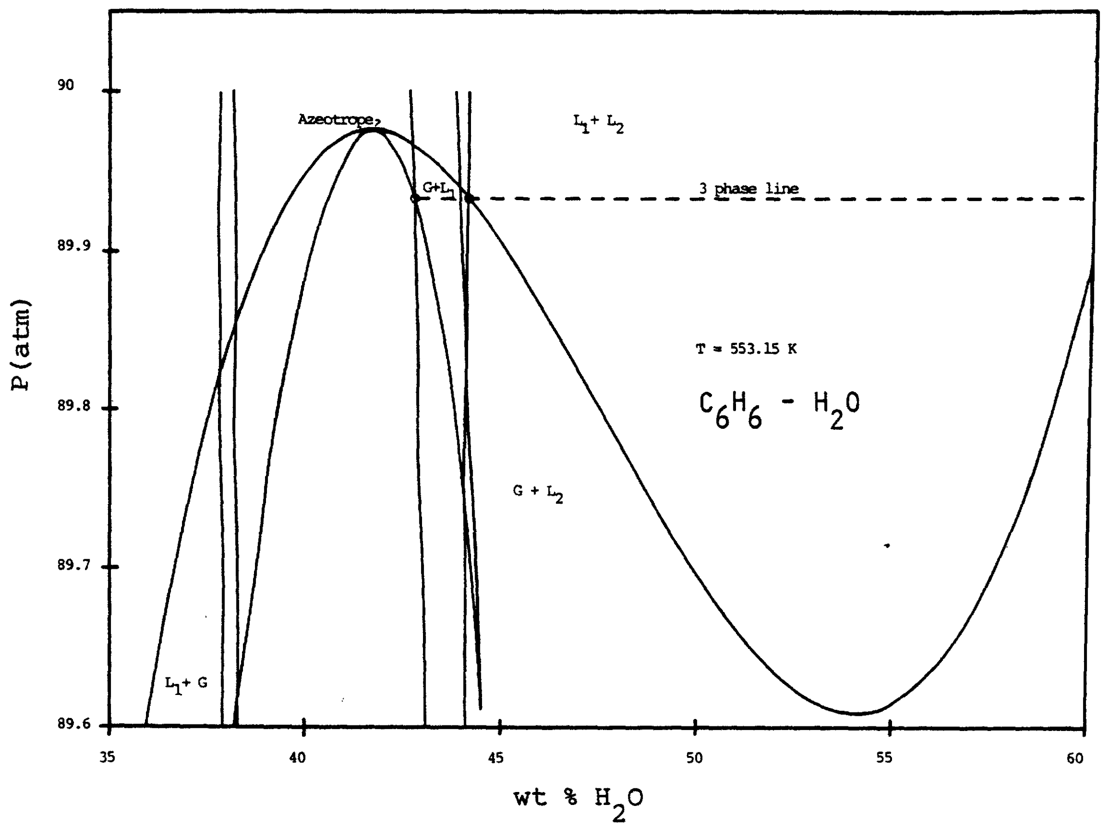

Figure 8.8b. The P-x section at 553.15 K in the vicinity of the azeotrope. The azeotrope is now stable, outside the region of liquid-liquid immiscibility.

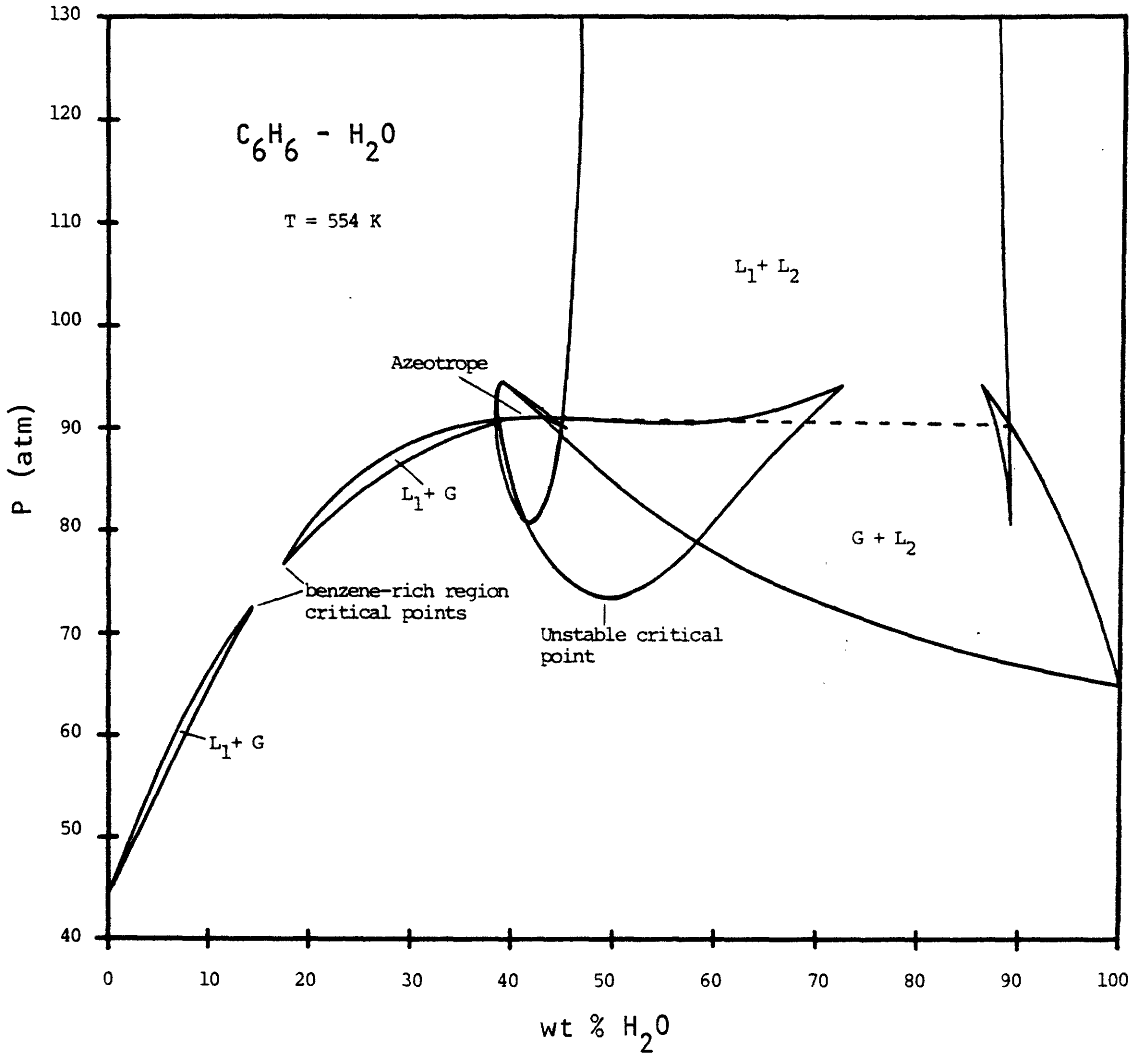

Figure 8.9. A P-x section slightly above the temperature minimum in the G-L critical line.

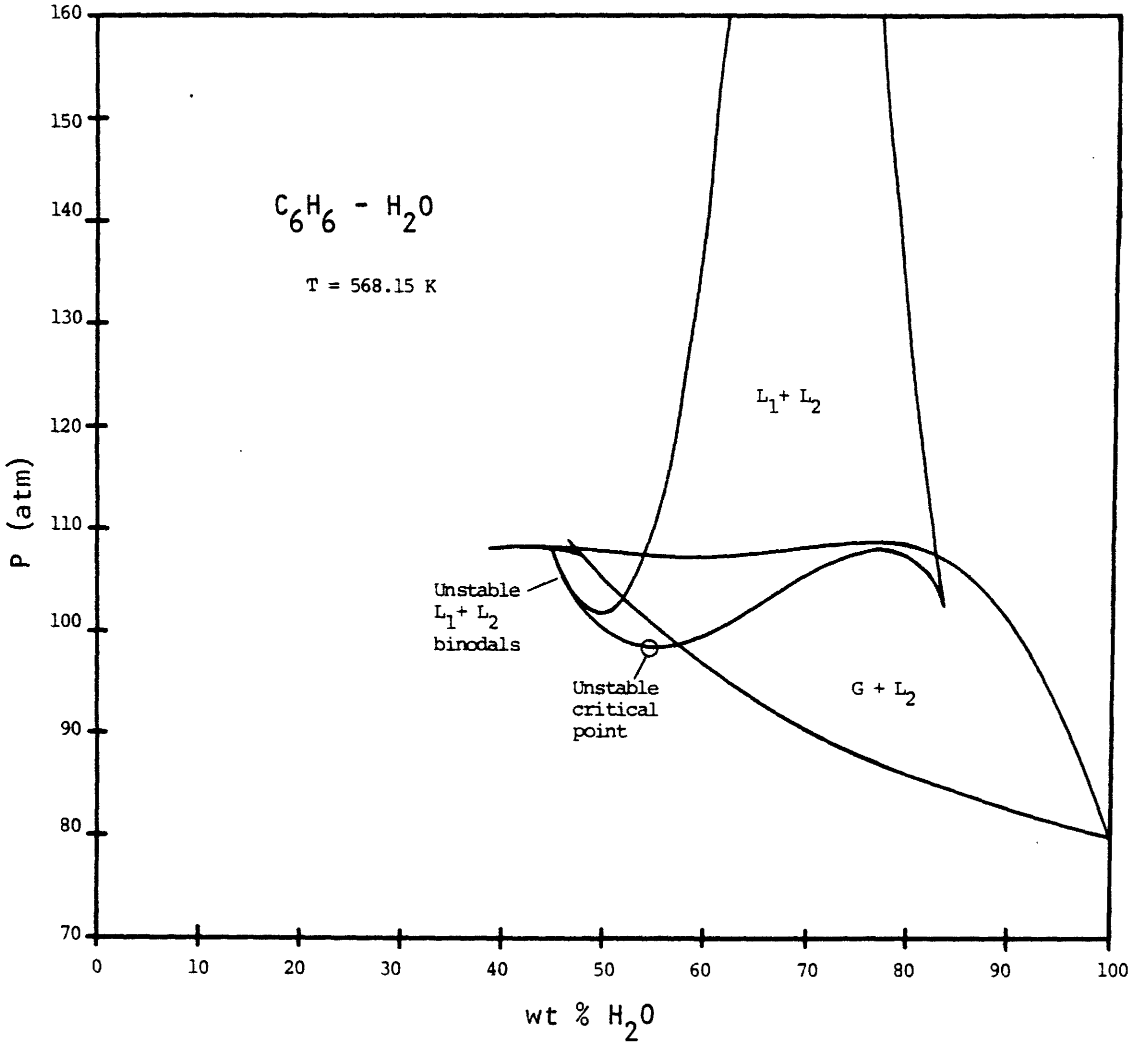

Figure 8.10a. A P-x section between benzene's critical point and the temperature minimum in the L-L critical line.

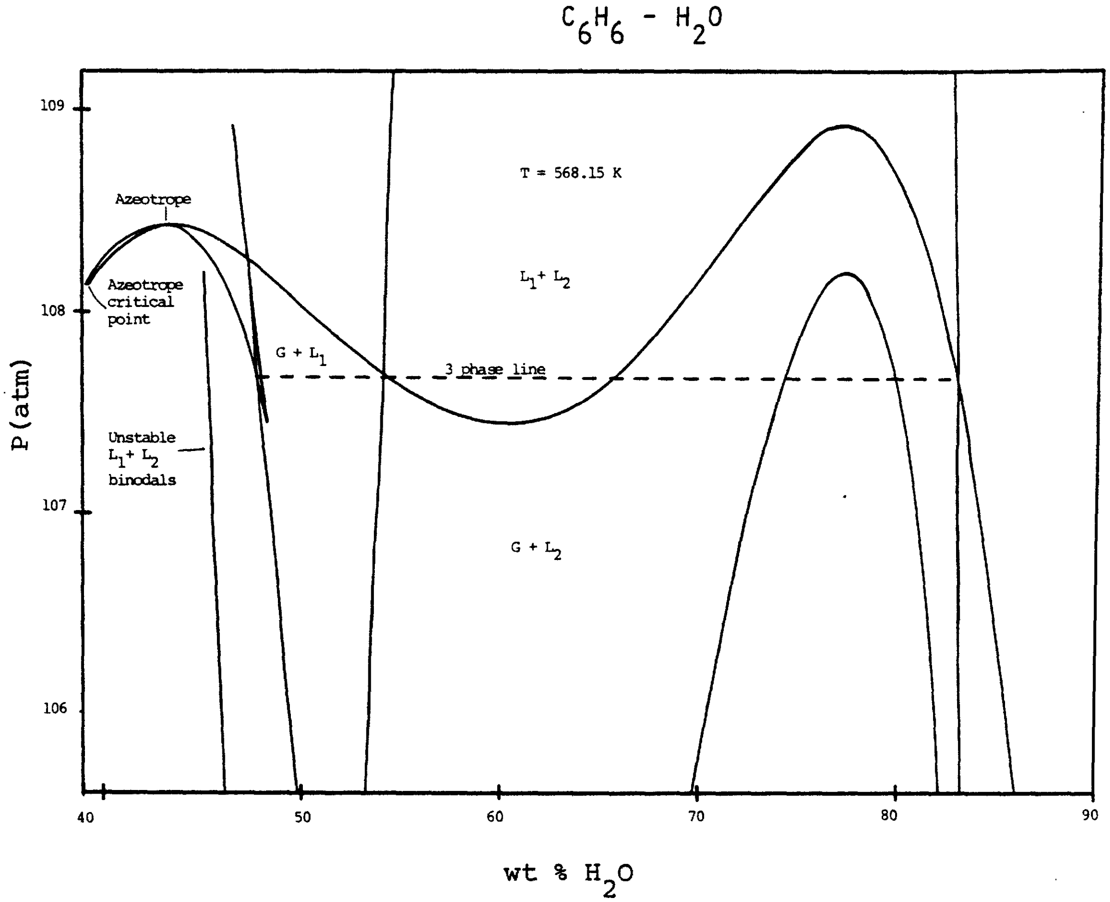

Figure 8.10b. The P-x section at 568.15 K in the vicinity of the three-phase line. The G+L_1 and G+L_2 binodals are continuous with one another.

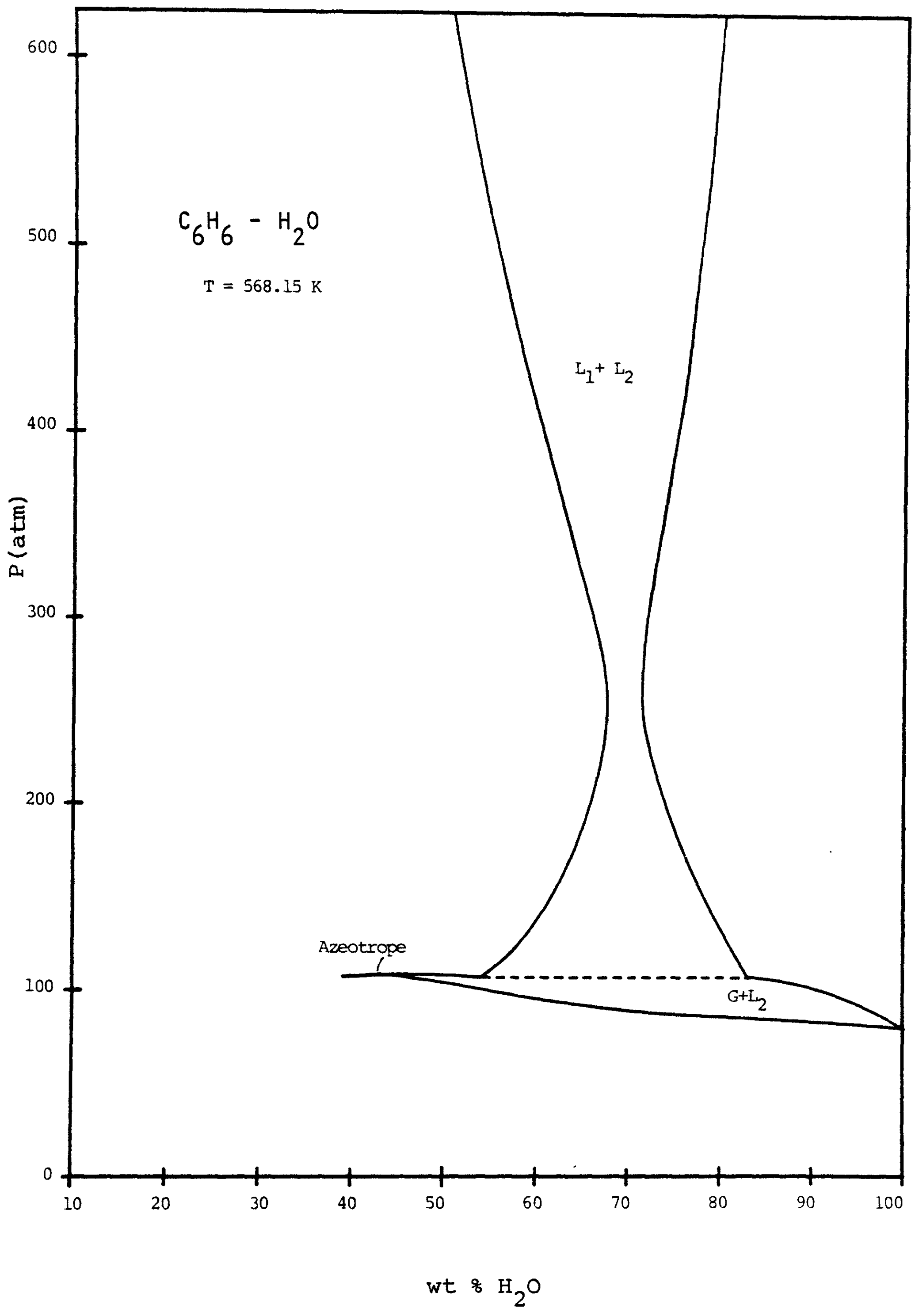

Figure 8.10c. The P-x section at 568.15 K extended to high pressures.

of the stable binodal curves. It is now the L_1+L_2 curve which of itself forms a closed loop, while the $G+L_1$ and $G+L_2$ curves are interconnected. Figure 8.10b shows these interconnections in an enlargement of the three-phase region. For comparison with the high pressure data in Figure 8.4d, Figure 8.10c has been included. The necking effect in the L_1+L_2 region, due to the proximity of the critical solution temperature, is evident.

As temperature is further increased, the benzene-rich branch of the azeotrope continues to shrink. Eventually, the azeotrope critical point of Figure 8.10b will meet the azeotrope point in a cusp. This behavior was illustrated in Figure 2.13. Figure 8.11a, at 573.15 K, is at a temperature slightly above the cusp temperature. A critical point appears very near the tip of the $G+L_1$ region. In Figure 8.11b, the section is redrawn to include high pressure data for comparison with Figure 8.4e. Although the predicted compositions are not accurate, the miscibility gap has been correctly predicted.

Figure 8.12 is a P-x section at a temperature just above that of the critical end point in Figure 8.2. The L_1+L_2 critical point has now become metastable, and will disappear as the L_1+L_2 region converges to a point. Figure 8.13a, drawn at 603.15 K, is at a temperature above the L_1+L_2 critical line termination. The VLE envelope is now of the

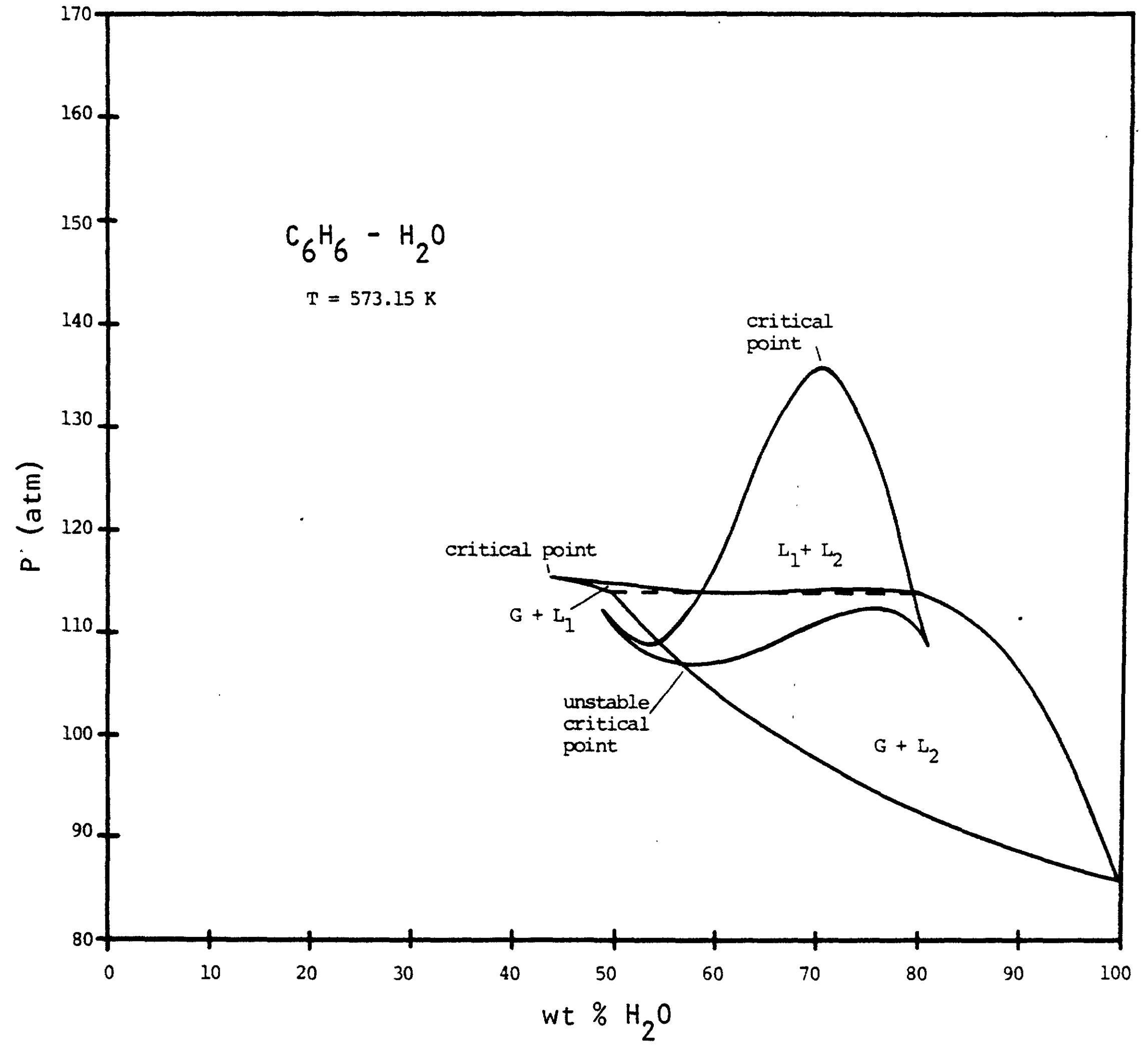

Figure 8.11a. A P-x section between the temperature minimum in the L-L critical line and the critical end point.

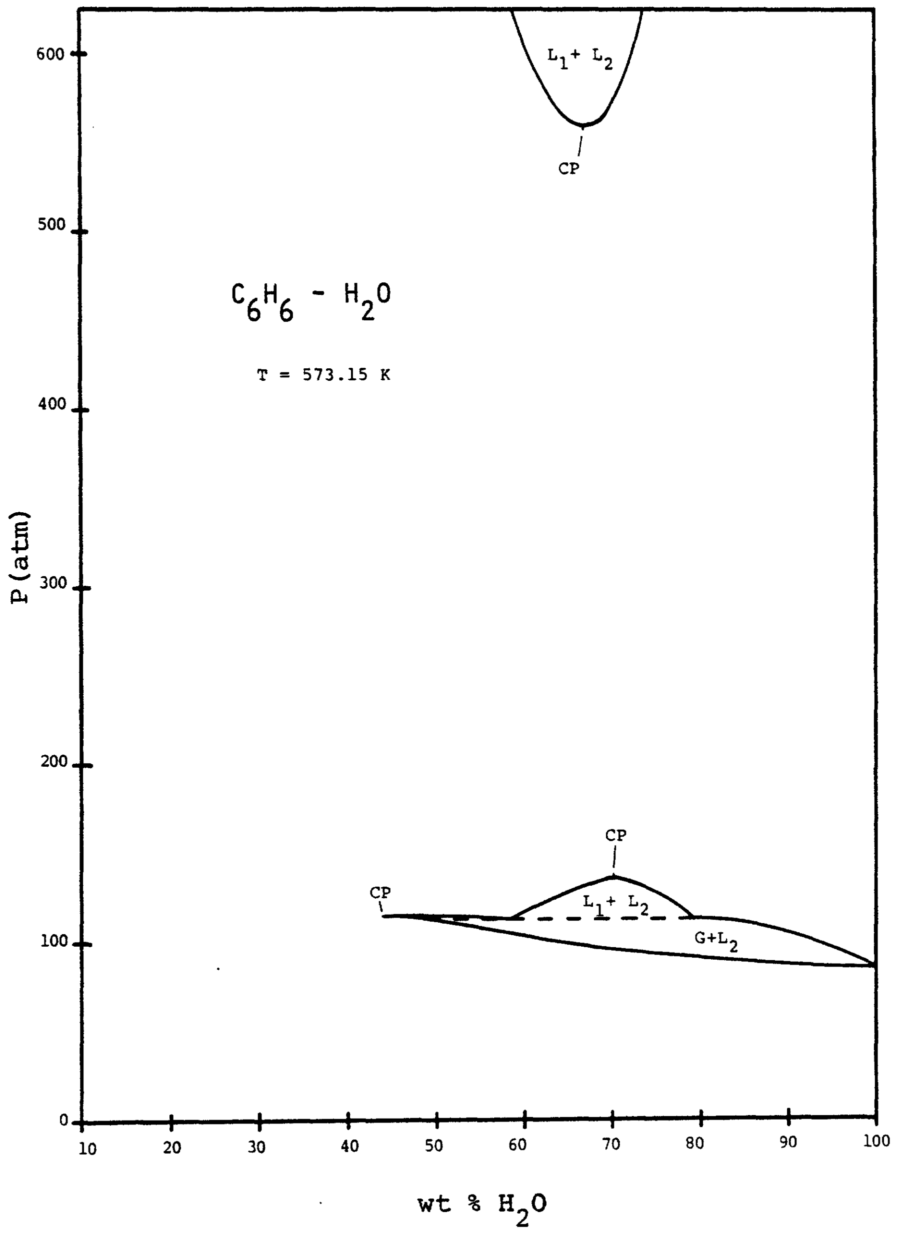

Figure 8.11b. The P-x section at 573.15 K extended to high pressures.

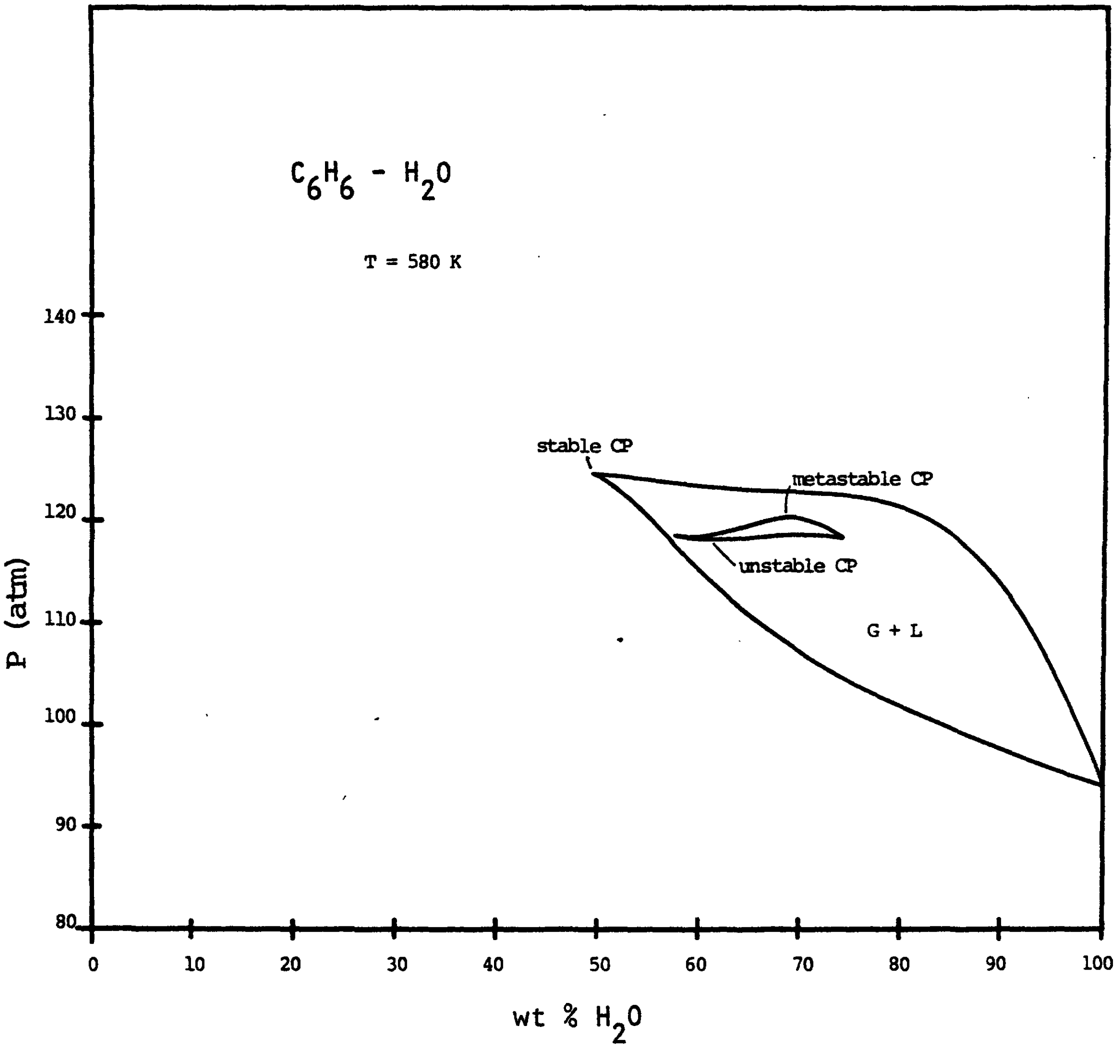

Figure 8.12. A P-x section slightly above the critical end point.

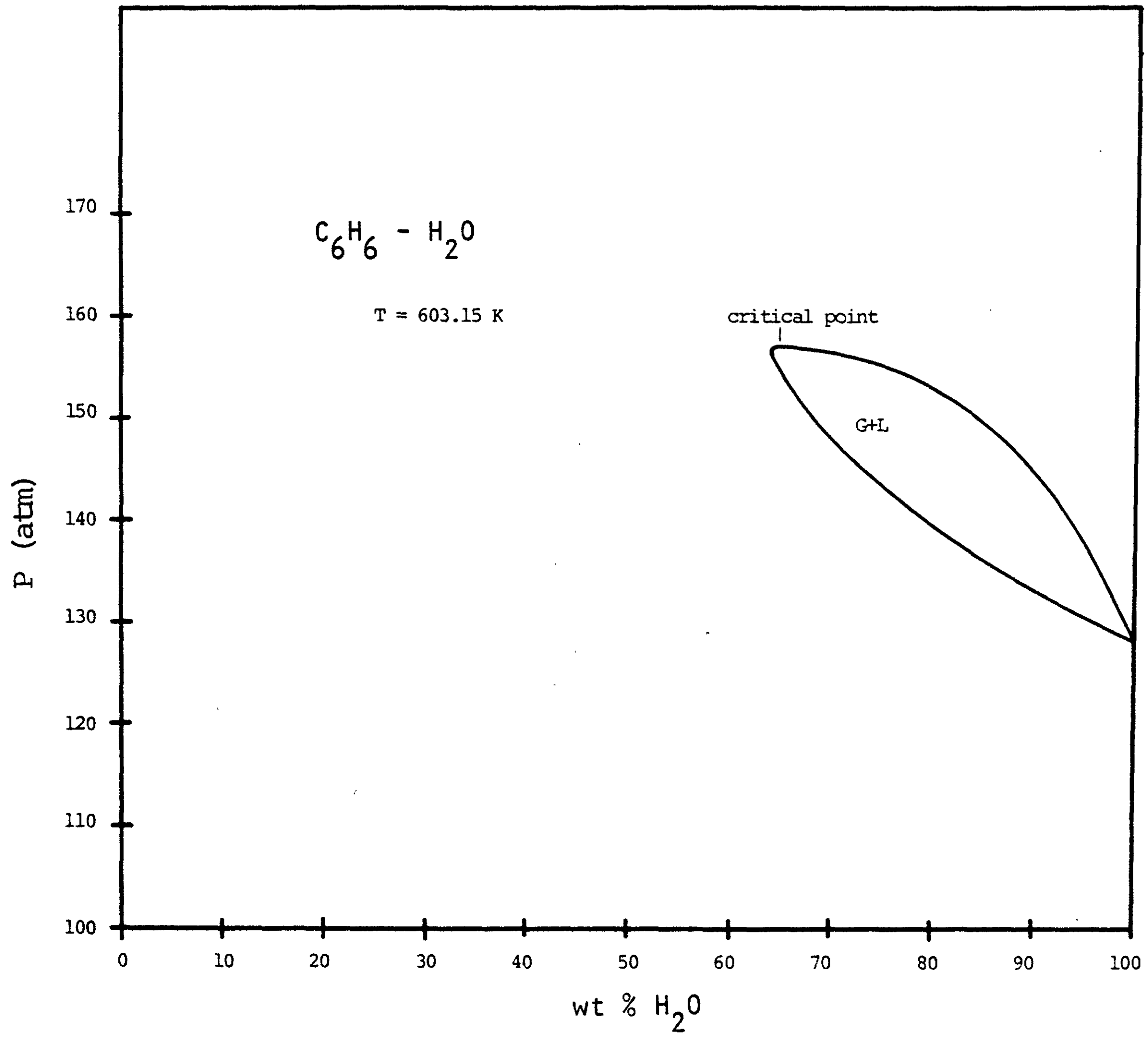

Figure 8.13a. A P-x section above the L-L critical line cusp.

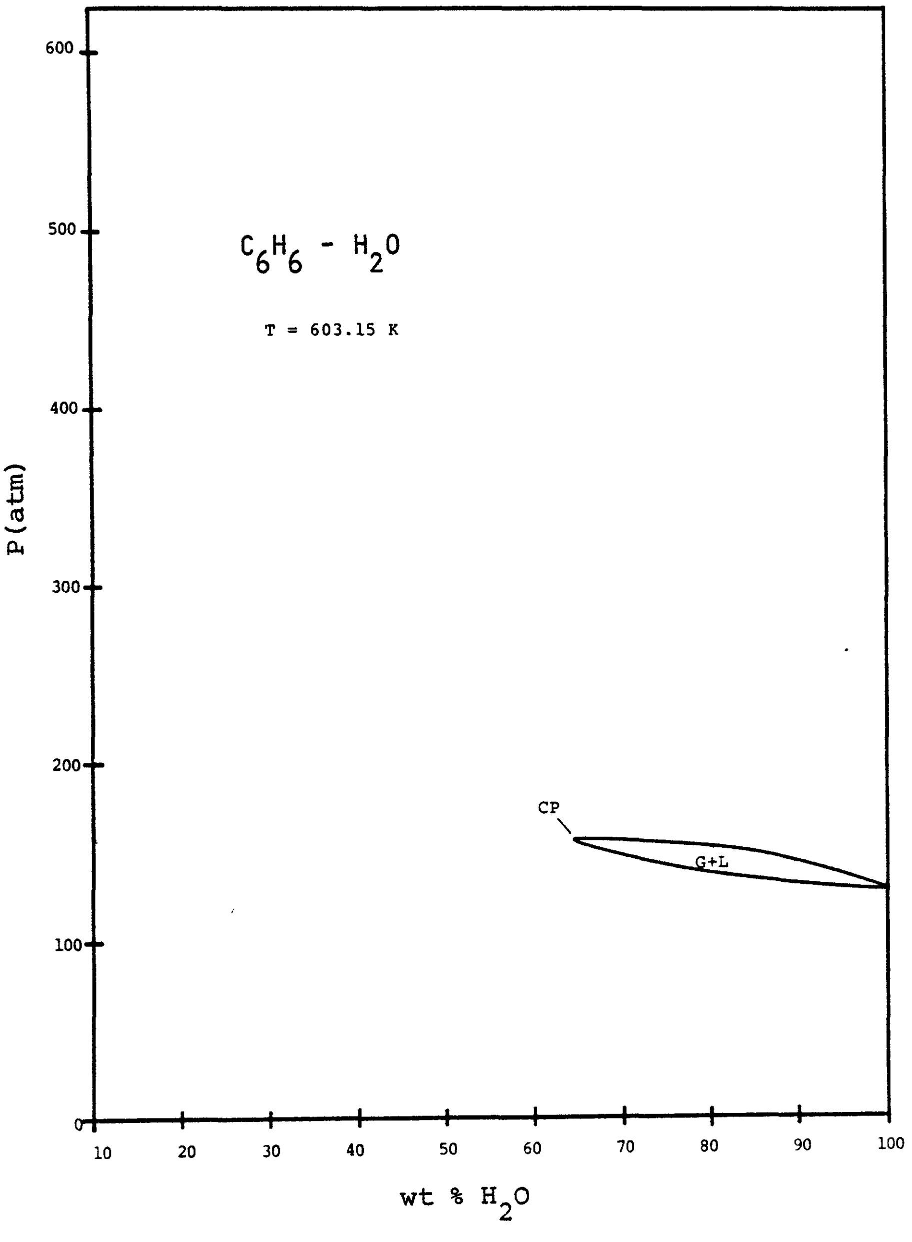

Figure 8.13b. The P-x section at 603.15 K extended to high pressures.

usual type. Figure 8.13b is the same section on a high pressure axis, for comparison with Figure 8.4f.

In generating the preceding P-x sections, several new types of fugacity curves were encountered. A pressure sequence of Cartesian f-x plots at 568.15 K is given in Figure 8.14. Figure 8.14a is a plot at 100 atm, which is different in several respects from the closed loop plots discussed in Chapter 3. The mechanically unstable or middle volume root no longer gives the middle value of fugacity. As shown in the figure, it yields the minimum fugacity over the entire multiple root range. Also, the two stable roots are no longer conveniently identified as liquid and gaseous. For most of the multiple root range, the monotonic solution gives the intermediate fugacity value, but it becomes the maximum fugacity value as the infinity point is approached. The second stable solution, which forms the top of the loop, has two maxima and one minimum for a total of three spinodal points. Continuation of the plot to the pure benzene axis does not yield any further spinodal points.

The f-x plots at this temperature exhibit an interesting transition in the region near the infinity point. Figure 8.14b focuses on this region at a pressure of 108.158 atm. The first infinity point is equivalent to the infinity point in Figure 8.14a, i.e., it is at the tip of the loop. The tip is now quite pointed, and the spinodal point is very close to

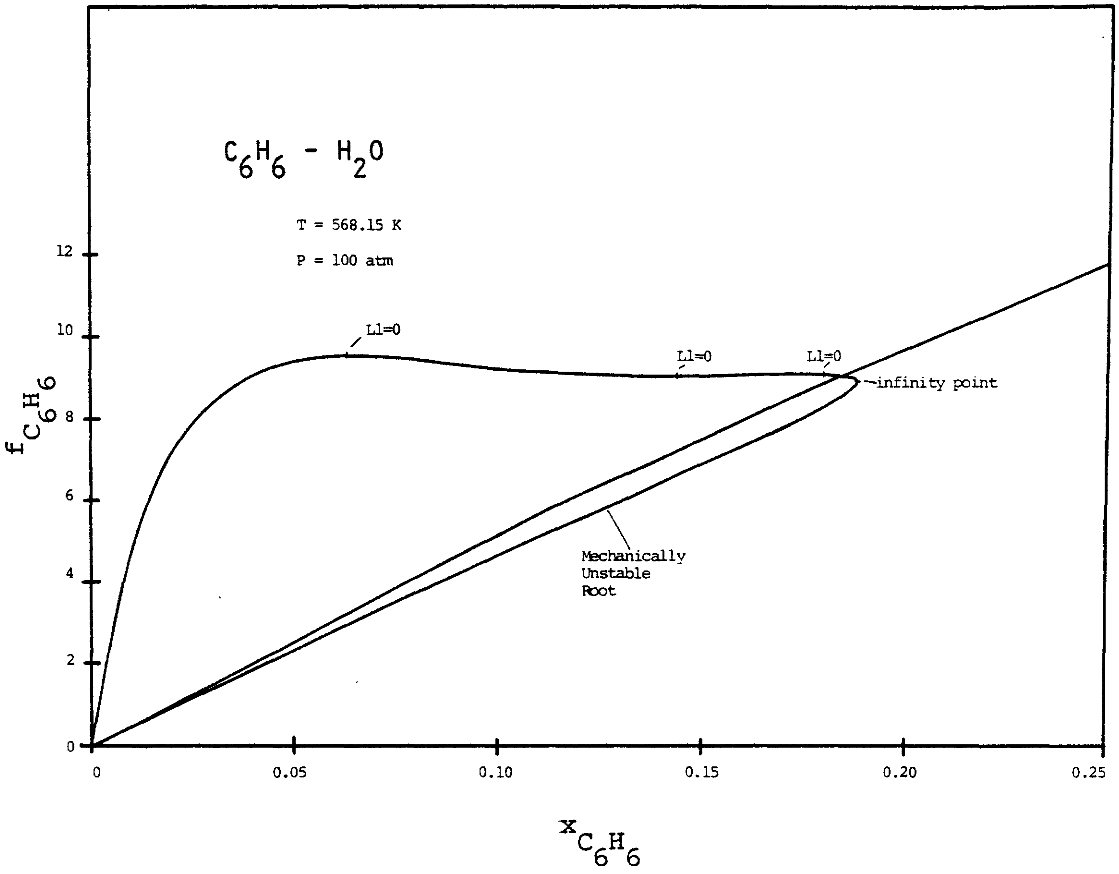

Figure 8.14a. An f-x plot. The mechanically unstable root always gives the minimum fugacity.

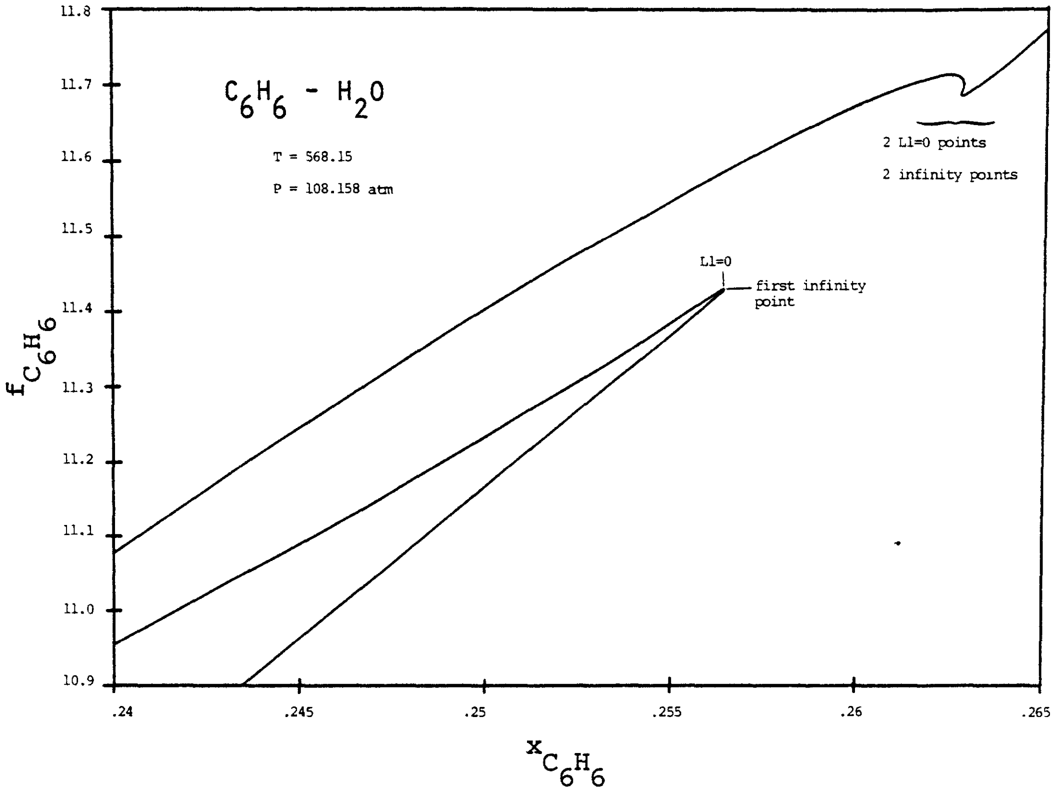

Figure 8.14b. An f-x plot in the region of the infinity points.

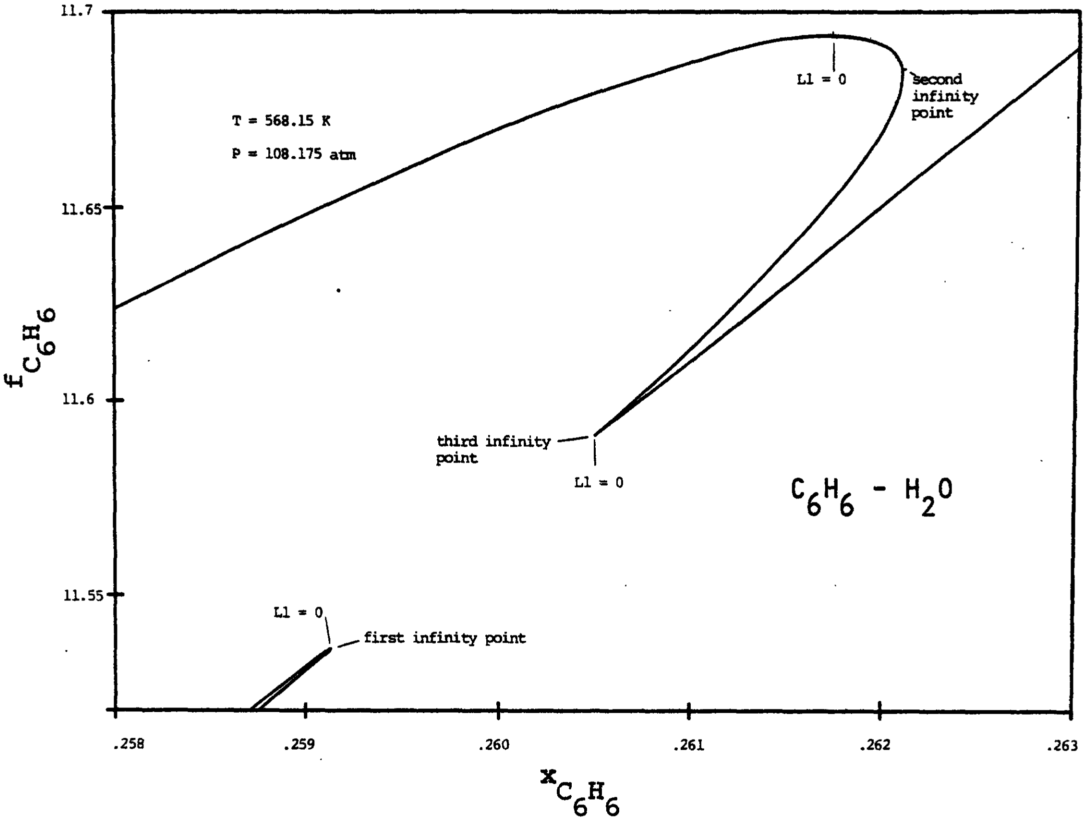

Figure 8.14c. An f-x plot in the region of the infinity points.

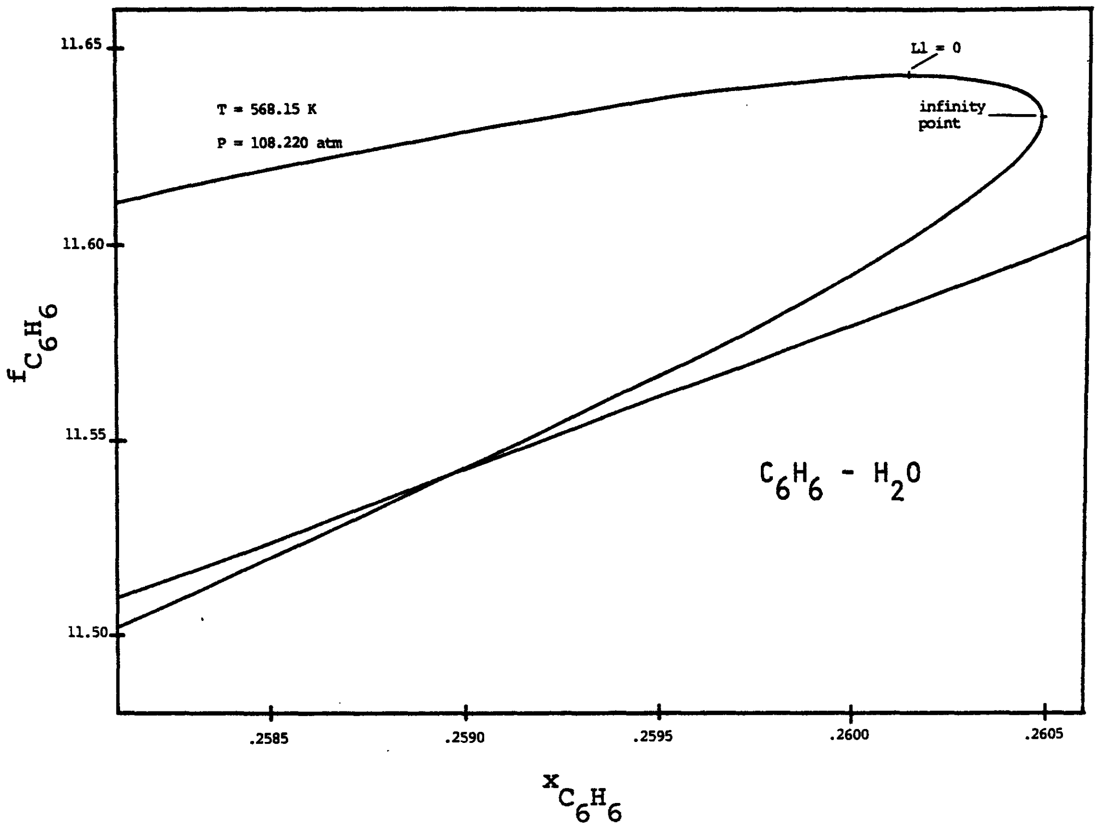

Figure 8.14d. An f-x plot. The first and third infinity points in Figure 8.14c. have merged.

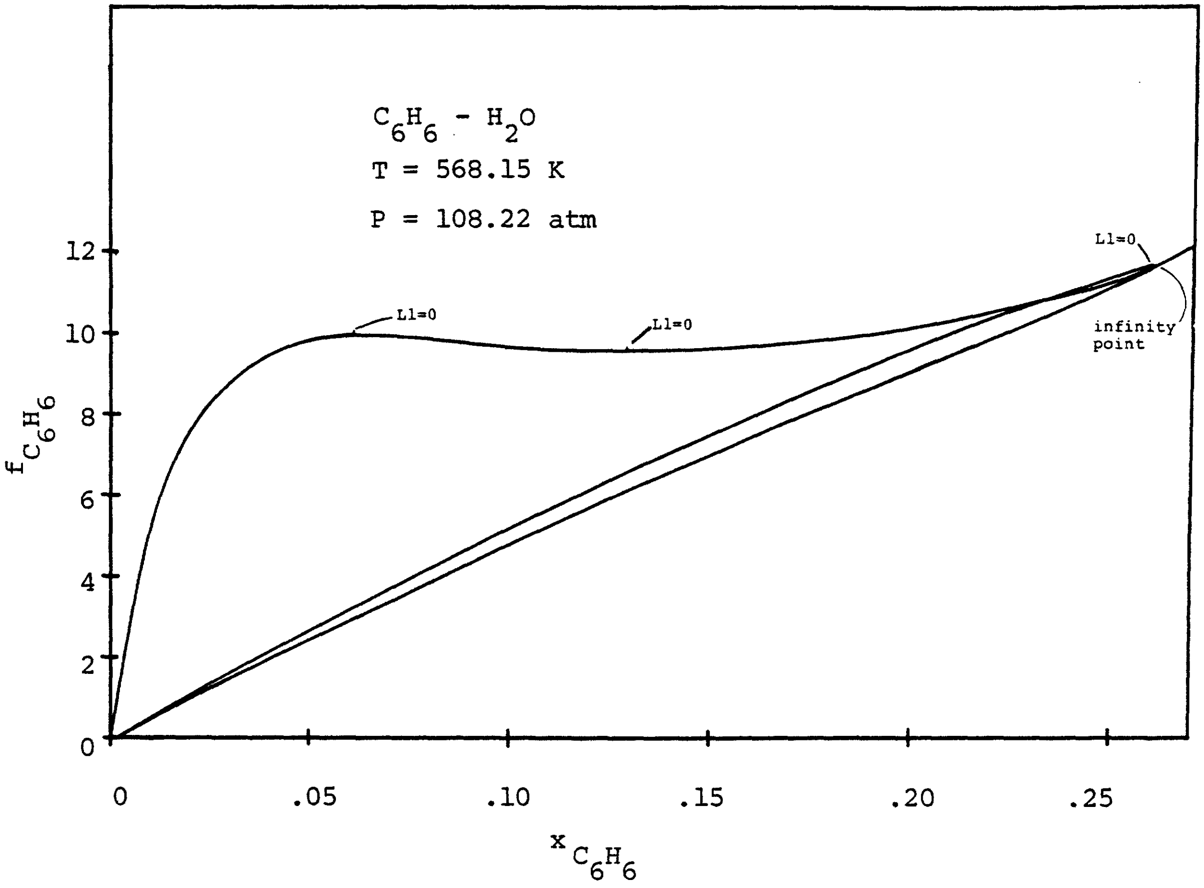

Figure 8.14e. The f-x plot of Figure 8.14d extended to the pure water axis.

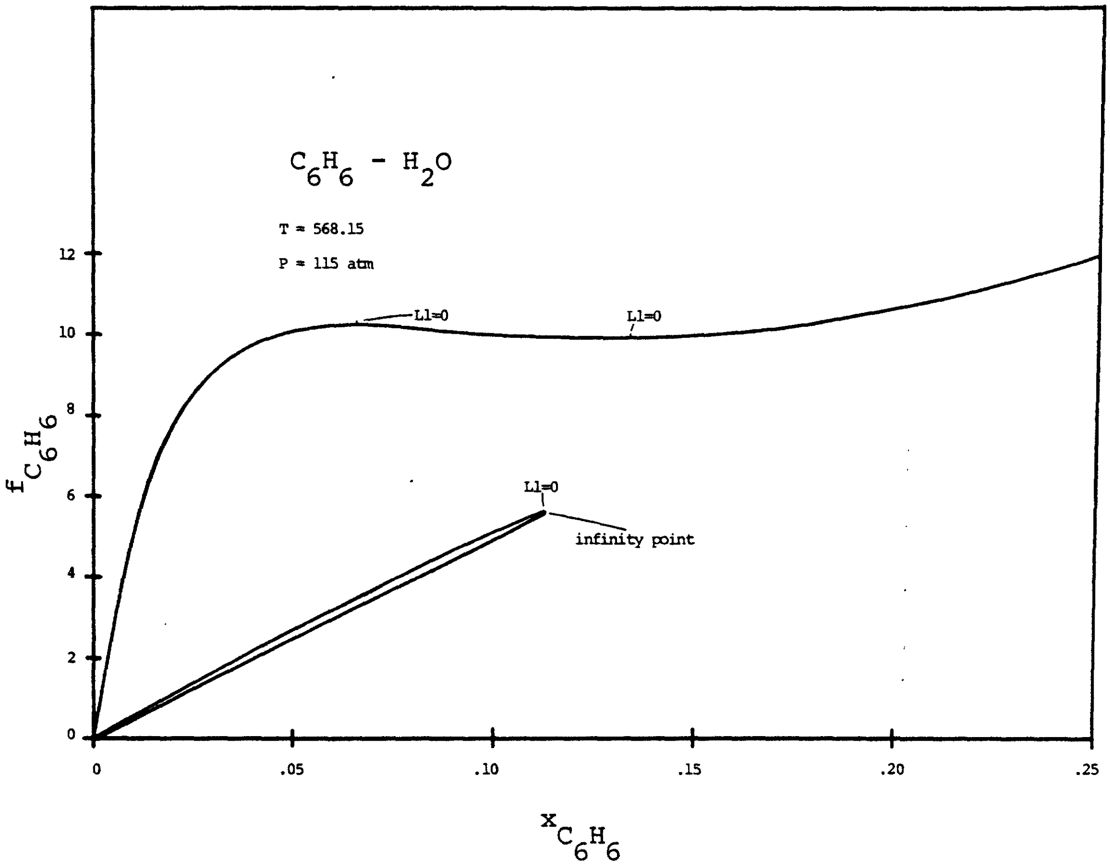

Figure 8.14f. An f-x plot. The region of three roots is shrinking toward the origin with increasing pressure.

the infinity point. The formerly monotonic solution now exhibits a kink, which adds two infinities and two spinodals for a total of three infinities and five spinodals at this pressure and temperature. The kink is associated with phase equilibrium solutions along the benzene-rich azeotropic branch. (At pressures and temperatures near benzene's vapor pressure curve, it moves over to the pure benzene axis to give a discontinuity of the type shown in Figure 3.3). As pressure is increased to 108.175 atm, the kink becomes sharper, and the first and third infinity points approach one another. This is shown in Figure 8.14c. Upon reaching 108.22 atm, the two infinities have merged, as illustrated by Figure 8.14d. Figure 8.14e shows the course of the entire loop at this pressure. The curve is quite similar to that given in Figure 8.14a, with a total of three spinodal points and one infinity. Now, however, the top half of the loop has only one spinodal point. This is more easily seen in Figure 8.14f, as the loop shrinks toward the pure water axis. The loop will disappear as pressure is further increased.

To summarize, a comparison of the experimental and predicted P-x sections shows that the qualitative picture provided by the equation of state is in large measure correct. The calculated P-x sections clarify the behavior of the normal azeotrope which was not investigated in the experimental work. The correctness of the predicted three-phase line and the G-L critical line is uncertain, pointing out the need for more careful experimental work in this region.

Chapter 9 Conclusions and Recommendations

Knowledge of the overall phase behvaior of systems is of importance in process design, since it indicates under what conditions a phase equilibrium process is most favorably carried out. For example, supercritical extraction of naphthalene with ethylene should probably be carried out near the UCEP rather than the LCEP. Although the pressures required are 3.5 times as high (174 atm versus 51 atm), the solubility of naphthalene is 85 times as high (0.17 versus 0.002 mole fraction). As a further example, suppose it was desired to dissolve benzene in water. The shape of the upper critical line for this system shows that conditions of about 300°C and 170 atm are sufficient to yield complete miscibility of these two substances.

In developing a methodology to predict overall P-T-x diagrams, a number of significant results were obtained. These are as follows:

- -Fugacity-composition plots provide an excellent means of representing the possible types of stable and metastable phase equilibrium at a given temperature and pressure.
- -If the material stability criterion reaches a point of discontinuity in the tracking of a stable system, that point may represent a limit of mechanical

stability. This is true even if the material stability criterion is satisfied on either side of the discontinuity.

- Material stability should be considered undefined in a region of mechanical instability, since alternate statements of the material stability criterion may give conflicting information in such a region.
- When the cubic equation has multiple roots, P-x and T-x sections may correctly indicate the existence of stable states within a region bounded by spinodal curves.
- In critical point determinations, the criterion M1=0 may be replaced by the alternate criterion

$$\left(\frac{\partial L1}{\partial x}\right)_{T,P} = 0.$$

- An unstable critical point may be identified as the terminus of an unstable binodal locus.

  Alternatively, $\left(\frac{\partial^2 L1}{\partial x^2}\right)_{T,P}$ is greater than zero for a stable critical point and less than zero for an unstable critical point.
- A necessary and sufficient criterion for the existence of a critical end point is the occurrence of a horizontal inflection point in the stable binodal locus in a P-x or T-x section.
- Solution of the two-phase eqilibrium problem is sufficient for the determination of three-phase

equilibrium, since three-phase equilibrium results from the intersection of binodal loci.

From the four systems investigated, the following conclusions have been drawn:

-The Peng-Robinson equation, with a single, constant interaction parameter, gives a qualitatively correct representation of phase behavior over the entire fluid region for nonpolar binary systems. The system may be nonideal with respect to molecular size of the components.

-The Peng-Robinson equation, with a single, constant interaction parameter, gives a reasonably correct representation of phase behavior over the entire fluid region for binary systems with one polar component. The qualitative picture may be incorrect in certain minor details.

-Semiquantitative predictions may be obtained in any region of interest by choosing an appropriate temperature dependent interaction parameter. In particular, the supercritical fluid region is amenable to such treatment.

-Analysis of fugacity-composition plots allows the development of phase equilibrium algorithms suitable for any region of the phase diagram.

-Metastable and unstable solutions to the phase equilibrium equations are always associated with

> three-phase equilibrium in a binary system. The solutions may exist over a substantial region of the P-T-x space, and if not accounted for can lead to erroneous predictions.

The significance of the last two conclusions for computer calculations of phase equilibrium must be strongly emphasized. Algorithms which fail to account for the behavior of the fugacity functionality are liable to experience convergence problems when this functionality takes on a complex shape. Complex shapes are found in three-phase regions, as well as near azeotropic coordinates and pure vapor pressure curves. Similarly, algorithms which fail to account for all phase equilibrium solutions to an equation of state may converge to an incorrect result. Erroneous prediction of both binodal curves and critical lines may occur. Careful development and application of phase equilibrium algorithms is necessary to avoid these difficulties.

Taken as a whole, these conclusions indicate that a simple, cubic equation of state is well suited to an orienting or preliminary study of binary phase behavior. The minimal computing time required by these equations makes them an obvious choice for such an application. The preliminary study maps out regions where more detailed investigation, in both the theoretical and experimental sense, is warranted. From the theoretical standpoint, once these regions have been defined, it may in some cases be desirable to switch to a more accurate equation of state. In other cases the cubic equation will provide sufficient accuracy with only a change in the interaction parameter. From the experimental standpoint, the preliminary study indicates the regions where further data should be taken, and serves as a check on the consistency of results.

Continued work on the topic of this thesis would be most worthwhile. Generation of P-T-x diagrams for other systems would provide additional verification of the above conclusions. Treatment of a system where both components are polar should be of interest. A categorization of the predicted P-T projections according to T , P , and ω of the species involved, as well as the value of δ_{12} employed, would be very useful. The categorization would make it possible to rapidly estimate the overall phase behavior of many systems. This is along the lines of van Konynenburg's (1968) work with the van der Waals equation.

Avenues for further development are several. Along the lines suggested by numerous workers, determination of a temperature and pressure functionality of the interaction parameter would lead to a more quantitative prediction of the P-T-x diagrams. It would also be instructive to generate the P-T-x space with a more complicated, and presumably more accurate equation to allow a comparison of the required computing time. For a non-cubic, pressure explicit equation of state, use of T and V as the independent variables may be an efficient approach.

Automation of the methodology, including provision for computer graphics, would increase its utility and convenience greatly. Finally, an attempt should be made to extend the techniques developed here to ternary and multicomponent systems.

Appendix A The Equation of State and Derived Expressions

The Peng-Robinson equation of state is

$$P = \frac{RT}{v - b} - \frac{a(T)}{v(v+b) + b(v-b)} \tag{A.1}$$

where a(T) is a temperature dependent attraction energy parameter. This equation may be rewritten in cubic form as

$$Z^3 - (1-B)Z^2 + (A-3B^2-2B)Z - (AB-B^2-B^3) = 0 \tag{A.2}$$

where

$$A = \frac{aP}{R^2T^2} \tag{A.3}$$

$$B = \frac{bP}{RT} \tag{A.4}$$

$$Z = \frac{Pv}{RT} \tag{A.5}$$

By requiring equation (A.1) to satisfy the pure component critical point criteria, equations (2.32) and (2.33), it is found that

$$a(T_c) = 0.45724 \frac{R^2T_c^2}{P_c} \tag{A.6}$$

$$b = 0.07780 \frac{RT_c}{P_c} \qquad (A.7)$$

$$Z_c = 0.307 \qquad (A.8)$$

For temperatures other than T_c, let

$$a(T) = a(T_c) \cdot \alpha\ (T_r,\ \omega) \qquad (A.9)$$

with

$$\alpha^{1/2} = 1 + \kappa(1-T_r^{1/2}) \qquad (A.10)$$

$$\kappa = 0.37464 + 1.54226\omega - 0.26992\omega^2 \qquad (A.11)$$

The fugacity of a pure component is derived from the relation

$$\ln\frac{f}{P} = \int_0^P \left(\frac{v}{RT} - \frac{1}{P}\right) dP \qquad (A.12)$$

Using equation (A.1), the integration yields

$$f = P\exp\left[Z - 1 - \ln(Z-B) - \frac{A}{2\sqrt{2}B} \ln\left(\frac{Z+2.414B}{Z-0.414B}\right)\right] \qquad (A.13)$$

For a mixture,

$$a = \sum_i \sum_j x_i x_j a_{ij} \qquad (A.14)$$

$$b = \sum_i x_i b_i \tag{A.15}$$

$$a_{ij} = (1-\delta_{ij})(a_i a_j)^{\frac{1}{2}} \tag{A.16}$$

where δ_{ij} is an empirically determined interaction parameter. The form of equations (A.14) and (A.15) for binary systems was given in equations (2.15) and (2.16). The fugacity of a component in a mixture is found from the relation

$$RT\ln \frac{f_i}{x_i P} = \int_{\underline{V}\to\infty}^{\underline{V}} \left(\frac{RT}{\underline{V}} - \left(\frac{\partial P}{\partial N_i}\right)_{T,\underline{V},\{N_i\}} \right) d\underline{V} - RT\ln Z \tag{A.17}$$

Substituting equation (A.1), the result for component 1 in a binary system is

$$f_1 = x_1 P\exp \left[\frac{b_1}{b}(Z-1) - \ln(Z-B) - \frac{A}{2\sqrt{2}B} \left(\frac{2(a_1x_1 + a_{12}x_2)}{a} - \frac{b_1}{b} \right) \cdot \ln \left(\frac{Z + (\sqrt{2}+1)B}{Z - (\sqrt{2}-1)B} \right) \right] \tag{A.18}$$

Use of the above fugacity expressions allows the calculation of phase equilibrium.

The mechanical stability of a phase is found from equation (A.1). For a stable system,

$$\left(\frac{\partial P}{\partial V}\right)_{T,x} = - \frac{RT}{(v-b)^2} - \frac{2a(v+b)}{v^2+2bv-b^2} < 0 \tag{A.19}$$

Determination of material stability spinodal curves was carried out using the L1 determinant of Beegle, et al. (1974b). This is given in intensive form for a binary system as

$$L1 = \begin{vmatrix} A_{VV} & A_{VX} \\ A_{VX} & A_{XX} \end{vmatrix} = A_{VV}A_{XX} - A_{VX}^{2} \tag{A.20}$$

Compositional derivatives (subscript x) are taken with respect to component 2.

This quantity is zero at a point on the stability limit. The M1 determinant of Reid and Beegle (1977) was used as the second criterion of criticality. This is expressed in intensive form for a binary system as

$$M1 = \begin{vmatrix} A_{VV} & A_{VX} \\ \left(\frac{\partial L1}{\partial V}\right)_{T,x} & \left(\frac{\partial L1}{\partial x}\right)_{T,V} \end{vmatrix} = A_{VV}A_{XX}A_{VVX} + A_{VV}^{2}A_{XXX} -$$

$$- 3A_{VV}A_{VX}A_{VXX} - A_{XX}A_{VX}A_{VVV} + 2A_{VX}^{2}A_{VVX} \tag{A.21}$$

At a critical point, this quantity is zero. Evaluation of L1 and M1 requires an expression for the Helmholtz free energy A = A(T, V, x). Using their equation, Peng and Robinson (1977) have formulated this expression as

$$A = RT\,\Sigma\, x_i \ln \frac{x_i RT}{v-b} - \frac{a}{2\sqrt{2}\, b} \ln \left(\frac{v+(\sqrt{2}+1)B}{v-(\sqrt{2}-1)B}\right) +$$

$$\int_{T_o}^{T} \Sigma\, x_i C_{Pi}^{*} dT - T \int_{T_o}^{T} \Sigma\, x_i \frac{C_{Pi}^{*}}{T} dT - RT \qquad (A.22)$$

where the asterisk denotes an ideal gas state.

Using equation (A.22), the derivatives in equations (A.20) and (A.21) are as follows:

$a_x = 2(-a_1x_1 + a_{12}(1-2x_2) + a_2x_2)$

$a_{xx} = 2(a_1 - 2a_{12} + a_2)$

$b_x = b_2 - b_1$

$r = a/b$

$$r_x = \frac{a_x b - ab_x}{b^2}$$

$$r_{xx} = \frac{a_{xx} - 2r_x b_x}{b}$$

$$r_{xxx} = \frac{-3r_{xx} b_x}{b}$$

$W = v^2 + 2bv - b^2$

$W_x = 2b_x(v-b)$

$W_{xx} = -2b_x^{\,2}$

$$X = v + (1+\sqrt{2})b$$

$$X_x = (1+\sqrt{2})b_x$$

$$Y = v + (1-\sqrt{2})b$$

$$Y_x = (1-\sqrt{2})b_x$$

$$A_{vv} = \frac{RT}{(v-b)^2} - \frac{2a(v+b)}{W^2}$$

$$A_{vx} = \frac{-RTb_x}{(v-b)^2} + \frac{a_x}{W} - \frac{aW_x}{W^2}$$

$$A_{xx} = RT\left(\frac{1}{x_1x_2} + \left(\frac{b_x}{v-b}\right)^2\right) - \left(r_{xx}\ln\frac{X}{Y} + 2r_x\left(\frac{X_x}{X} - \frac{Y_x}{Y}\right)\right.$$
$$\left. - r\left(\left(\frac{X_x}{X}\right)^2 - \left(\frac{Y_x}{Y}\right)^2\right)\right) \Big/ \sqrt{8}$$

$$A_{vvv} = \frac{-2RT}{(v-b)^3} + \frac{2a}{W^2}\left(\frac{4(v+b)^2}{W} - 1\right)$$

$$A_{vvx} = \frac{2RTb_x}{(v-b)^3} - \frac{2(a_x(v+b) + ab_x)}{W^2} + \frac{4aW_x(v+b)}{W^3}$$

$$A_{vxx} = \frac{-2RTb_x^2}{(v-b)^3} + \frac{a_{xx}W - 2a_xW_x - aW_{xx}}{W^2} + \frac{2aW_x^2}{W^3}$$

$$A_{xxx} = RT\left(\left(\frac{2x_2-1}{x_1x_2}\right)^2 + 2\left(\frac{b_x}{v-b}\right)^3 \right) - \left(r_{xxx}\ln\frac{X}{Y} + 3r_{xx}\left(\frac{X_x}{X} - \frac{Y_x}{Y}\right) - 3r_x\left(\left(\frac{X_x}{X}\right)^2 - \left(\frac{Y_x}{Y}\right)^2 \right) + 2r\left(\left(\frac{X_x}{X}\right)^3 - \left(\frac{Y_x}{Y}\right)^3 \right) \right) \Big/ \sqrt{8}$$

Appendix B

This appendix presents plots of n-hexadecane fugacity versus n-hexadecane mole fraction for a matrix of seven temperatures and sixteen pressures. Plots of naphthalene fugacity versus naphthalene mole fraction in the naphthalene - carbon dioxide and naphthalene - ethylene systems are very similar to those shown here.

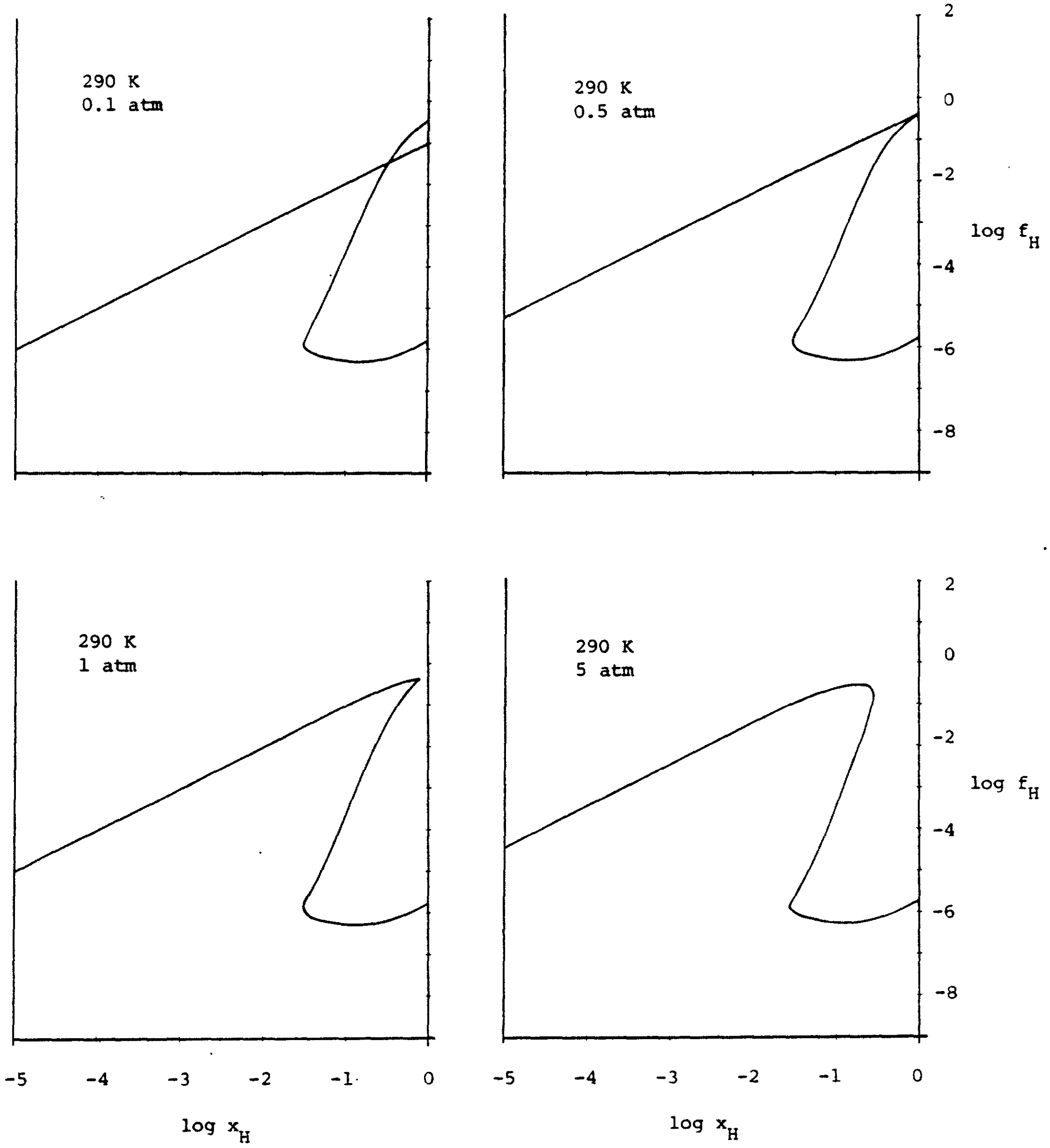
290 K
0.1 atm
290 K
0.5 atm
290 K
1 atm
290 K
5 atm
2
0
-2
-4
-6
-8
log f_H
2
0
-2
-4
-6
-8
log f_H
-5
-4
-3
-2
-1
0
log x_H
-5
-4
-3
-2
-1
0
log x_H

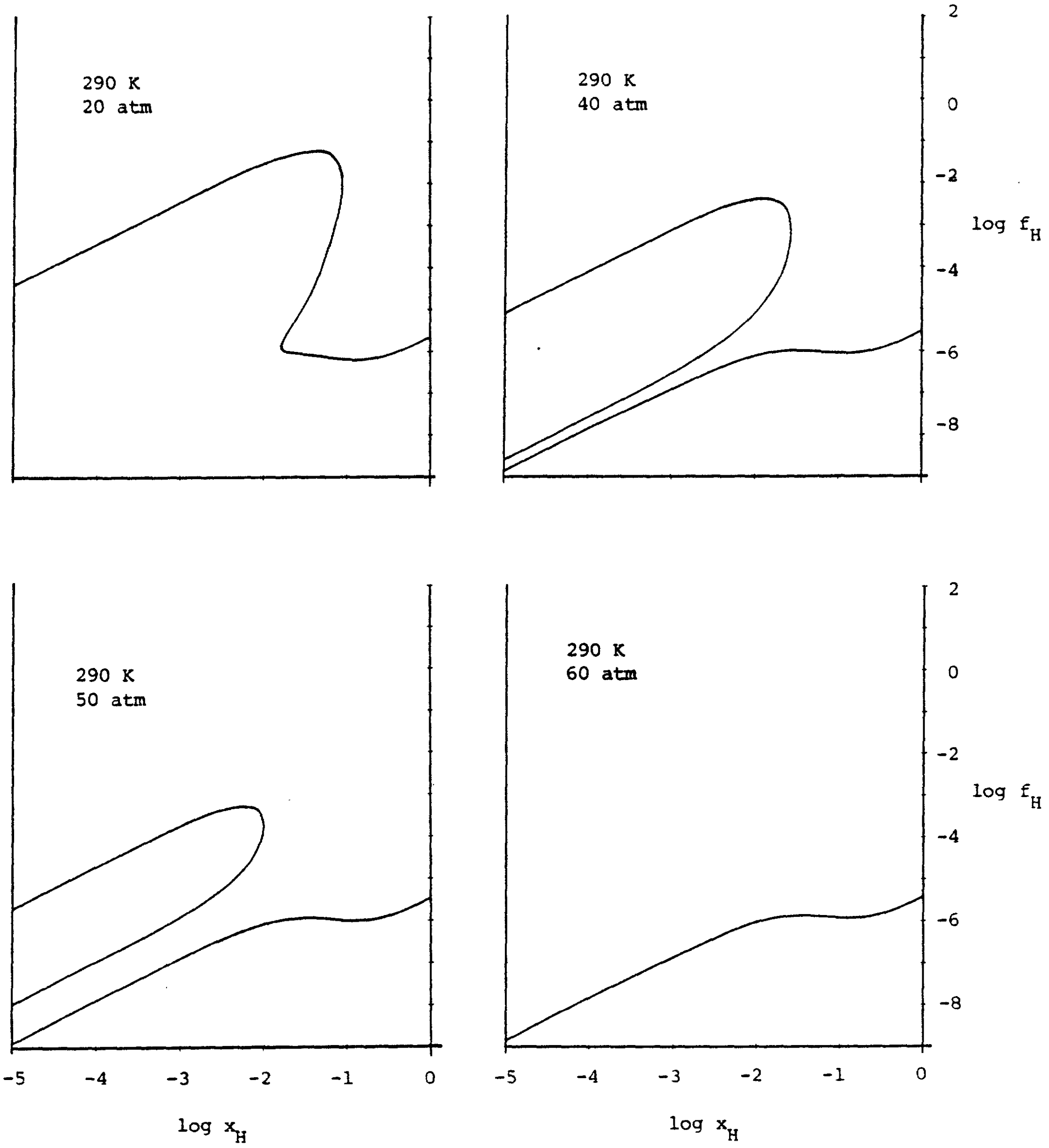
290 K
20 atm
290 K
40 atm
290 K
50 atm
290 K
60 atm
2
0
-2
-4
-6
-8
log f_H
2
0
-2
-4
-6
-8
log f_H
-5
-4
-3
-2
-1
0
log x_H
-5
-4
-3
-2
-1
0
log x_H

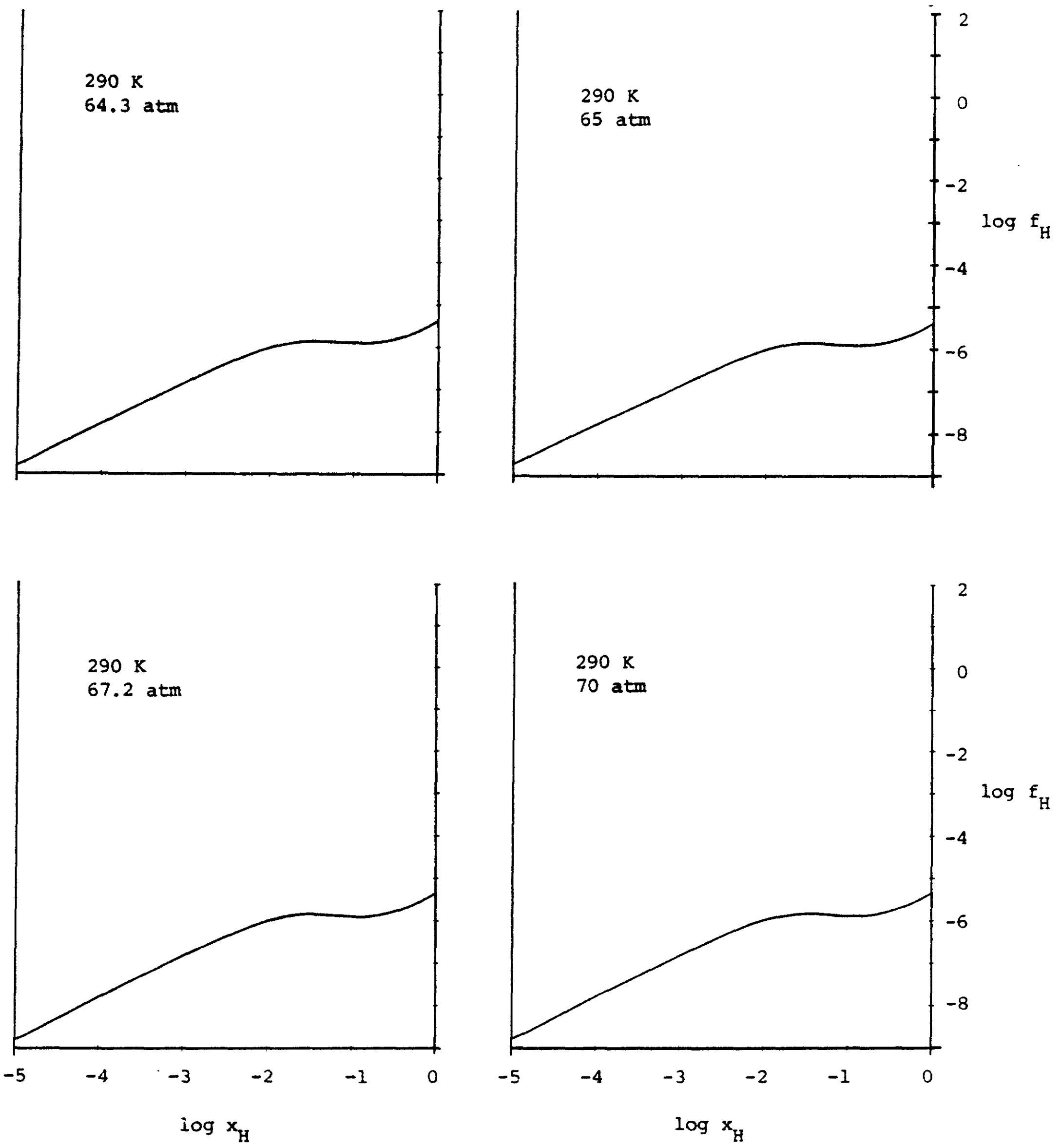
290 K
64.3 atm
290 K
65 atm
290 K
67.2 atm
290 K
70 atm
2
0
-2
-4
-6
-8
log f_H
2
0
-2
-4
-6
-8
log f_H
-5
-4
-3
-2
-1
0
log x_H
-5
-4
-3
-2
-1
0
log x_H

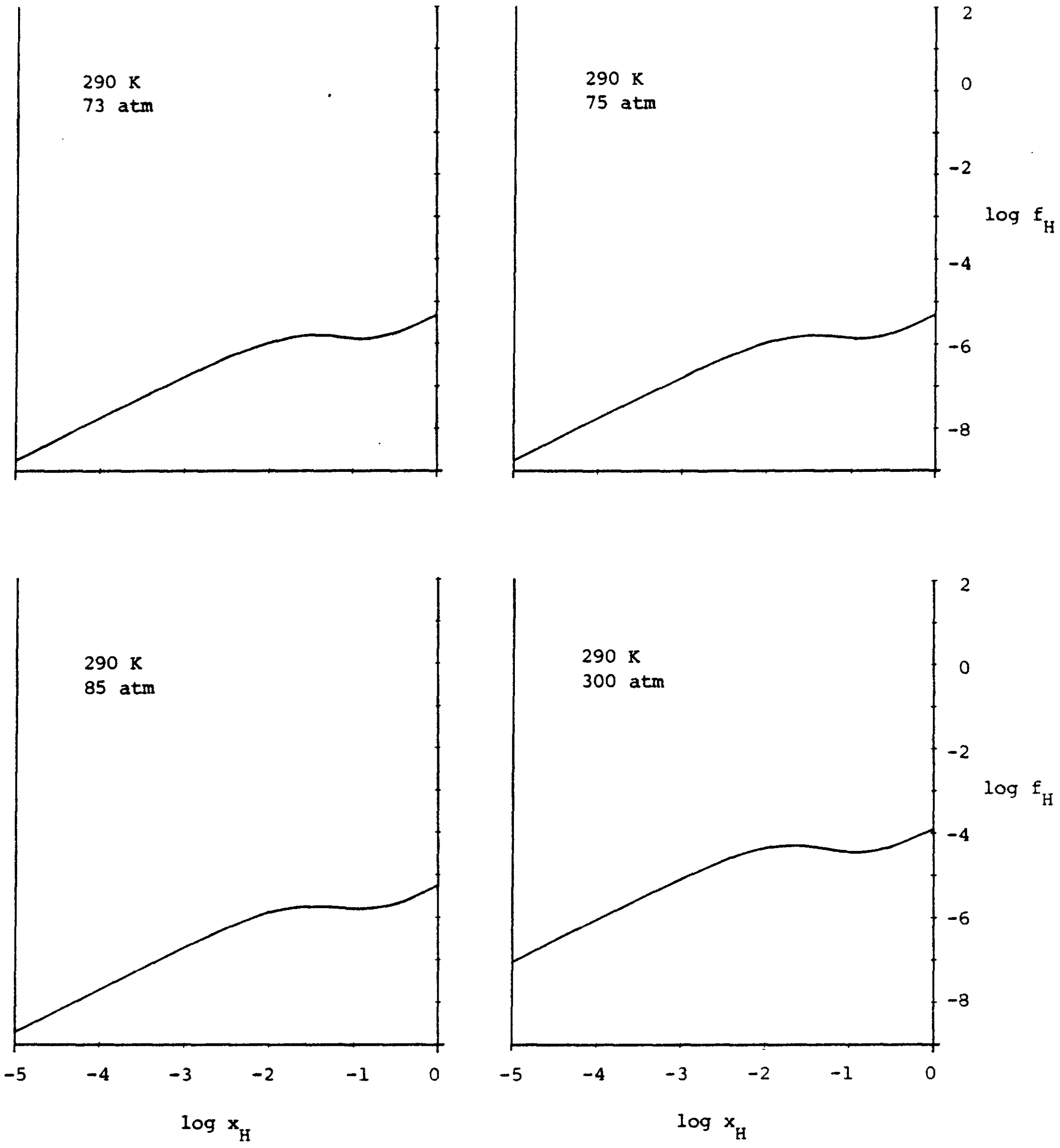
290 K
73 atm
290 K
75 atm
290 K
85 atm
290 K
300 atm
log f_H
log f_H
2
0
-2
-4
-6
-8
2
0
-2
-4
-6
-8
-5
-4
-3
-2
-1
0
-5
-4
-3
-2
-1
0
log x_H
log x_H

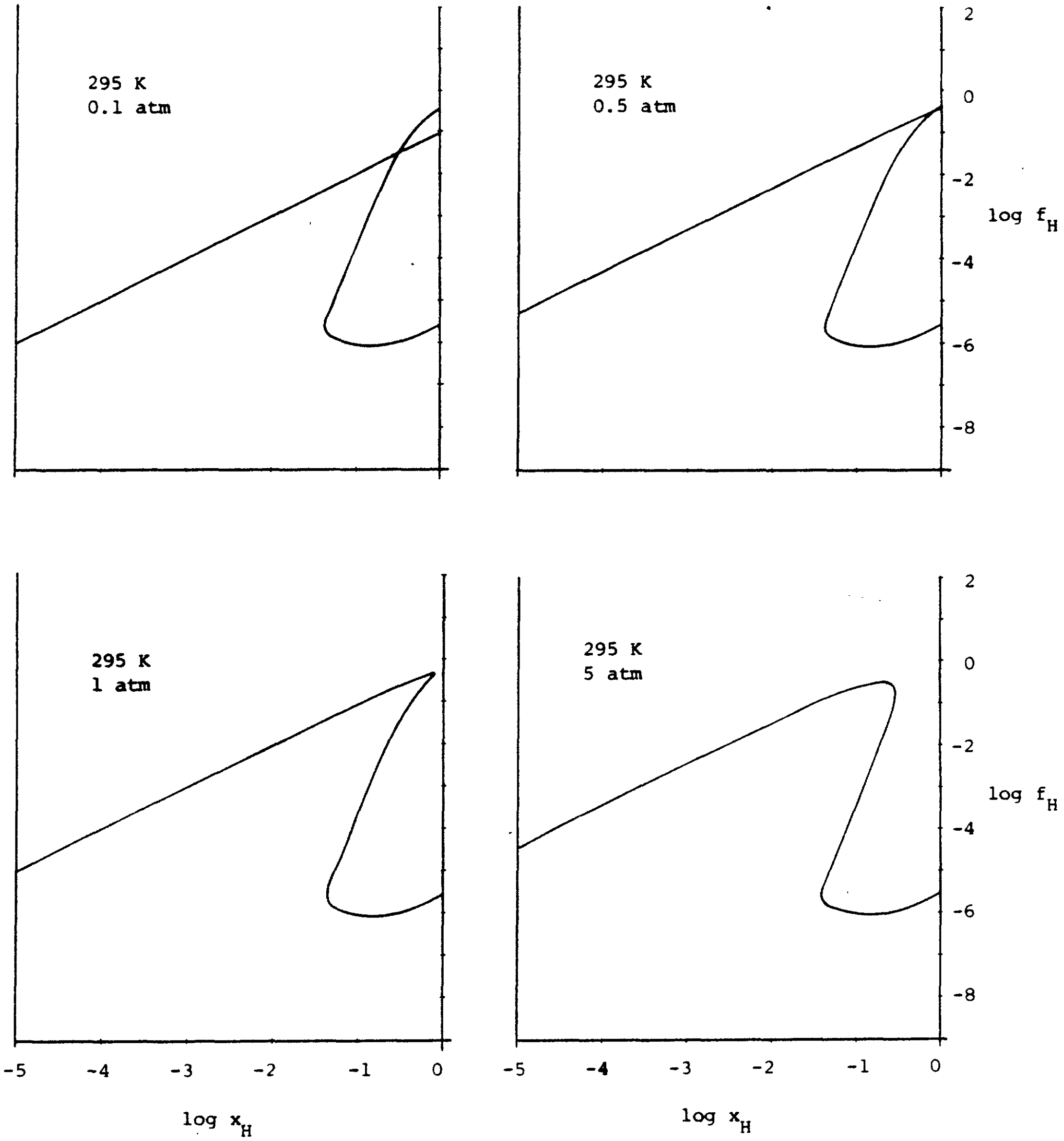
295 K
0.1 atm
295 K
0.5 atm
295 K
1 atm
295 K
5 atm
2
0
-2
-4
-6
-8
log f_H
-5
-4
-3
-2
-1
0
log x_H

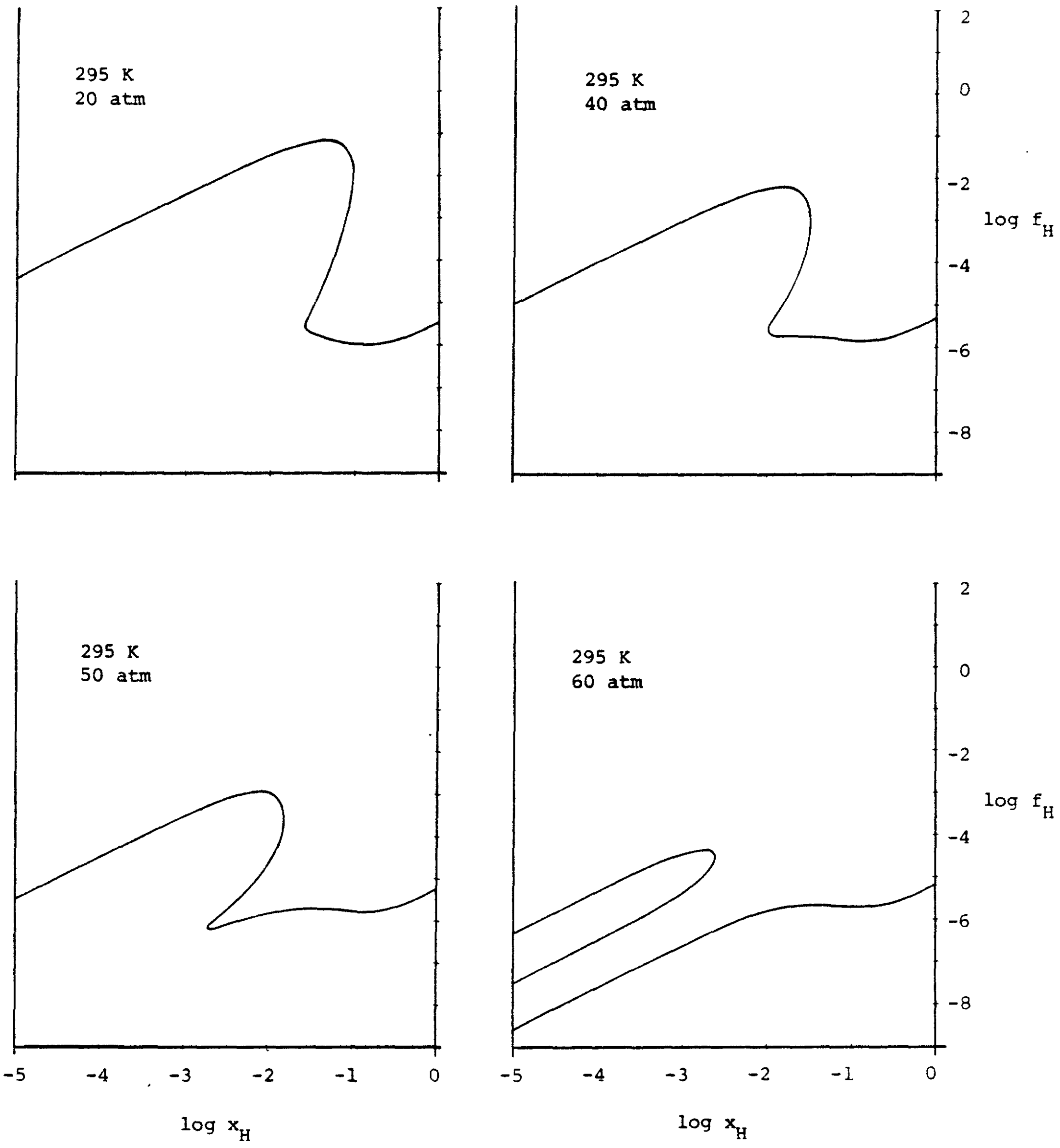
295 K
20 atm
295 K
40 atm
295 K
50 atm
295 K
60 atm
2
0
-2
-4
-6
-8
log f_H
2
0
-2
-4
-6
-8
log f_H
-5
-4
-3
-2
-1
0
log x_H
-5
-4
-3
-2
-1
0
log x_H

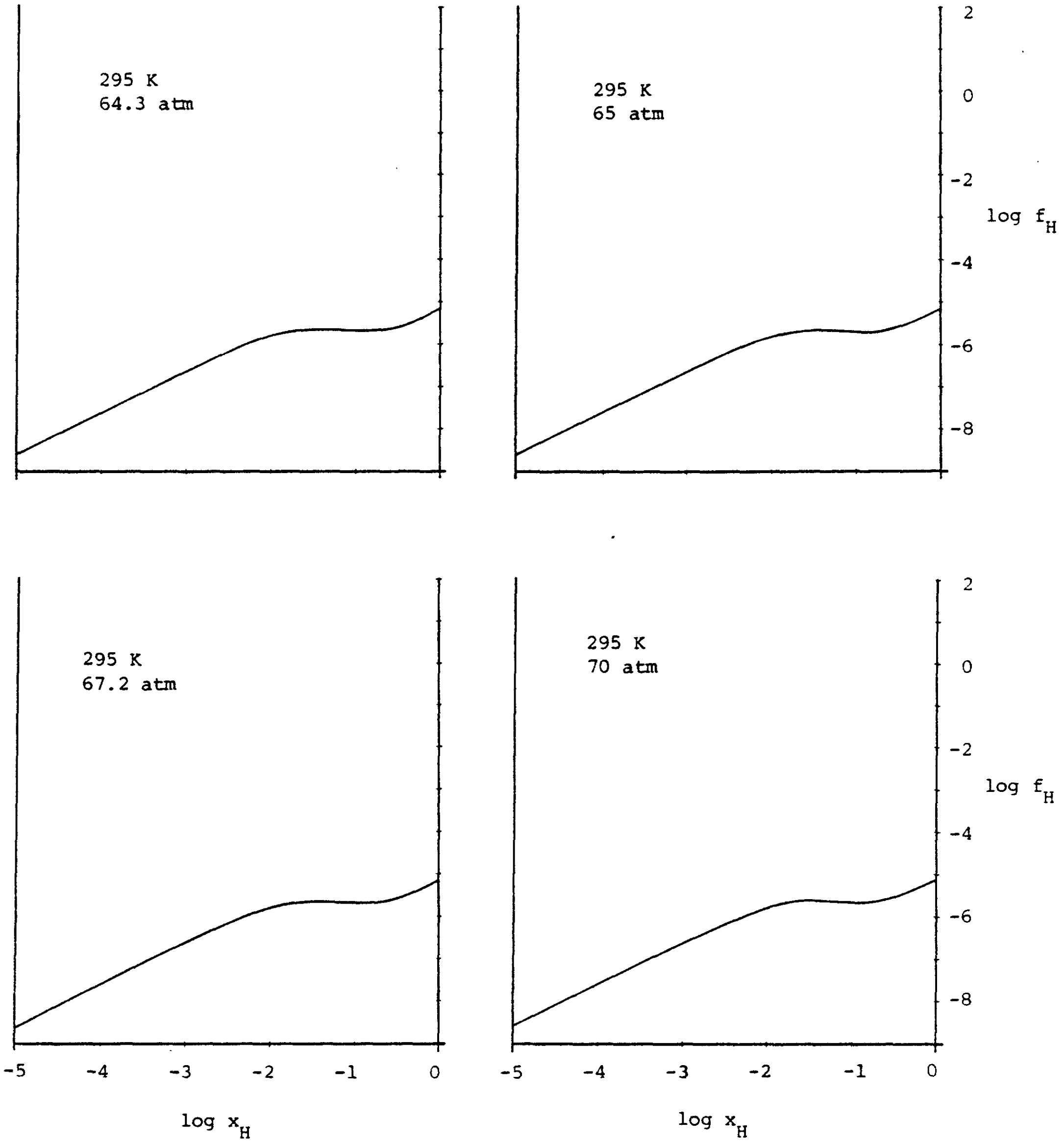
295 K
64.3 atm
295 K
65 atm
295 K
67.2 atm
295 K
70 atm
2
0
-2
-4
-6
-8
log f_H
2
0
-2
-4
-6
-8
log f_H
-5
-4
-3
-2
-1
0
log x_H
-5
-4
-3
-2
-1
0
log x_H

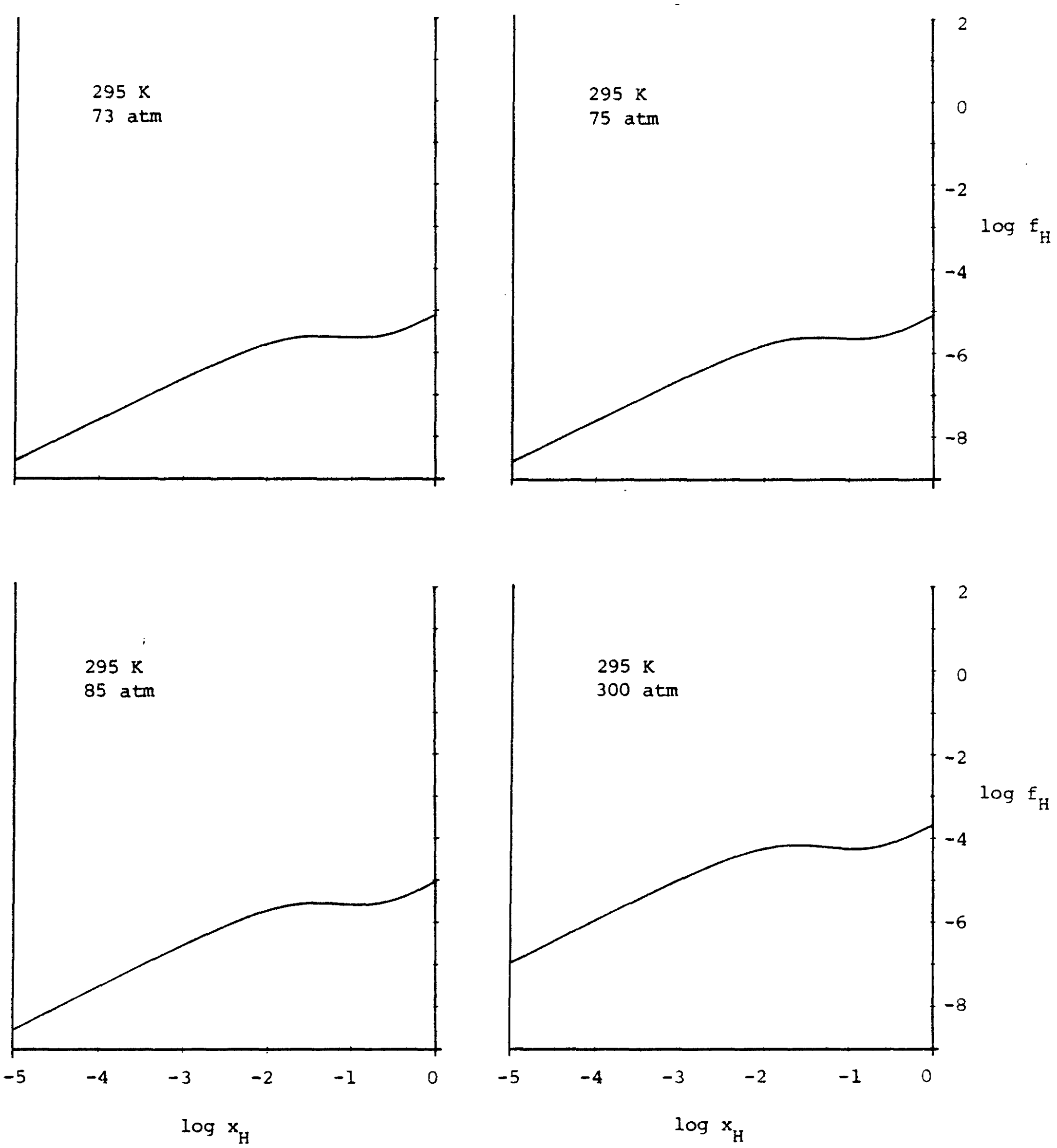
295 K
73 atm
295 K
75 atm
295 K
85 atm
295 K
300 atm
2
0
-2
-4
-6
-8
log f_H
2
0
-2
-4
-6
-8
log f_H
-5
-4
-3
-2
-1
0
log x_H
-5
-4
-3
-2
-1
0
log x_H

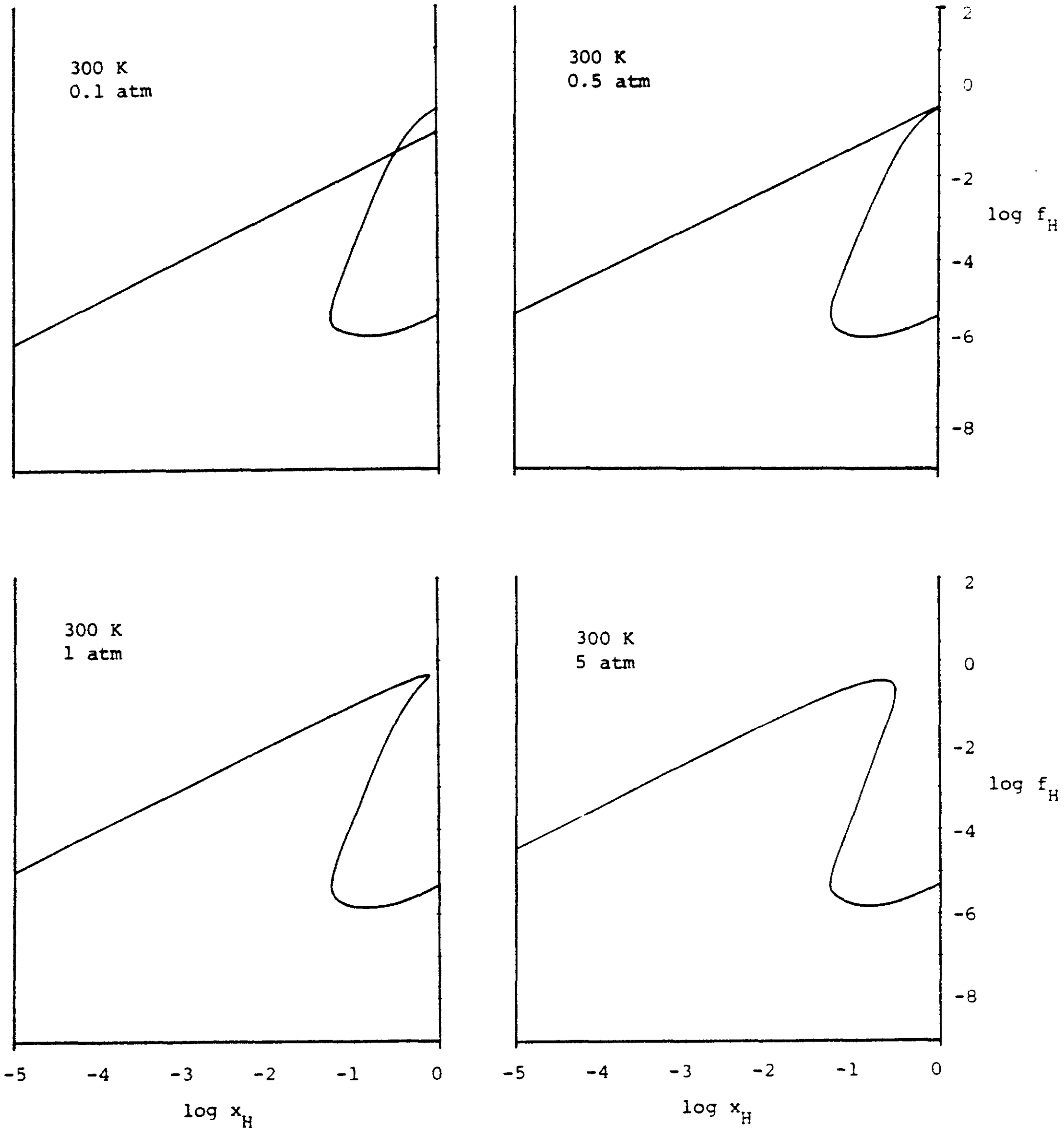
300 K
0.1 atm
300 K
0.5 atm
300 K
1 atm
300 K
5 atm
2
0
-2
-4
-6
-8
log f_H
-5
-4
-3
-2
-1
0
log x_H

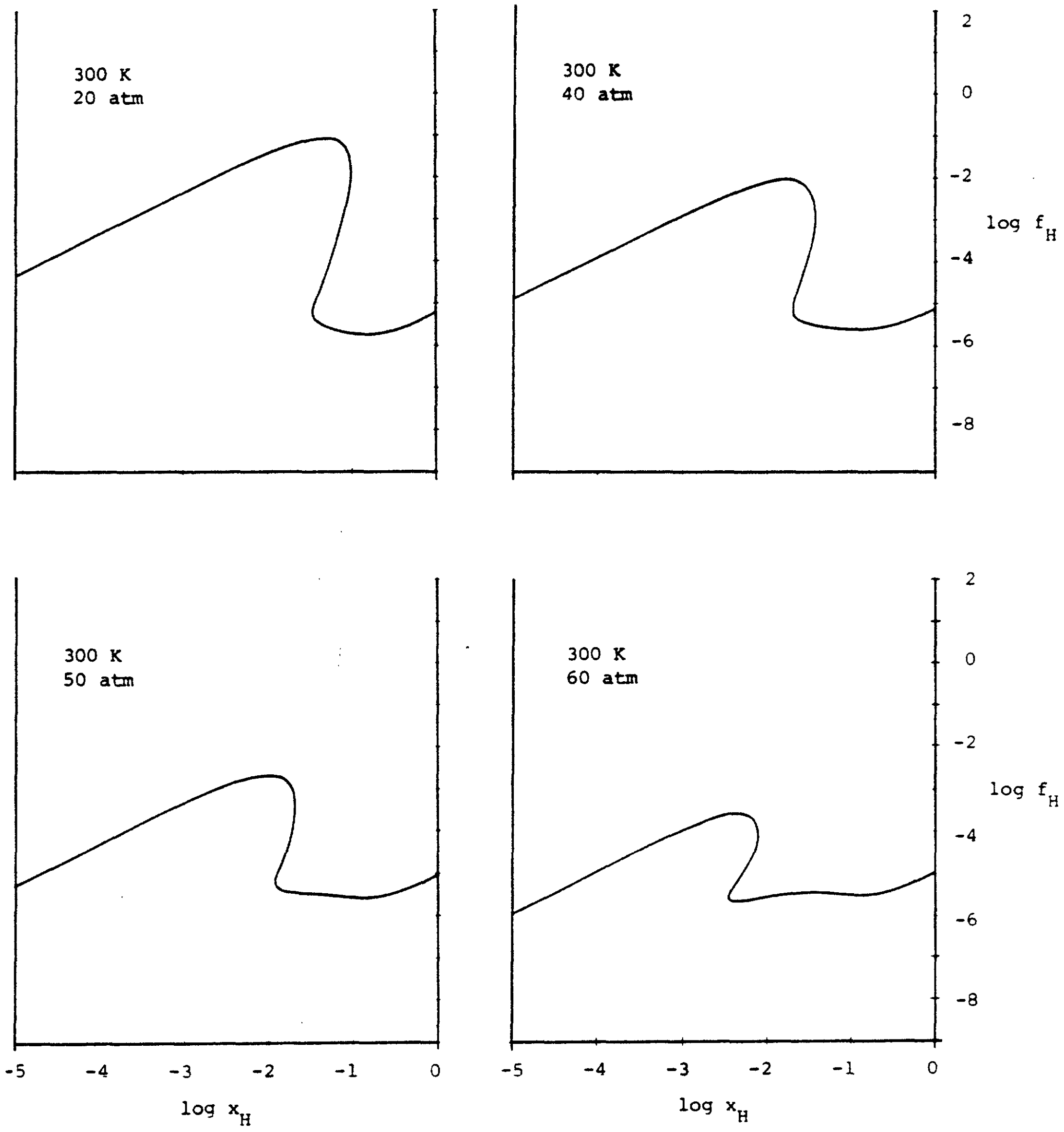
300 K
20 atm
300 K
40 atm
300 K
50 atm
300 K
60 atm
2
0
-2
-4
-6
-8
log f_H
2
0
-2
-4
-6
-8
log f_H
-5
-4
-3
-2
-1
0
log x_H
-5
-4
-3
-2
-1
0
log x_H

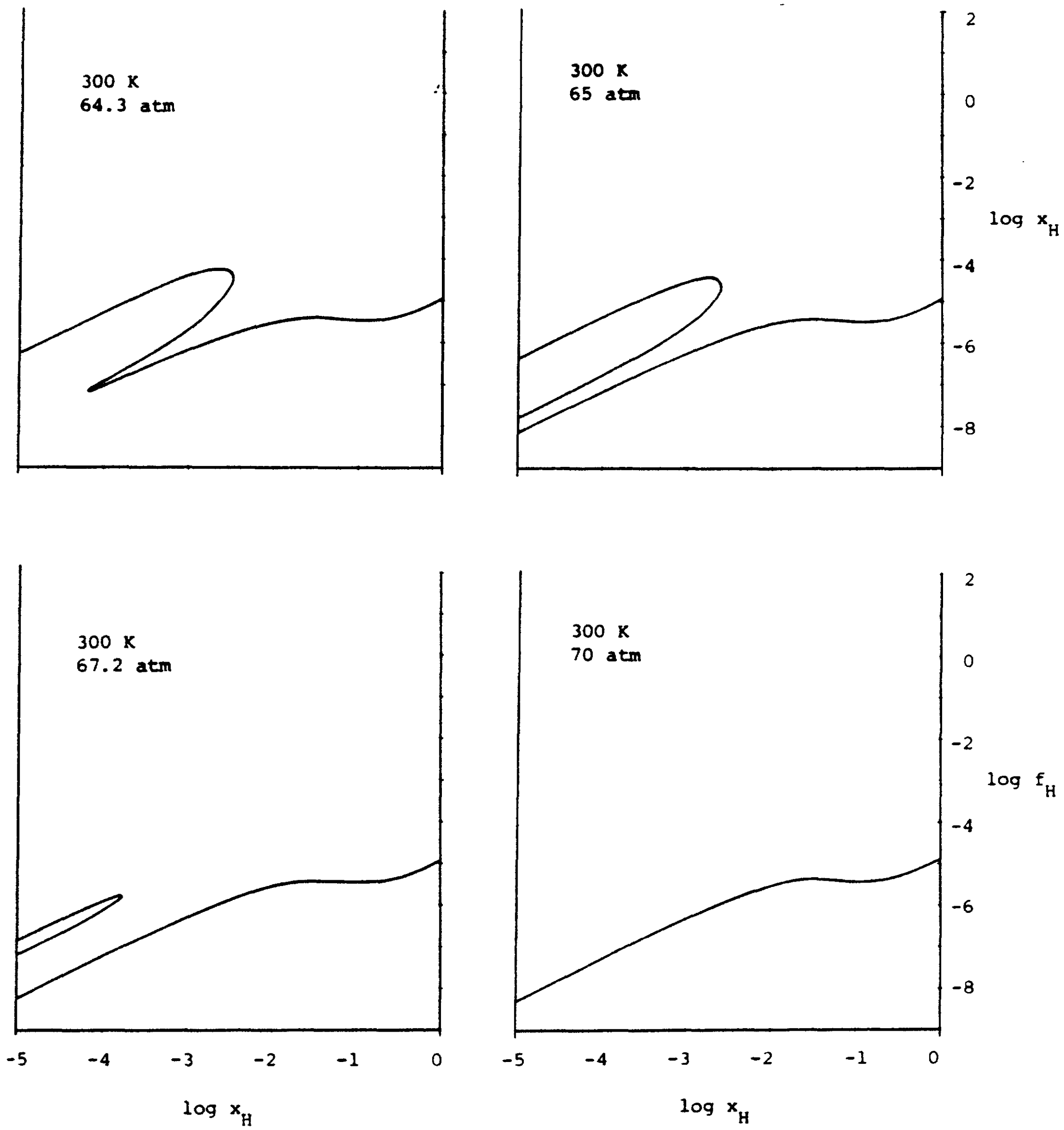
300 K
64.3 atm
300 K
65 atm
2
0
-2
-4
-6
-8
log x_H
300 K
67.2 atm
300 K
70 atm
2
0
-2
-4
-6
-8
log f_H
-5
-4
-3
-2
-1
0
log x_H
-5
-4
-3
-2
-1
0
log x_H

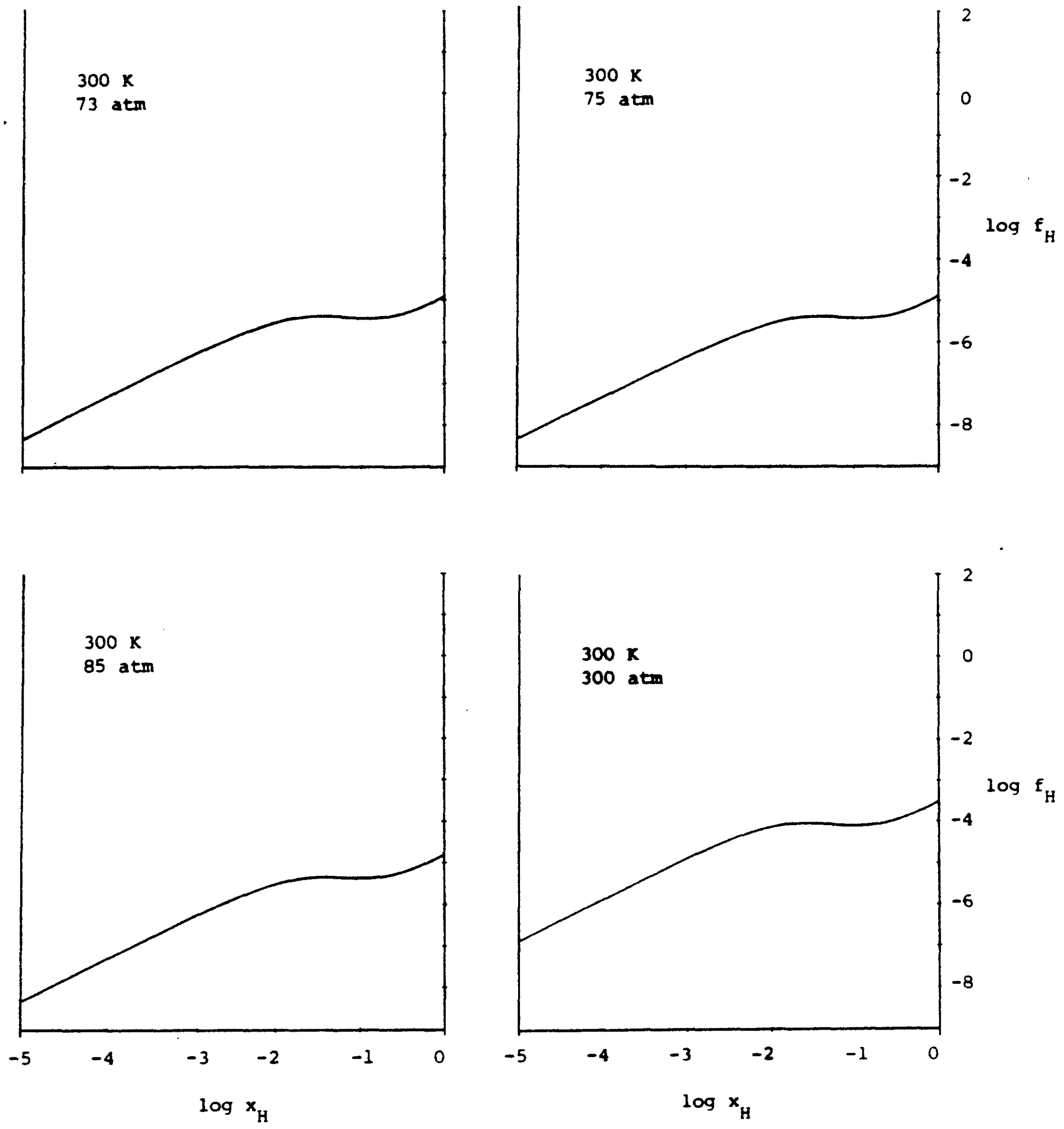
300 K
73 atm
300 K
75 atm
300 K
85 atm
300 K
300 atm
2
0
-2
-4
-6
-8
log f_H
-5
-4
-3
-2
-1
0
log x_H

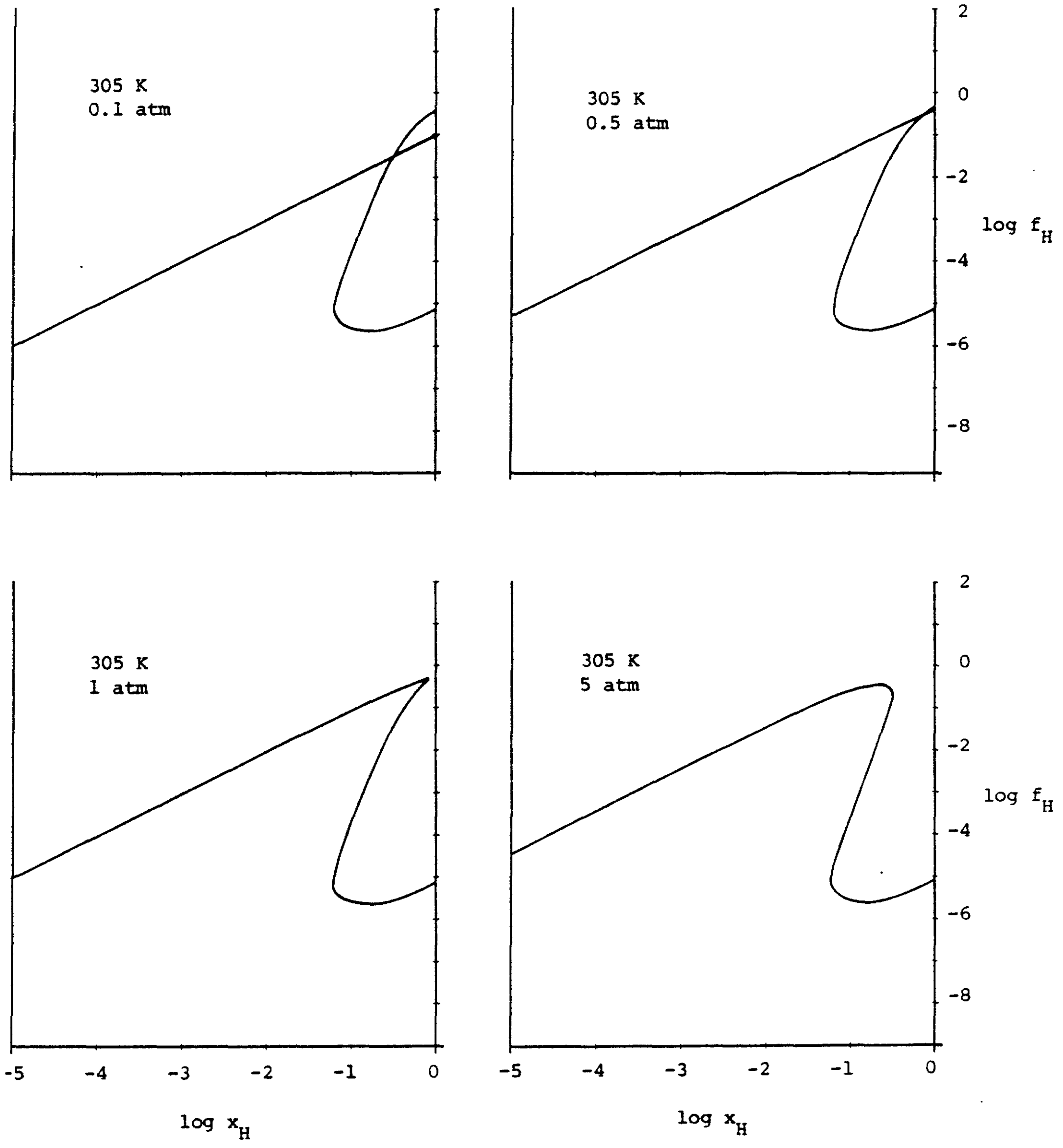
305 K
0.1 atm
305 K
0.5 atm
305 K
1 atm
305 K
5 atm
2
0
-2
-4
-6
-8
log f_H
-5
-4
-3
-2
-1
0
log x_H

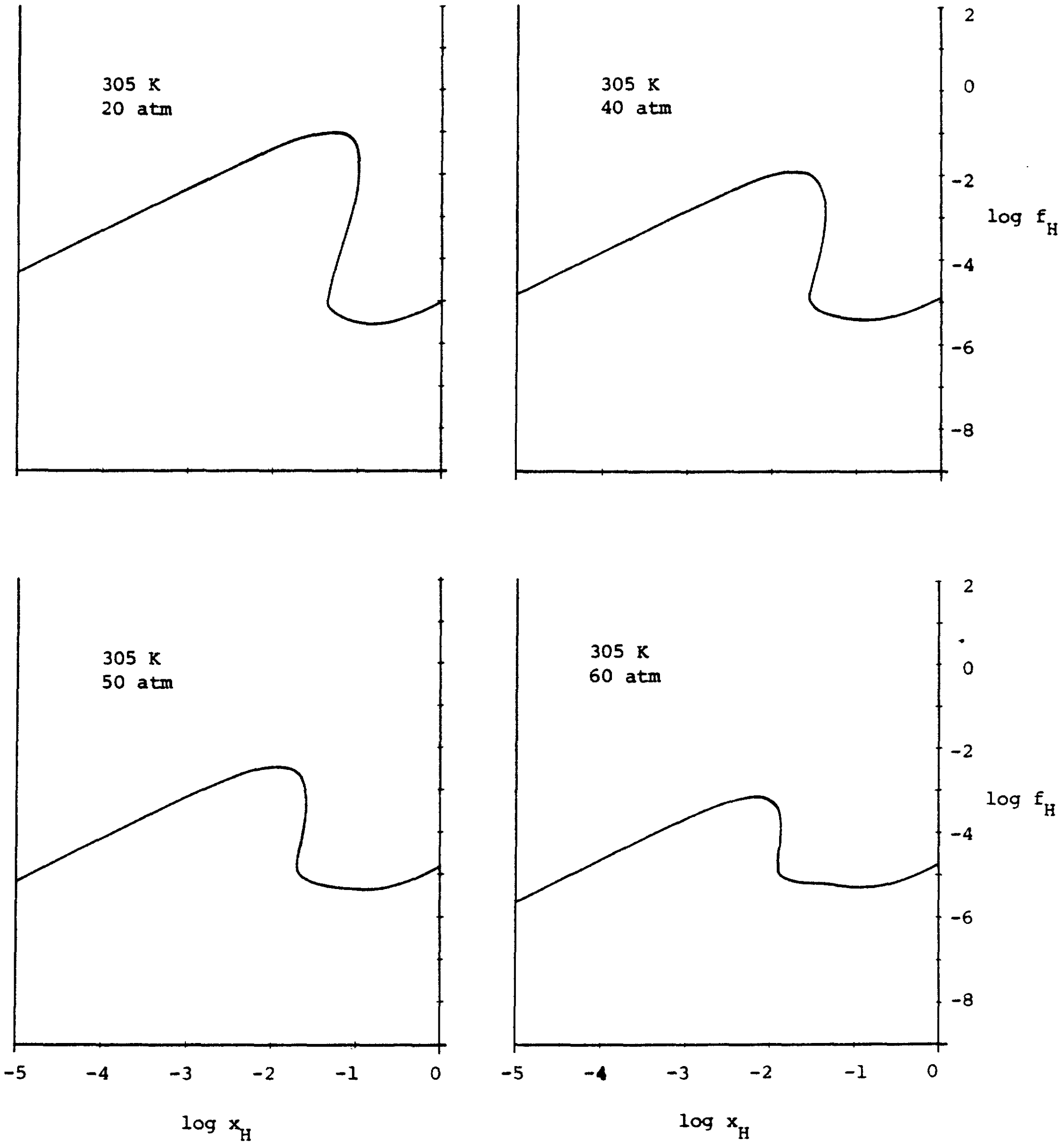
305 K
20 atm
305 K
40 atm
305 K
50 atm
305 K
60 atm
2
0
-2
-4
-6
-8
log f_H
-5
-4
-3
-2
-1
0
log x_H

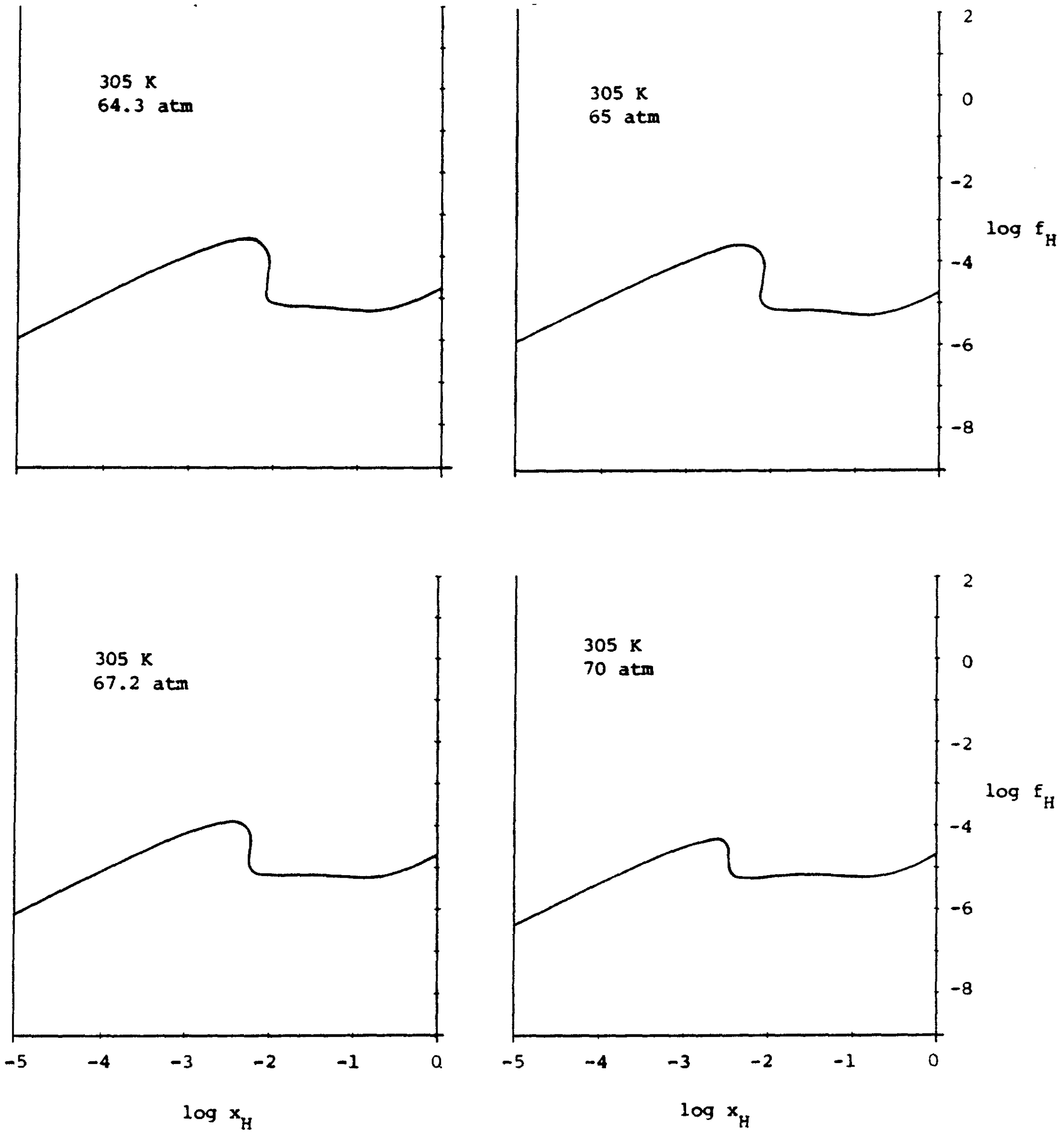
305 K
64.3 atm
305 K
65 atm
305 K
67.2 atm
305 K
70 atm
2
0
-2
-4
-6
-8
log f_H
2
0
-2
-4
-6
-8
log f_H
-5
-4
-3
-2
-1
0
log x_H
-5
-4
-3
-2
-1
0
log x_H

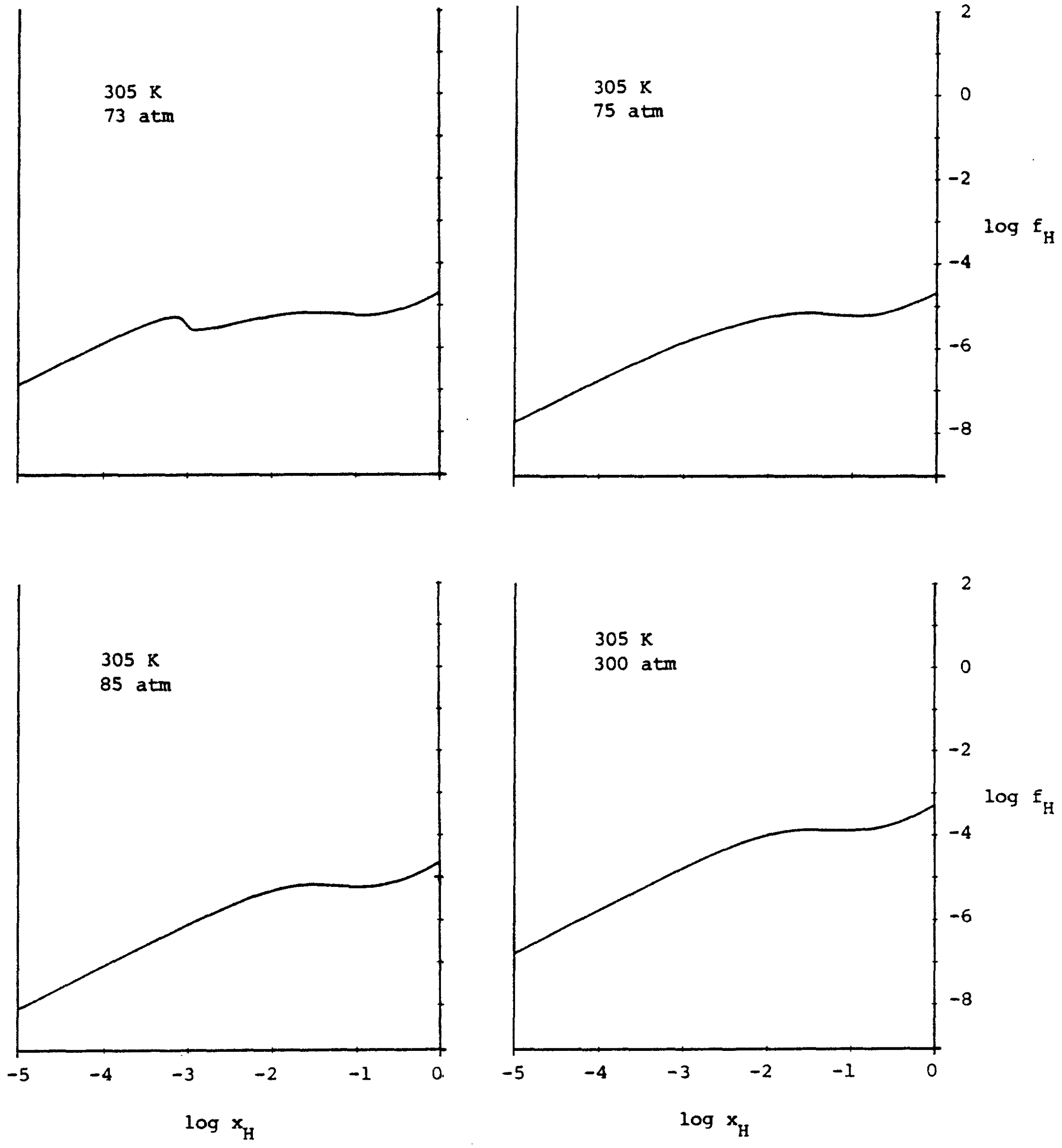
305 K
73 atm
305 K
75 atm
305 K
85 atm
305 K
300 atm
2
0
-2
-4
-6
-8
log f_H
2
0
-2
-4
-6
-8
log f_H
-5
-4
-3
-2
-1
0
log x_H
-5
-4
-3
-2
-1
0
log x_H

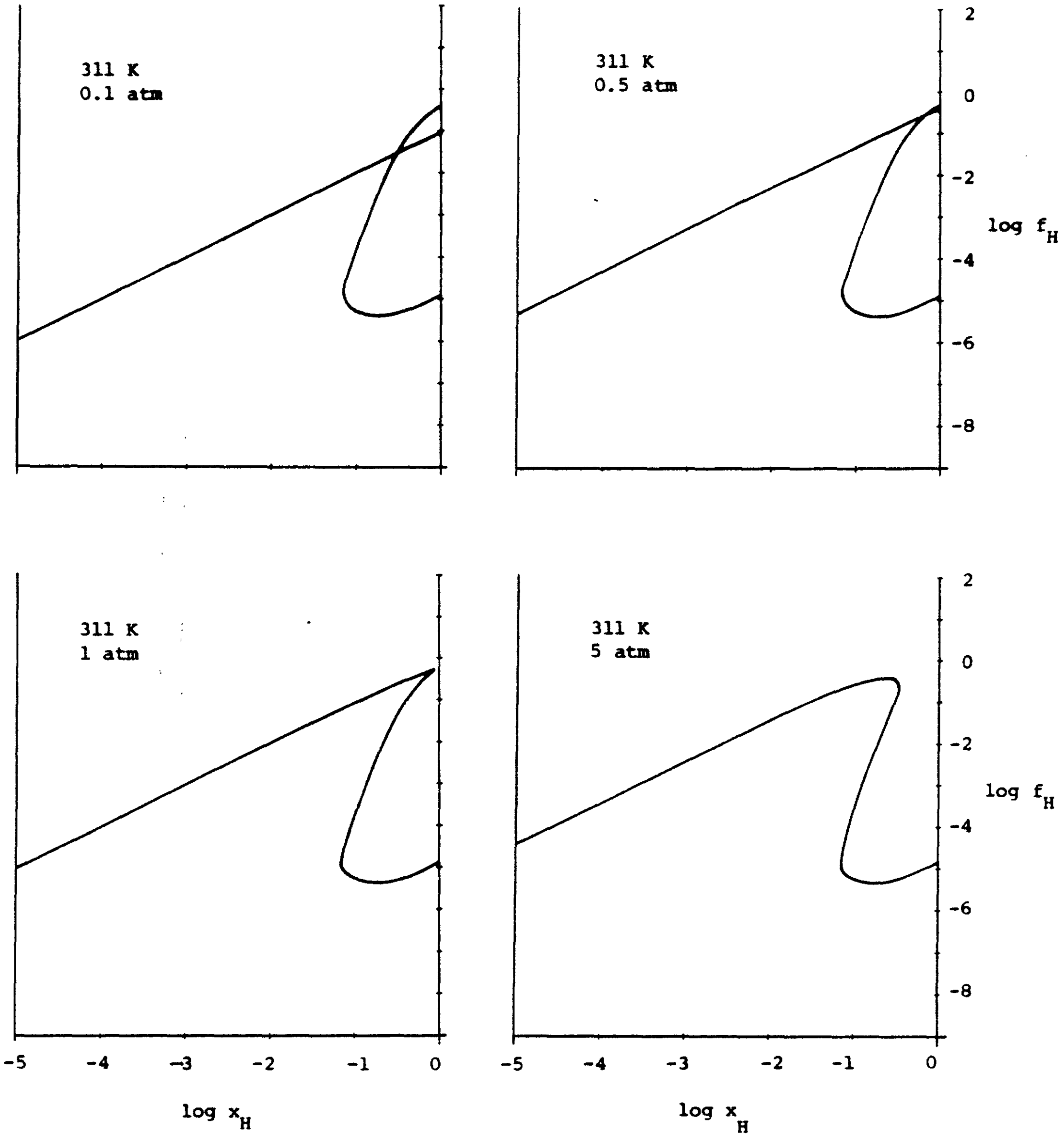
311 K
0.1 atm
311 K
0.5 atm
311 K
1 atm
311 K
5 atm
2
0
-2
-4
-6
-8
log f_H
-5
-4
-3
-2
-1
0
log x_H

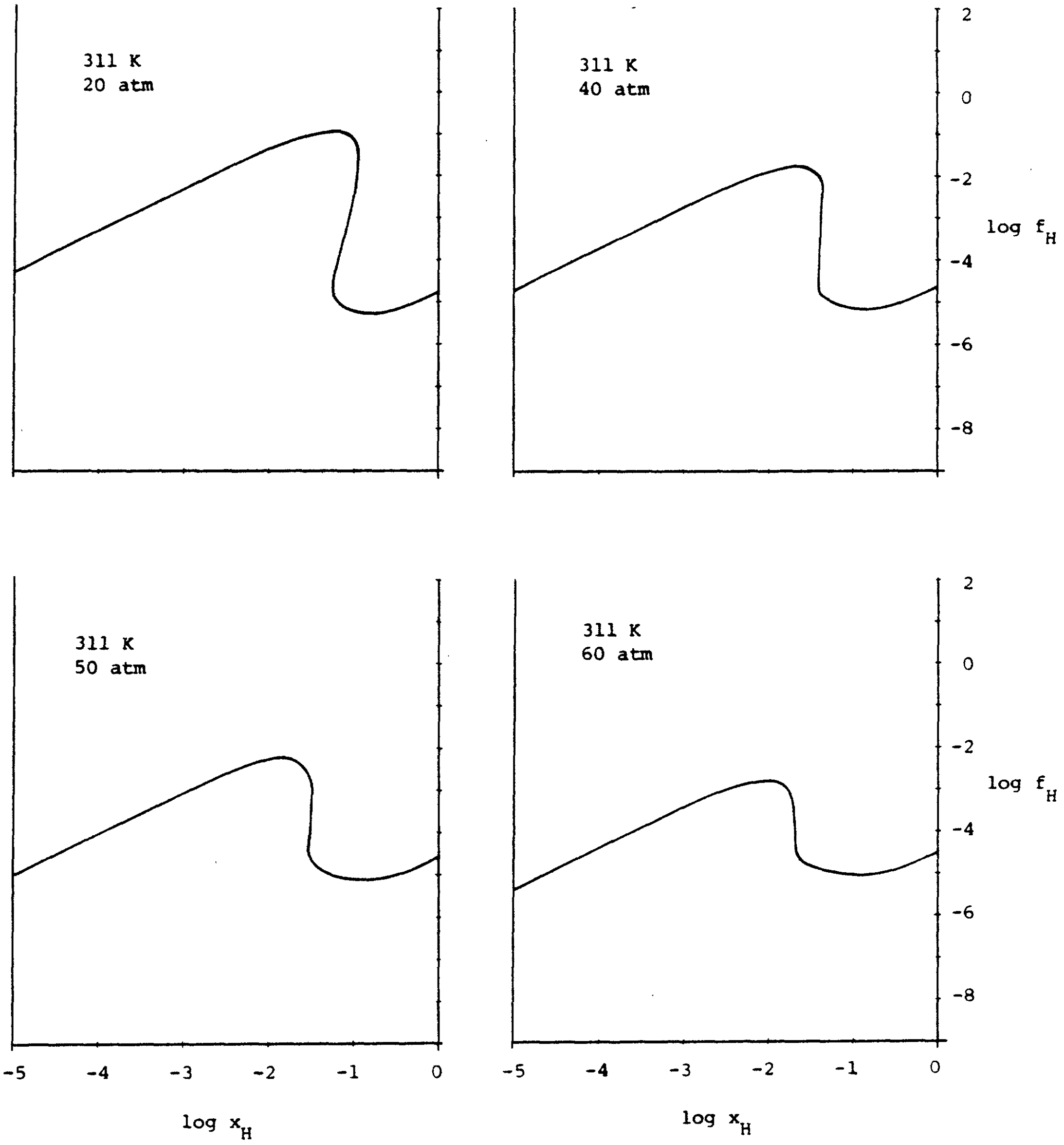
311 K
20 atm
311 K
40 atm
311 K
50 atm
311 K
60 atm
2
0
-2
-4
-6
-8
log f_H
-5
-4
-3
-2
-1
0
log x_H

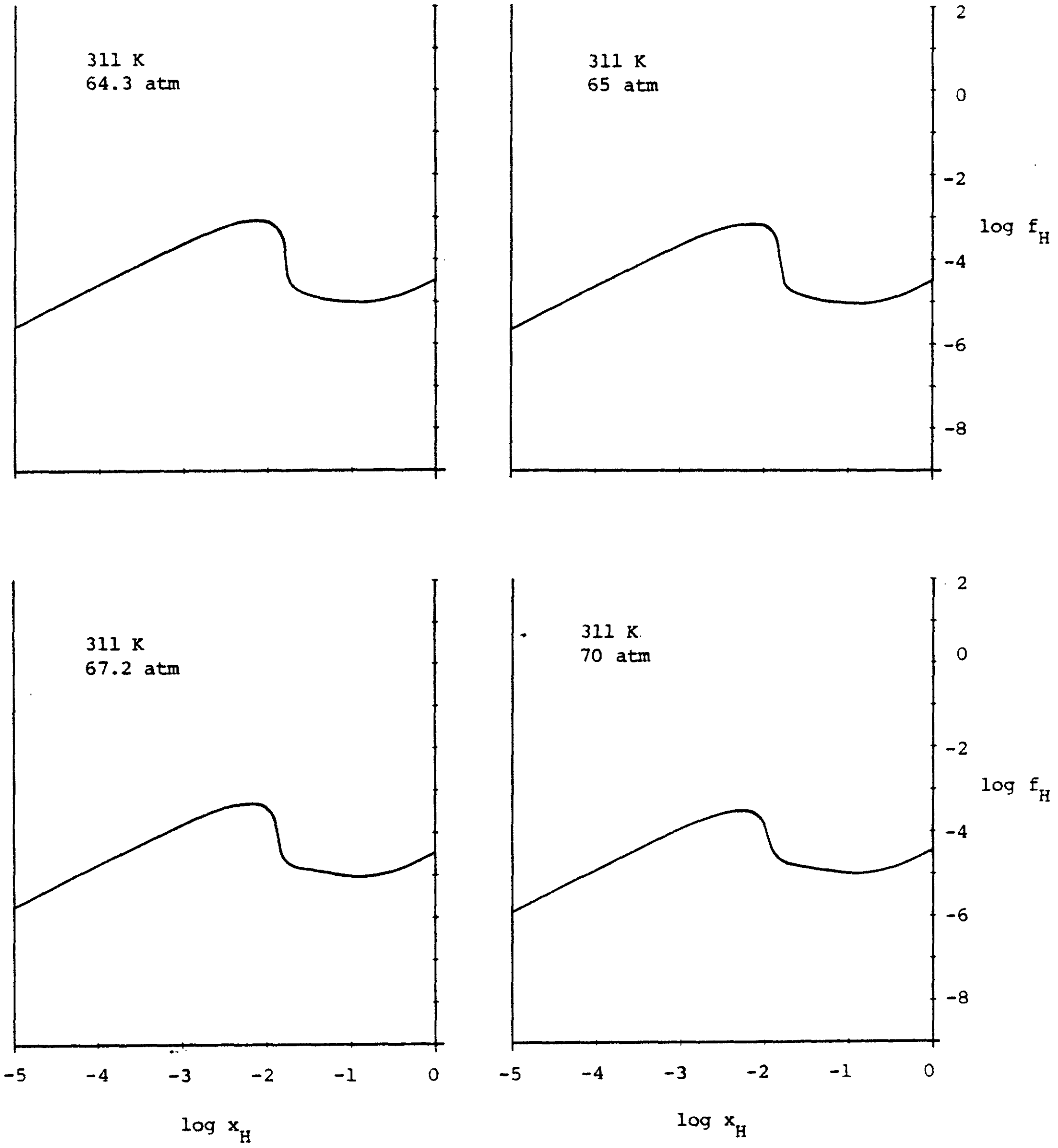
311 K
64.3 atm
311 K
65 atm
311 K
67.2 atm
311 K
70 atm
2
0
-2
-4
-6
-8
log f_H
-5
-4
-3
-2
-1
0
log x_H

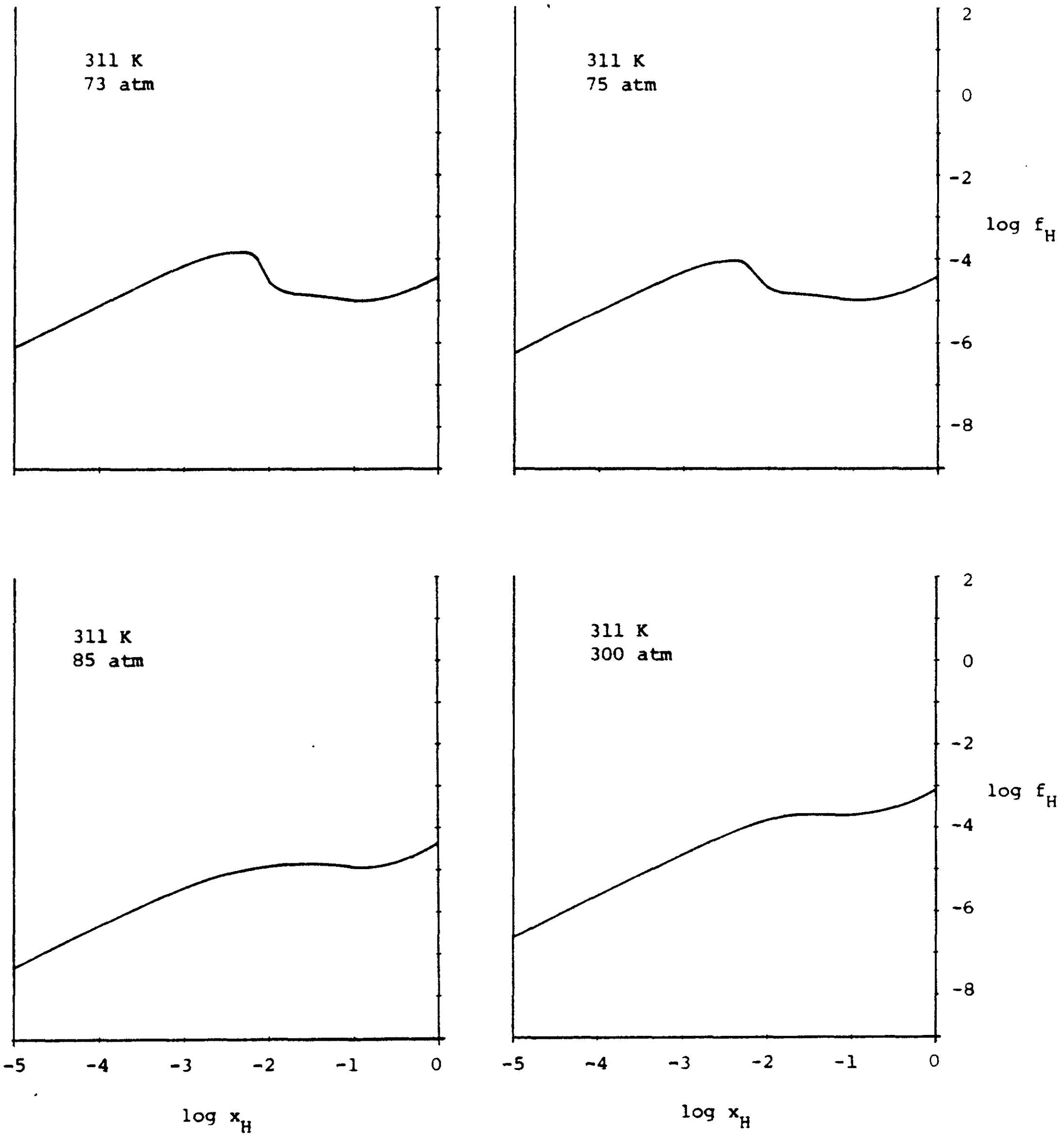
311 K
73 atm
311 K
75 atm
311 K
85 atm
311 K
300 atm
2
0
-2
-4
-6
-8
log f_H
-5
-4
-3
-2
-1
0
log x_H

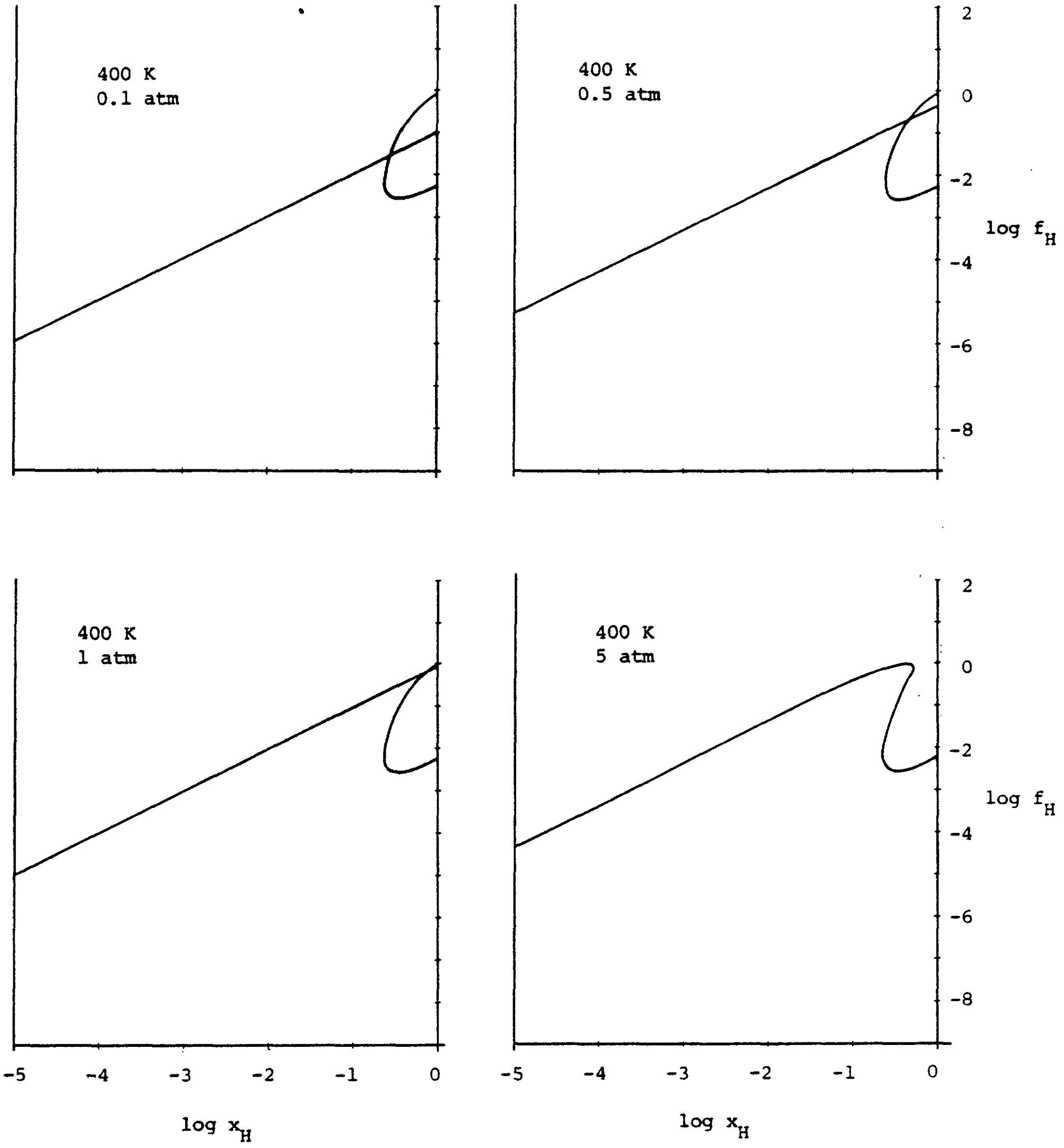
400 K
0.1 atm
400 K
0.5 atm
400 K
1 atm
400 K
5 atm
2
0
-2
-4
-6
-8
log f_H
2
0
-2
-4
-6
-8
log f_H
-5
-4
-3
-2
-1
0
log x_H
-5
-4
-3
-2
-1
0
log x_H

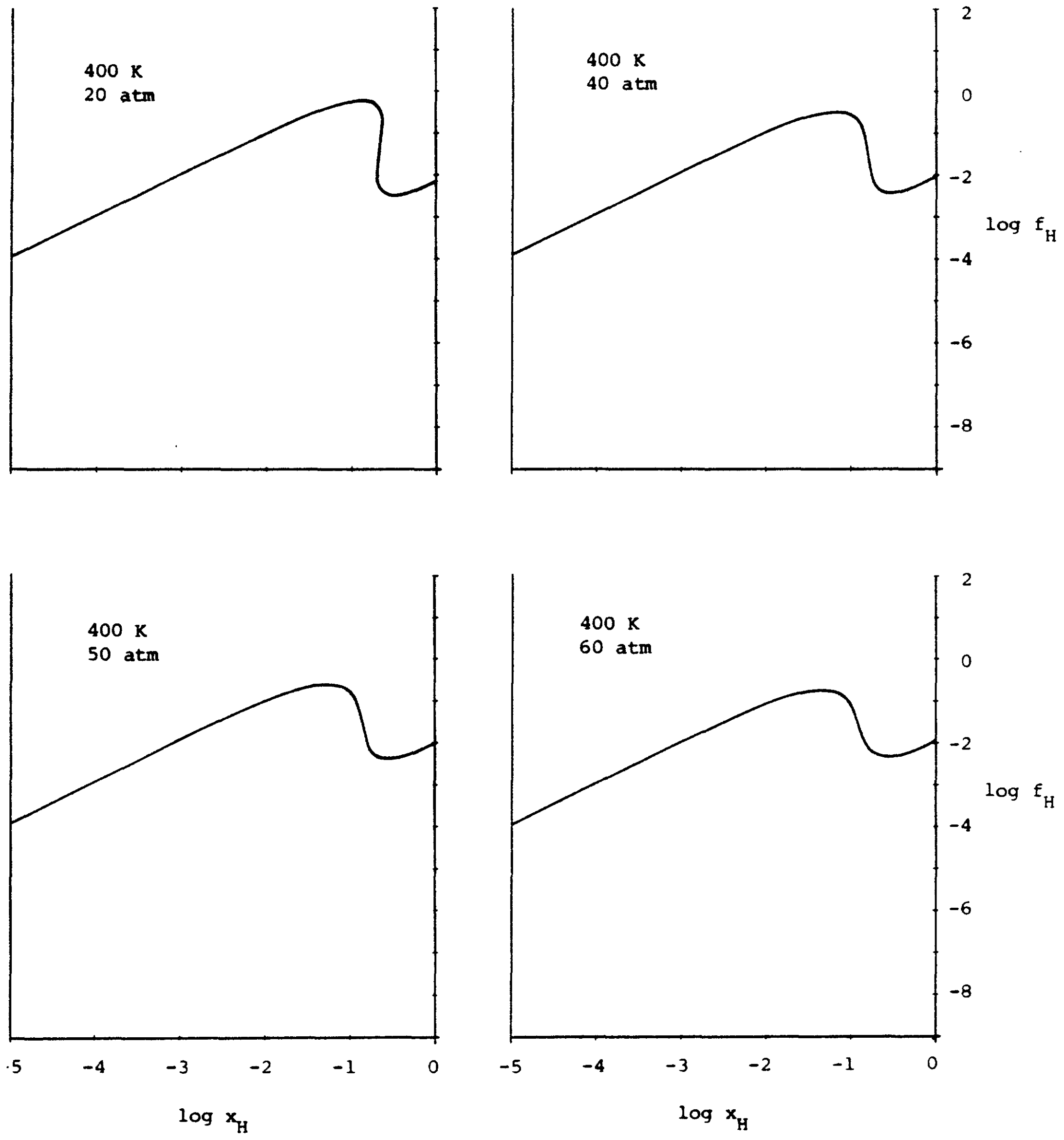
400 K
20 atm
400 K
40 atm
400 K
50 atm
400 K
60 atm
2
0
-2
-4
-6
-8
log f_H
2
0
-2
-4
-6
-8
log f_H
-5
-4
-3
-2
-1
0
log x_H
-5
-4
-3
-2
-1
0
log x_H

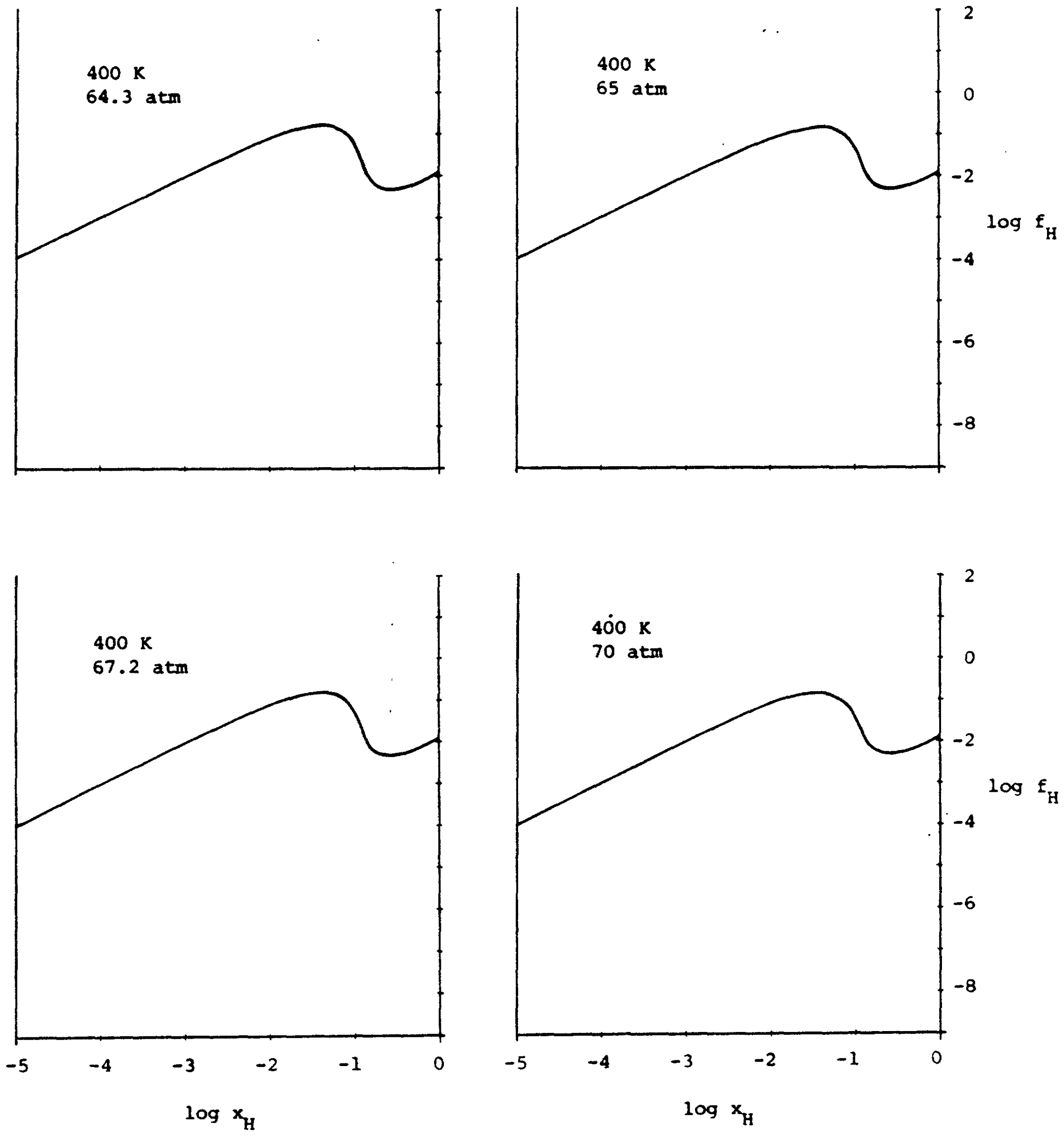
400 K
64.3 atm
400 K
65 atm
400 K
67.2 atm
400 K
70 atm
2
0
-2
-4
-6
-8
log f_H
-5
-4
-3
-2
-1
0
log x_H

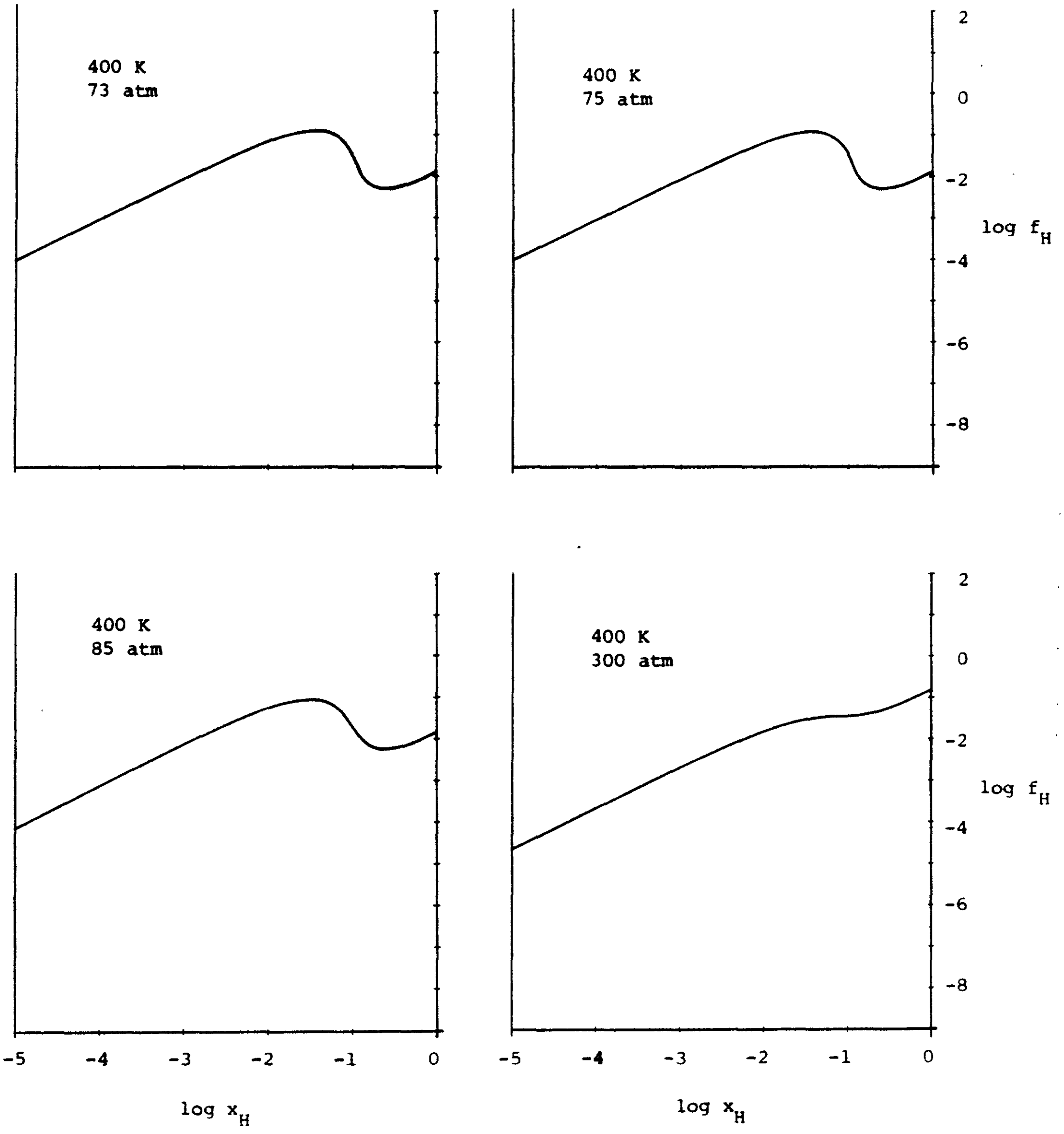
400 K
73 atm
400 K
75 atm
400 K
85 atm
400 K
300 atm
2
0
-2
-4
-6
-8
log f_H
-5
-4
-3
-2
-1
0
log x_H

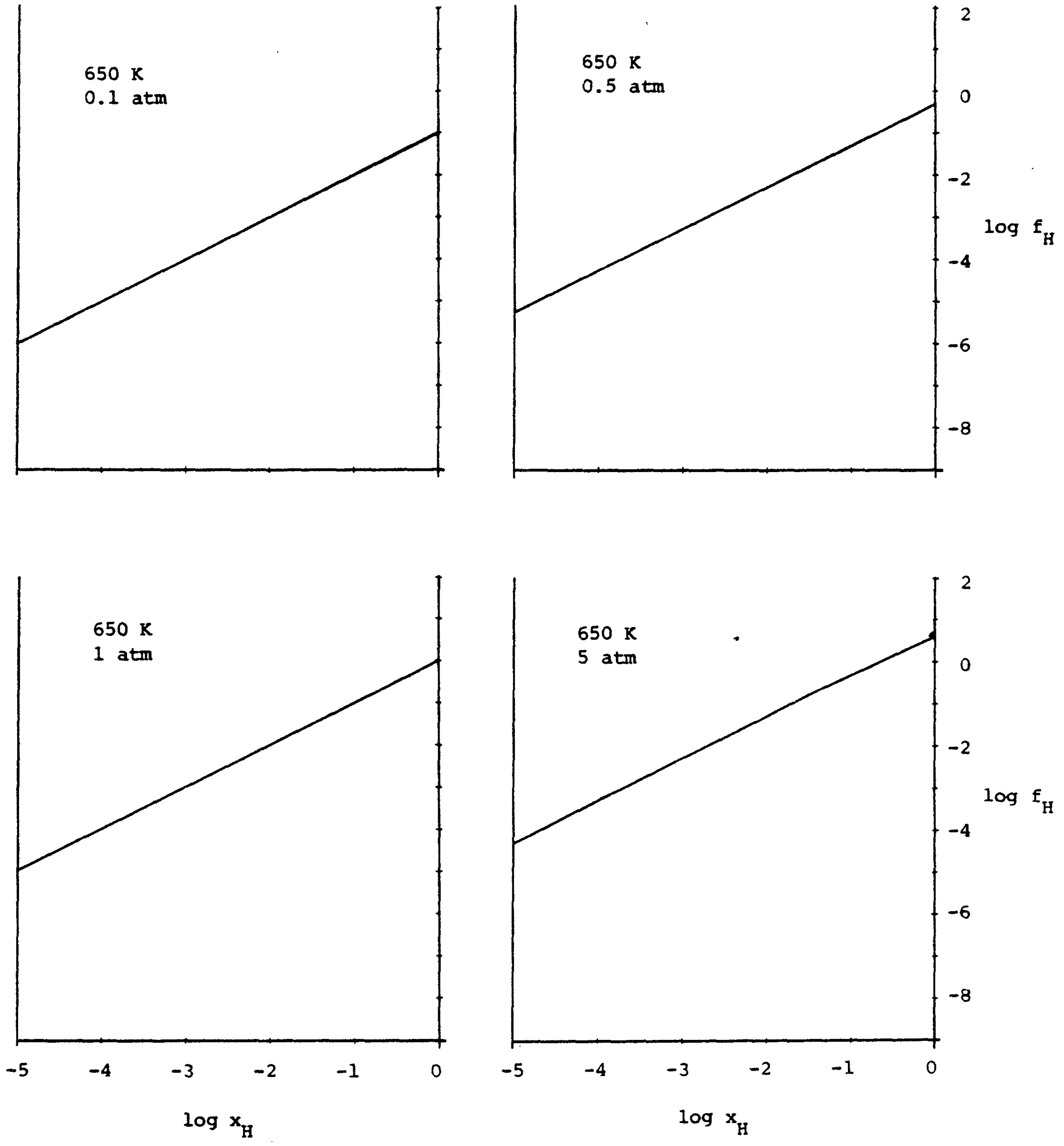
650 K
0.1 atm
650 K
0.5 atm
650 K
1 atm
650 K
5 atm
2
0
-2
-4
-6
-8
log f_H
-5
-4
-3
-2
-1
0
log x_H

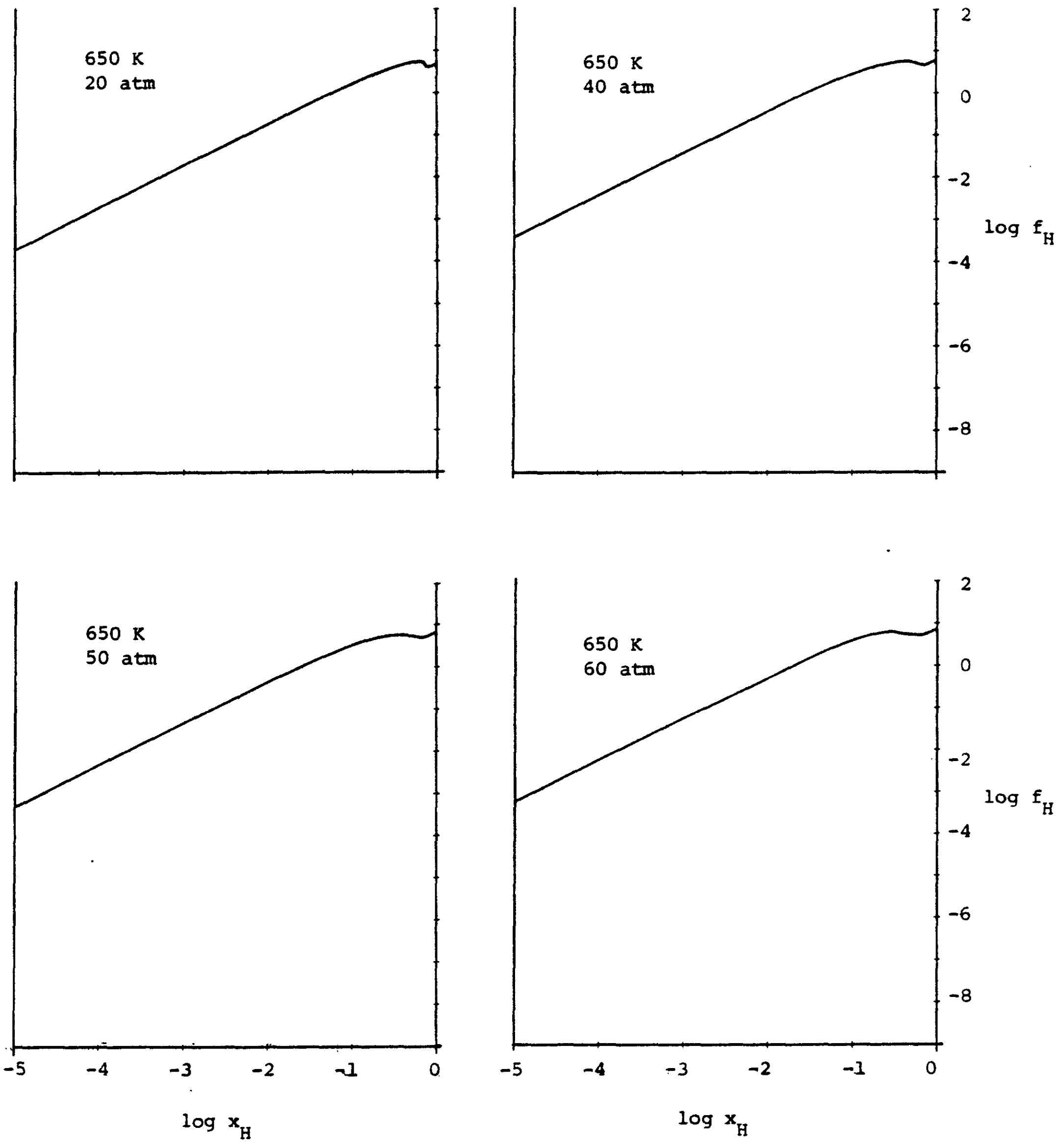
650 K
20 atm
650 K
40 atm
650 K
50 atm
650 K
60 atm
2
0
-2
-4
-6
-8
log f_H
2
0
-2
-4
-6
-8
log f_H
-5
-4
-3
-2
-1
0
log x_H
-5
-4
-3
-2
-1
0
log x_H

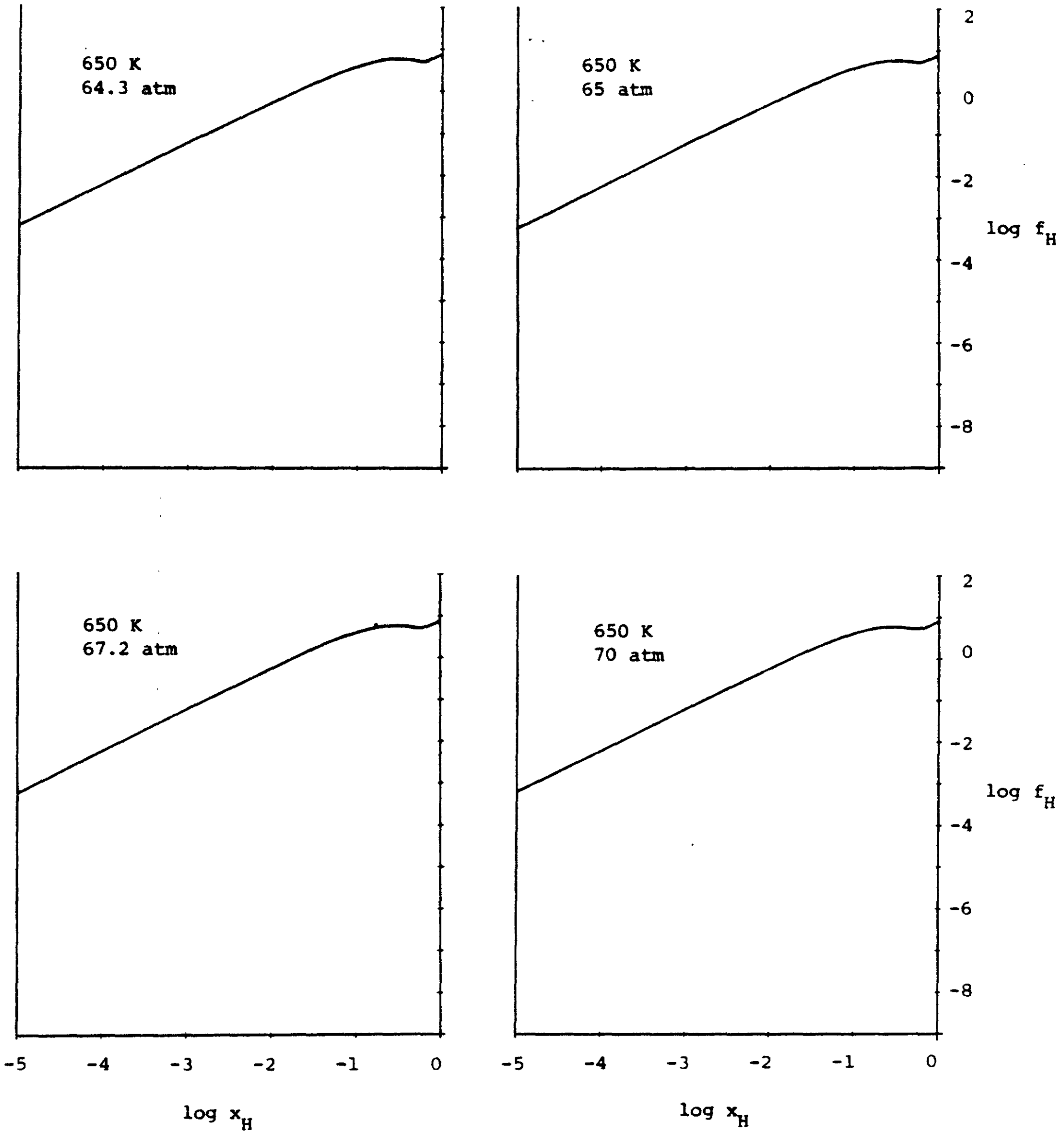
650 K
64.3 atm
650 K
65 atm
650 K
67.2 atm
650 K
70 atm
2
0
-2
-4
-6
-8
log f_H
2
0
-2
-4
-6
-8
log f_H
-5
-4
-3
-2
-1
0
log x_H
-5
-4
-3
-2
-1
0
log x_H

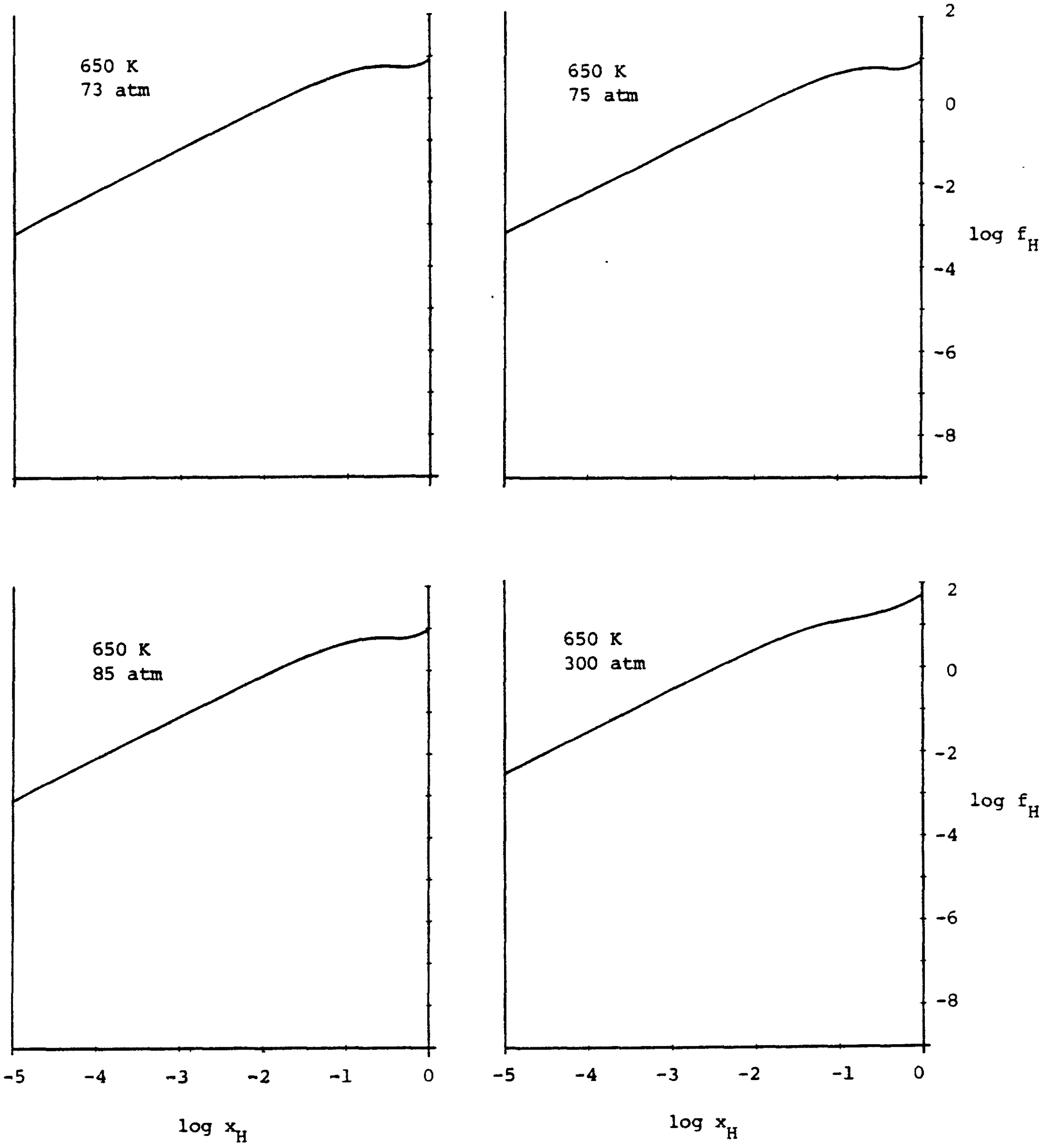
650 K
73 atm
650 K
75 atm
650 K
85 atm
650 K
300 atm
2
0
-2
-4
-6
-8
log f_H
-5
-4
-3
-2
-1
0
log x_H

Appendix C Algorithm and Documentation of Programs

C.1 Phase equilibrium algorithm

The basic algorithm used in the generation of the P-T-x diagrams is in principle quite simple, and involves the prediction of the equilibrium phase compositions at a given temperature and pressure. The f-x plot for component 2 (which may denote either substance) is first divided into monotonic segments to allow for convergence of the search routine. This division consists of locating the extrema and slope infinities in the fugacity functionality across the entire composition range. Figure C.1 gives an example of this procedure.

If prediction of a solid solubility is being carried out, each segment is checked for a composition at which

$$f_2^F = f_2^C \qquad (C.1)$$

These points correspond to solid-fluid equilibrium. If fluid-fluid equilibrium is desired, a segment is compared with another segment, and, if possible, a pair of compositions obtained for which

$$f_2^I = f_2^{II} \qquad (C.2)$$

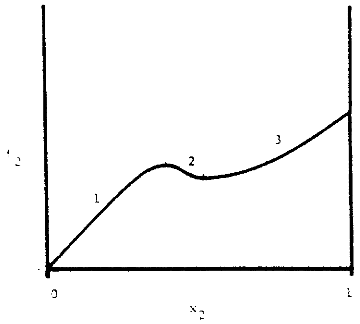

Figure C.1a. x_2 is incremented monotonically, starting from near 0, to locate the two extrema. The curve is then divided into the three segments shown.

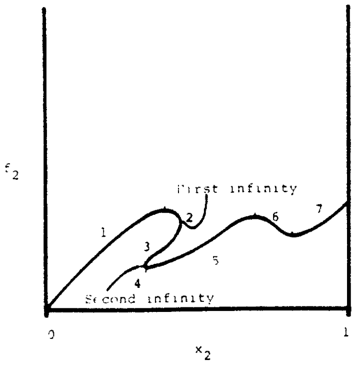

Figure C.1b. x_2 is increased along segments 1 and 2 until the first infinity is reached. (The second infinity is actually encountered first, but is skipped over). x_2 is then decreased along segment 3 until the second infinity is reached. The search now continues in a positive direction until $x_2 = 1$ is reached. Altogether seven segments are determined.

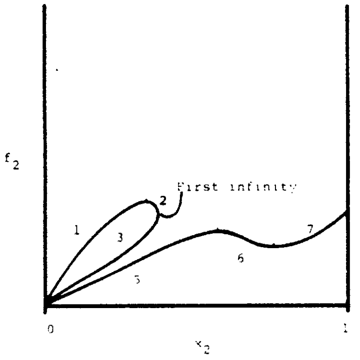

Figure C.1c. A closed loop f-x curve. The analysis of this curve is similar to that in Figure C.3b, with seven segments determined. In this case, however, segment 4 is of null length.

Here I and II refer to the two segments being compared. At these same compositions, a check is made to see if

$$f_1^{I} = f_1^{II} \tag{C.3}$$

If this equation is not satisfied, another set of compositions in these segments for which equation (C.2) holds is examined. If equation (C.3) is satisfied, conditions of fluid-fluid equilibrium have been determined. Depending upon the circumstances (see documentation of program peq), the same two segments will be searched for an additional phase equilibrium point, or the program moves on to the next pair of segments. All combinations of segments are compared in this manner, except for adjacent segments, for which it has been found that no equilibrium solutions can exist.

Once all segments have been compared, the procedure is complete for the given temperature and pressure. To construct a P-x section, the procedure is repeated for other pressures. Binodal curves are then drawn connecting the appropriate equilibrium points. If a three-phase tieline is present at the temperature chosen, it will be indicated by the intersection of two or more binodal curves at a common pressure. Critical points are located by noting when binodal tielines become of zero length. By analyzing a number of P-x sections in this fashion, a P-T projection or P-T-x space diagram for the system may be constructed.

C.2 General comments on programs

The twelve Fortran programs used for phase equilibrium calculations are documented in this appendix. The first of these, zer, is a trial and error search subroutine, and is used in calculations for both pure component and binary system diagrams. The next four programs, pure, zrp, Zvalp, and fp pertain only to pure component computations. Program pure is the main program, Zvalp is a subroutine, and zrp and fp are functions. The last seven programs pertain only to binary system computations. Program pr is the main program, Zv, sol, and peq are subroutines, while zr, LM, and f are functions. All programs are in double precision mode, since this was found to be necessary in a number of instances. Computations were carried out on the Honeywell Multics time-sharing system operated by the MIT Information Processing Center.

C.3 Subroutine zer

This subroutine searches a given composition interval to determine where some function of composition attains a given value. This function may be the fugacity, L1, M1, or the cubic determinant zr, and must be monotonic for the given interval. The trial and error search is performed by bisection (interval halving).

Variable list:

fx - Function under consideration. Possibilities were listed above.

i - Function definition. A dummy variable for function zr. For function LM, it specifies selection of L1 or M1. For fugacity, it specifies component 1 or 2.

nrt - Root specifier when multiple real roots to the cubic exist.

xlo - First endpoint of the composition range to be searched.

xhi - Second endpoint of the composition range to be searched.

fxm - The value which the function under consideration is to attain.

xapp - The composition at which the function has attained the desired value. This is the result which is returned to the calling program.

lox - Interval endpoint. Varies as the search narrows down the composition range.

```
COMPILATION LISTING OF zer (>user_dir_dir>HON>Hong>zer.fortran)

Compiled by: Multics New Fortran Compiler, Release 6a
Compiled on: 07/22/81  2049.6 edt Wed
    Options: ansi66 map

                                            Subroutine zer

       subroutine zer(fx,i,nrt,xlo,xhi,fxm,xapp,*)
       implicit double precision(a-h,o-z,A-Z)
       double precision lox
       lox=xlo
       hix=xhi
       asig=fx(lox/2+hix/2,i,nrt)/10^8
       do 40 j=1,60
       x=lox/2+hix/2
       if(abs(fx(x,i,nrt)-fxm)-abs(asig)) 50,50,10
10     if((fx(lox,i,nrt)-fxm)/(fx(x,i,nrt)-fxm))30,20,20
20     lox=x
       go to 40
30     hix=x
40     continue
       return 1
50     xapp=x
       return 2
       end
```

Figure C.3. Subroutine zer.

hix - Interval endpoint. Analogous to lox.

asig - Convergence criterion variable.

j - Do loop iteration variable.

x - Trial composition, midway between the endpoints of the interval being searched.

Flow scheme:

Line number - Operation

4,5 - Transfer input variables to working variables.

6 - Establish appropriate convergence accuracy.

7 - Enter or continue search loop. If 60 iterations already performed, go to line 15.

8 - Guess x.

9 - Test for convergence. If convergence sufficient, go to line 16. If not, go to line 10.

10 - If value of function is too high at x, go to line 13. If too low, go to line 11.

11 - Set new endpoint for interval to be searched.

12 - Go to line 14.

13 - Set new endpoint for interval to be searched.

14 - Proceed to line 7 to continue search.

15 - Contingency return to calling program. The convergence criterion has not been satisfied after 60 iterations.

16 - Set value to be returned to calling program.

17 - Return to calling program.

18 - End program.

C.4 Main Program pure

This is the main program for the generation of pure component diagrams. It is set up to calculate isotherms in a P-V plot, but also determines a phase equilibrium pressure when appropriate. Thus the program is also useful for determining tielines and P-T diagrams.

Variable list:

a - Peng-Robinson (P-R) attraction parameter.

b - P-R covolume.

T - Temperature.

v - Molar volume.

R - Gas constant.

Z - Compressibility factor.

Tc - Critical temperature.

Pc - Critical pressure.

w - Acentric factor.

ac - Value of attraction parameter at critical point.

Tlow - Lowest temperature isotherm to be calculated.

Thigh - Highest temperature isotherm to be calculated.

Tstep - Temperature increment between isotherms.

Plow - Lowest pressure for which volume is to be calculated.

Phigh - Highest pressure for which volume is to be calculated.

P - Pressure.

nrp - Root specifier when multiple real roots to the cubic exist.

```
COMPILATION LISTING OF pure (>user_dir_dir>HON>Hong>pure.fortran)

Compiled by: Multics New Fortran Compiler, Release 8a
Compiled on: 07/22/81  2049.7 edt Wed
    Options: ansi66 map

                                        Main Program

      implicit double precision(a-h,o-z,A-Z)
      common/pure/a,b,T,v,R,Z
      data Tc,Pc,w/304.2,72.8,.225/
      R=.082057
      ac=.45724*R^2*Tc^2/Pc
      b=.0778*R*Tc/Pc
      print,"Input Tlow,Thigh,Tstep,Plow,Phigh,Pstep"
      read,Tlow,Thigh,Tstep,Plow,Phigh,Pstep
      do 100 T=Tlow,Thigh,Tstep
      a=ac*(1+(.37464+1.54226*w-.26992*w^2)*(1-(T/Tc)^.5))^2
      do 100 P=Plow,Phigh,Pstep
      print,"T=",T,"       P=",P
      do 100 nrp=1,2-sign(1,zrp(P))
      call Zvalp(P,nrp)
      print,"v=",v
      if(nrp-2)100,100,10
10    if(fp(P,1,1)/fp(P-.99*Pstep,1,1))20,100,100
20    call zer(fp,1,1,P-.99*Pstep,P,0,Pvle,$100)
      print,"vle at P=",Pvle
100   continue
      end
```

Figure C.4. Main program pure.

zrp - Determinant function. See Section C.5.

Zvalp - Compressibility factor subroutine. See Section C.6.

fp - Fugacity function. See Section C.7

zer - Bisection subroutine. See Section C.3

Pvle - Pressure of vapor-liquid equilibrium at a given temperature.

Flow scheme:

Line number - Operation

5-7 - Assign values to constants.

8 - Request input of desired temperature and pressure grid.

9 - Read in temperature and pressure grid.

10 - Pick a new temperature. If greater than Thigh, go to line 22.

11 - Assign value to temperature dependent constant.

12 - Pick a new pressure. If greater than Phigh, go to line 10.

13 - Print out temperature and pressure.

14 - Enter or continue loop to calculate volume. If this is the second iteration and there is one real root to the cubic, go to line 12. If this is the fourth iteration and there are three real roots to the cubic, go to line 12.

15 - Call subroutine to calculate volume.

16 - Print out volume.

17 - If this is the third iteration, go to line 18. Otherwise, go to line 21.

18 - Evaluate function fp at the current pressure and at (approximately) the previous pressure. If the quotient of these two values is negative, a VLE pressure exists in this pressure interval. Go to line 19. If the quotient is nonnegative, go to line 21.

19 - Call subroutine zer to determine more accurately the VLE pressure. If VLE pressure cannot be determined, go to line 21.

20 - Print the VLE pressure.

21 - Go to line 14.

22 - End program.

C.5 Function zrp

This function calculates zrp, the determinant of the cubic equation. If zrp is positive, the cubic has one real root. If zrp is negative, the cubic has three real roots.

Variable list:

a, b, T, v, R, Z, P - Defined in main program pure.

zb, zc, zd, zp, zq - Intermediate variables in the calculation of zrp.

A - Dimensionless attraction parameter.

B - Dimensionless covolume.

Flow scheme:

Line number - Operation

6-7 - Assign values to constants.

8-12 - Assign values to intermediate variables.

13 - Calculate zrp.

14 - End program and return to calling program.

```
COMPILATION LISTING OF zrp (>user_dir_dir>HDW>Hong>zrp.fortran)

Compiled by: Multics New Fortran Compiler, Release 8a
Compiled on: 07/22/81  2349.7 edt Wed
    Options: ansi66 map

                                            Function zrp

      double precision function zrp(P)
      implicit double precision(a-h,o-z,A-Z)
      common/pure/a,b,T,v,R,Z
      common/Zvalp/zp,zq,zb
      common/fp/A,B
      A=a*P/(R*T)^2
      B=b*P/R/T
      zb=B-1
      zc=A-3*B^2-2*B
      zd=B^2+B^3-A*B
      zp=zc-zb^2/3
      zq=zd-zb*zc/3+2*zb^3/27
      zrp=(zp/3)^3+(zq/2)^2
      end
```

Figure C.5. Function zrp.

C.6 Subroutine Zvalp

This subroutine calculates the value of the compressibility factor, Z, and the molar volume v.

Variable list:

a, b, T, v, R, Z, P, nrp - Defined in main program pure.

zp, zq, zb - Defined in function zrp.

z - Array which stores the three values of Z when the cubic has three real roots.

zrp - Determinant function. See Section C.5.

zC, zD, zy - Intermediate variables in the calculation of Z when cubic has one real root.

n - Do loop iteration variable.

phi - Angle used in calculation of Z when cubic has three real roots.

Flow scheme:

Line number - Operation

6 - If three real roots to cubic, go to line 12. Otherwise, go to line 7.

7-9 - Assign values to intermediate variable.

10 - Calculate Z.

11 - Go to line 21.

```
COMPILATION LISTING OF Zvalp (>user_dir_dir>HDN>Hong>Zvalp.fortran)

 Compiled by: Multics New Fortran Compiler, Release 8a
 Compiled on: 07/22/81  2049.8 edt Wed
     Options: ansi66 map

                                                  Subroutine Zvalp

        subroutine Zvalp(P,nrp)
        implicit double precision(a-h,o-z,A-Z)
        common/pure/a,b,T,v,R,Z
        common/Zvalp/zp,zq,zb
        dimension z(3)
        if(zrp(P))20,10,10
   10   zC=abs(-zq/2+zrp(P)^.5)^(4./3)/(-zq/2+zrp(P)^.5)
        zD=-abs(zq/2+zrp(P)^.5)^(4./3)/(zq/2+zrp(P)^.5)
        zy=zC+zD
        Z=zy-zb/3
        go to 70
   20   do 30 n=1,3
        phi=acos((-27*zq^2/4/zp^3)^.5)
   30   z(n)=-(zq/abs(zq))*2*(-zp/3)^.5*cos(phi/3+2.0943951*(n-1))-zb/3
        go to (40,60,50) nrp
   40   Z=max(z(1),z(2))
        go to 70
   50   Z=min(z(1),z(2))
        go to 70
   60   Z=z(3)
   70   v=Z*R*T/P
        end
```

Figure C.6. Subroutine Zvalp.

12 - Enter or continue do loop to calculate three values of Z. If this is the fourth iteration, go to line 15.

13 - Calculate angle phi.

14 - Calculate a value for array z.

15 - Select the desired value of Z. For the gaseous value (large Z) go to line 16. For the liquid value (small Z) go to line 18. For the unstable value (intermediate Z) go to line 20.

16 - Assign Z the maximum value in the array z.

17 - Go to line 21.

18 - Assign Z the minimum value in the array z.

19 - Go to line 21.

20 - Assign Z the intermediate value in the array z.

21 - Calculate molar volume v.

22 - End program and return to calling program.

C.7 Function fp

This function calculates the difference between the fugacity of a pure vapor and the fugacity of the pure liquid at a given temperature and pressure. This quantity is important since, if equal to zero, the criterion of two-phase equilibrium is satisfied.

Variable list:

a, b, T, v, R, Z, P, nrp - Defined in main program pure.

j,k - Dummy variables, included for compatibility with subroutine zer.

A, B - Defined in function zrp.

f - Array which stores the values of the vapor and liquid fugacities. The value of the unstable fugacity is not stored.

Zvalp - Compressibility factor subroutine. See Section C.6.

Flow scheme:

Line number - Operation

6 - Enter or continue do loop to calculate vapor and liquid fugacities. If this is the third iteration, go to line 9.

7 - Call subroutine Zvalp to assign values to necessary variables.

8 - Calculate fugacity. Go to line 6.

9 - Calculate fp, the fugacity difference between vapor and liquid.

10 - End program and return to calling program.

```
COMPILATION LISTING OF fp (>user_dir_dir>HDW>Hong>fp.fortran)

 Compiled by: Multics New Fortran Compiler, Release 8a
 Compiled on: 07/22/81  2049.8 edt Wed
     Options: ansi66 map

                                               Function fp

       double precision function fp(P,j,k)
       implicit double precision(a-h,o-z,A-Z)
       common/pure/a,b,T,v,R,Z
       common/ fp/A,B
       dimension f(3)
       do 10 nrp=1,3,2
       call Zvalp(P,nrp)
   10  f(nrp)=P*exp(Z-1-alog(Z-B)-A/8**.5/B*alog((Z+(2**.5+1)*B)/(Z-(2**.5-1)*B)))
       fp=f(1)-f(3)
       end
```

Figure C.7. Function fp.

C.8 Main Program pr

This is the main program for the calculation of binary phase equilibrium, both fluid-fluid and solid-fluid. Most of the coding deals with analysis of the fugacity-composition functionality at a given temperature and pressure. Infinity points, extrema or spinodal points (L1=0) and inflection points (M1=0) are calculated. The fugacity curve is divided into monotonic segments, as described in Figures C.1a, b, and c, and the subroutines for determining equilibrium along these segments are called. In the following, all compositional derivatives refer to differentiation with respect to mole fraction of component 2.

Variable list:

d - Array which stores the end points of the monontonic segments. These occur at mole fractions of 0 and 1, as well as at slope infinities and extrema.

nr - Array which stores a root specifier for each interval. An element in this array is meaningful only if the cubic has three real roots in the given interval. If the cubic has one real root, the value of the root specifier is immaterial.

b1, b2 - Covolumes for components 1 and 2.

bx - Compositional derivative of mixture covolume.

T - Temperature.

a1, a2 - Attraction parameters for components 1 and 2.

```
COMPILATION LISTING OF pr (>udd>HDN>Hong>pr.fortran)

Compiled by: Multics New Fortran Compiler, Release 6a
Compiled on: 07/22/81  2125.5 edt wed
    Options: ansi66 map

                                   Main Program

          implicit double precision(a-h,o-z,A-Z)
          dimension d(15),nr(14)
          common/pr/b1,b2,bx,T,a1,a2,a12,P,R,vc
          data Tc1,Pc1,w1,Tc2,Pc2,w2,d12/304.2,72.8,.225,746.4,40,.302,.11/
          data c1,c2,d(1),nr(1)/1.000001,.999999,1d-8,1/
          R=.082057
          vc=.1248
          a1c=.45724*R^2*Tc1^2/Pc1
          a2c=.45724*R^2*Tc2^2/Pc2
          b1=.0778*R*Tc1/Pc1
          b2=.0778*R*Tc2/Pc2
          bx=b2-b1
          print,"Input Tlow,Thigh,Tstep,Plow,Phigh,Pstep,coarse grid,fine grid"
          read,Tlow,Thigh,Tstep,Plow,Phigh,Pstep,cg,fg
          do 200 T=Tlow,Thigh,Tstep
          a1=a1c*(1+(.37464+1.54226*w1-.26992*w1^2)*(1-(T/Tc1)^.5))^2
          a2=a2c*(1+(.37464+1.54226*w2-.26992*w2^2)*(1-(T/Tc2)^.5))^2
          a12=(1-d12)*(a1*a2)^.5
          do 200 P=Plow,Phigh,Pstep
          print,"T=",T,"       P=",P
          g=fg;l=1;inc=1;k=0;kf=0;x=1d-6
          if(zr(0d0,1,1).lt.0d0)kf=1
   40     y=x
          if(x.gt..15)g=cg
          if(l.ge.3)g=cg
          x=x+inc*g
          if(x)65,65,50
   50     if(x-1)70,60,60
   60     if(zr(1d0,1,1).gt.0.or.kf.gt.6)go to 180
   65     k=k+1
          kf=kf+1
          d(k+l)=idint(x)
          l=l+1
          nr(k+l)=k+1-2*(k/3+k/4)
          d(k+l)=idint(x)
          go to 100
   70     if(zr(y,1,1)/(zr(x,1,1))) 80,80,110
   80     kf=kf+1
          go to (110,90,90,110,110,90,90,110)kf
   90     k=k+1
          call zer(zr,1,1,x,y,0,d(l+k),$110)
          nr(k+l)=k+1-2*(k/3+k/4)
   100    inc=-inc
          if(mod(k,2).eq.1)x=c2*d(k+l)
          if(mod(k,2).eq.0)x=max(c1-1,c1*d(k+l))
          print,"zR zero at x2=",d(k+l)
          go to 40
   110    if(LM(y,2,nr(k+l))/LM(x,2,nr(k+l))) 140,150,150
   140    l=l+1
          nr(k+l)=k+1-2*(k/3+k/4)
          call zer(LM,2,nr(k+l),x,y,0,d(k+l),$150)
          print,"L1 zero at x2=",d(k+l),"     nr=",nr(k+l)
   150    if(LM(y,3,nr(k+l))/LM(x,3,nr(k+l))) 160,40,40
   160    call zer(LM,3,nr(k+l),x,y,0,M0,$40)
          print,"M1 zero at x2=",M0,"     nr=",nr(k+l)
          go to 40
   180    d(k+l+1)=1
          do 190 i=1,k+l
   190    call sol(max(d(i),d(i+1)),min(d(i),d(i+1)),nr(i))
          do 200 i=1,k+l-2
          do 200 j=i+2,k+l
          call peq(min(d(i),d(i+1)),max(d(i),d(i+1)),min(d(j),d(j+1)),max(d(j),d(j+1)),nr(i),nr(j))
   200    continue
          end
```

Figure C.8. Main program pr.

a12 - Parameter for attraction between components 1 and 2.

P - Pressure.

R - Gas constant.

vc - Molar volume of solid phase.

Tc1, Tc2 - Critical temperatures.

Pc1, Pc2 - Critical pressures.

w1, w2 - Acentric factors.

d12 - Interaction parameter.

c1 - Constant slightly greater than 1.

c2 - Constant slightly less than 1.

a1c, a2c - Attraction parameters at critical points.

Tlow - Lowest temperature for which phase equilibrium is to be calculated.

Thigh - Highest temperature for which phase equilibrium is to be calculated.

Tstep - Increment between temperatures for which phase equilibrium is to be calculated.

Plow - Lowest pressure for which phase equilibrium is to be calculated.

Phigh - Highest pressure for which phase equilibrium is to be calculated.

Pstep - Increment between pressures for which phase equilibrium is to be calculated.

cg - Large composition increment (coarse grid).

fg - Small composition increment (fine grid).

g - Current compositional increment.

1 - Associated with number of spinodal points located.

inc - Sets direction of compositional search. +1 for increasing mole fraction of component 2; -1 for decreasing mole fraction of component 2.

k - Associated with number of infinities located.

kf - Infinity flag. Associated with number of slope infinities encountered. A given infinity is sometimes encountered twice.

x - Current mole fraction of component 2.

zr - Determinant function. See Section C.9.

y - Previous mole fraction of component 2.

zer - Bisection subroutine. See Section C.3.

LM - Helmholtz derivative function. See Section C.11.

MO - Mole fraction of an inflection point.

i - Do loop iteration variable.

sol - Solid solubility subroutine. See Section C.12.

j - Do loop iteration variable.

peq - Fluid-fluid equilibrium subroutine. See Section C.13.

Flow Scheme:

Line number - Operation

6-12 - Assign values to constants.

13 - Request input of temperature, pressure, and composition grid.

14 - Read in temperature, pressure, and composition grids.

15 - Enter or continue do loop to calculate phase equilibria at a new temperature. If T is greater than Thigh, go to line 65.

16-18 - Assign values to temperature dependent constants.

19 - Enter or continue do loop to calculate phase equilibria at a new pressure. If P is greater than Phigh, go to line 15.

20 - Print out T and P.

21 - Initialize variables.

22 - Determine if three roots are present at x=0. If so, set the infinity flag to 1.

23 - Assign current value of x to previous value of x.

24-26 - Set composition step size to coarse or fine, depending on current value of x. It is sometimes necessary to search a particular composition range much more closely than the rest of the range. It becomes evident in the generation of a P-x diagram if and where such a fine search is necessary. The range given here for the fine search is x less than 0.15 or until the second extremum is found. The range is different for different temperatures and pressures, and is often in essence deleted by inputting a value of fg equal to cg at line 14.

27 - Assign new current value of x.

28 - If x is nonpositive (this occurs during the search of segment 3 in Figure C.1c) go to line 31. Otherwise, go to line 29.

29 - If x is greater than or equal to 1 go to line 30. Otherwise, go to line 38.

30 - If there is only one root at x=1, or if the three roots

at x=1 have already been accounted for, the search at this T and P is complete. Go to line 58.

31 - Increment number of infinities located.

32 - Increment infinity flag.

33 - Assign an interval endpoint the value of 0 if x<0, or the value of 1 is x>1.

34 - Increment number of extrema located.

35 - Assign proper value to root specifier.

36 - Same as line 33. Together, these statements have the effect of assigning a null length to segment 4 in Figure C.1c, or to an analogous segment occuring at x=1.

37 - Go to line 44.

38 - Test for a zero in the cubic determinant. A zero corresponds to an infinity in the fugacity plot. If a zero is present in the interval between x and y, go to line 39. Otherwise, go to line 49.

39 - Increment infinity flag.

40 - The value of the infinity flag determines if a new infinity is to be located and stored. If so, go to line 41. If not, go to line 49.

41 - Increment number of infinities located.

42 - Call subroutine to accurately locate infinity. Store location in array d. If infinity cannot be located, go to line 49.

43 - Assign proper value to root specifier.

44 - Change direction of composition search.

45, 46 - Bring x back into the range of 0 to 1.

47 - Print out location of infinity.

48 - Go to line 23.

49 - Test for an extremum (spinodal) in the x-y interval. If an extremum exists, go to line 50. Otherwise, go to line 54.

50 - Increment number of extrema located.

51 - Assign proper value to root specifier.

52 - Call subroutine to accurately locate extremum. Store location in array d. If extremum cannot be located, go to line 54.

53 - Print out location of extremum and root specified.

54 - Test for an inflection point in the x-y interval. If an inflection exists, go to line 55. Otherwise, go to line 23.

55 - Call subroutine to accurately locate inflection point. If inflection point cannot be located, go to line 23.

56 - Print out location of inflection point.

57 - Go to line 23.

58 - Set final segment end point at x=1.

59 - Enter or continue do loop to calculate solid solubilities. If all segments have been checked, go to line 61. This statement is deleted for systems in which no solid phase is present.

60 - Call subroutine to calculate solid solubility for a given segment. This statement is deleted for systems in which no solid phase is present.

61 - Enter or continue subroutine to calculate fluid-fluid equilibria. Specify the first segment of the two to be compared. If all necessary segments have been checked, go to line 65.

62 - Enter or continue subroutine to calculate fluid-fluid equilibria. Specify the second segment of the two to be compared. If all necessary segments have been specified, go to line 61.

63 - Call subroutine to calculate fluid-fluid equilibria between two segments.

64 - Go to line 62.

65 - End program.

C.9 Function zr

This function calculates zr, the determinant of the cubic equation. If zr is positive, the cubic has one real root. If zr is negative, the cubic has three real roots.

Variable lists:

x2 - Mole fraction of component 2.

d1,d2 - Dummy arguments for compatibility with subroutine zer.

b1, b2, bx, T, a1, - Defined in main program pr.
a2, a12, P, R, vc

a - Mixture attraction parameter.

b - Mixture covolume.

v - Molar volume of mixture.

Z - Compressibility factor of mixture.

A - Dimensionless mixture attraction parameter.

B - Dimensionless mixture covolume.

zb, zc, zd, zp, zq - Intermediate variables in the calculation of zr.

Flow scheme:

Line number - Operation

6-9 - Assign values to constants.

10-14 - Assign values to intermediate variables.

15 - Calculate zr.

16 - End program and return to calling program.

```
COMPILATION LISTING OF zr (>user_dir_dir>HDJ>Hong>zr.fortran)

Compiled by: Multics New Fortran Compiler, Release 8a
Compiled on: 07/22/81  2050.5 edt Wed
    Options: ansi66 map

                                                   Function zr

      double precision function zr(x2,d1,d2)
      implicit double precision(a-h,o-z,A-Z)
      common/pr/b1,b2,bx,T,a1,a2,a12,P,R,vc
      common/Zv/a,b,v,Z,A,B
      common/zr/zp,zq,zb
      a=a1*(1-x2)^2+2*a12*(1-x2)*(x2)+a2*(x2)^2
      b=b1*(1-x2)+b2*(x2)
      A=a*P/(R*T)^2
      B=b*P/R/T
      zb=B-1
      zc=A-3*B^2-2*B
      zd=B^2+B^3-A*B
      zp=zc-zb^2/3
      zq=zd-zb*zc/3+2*zb^3/27
      zr=(zp/3)^3+(zq/2)^2
      end
```

Figure C.9. Function zr.

C.10 Subroutine Zv

This subroutine calculates the value of the mixture compressibility factor Z, and the molar volume of the mixture, v.

Variable list:

x2 - Mole fraction of component Z.

nrt - Root specifier.

b1, b2, bx, T, a1, - Defined in main program pr.
a2, a12, P, R, vc

a, b, v, Z, A, - Defined in function zr.
B, zp, zq, zb

z - Array which stores the three vaues of Z when the cubic has three real roots.

zR - Value of the determinant zr at a given x2.

zr - Determinant function. See Section C.9.

zC, zD, zy - Intermediate variables in the calculation of Z when the cubic has one real root.

n - Do loop iteration variable.

phi - Angle used in calculation of Z when cubic has three real roots.

z1, z2, z3 - Intermediate variables in the determination of the middle (mechanically unstable) compressibility factor.

Flow scheme:

Line number - Operation

```
COMPILATION LISTING OF Zv (>user_dir_dir>HDN>Hong>Zv.fortran)

Compiled by: Multics New Fortran Compiler, Release 8a
Compiled on: 07/22/81  2050.3 edt Wed
    Options: ansi66 map

                                               Subroutine Zv

          subroutine Zv(x2,nrt,*)
          implicit double precision(a-h,o-z,A-Z)
          common/pr/b1,b2,bx,T,a1,a2,a12,P,R,vc
          common/Zv/a,b,v,Z,A,B
          common/zr/zp,zq,zb
          dimension z(3)
          zR=zr(x2,1,1)
          if(zR)20,10,10
     10   zC=abs(-zq/2+zR^.5)^(4./3)/(-zq/2+zR^.5)
          zD=-abs(zq/2+zR^.5)^(4./3)/(zq/2+zR^.5)
          zy=zC+zD
          Z=zy-zb/3
          go to 70
     20   do 30 n=1,3
          phi=acos((-27*zq^2/4/zp^3)^.5)
     30   z(n)=-(zq/abs(zq))*2*(-zp/3)^.5*cos(phi/3+2.0943951*(n-1))-zb/3
          go to (60,50,40) nrt
     40   Z=min(z(1),z(2),z(3))
          go to 70
     50   z1=max(z(1),z(2))
          z2=max(z(1),z(3))
          z3=max(z(2),z(3))
          Z=min(z1,z2,z3)
          go to 70
     60   Z=max(z(1),z(2),z(3))
     70   if((Z-B) .lt. 0) return 1
          v=Z*R*T/P
          end
```

Figure C.10. Subroutine Zv.

7 - Evaluate function zr at the input composition and assign this value to zR.

8 - If three real roots to cubic, go to line 14. Otherwise, go to line 9.

9-11 - Assign values to intermediate variables.

12 - Calculate Z.

13 - Go to line 26.

14 - Enter or continue do loop to calculate three values of Z. If this is the fourth iteration, go to line 17.

15 - Calculate angle phi.

16 - Calculate a value for array z.

17 - Select the desired value of Z. For the lowest value, go to line 18. For the mechanically unstable value, go to line 20. For the highest value, go to line 25. Z's must be chosen so that the monotonic segments are ordered as shown in Figure C.1.

18 - Assign Z the minimum value in the array z.

19 - Go to line 26.

20-22 - Assign values to intermediate variables.

23 - Assign Z the middle value in the array z.

24 - Go to line 26.

25 - Assign Z the maximum value in the array z.

26- Contingency return. The calculated value of Z has no physical meaning.

27 - Calculate molar volume v.

28 - End program and return to calling program.

C.11 Function LM

This function calculates values of the mechanical stability term $\left(\frac{\partial P}{\partial v}\right)_{T,x}$ (=Pv) , the material stability term L1, and the critical point term M1. The mechanical stability term is no longer used in any of the other programs since it was found to change sign only at infinities in the f-x functionality.

Variable list:

x2 - Mole fraction of component 2.

lorm - Function definition. Specifies whether the return value of the function is Pv, L1, or M1.

nrt - Root specifier.

b1, b2, bx, T, a1, a2, a12, P, P, vc - Defined in main program pr.

a, b, v, Z, A, B - Defined in function zr.

Zv - Compressibility factor function. See Section C.10.

ax - Compositional derivative of mixture attraction parameter.

axx - Compositional derivative of ax.

W, X, Y - Intermediate variables in the calculation of Pv, L1, and M1.

Wx, Xx, Yx - Compositional derivatives of W, X, and Y, respectively.

r - Ratio of attraction parameter to covolume.

rx - Compositional derivative of r.

```
COMPILATION LISTING OF LM (>user_dir_dir>HDN>Hong>LM.fortran)

Compiled by: Multics New Fortran Compiler, Release 8a
Compiled on: 07/22/81  2050.6 edt Wed
    Options: ansi66 map

                                        Function LM

        double precision function LM(x2,lorm,nrt)
        implicit double precision(a-h,o-z,A-Z)
        common/pr/b1,b2,bx,T,a1,a2,a12,P,R,vc
        common/Zv/a,b,v,Z,A,B
        call Zv(x2,nrt,$50)
        ax=2*(-(1-x2)*a1+(1-2*x2)*a12+x2*a2)
        axx=2*(a1-2*a12+a2)
        W=v^2+2*b*v-b^2
        Wx=2*bx*(v-b)
        X=v+(1+2^.5)*b
        Xx=(1+2^.5)*bx
        Y=v+(1-2^.5)*b
        Yx=(1-2^.5)*bx
        r=a/b
        rx=(ax*b-a*bx)/b^2
        rxx=(axx-2*rx*bx)/b
        Avv=R*T/(v-b)^2-2*a*(v+b)/W^2 .
        if(lorm-1)50,10,20
   10   LM=Avv
        return
   20   Avx=-R*T*bx/(v-b)^2+ax/W-a*Wx/W^2
        Axx=R*T*(1/x2/(1-x2)+(bx/(v-b))^2)-(rxx*alog(X/Y)+2*rx*(Xx/X-Yx/Y)-r*((Xx/X)^2-(Yx/Y)^2))/8^.5
        if(lorm-2) 50,30,40
   30   LM=Axx-Avx^2/Avv
        return
   40   Wxx=-2*bx^2
        rxxx=-3*rxx*bx/b
        Avvv=-2*R*T/(v-b)^3+2*a*(4*(v+b)^2/W-1)/W^2
        Avvx=2*R*T*bx/(v-b)^3+4*a*(v+b)*Wx/W^3-2*(ax*(v+b)+a*bx)/W^2
        Avxx=-2*R*T*bx^2/(v-b)^3+(axx*W-2*ax*Wx-a*Wxx)/W^2+2*a*Wx^2/W^3
        Axxx=R*T*((2*x2-1)/(x2*(1-x2))^2+2*(bx/(v-b))^3)-(rxxx*alog(X/Y)+3*rxx*(Xx/X-Yx/Y)-3*rx*((Xx/X)^2-(Yx/Y)^2)+2*r*((Xx/X)
^3-(Yx/Y)^3))/8^.5
        LM=Avvx*Axx/Avv-3*Avx*Avxx/Avv-Avvv*Avx*Axx/Avv^2+Axxx+2*Avvx*Avx^2/Avv^2
        return
   50   LM=-1
        end
```

Figure C.11. Function LM.

rxx - Compositional derivative of rx.

Avv, Avx, Axx, Avvv, Avvx, Axxx - Partial derivatives of the Helmholtz free energy. See Appendix A.

Wxx - Compositional derivative of Wx.

rxxx - Compositional derivative of rxx.

Flow scheme:

Line number - Operation

5 - Call subroutine to assign proper values to constants and calculate v. If a value of v cannot be calculated, go to line 34.

6-16 - Assign values to constants and intermediate variables.

17 - Calculate Avv.

18 - If Pv is the desired return value of the function, go to line 19. If not, go to line 21. Branch to line 34 is not used.

19 - Calculate -Pv (=Avv).

20 - Return to calling program.

21, 22 - Calculate derivatives of Helmholtz free energy.

23 - If L1 is the desired return value of the function, go to line 24. If not, go to line 26. Branch to line 34 is not used.

24 - Calculate L1.

25 - Return to calling program.

26, 27 - Assign values to intermediate variables.

28-31 - Calculate derivatives of Helmholtz free energy.

32 - Calculate M1.

33 - Return to calling program.

34 - Set LM equal to an error code value of -1.

35 - End program and return to calling program.

C.12 Subroutine sol

This subroutine searches a given monotonic segment of an f-x curve for points of equality with a solid fugacity. These points correspond to compositions of solid-fluid equilibrium.

Variable list:

y1 - High composition end point of segment to be searched.

y3 - Low composition end point of segment to be searched.

nj - Root specifier.

y - Array to store modified segment end points.

b1, b2, bx, T, a1, a2, a12, P, R, vc - Defined in main program pr.

js - Slope parameter. +1 if f_2 increases with increasing x_2 mole fraction. -1 if f_2 decreases with increasing x_2.

f - Fugacity function. See Section C.13.

xloj, xhij - Modified segment end points.

P2sat - Vapor pressure of pure solid phase.

fc - Fugacity of pure solid phase.

asig - Convergence criterion variable.

zer - Bisection subroutine. See Section C.3.

xj - Composition of fluid phase in equilibrium with solid phase. Refers to x_2.

```
COMPILATION LISTING OF sol (>user_dir_dir>HDN>Hong>sol.fortran)

Compiled by: Multics New Fortran Compiler, Release 8a
Compiled on: 07/22/81  2050.7 edt Wed
    Options: ansi66 map

                                        Subroutine sol

          subroutine sol(y1,y3,nj)
          implicit double precision(a-h,o-z,A-Z)
          dimension y(3)
          common/pr/b1,b2,bx,T,a1,a2,a12,P,R,vc
          if(y1.eq.y3)go to 140
          y(1)=(1-1d-9)*y1;y(3)=(1+1d-9)*y3
          js=sign(1,f(y(1),2,nj)-f(y(3),2,nj))
          xloj=y(2+js)
          xhij=y(2-js)
          P2sat=0.0001*exp(-8719/T+29.3)
          fc=P2sat*exp(vc*(P-P2sat)/R/T)
          if(max(f(xloj,2,nj),f(xhij,2,nj)).le.fc)go to 140
          if(min(f(xloj,2,nj),f(xhij,2,nj)).ge.fc)go to 140
          call zer(f,2,nj,xloj,xhij,fc,xj,$140,$90)
     90   print,"sfeq at x2=",xj,nj
     140  return
          end
```

Figure C.12. Subroutine sol.

Flow scheme:

Line number - Operation

5 - If segment is a null segment, go to line 17.

6 - Modify segment end points to insure monotonicity of segment.

7 - Determine slope of segment in f_2 vs x_2 coordinates.

8 - Set xloj as the modified segment end point of lower fugacity.

9 - Set xhij as the modified segment end point of higher fugacity.

10 - Calculate solid vapor pressure.

11 - Calculate solid fugacity.

12, 13 - Determine if segment spans a fugacity range including the solid fugacity. If not, go to line 17.

14 - Call subroutine to accurately determine phase equilibrium composition. If no convergence, go to line 17.

15 - Print out phase equilibrium composition and root specifier.

16 - Return to calling program.

17 - End program.

C.13 Subroutine peq

This subroutine searches a pair of monotonic segments of an $f_2 - x_2$ curve, nominally designated j and k, for compositions which satisfy the phase equilibrium criteria. The first step is to limit the original segments by considering only the overlapping range of fugacities, as illustrated in Figure C.13b. At the corresponding end points of these new segments, the fugacities of component 2 are equal. At the end points of lower fugacity, the difference

$$\text{dflo} = f_1(\text{xloj}) - f_1(\text{xlok})$$

is calculated, and at the end points of higher fugacity, dfhi is likewise calculated. If dflo and dfhi are of opposite sign, then a set of compositions must exist for which

$$f_2^j = f_2^k \quad \text{and} \quad f_1^j = f_1^k$$

This set of compositions represents fluid-fluid equilibrium. To determine these compositions accurately, a trial composition xj in the middle of segment j is chosen, and the composition xk in segment k which matches the fugacity of xj is determined. This step is illustrated in Figure C.13c. Now the difference

$$\text{df} = f_1(\text{xj}) - f_1(\text{xk})$$

```
COMPILATION LISTING OF peq (>udd>HON>Hong>peq.fortran)

Compiled by: Multics New Fortran Compiler, Release 3a
Compiled on: 07/22/81  2128.9 edt Wed
    Options: ansi66 map

                                             Subroutine peq

         subroutine peq(y1,y3,y2,y4,j,k)
         implicit double precision(a-h,o-z,A-Z)
         dimension y(4)
         if((y1.eq.y3).or.(y2.eq.y4))go to 200
         y(1)=(1+1d-6)*y1;y(2)=(1+1d-6)*y2;y(3)=(1-1d-6)*y3;y(4)=(1-1d-6)*y4
         js=sign(1,f(y(1),2,j)-f(y(3),2,j))
         ks=sign(1,f(y(2),2,k)-f(y(4),2,k))
         xlj=y(2+js)
         xhj=y(2-js)
         xlk=y(3+ks)
         xhk=y(3-ks)
         asig=f(xlk/2+xhk/2,1,k)/10^8
         do 10 n=1,2
         if(max(f(xlj,n,j),f(xhj,n,j)).le.min(f(xlk,n,k),f(xhk,n,k)))go to 200
    10   if(max(f(xlk,n,k),f(xhk,n,k)).le.min(f(xlj,n,j),f(xhj,n,j)))go to 200
         if(f(xlj,2,j)-f(xlk,2,k)) 20,40,30
    20   call zer(f,2,j,xlj,xhj,f(xlk,2,k),xlj,$200,$40)
    30   call zer(f,2,k,xlk,xhk,f(xlj,2,j),xlk,$200)
    40   if(f(xhj,2,j)-f(xhk,2,k)) 50,200,60
    50   call zer(f,2,k,xlk,xhk,f(xhj,2,j),xhk,$200,$70)
    60   call zer(f,2,j,xlj,xhj,f(xhk,2,k),xhj,$200)
    70   dflo=f(xlj,1,j)-f(xlk,1,k)
         dfhi=f(xhj,1,j)-f(xhk,1,k)
         if(dflo/dfhi)130,200,80
    80   do 100 n=1,19
         xj=xlj+n*(xhj-xlj)/20
         call zer(f,2,k,xlk,xhk,f(xj,2,j),xk,$200,$90)
    90   df=f(xj,1,j)-f(xk,1,k)
         if(df/dflo)110,100,100
   100   continue
         go to 200
   110   xjm=xj
         xkm=xk
         xjh=xhj
         xkh=xhk
         xhj=xj
         kf=2
         go to 140
   120   xlj=xjm
         xhj=xjh
         xlk=xkm
         xhk=xkh
         dflo=f(xjm,1,j)-f(xkm,1,k)
   130   kf=1
   140   xj=xhj/2+xlj/2
         call zer(f,2,k,xlk,xhk,f(xj,2,j),xk,$200,$150)
   150   df=f(xj,1,j)-f(xk,1,k)
         if(abs(df)-asig)190,190,160
   160   if(df/dflo)170,170,180
   170   xhj=xj
         xhk=xk
         go to 140
   180   xlj=xj
         xlk=xk
         go to 140
   190   print, "x =",xj,"   y =",xk
         if(kf.eq.2)go to 120
         return
   200   print, "1 phase"
         end
```

Figure C.13a. Subroutine peq.

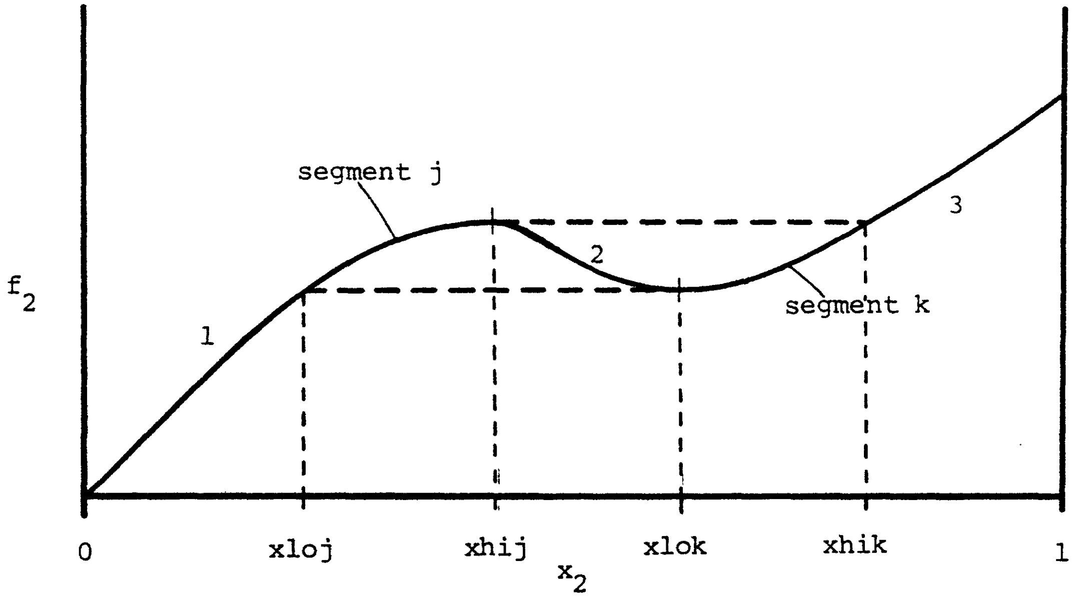

Figure C.13b. The search for fluid phase equilibrium between segments j and k. Equilibrium can only be found in regions of overlapping fugacity. Thus, the equilibrium composition in segment j must lie between xloj and xhij, and the equilibrium composition in segment k must lie between xlok and xhik.

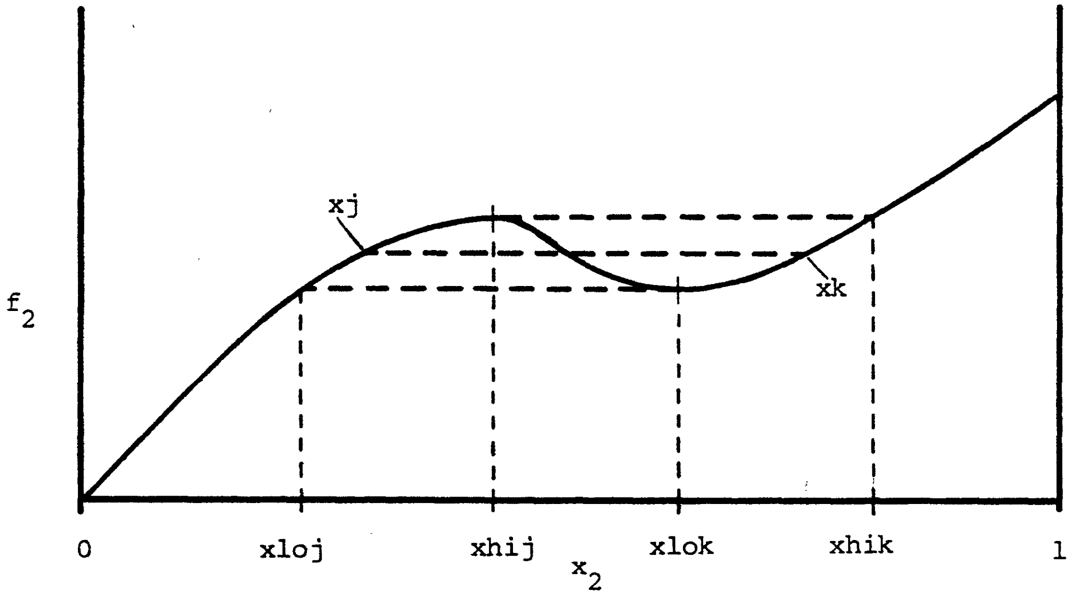

Figure C.13c. To determine the equilibrium compositions in segments j and k, a trial value of xj = (xloj + xhij)/2 is chosen. Then xk is chosen so that $f_2(xk) = f_2(xj)$.

is calculated. If df has the same sign as dflo, the compositions xj and xk become the new lower limits for segments j and k. If df and dfhi have the same sign, xj and xk become the new upper limits for the segments. The program proceeds in this fashion until df meets the convergence criterion. When this occurs, xj and xk are printed out as the phase equilibrium compositions.

When dflo and dfhi have the same sign, there is usually not phase equilibrium between the chosen pair of segments. However, in the vicinity of an azeotrope, the function df may have two zeroes so that dflo and dfhi have the same sign and two sets of phase equilibrium exist between a pair of segments. When this situation is encountered, the segments in question are split into two parts, so that two new pairs of segments with dflo and dfhi of opposite sign result. The preceding search method for phase equilibrium compositions may then be used. No instance has been found of two segments exhibiting more than two sets of phase equilibrium. Furthermore, equilibrium never exists between two adjacent segments.

Variable list:

y1 - Low composition end point of first segment (segment j).
y3 - High composition end point of segment j.
y2 - Low composition end point of second segment (segment k).
y4 - High composition end point of segment k.

j - Root specifier for segment j.

k - Root specifier for segment k.

y - Array to store modified segment end points.

js - Slope parameter for segment j. -1 if f_2 decreases with increasing x_2. +1 if f_2 decreases with increasing x_2.

ks - Slope parameter for segment k. Same sign convention as js.

f - Fugacity function. See Section C.14.

xlj, xhj - Modified end points for segment j.

xlk, xhk - Modified end points for segment k.

asig - Convergence criterion variable.

n - Do loop iteration variable.

zer - Bisection subroutine. See Section C.3.

dflo - Fugacity difference for component 1 for the composition pair xlj and xlk.

dfhi - Fugacity difference for component 1 for the composition pair xhj and xhk.

xj - Trial composition within segment j.

xk - Composition in segment k which has the same fugacity as xj.

df - Fugacity difference for component 1 for the composition pair xj and xk.

xjm - New segment end point within segment j. In an azeotropic region, segment j must be divided into two segments.

xkm - Variable which saves a value of xhj.

xkh - Variable which saves a value of xhk.

kf - Condition indicator. If equal to 2, the pair of segments is to be searched for a second set of phase equilibrium compositions. If equal to 1, both sets of compositions have already been determined, or only one such set exists.

Flow scheme:

Line number - Operation

4 - If either segment is a null segment, go to line 59.

5 - Modify segment end points to insure monotonicity of segments.

6 - Determine slope of segment j in f_2 vs x_2 coordinates.

7 - Determine slope of segment k in f_2 vs x_2 coordinates.

8 - Set xlj as the modified segment j end point of lower fugacity.

9 - Set xhj as the modified segment j end point of higher fugacity.

10 - Set xlk as the modified segment k end point of lower fugacity.

11 - Set xhk as the modified segment k end point of higher fugacity.

12 - Establish appropriate convergence accuracy.

13 - Enter or continue do loop to check for overlapping fugacity ranges between the segments. If ranges have been checked for both components, go to line 16.

14, 15 - Check for overlapping fugacity ranges between segments. If no overlap, go to line 59.

16-21 - Limit segments to overlapping fugacity ranges. See Figure C.13b.

22 - Calculate dflo, the fugacity difference at the low fugacity end points for component 1.

23 - Calculate dfhi, the fugacity difference at the high fugacity end points for component 1.

24 - If dflo and dfhi are of opposite sign, go to line 44. If of the same sign, go to line 25. If not in an azeotropic region, this statement is altered. For dflo and dfhi of the same sign, the program would proceed to line 59 rather than line 25. In this case lines 25 through 43 are skipped.

25 - Enter or continue do loop to find new segment end point. If end point has not been found after 20 iterations, go to line 31.

26 - Pick a trial composition xj in segment j.

27 - Call subroutine to determine composition xk in segment k which matches f_2 at xj. If xk cannot be found, go to line 59.

28 - Calculate df, the fugacity difference for component 1 at xj and xk.

29 - If df and dflo are of opposite sign, go to line 32. If of the same sign, go to line 30.

30 - Go to line 25.

31 - Go to line 59.

32 - Set new end point xjm at xj.

33 - Set new end point xkm at xk.

34 - Assign high fugacity end point of segment j to xjh.

35 - Assign high fugacity end point of segment k to xkh.

36 - Set high fugacity end point in first new j segment at xjm.

37 - Set condition indicator to 2.

38 - Go to line 45.

39 - Set low fugacity end point of second new j segment at xjm.

40 - Set high fugacity end point of second new j segment at the original high fugacity end point xjh.

41 - Set low fugacity end point of second new k segment at xkm.

42 - Set high fugacity end point of second new k segment at the original high fugacity end point xkh.

43 - Calculate dflo for second new set of segments.

44 - Set condition indicator to 1.

45 - Pick a trial composition xj in current segment j.

46 - Call subroutine to determine composition xk in segment k which matches f_2 at xj. If xk cannot be found, go to line 59.

47 - Calculate df, the fugacity difference for component 1 at xj and xk.

48 - Check convergence criterion. If df is sufficiently close to zero, go to line 56. If not, go to line 49.

49 - If df and dflo are of opposite sign, go to line 50. If

not, go to line 53.

50 - Set high fugacity end point of segment j to xj.

51 - Set high fugacity end point of segment k to xk.

52 - Go to line 45.

53 - Set low fugacity end point of segment j to xj.

54 - Set low fugacity end point of segment k to xk.

55 - Go to line 45.

56 - Print out phase equilibrium compositions.

57 - If condition indicator equals 2, go to line 39.

58 - Return to calling program.

59 - Print out message of no phase equilibrium.

60 - End program and return to calling program.

C.14 Function f

This function calculates the fugacities of components 1 and 2.

Variable list:

x2 - Mole fraction of component 2.

icomponent - Component specifier.

nrt - Root specifier.

b1, b2, bx, T, a1, a2, a12, P, R, vc - Defined in main program pr.

a, b, v, Z, A, B - Defined in function zr.

Zv - Compressibility factor function. See Section C.10.

Flow scheme:

Line number - Operation

5 - Call subroutine to assign proper values to constants and calculate Z. If Z cannot be calculated, go to line 11.

6 - If fugacity of component 1 desired, go to line 9. If fugacity of component 2 desired, go to line 7.

7 - Calculate fugacity of component 2.

8 - Return to calling program.

9 - Calculate fugacity of component 1.

10 - Return to calling program.

11 - Assign error code value of 0 to f.

12 - End program and return to calling program.

```
COMPILATION LISTING OF f (>user_dir_dir>HDN>Hong>f.fortran)

Compiled by: Multics New Fortran Compiler, Release 8a
Compiled on: 07/22/81  2050.7 edt Wed
    Options: ansi66 map

                                          Function f

        double precision function f(x2,icomponent,nrt)
        implicit double precision(a-h,o-z,A-Z)
        common/pr/b1,b2,bx,T,a1,a2,a12,P,R,vc
        common/Zv/a,b,v,Z,A,B
        call Zv(x2,nrt,$30)
        if(icomponent-2) 20,10,10
   10   f=x2*P*exp(b2/b*(Z-1)-alog(Z-B)-A/2/2^.5/B*(2*(a12*(1-x2)+a2*x2)/a-b2/b)*alog((Z+(2^.5+1)*B)/(Z-(2^.5-1)*B)))
        return
   20   f=(1-x2)*P*exp(b1/b*(Z-1)-alog(Z-B)-A/2/2^.5/B*(2*(a12*x2+a1*(1-x2))/a-b1/b)*alog((Z+(2^.5+1)*B)/(Z-(2^.5-1)*B)))
        return
   30   f=0.0
        end
```

Figure C.14. Function f.

C.15 Typical Printouts

Figure C.15a gives a printout from program pure for carbon dioxide. Molar volumes and the vapor pressure at the given temperature are reported. This run required about 1.4 seconds of CPU time. Figure C.15b gives a printout from program pr for the naphthalene - carbon dioxide system. Slope infinities, L1 zeroes, and M1 zeroes are first reported. Compositions of solid-fluid equilibrium are printed next, if appropriate. Finally, the compositions of coexisting fluid phases are given. "1 phase" signifies that no two-phase equilibrium was found between the two f-x segments being compared. This run required about 43 seconds of CPU time.

```
pure

Input Tlow,Thigh,Tstep,Plow,Phigh,Pstep

250,250,1,10,50,10

T=    .250000000000000000D+03       P=    .100000000000000000D+02
v=    .184739654974425603D+01
v=    .136009322667388695D+00
v=    .413429849452968378D-01
T=    .250000000000000000D+03       P=    .200000000000000000D+02
v=    .800238944381563493D+00
v=    .157720416125397523D+00
v=    .410769959094028311D-01
vle at P=    .174229796601172221D+02
T=    .250000000000000000D+03       P=    .300000000000000000D+02
v=    .410404707797054515D+00
v=    .205900244119081288D+00
v=    .408272375196663784D-01
T=    .250000000000000000D+03       P=    .400000000000000000D+02
v=    .405918843345159761D-01
T=    .250000000000000000D+03       P=    .500000000000000000D+02
v=    .403694139533885214D-01
r 19:44 1.417 1
```

Figure C.15a. Printout from main program pure. This run is for CO_2 at 250 K and 10-50 atm.

```
pr

Input Tlow,Thigh,Tstep,Plow,Phigh,Pstep,coarse grid,fine grid

300,1,1,65,1,1,.01,.0001

T=    .30000000000000000D+03      P=    .65000000000000000D+02
L1 zero at x2=    .36546687332151830 2D-02      nr=              1
zR zero at x2=    .41513453032059967 6D-02
zR zero at x2=    .00000000000000000D+00
L1 zero at x2=    .40912541208624839 7D-01      nr=              3
M1 zero at x2=    .14332752773708105 1D+00      nr=              3
L1 zero at x2=    .30095646513795852 7D+00      nr=              3
sfeq at x2=    .14370020605775599 6D-03             1
sfeq at x2=    .83292759269138378 9D-03             2
sfeq at x2=    .29678234784411864 6D-02             3
1 phase
1 phase
x =    .25620180586917003 7D-03    y =    .70127394711743811 9D-02
x =    .41206918100275391 9D-03    y =    .84659531524729419 0D-01
x =    .31326655820054385 9D-03    y =    .47129856894355734 1D+00
1 phase
1 phase
1 phase
1 phase
1 phase
x =    .18117857963875320 6D-02    y =    .94331374701827256 0D-01
x =    .15247978876661998 5D-02    y =    .46662211885260796 2D+00
1 phase
1 phase
x =    .10127418746496252 4D-01    y =    .47333402301715852 8D+00
r 20:36 42.905 24
```

Figure C.15b. Printout from main program pr. This run is for $C_{10}H_8$ - CO_2 at 300 K and 65 atm.

Appendix D Notation

A - Helmholtz free energy, parameter in cubic equation of state.

B - Parameter in cubic equation of state.

CEP - Critical end point.

CP - Critical point.

F - Fluid.

G - Gas (or vapor); Gibbs free energy.

H - Enthalpy; Hexadecane.

L - Liquid.

L1 - Spinodal (first criticality criterion) determinant.

LCEP - Lower critical end point.

LP - Limit point.

M1 - Critical (second criticality criterion) determinant.

N - Mole number; Naphthalene.

P - Pressure.

Q - Quadruple point.

R - Gas constant.

S - Solid; entropy.

T - Temperature.

TP - Triple point.

U - Internal Energy.

UCEP - Upper critical end point.

V - Vapor (or gas).

Z - Compressibility factor.

a,b - Parameters in cubic equation of state.

f - Fugacity.

v - Molar volume.

x - Mole fraction.

Subscripts

c - Critical property.

i, j, 1, 2, - Component indices.

r - Reduced property.

Superscripts

c - Crystalline.

g - Gas.

0 - Reference state.

I, II - Phase or segment indices.

Greek Letters

δ - interaction parameter

ω - acentric factor

μ - chemical potential

An underbar denotes a total property.

References

Alwani, Z. and G.M. Schneider. "Phasengleichgewichte, kritische Erscheinungen und PVT - Daten in binaren Mischungen von Wasser mit aromtischen Kohlenwasserstoffen bis 420°C und 2200 bar." Ber. Bunsenges., 73, 294 (1969).

Ambrose, D., I.J. Lawrenson and C.H.S. Sprake. "The Vapour Pressure of Naphthalene." J. Chem. Thermo., 1, 1173 (1975).

Baker, L.E., A.C. Pierce and K.D. Luks. "Gibbs Energy Analysis of Phase Equilibrium." Paper presented at the SPE/DOE Second Joint Symposium on Enhanced Oil Recovery of the Society of Petroleum Engineers, Tulsa, Oklahoma, April 5-8, 1981.

Beegle, B.L., M. Modell and R.C. Reid. "Legendre Transforms and Their Application in Thermodynamics." AIChE J., 20, 1194 (1974a).

________ "Thermodynamic Stability Criterion for Pure Substances and Mixtures." AIChE J., 20, 1200 (1974b).

Benedict, M., G.B. Webb and L.C. Rubin. "An Empirical Equation for Thermodynamic Properties of Light Hydrocarbons and Their Mixtures." J. Chem. Phys., 8, 334 (1940); J. Chem. Phys., 10, 747 (1942); J. Chem Phys., 47, 419 (1951).

Beris, A. personal communication (1981).

Brush, S.G. "Development of the Kinetic Theory of Gases. V. The Equation of State." Amer. J. Phys., 29, 593 (1961).

Büchner, E.H. "Flüssige Kohlensaure als Losungsmittel." Z. Phys. Chem., 54, 665 (1906a).

________ "Die beschränkte Mischbarkeit von Flussigkeiten das System Diphenylamine und Kohlensaure." Z. Phys. Chem., 56, 257 (1906b).

Calphad. Pergamon Press, New York, 1981.

Campbell. A.N. and R.M. Chatterjee. "Orthobaric Data of Certain Pure Liquids in the Neighborhood of the Critical Point." Can. J. Chem., 46, 575 (1967).

Chueh, P.L. and J.M. Prausnitz. "Vapor-Liquid Equilibria at High Pressures. Vapor-Phase Fugacity Coefficients in Nonpolar and Quantum-Gas Mixtures." Ind. Eng. Chem.

Fund., *6*, 492 (1967).

Chueh, P.L. and J.M. Prausnitz. "Vapor-Liquid Equilibria at High Pressures: Calculation of Partial Molar Volumes in Nonpolar Liquid Mixtures." *AIChE J.*, *13*, 1099 (1967).

Chueh, P.L. and J.M. Prausnitz. "A Generalized Correlation for the Compressibilities of Normal Liquids." *AIChE J.*, *15*, 471 (1969).

Connolly, J.F. "Solubility of Hydrocarbons in Water Near the Critical Solution Temperature." *J. Chem. Eng. Data*, *11*, 13 (1966).

Diepen, G.A.M. and F.E.C. Scheffer. "On Critical Phenomena of Saturated Solutions in Binary Systems." *J. Am. Chem. Soc.*, *70*, 4081 (1948a).

________ "The Solubility of Naphthalene in Supercritical Ethylene." *J. Am. Chem. Soc.*, *70*, 4085 (1948b).

________ "The Solubility of Naphthalene in Supercritical Ethylene - II." *J. Phys. Chem.*, *57*, 575 (1953).

Dodge, B.F. *Chemical Engineering Thermodynamics*. McGraw-Hill, New York, 1944.

Eckert, C.A. and J.M. Praunitz. "Phase Equilibria for Strongly Nonideal Liquid Mixtures at Low Temperatures." *AIChE J.*, *26*, 462 (1980).

Egloff, G. *Physical Constants of Hydrocarbons Vol. I*. Reihold, New York, 1939.

Francis, A.W. "Ternary Systems of Liquid Carbon Dioxide." *J. Phys. Chem.*, *58*, 1099 (1954).

Francis, D.C. and M.E. Paulaitis. "Solid Solubilities in Supercritical Fluids - High Pressure Phase Equilibrium Calculations Near the Upper Critical End Point Using the Lee-Kesler Equation of State." submitted for publication (1981).

Fowler, L., W.N. Trump and C.E. Vogler, "Vapor Pressure of Naphthalene." *J. Chem. Eng. Data*, *13*, 209 (1968).

Gibbs, J.W. "On the Equilibrium of Heterogeneous Substances." *Trans. Conn. Acad.*, *III*, 108 (1876).

Goldman, K. "Thermodynamic Properties of Ethylene Gas." in *Ethylene and its Industrial Derivatives*. S.A. Miller, ed., Ernest Benn, London, 1969.

Gomez-Nieto, M. "Comments on: `A New Two-Constant Equation of State'." Ind. Eng. Chem. Fund, 18, 197 (1979).

Gordon, P. Principles of Phase Diagrams in Materials Systems. McGraw-Hill, New York, 1968.

Gouw, T.H. and R.E. Jentoft. "Supercritical Fluid Chromotography." J. Chromoatogr., 68, 303 (1972).

Huang, E.T.S. and J.H. Tracht. "The Displacement of Residual Oil by Carbon Dioxide." SPE Paper 4735, Improved Oil Recovery Symposium, Tulsa, Oklahoma, April 22-24, 1974.

Hubert, P. and O.G. Vitzthum. "Fluid Extraction of Hops, Spices, and Tobacco with Supercritical Gases." Angew. Chem. Internat. Ed., 17, 710 (1978).

Johnston, K.P. and C.A. Eckert. "An Analytical Carnahan-Starling-van der Waals Model for Solubility of Hydrocarbon Solids in Supercritical Fluids." submitted to AIChE J. (1981).

Kammerlingh Onnes, H. Comm. Phys. Lab. Leiden., No.71 (1901).

Katz, D.L. and M.L. Rzasa. Bibliography for Physical Behavior of Hydrocarbons Under Pressure and Related Phenomena. Edwards, Ann Arbor (1946).

Keenan, J.H., F.G. Keyes, P.G. Hill and J.G. Moore. Steam Tables. John Wiley and Sons, New York, 1978.

Kleintjens, L.A. and R. Koningsveld. "Lattice Gas Treatment of Supercritical Phase Behavior in Fluid Mixtures." Paper presented at the 157th Meeting, The Electrochemical Society, St. Louis, May, 1980.

Klesper, E. "Chromatography with Supercritical Fluids." Angew. Chem. Internat. Ed., 17, 738 (1978).

Kurnik, R.T. "Supercritical Fluid Extraction: A Study of Binary and Multicomponent Solid-Fluid Equilibria." Sc.D. Dissertation, M.I.T. (1981).

Kurnik, R.T., S.J. Holla and R.C. Reid. "Solubility of Solids in Supercritical Carbon Dioxide and Ethylene." J. Chem. Eng. Data., 26, 47 (1981).

Lazalde-Crabtree, H., G.J.F. Breedveld and J.M. Prausnitz. "Solvent Losses in Gas Absorption. Solubility of Methanol in Compressed Natural and Synthetic Gases." AIChE J., 26, 462 (1980).

Lee, B.I. and M.G. Kessler. "A Generalized Thermodynamic

Correlation Based on Three-Parameter Corresponding States." AIChE J., 26, 462 (1980).

Lentz, H. and E.U. Franck, Ber.Bunsenges. Phys. Chem., 73, 28 (1969).

Levelt Sengers, J.M.H., W.L. Greer and J.V. Sengers. "Scaled Equation of State Parameters for Gases in the Critical Region." J. Phys. Chem. Ref. Data., 5, 1 (1976).

Lu, B.C. and S.S. Woods. "A Generalized Equation for Computer Calculation of Liquid Densities." AIChE J., 12, 95 (1966).

Mackay, M.E. and M.E. Paulaitis. "A Method to Calculate the Solubility of a Heavy Component in a Supercritical Solvent." Ind. Eng. Chem. Fund., 18, 149 (1979).

Martin, J.J. "Cubic Equations of State - Which?" Ind. Eng. Chem. Fund., 18, 81 (1979).

Martynova, O.I. "Solubility of Inorganic Compounds in Subcritical and Supercritical Water." in High Temperature, High Pressure Electrochemistry in Aqueous Solutions. (NACE-4), (1976).

Mason, E.A. and T.H. Spurling. The Virial Equation of State. Pergamon Press, New York, 1969.

McHugh, M. and M.E. Paulaitis. "Solid Solubilities of Naphthalene and Biphenyl in Supercritical Carbon Dioxide." J. Chem. Eng. Data., 25, 326 (1980).

Messmore, H.E. U.S. - Pat. 2420185, Phillips Petroleum Co. (1943).

Modell, M. "Criteria of Criticality." ACS Symp. Ser., No. 60, Estimation and Correlation of Phase Equilibria and Fluid Properties in the Chemical Industry. S.I. Sandler and T. Storvick, ed. (1977).

________ "Decontamination of Dredge Spoils by Extraction with Water Under Near Critical Conditions." Sea Grant Proposal R/T-1, M.I.T. (1979).

________ "Wastewater Treatment with Desorbing of an Adsorbate from an Adsorbent with a Solvent in the Near Critical State." U.S. Patent 4147624, Arthur D. Little, Inc. (1979).

________ "Gasification and Liquefaction of Forest Products in Supercritical Water." paper presented at the 89th National Meeting, AIChE, Portland, Oregon, August 20, 1980.

Modell, M., G.T. Hong and A. Heiba. "The Use of the Peng-Robinson Equation in Determining Supercritical Behavior." paper presented at the 72nd Annual Meeting, AIChE, San Francisco, California, November 26, 1979.

Modell, M. and R.C. Reid. *Thermodynamics and Its Applications*. Prentice-Hall, Englewood Cliffs, New Jersey. (1974).

Modell, M., R.J. Robey, V. Krukonis, R.P. de Filippi and D. Oestreich. "Supercritical Fluid Regeneration of Activated Carbon." paper presented at the 87th National Meeting, AIChE, Boston (1979).

Morey, G. "The Solubility of Solids in Gases." *Econ. Geol.*, *52*, 227 (1957).

Najour, G.C. and A.O. King, Jr. "Solubility of Naphthalene in Compressed Methane, Ethylene, and Carbon Dioxide. Evidence for a Gas-Phase Complex Between Naphthalene and Carbon Dioxide." *J. Chem. Phys.*, *45*, 1915 (1966).

Niggli, P. "Die Gase im Magma." *Centr. Min.*, 321 (1912).

Oellrich, L., U. Plöcker, J.M. Prausnitz and H. Knapp. "Methoden zur Berechnung von Phasengleichgewichten und Enthalpien mit Hilfe von Zustandsgleichungen." *Chem.-Ing. Tech.*, *49*, 955 (1977).

Peng, D.Y. and D.B. Robinson. "A New Two-Constant Equation of State." *Ind. Eng. Chem. Fundam.*, *15*, 59 (1976a).

________ "Two and Three Phase Equilibrium Calculations for Systems Containing Water." *Can. J. Chem. Eng.*, *54*, 595 (1976b).

________ "A Rigorous Method for Predicting the Critical Properties of Multicomponent Systems from an Equation of State." *AIChE J.*, *23*, 137 (1977).

________ "Calculation of Three-Phase Solid-Liquid-Vapor Equilibrium Using an Equation of State." paper presented at the 176th Meeting, ACS, Miami Beach, Florida, September 11-14, 1978; in *Advances in Chemistry Series 182*., American Chemical Society, Washington, D.C., 1979.

________ "Two- and Three-Phase Equilibrium Calculations for Coal Gasification and Related Processes." paper presented at AIChE-NBS-NSF symposium, Warrenton, Virginia, October 22-25, 1979; see *Thermodynamics of Aqueous Systems with Industrial Applications*. *ACS Symposium Series*., *133*, 393 (1980).

Plöcker, U.J., H. Knapp and J.M. Prausnitz. "Calculation of High-Pressure Vapor-Liquid Equilibria from a Corresponding-States Correlation with Emphasis on Asymmetric Mixtures." Ind. Eng. Chem. Proc. Des. Dev., 17, 324 (1978).

Prausnitz, J.M. "Fugacities in High-Pressure Equilibria and in Rate Processes." AIChE J., 5, 3 (1959).

________ "Solubility of Solids in Dense Gases." NBS Technical Note 316, July, 1965.

Prausnitz, J.M., T.F. Anderson, E.A. Grens, C.A. Eckert, R. Hsieh and J.P. O'Connell. Computer Calculations for Multicomponent Vapor-Liquid and Liquid-Liquid Equilibria. Prentice-Hall, Inc., Englewood Cliffs, New Jersey, 1980.

Quinn, E.L. "The Internal Pressure of Liquid Carbon Dioxide from Solubility Measurements." J. Am. Chem. Soc., 50, 672 (1928).

Rebert, C.J. and W.B. Kay. "The Phase Behavior and Solubility Relations of the Benzene-Water System." AIChE J., 5, 285 (1959).

Redlich, O. and J.N.S. Kwong. "On the Thermodynamics of Solutions. V. An Equation of State. Fugacities of Gaseous Solutions." Chem. Rev., 44, 233 (1949).

Reid, R.C. and B.L. Beegle. "Critical Point Criteria in Legendre Transform Notation." AIChE J., 23, 726 (1977).

Reid, R.C., J.M. Prausnitz and T.K. Sherwood. The Properties of Gases and Liquids. McGraw-Hill, New York, New York (1977).

Reisman, A. Phase Equilibria. Academic Press, New York, 1970.

Ricci, J.E. The Phase Rule and Heterogeneous Equilibrium. Van Nostrand, New York, 1951.

Rowlinson, J.S. Liquids and Liquid Mixtures. Butterworth, London, 1969.

Rowlinson, J.S. and M.J. Richardson. "Solubility of Solids in Compressed Gases." Adv. Chem. Phys., 2, 85 (1959).

Schneider, G.M. "Phase Equilibria in Fluid Mixtures at High Pressures." Adv. Chem. Phys., 17, 1 (1970).

Schneider, G.M., Z. Alwani, W. Heim, E. Horvath and E.U. Franck. "Phasengleichgewichte und kritische Erscheinungen in binaren Michsystemen bis 1500 bar."

Chem. Ing. Tech., 39, 649 (1967).

Schouten, J.A., C.A. ten Seldam and N.J. Trappeniers. "The Two-Component Lattice Gas Model." Physica., 73, 556 (1974).

Scott, R.L. and P.H. van Konynenburg. "Van der Waals and Related Models for Hydrocarbon Mixtures." Disc. Faraday Soc., 49, 87 (1970).

Sebastian, H.M., J.J. Simnock, H. Lin and K. Chao. "Vapor-Liquid Equilibrium in Binary Mixtures of Carbon Dioxide and n-Decane and Carbon Dioxide and n-Hexdecane." J. Chem. Eng. Data., 25, 138 (1980).

Sie, S.T., W. Van Beersum and G.W.A. Rijinders. "High-Pressure Gas Chromatography and Chromatography with Supercritical Fluids. I. The Effect of Pressure on Partition Coefficients in Gas-Liquid Chromatography with Carbon Dioxide as a Carrier Gas." Separation Sci., 1, 459 (1966).

Smits. A. "The Course of the Solubility Curve in the Region of Critical Temperatures of Binary Mixtures I." Proc. Roy. Acad. Sci. Amsterdam, 6, 171 (1903a).

________ "The Course of the Solubility Curve in the Region of Critical Temperatures of Binary Mixtures. II." Proc. Roy. Acad. Sci. Amsterdam, 6, 484 (1903b).

________ "On the Hidden Equilibria in the P-x Diagram of a Binary System in Consequence of the Appearance of Solid Substances." Proc. Roy. Acad. Sci. Amsterdam, 8, 196 (1905a).

________ "On the Hidden Equilibria in the P-x Sections Below the Eutectic Point." Proc. Roy. Acad. Sci. Amsterdam, 8, 568, (1905b).

Soave, G. "Equilibrium Constants from a Modified Redlich-Kwong Equation of State." Chem. Eng. Sci., 27, 1197 (1972).

Stalkup, F.I. "Carbon Dioxide Miscible Flooding: Past, Present, and Outlook for the Future." J. Pet. Tech., Aug. 1978, 1102.

Starling, K.E. Fluid Thermodynamic Properties of Light Petroleum Systems. Gulf Publishing Co., Houston, 1973.

Timmermans, J. Physico-Chemical Constants of Pure Organic Compounds. Elsevier, Vol. I, 1950; Vol. II, 1965.

Trappeniers, N.J., J.A. Schouten and C.A. ten Seldam.

"Gas-Gas Equilibrium and the Two-Component Lattice-Gas Model." Chem. Phys. Letters., 5, 541 (1970).

Tsekhanskaya, Y.V., M.B. Iomtev and E.V. Mushkina. "Solubility of Diphenylamine and Naphthalene in Carbon Dioxide Under Pressure." Russ. J. Phys. Chem., 36, 117 (1962).

_______ "Solubility of Naphthalene in Ethylene and Carbon Dioxide Under Pressure." Russ. J. Phys. Chem., 38, 1173 (1964).

Tsekhanskaya, Y.V., N.G. Roginskaya and E.V. Mushkina. "Volume Changes in Naphthalene Solutions in Compressed Carbon Dioxide." Russ. J. Phys. Chem., 40, 1152 (1966).

Tsiklis, D.A. and V.Y. Maslennikova. "Limited Mutual Solubility of the Gases in the Water-Nitrogen System." Akad. Nauk. SSSR Proc., Phys. Chem. Sec., 161, 262 (1965).

van der Waals, J.D. Thesis. A.W. Sigthoff, Leiden (Dutch ed.); Barth, Leipzig (German ed.), 1873.

________ "Molekulartheorie eines Körpers, der aus zwei verschiedenen Stoffen besteht." Z. Phys. Chem., 5, 133 (1890).

Van Gunst, C.A., F.E.C. Scheffer and G.A.M. Diepen. "On Critical Phenomena of Saturated Solutions in Binary Systems. II." J. Phys. Chem., 57, 578 (1953).

Van Konynenburg, P.H. "Critical Lines and Phase Equilibria in Binary Mixtures." PhD. Dissertation, U.C.L.A., (1968).

Van Welie, G.S.A. and G.A.M. Diepen. "The P-T-x Space Model of the System Ethylene-Naphthalene (III)." Rec. Trav. Chim., 80, 673 (1961).

Vargaftik, N.B. Tables on the Thermophysical Properties of Liquids and Gases. John Wiley and Sons, New York, 1975.

Vukalovich, M.P. and V.V. Altunin. Thermophysical Properties of Carbon Dioxide. Collets, London, 1968.

Wilke, G. "Extraction with Supercritical Gases - A Foreword." Angew. Chem Internat. Ed., 17, 701 (1978).

Wise, W.S. "Solvent Extraction of Coal." Chem. Ind. (London), 950 (1970).

Woerner, G.A. "Thermal Decomposition and Reforming of

Glucose and Wood at the Critical Conditions of Water." M.S. thesis, M.I.T., August, 1976.

Yen, L.C. and S.S. Woods, "A Generalized Equation for Computer Calculation of Liquid Densities." *AIChE J.*, *12*, 95 (1966).

Zhuse, T.P. and A.A. Kapelyushnikov, USSR - Pat. 113325 (1955).

Zhuse, T.P., G.N. Yushkevic and J.E. Gekker. *Maslob.-Zhir. Prom.*, *24*, 34 (1958).

Zosel, K. DBP 2005293, Studiengesellschaft Kohle (1970).

Zudkevitch, D. and J. Joffe. "Correlation and Prediction of Vapor-Liquid Equilibria with the Redlich-Kwong Equation of State." *AIChE J.*, *16*, 112 (1970).

Biographical Sketch

Glenn Thomas Hong was born on March 28, 1954 in East Meadow, Long Island, New York. He graduated as salutatorian from Freeport High School, Freeport, New York, in June of 1972. He thereafter attended the State University of New York at Albany, as a National Merit Scholar, and graduated with a Bachelor of Science degree in biology, summa cum laude, in May of 1976.

Mr. Hong entered the chemical engineering department at MIT in September of 1976. He was married to Karen Lorraine Sullivan on July 31, 1977. He is a member of the American Institute of Chemical Engineers, Sigma Xi, and Phi Beta Kappa, and is the coauthor of one technical paper. Following graduation, Mr. Hong will continue his work on supercritical water at Modar, Inc. in Natick, Massachusetts.